

S. Wiak, A. Krawczyk and M. Trlep (Eds.)

Computer Engineering in Applied Electromagnetism

$$\operatorname{rot} \mathbf{H} = \mathbf{J} + \frac{\partial \mathbf{D}}{\partial t}$$

$$\operatorname{rot} \mathbf{E} = -\frac{\partial \mathbf{B}}{\partial t}$$

$$\operatorname{div} \mathbf{B} = 0$$

$$\operatorname{div} \mathbf{D} = \rho$$

COMPUTER ENGINEERING IN APPLIED ELECTROMAGNETISM

Computer Engineering in Applied Electromagnetism

Edited by

S. WIAK

Technical University of Lodz, Poland

A. KRAWCZYK

Institute of Electrical Engineering, Warsaw, Poland

and

M. TRLEP

University of Maribor, Slovenia

A C.I.P. Catalogue record for this book is available from the Library of Congress.

ISBN 1-4020-3168-8 (HB)
ISBN 1-4020-3169-6 (e-book)

Published by Springer,
P.O. Box 17, 3300 AA Dordrecht, The Netherlands.

Sold and distributed in North, Central and South America
by Springer,
101 Philip Drive, Norwell, MA 02061, U.S.A.

In all other countries, sold and distributed
by Springer,
P.O. Box 322, 3300 AH Dordrecht, The Netherlands.

Printed on acid-free paper

All Rights Reserved
© 2005 Springer

No part of this work may be reproduced, stored in a retrieval system, or transmitted in any form or by any means, electronic, mechanical, photocopying, microfilming, recording or otherwise, without written permission from the Publisher, with the exception of any material supplied specifically for the purpose of being entered and executed on a computer system, for exclusive use by the purchaser of the work.

Printed in Great Britain by MPG Books Ltd., Bodmin, Cornwall.

TABLE OF CONTENTS

Preface

<i>S. Wiak, A. Krawczyk, M. Trlep</i>	ix
---	----

Invited Paper**Computational Electromagnetics: A Tool, an Art or Black Magic?**

<i>J.K. Sykulski</i>	3
----------------------------	---

I. Computational Techniques**Introductory Remarks**

<i>S. Wiak, A. Krawczyk, M. Trlep</i>	11
---	----

1. Study of the Electromagnetic Field Induced by Currents Flowing in the Circular Conductors

<i>S. Apanasewicz, S. Pawłowski</i>	13
---	----

2. Improvement of Effectiveness of High-Current Lines Optimization by Modification of Genetic Algorithms and Paralleling of the Computation Process

<i>K. Bednarek</i>	19
--------------------------	----

3. Shape Optimization with Adaptive Simulated Annealing and Genetic Algorithms

<i>H. Brauer, M. Ziolkowski</i>	25
---------------------------------------	----

4. The Design of Optimised Planar Thick Film Filters

<i>V. Desnica, Lj. Živanov, O. Aleksić, M. Luković, L. Lukić</i>	31
--	----

5. Active Shielding Optimisation

<i>P. Dessante, J.C. Vannier, B. Bonafos</i>	35
--	----

6. Cost-Effective Optimal Design of Screens in Power Transformers

<i>P. Di Barba, M.E. Mognaschi, A. Savini, J. Turowski</i>	41
--	----

7. A Comparison of Error Estimators for Adaptive MESH Refinement for Electromagnetic 2D/3D Problems

<i>K. Gawrylezyk, F. Alkhatib</i>	47
---	----

8. Multi-Objective Optimization of Permanent Magnet Motor Using Taguchi Method

<i>K. Hot, P. Bodlovic</i>	53
----------------------------------	----

9. Optimization of Barrier Type SRMs with Response Surface Methodology Combined with Moving Least Square Method

<i>Y.K. Kim, J.Y. Lee, J.P. Hong, J. Hur</i>	59
--	----

10. The Advanced Methods of Interaction and Data Analyze in the Visualization System for Electromagnetic Fields

<i>A. Krolewiak, E. Napieralska-Juszczak, M. Pietruszka</i>	65
---	----

11. Imaging of Two-Dimensional Current Density Distributions from their Magnetic Field

<i>G. Krukowski, S. Gratkowski, R. Sikora</i>	71
---	----

12. Some Applications of the Coupled Field-Circuit Method

<i>E. Napieralska-Juszczak, T. Niewierowicz, L. Kawecki</i>	77
---	----

13. Permanent Magnet Dealt with Boundary-Integral Approach <i>K.Pawluk</i>	83
14. Comparison of the General Load Line Method with the Finite Element Method <i>R.I. Román B., A. Konrad, J.F. Brudny</i>	89
15. Optimization for High Voltage Composite Insulators Using Experimental Design Theory <i>I. Sebestyén</i>	95
16. Modelling and Optimisation of Intelligent Electrostatic Comb Accelerometer <i>S. Wiak, K. Smólka, M. Rudnicki</i>	99
17. The Optimal Design of Passive Shimming Elements for High Homogeneous Permanent Magnets Utilizing Sensitivity Analysis <i>Y. Yao, C.S. Koh, G. Ni, S. Yang, D. Xie</i>	105
18. Reconstruction of the Interface Between Two Conducting Fluids with Modified Genetic Algorithms <i>M. Ziolkowski, H. Brauer, M. Kuilekov</i>	111
<u>II. Electromagnetic Engineering</u>	
Introductory remarks <i>S. Wiak, A. Krawczyk, M. Trlep</i>	117
1. On the Use of the Current and Flux State Variables in the Dynamic Analysis of Magnetolectric Networks <i>A. G. Beccuti, S. Leva, A.P. Morando</i>	119
2. Calculation of Linear Motor Performance Using Finite Element Method <i>M. Bugeza, D. Makuc, R. Fišer</i>	125
3. Analytical Model of the Magnetic Field in Doubly Slotted Electrical Machines with Distributed Windings and Evaluation of E.M.F. and Torque <i>A. Di Gerlando, G.M. Foglia, R. Perini</i>	129
4. The 3D-Analysis of the Field Distribution of Fractional Power Induction Motor <i>K. Komeza, M. Dems, P. Jastrzqbek</i>	137
5. Improvement of the Electric Strength of an Insulation System of a Medium Voltage Instrument Transformer Using Field Analysis <i>E. Leśniewska</i>	143
6. A Method for Reduction of Cogging Torque in PM Machines Using Stepped Magnets <i>M. Łukaniszyn, R. Wróbel, M. Jagiela</i>	149
7. Electric Field Analysis of the Insulation Structure of Power Transformer <i>D. Makuc, J. Ikanonić, K. Lenasi</i>	155
8. A Study on Improvement in Energy Efficiency of Skeleton Type Single-Phase PM Motor Using Finite Element Method <i>T. Masuda, Y. Takashima, M. Murase, Y. Kawase, T. Yamaguchi, T. Okouchi</i>	161
9. Analysis of Characteristics of Induction Motor by Three-Dimensional Axi-Symmetric Finite Element Method <i>T. Matsusaka, K. Harada, Y. Ishihara, T. Todaka, S. Kitamura, T. Shimomura</i>	165
10. An Influence of Permanent Magnet Shape on the Torque Ripple of Disc-Type Brushless DC Motors <i>E.A. Mendrela, M. Jagiela, R. Wróbel</i>	171
11. Analysis of Magnetization Characteristics of HTS Bulk Rotor in a Rotating Magnetic Field <i>T. Nakamura, H.J. Jung, N. Tanaka, I. Muta, K. Fukui</i>	177

12. Equivalent Circuit Analysis of Pole-Change Single-Phase Induction Motor Considering Harmonic Components <i>H. Nam, S.K. Jung, J.P. Hong</i>	183
13. The 3D Dynamic Simulation of the Inverter Fed Electromechanical Actuators Including Eddy Currents <i>L. Nowak</i>	189
14. An Optimal Determination of Stranded Wires Used in Windings of Switched Mode Power Transformers <i>F. Pavlovčič, K. Lenasi, J. Nastran</i>	193
15. Chart and Expressions for Eddy Current Losses Calculation in Steel Laminations Derived from Finite Element Numerical Results in 2D <i>P.G. Pereirinha, C.F.R. Lemos Antunes</i>	197
16. AC Motor Magnetic Signature: Contribution of Stator Laminations <i>D. Roger, A. Henneton</i>	203
17. A Comparison Between Surface Magnets and Embedded Magnets in Fractional Slot Wound PM Motors <i>P. Salminen, J. Pyrhönen, M. Niemelä</i>	209
18. Evaluation of New Surface Mounted Permanent Magnet Synchronous Machine with Finite Element Calculations <i>T. Schneider, A. Binder</i>	215
19. Numerical Analysis of the Brushless Motor Magnetic Field and Torque <i>I. Tičar, A. Stermecki, I. Zagradišnik</i>	221
20. Magnetic Field and Short-Circuit Reactance Calculation of the 3-Phase Transformer with Symmetrical Amorphous Core <i>B. Tomczuk, K. Zakrzewski, D. Koterak</i>	227
21. Analysis of Instantaneous Voltage Distribution in Permanent Magnet Brushless Generator <i>B. Wawrzyniak, P. Witczak</i>	231
22. Development of Mathematical Model and Computation of Electromagnetic Drum-Type Separator by Boundary Element Method <i>M.V. Zagirnyak, O.S. Akimov</i>	237

III. Special Applications

Introductory remarks <i>S. Wiak, A. Krawczyk, M. Trlep</i>	243
1. The Rotational Power Loss Calculation in the Square Sample <i>W. Anuszczyk, Z. Gmyrek</i>	245
2. A Method for Studying the Current Field Generated by Interconnected Grounding Systems <i>M. Bronzini, G. Delvecchio, N. Mitaritonna, P. Pugliese, M. Sylos Labini</i>	251
3. The Comparison of Phantom Model and Simulation Results in SAR Analysis <i>K. Ciosk, A. Krawczyk, R. Kubacki</i>	257
4. Electric Circuit Representation of a Magnetic Circuit with Hysteresis <i>L. Cristaldi, S. Leva, A. P. Morando</i>	261
5. Simulation of 3D End Effects in a Superconductive Magnet with a Ferromagnetic Core <i>H. DeGersem, T. Weiland</i>	267

6. Modelling of Temperature-Dependent Effective Impedance of Nonferromagnetic Massive Conductor <i>I. Doležel, L. Musil, B. Ulrych</i>	273
7. The Magnetic Noise of a DC Electric Motor – Modeling of Three-Times-Coupled Electromagnetic, Mechanical and Acoustic Phenomena <i>M. Furlan, M. Boltežar</i>	279
8. Measurement of 2-D Magnetic Properties of Grain Oriented Silicon Steel Sheet Using RRSST <i>V. Goričan, M. Jesenik, A. Hamler, B. Štumberger, M. Trlep</i>	287
9. The Heat Circumstances in Switch by Permanent Load <i>G. Hrovat, A. Hamler</i>	293
10. Eddy Current Effects in the Sample of 2D R.R.S.S.T. and the Sample of 2D S.R.S.S.T. <i>M. Jesenik, V. Gorican, M. Trlep, A. Hamler, B. Stumberger</i>	297
11. 3-D Finite Element Analysis of Attractive Force by Residual Magnetization of DC Electromagnets <i>Y. Kawase, T. Yamaguchi, K. Iwashita</i>	301
12. Characteristic Comparisons Between Iron Powder Materials and Lamination Cores in Brushless Motors <i>Y.K. Kim, J.P. Hong, K.H. Ha, J. Hur, H.K. Sung</i>	305
13. Electroheating in Surface Treatment Process <i>K. Kurek, D. Dolega</i>	311
14. Magnetodynamic Performance in Cage Induction Motors with a Broken Bar <i>X. M. López-Fernandez, M. Piper</i>	317
15. Soft Magnetic Composite in Design of Motor With Oscillatory Starting <i>D. Miljavec, B. Šuštaršič, Ž. Turk, K. Lenasi</i>	323
16. Analysis of Core Loss in Variable Reluctance Permanent-Magnet Motors <i>H. Öztura</i>	329
17. A Novel Axial Flux Permanent Magnet Machine to Laboratory Use <i>A. Parviainen, M. Niemelä, J. Pyrhönen</i>	333
18. Electromagnetic Hyperthermia – Foundation and Computer Modelling <i>J. Plewako, A. Krawczyk, B. Grochowicz</i>	337
19. 2D FEM Analysis of 3D Magnetic Structures by Using Topological Transformations. Application to the Design of a Micro-Relay <i>J. Roger-Folch, E. Gómez, M. Riera, V. Lázaro</i>	343
20. Health Effects of Base Stations <i>O. Sahin</i>	349
21. Two Dimensional Finite-Element Simulation of a High Temperature Superconducting Synchronous Generator During Three-Phase Short-Circuit Fault Condition Using Full Transient Non-Linear Rotating Machine Model <i>K.S. Ship, K.F. Goddard, J.K. Sykulski</i>	355
22. Coupled Electromagnetic Fields and Temperature Fields to Analyze the Voltage Fluctuation of a Synchronous Generator with the Consideration of Insulation Layers <i>L. Weili, Z. Feng, Z. Dong, H. Yunpeng, D. Shuye</i>	359
23. Magnetic Diagnosis of Structural Materials and These Monte-Carlo Simulations <i>K. Yamada, B. Liu, A. Shinagawa, Z. Honda, Y. Isobe, K. Yamaguchi, A. Krawczyk</i>	365

PREFACE

This book contains the papers presented at the International Symposium on Electromagnetic Fields in Electrical Engineering ISEF'03 which was held in Maribor, Slovenia on September 18-20, 2003. ISEF conferences have been organized since 1985 as a common initiative of Polish and European researchers who deal with electromagnetic fields applied to electrical engineering. Until now the conferences have been held every two years, either in Poland or in one of the European academic centres known from its electromagnetic research. The city of Maribor is well-known in the world for its beauty and academic flavour as well as for its researchers' achievements in the area of applied and computational electromagnetism.

Almost 200 papers were submitted as abstracts and after selection process 159 papers were accepted for the presentation at the Symposium, and almost all of them (ca. 90%) were presented both orally and in poster sessions. The papers published in this book were refereed by the sessions' chairmen and the papers accepted for further publication were divided into two parts: these of more computational aspect and those of more applicable nature. The latter are published here, while the first part went to COMPEL journal.

It is the tradition of the ISEF meetings that they comprise a vast area of computational and applied electromagnetics. Moreover, the ISEF symposia aim at joining theory and practice, thus the majority of papers are deeply rooted in engineering problems, being simultaneously at a high theoretical level. Bearing this tradition, we hope to touch the heart of the matter in electromagnetism. The main topics of ISEF meetings are listed below:

- *Computational Electromagnetics*
- *Electromagnetic Engineering*
- *Computational Techniques*
- *Coupled Field and Special Applications*
- *Bioelectromagnetics and Electromagnetic Hazards*
- *Magnetic Materials Modelling.*

The papers in the book have been grouped in three sections which cover the above topics:

- *Computational Techniques*
- *Electromagnetic Engineering*
- *Special Applications.*

It makes some order in reading but also it somehow represents the main directions which are penetrated by researchers dealing with contemporary electromagnetics. Looking at the content of the book, one may also notice that more and more researchers go into the investigation of new applications of electromagnetics, especially these connected with medicine, biology and material sciences. The computational techniques which were under development during the last three decades and which are being still developed serve as good tools for discovering new electromagnetic phenomena. This conclusion is unnecessarily shared by all the readers but we try to show here the trend which can be clear from the book.

A more conventional approach is presented in the first paper of the volume which was the invited paper at the conference. The author is Professor Jan Sykulski from Southampton University, UK, who is well-known for being the key person of the International Compumag Society from its beginning. His writing shows contemporary computational techniques placed in the history of the subject, and the examples which are quoted in the paper are just confined to classical applications, as electrical machines and the like.

The three chapters are prefaced by short introductory remarks. They will help readers in looking for some particular topic in which they are interested.

We, the Editors of the book, would like to express our thanks to our colleagues who have contributed to the book by refereeing the papers at the conference as well as in the publishing process. We also convey our thanks to Kluwer Academic Publishers for their effective collaboration in shaping this editorial enterprise. As ISEF conferences are organised biannually, we do hope to keep our strong links with Kluwer.

Mladen Trlep
Chairman of the
Organising Committee

Andrzej Krawczyk
Scientific Secretary

Sławomir Wiak
Chairman of the ISEF
Symposium

ISEF 2003 – 11th International Symposium on Electromagnetic Fields in Electrical Engineering

Maribor, Slovenia, September 18-20, 2003

INVITED PAPER

COMPUTATIONAL ELECTROMAGNETICS: A TOOL, AN ART OR BLACK MAGIC?

Jan K. Sykulski, FIEE, SMIEEE, FInstP

University of Southampton, Southampton SO17 1BJ, United Kingdom, jks@soton.ac.uk

Abstract – The paper is an attempt to review the state of the art in Computational Electromagnetics (CEM) with a focus on applications related to electrical engineering. Design and optimisation, as well as development of new materials, are emphasised as of paramount importance in the real engineering world. Modern computational methods based on finite elements and related techniques have now become a mature design tool, but the complexity of the underlying mathematics and physics often hampers widespread use of these efficient techniques. Recent advances in general purpose software are encouraging but much remains to be done in improving the standards of education to remove the mist of mystery surrounding the subject.

Introduction

The research activity known as Computational Electromagnetics (CEM) has evolved alongside the modern developments in the digital computing hardware. Moreover, CEM is both a special case and part of the broader subject of computational mechanics. The speciality arises in many obvious ways, e.g. free space is an unbounded magnetic ‘material’, there is a vast range of physical dimensions encountered with critical feature sizes often varying over many orders of magnitude, the fundamental properties of Maxwell’s equations are different to equations governing other physical phenomena. There is also a very broad spectrum of frequencies encountered: from DC to daylight. Activities of the CEM community are well organised within the International Compumag Society [1,2], an independent international organisation in existence since 1993 with nearly 700 members from over 40 countries. The IEE Professional Network on Electromagnetics [3] is also gaining momentum and establishing itself as an international forum for discussion. The IEEE Magnetics Society [4] and ACES [5] manage the activities in North America. Journals such as IEE Proceedings [6], IEEE Transactions on Magnetics [7] and COMPEL [8] contain a significant number of papers showing fundamental advances and applications of CEM. There are many conferences reporting regularly on recent developments, including COMPUMAG [9,10], CEFC [11], CEM [12,13] and, of course, ISEF [14].

There exist many books on fundamental aspects of field computation in applications relevant to electrical engineering (see for example [15-17]), as well as monographic publications devoted more specifically to finite-element aided modelling and simulation of electromechanical devices in electrical power engineering [18,19]. Design and optimisation feature prominently in literature; it is worth mentioning here some of the books devoted to optimal design in electricity and magnetism [20] and more general monographs on multi-objective optimisation [21,22]. Recent advances in material science and discovery of new types of materials (e.g. high temperature superconductivity) have an immense impact on the way in which modern designs of electromechanical devices are approached and present a continuing challenge to fundamental sciences in terms of development of new, cheaper, more efficient and accurate methods for electromagnetic field modelling and simulation. Coupled field systems are of particular importance as practical designs have to address simultaneously all aspects of performance of the device: electromagnetic, mechanical, thermal and economic. One of the reasons why progress is impeded is because the mathematics and physics behind the numerical formulations are often quite complex and thus few designers have sufficient skills to master available software. Nevertheless, recent progress with the general purpose software – such as OPERA [23], MAGNET [24], or ANSYS [25] – makes these programs extremely powerful tools in the hands of an expert.

CAD of Electromechanical Devices

Recent advances in CEM, supported by continuing increases of power and speed of computers, make finite element modelling an attractive alternative to well established semi-analytical and empirical methods, as well as to the still popular ‘trial and error’ approach. A typical system incorporating FE computation is demonstrated by Fig. 1 [15,16]. First, a designer has to build a computational model of his physical problem. This is a vital step, often underestimated, which may decide on a success or a failure of the whole process. Clearly, the model must be adequate for the results to be meaningful. This emphasises the significance of human input to the design and importance of an experiment and/or alternative models for solving the same problem, so that comparisons can be made. Once the model has been formulated the CAD system will facilitate finding a solution.

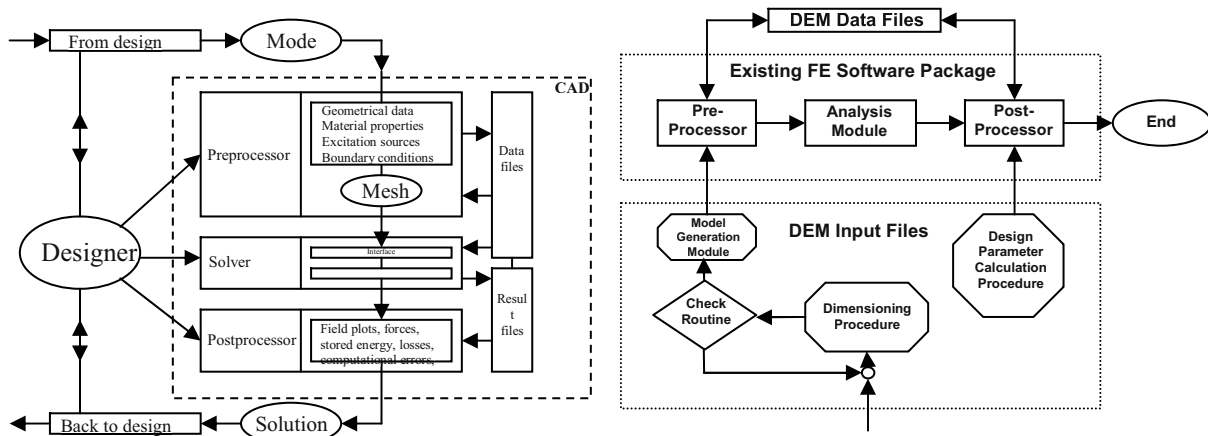


Fig. 1. A typical CAD system for electromagnetics

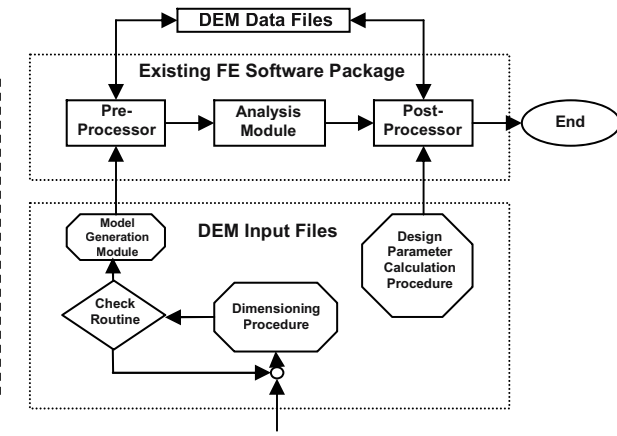


Fig. 2. A general DEM and its relation to FE package

Parameterisation of the model is often desired, so that various parts – as well as the whole device – may be constrained in a convenient way, for example for optimisation or sensitivity analysis. A typical example of software development addressing this issue is the concept of Design Environment (DEM) [23,26,27] – see Fig. 2. A DEM facilitates the use of electromagnetic analysis software by providing an application specific shell to guide a non-specialist through the geometric design and physical property specification of a class of device. DEMs are created by experts and contain a parameterised model of a device with a set of decision making routines suggesting optimal representation of materials and boundary conditions, followed by automatic analysis of performance. The post-processor offers top level commands for specific tasks such as calculation of device parameters.

One of the more important issues associated generally with such CAD systems is the question of error estimation and the ability of the system to refine the model to improve the accuracy. Various adaptive schemes are available based on h , p or r mesh refinement [16] or dynamic bubbles shown in Fig. 3.

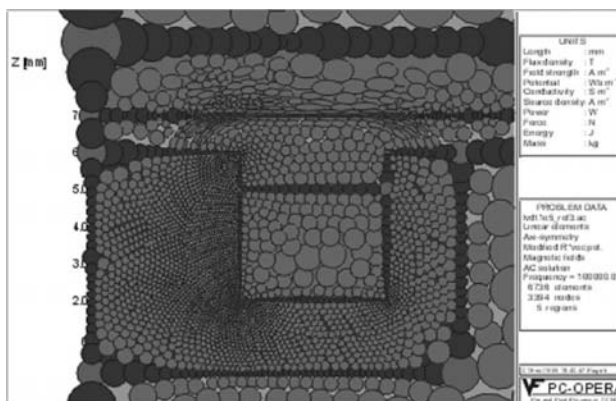


Fig. 3. Anisotropic mesh using dynamic bubbles [28]

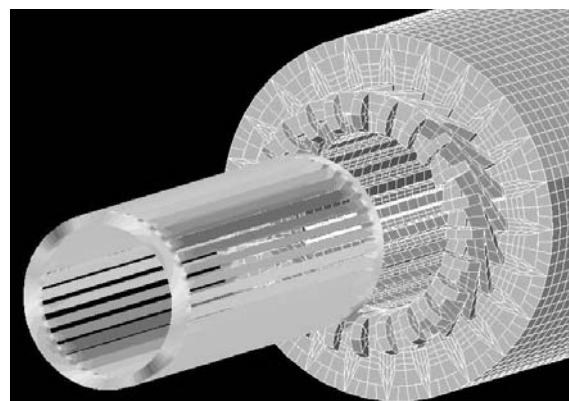


Fig. 4. 3D model of an induction motor

The CEM community has gone a long way to address the needs of designers and contemporary commercial software is capable of solving static, quasi-static and full transient problems in 2D as well as in 3D. Nonlinearity of materials, permanent magnets, various shapes of excitation coils – these are just examples of what can easily be solved (see an example of Fig. 4). Finally, coupled problems can be handled involving interactions between electromagnetic field, motion and supplying circuit [29].

Fundamental Formulations and Techniques

There has been important progress in fundamental formulations providing more solid foundations for numerical field analysis. These have been reported at COMPUMAG [9], CEFC [11] and CEM [12]. Lack of space does not permit to elaborate on these developments here but some more exciting advances are mentioned. Equally, progress has been made in implementation of new techniques leading to more efficient, faster, more accurate and numerically stable algorithms. The following is a non-exhaustive list of such advances which have made the greatest impact on the CEM community.

- a new *Finite Element Difference* (FED) method,
- higher order *Finite Difference Time Domain* (FDTD) approach,
- further developments of the *Transmission Line Matrix* (TLM) method,
- advances of the *Multiple Multipole Technique* (MMT),
- the use of *Finite Integration Technique* (FIT),
- a new *Subspace Projection Extrapolation* (SPE) scheme,
- working field theory problems with *Random Walks*,
- formulations in terms of differential geometry,
- the usage of total/reduced magnetic vector potential and electric scalar potential,
- an introduction of *Lie derivative* as a tool for force computation,
- implementation of edge and facet elements,
- improved anisotropy models,
- efficient application of *Continuum Design Sensitivity Analysis* (CDSA).

Modelling of New Types of Materials

Discovery and/or development of new materials present a modelling challenge and often lead to reformulation of fundamental equations or methods of solution. We will focus here on recent advances in superconductivity. Ceramic superconducting materials were discovered in 1986 and their main advantage is that they can operate at liquid nitrogen temperature (78K) – hence the name High Temperature Superconductors (HTS) – and thus offer cheap and reliable technology (often compared to water cooling). With practical current densities 10 to 20 times larger than in conventional copper windings they have great potential in electric power applications (generators, motors, fault current limiters, transformers, flywheels, cables, etc.), as losses are significantly reduced. From the design point of view they offer a challenge because of very highly non-linear characteristics and anisotropic properties of materials, and due to unconventional design solutions. Fundamental characteristics and underlying physical processes are well described in literature. Some recent advances at Southampton University in the application of the HTS technology to electric power devices are described in [30-39].

There is continuing significant activity around the world in the development of HTS tapes and wires, applications of the technology to power devices and modelling of fundamental processes in the superconducting materials. From the practical point of view the ability to predict and reduce all ‘cold’ losses is of paramount importance to demonstrate economic advantages of HTS designs. The behaviour and characteristics of the highly non-linear and anisotropic HTS materials is markedly different to conventional conductors. A typical field distribution is depicted in Fig. 5, whereas the dependence of AC losses on field level is shown in Fig 6 [33]. It can be clearly seen that field direction is of paramount importance and thus steps need to be taken to ‘shape’ the leakage field in the device to avoid excessive losses and prevent the conductor from being exposed to fields higher than critical.

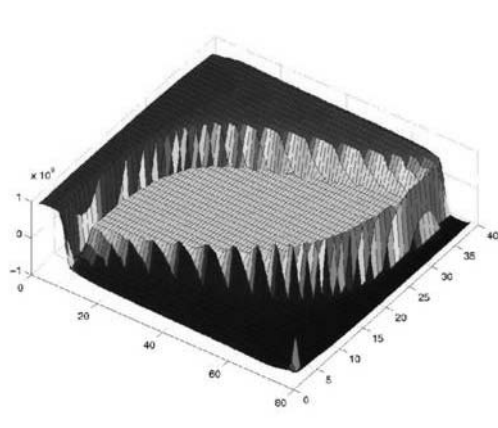


Fig. 5. Current density distribution (applied field at 45°)

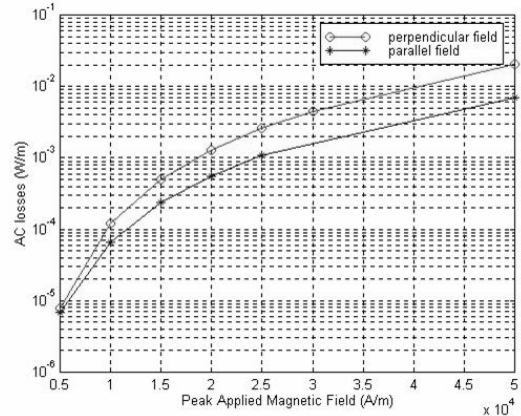


Fig. 6. AC loss as a function of peak magnetic field

Low Temperature Superconductivity has not been very successful in electric power applications due to low reliability, high cost and difficult technology. HTS offer better thermal stability, cheaper cooling and improved reliability. Currently all conceptual HTS designs and small demonstrators use BSCCO tapes at temperatures between 20K and 30K because critical fields and currents are an order of magnitude better than at 78K and it is possible to have a core-less design. However, liquid neon or helium gas is needed leading to increased cost and complexity of refrigeration plant, reduced thermodynamic efficiency and worse reliability and higher maintenance requirements. All Southampton designs use cooling at 78/81/65/57 K (liquid nitrogen or air / sub-cooled nitrogen or air).

The first device built and successfully tested in Southampton in 1997/98 was a small 10kVA demonstrator transformer (Fig. 7) [39]. A particularly satisfying result was the two-fold reduction of losses through introduction of magnetic flux diverters as demonstrated by Figs. 8.

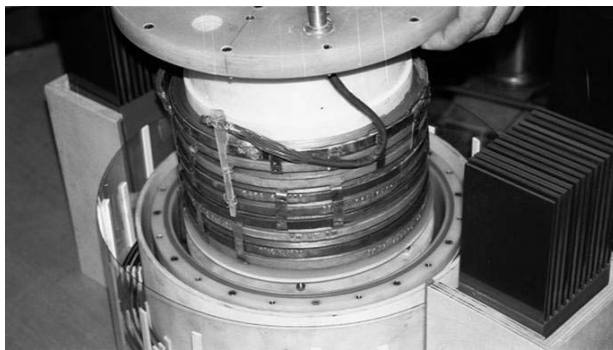


Fig. 7. HTS winding in a 10kVA transformer

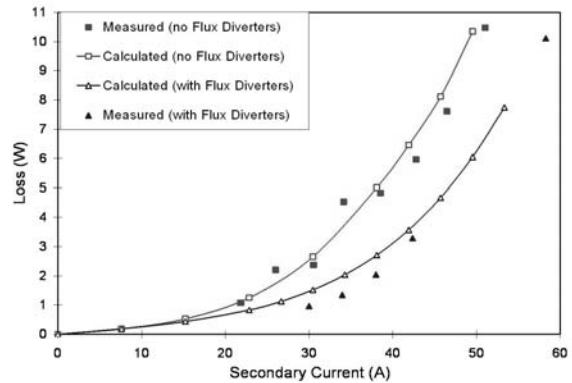


Fig. 8. Power loss in HTS winding vs load current

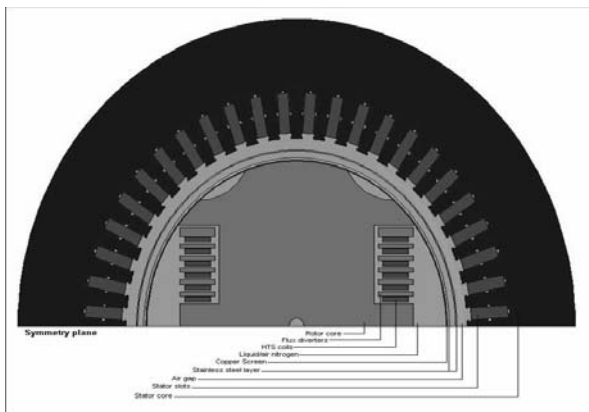


Fig. 9. A cross-section through 100kVA HTS generator

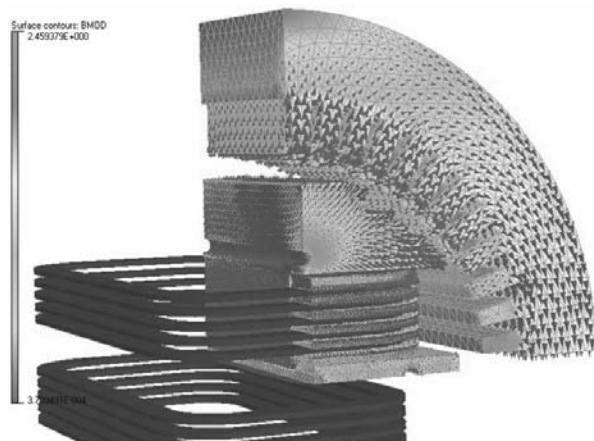


Fig. 10. 3D flux density and its distribution

A new 100 kVA, 2 pole HTS synchronous generator – nearing completion at Southampton – uses a magnetic core made of 9% cryogenic steel to lower the ampere-turns required by a factor of ten and to significantly reduce fields in the pancake coils made of BSCCO (Fig. 9). In terms of modelling the important issues are no-load tooth ripple losses due to the distortion of the fundamental flux density wave by the stator slotting, and full-load losses that include the effects of the MMF harmonics of the stator winding. Two models were used: full transient non-linear rotating (no-load, see Fig 10), and a combination of static and steady-state (full-load), respectively. Losses are released into liquid nitrogen and have to be removed using inefficient refrigeration system. Each 1W of loss requires between 15 – 25 W of installed refrigeration power at 78K (a similar figure at 4K would be about 1000 W).

Optimisation

Optimal design of electromechanical devices often necessitates repetitive usage of finite-element (FE) solvers, or other numerically intensive field computation. A direct way of incorporating field modelling into an optimisation loop is to call the FE package every time a function evaluation is needed. Although fairly straightforward in implementation, this on-line approach will normally lead to unacceptable computing times, as for each set of selected design parameters a full field analysis needs to be undertaken. The number of necessary calls to the FE software escalates as the number of design variables increases; moreover, additional calls are normally required to calculate each gradient of the objective function. Although theoretically this is of no consequence, in the design office environment such an approach becomes impractical.

The *Minimum Function Calls* (MFC) approach relies on evaluating the objective function a priori for a number of pre-determined cases and fitting an interpolating function through the data points [40]. The optimiser then uses the interpolating function rather than calling the FE directly. In this *Response Surface Methodology* (RSM) approach it is usual to use polynomial interpolating functions. Using the RSM reduces computing times dramatically, but care must be taken not to sacrifice accuracy. Extensive numerical experiments have shown that further significant improvements may be achieved by introducing *on-line learning* with *dynamic weighting* [40]. To illustrate the process a brushless permanent magnet (PM) motor has been optimised for efficiency (with minimum torque constraint) in terms of magnet height, tooth width and stack length. The convergence is illustrated in Fig. 11.

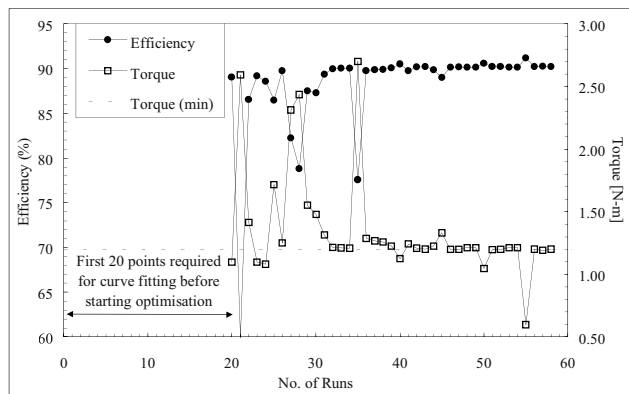


Fig. 11. Convergence of efficiency and torque in a PM motor

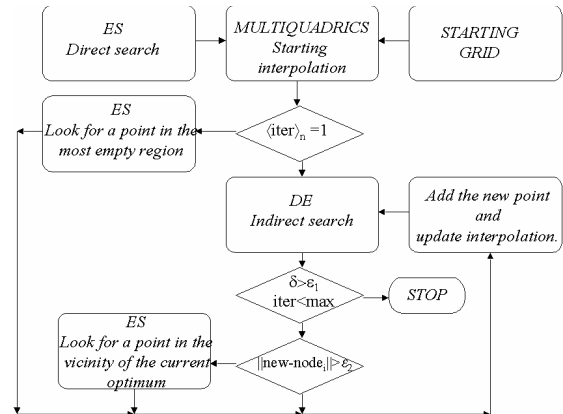


Fig. 12. Flowchart of the ES/DE/MQ method [41]

The deterministic approach, despite the addition of learning points, may not be able to avoid local minima traps. If this is identified as a potential problem stochastic techniques may offer a better choice. Most such techniques are very expensive in terms of number of necessary function evaluations and thus impractical. Some more recent methods, however, look more promising and one such technique introduced originally in [41] is reported here. It uses a combination of *Evolution Strategy*, *Differential Evolution* and *Multiquadrics Interpolation* (ES/DE/MQ) as shown in Fig. 12. This hybrid method has been shown to be able to avoid local minima traps for a number of test functions and achieves a significant reduction of the number of necessary function calls, making the approach

suitable for computationally intensive FE design/optimisation problems. Moreover, the quality of the resultant optimum is comparable to, or better than, those obtained using other methods.

The *Neuro-Fuzzy Modelling* (NFM) [42] uses optimisation based on the Genetic Algorithm (GA) and the *Sequential Quadratic Programming* (SQP) method. In the NF/GA/SQP approach, an n -dimensional hyper-space is sampled initially using a grid structure or a suitable *Design of Experiment* (DoE) orthogonal array if the number of variables is high. The model data is subsequently employed to create a neuro-fuzzy model which provides an approximation of real function. The notion of *Membership Functions* (MFs) is introduced which can be described by Gaussian, generalised bell or other curves. During the supervised training process the parameters of each MF are modified using the back-propagation algorithm and the consequent parameters established using least squares, ultimately providing an approximation of the system under investigation. This empirical model effectively replaces the actual function generator – in this case the finite element solver – easing the computational cost when applying the optimisation routine. This comprises a GA to identify the locality of the global optimum followed by the SQP method to isolate it accurately. The latter is possible due to the extraction of derivative information from the neuro-fuzzy model.

There is growing interest in the ways in which the performance of a specific device could be modelled using a *neural network*. Such a network learns the shape of the hyper-surface and provides a fast evaluation of any point in it. Typically, the neural network is trained in a batch mode, prior to the optimisation process – essentially “off-line”. A recent attempt has been made to construct a system which can provide “on-line” training, i.e. a network which is capable of learning and modifying its behaviour as it is used [43]. Such a network has major benefits over a static system in that it can handle a large number of variations of a device and track developments in design related to material changes and manufacturing processes.

Design has to be put in the context of general trends in optimisation methods. The role of multi-objective tasks is increasing as practical designs often involve conflicting requirements. Such problems may be converted into single-objective tasks with a priori application of knowledge or imposition of a decision (e.g. weighting factors), but it is argued that information can easily be lost in the process. Instead the application of *Pareto Optimal Front* (POF) approximation is advocated. The mathematical theory of Pareto optimisation may be somewhat complicated [44], but some basic definitions and properties are easily explained using a special case of two objective functions being minimised as shown in Fig. 13.

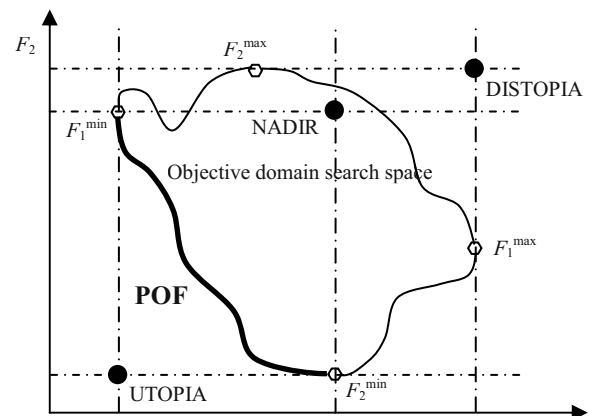


Fig. 13. Example showing Pareto Optimal Front and UTOPIA, DISTOPIA and NADIR points

Finally, often in practice, it is the improvement to the design, not necessarily a global optimum, which is of interest. Hence the *sensitivity analysis* is of great value as computing times are not affected by the number of design variables. The *Continuum Design Sensitivity Analysis* (CDSA) is particularly to be recommended as standard EM software may be used for extracting gradient information [45].

Industrial and Educational Requirements

From the industrial perspective it is probably true to say that many managers still perceive computational electromagnetics as a kind of “black magic” – and yet these are the very people who would benefit most from using CEM techniques to reduce design times and costs. There is lack of appropriate skills to benefit fully from the enormous power and versatility of the available CEM tools. It may be argued that three categories of users are required in industry:

- those able to run EM software with basic understanding of field displays and ability to interpret the numerical results to incorporate them into design processes;

- design experts who understand the language of electromagnetics and are capable of creating computational models using available software;
- EM software developers – the ultimate CEM experts producing computational tool.

Decision makers in industry – in their very best interest – need to support the universities and government in providing sufficient funding for both the development of CEM tools and for providing sufficient education at different levels. Academic institutions face a great opportunity of reversing the current trend of reducing the amount of EM teaching and making sure that relevant courses are available to undergraduates and engineers in industry. There is some cause for optimism as progress with CEM software development is accelerating and more programs find their way to design offices.

Future Developments

Further progress is required and a possible list of topics for research and development may include:

- adaptive meshing with particular emphasis on problems with strong skin effect,
- reliable error estimation (a posteriori and a priori),
- code development for high speed computing,
- efficient handling of non-linearity, hysteresis and anisotropy,
- modelling of new types of materials (e.g. composite, superconducting),
- incorporation of linear movement and rotation of some parts of the device,
- combined modelling of fields and circuits (e.g. supply electronic circuits),
- coupled problems (electromagnetic + stress + temperature, etc),
- optimisation (deterministic and stochastic, practical implications),
- integrated design systems (combined mechanical, electromagnetic, thermal, economic).

It can be argued, however, that CAD in Magnetics is already a mature practical tool for design and optimisation of a variety of electromechanical devices and the engineering community can benefit from tremendous advances that occurred in the field over the past many years.

References

- [1] *International Compumag Society*, <http://www.compumag.co.uk/>
- [2] Sykulski J.K. (editor), *International Compumag Society Newsletter*, ISSN 1026-0854
- [3] *Professional Network Electromagnetics, IEE*, <http://www.iee.org/OnComms/pn/electromagnetics/>
- [4] *Magnetics Society* <http://www.ieemagnetics.org/>
- [5] *ACES* <http://aces.ee.olemiss.edu/>
- [6] *IEE Proceedings* <http://www.iee.org/Publish/Journals/ProfJourn/Proc/>
- [7] *IEEE Transactions on Magnetics* <http://www.ieemagnetics.org/>, ISSN 0018 9464
- [8] *COMPTEL* <http://www.emeraldinsight.com/compel.htm>, ISSN 0332 1649
- [9] COMPUMAG 2003 Proceedings, Saratoga Springs, New York, July 13 – 17, 2003, ISBN 0 9743535 0 7, CD-ROM: ISBN 0 9743535 5 8, <http://www.compumag2003.com/>
- [10] COMPUMAG 2001, *IEEE Transactions on Magnetics*, Vol 38, No 2, March 2002, ISSN 0018 9464
- [11] CEFC 2002, *IEEE Transactions on Magnetics*, Vol 39, No 3, May 2003, ISSN 0018 9464
- [12] Special Issue on Computational Electromagnetics, *IEE Proceedings; SMT*, Vol 149, No 5, September 2002
- [13] Computation in Electromagnetics CEM2002, Proceedings, 8 – 11 April 2002, Bournemouth, UK, <http://www.iee.org/oncomms/pn/electromagnetics/CEMconf.cfm>
- [14] Electromagnetic Fields in Electrical Engineering ISEF'01, *Studies in Applied Electromagnetics and Mechanics*, Vol 22, 2002, IOS Press, ISSN 1383 7281
- [15] Hammond P. and Sykulski J.K., *Engineering Electromagnetism, Physical Processes and Computation*, Oxford Science Publications, New York, 1994, ISBN 0 19 856289 6
- [16] Sykulski J.K., *Computational Magnetics*. Chapman & Hall, 1995, ISBN 0 412 58570 7
- [17] Binns K.J., Lawrenson P.J. and Trowbridge C.W., *The Analytical and Numerical Solution of Electric and Magnetic Fields*, John Wiley & Sons, 1992, ISBN 0 471 92460 1
- [18] Hameyer K. and Belmans R., *Numerical Modelling and Design of Electrical Machines and Devices*, WIT Press, 1999, ISBN 1 85312 626 8
- [19] Reece A.B.J. and Preston T.W., *Finite Element Methods in Electrical Power Engineering*, Oxford Science Publications, 2000, ISBN 0 19 856504 6

- [20] P. Neittaanmaki, M. Rudnicki, and A. Savini, *Inverse Problems and Optimal Design in Electricity and Magnetism*, Oxford Science Publications, Oxford, 1996
- [21] K. Miettinen, *Nonlinear Multiobjective Optimisation*, Kluwer Academic Publishers, Dordrecht, 1999
- [22] K. Deb, *Multi-objective Optimization Using Evolutionary Algorithms*, John Wiley and Sons, 2001
- [23] OPERA, Vector Fields, <http://www.vectorfields.co.uk/>
- [24] MAGNET, Infolytica, <http://www.infolytica.com/>
- [25] ANSYS, <http://www.ansys.com/>
- [26] Biddlecombe, C.S., Sykulski, J.K. and Taylor, S.C., 'Design Environment Modules for Non-specialist Users of EM Software,' *IEEE Transactions on Magnetics*, Vol. 30, pp. 3625-8, 1994
- [27] Parker, C.F., Sykulski, J.K., Taylor, S.C. and Biddlecombe, C.S., 'Parametric environment for EM computer aided design,' *IEEE Transactions on Magnetics*, Vol. 32, pp. 1433-6, 1996
- [28] Taylor S. and Sykulski J.K., 'Anisotropic adaptive mesh refinement for EM finite element analysis in 2 dimensions,' *IEEE Transactions on Magnetics*, Vol. 35, pp. 1322-5, 1999
- [29] Biddlecombe C.S., Simkin J., Jay A.P., Sykulski J.K. and Lepaul S., 'Transient electromagnetic analysis coupled to electric circuits and motion,' *IEEE Transactions on Magnetics*, Vol. 34, pp.3182-5, 1998
- [30] J. Rhyner, 'Magnetic properties and ac losses of superconductors with power law current-Voltage characteristics,' *Physica C*, Vol. 212, pp. 292-300, 1993.
- [31] J. K. Sykulski, R. L. Stoll, A. E. Mahdi, and C. P. Please, 'Modelling HTc Superconductors for AC Power Loss Estimation,' *IEEE Transactions on Magnetics*, Vol. 33, no. 2, pp. 1568-71, March 1997
- [32] J.K. Sykulski, M. Rotaru and R.L. Stoll, 'Highly Non-Linear Field Diffusion in HTc Superconducting Tapes,' *COMPEL*, Vol. 18, no. 2, pp. 215-224, 1999
- [33] J.K. Sykulski, M. Rotaru and R.L. Stoll, '2D modelling of field diffusion and AC losses in high temperature superconducting tapes,' *IEEE Transactions on Magnetics*, Vol. 36, no. 4, pp. 1178-82, 2000
- [34] J.K. Sykulski, K. Goddard and R.L. Stoll, 'A method of estimating the total AC loss in a high-temperature superconducting transformer winding,' *IEEE Transactions on Magnetics*, Vol. 36, no. 4, pp. 1183-7, 2000
- [35] K.S. Ship, K.F. Goddard and J.K. Sykulski, 'Field Optimisation in a Synchronous Generator with High Temperature Superconducting Field Winding and Magnetic Core,' *IEE Proceedings; Science, Measurement and Technology*, Vol. 149, No 5, pp. 194-8, September 2002
- [36] J.K. Sykulski, K.F. Goddard and K.S. Ship, 'Modelling and Evaluation of Eddy-Current Loss in High Temperature Superconducting Synchronous Generator,' *Studies in Applied Electromagnetics and Mechanics*, Vol. 22, pp. 142-7, 2002
- [37] K.F. Goddard, J.K. Sykulski and R.L. Stoll, R.L. 'A new approach to modelling dominant AC loss in HTc superconducting solenoidal windings,' *IEEE Transactions on Magnetics*, Vol. 35, no. 3, pp. 1195-8, 1999
- [38] J.K. Sykulski, C. Beduz, R.L. Stoll, M.R. Harris, K. Goddard and Y. Yang, 'High temperature superconducting power transformers: conclusions from a design study,' *IEE Proceedings; Electrical. Power Applications*, Vol. 146, no 1, pp. 41-52, 1999
- [39] J.K. Sykulski, K. Goddard and R.L. Stoll, 'High temperature super-conducting demonstrator transformer: design considerations and first test results,' *IEEE Trans. on Magnetics*, Vol. 35, no. 5, pp. 3559-61, 1999
- [40] Sykulski J.K., Al-Khoury A.H. and Goddard K.F., 'Minimal function calls approach with on-line learning and dynamic weighting for computationally intensive design optimization,' *IEEE Transactions on Magnetics*, Vol. 37, pp. 3423-6, 2001
- [41] M. Farina, and J. K. Sykulski, 'Comparative Study of Evolution Strategies Combined with Approximation Techniques for Practical Electromagnetic Optimisation Problems,' *IEEE Transactions on Magnetics*, Vol. 37, no. 5, pp. 3216-20, September 2001
- [42] K. Rashid, M. Farina, J. A. Ramirez, J. K. Sykulski, and E. M. Freeman, 'A Comparison of Two Generalized Response Surface Methods for Optimisation in Electromagnetics,' *COMPEL*, Vol. 20, No 3, pp. 740-52, 2001
- [43] J. Seguin, F. Dandurand, D. A. Lowther, and J. K. Sykulski, 'The Optimization of Electromagnetic Devices Using a Combined Finite Element/Neural Network Approach with On-Line Training,' *COMPEL*, vol. 18, no 3, pp. 266-274, 1999
- [44] M. Farina, 'Cost-effective Evolutionary Strategies for Pareto Optimal Front Approximation to Multi-objective Shape Design Optimization of Electromagnetic Devices,' *Ph.D. dissertation*, Department of Electrical Engineering, University of Pavia, Italy, 2002
- [45] Kim, Dong-Hun and Ship, K.S. and Sykulski, J.K., 'Applying Continuum Design Sensitivity Analysis combined with standard EM software to shape optimisation in magnetostatic problems,' *Proceedings COMPUMAG*, Vol. 2, pp 112-113, Saratoga Springs, NY, USA, 2003, ISBN 0 9743535 2 3

SECTION I COMPUTATIONAL TECHNIQUES

Introductory Remarks

The first section is devoted to the problems connected with computational electromagnetics. The subject has been intensively developed in the last decades – one can place in time very roughly the starting date of the subject in the mid-seventies when the first COMPUMAG conference was held in Oxford, UK. Since that time many conferences have been held and the ISEF conference is one of them. Elderly participants can probably remember the first activities in this field which in the main were devoted to making numerical models in simple two-dimensional modes with stationary or quasi-stationary time variation. The content of the section shows that research on the problems is much more advanced: the 3-D numerical code regarding all the sophisticated material features, complicated geometry and arbitrary course in time is nowadays the tool for optimizing and designing processes. Very few authors consider the so-called direct problems, i.e. the problems of electromagnetic field computation. Just the opposite, most papers deal with the so-called inverse problems, i.e. the problems of shape or parameters designing. That is *signum temporis* (the sign of the times).

The papers which belong to this section can be divided into two subgroups, regarding the subject of their contents:

- improvement of computational techniques,
- optimization problems,

The first subgroup concerns the problems which can be divided into two piles: one pile is represented by papers I-1, I-11, I-13 and I-14 and comprises some methodological considerations. They are very interesting, indeed, as they introduce analytical formulae to the algorithm or they analyze the features of the algorithm. Paper I-1 gives the solution of the problem which seems to be simple as its geometry is simple but, as a matter of fact, it is not a trivial problem. The authors give some analytical solutions of the problem and discuss them from the point of view of assumptions adopted. The authors of paper I-11 consider the problem of imaging two-dimensional current density distributions on the basis of the magnetic field that is generated by the currents. It is, in other words, the problem of regularization which appears when dealing with inverse problems. Paper I-13 deals with the calculation of magnetic fields created by permanent magnets by the use of the indirect boundary-integral model. One meets here a creative introduction of the boundary-integral method. Fictitious sources are introduced and considered as unique sources of the conservative magnetic field. The approach leads to advanced analytical expressions for usual magnetic quantities, by means of which various technical objects containing permanent magnets can be analyzed. Paper I-15 describes the application of the general load line method to a magnetic circuit problem with series and parallel branches of uniform cross sections consisting of the same homogeneous ferromagnetic core material. It also compares the results with those obtained by finite element analysis.

The second pile of papers considering computational techniques is more or less connected with computer software. Two of them (I-7, I-10) concern the problems of peripheries of numerical software: in (I-7) one can find the method of mesh generation, while in (I-10) the method of visualization is described. Paper (I-12) introduces some new technique of calculation, namely the coupling of field and circuit method.

The second group is connected with optimization and design techniques. As has already been mentioned, the main stream of activity in computational electromagnetics is directed at solving such problems. Indeed, one can find in the section many techniques of optimization as well as many objects

to be optimized and designed. As to the techniques, three of them are mostly quoted: genetic and evolution strategies (I-2, I-18), simulated annealing (I-3) and methods based on sensitivity analysis (I-17).

The rest of the papers deal with other methods of optimization, such as experimental method (I-4, I-5, I-15), Taguchi method (I-8) and combined. One can observe even bigger variety when one looks at objects either designed or/and optimized. We have here power transformers and shielding technique (I-5, I-6), small electric motors and devices (I-8, I-9, I-16), magnets (I-17), planar thick film filters (I-4), high voltage lines and insulators (I-2, I-15).

Of course, the techniques and the objects are crossed mutually and there is no rule which would prescribe one method to one object or there is neither this nor that method in its pure form.

The papers placed in the section show, more or less, the state of the art of computational techniques in applied electromagnetics. We devoted a little bit more space to papers dealing with some analytical solutions. It seems a little strange to work out such approaches, especially if one takes into account the common use of numerical modeling. It is believed, however, that such approaches can enrich pure numerical models providing them with *a priori* information on the problem considered. And, above all other aspects, the analytical solutions are pretty and they will never pass into oblivion.

I-1. STUDY OF THE ELECTROMAGNETIC FIELD INDUCED BY CURRENTS FLOWING IN THE CIRCULAR CONDUCTORS

Stanisław Apanasewicz

Technical University of Rzeszow
ul. W.Pola 2, 35-959 Rzeszow
Poland
sapanas@prz.rzeszow.pl

Stanisław Pawłowski

Technical University of Rzeszow
ul. W.Pola 2, 35-959 Rzeszow
Poland
spawlo@prz.rzeszow.pl

Abstract – Equations, describing the distribution of electromagnetic field induced by currents of (1.1) type flowing in the circular coil, including symmetrically infinitely long metal cylinder (fig.1), are presented in the paper. In spite of simply physical configuration, they are very complicated. Main research goals set by authors are presented below: a/ general analyze of electromagnetic field in the considered configuration, b/ examination of electromagnetic waves in the distant zone with respect to possible interferences, c/ examination of influence of Maxwell displacement currents on distribution of field in the environment of metal wall (circular cylinder) of curved surface. It is obvious, that in the case of surface, which is not curved, influence of Maxwell displacement currents on distribution of field in the near zone is negligible. Influence on the distribution of electrical field is essential and cannot be omitted even during the approximation [1]. However, in the case of cylindrical wall, Maxwell currents may influence significantly even on the distribution of magnetic field (in the case of exciting currents flowing in the linear conductors, which are parallel to the axis of cylinder) [2].

1. Electromagnetic field induced by current flowing in the circular coil without inside cylinder ($R_0 = 0$)

We assume, that current flowing in the conductor has the following form:

$$i(t, \theta) = i_0 \exp(j\omega + n\theta), \quad j = \sqrt{-1} \quad (1.1)$$

We will calculate spatial, complex amplitudes of electromagnetic field excited by the current of this type. Equation (1.1) can be treated as one of terms of complex Fourier series of angular function periodical with respect to the angle θ .

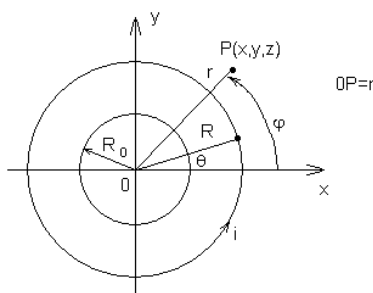


Fig.1. Diagram of analyzed configuration

Retarded electromagnetic potential is a mathematical base for the calculations \vec{A} [3]:

$$\begin{aligned}\vec{A} &= \frac{i_0 \mu_0}{4\pi} \int_{-\pi}^{\pi} e^{jn\theta} W_0(\rho) d\vec{l}, & d\vec{l} &= R(-\sin\theta, \cos\theta, 0) d\theta \\ W_0 &= \frac{e^{-jk\rho}}{\rho}, & k &= \frac{\omega}{c} = \omega\sqrt{\mu_0 \varepsilon_0}, & \rho^2 &= R^2 + r^2 + z^2 - 2rR\cos(\theta - \varphi)\end{aligned}\quad (1.2)$$

Differential $d\vec{l}$ is written in the Cartesian coordinates (x, y, z) ; all next calculations are carried out in the cylindrical coordinates (r, θ, z) . Electric field \vec{E} and magnetic field \vec{H} can be expressed in the following form:

$$\vec{H} = \frac{1}{\mu_0} \text{rot} \vec{A}, \quad \vec{E} = \frac{1}{j\omega\varepsilon_0} \text{rot} \vec{H} \quad (1.3)$$

After some rather arduous mathematical calculations, on the basis of these equations we obtain [4]:

- (radial E_1 , circumferential E_2 and axial E_3) components of electric field:

$$\begin{aligned}E_1 &= h(\varphi) \int_0^{\pi} [W_3 - r(r - R \cos \tau) W_2] \sin n\tau \sin \tau d\tau, & E_2 &= jh(\varphi) \int_0^{\pi} [W_3 \cos \tau - Rr W_2 \sin^2 \tau] \cos n\tau d\tau \\ E_3 &= -h(\varphi) z r \int_0^{\pi} W_2 \sin n\tau \sin \tau d\tau, & h(\varphi) &= \frac{i_0 R e^{jn\varphi}}{2\pi\varepsilon_0 \omega}, & W_1 &= \frac{1}{\rho} \frac{dW_0}{d\rho} = -\left(\frac{jk}{\rho} + \frac{1}{\rho^2}\right) W_0, \\ W_2 &= \frac{1}{\rho} \frac{dW_1}{d\rho} = \left(\frac{3}{\rho^4} + \frac{3jk}{\rho^3} - \frac{k^2}{\rho^2}\right) W_0, & W_3 &= 2W_1 + \rho^2 W_2 = \left(\frac{1}{\rho^2} + \frac{jk}{\rho} - k^2\right) W_0\end{aligned}\quad (1.4)$$

- and adequately of magnetic field:

$$\begin{aligned}H_1 &= -zh_*(\varphi) \int_0^{\pi} W_1(\rho) \cos n\tau d\tau, & H_2 &= -jh_*(\varphi) \int_0^{\pi} W_1(\rho) \sin n\tau \sin \tau d\tau \\ H_3 &= h_*(\varphi) \int_0^{\pi} [r \cos \tau - R] W_1(\rho) \cos n\tau d\tau, & h_*(\varphi) &= \frac{i_0 R e^{jn\varphi}}{2\pi}\end{aligned}\quad (1.5)$$

If the influence of Maxwell currents ($k=0 \equiv c=\infty$ in equations (1.2)) is omitted and it is assumed, that i current does not change along the conductor ($n=0$), we achieve the distribution of field in accordance with Biot-Savart formulas:

$$E_1 = E_3 = 0, \quad E_2 = jh(\varphi) \int_0^{\pi} [W_3 \cos \tau - Rr W_2 \sin^2 \tau] d\tau \quad (1.6)$$

$$H_2 = 0, \quad H_1 = -zh_* \int_0^\pi W_1 d\tau, \quad H_3 = h_* \int_0^\pi [r \cos \tau - R] W_1 d\tau \quad (1.7)$$

2. Description of electromagnetic field in the distant and near zone

On the basis of formulas (1.4), (1.5), we may present description of field in the distant zone. Consequently, in this zone $\rho^2 = r^2 + z^2$; functions W_0, W_1, W_2 do not depend on the integration parameter τ . In this case, components of field different from zero will exist only if $n = 1$. Namely:

$$E_1 = \frac{\pi}{2} h(\varphi) (W_3 - r^2 W_2), \quad E_2 = \frac{\pi}{2} j h(\varphi) W_3, \quad E_3 = -\frac{\pi}{2} h(\varphi) z r W_2 \quad (2.1)$$

$$H_1 = 0, \quad H_2 = -\frac{\pi}{2} j h_*(\varphi) W_1, \quad H_3 = \frac{\pi}{2} h_*(\varphi) r W_1 \quad (2.2)$$

Additionally, by rejection of non significant values, we may assume:

$$W_1 = -\frac{jk}{\rho} W_0, \quad W_2 = -\frac{k^2}{\rho^2} W_0, \quad W_3 = -k^2 W_0 \quad (2.3)$$

Similarly in the near zone (induction)

$$W_0 = \frac{1}{\rho}, \quad W_1 = -\frac{1}{\rho^3}, \quad W_2 = \frac{3}{\rho^5}, \quad W_3 = \frac{1}{\rho^3} \quad (2.4)$$

3. Description of electromagnetic field, taking into account eddy currents in the metal cylinder

For the sake of range of paper, we limit the examination of influence of Maxwell displacement currents on the distribution of electromagnetic field on the surface of metal cylinder, to the case of axial symmetry only. With such an assumption, we may also take into account displacement current, though exciting current does not change along the circular conductor. There is another situation, when current flows in the infinite long straight conductor; In such a situation, it is possible to omit the displacement current only, if exciting current does not change along the conductor.

In the axially symmetrical case, electric field will have the circumferential component E only and magnetic field will have the radial component H_1 and axial component H_3 :

$$\vec{E} = (0, E, 0), \quad \vec{H} = (H_1, 0, H_3) \quad (3.1)$$

These components meet the equation:

$$\Delta E + \left(k^2 - \frac{1}{r^2}\right)E = 0, \quad \Delta H_1 + \left(k^2 - \frac{1}{r^2}\right)H_1 = 0, \quad \Delta H_3 + k^2 H_3 = 0, \quad k = \frac{\omega}{c} \quad (3.2)$$

Additionally, we assume, that radius R_0 is great comparing to the depth of field penetration in the metal:

$$R_0 \gg \sqrt{\frac{2}{\omega\mu\gamma}} \quad (3.3)$$

So, we may apply the impedance boundary conditions for $r = R_0$:

$$E = -\frac{\alpha}{\gamma} H_3, \quad \alpha^2 = j\omega\mu\gamma \quad (3.4)$$

Solutions of equations (3.2) may be presented using Fourier integrals; If impedance condition (3.4) is met, we obtain:

a/ if Maxwell displacement currents are omitted ($k = 0 \equiv c = \infty$):

$$E = \int_0^{\infty} S(\tau) K_1(\tau r) \cos \tau z \, d\tau + E_*(r, z), \quad E_* = \begin{cases} \int_0^{\infty} Q(\tau) K_1(\tau r) \cos \tau z \, d\tau, & r \geq R \\ 0 \\ \int_0^{\infty} Q_*(\tau) I_1(\tau r) \cos \tau z \, d\tau, & r \leq R \end{cases} \quad (3.5)$$

where:

$$Q_* = \frac{K_1(\tau R)}{I_1(\tau R)} Q, \quad Q = \frac{\pi j \omega \mu_0 i_0 I_1(\tau R)}{4[K_0(\tau R)I_1(\tau R) + K_1(\tau R)I_0(\tau R)]\tau} \quad (3.6)$$

$$S = \frac{\frac{\alpha}{\gamma} I_0(\tau R_0) - j\omega\mu_0 I_1(\tau R_0)}{\frac{\alpha}{\gamma} \tau K_0(\tau R_0) + j\omega\mu_0 K_1(\tau R_0)} Q_*$$

$$H_1 = -\frac{1}{j\omega\mu_0} \int_0^{\infty} \tau \cdot S(\tau) K_1(\tau r) \sin \tau z \, d\tau + H_{1*}$$

$$H_{1*} = \begin{cases} -\frac{1}{j\omega\mu_0} \int_0^{\infty} \tau \cdot Q K_1(\tau r) \sin \tau z \, d\tau, & r > R \\ -\frac{1}{j\omega\mu_0} \int_0^{\infty} \tau \cdot Q_* I_1(\tau r) \sin \tau z \, d\tau, & r < R \end{cases} \quad (3.7)$$

$$H_3 = \frac{1}{j\omega\mu_0} \int_0^\infty \tau \cdot SK_0(\tau r) \cos \tau z \, d\tau + H_{3*}, \quad H_{3*} = \begin{cases} \frac{1}{j\omega\mu_0} \int_0^\infty \tau \cdot QK_0(\tau r) \cos \tau z \, d\tau, & r \geq R \\ -\frac{1}{j\omega\mu_0} \int_0^\infty \tau \cdot Q_*I_0(\tau r) \cos \tau z \, d\tau, & r \leq R \end{cases} \quad (3.8)$$

b/ taking into account Maxwell displacement currents ($k \neq 0$):

$$E = \int_0^{\tau_0} C_5 H_1^{(2)}(\delta r) \cos \tau z \, d\tau + \int_{\tau_0}^\infty C_6 K_1(\delta_* r) \cos \tau z \, d\tau + E_0$$

$$E_0 = \begin{cases} \int_0^{\tau_0} C_1 J_1(\delta r) \cos \tau z \, d\tau + \int_{\tau_0}^\infty C_3 I_1(\delta_* r) \cos \tau z \, d\tau, & r \leq R \\ \int_0^{\tau_0} C_2 H_1^{(2)}(\delta r) \cos \tau z \, d\tau + \int_{\tau_0}^\infty C_4 K_1(\delta_* r) \cos \tau z \, d\tau, & r \geq R \end{cases} \quad (3.9)$$

$$\delta^2 = k^2 - \tau^2, \quad \delta_*^2 = \tau^2 - k^2, \quad \tau_0 = \frac{\omega}{c} = k$$

$$H_3 = -\frac{1}{j\omega\mu_0} \left[\int_0^{\tau_0} C_5 \delta H_0^{(2)}(\delta r) \cos \tau z \, d\tau - \int_{\tau_0}^\infty C_6 \delta_* K_0(\delta_* r) \cos \tau z \, d\tau \right] + H_{30}$$

$$H_{30} = -\frac{1}{j\omega\mu_0} \begin{cases} \int_0^{\tau_0} C_2 \delta H_1^{(2)}(\delta r) \cos \tau z \, d\tau - \int_{\tau_0}^\infty C_4 \delta_* K_0(\delta_* r) \cos \tau z \, d\tau, & r \geq R \\ \int_0^{\tau_0} C_1 \delta J_0(\delta r) \cos \tau z \, d\tau + \int_{\tau_0}^\infty C_3 \delta_* I_0(\delta_* r) \cos \tau z \, d\tau, & r \leq R \end{cases} \quad (3.10)$$

where:

$$C_1 = -\frac{j\omega\mu_0 i_0}{\pi\delta} \cdot \frac{H_1^{(2)}(\delta R)}{M_1}, \quad C_2 = -\frac{j\omega\mu_0 i_0}{\pi\delta} \cdot \frac{J_1(\delta R)}{M_1}, \quad M_1 = J_1(\delta R)H_0^{(2)}(\delta R) - J_0(\delta R)H_1^{(2)}(\delta R)$$

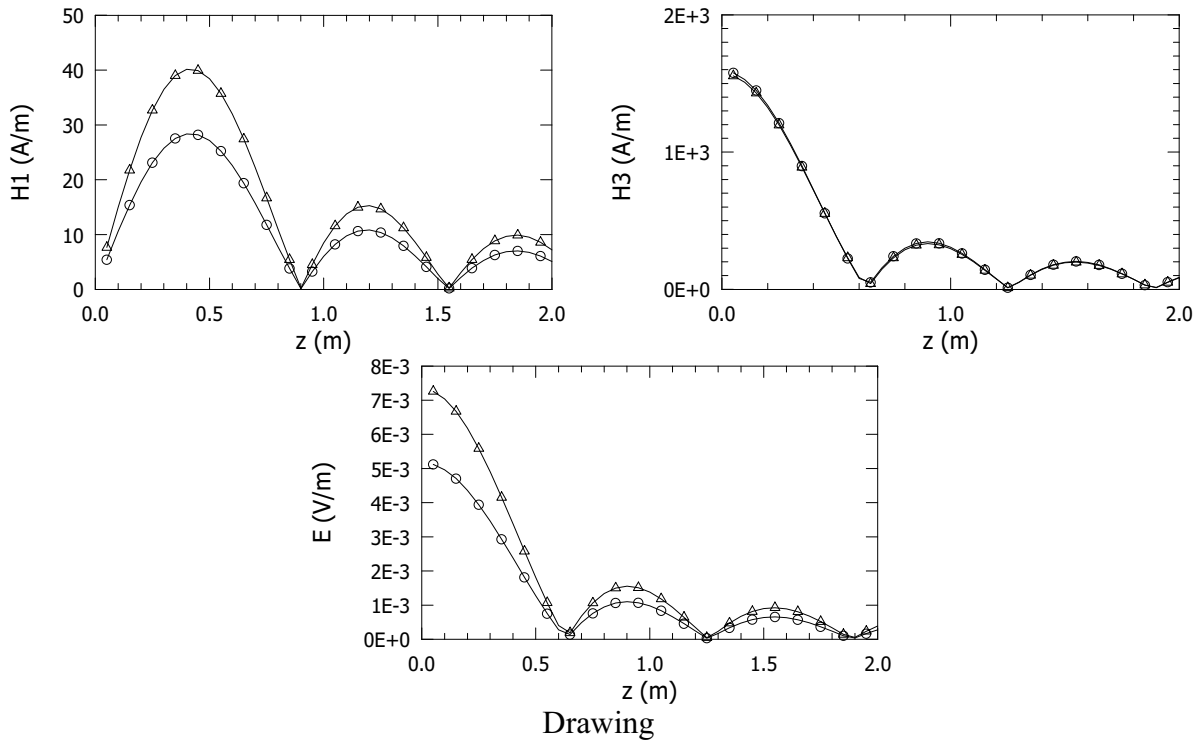
$$C_3 = \frac{j\omega\mu_0 i_0}{\pi\delta_*} \cdot \frac{K_1(\delta_* R)}{M_2}, \quad C_4 = \frac{j\omega\mu_0 i_0}{\pi\delta_*} \cdot \frac{I_1(\delta_* R)}{M_2}, \quad M_2 = K_0(\delta_* R)I_1(\delta_* R) + I_0(\delta_* R)K_1(\delta_* R)$$

$$C_5 = \frac{\frac{\delta\mu_r}{\alpha} J_0(\delta R_0) - J_1(\delta R_0)}{H_1^{(2)}(\delta R_0) - \frac{\delta\mu_r}{\alpha} H_0^{(2)}(\delta R_0)} C_1, \quad C_6 = \frac{\frac{\delta_*\mu_r}{\alpha} I_0(\delta_* R_0) - I_1(\delta_* R_0)}{K_1(\delta_* R_0) + \frac{\delta_*\mu_r}{\alpha} K_0(\delta_* R_0)}$$

$$\alpha^2 = j\omega\mu\gamma$$

We may determine the component H_1 from the formula:

$$H_1 = \frac{1}{j\omega\mu_0} E_2 = -\frac{1}{j\omega\mu_0} \int_0^\infty \tau Q \cdot \sin \tau z \, d\tau \quad (3.11)$$



Conclusions

On the basis of performed calculations, the following conclusions may be presented:

- a/ In the distant zone, electromagnetic field excited by currents, flowing in the circular coil, appears only, if $n=1$ in the equation (1.2).
- b/ If axial symmetry does not exist ($n \neq 0$), all components of electromagnetic field occur in the cylindrical coordinates.

References

- [1] S. Apanasewicz, An investigation of the influence of the displacement currents on the electromagnetic field distribution at metallic body surface, *Compel*, Vol.19, Nr 2, pp.205-210, 2000
- [2] S. Apanasewicz, S. Pawłowski, Assessment of effect of Maxwell displacement currents on the distribution of electromagnetic field in the environment of metal wall of curved surface, Warsaw: ISTET'03
- [3] L.D. Goldstein, N.W. Ziernow, *Electromagnetic fields and waves* (in rus), Moscow, 1971
- [4] S. Apanasewicz, On some properties of retarded potential for electromagnetic field calculation, Warsaw: ISTET'03

II-2. IMPROVEMENT OF EFFECTIVENESS OF HIGH-CURRENT LINES OPTIMIZATION BY MODIFICATION OF GENETIC ALGORITHMS AND PARALLELING OF THE COMPUTATION PROCESS

K. Bednarek

Institute of Industrial Electrical Engineering, Poznan University of Technology
Piotrowo 3a, 60-965 Poznan, Poland, e-mail: Karol.Bednarek@put.poznan.pl

Abstract – The work presents a mathematical model of electrodynamic parameters calculation, determining the optimization process of high-current lines. Special attention was paid to speeding up the optimization calculation with the use of genetic algorithms with different modifications and with the use of the computers including several parallel operating processors. The optimization calculation and the discussion of obtained results were presented.

Introduction

Optimization of engineering systems is often a highly complex process. Introduction of multi-criterial analysis of systems and more and more sophisticated mathematical methods designed for calculating of object parameters give rise to the problems of accuracy and duration of the optimization process. An important factor in such cases is appropriate choice of optimization method and the use of suitable modifications of the chosen method (according to considered technical problem). Additionally, parallel execution of the calculation may be considerably helpful in efficient realization of the task. The paper presents optimization problem of three-phase high-current lines. For the purpose of optimizing the genetic algorithms were applied, with their various modifications. For particular modification variants the effectiveness of optimization process was analyzed. The effect of parallel organization of the calculation process on the time of optimization search was examined.

Description of the system and electrodynamic computation methods

The object of the analyses of the present paper is a three-phase screened air-insulated high-current line (power busway). It consists of three phase conductors, made in the form of oval cross-section tubes, distributed symmetrically each 120°, inside a screen of circular cross-section.

Geometry of the system (Fig. 1) is characterized by the following values: thickness of conductor wall (g), major (a) and minor (b) axis of the oval cross-section, height of conductor suspension (h) and internal radius of the screen (R_s). Thickness of screen wall (t_s) is assumed to be constant and amounts to 3 mm.

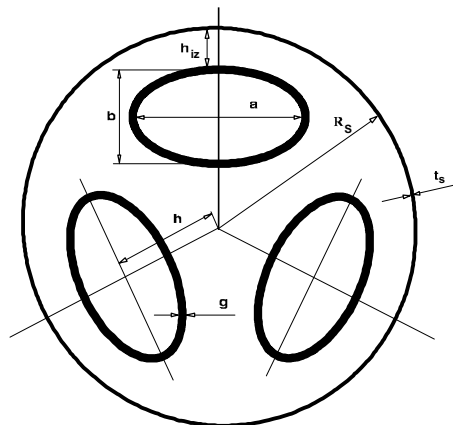


Fig 1. Geometrical parameters of the system

External radius of the screen (R_{sz}) and height of insulator (h_{iz}) are determined by the above mentioned values. Hence, the analyzed system is characterized by five independent variables: a , b , g , h , R_s .

In order to determine selected electrodynamic parameters (reckoned among optimization elements) of shielded three-phase power busways (power loss, temperatures, electrodynamic forces, voltage gradients) the method of integral equations was used. Starting from the equations of magnetic vector potential \mathbf{A} written for the areas of the analyzed system respectively one may define the distribution of current density $\mathbf{J}(r, \varphi)$ of the phase conductor on the ground of an approximate solution of the system of integral equations obtained from the known relationship of electromagnetic field $\mathbf{E} = -j\omega\mathbf{A}$ and $\mathbf{J} = \gamma\mathbf{E}$:

$$\mathbf{J}(r, \varphi) - \mathbf{J}(r_0, \varphi_0) + \frac{3}{4\pi} j\omega\mu_0\gamma_c \int_s \mathbf{J}(r', \varphi') [\mathbf{K}(r', \varphi', r, \varphi) - \mathbf{K}(r', \varphi', r_0, \varphi_0)] dr' d\varphi' = 0 \quad (1)$$

$$\int_{S_c} \mathbf{J}(r', \varphi') r' dr' d\varphi' = I \quad (2)$$

where: (r_0, φ_0) is a reference point, γ_c is conductivity of conductor material, I - current intensity in the phase, $\mathbf{K}(r', \varphi', r, \varphi)$ - a kernel of the integral equation:

$$\mathbf{K}(r', \varphi', r, \varphi) = \sum_{i=1}^{\infty} [a_i \sin i(\varphi - \varphi') + b_i \cos i(\varphi - \varphi')] \frac{x_i}{i} r' + \sum_{i=1}^{\infty} [F_{1i} \sin i(\varphi - \varphi') + F_{2i} \cos i(\varphi - \varphi')] (r r')^i r \quad (3)$$

Coefficients occurring in the equation were defined by the works [3, 4].

It results from symmetry of the system that distribution of current density of two remaining phase conductors (S and T) is the same as in R but shifted by $+120^\circ$ and -120° , respectively.

Similar relationship remains in force for the shield, with an additional equation:

$$\int_{S_s} \mathbf{J}_s(r', \varphi') r' dr' d\varphi' = 0 \quad (4)$$

The presented system of integral equations may be solved in approximate manner using a moment method, being a variation of Ritz method. Methods of solving the above questions and determining the coefficients occurring in equations are discussed in detail in the works [3, 4].

Knowledge of approximate distribution of current density vector enables to determine the value of active power loss in the conductor and its shield (based on Joule's law). Knowledge of the active power losses and the distribution of power density emitted in the conductors and in the screen is necessary for determining thermal conditions of the system [3, 4]. Due to voltage and current values the optimization results depend rather on temperature distribution than on electrodynamic forces and voltage gradients. However, these parameters are also determined during the optimization process.

Optimization criterion

The optimization is aimed at determining such dimensions of the system for which a minimal amount of conductor and screen material shall be used, for assumed values of rated voltage, rated current, and the parameters characterizing the conductors and the screen. Therefore, the optimization consists in minimization of a function $S(\mathbf{u})$ determining the area of the busway cross-section, written in a general form [2, 3]:

$$S(\mathbf{u}) = f(u_1, u_2, u_3, \dots, u_r) \quad (5)$$

where: $u_1, u_2, u_3, \dots, u_r$ - decisive variables ($r=5$), namely the values of a, b, g, h , and R_s .

Constraints of the optimization process are admissible electrodynamic and thermal parameters (temperatures of working lines $T_{C_{max}}$ and of the screen $T_{S_{max}}$, electrical strength of the system - E_{max} , the forces acting in steady conditions and in short-circuit state F_{max}), as well as admissible ranges of variation of the geometrical dimensions.

A set of the above mentioned constraints Z_i in a general form is given by the function:

$$\mathbf{Z}(\mathbf{u}) = [Z_1(\mathbf{u}), Z_2(\mathbf{u}), \dots, Z_k(\mathbf{u})] \quad (6)$$

In order to convert the presented problem to a constraint-free optimization problem the criterion function $S_z(\mathbf{u})$ has been modified:

$$S_z(\mathbf{u}) = S(\mathbf{u}) + \sum_{i=1}^k P_i (Z_i)^2 N[Z_i] \quad (7)$$

where: $N[Z_i] = \begin{cases} 1 & \text{for } Z_i > 0 \text{ infringement of the constraints} \\ 0 & \text{for } Z_i \leq 0 \text{ fulfilment of the constraints} \end{cases}$

The formula (7) includes P_i - a so-called penalty factor, of high value, being positive for the case of minimization $S(\mathbf{u})$ (and negative for maximization).

Due to the dependence of criterion function included extremized variables on delimiting parameters (the values of which are to be determined in result of complex numerical calculation) and due to the constraints included in the objective function, the modified criterion function can not be written in an explicit form. This imposes an additional problem that complicates the optimization calculations and considerably extends the time consumed for getting the results.

The optimizing method is based on genetic algorithms. Therefore, the criterial function was converted into an adaptation function (bringing the problem to a maximization task) [2].

Genetic algorithm and effectiveness of its modification

The genetic algorithm in its elementary version includes the following operations: selection according to the roulette rule, simple crossing with random linking, and simple mutation.

Optimization methods in their classical forms often do not take into account the nature of considered problem and, therefore, are less effective. However, their effectiveness may be improved in result of some modifications.

The selection according to the roulette principle is a process characterized by considerable variation, i.e. providing important spread of actual number of the copies around its expected value. The paper presents and implements modification of the selection operation based on the model of De Jong's expected values and Brindle's random selection using the remainders without repetitions.

In order to avoid the loss of the best existing individual two variants of a method of keeping the best of existing solutions were proposed: such a solution is kept 1) always, or 2) provided that the adaptation factor of the best individual of the $P(t+1)$ population is lower than for the best individual of the $P(t)$ population (exclusivity model).

Another modification method consists in scaling of the adaptation. In the presented algorithm linear scaling was applied. Adjustment scaling is aimed at preventing domination of the above average individuals at the beginning of the computation process, that could result, on the one hand, in stagnation of the procedure in a local maximum, and, on the other hand, in increasing the differences in accommodation factors of the individuals in final stage of the computation, when the average accommodation factor only slightly departs from its maximal value [2, 3].

During the calculation the course of the genetic algorithm was monitored for 100 generations. Probabilities of crossing and mutation were constant and amounted to 0.8 and 0.005, respectively. For computation purpose binary coding was used. Every individual (chromosome) included 20 genes (bits). Constant population size was maintained, including 20 individuals.

Examples of optimization search are shown in Figs. 2 - 9. In order to depict better the existing relationships the charts of absolute values of the adaptation coefficients have been used (referred to optimal values for each of the solutions).

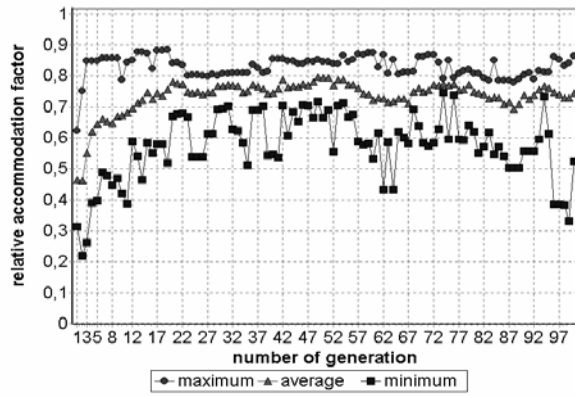


Fig. 2. Optimization course in case of selection according to the roulette principle

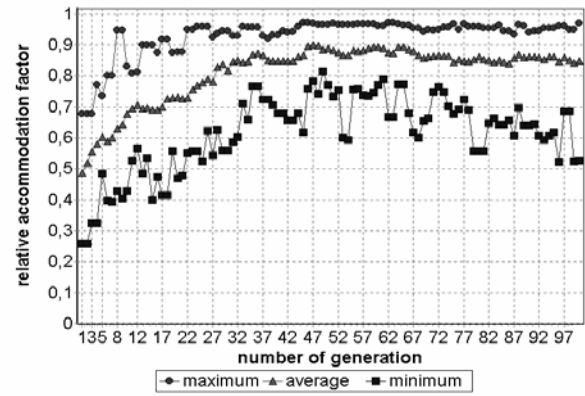


Fig. 3. Optimization course in case of selection with regard to remainders without repetitions

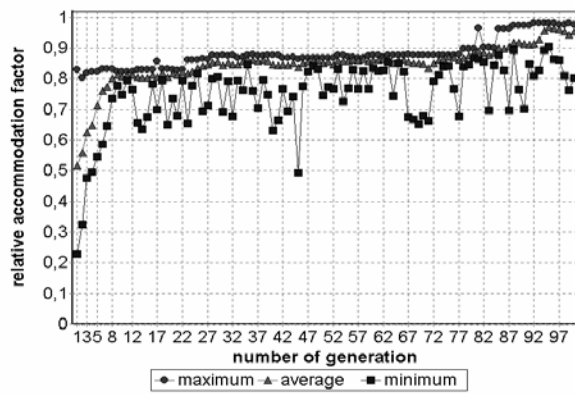


Fig. 4. Optimization course in case of selection according to the roulette principle, scaling of accommodation factor

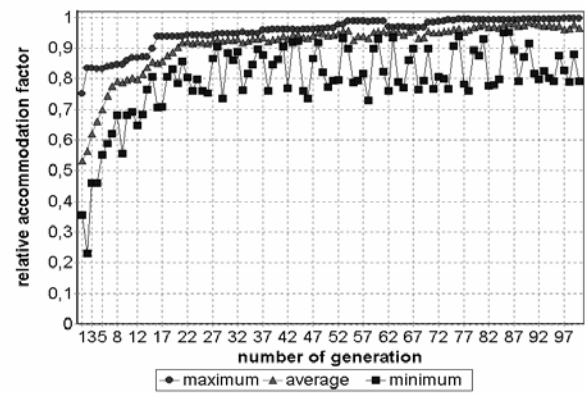


Fig. 5. Optimization course in case of selection with regard to remainders without repetitions, scaling of accommodation factor

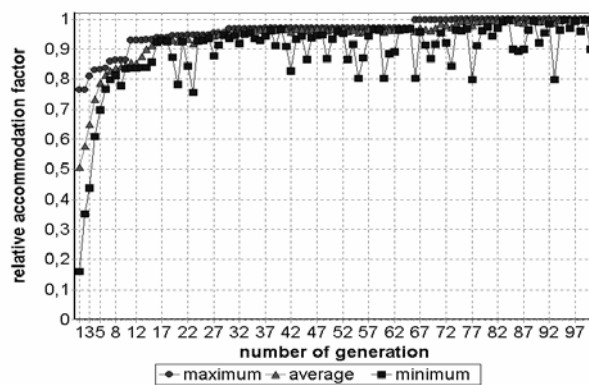


Fig. 6. Optimization course in case of selection according to the roulette principle, scaling of accommodation factor, "unconditional" transferring of the best individual

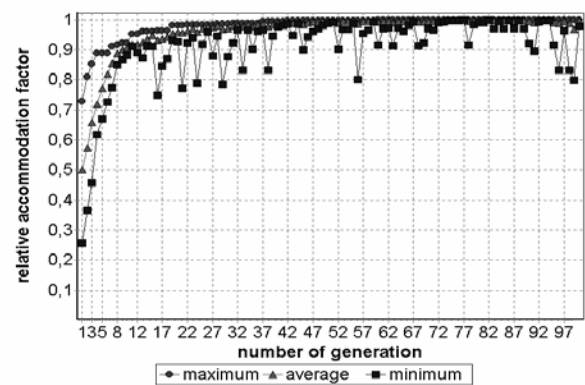


Fig. 7. Optimization course in case of selection with regard to remainders without repetitions, scaling of accommodation factor, "unconditional" transferring of the best individual

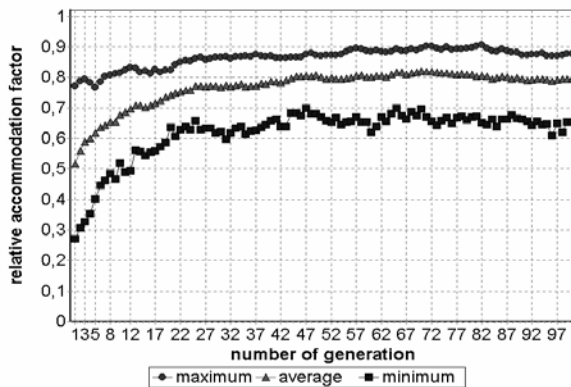


Fig. 8. Selection according to the roulette principle (average points for 10 trials)

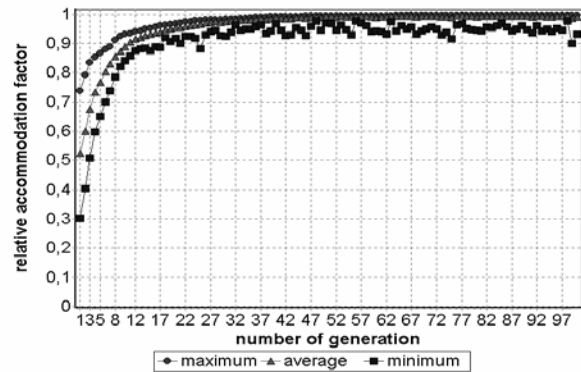


Fig. 9. Selection with regard to remainders without repetitions, with accommodation scaling and "unconditional" transferring of the best individual (average points for 10 trials)

Every computation trial is of exclusive character, as the genetic algorithms consist in a random optimization method. Therefore, in order to come to generalized conclusions (for given variants) values depicted by particular points of the diagrams included in the paper are the averages taken from 10 trials (Figs. 8 - 9). This enables more reliable analysis of effectiveness of particular modifications.

A selection process more advisable than the roulette rule is the selection method with remainders without repetitions.

The non-exclusivity reproduction methods, i.e. the ones keeping no the best individual from the last generation, characterize with the possibility of a loss of promising solutions, that could result in wrong orientation of the whole optimization process. This might result in longer computation time or even lead to wrong results (the loss of the global optimum - which occurred in both selection cases without the modification (Figs. 2-5)). Thus, an important part of the optimization process carried out with the method of genetic algorithm is its modification consisting in transferring of the best individual.

Scaling of the accommodation function causes an increase in averaged factors of maximal accommodation of the individuals belonging to the population (Figs. 4-7). In result the average and minimal accommodation factors also increase (approach the maximal value).

Application of parallel computation

The genetic optimization algorithm gives a possibility to separate the operations of determining values of adaptation functions (for particular individuals of given generation) among several computation units. This enables shortening of computation time of the most time-consuming tasks of the optimization procedure [1, 3]. Fig. 10 presents relative per cent time of optimization calculations performed with genetic method for various numbers of calculating units, compared to the same process performed with a single processor. The following denotation has been adopted: T_k - calculation time with k processors (where $k = 1, 2, 3,$ or 4), T_1 – calculation time for a single processor. Errors of solutions obtained during the test calculations were similar.

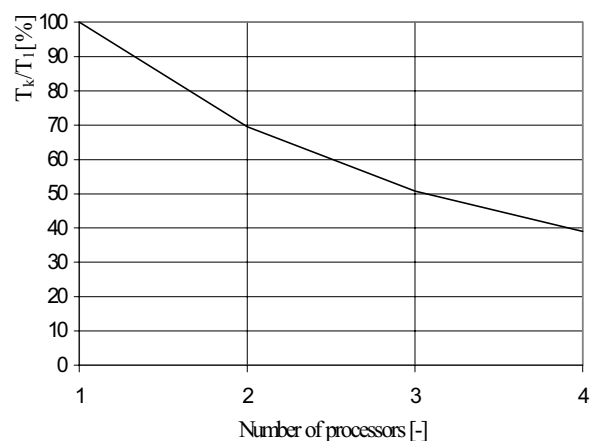


Fig. 10. Relative time of optimization calculations as a function of the number of processors

Results of optimization calculations

In the optimization calculations the following operation data and material parameters are assumed: rated voltage 1 kV and 17.5 kV, rated current 1-4 kA, conductivity of conductor and screen materials $37 \cdot 10^6$ S/m, frequency 50 Hz, environment temperature 308 K, thermal resistance of conductor and screen materials 0.004 1/K, emissivity coefficient of outside conductor surface 0.45, emissivity coefficient of outside screen surface 0.5, maximal operation temperature of the conductors 363 K, assumed temperature of the shield 338 K. Figure 11 shows the results of optimization calculations of cross-section area of the busways $S[\text{mm}^2]$ as functions of the rated current $I[\text{kA}]$.

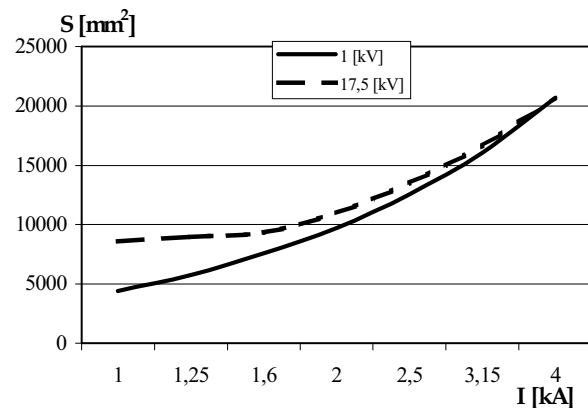


Fig. 11. Dependence of optimal entire section area of the busways as a function of the current, for voltage values 1 kV and 17.5 kV.

Final notes and conclusions

- The genetic algorithms are effective methods of searching of optimal solutions in the global sense.
- The selection based on the roulette principle gives worse results than the method of remainders without repetitions. In the second case the algorithm gave higher averaged accommodation factor.
- In case of modification consisting in transferring of the best individual and accommodation scaling similar results are obtained - the modifications improve the rate and accuracy of achieving the optimal point.
- The use of a 4-processors computer enables shortening of computation time by more than 60 percent. The use of more processors leads to further shortening of the solving procedure.
- The presented tests of parallel computing were carried out on a multi-processor computer. At present further work aimed at paralleling of computation with the use of parallel virtual machine of cluster type is in the course.
- Both the modification of the classical genetic algorithm and parallel organization of the computation process considerably improve effectiveness of the optimization search.
- As an optimization assumption a material criterion has been adopted. This leads to an increase of power loss falling to unit length of the busway.
- Appropriate selection of calculation methods of electrodynamic parameters of the power busways and their optimization methods allow to achieve remarkable savings during the designing and exploitation processes if these devices.

References

- [1] C. Vollaire, L. Nicolas, Parallel Computing for Scattering Problems, International Conference on Parallel Computing in Electrical Engineering, PARALEC'98, Bialystok, Poland, 1998, p.283-286.
- [2] D.E. Goldberg, Genetic Algorithms in Search, Optimization and Machine Learning, Addison-Wesley Publishing Company, Inc. Reading, Massachusetts, 1989.
- [3] K. Bednarek, R. Nawrowski, A. Tomczewski, An application of genetic algorithm for three phases screened conductors optimization, PARELEC'2000 International Conference on Parallel Computing in Electrical Engineering, Trois-Rivieres, Canada, August 2000, p. 218-222.
- [4] K. Bednarek, R. Nawrowski, Numerical optimization of 3-phase screened conductor, Conference Computer Applications in Electrical Engineering ZKwE'96, Poznan – Kiekrz, 1996, pp. 245-248 (in Polish).

I-3. SHAPE OPTIMIZATION WITH ADAPTIVE SIMULATED ANNEALING AND GENETIC ALGORITHMS

Hartmut Brauer¹, Marek Ziolkowski^{1,2}

¹ Technische Universitaet Ilmenau, Am Helmholtzplatz 2, D-98684 Ilmenau, Germany

² Technical University of Szczecin, Sikorskiego 37, PL-70313 Szczecin, Poland

email: hartmut.brauer@tu-ilmenau.de

Abstract – Stochastic methods offer a certain robustness quality to the optimization process. In this paper, the Adaptive Simulated Annealing (ASA) and two Genetic Algorithms (GA) are used for the shape optimization of a shimming magnet pole. The magnetic field is computed using the finite element method in 2D. The aim of optimization is the search for a pole shape geometry which leads to a homogeneous magnetic field in the region of interest.

Introduction

For optimal performance of electromagnetic devices, it is necessary to perform design optimization of the shape and parameters of their magnetic circuit, size and position of the current windings, magnetic properties of the used magnetic materials, etc. The traditional optimization methods based on trial-and-error procedures are not very suitable, especially for highly complex and multivariable optimization problems because they are very laborious, time consuming and not enough accurate. Therefore, the development of new and more efficient methods for inverse optimization and automation of the entire optimization process are always desired.

Optimization methods are usually classified into two categories: the gradient-based (deterministic) search methods and non-gradient-based (stochastic) search methods. While the former ones need computation of the gradient of the objective function, the latter ones work directly with the values of the objective function, and are more convenient in cases where it is difficult or even impossible to compute exactly the gradient of the objective function [1].

In electromagnetic device optimization the problem of obtaining such devices which will result with desired values of the magnetic flux density at several certain points, is a very common problem. However, since the exact expression of the gradient function is impossible, therefore, usage of the deterministic optimization methods is excluded. Consequently, for such optimization problems designers usually utilize stochastic methods. Genetic Algorithm (GA), Simulated Annealing (SA), Evolution Strategy (ES), or Tabu Search (TS) are such stochastic methods which become very popular in the design of electromagnetic devices [2-4].

In this paper, we compare ASA and two different versions of GA to the shape optimization of the pole shape geometry of a simple shimming magnet, where we are searching for the pole shape modifications leading to a homogeneous magnetic flux density in a certain region.

Shape Optimization Problem

The proposed framework to optimize is presented in Fig. 1. It is a simplified 2D configuration of a shimming magnet where the optimization goal is to obtain a modified magnetic pole shape generating a constant magnetic flux density in a certain part of the central region of the air gap.

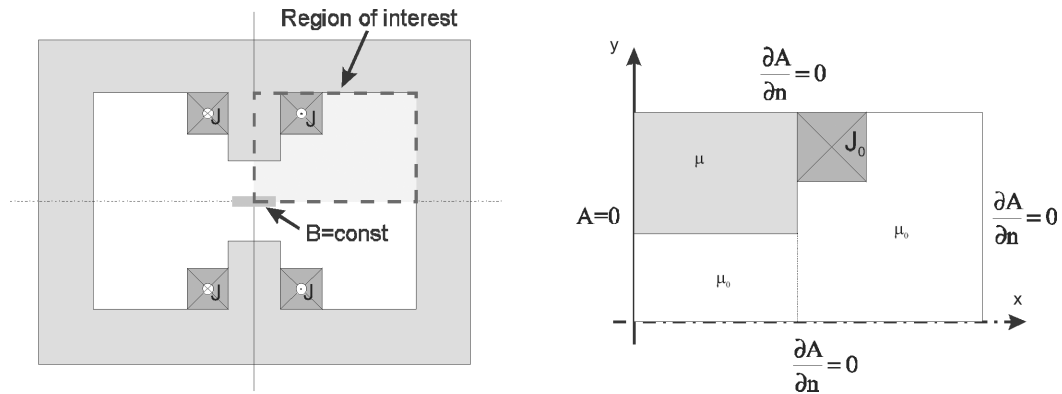


Fig. 1. Layout of the considered shape optimization problem in a simplified 2D shimming magnet system (left), and the field problem used for the shape optimization, with iron core, impressed current density \mathbf{J} , and boundary conditions (right).

The magnetic flux in the iron core, which is assumed to be linear or nonlinear, is driven by the current density \mathbf{J} indicated in Fig. 1. Because of the symmetry only a part of the framework has to be taken into account. This region of interest is indicated by the dashed line. Extracting this region of interest we get the configuration to which the stochastic optimization methods were applied (Fig. 1).

A current density of 1 A/mm^2 was applied to the coil, and two different cases of magnetic material were considered: a linear one with $\mu_r = 100$ and a nonlinear one where a material characteristic of steel M19 was assumed. The magnetic fields were computed using the free available finite element software code FEMM (<http://femm.berlios.de>). The goal of the shape optimization is getting a constant magnetic flux density at $y = 0$ and $0 \leq x \leq 80 \text{ mm}$.

To develop our idea, first, let us briefly describe the strategy for shape optimization based on the searching techniques employed in our approach. First, we have to define the searching space, and establish several control points along the outline of the device which shape optimization is desired as shown in Fig.2.

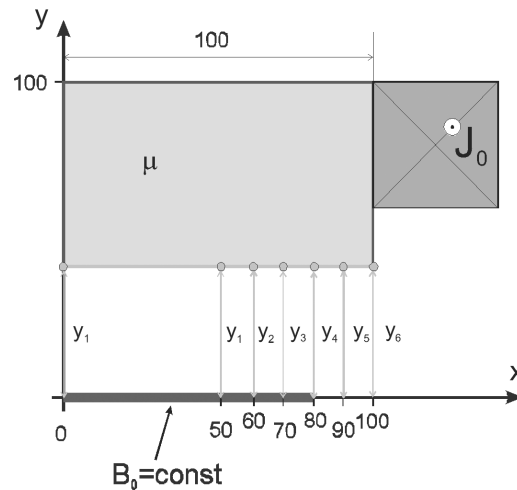


Fig. 2. Field problem used for the shape optimization, with positions of the six control points y_1, \dots, y_6 .

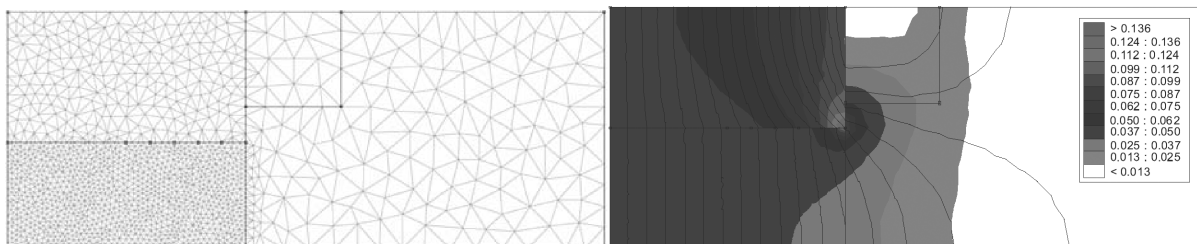


Fig. 3. Finite element mesh (left) and magnetic flux density distribution (right) of the starting configuration computed with the FEM code FEMM.

In this example, we are interested in an optimal shape of the iron core, and for that purpose, we have chosen a set of six control points, indicated by the variables y_1 through y_6 (Fig. 2). Each point is fixed in the x -coordinate, while it can move freely within the searching space (y -direction), which is defined by the interval of $10\text{mm} \leq y_i \leq 65\text{mm}$. The control point y_1 is doubled which means that the control points at $x = 0\text{mm}$ and at $x = 50\text{mm}$ can be moved only together. Between the control points no smooth approximation of the core shape has been done. The control points are connected by polygons corresponding to the finite element mesh (Fig. 3, left). The magnetic flux density distribution for this starting configuration is given in Fig. 3 (right).

Optimization using Adaptive Simulated Annealing (ASA)

Annealing is actually a term from metallurgy. If a metal is heated to a very high temperature, the atoms move at high speed. If they are cooled now very slowly, they settle into patterns and structures, rendering the metal much stronger than before.

Simulated Annealing (SA) is a stochastic relaxation technique which is based on the analogy to the physical process of metal annealing: at high temperatures the atoms are randomly distributed. With decreasing the temperature they tend to arrange themselves in a crystalline state which minimizes their energy. Using this analogy, the algorithm generates randomly new configurations by sampling from probability distribution of the system. New configurations are accepted with a certain acceptance probability depending on the temperature. It has been shown that the algorithm converges to a global energy minimum if the temperature is reduced slowly enough [8].

In this study we have applied the Adaptive Simulated Annealing (ASA) Code which is a C-language code developed to statistically find the best global fit of a nonlinear constrained non-convex cost function over a N -dimensional space [7]. This algorithm permits an annealing schedule for “temperature” T decreasing exponentially in annealing-time k ,

$$T = T_0 \exp(-c k^{1/N}).$$

The introduction of re-annealing also permits adaptation to changing sensitivities in the multi-dimensional parameter space. This annealing schedule is faster than fast Cauchy annealing, where $T = T_0/k$, and much faster than Boltzmann annealing, where $T = T_0/\ln k$.

The ASA algorithm consists of three main parts [8]:

Generating probability density function

In a N -dimensional parameter space with parameters p^i having ranges $[A_i, B_i]$, about the k -th saved point (e.g., a local optima), p^i_k , a new point is generated using a distribution defined by the product of distributions for each parameter, $g^i(y^i; T_i)$ in terms of random variables $y^i \in [-1, 1]$, where $p^i_{k+1} = p^i_k + y^i(B_i - A_i)$, and “temperatures” T_i ,

$$g^i(y^i; T_i) = \frac{1}{2 \cdot (|y^i| + T_i) \cdot \ln(1 + 1/T_i)}$$

Acceptance probability density function

The cost functions, $C(p_{k+1}) - C(p_k)$, are compared using a uniform random generator, $U \in [0, 1]$, in a “Boltzmann” test:

$$\exp[-(C(p_{k+1}) - C(p_k))/T_{cost}] > U,$$

where T_{cost} is the “temperature” used for this test. If the above inequality is fulfilled then the new point is accepted as the new saved point for the next iteration. Otherwise, the last saved point is retained.

Reannealing temperature schedule

The annealing schedule for each parameter temperature, T_i from a starting temperature T_{i0} , is

$$T_i(k_i) = T_{i0} \exp(-c_i k_i^{1/N}).$$

The annealing schedule for the cost temperature is developed similarly to the parameter temperatures. However, the index for re-annealing the cost function, k_{cost} , is determined by the number of accepted points, instead of the number of generated points as used for the parameters. This choice was made because the Boltzmann acceptance criterion uses an exponential distribution which is not as fat-tailed as the ASA distribution used for the parameters. As determined by the selected program options, the parameter “temperature” may be periodically adaptively re-annealed, or increased relative to their previous values, using their relative first derivatives with respect to the cost function, to guide the search “fairly” among the parameters. The re-annealing of the cost temperature resets the scale of the annealing of the cost acceptance criteria as

$$T_{cost}(k_{cost}) = T_{0_{cost}} \exp(-c_{cost} k_{cost}^{1/N}).$$

The new $T_{0_{cost}}$ is taken to be the minimum of the current initial cost temperature and the maximum of the absolute values of the best and last cost functions and their difference. The new k_{cost} is calculated taking T_{cost} as the minima of the cost function, constrained not to exceed the current initial cost temperature. This procedure essentially resets the scale of the annealing of the cost temperature within the scale of the current best or last saved minimum.

Optimization using Genetic Algorithms (GA)

Various searching techniques based on the GAs have already been applied for inverse shape optimization of electromagnetic devices, mainly due to their ability to avoid trapping into local optimum of the objective function [1-4]. *Genetic Algorithms* work with the coded information rather than directly with the optimized functions. Therefore, they can be adjusted to the particular problem relatively easily.

In this study we have applied a C++ library of genetic algorithm components (GAlib) developed at the M.I.T. [5]. From the implemented algorithms offered by the GAlib we have chosen the standard, simple genetic algorithm which uses non-overlapping populations, optional elitism and roulette-wheel selection scheme. We have applied the 16 bit binary-to-decimal genome (which converts binary strings to decimal values) and modified the crossover and mutation probabilities for population sizes of 60 individuals.

We have also applied the Genetic Algorithm Optimization Toolbox (GAOT) developed at the North Carolina State University [6]. GAOT implements simulated evolution in the Matlab environment using both binary and real representations. Here the crossover and mutation operators were chosen much more sophisticated. Arithmetic, heuristic and simple crossover operators were applied with different frequencies [6].

Table I. Applied frequencies of the crossover operator and the mutation operator in GAOT, where G_{max} is the maximum number of generations and b is a certain shape parameter describing the mutation rate.

Crossover	Applied frequency	n	Mutator	Applied frequency	G_{max}	b
arithmetic	4	0	boundary	1	0	0
heuristic	1	3	uniform	1	0	0
simple	4	0	non-uniform	4	200	2
			multi non-uniform	4	200	2

Optimization results

The aim of the simulation study is the investigation of the effects of modified stochastic operators on the shape optimization process. We minimized the cost function

$$CF = 100\% \frac{\sqrt{\sum_{i=1}^N (B_i - B_0)^2}}{B_0}$$

where B_0 is the desired constant magnetic flux density along the symmetry line ($0 < x < 80\text{mm}$; $y = 0$). With the impressed current density of 1 A/mm^2 we defined a value of $B_0 = 40 \text{ mT}$. The GA simulations were performed for crossover rates of 0.55, 0.65, 0.75, 0.85, and 0.95, and for mutation rates of 0.01, 0.1, and 0.2. The search for the optimal shape was terminated after 100 generations.

Fig. 4 shows the results of both GA and ASA optimization, respectively, for the linear case (iron core with $\mu_r = 100$) and for the nonlinear case (iron core with steel M19). The population contained 60 individuals. The best results were obtained with a mutation probability of 0.01 and crossover probabilities of 0.65 and 0.85 for the linear case and the nonlinear case, respectively.

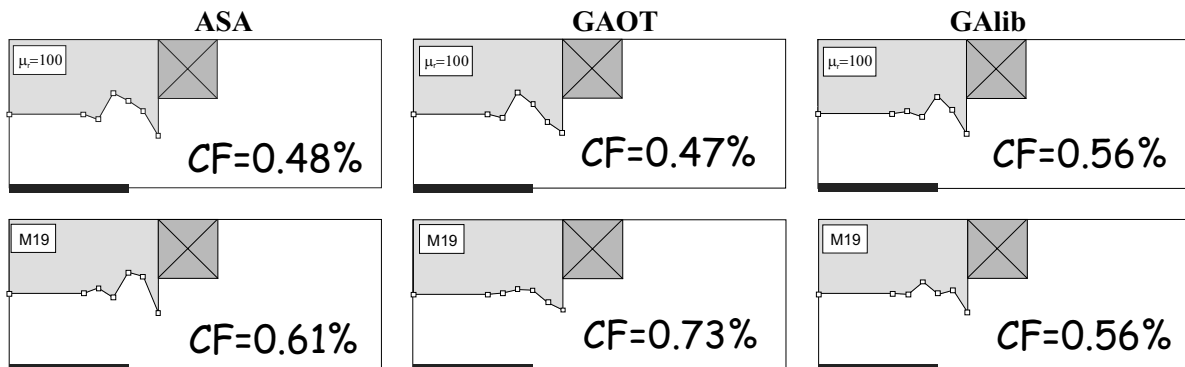


Fig. 4. Results of the optimization for the linear ($\mu_r = 100$) and the nonlinear problem (steel M19)

Because of the stochastic characteristics of the applied methods it is not sure that we have got the “best” result if the process is terminated by the maximum number of generations, i.e. in some cases we have got lower cost function values for other crossover rates or mutation rates than given here. But in all cases we found that it makes no sense to increase the mutation rate considerably. Usually, a mutation probability of 0.01 is a good choice. Another essential parameter is the population size. We could improve the results if their number was increased (e.g., $30 \rightarrow 60$).

Fig. 5 shows the magnetic flux density distribution at the symmetry line for linear and nonlinear problems together with the solution for the start configuration.

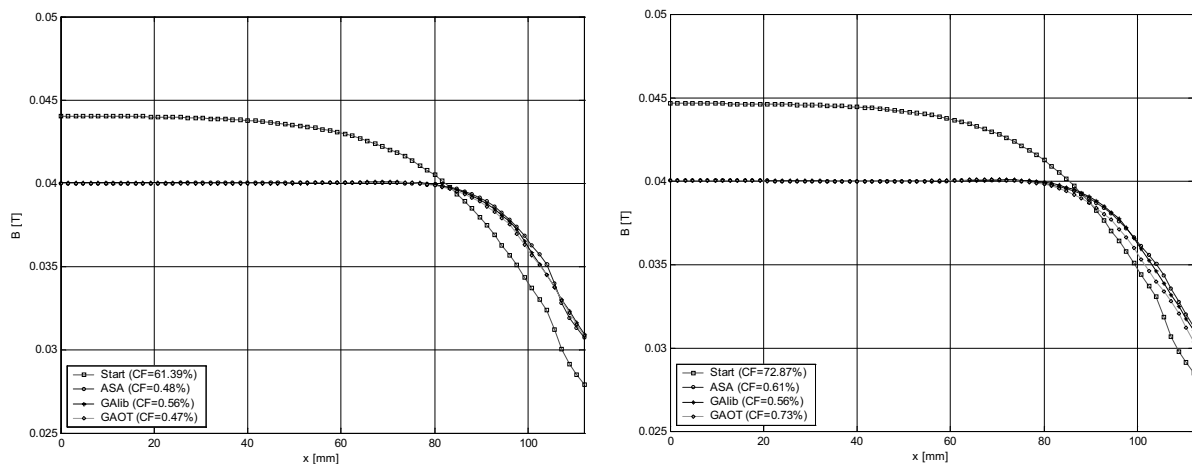


Fig. 5. Magnetic flux densities at the line of symmetry for the linear case (left), for the nonlinear case (right)

The three methods (GA/ASA) have given similar results (CF around 0.5%) although the shapes of the iron core are slightly different. The time of calculations has been also comparable i.e. several minutes on 1GHz Pentium4. The only difference has consisted in the fact that GA demanded more carefully tuning (choosing the adequate population size, the crossover and the mutation probabilities) than ASA which has been applied with the standard options only.

Conclusions

In optimization problems where derivatives of the cost function are not available stochastic methods like *Genetic Algorithm* or *Simulated Annealing* can be applied. In this paper both these methods have been used to optimize the pole shape of a simple shimming magnet configuration. Different optimization algorithms (GA, ASA) known from the literature have been combined with the finite element code FEMM to study their performance for shape optimization problems.

The true strength of SA lies in its ability to statistically deliver a true global optimum, but there are no theoretical reasons for assuming that it will be more efficient than GA which also can find the global optimum. Thus, a possible comparison of GA and SA must be viewed in the context of “judging” these algorithms only specific to the problem just being tested. It should be expected that there are systems for which one of GA or SA will be better suited than the other. For our problem no one could be preferred. With GALib we found in both the linear and nonlinear cases exactly the same value of the cost function, whereas GAOT gave the best result in the linear case but the most wrong result in the nonlinear case. On the other hand, ASA is easier to handle and works more robust than the GA codes. In the next future, further modifications of the so far used standard algorithms will show under which conditions these conclusions can be maintained.

References

- [1] Rahmat-Samii, Y., E. Michielssen: “*Electromagnetic Optimization by Genetic Algorithms*”, Wiley, 1999
- [2] Lukas, D.: “*Shape optimization of homogeneous electromagnets*”. In: *Lecture Notes in Computational Science and Engineering*, Springer, 2001, vol. 18, pp. 145-152
- [3] Zaoui, F., C. Marchand: “*Using genetic algorithm for the optimization of electromagnetic devices*”. *COMPEL*, vol. 17, No. 1/2/3, 1998, pp. 181-185
- [4] Yokose, Y., V. Cingoski, K. Kaneda, H. Yamashita: “*Performance comparison between gray coded and binary coded genetic algorithms for inverse shape optimization of magnetic devices*”. *Proc. 1st Japanese-Bulgarian-Macedonian Joint Seminar on Applied Electromagnetics and Mechanics*, Sofia, 1998
- [5] Wall, M.: “*GALib: A C++ Library of Genetic Algorithm Components*”. V2.4, 1996, <http://lancet.mit.edu/ga/>
- [6] Houck, C.R., J.A. Joines, M.G. Kay: “*A genetic algorithm for function optimization: a Matlab implementation*”. North Carolina State University, NCSU-IE TR 95-09, 1995
- [7] Ingber, L.: “*Adaptive Simulated Annealing (ASA)*”. *ASA-User Manual*, 2003, <http://www.ingber.com/>
- [8] Ingber, L.: “*Simulated annealing: Practice versus theory*”. *Math. Comput. Modelling*, vol. 18, No. 11, 1993, pp. 29-57

I-4. THE DESIGN OF OPTIMISED PLANAR THICK FILM FILTERS

V. Desnica, Lj. Živanov, O. Aleksić¹, M. Luković¹, L. Lukić²

University of Novi Sad, Faculty of Technical Science, Trg Dositeja Obradovića 6, 21000 Novi Sad

¹University of Belgrade, Faculty of Electrical Engineering, Bulevar Revolucije 73, 11000 Belgrade

²IRITEL AD, Batajnički put 23, 11000 Belgrade, Serbia and Montenegro.

Abstract – This paper presents planar thick film components and their practical implementations to filters. Different thick film LC filter geometries were designed, printed on alumina, fired and characterized in the HF range. They were asymmetric to input and output terminations, and to positive and negative (or ground) applied voltages and HF signals. L-inductive, C-capacitive parameters were distributed using different planar thick film constructions: inductor windings were printed as the top electrode of capacitor and vice versa, planar capacitors were printed between the windings. In addition, four types of optimised planar thick film filter are built using dielectric and ferrite middle layer. As a result, the groups of cells were realized on 0,5x1, 1x1 inch alumina substrate as DIL (dual-in-line package) matrix to serve as filter arrays in EMI (Electromagnetic Interference) suppression.

Introduction

Wireless communications continue to grow at a very fast rate, notably enhanced by the rapid expansion of portable communication systems and open an important market opportunity to electronic interconnect technologies, having excellent performance in the high frequency range. Applications for filters circuitry are in rapid expansion, particularly in the field of portable communications systems, and the operating speeds of digital integrated circuits (DIC) continue to increase, creating the need for suitable optimised thick film structures. A lot of efforts take place to integrate or embed passives not only to reduce size and weight but also to enhance the performance and necessarily or hopefully to lower the costs [1]. Several papers [2-6] have been written in the last five years to describe the characterization and the performance of thick film symmetrical thick film filters and to compare these properties mutually under the same test conditions. These scientific results are good basis for future research.

The first part of presentation will deal with the development of the asymmetrical thick film filter, while the second part of the presentation will deal with optimised planar thick film filters.

Fig. 1 explains the expected frequency profile of the proposed thick film RF noise filter. The transmission line basically has a passband that covers the signal frequency range. Without the filter, the noise harmonics of the signal pass through the transmission line with only a little attenuation.

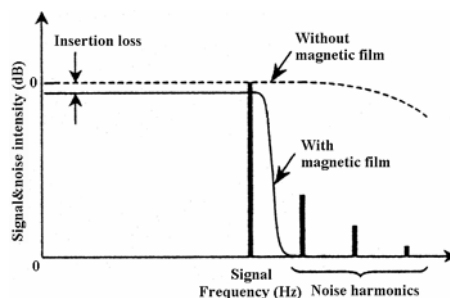


Fig. 1 Desired transfer characteristics of the thick film filter [7].

The ideal role of filter is not to raise attenuation in the passband and to give as large attenuation as possible to eliminate the noise harmonics at the stop band, where the frequency range is higher than the meaningful signal.

Design of the asymmetrical and optimised planar thick film filters

The traditional additive ceramic based thick film technology is used for asymmetrical and optimised planar filters, Fig. 2 and Fig. 4, on the surface of alumina (Al₂O₃), substrate.

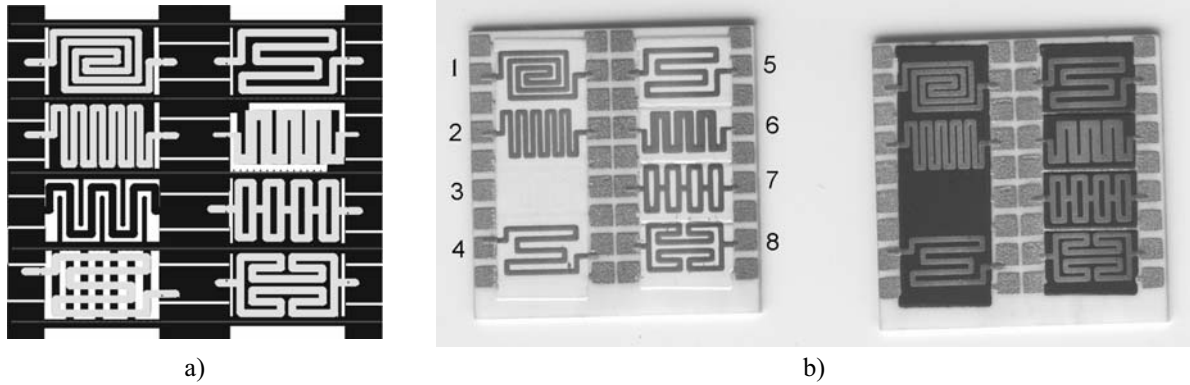


Fig. 2 Top view of asymmetrical thick film filters: a) schematic enlarge layout, b) picture of realized filter.

Fig 3 compares the measured attenuations of asymmetrical filters versus frequency with dielectric and ferrite material for filter number 4 and 7, where the largest attenuation enhancement is obtained using ferrite midlayer.

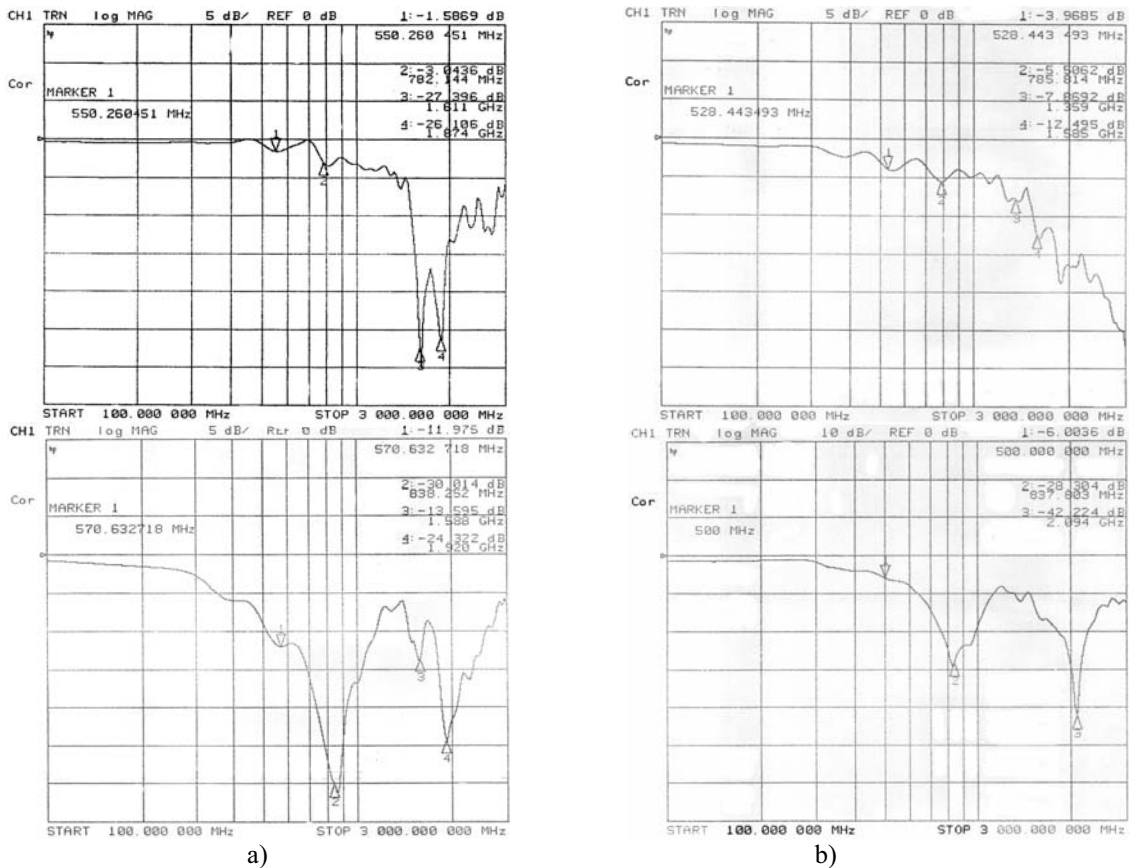


Fig. 3 Attenuation of two different filters: a) Filters number 4 and 7 with dielectric midlayer; b) Filters number 4 and 7 with ferrite midlayer.

Optimised planar thick film filters

In [3] basic LC filters, series combination of two filters, and series combination of three filters are being compared. Using these results we realized the optimised symmetrical thick film filters with dielectric and ferrite middle layer, shown on Fig. 4. These filters are symmetrical looking from input to output. Symmetrical design means operation is the same for wave forms propagation in the opposite direction.

Lumped-element and distributed circuit models are used for each optimised planar thick film filter [2-4]. In the case where the middle layer is ferrite material, filter model is little modified, because the permittivity and permeability of ferrite material are complex parameter consisting of real and imaginary part. The real component represents the reactive portion and the imaginary component represents the losses. R_f given by

$$R_f = 2 \cdot \pi \cdot f \cdot L_o \cdot \mu_r'' \tag{1}$$

where f is frequency, L_o is inductance of inductor in vacuum environment and μ_r'' imaginary part of complex permeability. The impedance curve can be translated to a pure material curve, the so-called complex permeability curve. As impedance consists of reactive and resistive part, permeability should have two parts too to represent this. The real part corresponds to the reactance, positive for an inductance, negative for a capacitance, and the imaginary part to the losses. The impedance of the filter is given by

$$Z = j\omega(\mu' - j\mu'') \cdot L_o = \omega\mu'' \cdot L_o + j\omega\mu' \cdot L_o, \quad Z = R + jX \rightarrow R = \omega\mu'' \cdot L_o, \quad X = \omega \cdot \mu' \cdot L_o (\omega = 2 \cdot \pi \cdot f)$$

$$|Z| = \sqrt{R^2 + X^2} = \omega \cdot L_o \cdot \sqrt{\mu''^2 + \mu'^2} \tag{2}$$

Optimised symmetrical filters performances are investigated and compared in terms of attenuation (A) as shown in Fig. 5 for optimised thick film filter B from Fig. 4.

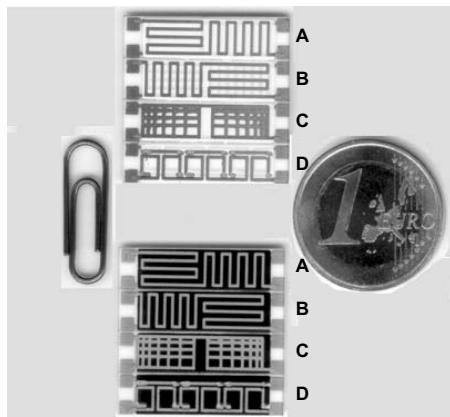


Fig. 4. Photograph of realized optimised planar thick film filters.

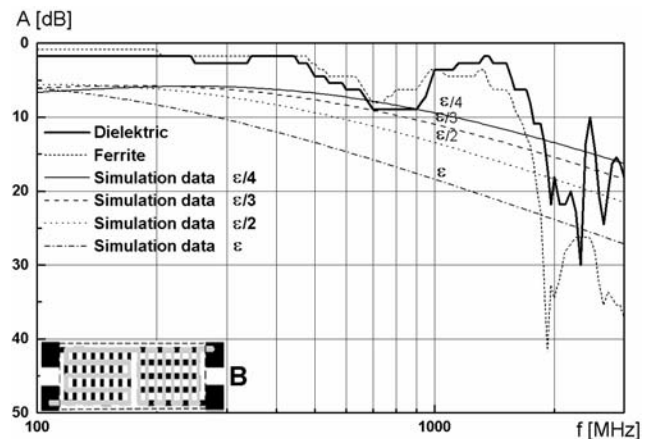


Fig. 5. Measured and simulated attenuation for optimised planar thick film filter B.

Fig. 5 shows the simulated and measured values of attenuation for optimised symmetrical planar thick film filter B. We compared the influence of dielectric middle layer for dielectric constants of interest.

The equivalent circuit analysis shows the contribution of the magnetic film to the optimised planar thick film filter. By applying the magnetic film to the dielectric middlelayer filter attenuation was increased from 1 to 3 GHz.

Conclusion

Filters from EMI suppression have been fabricated using magnetic and dielectric materials that have good properties and can be incorporated into a thick film process without any additional technological steps. The use of advanced functional modules illustrate that it is necessary to have suitable CAD software that can handle with technological and geometrical demands.

Characteristics of the asymmetric filters are measured and investigated. Further extensions may also allow realisation of novel filter that consist of series combination of presented asymmetrical filters as was done for symmetrical filters. Wider bandwidths can be obtained using more than two asymmetrical thick film filters. Desired attenuation characteristic will be achieved using this optimised structure. The results of this work will be published at a latter date.

Acknowledgement

The authors of this paper have, along with a number of Serbian partners, spent the last few years working on a Serbian Ministry of Science, Technology and Development funded project, ETR.6.04.32023B. The authors highly appreciate the important support of the Republic of Serbia.

References

- [1] S. Norlyng, "An overview of integrated component technologies", *Advanced Microelectronics*, vol. 30, no. 3, pp. 9-13, 2003.
- [2] V. Desnica, Lj. Živanov, O. Aleksić, "The modeling and de-sign of symmetrical thick film EMI/EMC cells", *Studies in Applied Electromagnetics and Mechanics: Electromagnetic Fields in Electrical Engineering*, vol. 22, pp. 395-400, IOS Press, Amsterdam, 2002.
- [3] O. Aleksić, V. Desnica, M. Luković Lj. Živanov, "Thick film symmetrical EMI LC cells", *Microelectronics International*, vol. 19, no. 2, pp. 19-25, 2002.
- [4] V. Desnica, Lj. Živanov, M. Nimrihter, O. Aleksić, M. Luković, "A Comparative Characteristics of Thick Film Integrated LC Filters", *IEEE Transactions on Instrumentation and Measurement*, Vol. 51, no. 4, pp. 570-576, August 2002.
- [5] V. Desnica, Lj. Živanov, O. Aleksić, M. Luković, L. Lukić, "Symmetrical Two-port Integrated Thick Film Filters", *Inter-connection and Packaging Symposium IMAPS 2002 Proceedings*, pp. 312-316, Cracow, Poland.
- [6] Desnica, V., Živanov, Lj., Aleksić, O. (2002), "Symmetrical thick film EMI/RFI filters", *23rd International Conference on Microelectronics MIEL 2002*, Niš, Yugoslavia, vol. 1, pp. 361-364.
- [7] M. Yamaguchi, Ki Kim, T. Kuribara, "Thin-film RF noise suppressor integrated in a transmission line", *IEEE Trans. on Magnetics*, vol. 38, no. 5, pp. 3183-3185, 2002.

5. ACTIVE SHIELDING OPTIMISATION

Ph. Dessante, J.C. Vannier, B. Bonafos

Supelec EEI, 91192 Gif/Yvette, France, philippe.dessante@supelec.fr

Abstract: – This paper describes the analysis and the optimisation of an active shielding. The shield is designed for space application. A comparison of the performances of two magnetic shields is first used to have a point of comparison. The second shield is 2 times thicker than the first. A Finite Element Analysis of the cylindrical metallic shield in a 1 Gauss flux density is performed in 2D. An active shielding is achieved by placing coils around the cavity inside the thinner shield. Another FEA is made to explore the effect of each coil when they are fed with a current density of 1A/m^2 . An optimisation method is used to establish the best current density to apply in the coils to neutralise the exterior magnetic field in the inner cell. Finally an introduction to multiple shells shielding is given.

1. Introduction

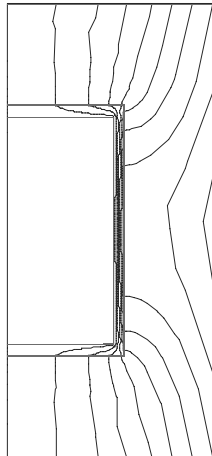


Figure 1. Thin Shield

The goal of this study is to shield an apparatus from an exterior magnetic field. As the apparatus will be finally dedicated to an application aboard a satellite, the mass of the system is a very critical parameter. A first system is presented where we compare two shields of different thickness. We define then the characteristics of an active shielding and finally we introduce double shell shielding. The performances of these different systems are discussed.

2. Standard shield analysis

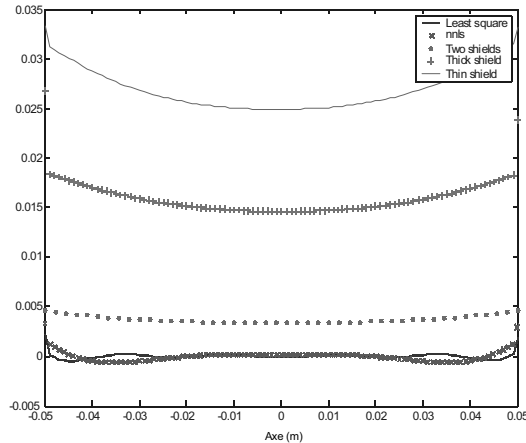


Figure 2 Comparison of shielding methods. Residual flux density on the axis $y=0$

The shields analysed here are cylindrical and a typical model is shown in the figure 1. They are excited by and applied external flux density of 1 Gauss. The efficiency of the shielding is estimated with level of internal residual field on the axis. The first shield is made with magnetic material whose thickness is 5mm and the relative magnetic permeability value is 1000. The residual magnetic field is evaluated by FEA, as shown in figure 2, its value at the centre of the cell is 25mG . The other shield with the same permeability and a thickness of 1cm give a residual field whose value is 14mG at the centre of the cell. On the other side a sensibility analysis shows that the attenuation factor should vary proportionally with the thickness of the shield. These results prove the validity of this analysis. Unfortunately the weight of the shield varies with the thickness too.

3. Active shield analysis

To limit the weight augmentation and to increase the axial attenuation factor of the shield, we propose the use of coils to neutralise the external axial flux density excitation. The coils are located in the inner cell of the shield and are cylindrical. We have to define the right current distribution in a given number of coils.

3.1 Effect analysis of each coil

The first step of this active shielding optimisation is to analyse the effect of each coil on the induction. We apply successively in each coil a current density of 1A/m^2 . The resultant induction on the axis is shown in figure 3. The induction is superposable, here with no saturation, so we can put different currents in each coil to neutralize the exterior magnetic field. This is done by a least square optimisation to optimise the attenuation factor by searching the current density distribution in each coil.

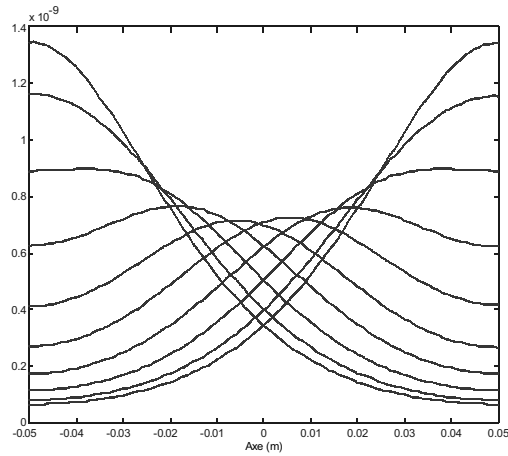


Figure 3. Effect analysis of each coil separately. Flux density on the y-axis = 0

3.2 Least square optimisation

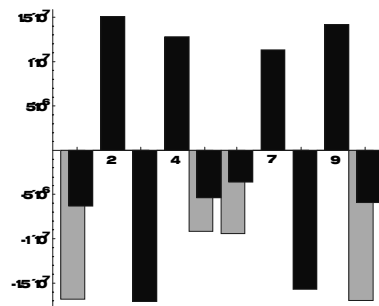


Figure 4. Currents applied to the coils. Black: standard least square, grey : *nls*

With the data of the induction distribution of each coil, it is possible with a least square fit to try to neutralize the external axial excitation flux density. Two methods are presented, the first use a least square minimisation, in this case the current densities can be positive or negative. The second use a *non negative least square (nls)* minimisation; in this case the current densities are of the same sign. Evidently the first method give the best result in term of shielding, but it can be difficult to have a small apparatus to deliver positives and negatives currents. A typical current distribution in each coil is given for the two methods in the figure 4.

3.3 Results

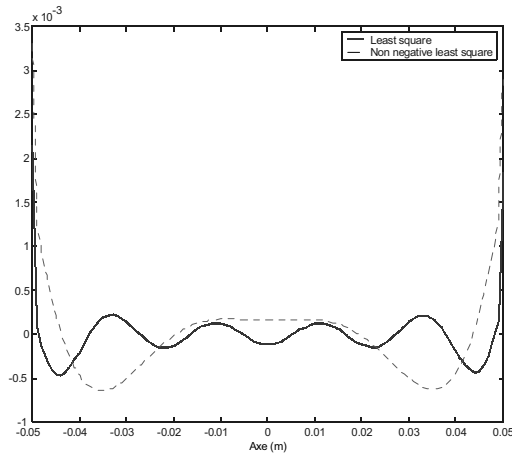


Figure 5. Ten coils. Residual flux density on the y-axis = 0

Figures 5, 6, 7, show the residual flux density distribution on the axe for respectively 10, 30 and 50 coils. In each figures are reported the resultant induction for *nmls* and standard least squares. Let's introduce some results:

- The shielding for standard least square optimisation is always more efficient than *nmls*.
- The attenuation factor increase with the number of coils for standard least square optimisation.
- The attenuation factor is almost constant with the augmentation of coils for *nmls* optimisation. This is explained as we can see in the figure 4 that the distribution of current in the coils is distributed in only three regions: each border and the centre. This distribution doesn't vary with the number of coils.

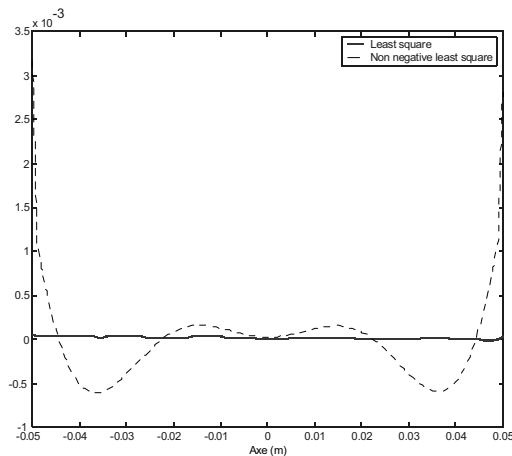


Figure 6. Thirty Coils. Residual flux density on the y-axis = 0

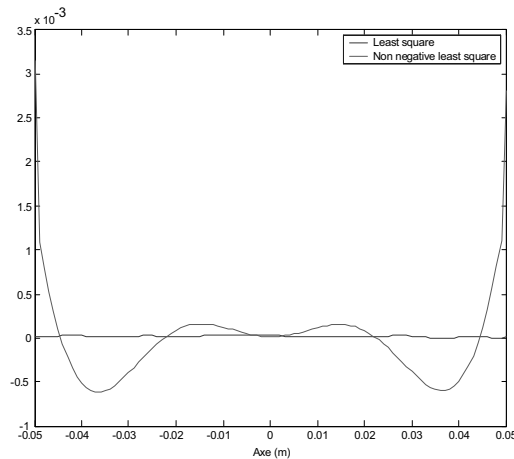


Figure 7. Fifty coils. Residual flux density on the y-axis = 0

3.4 Multiple shells

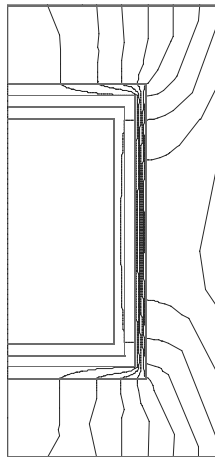


Figure 8. Double shells shield

Another method to shield this apparatus is to use multiple shells of shielding material. An example is given in the figure 8 with the resultant line field. The induction on the axe is shown altogether with the other methods in figure 2. The figure 9 shows the induction at the centre of the shield in function of the distance of the two shells. This distance is indicated in abscises by the rapport of gap distance over the thickness of the shield (supposed constant). We can see that there is an extremum for the attenuation factor located between a distance between 6 and 8 times the thickness of the shell. We will explore this study in a further article.

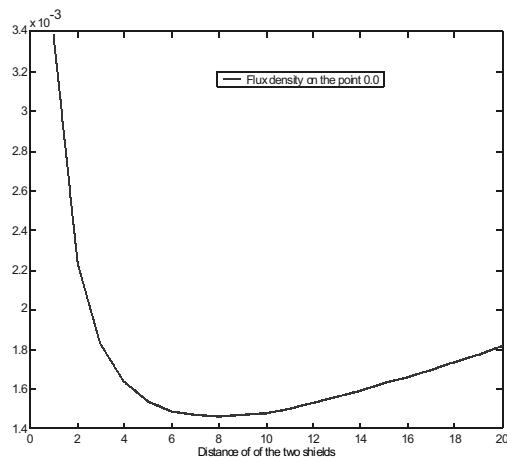


Figure 9. Flux density in function of the shield's distance.

4. Comparisons and conclusions

As shown in figure 2 the best attenuation factor is given by the active shield. It's far better the double shell shield presented in the precedent section, and much better than the simple shield. Moreover the weight of shield itself and the coils is less than the necessary iron to achieve the same shielding with a standard or double shield. In this study we have shown the efficiency of coupling a standard iron shield with electrical coils to realise an active shield. The obtained attenuated factor is around 4000 with the active shield, while with the thick shield it is around 70. The weight of the active shield is lower if we do not consider the supply circuit. The further study will be to compare with multiple shells of shields.

References

- [1] A.J Mager, *Magnetic Shield*, *IEEE Transactions on Magnetics*, Vol. MAG-6, N°1, pp 67-75, 1970
- [2] F. Schweizer, *Magnetic Shielding Factors of a System of Concentric Spherical Shells*, *Journal of Applied Physics*, Vol. 33 number 3, pp 1001-1003, 1962
- [3] D.U. Gubser, S.A. Wolf and J.E. Cox, *Shielding of longitudinal magnetic fields with thin, closely spaced, concentric cylinder of high permeability material*, *Rev. Sci. Instrum.*, Vol. 50(6), pp 751-756, 1979
- [4] A. Mager, *Magnetic shielding efficiency of cylindrical shells with axis parallel to the field*, *J. Appl. Phys.*, Vol. 39, p 1914, 1968
- [5] B. Bonafos, Ph. Dessante, J.C. Vannier, *Analysis and Parameter Identification of a PM linear actuator for Space Application*, ISEM 2003, pp 252-253, 2003

I-6. COST-EFFECTIVE OPTIMAL DESIGN OF SCREENS IN POWER TRANSFORMERS

P. Di Barba¹, M.E. Mognaschi¹, A. Savini¹, J. Turowski²

¹Department of Electrical Engineering, University of Pavia, I-27100 Pavia, Italy

e-mail: di_barba@etabeta.unipv.it

²Institute of Mechatronics and Information Systems, Technical University of Lodz, 90-924 Lodz, Poland

Abstract – The Reluctance Network Method, which has already proven to be very fruitful for the 3D analysis of power transformers, is here proposed to design screen and tank in order to fulfil two conflicting objectives: to minimize power losses and tank volume. It is shown how non-dominated design geometries follow from fast magnetic analyses carried out by the reluctance network method.

1. Introduction

It is well known that many important phenomena in power transformers are strongly connected with leakage field distribution which, in turn, depends on the ratio of distances of tank wall a_t and core limb a_c from the interwinding gap, respectively, and also on the thickness d of the screen covering the tank wall [1]. In fact, the stray flux in the interwinding gap is almost constant, only the flux to the core and the flux to the tank wall vary, when tank distance or screen are changed [2] [3].

In particular, in the case of electromagnetic screens, the screening effect gives rise to a conflict of design objectives: on one hand, the flux entering into the core limb is increased with respect to the flux into the tank wall; on the other hand, axial forces and additional losses from the radial component of flux density in the LV winding are increased too. Moreover, when distance between windings and tank increases, power losses in tank decrease, but volume and cost of the whole device are increased in turn.

Moving from this background, the shape design of the screen could be tackled in a systematic way in terms of the identification of the non-dominated solutions, namely the set of solutions such that no decrease of an objective is possible without a simultaneous increase of the other objectives [4]. More specifically, the inverse problem could be stated e.g. as follows: starting from a set of feasible geometries, identify the corresponding non-dominated geometries, such that power losses are minimum and tank volume is minimum too (two-objective shape design).

In the case of a single screen, three design variables can be selected, namely: radial position, height and thickness of the screen itself. In order to meet the requirement of a rapid-design method for industrial environment, the following computational scheme is adopted: given a prototype transformer, a sequence of fast magnetic analyses, based on reluctance-network method, is performed first, by varying the design variables in the feasible design space. Then, the solutions so obtained are sorted in the objective space according to the definition of non-dominated solutions. As a result, an approximation of the set of best-compromise design is identified without the use of a time-consuming optimisation algorithm linked e.g. to a finite-element solver.

2. Case study

A three-phase transformer with tank is considered; its geometric and electric data are summarized in Tab. I and Fig.1; the transformer is symmetrically placed inside the tank.

Rated power S [MVA]	240
Rated current I_{HV} [A]	346.41

Tab. I. Transformer data.

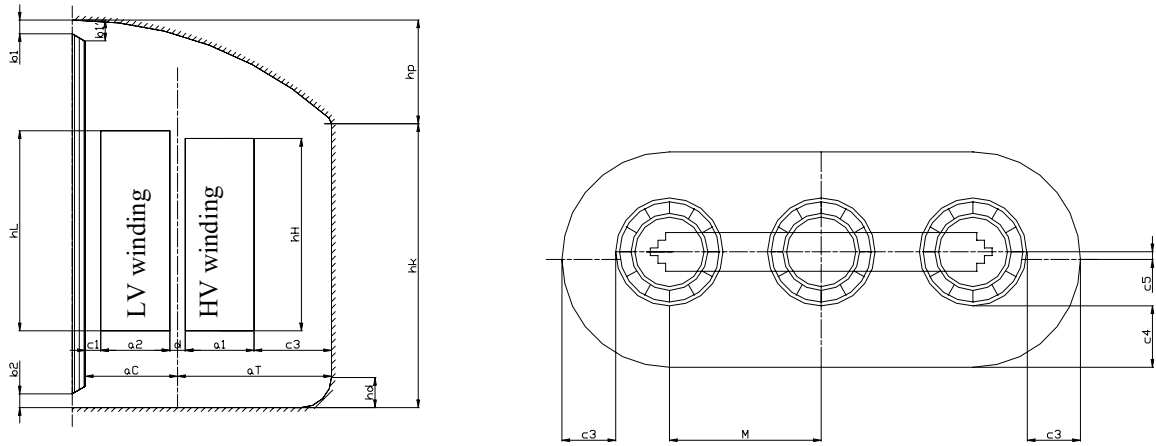


Fig. 1. Vertical (left) and horizontal (right) cross-section of transformer.

For the purpose of magnetic analysis, the transformer is discretized by means of the three-dimensional reluctance network shown in Fig.2, taking into account the magnetization curve of steel by means of an analytical approximation [7].

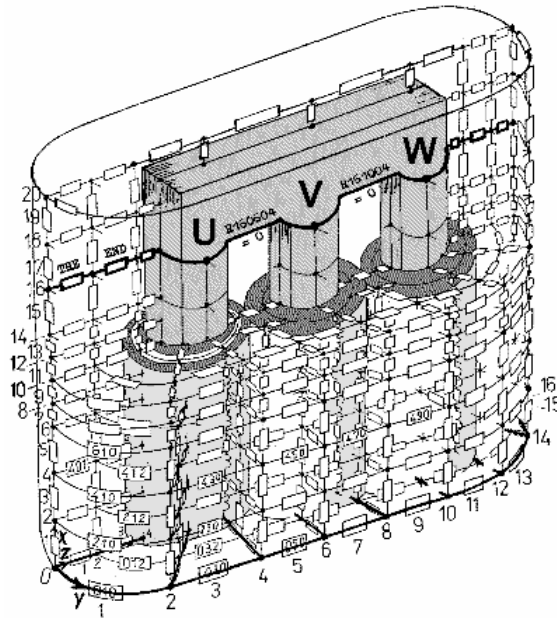
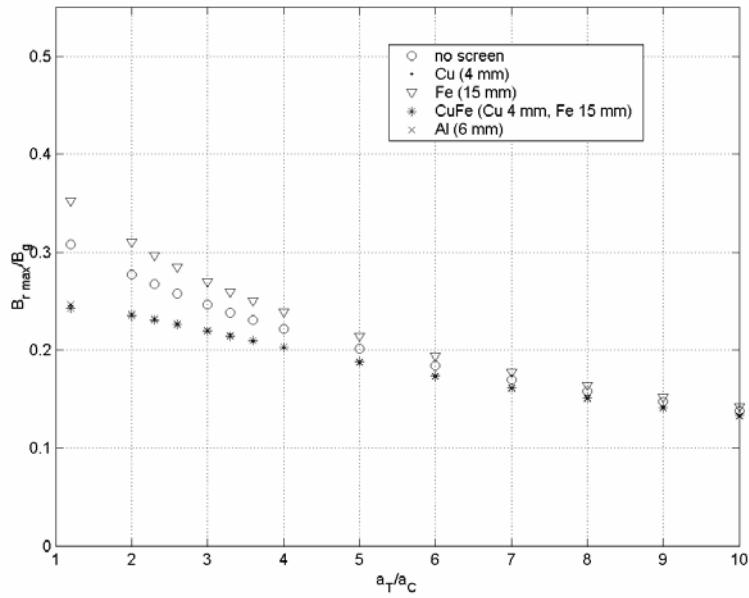
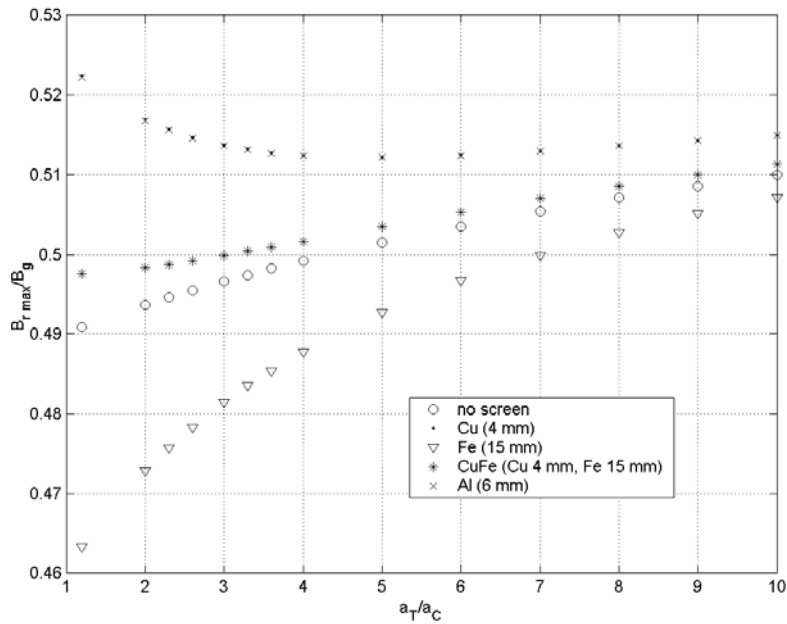


Fig. 2. Reluctance network discretizing the device [5].

3. Results

All results have been obtained using the code RNM-3D [5] referring to the device described above; local quantities have been considered first. In Fig.3 and Fig.4 the flux density ratio $B_{r \max} / B_g$ is plotted against the distance ratio a_t / a_c of the interwinding gap from the tank and the core, respectively. The former is referred to the HV winding, while the latter to the LV winding. $B_{r \max}$ is the maximum value of radial flux density along the winding at $y=0$ (see Fig.2) while B_g is the flux density supposed to be constant at the interwinding gap at $x=0$. The effect of different materials of the screen is compared, considering a full-height screen with various thickness.

Fig. 3. Radial flux density along HV winding at $y=0$ vs distance ratio a_t / a_c .Fig. 4. Radial flux density along LV winding at $y=0$ vs distance ratio a_t / a_c .

Ratios $B_{r,max} / B_g$ and a_t / a_c can be considered as indexes of performance and cost, respectively; in fact, the former is proportional to the axial force exerted on a winding, while the latter is related to the tank volume [1]. By comparing Fig.3 and Fig.4 a conflict between the two windings of the same phase arises. In fact, for a given value of a_t / a_c , in the HV winding the radial flux density in the case of magnetic screen is higher than in the case of no screen, while in the LV winding the corresponding radial flux density is lower than the in case with no screen. Conversely, in the case of electromagnetic screen the radial flux density in the HV winding is lower than in the case of no screen, while the radial flux density in the LV winding is higher than in the case of no screen.

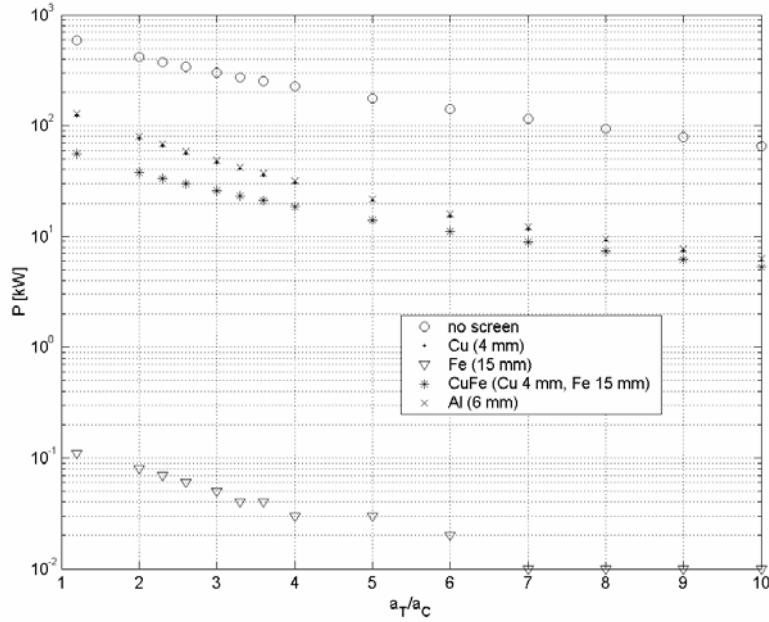


Fig. 5. Power loss vs distance a_t / a_c: effect of screen material.

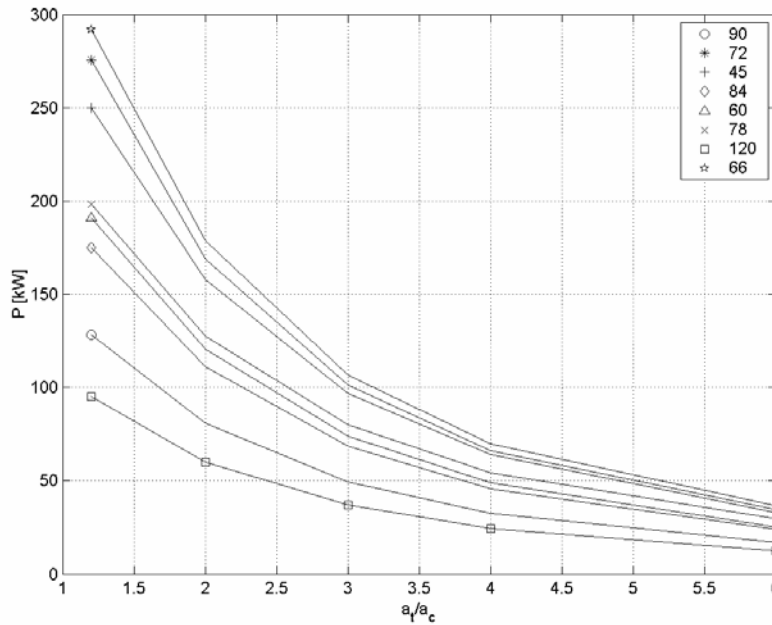


Fig. 6. Power loss vs distance ratio a_t / a_c for different costs of an Al screen.

Moving from fields to global quantities, in Fig.5 the power loss in tank and screen is plotted against the distance ratio of the tank, comparing different materials for a full-height screen of variable thickness. Again P and a_t/a_c may be considered as indexes of performance and cost, respectively; therefore, curves represented in Fig.5 may be regarded as sets of non-dominated curves by varying the screen material.

Finally, in Fig.6 the effect of screen cost is investigated for an Al screen; the (dimensionless) cost is proportional to the product of screen thickness times its height; given a cost, there are several possible combinations of thickness and height, each of which has a different screening effect. Results of repeated analyses are represented as power loss in tank and screen against distance ratio of the tank, each curve corresponding to a given screen cost. For thickness and height of the screen are

independent variables, the curves shown in Fig.6 cannot be ranked monotonically with respect to the resulting screen cost. Best-compromise solutions can be identified by selecting the non-dominated curve, *i.e.* the one such that no reduction of power loss is possible without a simultaneous increase in the tank volume. Non-dominated curve corresponds to the curve of maximum screen cost; in particular, it is meaningful to extract the points located along it as shown in Tab. II, where they have been ranked from the solution of minimum tank volume to the solution of minimum power loss.

a_t/a_c	power loss [kW]	screen thickness [mm]	screen height [mm]
1.2 (minimum tank volume)	95.35	8	4200
2	60.06		
3	36.85		
4	24.33		
6	12.54 (minimum power loss)		

Table II. Example of best-compromise design.

Moreover, the distribution of specific power on the tank wall has been investigated for both solutions outlined in Tab. II; no hazard of local over-heating has been detected.

4. Conclusion

The RNM-3D code, based on non-linear reluctance network method in three dimensions, has proved to be an effective tool for fast analysis of power transformers, with accuracy and runtime fulfilling the requirements of industrial design. Moreover, the use of this kind of computational tool makes it practical to apply the concept of non-dominated solution to the shape design of the transformer screen, considering design criteria that may be in conflict.

The problem solved has considered a single and continuous screen. Usually screens are not continuous, are laminated and are located in various positions depending on flux concentration and distribution. Their optimisation is a more complicated and challenging problem for which, however, it is believed that RNM can turn out to be a profitable tool again.

References

- [1] A. Savini and J. Turowski, Influence of structure geometry, screens and eddy currents on the critical distance of tank wall in power transformers. In: A. Savini and J. Turowski (Editors), *Electromagnetic Fields in Electrical Engineering*, New York, Plenum Press, 1988.
- [2] D.A. Koppikar, S.V. Kulkarni and J. Turowski, Fast 3D interactive computation of stray field and losses in asymmetric transformers. *IEE Proceedings, Gener. Trans. Distrib.*, vol.147, no.4, 2000.
- [3] J. Turowski, I. Kraj and K. Kulasek, Industrial verification of rapid design methods in power transformers. *Proc. TRANSFORMER'01*, Bydgoszcz, Poland, 2001.
- [4] P. Di Barba, A fast evolutionary method for identifying non-inferior solutions in multicriteria shape optimization of a shielded reactor, *COMPEL*, Vol.20, No.3, pp.762-776, 2001.
- [5] J. Turowski, M. Turowski et al, Method of three-dimensional network solution of leakage field of three-phase transformers, *IEEE Trans. on Magnetics*, vol.26, pp.2911-2919, September 1990.
- [6] J. Turowski, M. Kopec, M. Turowski, Fast 3-D analysis of combined Cu and Fe screens in three-phase transformers, *COMPEL*, pp. 113-116, 1990.
- [7] J. Turowski, *Reluctance Networks*, In: J.K. Sykulski (Editor), *Computational Magnetics*, London, Chapman & Hall, 1995.

I-7. A COMPARISON OF ERROR ESTIMATORS FOR ADAPTIVE MESH REFINEMENT FOR ELECTROMAGNETIC 2D/3D PROBLEMS

Konstanty Marek Gawrylczyk, Fawwaz Alkhatib

Chair of Theoretical Electrotechnics and Computer Science, Technical University of Szczecin
70 – 313 Szczecin, St. Gen. Sikorskiego 37, Poland E-mail: kmg@ps.pl , fawwaz@ps.pl

Abstract: – To obtain a high accuracy solution from the finite element method the mesh should be suitable to the field distribution. Adaptive mesh refinement offers an automatic way to generate meshes fitting the problem. An a posteriori error estimation has a key role in the adaptive mesh refinement, since the accuracy of the solution depends on how effective is it in locating elements with larger local error. In this paper different error estimation techniques for 2D and 3D cases are discussed. A comparison was made between them to show the effectiveness of the estimators.

Introduction

Adaptive techniques has been proved to be a necessary tool for the numerical treatment of partial differential equations (PDE) with FEM. In order to reduce the size of the arising computational effort, work is put only into subregions where a large local error of the current discrete solutions assumed. The adaptive algorithm uses two types of error estimation, namely *a priori* and *a posteriori* error estimators.

The shape of the element is of great importance. At the beginning or after of solving the problem some poorly shaped elements could exist in the mesh. This may make further refinement impossible, which affects directly the accuracy of the solution. To locate these elements, an *a priori* error estimator exploiting the geometrical properties of the element is used. Then using some topological transformations techniques the quality of the elements can be improved.

In order to increase the accuracy of the FE solution, the mesh should be suitable to the field distribution. So the number of elements should be increased in some regions to fit the field behavior. A locally working *a posteriori* error estimator is used to identify the subregions of high discretization error. Then elements within these subregions are refined. Many such estimators are known, as well as their theoretical foundation. The most crucial part of an adaptive FE computation is the availability of an efficient and reliable error estimation technique to predict accurately the error in the solution. In this paper different error estimators were implemented to the adaptive algorithm. Test problems in 2D and 3D were considered. A comparison was performed between the results of these error estimators to show the efficiency. The criteria of comparison are the reduction of the error in energy norm

A priori Error Estimation

This type of error estimation is performed before a numerical computation to enhance the quality of the mesh. Because no solution is known, geometrical properties, such as shape of a finite element of the mesh, are chosen to estimate the quality of discretization [1]. The quality factor of the generated elements according to Lindholm [2] is obtained for 2D, 3D elements as following:

$$2D: Q = 2 \cdot \frac{r}{R}, \quad 3D: Q = 3 \cdot \frac{r}{R} \quad (1)$$

r – the diameter of the inscribed circle (2D) or sphere (3D) in the element

R – the radius of the circumscribed circle (2D) or sphere (3D) on the element

The quality factor of an element is 0 if the element is degenerated to a line segment and 1 if it is regular. In order to get a better picture of the quality of the generated mesh, a quality factor for the mesh is calculated as the arithmetic mean of the quality factors of the elements. This mean is defined by:

$$Q_m = \frac{1}{NE} \cdot \sum_{i=1}^{NE} Q_i \quad (2)$$

where: NE – number of elements.

Mesh Modification

The adaptive mesh generation is started with a coarse mesh which represents the geometrical properties of the model. The mesh refinement scheme chosen in the algorithm is the edge-based refinement, i.e. new nodes are inserted along the edges of the element. Using this scheme of mesh refinement the number of new elements per refined element is high (Fig. 1)

The subdivision of elements produces poorly shaped elements that cause the numerical solution to be less accurate and more difficult to compute. That is bad conditioning of stiffness matrix [5] and the shape functions cannot approximate the continuous quantity with accuracy [6]. Therefore, an algorithm consisting of different smoothing techniques was used to improve the shape of distorted elements. These techniques are:

1. Node relaxation : in 2D case each node that has no fixed position, not being a node on the external boundary or on the interface between different media, can be moved to a new position which is the centroid of the polygon, formed from its neighboring nodes [6]. In 3D case it is extension of the 2D case. The new position of the node is the centroid of the polyhedron. In some cases the new position of the node may be outside the space of the polyhedron, so a check must be applied to avoid misshapen and overlapping tetrahedra [7].
2. Swapping diagonals : in 2D case the algorithm applies swapping diagonals on elements. Basing on Delaunay criterion i.e. circle criterion [6]. In 3D case this technique can be employed only in the case when the two faces lie on the same surface[7].
3. Local mesh reconfiguration : there are two techniques: face swapping and edge swapping. Face swapping reconnects the tetrahedra separated by a single interior face[3]. So, two tetrahedra can be transformed to 3 and vice versa. Edge swapping reconfigures N tetrahedra incident on the longest edge of the mesh by removing that edge and replacing the original N tetrahedra by $2N - 4$ tetrahedra. This reconfiguration is performed only if every new tetrahedron has better quality than the worst of the N original tetrahedra[3].

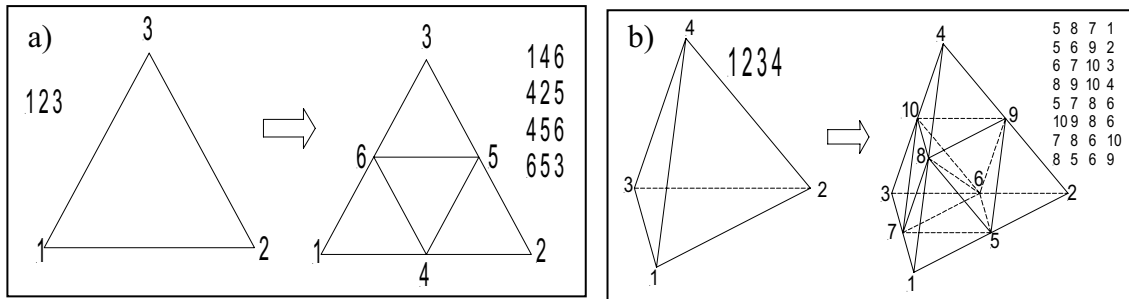


Figure 1. Subdivision of element: a) 2D b)3D

A posteriori Error Estimation

An *a posteriori* error estimator evaluates the local error e_k per element, based on a previously computed solution. To obtain a local error between 0 and 1, it is normalized, i.e. divided by maximum error over all elements in the mesh.

$$\varepsilon_k = \frac{e_k}{\max(e_k)} \quad (3)$$

A maximum accepted local error $\varepsilon_{\text{local}}$ (e.g. 10%) can be specified by the user and all elements with a larger error bound are considered for refinement [1].

Flux density and refraction of the field lines on the interface between elements is used as error indicators.

The flux density in the element can be estimated by two ways:

1. Flux density at a node : The magnetic flux density $\mathbf{B}_{n,i}$ at a node i is the weighted average of the values of the magnetic flux density $\mathbf{B}_{e,k}$ of the surrounding elements k belonging to the same label. The weighting factor in 2D is the area Δ_k of the elements [1] and in 3D is the volume of the elements.

$$2D: B_{n,i} = \frac{\sum_{k=1}^N B_{e,k} \cdot \Delta_k}{\sum_{k=1}^N \Delta_k}, \quad 3D: B_{n,i} = \frac{\sum_{k=1}^N B_{e,k} \cdot V_k}{\sum_{k=1}^N V_k} \quad (4)$$

The local error e_k of an element is calculated by:

$$2D: e_k = \left| B_{e,k} - \frac{\sum_{i=1}^3 B_{n,i}}{3} \right|, \quad 3D: e_k = \left| B_{e,k} - \frac{\sum_{i=1}^4 B_{n,i}}{4} \right| \quad (5)$$

2. Flux density in the surrounding elements : The magnetic flux density $\mathbf{B}_{n,i}$ in element i is the weighted average of the values of the magnetic flux density $\mathbf{B}_{e,k}$ of the surrounding elements k belonging to the same label. The weighting factor in 2D is the area Δ_k of the elements [5] and in 3D is the volume of the element.

$$2D: B'_{e,i} = \frac{\sum_{k=1}^3 B_{e,k} \cdot \Delta_k}{\sum_{k=1}^3 \Delta_k}, \quad 3D: B'_{e,i} = \frac{\sum_{k=1}^4 B_{e,k} \cdot V_k}{\sum_{k=1}^4 V_k} \quad (6)$$

The local error e_k of an element is calculated by:

$$e_k = \left| B_{e,i} - B'_{e,i} \right| \quad (7)$$

The second, *a posteriori* error, basis on the field intensity inside the elements. The field intensity lines in inhomogeneous environment, reveal an angle of refraction α at the interface between elements (Fig. 2). Angle of refraction is uses as an error indicator. It is calculated for each side of the element i between this side and its next element e by two ways:

1. by dot product :

$$\delta' = 1 - \cos \alpha = 1 - \frac{\mathbf{H}_i \cdot \mathbf{H}_e}{H_i \cdot H_e} \quad (8)$$

2. by vector product :

$$\delta'' = \sin \alpha = \frac{|\mathbf{H}_i \times \mathbf{H}_e|}{H_i \cdot H_e} \quad (9)$$

The local error e_k is then estimated for the element as mean of the δ'_{sm} or δ''_{sm} of the element sides as following:

$$2D: e_k = \frac{1}{3} \cdot \sum_{i=1}^3 \delta_{sm} \quad (10)$$

$$3D: e_k = \frac{1}{4} \cdot \sum_{i=1}^4 \delta_{sm}$$

The maximum accepted local error \mathcal{E}_{local} value will determine the elements to be refined.

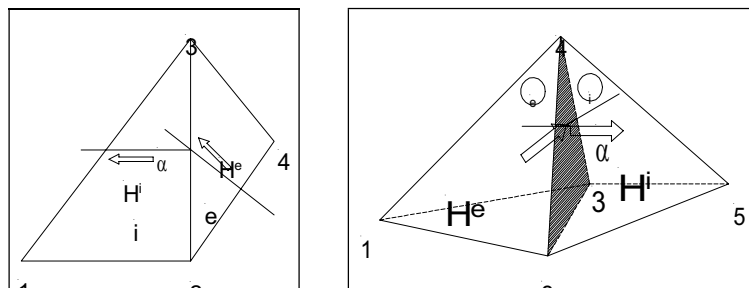


Figure2. Refraction of the field intensity lines at the interface between elements a)2D b)3D

Problems

A . 2D Problem:

As an example for the 2D case a simple magnetostatic problem has been chosen (Fig.3).

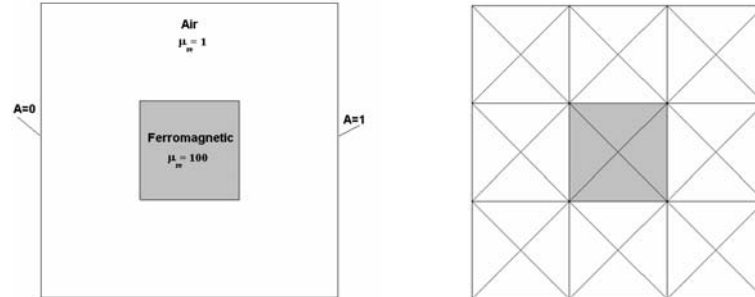


Fig. 3. 2D sample problem with initial mesh

The problem has been calculated up to 4705 nodes and 9126 elements, in order to compare the adaptive and uniform refinement (Fig. 4).

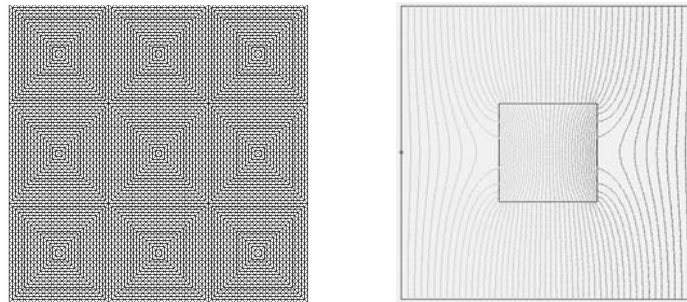


Fig. 4. Uniform refinement mesh and field lines

The adaptive refinement was performed using different *a posteriori* error estimators discussed above. The total energy of the model was chosen as a global error. The memory requirements is expressed by the number of nodes. Figure 5 shows the results for the uniform and the adaptive refinement. It can be clearly noticed, that the error estimators based on the flux density gives better results than these based on field lines refraction for this kind of problems. Figure 6 shows the adaptive mesh and the field lines using error estimators a) based on flux density from elements nodes, b) based on the refraction of the field lines (vector product)

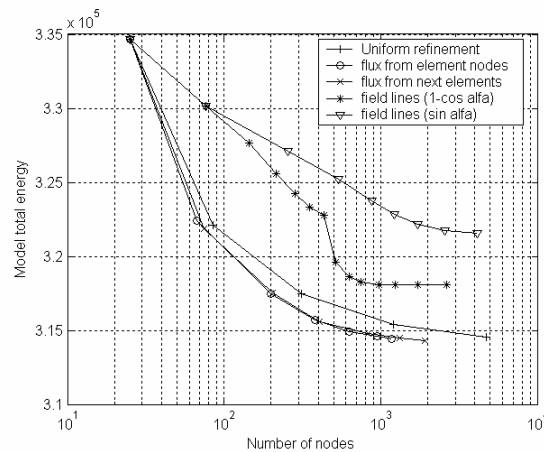


Fig. 5. Total energy of the model and the number of nodes for uniform and adaptive refinement

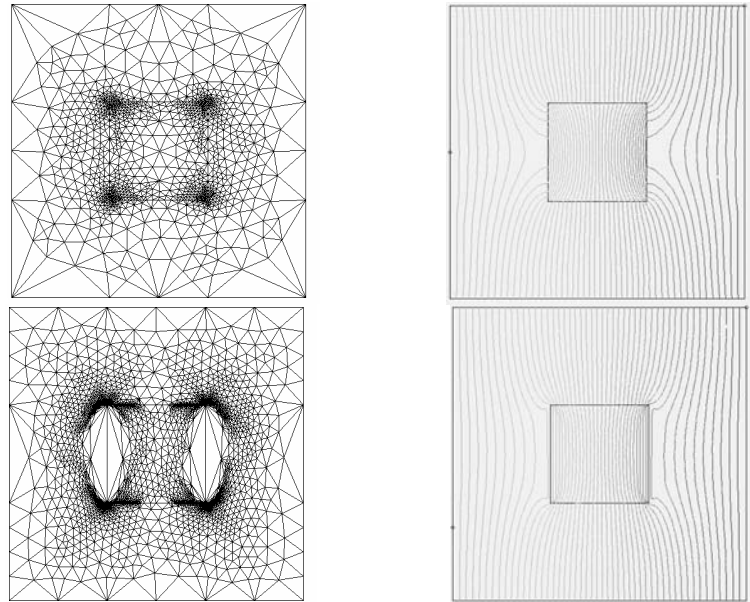


Fig. 6. Adaptive mesh and field lines using error estimators: a) based on flux density from the element nodes, b) based on the refraction of the field lines.

B. 3D problem

As an example for the 3D case an L-shape problem has been chosen. Figure 7 shows the surface view of the initial mesh with boundary conditions and the uniform refinement. The initial mesh has 33 nodes and 72 elements with a mean quality of 0.25, the uniform refined mesh has 7089 nodes, 36864 elements with a mean quality of 0.20.

Figure 8 shows the surface view of the adaptively refined mesh using error estimators a) based on flux density from next elements with 1771 nodes and 8716 elements and mean quality factor of 0.2, b) based on field lines refraction with 1874 nodes, 8868 elements and mean quality factor of 0.18.

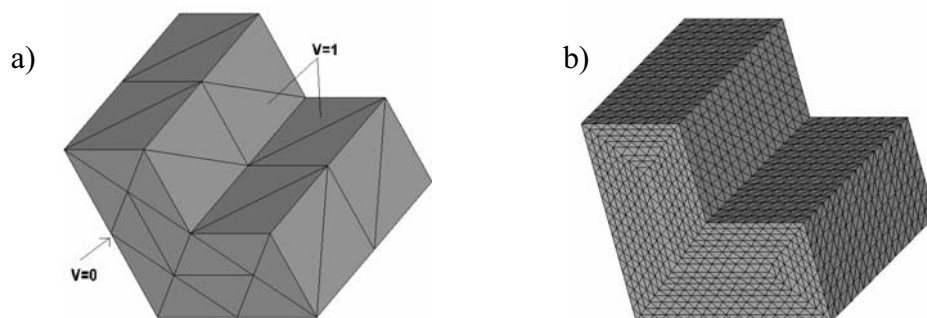


Fig. 7. Initial and uniform refined mesh for 3D sample problem

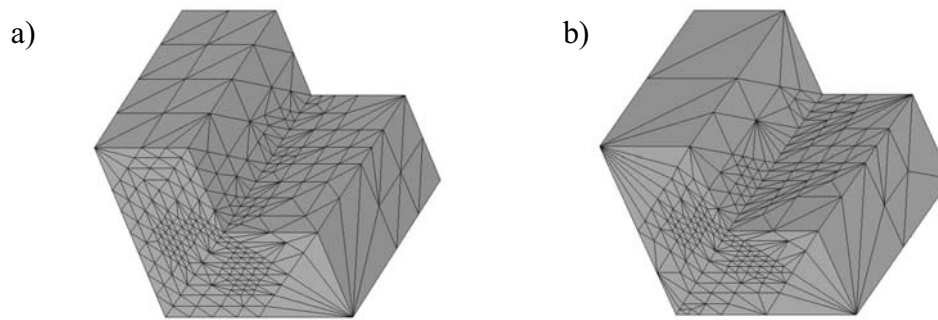


Fig. 8. Adaptively refined mesh using error estimators based on: a) flux density from next elements, b) field lines refraction

Conclusions

The effectiveness of the adaptive mesh generation has been examined for a 2D and a 3D example. For both cases, the adaptive refinement has shown significant advantages with respect to the accuracy of the solution and the computational effort (expressed by the number of the nodes). Weighing the parameter of refinement by the element area (2D) or volume (3D) gives good results. The reason behind this weighting is that the field in larger elements provide a greater contribution to the global error than the same error in a smaller element.

References

- [1] K. Hamyer, R. Belmans, Numerical Modelling and Design of Electrical Machines and Devices, Southampton, Boston: WITpress, 1999
- [2] D.A. Lindholm, Automatic triangular mesh generation on surfaces of polyhedra, IEEE Transactions on Magnetics, Vol. MAG-19, No. 6 pp. 2539-2542, 1983
- [3] L.A. Freitag, C. Olivier-Gooch, Tetrahedral Mesh Improvements Using Swapping and Smoothing, International Journal for Numerical Methods in Engineering, Vol. 40, pp. 3979-4002, 1997
- [4] K.M. Gawrylczyk, Quality and Optimization of Tetrahedral Finite Element Mesh, 18-th Seminar on Fundamentals of Electromagnetics and Circuit Theory, pp. 65-69, 1995
- [5] K.M. Gawrylczyk, Adaptiven Algorithmen auf Der Basis Der Methode Der Finiten Elemente, Prace Naukowe Politechniki Szczecińskiej, 1992
- [6] N.A. Goliias, T.D. Tsiboukis, Adaptive refinement in 2-D Finite Element applications, International Journal of Numerical Modelling: Electronic Networks, Device and Fields, Vol. 4, pp. 81-95, 1991
- [7] N.A. Goliias, T.D. Tsiboukis, Three- Dimensional Automatic Adaptive mesh generation, IEEE Trasaction on Magnetics, Vol. 28, No.2, pp. 1700-1703, 1992

I-8. MULTI-OBJECTIVE OPTIMIZATION OF PERMANENT MAGNET MOTOR USING TAGUCHI METHOD

K. Hot and P. Bodlovic

Electrical Engineering Dept., Polytechnic of Zagreb, Croatia, e-mail: khot@public.srce.hr

Abstract – The performance of permanent magnet motor can be improved by optimization of its magnetic circuit. That can be achieved by means of finite element method in torque calculation and statistical analysis using orthogonal arrays and multi-objective approach. The magnetic field was calculated taking into account non-linear density and effect of current commutation. The electromagnetic torque was determined from magnetic vector potentials of moving conductors. The effect of change for every geometric parameter was particularly calculated. A fast improvement in shapes of the motor magnetic parts was achieved by an appropriate number of field and torque calculations.

Introduction

The design and development of various electric machines include the methods of optimization described in [1] and some recent methods of genetic algorithm, experiment planning, quality engineering, etc. The design is governed by the aim of maximum efficiency in electromechanical energy conversion with minimum needs of material and space.

An optimal magnetic field distribution giving the acceptable local magnetic saturation and permanent magnetization is essential prerequisite in order to reach this aim. Such a field distribution can be achieved using appropriate optimization method together with numerical field calculation method and parametric sensitive geometric model. With presented methods and technique it is possible to calculate magnetic field and optimal shapes for arbitrary parts of a permanent magnet DC motor.

The well-known methods for optimization with or without constraints [1] demand a large number of field calculations to determine optimal magnetic field. Some of them include also very sensitive calculations of field derivatives searching for the most appropriate shape changes. During the optimization computation sequence one can't have real quantitative information on the effect of each parameter because of possible different paths of optimization procedure.

The parametric CAD modeling software can generate the geometry of the motor cross-section for determined values of chosen parameter set. The magnetic field analysis program calculates nonlinear FEM model prepared by CAD program and passes the electromagnetic torque values to an optimization procedure based on a method introduced by G. Taguchi and known from quality engineering [2,3].

The software package for a motor optimization usually contains three major parts: parametric (CAD) pre/post-processor, electromagnetic field (FEM) solver and numerical optimization program (TAM). The mathematical method and software accessories must fulfill the conditions outlined in recent papers [4, 5].

The governing equations included the space with permanent magnetization and nonlinear magnetic properties. Every solution of magnetic field was consisted of a stationary spatial distribution of the magnetic vector potential. The electromagnetic torque was calculated directly from vector potential difference of a conductor according to [6]. The procedure of Taguchi method was adopted for this particular problem and shown with an orthogonal array including 25 consecutive experimental calculations. The main equations, figures and diagrams for calculated PMDC motor are presented and can be compared with recent results [7, 8].

Orthogonal Array and Objective Functions

We choose a set of field calculations where we change the settings (levels) of the parameters we want to study from one calculation to another. The data from all calculations in the set taken together are analyzed to determine the effects of the various parameters.

The use of special matrices called orthogonal arrays [2, 3] allows the effects of several parameters to be determined very efficiently. As the name suggests, the columns of an orthogonal array are mutually orthogonal. Consider the linear form $L_i = w_{i1} \cdot \eta_1 + w_{i2} \cdot \eta_2 + \dots + w_{ik} \cdot \eta_k$ which is a weighted sum of k calculations. Recall that the linear form L_i is called a contrast if the weights add up to zero ($w_{i1} + w_{i2} + \dots + w_{ik} = 0$). Two contrasts, L_i and L_j , are said to be orthogonal if the inner product of the vectors corresponding to their weights is zero ($w_{i1} \cdot w_{j1} + w_{i2} \cdot w_{j2} + \dots + w_{ik} \cdot w_{jk} = 0$).

The orthogonality is interpreted in the combinatorial sense, i.e. for any pair of columns all combinations of parameter levels occur in an equal number of times. This is a balancing property that implies orthogonality.

The columns of the standard orthogonal arrays are commonly arranged in increasing order of the number of changes. The number of times the level of a parameter has to be changed in running the calculations in the numerical order is less for the columns on the left when compared to the columns on the right. Hence we should assign a parameter whose levels are more difficult to change to columns on the left.

For optimization of electromagnetic torque a quadratic quality loss function can be used and a larger-the-better characteristic that has to be continuous and non-negative

$$L(y) = A_0 \cdot \Delta_0^2 \cdot (1/y^2) \quad (1)$$

where A_0 is the loss at the tolerance Δ_0 for variable y . We would like the characteristic to be as large as possible and we do not have any adjustment factor. The objective function to be maximized in this case is given by

$$\eta = -10 \cdot \log_{10} \left(\frac{1}{n} \cdot \sum_{i=1}^n \frac{1}{y_i^2} \right) \cong -10 \cdot \log_{10} \left[\frac{1}{\mu^2} \cdot \left(1 + 3 \cdot \frac{\sigma^2}{\mu^2} \right) \right] \quad (2)$$

where μ and σ are the mean and variance of the quality characteristics. As we need to focus our attention on (μ^2/σ^2) , it is common practice to call it signal-to-noise (S/N) ratio (because σ^2 is the effect of noise factors and μ is the desirable part of the calculated data) and take log transform to express it in decibels. For optimization for some other objective function (e.g. ratio of the motor weight to torque) a quadratic quality loss function can be used but with a smaller-the-better characteristic (continuous and nonnegative)

$$L(y) = A_0 \cdot \Delta_0^2 \cdot y^2 \quad (3)$$

We would like the characteristic to be as small as possible and we do not have any adjustment factor. The objective function to be maximized in this case is given by

$$\eta = -10 \cdot \log_{10} \left(\frac{1}{n} \cdot \sum_{i=1}^n y_i^2 \right) \quad (4)$$

If carefully modeled, one set of field calculations for chosen parameters can be used for optimization of more than one objective function which can be calculated from the field results. The total influence of the parameter change in its range can be calculated as design effect for every parameter. Hence, in the case of additional limitations one is free to choose another combination of parameters than that larger-the-better (or smaller-the-better) characteristic. The influence of every parameter can be recalculated per unit for the purpose of easier use in further design analysis.

In the particular case of electrical machine optimization four or five levels are necessary to ensure good approximation of parameter influence in nonlinear conditions. It means that 64 calculations for (up to) 21 parameters and 50 calculations for (up to) 11 parameters respectively have to be performed.

Magnetic Field and Torque

We want to optimize some of the main dimensions in a representative (middle) cross-section of a PMDC motor. The vector potential is defined by $B = \text{rot } A$. Using Stokes theorem in two-dimensional domain we obtain

$$\frac{1}{\partial x} \left(\frac{1}{\mu_y} \frac{\partial A}{\partial x} \right) + \frac{1}{\partial y} \left(\frac{1}{\mu_x} \frac{\partial A}{\partial y} \right) = -(J + J_m) \quad (5)$$

where J is real current density and J_m is an equivalent permanent magnet excitation through a current defined by

$$J_m = \oint (M_{0x}/\mu'_x + M_{0y}/\mu'_y) dl \quad (6)$$

Quasi-Poisson equation (5) is commonly solved by finite element method with prescribed boundary conditions. Assuming no change of energy storage in motor space due to losses, an infinitely small shift of the rotor $d\alpha$ will cause the change of conservative (magnetic) field energy that must be equal to the difference of electrical (input) energy and mechanical (output) energy

$$dW_m = u \cdot i \cdot dt - T_e \cdot d\alpha \quad (7)$$

The electromagnetic torque has to be independent on the current change during a very small shift of rotor and hence given by

$$T_e = -\frac{\partial W_m}{\partial \alpha} + i \cdot \frac{\partial \Psi}{\partial \alpha} \quad (8)$$

where $\Psi = u \cdot dt$ is a linked flux. The magnetostatic treatment of the field can be applied after any discrete shift of rotor and its energy and the linked flux are respectively

$$W_m = \frac{1}{2} \int_V \vec{A} \cdot \vec{J} \cdot dV \quad \text{and} \quad \Psi = l \cdot \sum_{j=1}^N \sum_{k=1}^{w'} (A'_{j,k} - A''_{j,k}) \quad (9)$$

where A' and A'' are respectively the average vector potentials of the left and the right hand side of a turn located in (two electrically nearly diametrical) slots, l is axial length of slots and $w' = w/N$ where w is total number of conductors and N is a total number of slots around the armature. If the winding has $2 \cdot a$ parallel branches and p poles, the voltage E_i induced during the shift $\Delta\alpha$ (rad) at speed n (rpm) is

$$E_i = \frac{p}{a} \cdot \frac{n}{60} \cdot l \cdot \frac{\alpha_p}{\Delta\alpha} \cdot \sum_{i=1}^w (A'_i - A''_i) \quad (10)$$

where α_p is the angle of a pole pitch. If current I is the only independent variable, a total electromagnetic torque is

$$T_e = \frac{p}{\pi} \cdot \frac{I}{2 \cdot a} \cdot l \cdot \frac{\alpha_p}{\Delta\alpha} \cdot \sum_{j=1}^N \sum_{k=1}^{w'} (A'_{j,k} - A''_{j,k}) \quad (11)$$

Optimization Procedure and Results

We have analyzed a PMDC two-pole motor with 12 armature slots and 192 turns. The magnets are longer than the armature to give some flux concentration. The yoke is also longer than the magnets to reduce yoke saturation. The characteristics of iron sheets, yoke and ferrite permanent magnets were smoothly interpolated according to manufacturer data. Many details of calculation were presented in [6]. Its magnetic field at load is shown in Fig.1 with material boundaries in the middle cross-section and geometry parameters we have chosen in advance. Parameter A is thickness of magnet holding part, B is housing thickness, C is tooth width, D is inner slope of tooth-tip overhang, E is thickness of the armature core and F is an angle of one half of the magnet.

Table 1: Parameters of motor geometry

Level #	1	2	3	4	5
A (mm)	0.00	0.40	0.80	1.20	1.60
B (mm)	3.15	3.40	3.65	3.90	4.15
C (mm)	4.00	4.50	5.00	5.50	6.00
D (deg)	0.0	5.0	10.0	15.0	20.0
E (mm)	7.00	8.00	9.00	10.0	11.0
F (mm)	59.5	61.5	63.5	65.5	67.5

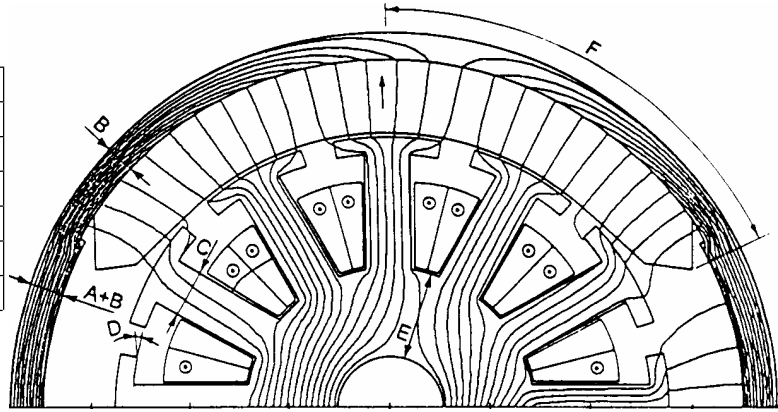


Fig. 1 Motor cross-section with geometry parameters

The parameter range is given in Table 1 for five levels in equal steps (mm or deg). The number of levels should be high enough to describe non-linearity in parameter changes. The parameter range has to be adequate to shape possibilities in manufacturing. The dimensions of permanent magnets (inner 57.0 mm and outer diameter 71.1 mm), shaft (10.5 mm) and air-gap (2 mm) were constant for the manufacturing reasons. The end regions of magnet were already shaped to minimize problems in current commutation and vibrations (plain part and angular end) and were not changed for the clarity of the example results, i.e. parameter F was changed by enlargement of middle part of magnet profile.

Table 2: Orthogonal array L_{25} with calculated torque and weight

Calc.#	A	B	C	D	E	F	t_e (p.u.)	w (p.u.)	t_e/w
1	1	1	1	1	1	1	1.000	1.000	1.000
2	1	2	2	2	2	2	1.105	1.097	1.056
3	1	3	3	3	3	3	1.208	1.197	1.062
4	1	4	4	4	4	4	1.307	1.300	1.038
5	1	5	5	5	5	5	1.399	1.406	0.997
6	2	1	2	3	4	5	1.207	1.181	1.071
7	2	2	3	4	5	1	1.261	1.248	0.949
8	2	3	4	5	1	2	1.201	1.166	1.072
9	2	4	5	1	2	3	1.277	1.248	1.057
10	2	5	1	2	3	4	1.279	1.205	1.088
11	3	1	3	5	2	4	1.222	1.145	1.110
12	3	2	4	1	3	5	1.299	1.229	1.093
13	3	3	5	2	4	1	1.211	1.293	0.967
14	3	4	1	3	5	2	1.212	1.255	0.999
15	3	5	2	4	1	3	1.276	1.173	1.126
16	4	1	4	2	5	3	1.233	1.280	0.997
17	4	2	5	3	1	4	1.296	1.197	1.113
18	4	3	1	4	2	5	1.295	1.151	1.153
19	4	4	2	5	3	1	1.207	1.213	1.029
20	4	5	3	1	4	2	1.322	1.305	1.019
21	5	1	5	4	3	2	1.227	1.238	1.012
22	5	2	1	5	4	3	1.225	1.197	1.054
23	5	3	2	1	5	4	1.301	1.287	1.046
24	5	4	3	2	1	5	1.367	1.207	1.159
25	5	5	4	3	2	1	1.281	1.264	1.030

There was no change in the electric circuit of the motor during the optimization procedure and a strongly stabilized voltage source was assumed. The magnetic field was evaluated under 25 shape conditions with parameters given in an orthogonal array (Tab. 2). The electromagnetic torque calculations were performed using eq. (11). The change of weight was calculated for magnetic active parts of the motor. Further analysis was performed by the statistical technique based on (2) and (4) to determine the contribution of each parameter.

The results for electromagnetic torque are presented as S/N ratio for every parameter at every level in Fig. 2. It is obviously that the inner slope of tooth-tip overhang D and armature core thickness E have smaller influence on electromagnetic torque than the other parameters. The influence of every parameter can be helpfully re-calculated per millimeter or per degree in design analysis according to Table 1. Hence, in the case of additional limitations one is free to choose another combination of parameters than the larger-the-better characteristic (levels A5, B5, C5, D4, E4 and F5) that gives maximum torque 1.060 Nm in an added calculation. The results for motor weight are presented as S/N ratio for every parameter at every level in Fig. 3 based on smaller-the-better calculation. The results for electromagnetic torque per weight of magnetically active motor parts are presented as S/N ratio for every parameter at every level in Fig. 4. The optimum of the design is at new parameter set (levels A4, B3, C2, D3, E1 and F5). The total influence of the parameter change was calculated as design effect for every parameter and given in Table 3.

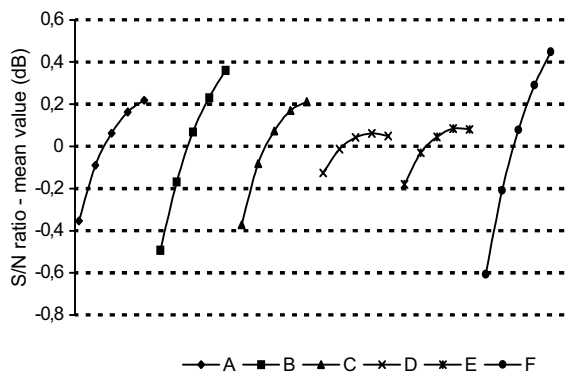


Fig. 2: S/N ratio of torque for parameter levels

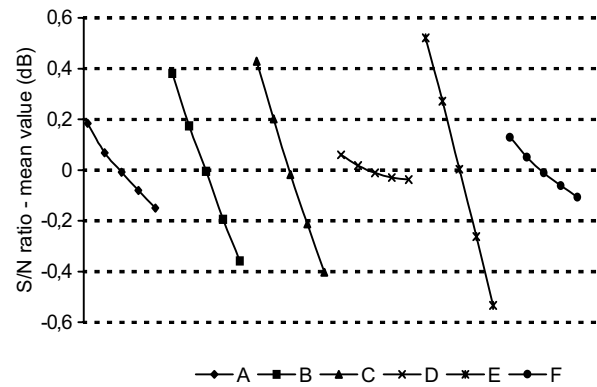


Fig. 3: S/N ratio of weight for parameter levels

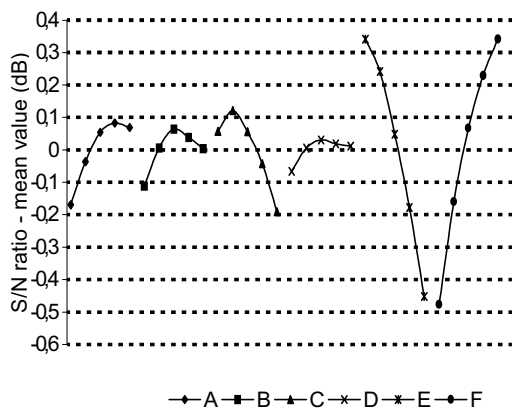


Fig. 4: S/N ratio of torque per weight

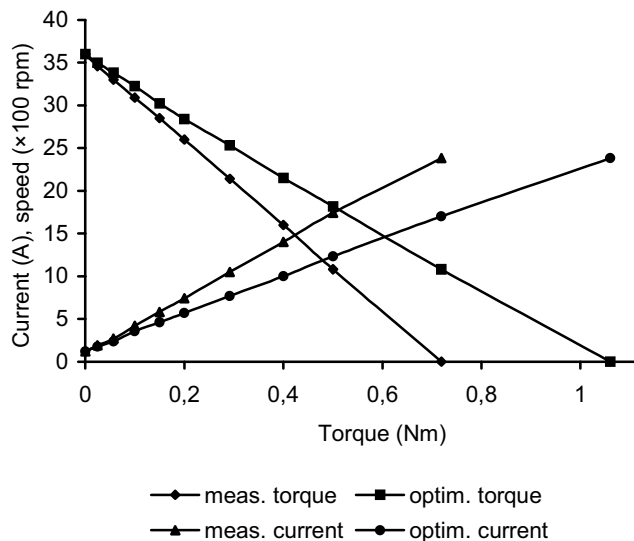


Fig. 5: Speed-torque and current-speed characteristics

Table 3: Parameter effects (%) for torque, weight and torque per weight calculation

Parameter	A	B	C	D	E	F
Electromagnetic torque	12.974	30.936	16.796	3.051	5.833	30.041
Weight of active parts	4.178	21.577	27.395	0.397	44.262	2.191
Torque per weight	4.596	1.871	6.129	0.061	42.688	44.105

The first result of optimization was maximum torque increase of 47% compared with starting shape where we had performed the measurements of speed and current at a full range of load (Fig. 5). The heating effect was obviously neglected at this stage of torque calculation but the characteristic was still

slightly non-linear. The losses at no-load condition were determined as a correlation between measured (mechanical torque on the shaft) and calculated (electromagnetic torque) values at initial geometry of motor cross-section. The second result of optimization was maximum torque per motor weight and parameter set strongly differs from previous one (A4, B3, C2, D3, E1 and F5).

Conclusions

The optimal geometry was determined by Taguchi method using the combination of values given in an appropriate table. Instead of a number of possible combinations for six parameters and five discrete values (levels) for each of them ($5^6=15625$), one had to consider only 25 patterns defined by L_{25} orthogonal array. The optimal shape had to be selected from given patterns in 25-dimensional design space. The effect of each parameter change was estimated by means of FEM calculation and Taguchi method from the point of view of quality engineering. Signal-to-noise (S/N) ratio for each calculated combination of parameters was evaluated by the analysis using FEM to get results of starting electromagnetic torque as an objective function, Taguchi method to reduce the number of calculations and standard statistical analysis. S/N ratio of every level on every parameter had to be calculated. The effects (in dB) of the relative influence were presented for all parameters. The optimal model from given levels was selected using S/N ratio's maximization and confirmed by an additional calculation. A very moderate number of field calculations in the optimization procedure were used without any field derivatives. The same set of field calculations was used also for other objective functions (motor weight and torque per motor weight).

References

- [1] G. N. Vanderplaats, Numerical optimization techniques for engineering design, New York: McGraw-Hill, 1984, pp 153-195
- [2] G. Taguchi and S. Konishi, Orthogonal arrays and linear graphs, Dearborn (MI-U.S.A.): ASI Press, 1987, p 59
- [3] R. K. Roy, Design of experiments using the Taguchi approach, New York: Wiley-Interscience, 2001, pp 172-204
- [4] B. J. Reece and T. W. Preston, Finite element methods in electrical power engineering, Oxford (U.K.): Oxford University Press, 2000, pp 195-200
- [5] Benhama, A. C. Williamson and A. B. J. Reece, Force and torque computation from 2-D and 3-D field solutions, IEE Proceedings – Electric Power Appl., Vol. 146, No.1, pp 25-31, 1999.
- [6] K. Hot and P. Bodlovic, Direct approach in performance calculation on permanent-magnet DC motor, in Proceedings 10th Int. Symp. on Electromagnetic Fields in El. Eng., Cracow (Poland), pp 55-58, 2001
- [7] T. Tsunoda, Y. Ishihara, T. Todaka and K. Hirata, Geometry optimization of DC motor by Taguchi method, in Proceedings 10th Int. Symp. on Electromagnetic Fields in El. Eng., Cracow (Poland), pp 489-492, 2001
- [8] K. Hot and P. Bodlovic, Optimization of Permanent-Magnet DC Motors Using Orthogonal Arrays, in *Optimization and Inverse Problems in Electromagnetism* (Eds. M. Rudnicki and S. Wiak), Dordrecht (Netherlands): Kluwer Acad. Publ., 2003

I-9. OPTIMIZATION OF BARRIER TYPE SRMs WITH RESPONSE SURFACE METHODOLOGY COMBINED WITH MOVING LEAST SQUARE METHOD

¹Young-Kyoun Kim, ¹Ji-young Lee, ¹Jung-Pyo Hong, Senior Member, *IEEE*, and ²Jin Hur

¹Dept. of Electrical Eng., Changwon Nat'l Univ., Changwon, Kyungnam, 641-773, Korea

²Precision Machinery Research Center of Korea Electronic Technology Institute, Korea
(ensigma@hitel.net, jyecad@korea.com, jphong@sarim.changwon.ac.kr, jinhur@keti.re.kr)

Abstract – While Switched Reluctance Motors have good performances, such as high torque/volume ratio, high speed, and high reliability, the motor has serious disadvantage on large torque ripple. In this paper, therefore, the Switched Reluctance Motor having barriers in the rotor is proposed to improve the torque performance of the motor. In order to reduce the torque ripple, the shape optimization of the barrier is accomplished by a combination technique employing Response Surface Methodology, Moving Least Square Method, and Genetic Algorithm.

Introduction

The applications of switched reluctance motors are recently received much attention in various industrial fields due to its superior advantages, such as high speed, efficient variable speed, and high reliability [1-2]. However, the SRM has severe nonlinear characteristics and suffers from high torque ripple and the torque/volume ratio depends on the designed shape of salient poles, which lead to limit their applications in industrial fields. Therefore, in order to improve the torque performance, this paper introduces a SRM having barriers [3] in the rotor and describes the optimum design of the barrier shape.

A computational optimization can be complicated and time-consuming because the numerous design variables are used and have usually a lot of interactions each other. Therefore, in order to introduce an effective computational approach, the Response Surface Methodology (RSM) is employed [4-6]. The RSM is used to build an analytical expression, which is utilized as an objective function or constraint in the optimization process. Moreover, to enhance the accuracy of the analytical model, the regression coefficients in the RSM are estimated by using the Moving Least Square (MLS) method [7]. The RSM combined with the MLS method is able to display an overall perspective of the torque performance according to the behavior of design variables, which are the components of the barrier shape. Although, several different search methods can be available for the optimization problem, Genetic Algorithms [8] have been selected to use as the search method because the genetic algorithms are able to find the global optimum. And the electromagnetic field within the motor is computed by using the time-stepping procedure, which is coupled with 2D-FEM and the voltage equation together.

Concept of the Statistical Fitting Method

Response Surface Methodology

The RSM is very powerful method, which seeks the relationship between input variable and output variable through statistical fitting method, to make simple model for a complex problem. A polynomial approximation model is commonly used for a second-order response and can be written as following [4-6].

$$U = \beta_0 + \sum_{j=1}^k \beta_j x_j + \sum_{j=1}^k \beta_{jj} x_j^2 + \sum_{i \neq j}^k \beta_{ij} x_i x_j + \varepsilon \quad (1)$$

where β is regression coefficients and ε denotes the random error. The least squares method is used to estimate unknown coefficients. The least squares method, which is to minimize the sum of the squares of the random errors, is used to estimate unknown vector β . The least squares function can be expressed as follows:

$$L = \sum_{i=1}^n e_i^2 = e'e = (\mathbf{U} - \mathbf{X}\beta)'(\mathbf{U} - \mathbf{X}\beta) \quad (2)$$

The estimated vector $\hat{\beta}$ of the unknown vector β must satisfy as (3).

$$\left. \frac{\partial L}{\partial \beta} \right|_{\beta} = -2\mathbf{X}'\mathbf{U} + 2\mathbf{X}'\mathbf{X}\beta = 0 \quad (3)$$

Therefore, the estimated vector $\hat{\beta}$ can be written as (4) and the fitted response vector $\hat{\mathbf{U}}$ is given by (5). Matrix notations of the fitted coefficients and the fitted response model should be

$$\hat{\beta} = (\mathbf{X}'\mathbf{X})^{-1}\mathbf{X}'\mathbf{U} \quad (4)$$

$$\hat{\mathbf{U}} = \mathbf{X}\hat{\beta} \quad (5)$$

Moving Least Square Method

In the traditional regression, coefficients of the functional approximation are estimated by the Least Square (LS) method. The LS method has a weak point increasing approximation errors in some cases because of minimizing the sum of the squares of the errors through whole sample points. To overcome its disadvantage, the MLS method is proposed to fit relationship between inputs and outputs. Unknown coefficients of the functional response modeling are estimated by the MLS method. The main idea of the MLS method is that a whole approximation $U^h(x)$ of a sampling space can be accomplished by going through a moving process.

In domain Ω , an unknown relationship between inputs and outputs can be expressed as follows:

$$U(x) = U^h(x) + \varepsilon \quad (6)$$

where ε denotes the random error mean zero and variance σ^2 , $U^h(x)$ is an approximation function in the unknown relationship, and x is an design variable.

$$U^h(x) = \sum_{i=1}^m P_i(x) a_i(x) = \mathbf{P}(x)^T \mathbf{a}(x) \quad (7)$$

where m is the number of the polynomial basis, $P_i(x)$ is a complete polynomial basis, and $a_i(x)$ is unknown coefficients.

The coefficients can be estimated by minimizing a weighted least square function, which is shown as follows:

$$J(d) = \sum_1^N W_1(d) \varepsilon_1^2 = \sum_1^N W_1(d) (U(x_1) - U^h(x_1))^2 \quad (8)$$

where $W_1(d)$ is a weight function depend on the distance (d) between approximation point and point I in a influence domain and N is the number of points in that.

In this work, the quartic spline function is used as the weight function [7].

$$W(d) = \begin{cases} 1 - 6\left(\frac{d}{r}\right)^2 + 8\left(\frac{d}{r}\right)^3 - 3\left(\frac{d}{r}\right)^4 & \text{for } \frac{d}{r} \leq 1 \\ 0 & \text{for } \frac{d}{r} > 1 \end{cases} \quad (9)$$

where $r = \alpha d_1$ is the radius of influence domain and α is the scaling factor.

Substituting (7) and (9) into (8), the matrix notation of the unknown coefficients can be rewritten as follows:

$$\mathbf{a}(x) = \mathbf{A}^{-1} \mathbf{B} \mathbf{U} \quad (10)$$

$$\mathbf{A} = \mathbf{P}^T \mathbf{W} \mathbf{P}, \quad \mathbf{B} = \mathbf{P}^T \mathbf{W} \quad (11)$$

where \mathbf{P} and \mathbf{U} are composed with a set of sample points regarding design variables and outputs, respectively.

Application to the Optimization Design in Barrier Type SRM

Barrier Type SRM and Field computation Method

The proposed barrier type 8/6 SRM is shown in Fig. 1 and the barrier is employed to improve the torque characteristic. The voltage equation of the motor is written as follows:

$$V_a = R_a i_a + L_a \frac{d i_a}{d t} + E_a \quad (12)$$

where E_a denotes the motor back emf, R_a is the resistance of windings, and L_a is inductance of that, per a phase. The governing equation of the electromagnetic field in the motor can be described by magnetic vector potential \vec{A} .

$$\nabla \times [\nu(\nabla \times \vec{A})] = \vec{J} \quad (13)$$

where ν is the magnetic reluctivity and \vec{J} is the z-component of the density of the current.

To consider the nonlinear nature of inductance as a function of exciting current and rotor angular displacement, it is necessary to solve the differential circuit equations for the appropriate switched conditions and transient performance. Therefore, system matrix is composed of coupling the voltage equation (1) with the governing equation (2), and solved by the time-stepping procedure. The reluctance torque is calculated by using the Maxwell stress tensor.

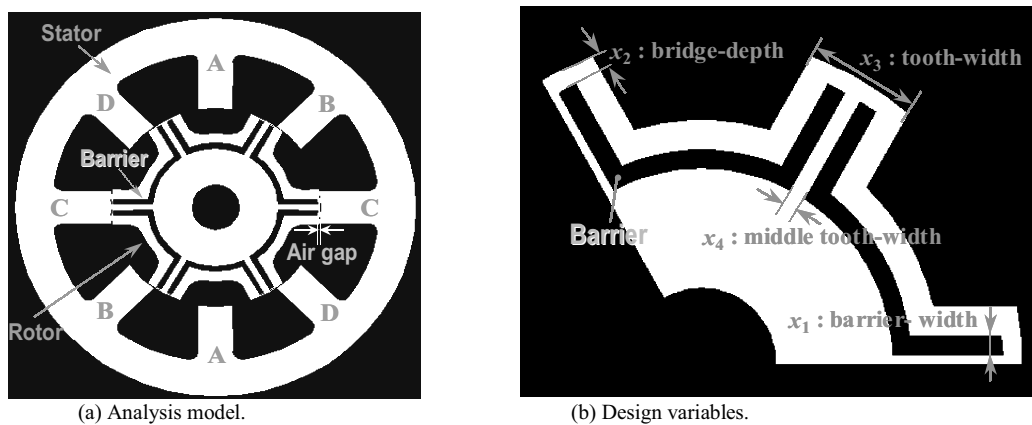


Fig. 1. Analysis model and design variables.

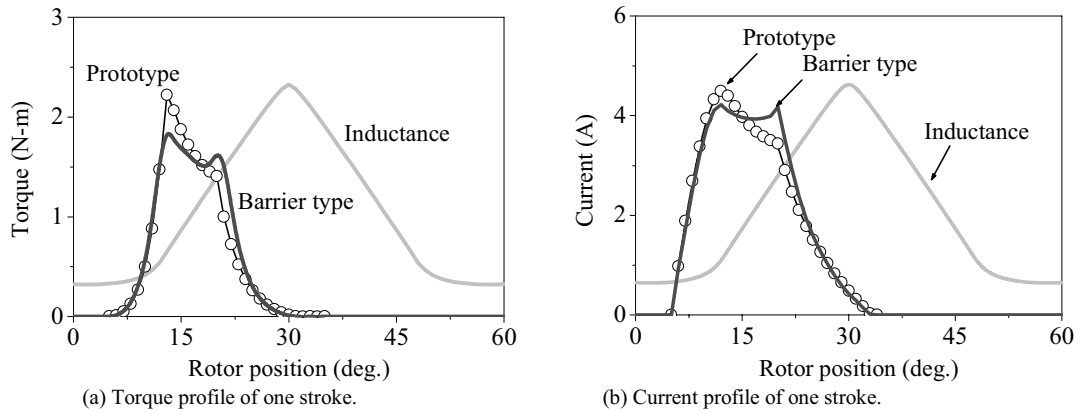


Fig. 2. Analysis results of the barrier type SRM.

When an input voltage is 150 V and a speed is 1800 rpm, Fig. 2 shows the comparison of analysis results of the prototype SRM and the barrier type SRM. The analysis results are computed by time-stepping procedure, and as will be seen, the reduction of the torque ripple is achieved in the barrier type SRM.

Objective function and Procedure of Optimization

While several different optimization methods can be applied at the motor design, the optimization technique based on the genetic algorithms has been used in this paper. The genetic algorithms research in the design space of the motor by means of a process of reproduction, crossover and mutation [8], which is able to avoid the local minimum as contrasted with gradient based method.

The schematized procedure of the optimization is shown in Fig. 3. In order to apply the shape optimization of the barrier, an objective function is defined as the torque ripple of the barrier type SRM and the constraint condition is defined to satisfy the running torque of the prototype SRM as follows:

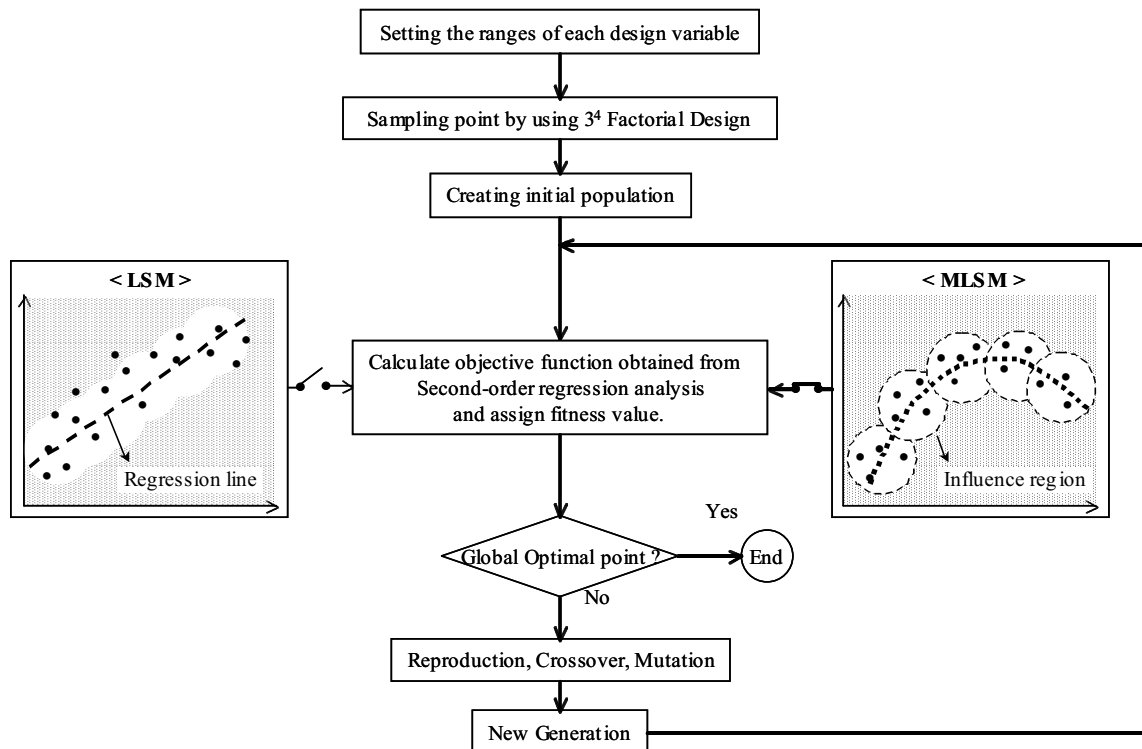


Fig. 3. Description of Optimization Based on RSM associated with Genetic Algorithms.

Minimize:

$$f(x) = U^h(x)_{Torque\ ripple} \text{ (N - m)} \tag{14}$$

Subject to:

$$g(x) = U^h(x)_{Torque} \text{ (N - m)} \geq 1.37 \tag{15}$$

Design space:

$$0.6 \leq x_1 \leq 2.2, 0.3 \leq x_2 \leq 1.1, 18 \leq x_3 \leq 20, 1.2 \leq x_4 \leq 2.4 \tag{16}$$

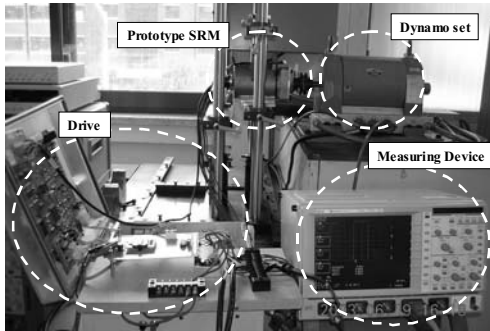
In this paper, the functional expressions of the objective function and constraint are obtained by the sampling point based RSM combined with MLS and the full factorial design is used for building the second-order fitted model. This design of experiments involving four factors is required to conduct 81 experiments. And then the time-stepping procedure, which is coupled with 2D-FEM and the voltage equation together, is used for acquiring the samples.

Results of Numerical Optimizaton and Discussion

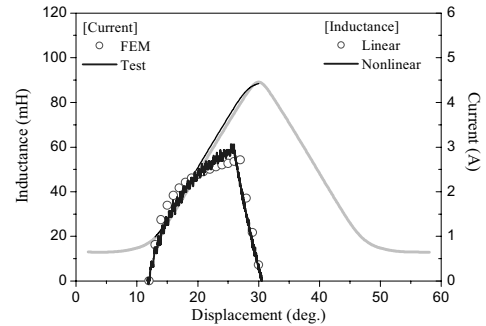
Fig. 4(a) shows the overall experimental test-bed, built at Changwon University in Korea and it was tested under the conditions for experiment with 80V input voltage and 800 rpm speed. As shown in Fig. 4(b), it is noted that the simulation results has a good agreement with the experimental results.

Figs. 5 and 6 show the perspective response surface of the torque characteristics that have been fitted with 81 samples where solid black dots represent the simulation results of 2D-FEM. From these results, it can be confirmed that the MLSM gives a response surface, which is much closer to the results of 2D-FEM.

In this paper, The RSM combined with the genetic algorithms is applied to the optimum design of the barrier shape in the proposed barrier type 8/6 SRM. The design parameters of the proposed motor and torque performances are shown in Table 1. The torque ripple of the proposed motor is less than that of the prototype SRM and its running torque becomes greater than that of the prototype SRM.

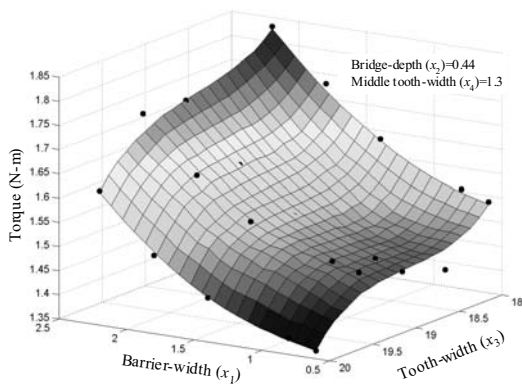


(a) Experimental set.

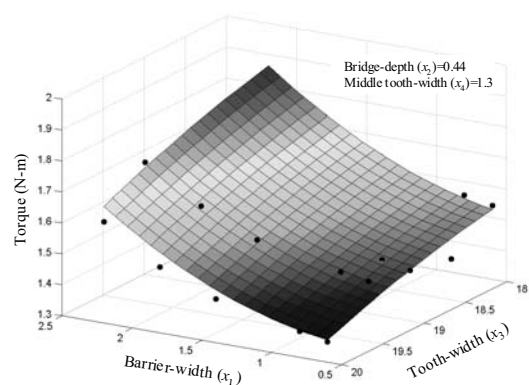


(b) Comparison of phase current.

Fig. 4. Experimental set and comparison of phase current about prototype SRM.



(a) Moving Least Square method.



(b) Conventional Least Square method.

Fig. 5. Response surface of torque with both fixed x_2 and x_4 .

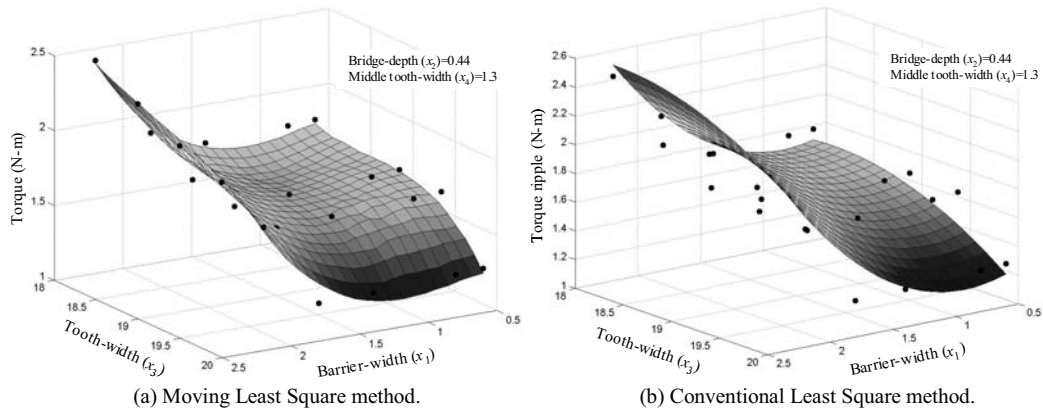


Fig. 6. Response surface of torque ripple with both fixed x_2 and x_4 .

Table 1. Analysis model and design variables.

Item	Prototype SRM	Barrier type SRM	
Torque	1.37 (N-m)	1.4 (N-m)	
Torque ripple	1.65 (N-m)	1.27 (N-m)	
Optimized shape of barrier in the proposed motor			
Barrier-width (x_1)	Bridge-depth (x_2)	Tooth-width (x_3)	Middle tooth-width (x_4)
1.0 (mm)	0.44 (mm)	20 (deg.)	1.3 (mm)

Conclusion

In this paper, the Barrier Type SRM is proposed in order to improve the torque performances. Also, taking advantages of barrier shape, the optimization technique based on the statistical fitting method has been developed. Moreover, Moving Least Square method is introduced to enhance the accuracy of the predictive performance according to varieties of design parameters. The comparison with the prototype SRM has been performed and the result of the comparison indicates that the torque performance of the Barrier type SRM is superior to that of the prototype SRM.

References

- [1] M. Stiebler and Ke Liu, "An Analytical Model of Switched Reluctance Machines," *IEEE Trans. Energy Conversion, Magn.*, vol. 14, No. 4, pp. 1100-1107, December 2000.
- [2] Yasuharu Ohdachi, Yoshihiro Kawase, Yutaka Miura, and Yoji Hayashi, "Optimum Design of Switched Reluctance Motors using Dynamic Finite Element Analysis," *IEEE Trans. On Magnetics*, Vol. 33, No. 2, pp. 2033-2036, March 1997.
- [3] Hiroyuki Kiriya, Shinichiro Kawano, Yukio Honda, Toshiro Higaki, Shigeo Morimoto, and Yoji Takeda, "High Performance Synchronous Reluctance Motor with Multi-Barrier for the Appliance Industry," *IEEE Industry Application Conference*, pp. 111-117, 1998.
- [4] R. Rong, D. A. Lowther, Z. Malik, H. Su, J. Nelder, and R. Spence, "Applying Response Surface Methodology in the Design and Optimization of Electromagnetic Devices," *IEEE Trans. On Magnetics*, Vol. 33, No. 2, pp. 1916-1919, MARCH 1997.
- [5] F. Gillon and P. Brochet, "Screening and Response Surface Method Applied to the numerical optimization of electromagnetic devices," *IEEE Trans. On Magnetics*, Vol. 36, No. 4, pp. 1163-1167, JULY 2000.
- [6] R. H. Myers and D. C. Montgomery, *Response Surface Methodology*, John Wiley & Sons, INC., 1995.
- [7] Vlatko Čingoski, N. Miyamoto, and H. Yamashita, "Element-Free Galerkin Method for Electromagnetic Field Computations," *IEEE Trans. On Magnetics*, Vol. 34, No. 5, pp. 3236-3239, 1998.
- [8] N. Bianchi and S. Bolognani, "Brushless DC Motor Design: An Optimisation Procedure Based On Genetic Algorithms," *EMD97 Conference Publication*, No. 444, pp. 16-20, September 1997.

I-10. THE ADVANCED METHODS OF INTERACTION AND DATA ANALYZE IN THE VISUALIZATION SYSTEM FOR ELECTROMAGNETIC FIELDS

Adam Krolewiak (*), Ewa Napieralska-Juszczak (*), Maria Pietruszka (**)

*L.S.E.E., Université d'Artois, Technoparc Futura, 62400 Bethune, France, napieralska@univ-artois.fr

**Institute of Computer Science, FTIMS Technical University of Lodz, Poland

Abstract – This paper presents the solutions of human-machine communication in scientific visualization, especially in the electromagnetic fields visualization. The methods described concern three issues: the navigation in three-dimensional result space connected with the position manipulation of the results set's graphical representation, the user communication with the application using the special menu system and the value obtaining directly from the graphical representation. The method described in this paper was implemented by authors in own interactive and 3D stereo visualization system for electromagnetic fields having the virtual reality features.

Introduction

The User–Application Interface

The interaction between a user and the computer systems is a problem which accompanies constantly the computer science development. With a progress in domain of the computer peripheral devices, grow both the possibilities but also the requirements for user–application communication systems. The interaction plays particular role in the systems of graphical data analyses. The basic aim of interaction is the simplification of passing the visualization's parameters. The earlier solutions such as modifiable text files or scripts controlling the data analyze process, created by the user in a script language dedicated for given system or in one of the popular programming languages, have typical features of batch processing. The necessity to set up many parameters in a text configuration file or to create the script controlling visualization process before each results generation process, was not conducting to efficacy nor comfort of the analyze. The significant step ahead was the command line introduction. It allows controlling the data analyze or visualizations interactively. Similar to batch scripts the user should know the command syntax. But it can significantly increase the work efficiency. Additionally the functionality of that solution could be increase with the defining possibility of own commands and functions. It allowed to personalize the user work environment.

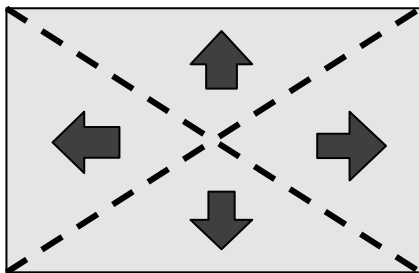
Currently the hierarchical menu systems are the standard. They give the access to indispensable options and graphical dialog windows allowing the parameters input or the requested information (such as cipher results) output. Such solutions featuring with high degree of data analyze environment integrations. They do not require the knowledge of any internal language nor the structure of configuration files, creating graphical communication layer above their level. The user can focus exclusively of content-related layer of the issue. The graphical environments of data analyze having the context menu pose the new quality of interaction. The idea of a context menu is the obtaining access to program's options or numerical values concerning nothing but the indicated object, the area or the point. Thanks to such a mechanism it is possible to know the values featuring the particular point from graphical data representation indicated by the cursor. These values can relate to the quantity currently shown but also they can inform about any quantity existing in data set, but not illustrated. Unfortunately, the advanced interaction mechanisms are not widely applied in commercial data analyze systems.

In the analyze systems placed in three-dimensional space where the user observe the scene projected on monitor screen the essential problem is the manipulation of data set graphical representation in relation to observer position. The advantage of interaction between user and application is taken in order to change the direction the observation or the distance from observer to data set. The smoothness of these changes depends on the interaction method applied in given system. If it is required to enter precisely the coordination of observer position and observation direction in the scene coordination system, in order to change the direction of the observation, the user suffer not only from harshness but also from discomfort of the work. Applying the intuitive navigation mechanism in three-dimensional space presented on computer monitor improves the comfort of work with application exempting the user from necessity of using the coordination values or frames of reference. Such approach is the base assumption of the virtual reality environment but it is not fully applied in the graphical data analyze systems.

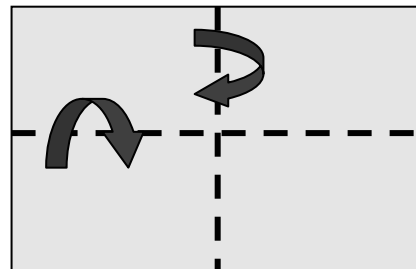
In this paper the methods and the solutions developed by authors and applied in visualization system for the results from electromagnetic calculations are presented. These methods concern either the navigation during the observation or the control of application's by menu system. The main goal of developed methods was to create the virtual reality environment for scientific data presentations, allowing the intuitive and functional process of observation and data analyze and giving the access to indispensable options and functions.

Interactive navigations in three-dimensional result space

The issue of the data space exploration in authors' system was realized base on virtual reality idea. It had been assumed to use PC mouse as a most popular PC peripheral tool. The main trump of PC mouse is a possibility of widely application. Since the graphical application and graphical operating systems were appeared, almost all desktop computers or workstations are equipped with this tool. The main problem to solve was the organization of the movement in three-dimensional space using the PC mouse operating in two dimensions. The idea of the movement is compatible with the standard of virtual reality environment. It consist in dividing the computer screen's plane into a few areas. Each of them is related to specific direction or kind of movement.



Picture 1. The conventional screen dividing for navigation

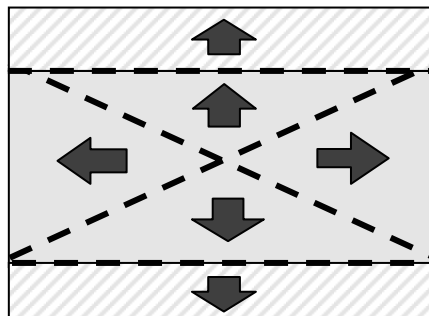


Picture 2. The idea of object's rotation

Pressing the mouse button in the upper area determined by crossing diagonals causes the movement of observer deep into the scene (in the direction perpendicular to screen's plane). Pressing the button when the cursor is in one of the side areas generates, depending on implementation: the rotation of the observer around the vertical axe of the scene coordinates system, the rotation of the observer around his own axe or the movement in parallel direction to screen's plane to the left or right. This solution gives the possibilities of free and easy observer's movement through the scene. It is easy to find out, however, that the movement can be realize only in one plane XZ of the world coordinates system with constant y coordinate value, it is also not possible to change the view direction vertically. The possibilities of all space penetration are then significantly limited. Two different solution of this problem was proposed in authors' visualization system. The first consist in the rotation possibility of the object representing the data set using the separate navigation mode: "the rotation". Pressing the

mouse button in this mode causes the conventional object holding, then the vertical movement generates rotation around the x axis, the horizontal – around the y. Thanks this solution, even though the observer moving only in the range of one given plane, it is possible to reach any point in the examined data set. Additionally the observer's orientation vector is still directed toward the center of the scene. It is an essential advantage in the case of stereoscopy presentation mode, where the center of the scene is a point of reference for direction of cameras associated with moving observer. Moreover, described solution forces the graphical data representation retaining in the view area the whole visualization process. The idea of making rotation is presented on the illustration below.

The second solution, setting free from operating on the only one plane, is the possibility to making rotations around the own operator x axis. This cause the change of the y component of observer's direction vector. In order to organize additional movement possibilities using a mouse as a manipulator, two additional areas on the top and bottom were separated. The new conventional screen divide is presented on illustration below.



Picture 3. The additional solution for vertical movement

Pressing the mouse button at one of the extreme areas cause the camera's rotation around its own x axis. This is the way to change vertical component of camera's orientation vector. The camera represents the observer, so in effect the user have impression looking up or down. For the camera's orientation changes are kept after rotation, so the movement forward causes the changes not only in the range of x and z coordinates but y coordinate as well.

During the free exploration through the space fulfils with graphical data representation, taking to consideration the scientist's or engineer's goals of visualization, getting the information about current observer position in scene coordination system is necessary. This information in the three component vector form and other numerical values indispensable in visualization process can be presented in additional window displayed dynamically during application process. This information window is placed in the bottom left-handed corner so as not to blind visualized data. It can be easily hidden by the simple mouse click over.

Visualization control process

The menu construction

In graphical data analyze process the possibility of the visualization course control is profitable or even necessary. The user should be able to for instance change the current data visualization method, set the observer position to the one of predefined points or run the special application function. This problem was called *the control of the visualization's parameters*. The control's organization has the particular importance in the data analyze system based on virtual reality environment. In this case the most important is the possibly effective showing of the graphical data representation, which can be viewed from all directions using free navigation in data space. All remaining application control functions should be realized in intuitive and simplified manner so that not to interfere with observation nor cause the loss of the data view. In the application adopted to the

stereo observation the necessity of work in a full screen mode is an additional difficulty. Usually, in this kind of applications it is not possible to use standard menu from graphical window systems.

The control of visualization parameters proposed in the graphical analyze system developed by the authors for electromagnetic fields, was realized using the dynamic, auto-hidden, hierarchical menu. During the space exploration the menu is invisible. Placing the cursor near the screen's top edge cause the displaying of the main horizontal menu bar. On this menu bar the names of functions group available in application are displayed. Positioning the cursor over the one of the names cause the field highlighting and rolling down the vertical list containing the functions names from chosen group. The rolled down list can contain fields starting application's functions or the names of menu's group of the next level. The menu prototype used in authors' system and described in this paper assumes the groups of first level only. The following can be added in similar way. The menu function is activated by the mouse button pressing when its name is highlighted. Moving the cursor out from rolled down menu area causes the menu hiding.

Although the idea of the menu implemented in authors' system poses the standard in modern hierarchical menu system, its implementation in the stereoscopy graphical data analyze system is a new solution related to current commercial packet.

The example of menu implementation was created for Windows operating system using object oriented programming language Visual C++. The menu was realized as a set of independent windows. Its construction bases on definition of objects of three class: the menu command class CDxMenuCommand, the main menu class CDxMenu and the menu of first level CDxSubMenu. The objects of the first class are responsible for menu's content, the objects of two other classes – for appropriate displaying, positioning and interaction with a user.

The Objects of CDxMenuCommand class represent individual menu's positions with their labels (*m_Label*), assigned function (*m_Command*) and with determination of group's position in main menu (*m_MenuPos*) and in submenu (*m_SubMenuPos*). The scheme of the class is presented in the table 1.

CDxMenuCommand
<i>m_MenuPos</i>
<i>m_SubMenuPos</i>
<i>m_Label</i>
<i>m_Command</i>
<i>CDxMenuCommand()</i>
<i>~CDxMenuCommand()</i>

Table 1. The menu command class

The object of CDxMenu class representing the main menu bar derives the methods and properties of CWnd window class from MFC library. Moreover it owns the specific method and properties presented in table 2.

CDxMenu
<i>m_MenuNum</i>
<i>m_lpMenuText</i>
<i>m_PrevMenu</i>
<i>m_lpSMenu</i>
<i>m_lpSMenuNbPos</i>
<i>InitMenu()</i>
<i>CDxMenu()</i>
<i>~CDxMenu()</i>

Table 2. The main menu class

The object properties include: the information of currently chosen menu group (`m_MenuNum`), the information of previously selected menu group (`m_PrevMenu`), the pointer to the table containing the labels of individual groups (`m_lpMenuText`), the pointer to the objects table representing first level menu (`m_lpSMenu`) and the table with number of positions in each of submenus (`m_lpSMenuNbPos`). The `InitMenu()` method fills in the table `m_lpMenuText` with labels texts, creates instances of all submenu objects and sets their properties.

The objects of `CDxSubMenu` make the first level menu functionality and appearance.

CDxSubMenu
<i>m_MenuNum</i>
<i>m_lpMenuText</i>
<i>m_PrevMenu</i>
<i>m_left</i>
<i>m_right</i>
<i>m_lpParentMenu</i>
<i>m_SubNum</i>
<i>m_SubID</i>
<i>InitSubMenu()</i>
<i>CDxSubMenu()</i>
<i>~CDxSubMenu()</i>

Table 3. The submenu class

The properties `m_left`, `m_right`, `m_SubNum` determine the size and the position of each submenu window. The submenu windows are identified by integer value assigned to `m_SubID` field.

At the begin of application the two dimension table `MenuTab[][]` of `CDxMenuCommand`

Group_1	Group_2	Group_3	Group_4	Group_5
SubMenu_1_1	SubMenu_2_1	SubMenu_3_1	SubMenu_4_1	SubMenu_5_1
SubMenu_1_2	SubMenu_2_2	SubMenu_3_2	"" (NULL)	SubMenu_5_2
"" (NULL)				

MainMenu window	SubMenu window
-----------------	----------------

Table 4. The hierarchical menu construction schema.

objects are created, then the functions, exact the pointers to the functions which execute given tasks, the labels and the positions in menu structure are assigned to these objects. The position in `MenuTab` table corresponds with position in graphical menu structure.

While the main visualization window is being created, the object of `CDxMenu` and `CDxSubMenu` classes are forming. These object thanks to method and properties derived from `CWnd` class are windows in Windows system meaning. They are not visible during visualization process. Only the cursor placing near the top edge of visualization area causes the displaying the main menu bar – the window of `CDxMenu` object. Then the cursor movement are traced by the Windows system and the system message containing cursor position coordinates is passed to `CDxMenu` object and handling by the event handler `OnMouseMove()`. In this way, the cursor movement along the menu strip causes the displaying the consecutive submenu windows representing by `CDxSubMenu` object. In the similar

way the cursor movement and position is tracing and handling by this object. Based on cursor position all the menu fields are consecutively highlighted, the mouse button pressing causes function execution assigned to one of CDxMenuCommand objects placed in MenuTab table. The indexes in the table are determined by fields m_SubID and m_MenuNum of CDxSubMenu object. Placing the cursor out of main and submenu window area causes their disappearing.

Thanks the system menu constructed like that, it is possible to free control of the menu window position and to show it in full screen application particularly for different stereo visualization format. Also it is possible to change dynamically of individual fields or even the whole groups of menu so that the function set available from the menu could be adequate to visualization's state and in the same time simple and easy to reach.

Data querying in the analyze process

The interaction problem includes also the methods of data querying directly from graphical data representation during visualization process. The only graphical representation, although it gives general view of the phenomenon, is not enough for engineer or scientist requiring the precise values of interesting quantity in specific well defined areas. The values are required to be expressed with a high precision relating to calculation results precision. The possibility to obtain a value from any point of data set in a simply and intuitive way is a necessity. Authors developed appropriate method for obtaining values from the points indicated with mouse cursor. These points are indicated on isosurfaces using two dimensional cursor. Additionally any point from the space can be chosen using special cursor moving easily through entire volume. The values are displayed in a specially prepared windows taking to consideration the possibilities of using several different stereo formats. Using the spatial cursor, the user can chose a set of points creating for instance the data analyze path. The points indicated by cursor can also determine the position of plane which is made to cut data set for colored map creation. Presented method allows to combine generality of data graphical model with a precise of analyzing result required by engineers and scientist.

Conclusions

Developed by authors and presented in this paper methods of interaction between the user and the visualization system concern: the navigation in the space, the object manipulations, the user-application communication and the extracting values directly from graphical data image. They allow to project and develop the comfortable visualization system featuring with interactive engineering data analyze. The method described in this paper was implemented and tested in developed by authors the interactive and stereoscopy visualization system based on virtual reality environment for electromagnetic field analyze.

References

- [1] Yamashita H., Johkoh T., Nakamae E.: „*Interactive Visualization of Interaction between Magnetic Flux Density and Eddy Current in 3D Steady State Field*”, IEEE Transaction on Magnetics, Vol. 28, No. 2, March 1992
- [2] Zabrodzki J. (Editor): „*Grafika komputerowa, metody i narzędzia*”, WNT Warsaw 1994
- [3] Fujiwara K.: „*3D Magnetic field computation using edge elements*”, 5th IGTE Symposium, Graz 1992
- [4] A.Królewiak, M.Pietruszka, E.Napieralska-Juszczak, T.Niewierowicz „*The interactive and stereo visualization of electromagnetic fields in transformers*”, Proc. of IEEE, Acapulco, Mexico, 2001
- [5] Raskin J.: „*The human interface for designing interactive system*”, ACM Press, 2001

I-11. IMAGING OF TWO-DIMENSIONAL CURRENT DENSITY DISTRIBUTIONS FROM THEIR MAGNETIC FIELD

G. Krukowski, S. Gratkowski, R. Sikora

Faculty of Electrical Engineering, Technical University of Szczecin, Poland

Abstract - In this paper we consider different aspects of imaging two-dimensional current density distributions from their magnetic field. Such an imaging is important for its application in nondestructive testing of thin conducting plates. Maps of magnetic fields of currents injected into the plates can be converted through a solution to the inverse problems into images of the currents, and next maps of the conductivity distributions can be created throughout the plates. The inverse problem is equivalent to the solution of the Fredholm integral equation of the first kind, which belongs to the class of ill-posed problems. There is a wide variety of inverse algorithms for such kind of problems. In this paper different methods are compared.

Introduction

The inverse problems have been intensively developed in recent years. One of the methods used for the nondestructive evaluating is the visualisation of the currents injected in to the conducting object, when the magnetic field above it is known. The magnetic field is described by the law of Biot-Savart:

$$\mathbf{B} = \frac{\mu_0}{4\pi} \int_{\Omega} \frac{\mathbf{J} \times \mathbf{r}}{|\mathbf{r}|^3} d\omega \quad (1)$$

which can be rewrite to the discrete form:

$$\mathbf{B} = \mathbf{A}\mathbf{J} \quad (2)$$

or

$$\mathbf{B} = \mathbf{K} \otimes \mathbf{J} \quad (3)$$

where \mathbf{A} is the discrete equivalent of the integral operator of the equation (1), \mathbf{K} is the discrete equivalent of the kernel of the integral equation (1), \otimes is the convolution operator.

To obtain the image of the current from the magnetic field, which was measured at height h above the plate it is necessary to use the inversion of the equations (1), (2) or (3). The equation (1) is the Fredholm equation of the first kind if the function $\mathbf{J}(\dots)$ is treated as an unknown quantity, and the equations (2), (3) are its discrete equivalents. The discrete forms of the Fredholm equation are often used in practice. The solution to equation (2) can be written as:

$$\mathbf{J} = \mathbf{A}^{-1}\mathbf{B} \quad (4)$$

The equation (4) is ill-posed, that means its solution is unstable, and cannot be solved by the standard numerical methods.

This paper describes two methods of solution of the equation (4): the method of Tikhonov regularization and the method of Hosaka-Cohen transformation. The method of Tikhonov regularization will be described in two variants: the direct solution of equation (4) and solution by means of the Fourier Transform (3). For each method it is described: the algorithm property, cost of computation and sensitivity to changes of different parameters of the system.

The inverse problems

The Tikhonov regularization method [1]

This method relies on minimisation of the functional:

$$F = \|AJ - B\|^2 + \lambda \|J\|^2 \quad (5)$$

The λ is the regularization parameter and J is the unknown quantity. The quality of solution depends on the regularization parameter. At present there are many methods of choosing λ (for example: the L-curve method, the general discrepancy method). The functional (5) has a minimum for J satisfying the equation:

$$(A^T A + \lambda I)J = A^T B \quad (6)$$

in other words:

$$J = (A^T A + \lambda I)^{-1} A^T B \quad (7)$$

For correctly chosen λ , the solution (7) is numerical stable.

The Tikhonov regularization by means of the Fourier Transform [1,2]

The equation (1) is a convolution-type equation, so use of the Fourier Transform is possible for its solution. This method is very fast and powerful, especially for large equation systems. The discrete convolution equation has the Fourier transform:

$$K \otimes J = \text{IFFTn}(\text{FFTn}(K) \cdot \text{FFTn}(J)) \quad (8)$$

where FFTn is the n -dimensional Discrete Fourier Transform (Fast Fourier Transform), IFFTn is the inverse n -dimensional Discrete Fourier Transform. The equation (8) says us that the convolution in the time domain is equal to multiplication of frequencies in the frequency domain.

The equation (7) can be written as:

$$J = \text{IFFTn} \left(\frac{\text{FFTn}(K)^* \cdot \text{FFTn}(B)}{\text{FFTn}(K)^* \cdot \text{FFTn}(K) + \lambda} \right) \quad (9)$$

where K^* is the complex conjugate.

The equation (9) describes the Tikhonov regularization by means of the Fourier Transform.

The real magnetic field above the plate is described by:

$$B = K_\infty \otimes J_m \quad (10)$$

where K_∞ is the unbounded kernel, J_m is the current injected into the plate, but we can calculate only:

$$B = K \otimes J_c \quad (11)$$

where K is the kernel with local support and J_c is the wanted current.

When we solve the inverse problem on the basis of the magnetic field we get form (10) and (11):

$$K_\infty \otimes J_m = K \otimes J_c \quad (12)$$

therefore

$$J_m \neq J_c \quad (13)$$

what marks that we never calculate exactly the current which generates the magnetic field, but only its approximate value.

The Hosaka-Cohen transformation [2]

A “current-pattern” in the xy -plane can be obtained from z -component of the flux density vector by the Hosaka-Cohen transformation

$$HC \equiv \frac{\partial B_z}{\partial y} \vec{i} - \frac{\partial B_z}{\partial x} \vec{j}, \quad (14)$$

where the field is measured a distance h above the currents. It was shown in [2] that the components of the current density vector in the conducting plate of thickness d can be calculated as:

$$J_x \approx \frac{2\pi h}{\mu_0 d} \frac{\partial B_z}{\partial y}, \quad (15)$$

$$J_y \approx -\frac{2\pi h}{\mu_0 d} \frac{\partial B_z}{\partial x}. \quad (16)$$

The Hosaka-Cohen transformation is the first-order approximation of the exact inverse solution. The approximation is best for small values of h .

Simulations

The test problem

The methods described above were tested by using the structure shown in Figure 1.

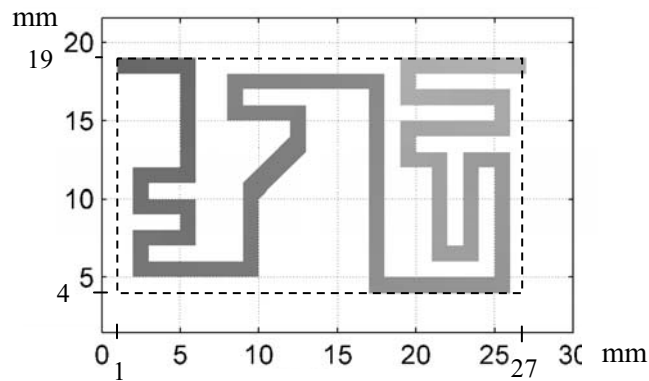


Fig. 1. The structure under test

Figure 1 shows a printed circuit pattern with current 1 A. The printed pattern width is 1 mm, the thickness is 0.01 mm. The measuring area is the rectangle shown in Fig. 1 (dashed line). The measuring area was divided by the grids described in Table 1. For all grids the magnetic field was calculated at heights h : 0.5 mm, 1 mm, 2 mm, 3 mm, 5 mm; 10 mm. The noise was modelled by the Gaussian noise with amplitudes: 1 μ T, 5 μ T, 10 μ T, 20 μ T. The grids for the Tikhonov regularization by means of the Fourier Transform is described in Table 2. The normal grids (Table 1) are central parts of Fourier grids (Table 2).

Tab. 1 - Grid description

Grid no.	Mesh size [mm]	Grid size [nodes]
Grid 1	1.0	[26 × 15]
Grid 2	0.50	[52 × 30]
Grid 3	0.25	[104 × 60]
Grid 4	0.125	[208 × 120]

Tab. 2 - Grid for FFT based regularization

Grid no.	Mesh size [mm]	Grid size [nodes]
Grid 1F	1.0	[76 × 43]
Grid 2F	0.50	[154 × 88]
Grid 3F	0.25	[310 × 178]
Grid 4F	0.125	[622 × 358]

Results

The Tikhonov regularization method

- Simulations:** The simulations have been done for the first two grids. For the Grid 1 the size of matrix A is [390×390], memory consumption is 1.16 Mb, calculation time of inverse problem is about 2 seconds. For Grid 2 the size of matrix A is [1560×1560], memory consumption is 18 Mb, calculation time of inverse problem is about 40 seconds. The size of matrix A is a second power of geometrical size of analysed region.
- Sensitivity:** If the scanning height h is small in comparison to the size of analysed region, the solution of the inverse problem is numerical stable. Above this height the regularization is necessary for solving the inverse problem. For any plate it is possible to find the height below it the regularization is not necessary and the numerical solution is stable. In this case the solution with or without regularization is identical and the error of the solution is minimal. Above this height it is necessary to use the regularization for correct solution of the inverse problem. For each height h it is possible to find the regularization parameter λ that the error of solution is minimal. When the height and the noise level grow up the error of the solution grows as well.
- Conclusions:** The Tikhonov regularization method is perfect to solve small problems. It is reference method for other ones. For big problems the method is too slow and uses too many computer resources (Figs. 6, 7, 8, 9, 10).

The Tikhonov regularization by means of the Fourier Transform

- Simulations:** The simulations have been done for all grids. The time of calculation are: Grid 1 - less than 1 second, Grid 2 - less than 1 second, Grid 3 - ≈ 1.5 second, Grid 4 - ≈ 14 seconds. This algorithm uses significantly less memory than the previous method.
- Sensitivity:** The conclusions are as in the previous case, but it introduces additional error to the solution.
- Conclusions:** This method is faster than normal Tikhonov regularization and uses less memory. Nowadays there are known very speed and powerful algorithms for the Fourier Transform. This method is perfect for big problems if we can accept the introduced error (Figs. 4, 12).

The method of Hosaka-Cohen transform

- Simulations:** The simulations have been done for all grids. The time of calculation is a linear function of data size and the memory requirement is very small.
- Sensitivity:** This method is height-dependent. The quality of the solution dramatically falls down with the height. This method is relatively resistant to noise in the input signal. For the test problems, if the height h is smaller than 1 mm then we can interpret the solution.
- Conclusions:** This is the fastest method, but it has a big disadvantage: it works correctly if the height h is very small (Figs. 5, 13).

Conclusions

We can classify described methods on many criteria: speed, accuracy and sensitivity. For example, if the criterion is the speed of algorithm, the sequence is: 1) the Hosaka-Cohen method, 2) the Tikhonov regularization by means of the Fourier Transform, 3) the Tikhonov regularization. If the criterion is the insensitivity on the height at which the magnetic field is measured, the sequence is reverse. It should be stressed that all the conclusions have no general use, as they depend strongly on the nature of the problem. In each particular case it is necessary to perform the calculations according to the individual requirements.

Acknowledgement

This work has been supported by the KBN, Poland, under the Grant no: 4T10A 024 24 (2003-2006).

References

- [1] A. N. Tikhonov and A. V. Goncharsky, editors. *Ill Posed Problems in the Natural Sciences*, MIR Publishers, Moscow, 1987
- [2] J.P. Wikswo, *The Magnetic Inverse Problem for NDE*. In H. Weinstock, editor, *SQUID Sensors: Fundamentals, Fabrication and Applications*, pages 629-695, Kluwer Academic Press, 1996

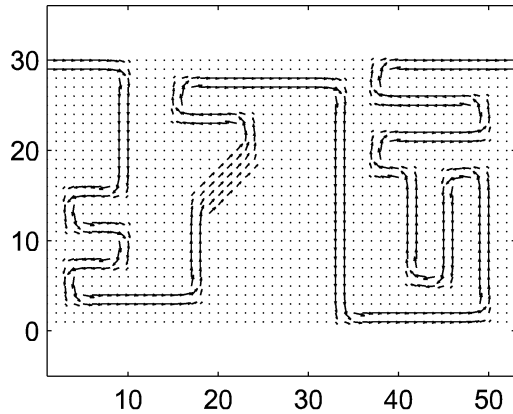


Fig. 2. Forward problem

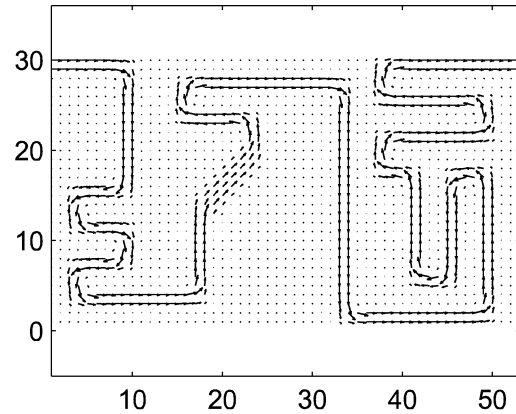


Fig. 3. Inverse problem without regularization and noise, $h=1$ mm

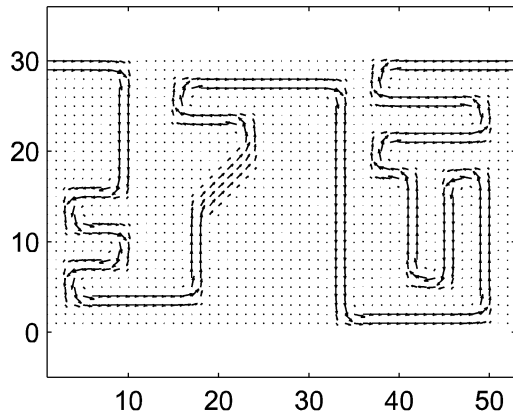


Fig. 4. Inverse problem with Tikhonov regularization + FFT, without noise, $h=1$ mm

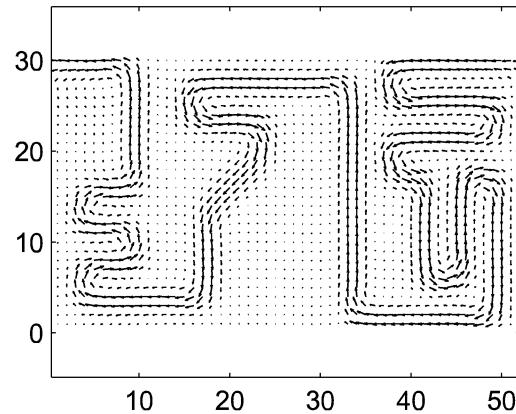


Fig. 5. Inverse problem with Hosaka-Cohen transformation, without noise, $h=1$ mm

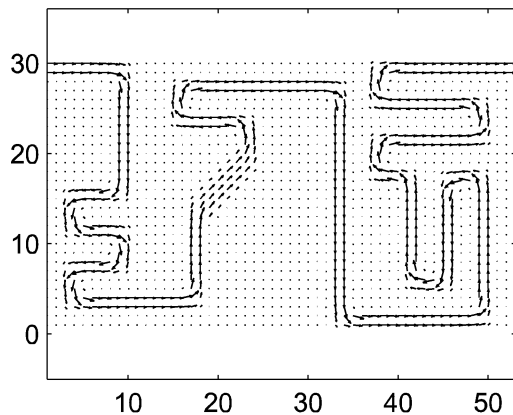


Fig. 6. Inverse problem with Tikhonov regularization, without noise, $h=1$ mm

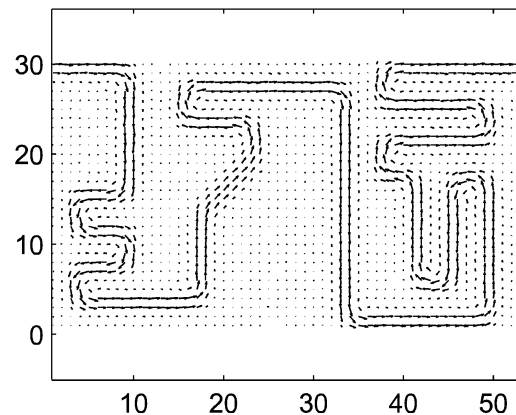


Fig. 7. Inverse problem with Tikhonov regularization, noise $1\mu\text{T}$, $h=1$ mm

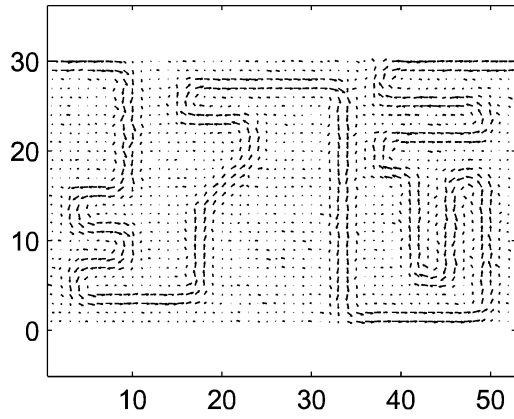


Fig. 8. Inverse problem with Tikhonov regularization, noise $5 \mu\text{T}$, $h=1 \text{ mm}$

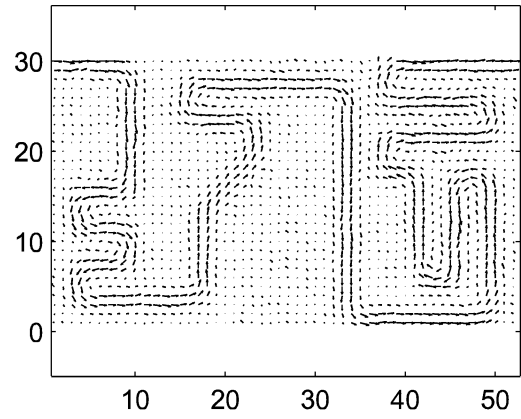


Fig. 9. Inverse problem with Tikhonov regularization, noise $10 \mu\text{T}$, $h=1 \text{ mm}$

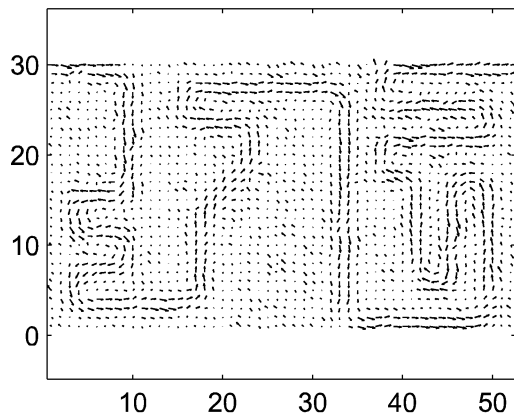


Fig. 10. Inverse problem with Tikhonov regularization, noise $20 \mu\text{T}$, $h=1 \text{ mm}$

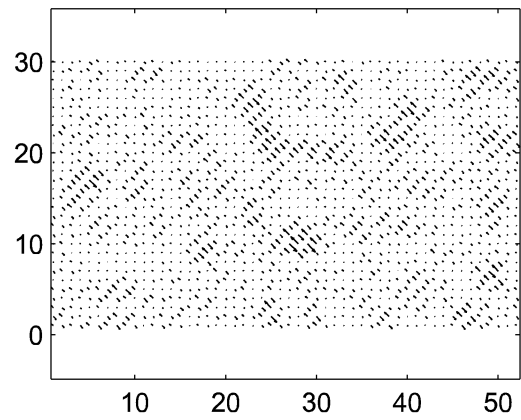


Fig. 11. Inverse problem without regularization, noise $20 \mu\text{T}$, $h=1 \text{ mm}$

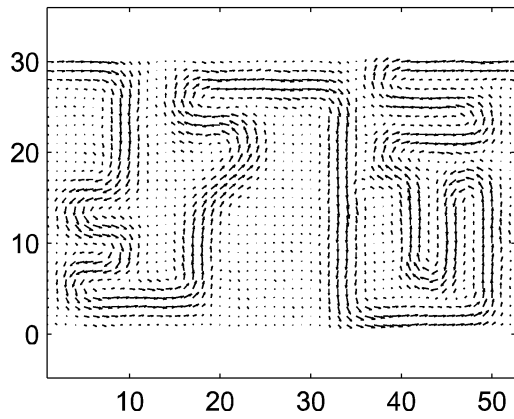


Fig. 12. Inverse problem with Tikhonov regularization + FFT, noise $20 \mu\text{T}$, $h=1 \text{ mm}$

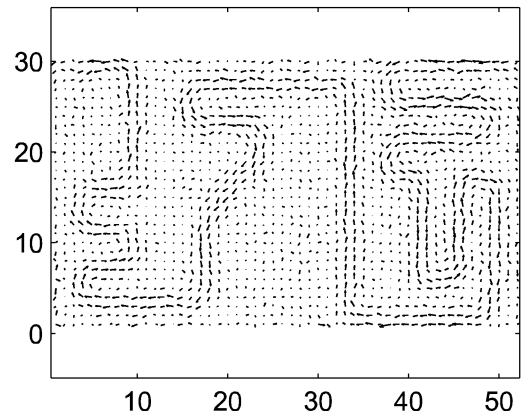


Fig. 13. Inverse problem with Hosaka-Cohen transformation, noise $20 \mu\text{T}$, $h=1 \text{ mm}$

I-12. SOME APPLICATIONS OF THE COUPLED FIELD-CIRCUIT METHOD

E. Napieralska-Juszczak*, Tadeusz Niewierowicz**, Leszek Kawecki**

*L.S.E.E., Université d'Artois, Technoparc Futura, 62400 Bethune, France, napieralska@univ-artois.fr

**ESIME-Instituto Politecnico Nacional, Mexico, Unidad Zacatenco, Edificio #5, 3er piso, 07738 México

Abstract - The method presented in this paper is based on the incomplete coupling of circuit and field models for the simulation of electromagnetic fields in a transformer, which provides power to the converter system during different modes of operation and failures. With this method the coefficient matrix remains symmetric and banded and circuit and field equations are solved simultaneously. The presented model allows the analysis of the currents, voltages and the flux density distribution in several converter sets. Two examples are presented here. The first analysed model was a converter transformer applied for railways. The second example concerns a specially prepared three-limb, two-winding model transformer supplying a three phase 6D bridge.

Introduction

The model presented here is the result of the authors' ongoing research activities on the subject since many years. The aim was the creation of a universal mathematical model for simulation of phenomena, which could arise during the performance of the converter set supplied with a three-phase transformer, both during proper operation and failures. There are two different approaches to the coupling of finite element models with circuit equations. The equations of the finite element model and the circuit model may be handled as a single system of equations, or alternatively, the finite element part may be handled as a separate system, which communicates with the circuit model by the aid of coupling coefficients. The first approach is called direct coupling, the second one indirect coupling [1]-[3]. An important reason for the popularity of the direct coupling is the fact that one obtains quite effective convergence of computation by applying multidimensional Newton-Raphson iteration on the combined field-circuit equations. Usually the number of the node points in the finite element mesh is so large that a sparse matrix solution technique has to be used when handling the Jacobian matrix of the Newton-Raphson algorithm for the combined field/circuit equations [2]. A drawback of the direct coupling is the fact that we have to formulate the circuit equations in such a way that the sparse matrix solution technique still works when the circuit models are added in parallel with the finite element model. This, of course, limits our freedom with the circuit modelling. By using the indirect coupling, we do not have to destroy desirable properties like symmetry and positive definiteness of the large coefficient matrix of the combined finite element/circuit equations. The method is based on incomplete coupling of circuit and field models, making it possible to maintain matrix features convenient for programming. The finite element model was treated as a multi-input, nonlinear macro element connected to the electric circuit. The circuit may contain resistors, inductors, mutual inductances, capacitors, voltage sources, diodes, controllable power electronic components such as thyristors, and other components. This facilitates the simulation of different faults such as a short circuit or the disconnection of a diode in the converter system.

Basic equations of the electric circuit and 2D electromagnetic field of the transformer

At low frequencies, with displacement currents neglected, the governing equation for transient, eddy current problems can be expressed in terms of the magnetic vector potential A . The electromagnetic field was assumed to be *flat-parallel*, with two flux density components in the x - and y -directions, one component of current density J in the z -direction, as well as one component of the vector potential A

in the z-direction. Hysteresis was not taken into consideration in the field model. The materials in the domain of computation may be inhomogeneous and anisotropic. The magnetic vector potential A satisfies the equation

$$\nabla_{xy}(\nu(B|\alpha)\nabla_{xy}A)=-\gamma\nabla V+\gamma\frac{\partial A}{\partial t} \quad (1)$$

where ν is the reluctivity of the material, which depends on the magnitude of the flux density and angle of anisotropy, γ is the electrical conductivity, ∇V is the gradient of the electric scalar potential. To describe a 2D field we can use a scalar $a(x,y)$ defined as $a(x,y)=I_z A(x,y)$ where I_z is the equivalent depth of the region. By introducing the scalar $a(x,y)$ we obtain:

$$\text{div}(\nu(B|\alpha)_{z^{-1}}\text{grad}(a(x,y)))=-\gamma_{z^{-1}}\left(-\frac{\partial a(x,y)}{\partial t}-u_{pk}(x,y)\right) \quad (2)$$

where $u_{pk}(x,y)$ is in *flat-parallel* field the voltage between the ends of the single coils, passing by the point (x,y) . The right-hand side of (4) depends on the type of conductor in the finite element analysis. Consider a conductor made of many thin strands, each strand too thin to model in a practical finite element grid. Instead we lump them together in one finite element region and assume that their contributions to the current density are averaged over the area of the region. The strands are wound in n turns connected in series. We assume that the current density is uniform over the cross section of one coil. The voltage drop in the winding can be expressed as a function of current

$$\text{div}(\nu(B|\alpha)_{z^{-1}}\text{grad}(a(x,y)))=S_p^{-1}i \quad (3)$$

where S_p is the cross sectional area of the coil. The voltage of every coil is given by $u_{pk}=R_{kik}$, where n is the number of turns. After the finite element discretization of the transformer volume we obtain the following global system of differential equations:

$$[S(\mathbf{a})][\mathbf{a}]+[G]\frac{\partial}{\partial t}[\mathbf{a}]-\frac{1}{l}[Q]^T[\mathbf{i}_{pk}]-[Z]=0 \quad (4)$$

where: $[\mathbf{a}]$ is the column matrix of the values of vector a in the current nodes; $[\mathbf{i}_{pk}]$ is the column matrix of currents in the windings; $[S(\mathbf{a})]$ is the stiffness matrix, which depends on the shape function of elements and on the anisotropic magnetic permeability of the material; $[Q]$ is the coupling matrix; $[G]$ is the conductivity matrix, which depends on the shape function of the conductor elements and on the conductivity of the material; $[Z]$ is the matrix representing boundary conditions. The contribution of each element and each winding to the coupling matrix is given by

$$Q(in,ic)_e=\int_{se}^{\gamma_e} \frac{N_{in}dx dy}{l_z} \quad (5)$$

where e is the number of the element containing node in , ic is the winding number containing element e , N_{in} is the function of the shape associated into node and element. The vector of voltages is given as: $[\mathbf{u}_{pk}]=[R][\mathbf{i}_{pk}]$, where $[R]$ is the diagonal matrix of resistivity of the winding. The time dependence is discretized by a time stepping trapezoidal rule. The vector potential, currents and voltages are calculated at the time instant $k+1$ from

$$\left\{ [S_{k+1}(\mathbf{a}_{k+1})+\frac{2}{h}G][\mathbf{a}_{k+1}]-\frac{1}{l}[Q]^T[\mathbf{i}_{pkk+1}]+[-S_k(\mathbf{a}_k)+\frac{2}{h}G][\mathbf{a}_k]+\frac{1}{l}[Q]^T[\mathbf{i}_{pkk}]+[Z_{k+1}]+[Z_k] \right\}=0 \quad (6)$$

$$[\mathbf{u}_{pkk+1}]=[R][\mathbf{i}_{pkk+1}]+[R][\mathbf{i}_{pkk}]-[\mathbf{u}_{pkk}]$$

These equations may be seen as a nonlinear, multiport macro element with the nodal values of the vector potential $[\mathbf{a}_{k+1}]$ as internal variables of this element. It is connected to the electric circuit by the

voltages and currents in the windings. The equation of the electric circuit model is given below in order to show the coupling of the circuit with the multiport element representing the finite element model. Supply voltages U_a, U_b, U_c feed the primary windings, and the secondary windings are only converter-loaded. The formulation of the electrical equations depends on the winding connections. Three types of connections are possible:

(a) star-connected windings with active neutral Y_n ; the electrical equations are given by

$$U_k = n \frac{d\phi_k}{dt} + R i_k + L \frac{d i_k}{dt} \quad (7)$$

$$i_k = i_{rk} + \frac{n}{R} \frac{d\phi_k}{dt}$$

where ϕ_k is flux coupled with the winding, R is resistance, L is inductance of the winding, $k = 1, 2, 3$.

(b) star-connected windings without neutral terminal Y :

$$u_k = V_k - V_0 = n \frac{d\phi_k}{dt} + R i_k + L \frac{d i_k}{dt} \quad i_1 \neq i_2 \neq i_3 \quad (8)$$

(c) delta-connected windings:

$$U_k = n \frac{d\phi_k}{dt} + R i_k + L \frac{d i_k}{dt} + M \frac{d i_\Delta}{dt}$$

$$i_k = i_{rk} + \frac{n}{R} \frac{d\phi_k}{dt} - i_\Delta \quad (9)$$

The number of equations corresponds to the number of windings, but every delta connection needs an additional equation of the following form:

$$n \frac{d(\phi_1 + \phi_2 + \phi_3)}{dt} + 3R_\Delta i_\Delta + 3L \frac{d i_\Delta}{dt} + M \frac{d(i_1 + i_2 + i_3)}{dt} = 0 \quad (10)$$

$R(t)$ is the equivalent resistance in series with the winding. $R(t)$ is a variable containing the time-dependent switching action of particular elements (faults and disconnection of diodes by the fuses and current-dependent nonlinearity like in power electronic components such as diodes and thyristors). The power electronics components are modelled with the Ebers-Moll model [4]. The model allows simulating barrier state, one directional conductivity state, two-directional conductivity state: $u_d = f(i_d)$, where i_d is the diode current. The function $f(i_d)$ is defined as follows

$$f(i_d) = \alpha R_s i_d + (1 - \alpha) C * \ln((i_d + I_s)/I_s) + i_d (1 - \alpha) R_d \quad (11)$$

where $\alpha [0, 1]$ is the control parameter defining the state, the coefficient $C = 40$, $I_s = 2V_T/R_s$, V_T is the threshold voltage of the diode, and R_s is the barrier resistance. The fault (a) and disconnection (b) of the diode is based on two basic states: (a) No conducting state – large impedance $R = R_s = 1 \text{ M}\Omega$, $\alpha = 1$; (b) Conducting state in both directions – small impedance $R = R_d = 1 \mu\Omega$, $C = 100000$, $\alpha = 0$. The thyristor needs simultaneous fulfilment of two conditions: forward voltage and effect of gate impulse delayed with an angle β releasing the thyristor blockade in the forward direction. The impulse, that means releasing condition, in the three phase bridge has to be either long ($> \frac{\pi}{3}$) or short, but repeated after $\frac{\pi}{3}$. This condition can be easily realized in the program cancelling the blockade of the thyristor in proper instance according to the angle β either for long time (e.g. $\frac{\pi}{2}$) or for a short time (e.g. $\frac{\pi}{36}$) but repeated after $\frac{\pi}{3}$. The operation of a fuse can be represented in an approximate manner. Beginning the initial instant of S.C. the value of $\int i^2 dt$ is computed and reaching the critical value for considered fuse introduces an additional resistance rising with given nonlinear steepness to R_d . The information

about the damage of any diode or change in receiver branch providing the transient can be introduced in discrete form in an arbitrary instant of the operation. All these operations are included in the parameter R_{dj} . All currents in the circuit are expressed as combination of the loop currents. The construction of the circuit equations is based on Kirchhoff's voltage law $[B][u]=0$, where $[u]$ is the column matrix of branch voltages and $[B]$ is the incidence matrix. The elements of the matrix are 1 if the branch current has the same direction as the loop current, -1 if opposite, 0 if the branch does not belong to the loop. Let N_e represent the number of electric circuit branches, N_o the number of electric circuit independent loops. The j -th branch includes the transformer winding with w_j turns, external resistance R_j , inductance L_j and external sources e_j . The system of circuit equations can be written in the following form:

$$\frac{d\phi_j}{dt} + R_j i_j + L_j \frac{di_j}{dt} + L_{SRj}(i_j) + R_{dj}(f(i_j)) i_j + e_j = u_j \quad j = 1, 2, \dots, N_e \quad (12)$$

where $L_{SRj}(I_j)$ is the nonlinear inductance of smoothing reactor. The magnetic flux coupled with the winding is given by:

$$\frac{d\phi_k}{dt} = \frac{d}{dt} \sum_{e=1}^{ws} a(x,y) = u_{wind} \quad (13)$$

where ws is the total number of discretized elements in the winding area;

$$u_{windj} + R_j i_j + L_j \frac{di_j}{dt} + L_{SRj}(i_j) \frac{di_j}{dt} + R_{dj}(f(i_j)) i_j + e_j = u_j \quad j = 1, 2, \dots, N_e \quad (14)$$

where z_j is the number of turns of the j -th winding, V_{kj} is the volume and S_{kj} is the cross sectional area of the j -th winding. In matrix form the equation (14) is:

$$[u] = [R_b][i] + \frac{d}{dt} \{ [L_b][i_o] \} + \frac{d}{dt} \{ [L_n][i_o] \} - [k_p] R_s [i_d] + [k_{kp}][u_{kp}] + [k_e][e] \quad (15)$$

where the matrices $[K_d]$, $[K_{pp}]$, $[K_e]$ are the incidence matrices. The branch currents are obtained from the loop currents $[i] = [B]^T [i_l]$, where $[i_l]$ is the column matrix of loop currents. After substituting we obtain

$$[B][R_b][B]^T [i_o] + \frac{d}{dt} \{ [B][L_b][B]^T [i_o] \} + \frac{d}{dt} \{ [B][L_n][B]^T [i_o] \} - R_s [B][k_p][i_d] + [B][k_{kp}][u_{kp}] + [B][k_e][e] = 0 \quad (16)$$

The presented circuit equation is discretized by the trapezoidal rule. The Newton-Raphson iteration procedure is applied to the time-discretized circuit equations. The Gauss-Jordan algorithm solves the system. The multiport element presented in section 2 is connected with the circuit system by the currents in the coils of particular windings.

Applications

The presented model allows the analysis of the currents, voltages and the flux density distribution in several converter sets. Two examples are presented here. The computer used for simulation was an IBM RISC System 600/250, workstation. The first analysed model was a converter transformer applied for railways. The main parameters of the transformer were: $S = 5851$ kVA, $\Phi = 0.1523$ Wb, turn voltage $e' = 33.862$ V/turn, the primary windings were star-connected with 311 turns per phase wound with two parallel conductors as cylindrical continuous winding consisting of discs (every second disc reversed), the rated current was 168.9A, the rated phase voltage was $20/\sqrt{3}$ kV. There were two secondary windings: the first one was star-connected with 22 turns, the rated winding current was 1310A, the second winding was delta-connected with 38 turns. The rated winding current of the delta was 756.3A. The secondary line voltages in the star-connected windings were 1286.76V, in the delta-connected windings 1290.323V. On the DC side no load voltage $U_{dco} = 3480.3$ V, rated load current $I_{dc} = 1604.4$ A. Both secondary windings form a cylinder where the coils of particular windings are

interlaced (pancake system). The transformer supplies a 12-pulse double bridge set connected in series. For the s.c. test only the smoothing reactor loads the system, $R=0$ and $E=0$. This reactor is practically linear up to 120% of the rated current ($L=0.01H$), over this value it begins to saturate and by 400% its dynamic inductance achieves only 0.0005H. Such situation appears during S.C. on DC terminals [5]. In Figure 1a the equivalent circuit connected with the macro-element is shown.

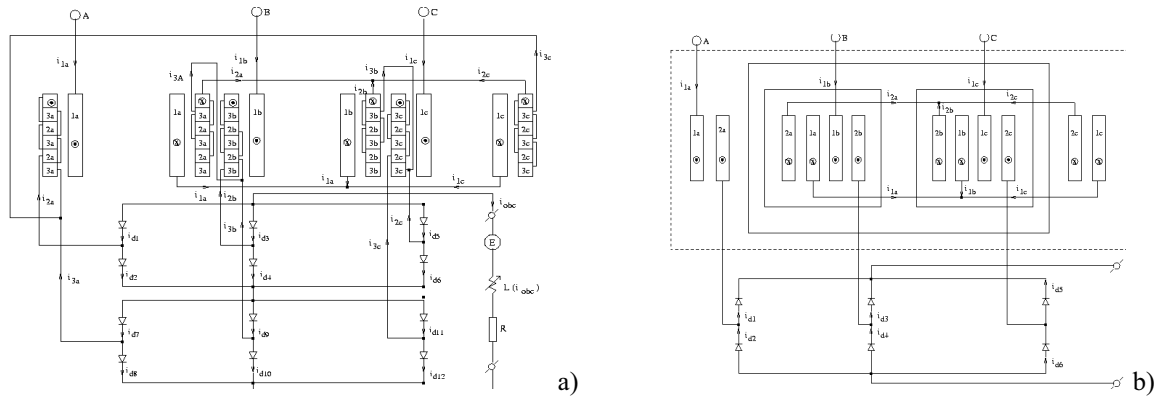


Fig.1. (a) Equivalent circuit of Yd connected transformer with macro-element; (b) The equivalent circuit of the two-winding transformer

The macro-element is a finite element model with the quadratic triangle and quadrilateral. The finite element mesh contains 5184 quadratic, isoparametric, triangular and rectangular elements and 12909 nodes. The winding currents connect both the model macro-element and the electrical circuit. Application of rated load on the DC side as well as a transient during short circuit on the output terminals, including only non linear smoothing reactor are presented in Figure 2.

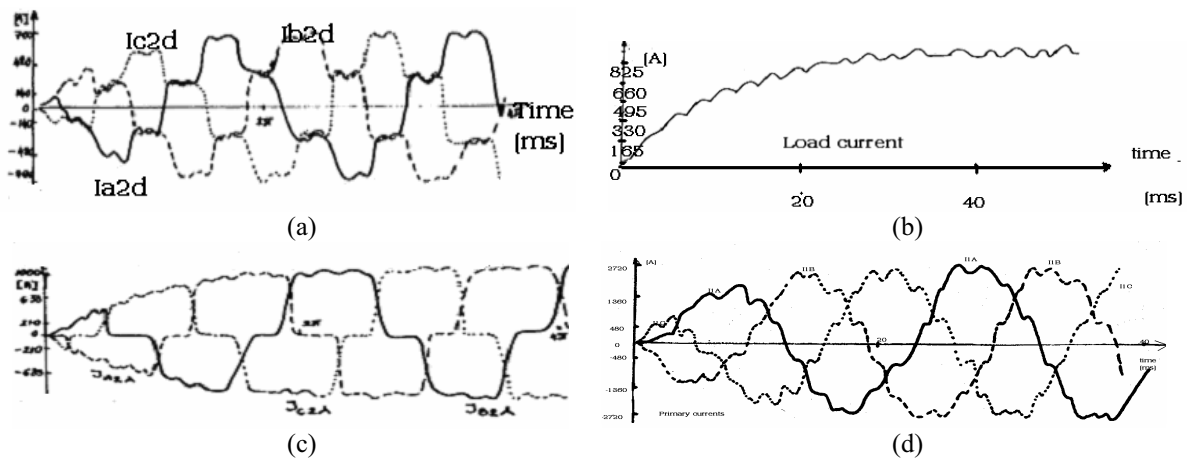


Fig.2. The computed load current on the DC side: (b) primary currents, (d) both secondary currents, (a) delta currents, (c) star currents, during short circuit through non-linear smoothing reactor in DC output.

In order to get information about the efficiency of the proposed method in case of different types of windings, a star-connected cylindrical primary winding and a star/delta-connected pancake secondary winding were tested. This example enabled us to test the influences of non linearity of the smoothing reactor on the dc current. The computed values of current agree in the limits of 8% with the measured ones. The second example concerns a specially prepared three-limb, two-winding model transformer supplying a three phase 6D bridge (Fig 1b). It has the following rated primary parameters: $S = 23.65$ kVA; $U_{line} = 167,4V$; $I = 81,65A$; winding connections Yy0 (primary winding 62 turns, secondary winding 64 turns); short circuit data: $z_{sc} = 7,63\%$, $x_{sc} = 6,5\%$, $r_{sc} = 4\%$; $B_m = 1,4T$; on the DC side: $U_{dco} = 226$ V, $I_d = 100A$. For this set a series of tests has been done concerning different conditions of operation and different kinds of failures. In the computer simulation the anisotropy, the overlapping and equivalent air gaps were all taken into account. The macro-element is a finite element model with

the quadratic triangle and quadrilateral. The transformer space is divided into 3458 triangular elements and 7065. The computation of the circuit with the above given parameters was done for the case of a break through of one diode disconnected by the fuse during rated load. The system was maintained in work with one valve shut off. The voltage on the D.C. output decreases under such conditions to 83 % of rated voltage. Short circuiting the diode for five periods (meaning 0.1s) is long enough to obtain full saturation of the core with D.C. (Figure 3).

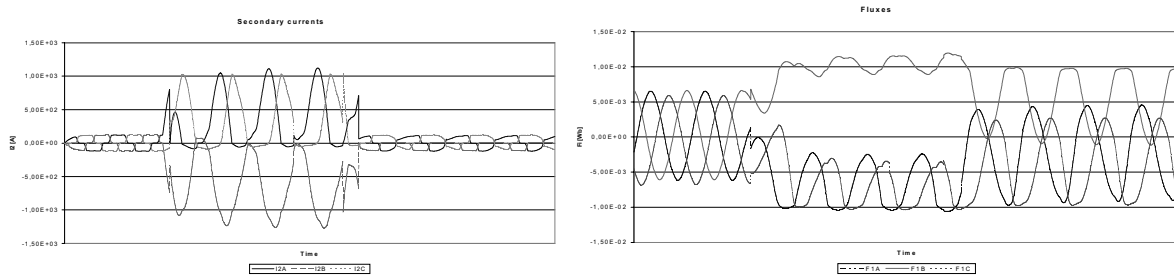


Fig. 3. The secondary currents and the flux in limb B after disconnecting the valve.

After disconnecting the valve, the primary current in the phase B diminishes and is at first unidirectional. With passing time the primary D.C. component diminishes exponentially to zero, the current rises and begins to be alternating, considerably deformed. The saturation of the core due to the D.C. component of the secondary current caused a strong noise during the test not only because of magnetostriction, but first of all due electromagnetic vibrations amplified with high D.C. submagnetization of the core (effect of diaphragm). The simulation of such an operation for different load conditions was accomplished. The results of the simulation have been validated by experiment. Figure 4 shows the results of calculated and measured currents on the primary side.

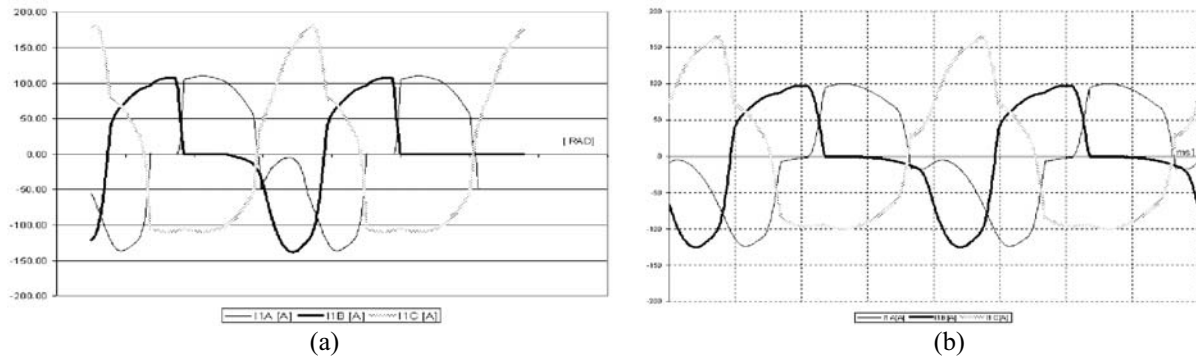


Fig.4. (a) Primary currents calculated by applying the presented method. (b) Measured primary currents.

The above-presented computations are only a few selected examples from the wide possibilities covered by the described mathematical model. The presented 2D model is interesting in case of computation concerning the distribution of magnetic field in transformer cores, proper selection of interlacing mode and core design as well as methods of calculation for the iron losses. This work was made within the framework of a French-Mexican collaboration.

References

- [1] I.A.Tsukerman, A. Konrad, G. Meunier, and J.C. Sabonnadière "Coupled Field-Circuit Problems: Trends and Accomplishments," *IEEE Trans. Magn.*, vol.29, No.2, 1993, pp 1701-1704.
- [2] A. Nicolet, F. Delincé, N. Bamps, A.Genon, W.Legros "A Coupling between Electric Circuit and 2D Magnetic Field Modeling," *IEEE Trans. Magn.*, Vol.29, No.2, 1993, pp.1697-1699.
- [3] J. Väänänen, "Circuit Theoretical Approach to Couple Two-Dimensional Finite Elements," *IEEE Trans. Magn.*, March 1996, Vol.32, Nb.2, pp.400-406.
- [4] M. Tadeusiewicz, *Method of computer-aided analysis of nonlinear electronic circuit*, WNT Warsaw Poland, ISBN 83-204-1263-3
- [5] M. Jablonski "The simple method of smoothing reactors in the converter sets," *Rozprawy elektrotechniczne*, No.21, 1978, Poland.

I-13. PERMANENT MAGNETS DEALT WITH BOUNDARY-INTEGRAL APPROACH

K. Pawluk

Electrotechnical Institute, 04-703 Warsaw, Poland
ul. Pożaryskiego 28, E-mail: pawluk@iel.waw.pl

Abstract – The magnetic field created by permanent magnets can be effectively analysed by the use of the indirect boundary-integral model. The fictitious magnetic densities upon both pole surfaces are imagined. They are considered as unique sources of the conservative magnetic field. The approach leads to the advanced analytical expressions for usual magnetic quantities, by means of which various technical objects containing the permanent magnets can be analysed. In the case of disc- or ring magnets, special solutions are obtained, when Lipschitz-Hankel integrals are employed to express the magnetic scalar potential. Special considerations are devoted to the magnetic energy created by permanent magnets. The original test software has been performed and the test results of the magnetic energy computation are presented

Introduction

The subject of problems, which are presented in the paper, belongs, generally, to the magneto-statics, or, more precisely, to the magnetic fields created by permanent magnets. In particular, the magnetic energy is examined. We deal with such quantity that is not directly measurable, and because of that, probably, the quantity magnetic energy is not largely exploited in engineering design. The aim of the paper is to show that it is possible to perform the reliable considerations and calculations devoted to determining the magnetic energy in engineering structures, going thoroughly into the matter.

We consider the yoke-less permanent magnet of a cylindrical or ring shape (radii R_e , R_i , length l_m) that is flat ($l_m < 2R_m$) and sufficiently small to suppose be uniformly magnetized in axial direction. It means that the magnetic polarization $\mathbf{J}(r, \varphi, z) = \text{const}$ is steadily distributed in the whole magnet body. A value of \mathbf{J} is not given *a priori*, but it shall be determined basing on the magnet size and its magnetic curve – see [4]. It is not to conclude from the above that the magnet quantities \mathbf{B} and \mathbf{H} would be constant inside the magnet piece, indeed, as it is generally supposed when the magnet forms a part of a magnetic circuit.

Two equivalent boundary models of a permanent magnet may be used in such form that was defined by the author. The reader may find the author's treatment of such problems in [1-2], [4-5], [9]. We use, here, the first boundary model with analogy between magneto- and electrostatic approach based on a fictitious polar quantity attributed to the magnet polar surfaces, that we call *surface monopole density of the magnetic charge*, symbol σ . When the magnet piece is homo-geneously magnetized lengthwise the z -axis of the magnet piece, it is supposed that $\sigma = \pm \mathbf{J}$ on the N-or S-surface, respectively.

Magnetic scalar potential

The magnetic scalar potential created by the both $\pm\sigma$ distributed upon N- and S-pole surface can be analytically expressed [4] by means of the following integral of Lipschitz-Hankel type

$$\psi_m(r, z) = \frac{\sigma}{2\mu_0} \int_0^\infty [R_e J_1(R_e u) - R_i J_1(R_i u)] \cdot J_0(ru) \left(e^{-|z-l|u} - e^{-|z+l|u} \right) u^{-1} du \quad (1)$$

where r, z – cylindrical coordinates, J_1, J_0 – Bessel functions, $l = l_m/2$, u – internal variable. For $R_i = 0$,

the formula covers the case of a disc magnet, as well. The Lipschitz-Hankel integral is a very effective tool to analyze cylindrical permanent magnets being set in free space. To obtain magnetic quantities within the magnet body as well as in neighboring region a relevant differentiation on the integrand with respect to r and z should be easy performed. A space distribution of the magnetic quantities can be easily computed by means of elliptic integrals, to which integrals (1) and the similar ones are reducible.

Magnetic energy

The polar densities $\pm\sigma$ uniformly distributed on the polar surfaces are considered as unique sources of the magnetic energy in \mathbb{R}^3 , thus, it can be evaluated by integration of the magnetic scalar potential upon the both N and S polar surfaces. The magnetic energy W_m created by the inherent magnetization of the magnet alone and stored within the whole space should be determined as the sum of four terms:

$$W_m = W_N + W_S + W_{SN} + W_{NS} \quad (2)$$

where: W_N – self energy of the N-pole surface, W_S – self energy of the S-pole surface, W_{NS} – mutual energy created by $\sigma_S = +\sigma$ acting on the N-pole surface, W_{SN} – mutual energy created by $\sigma_N = -\sigma$ acting on the S-pole surface. To summarize, we have readily $W_N = W_S$ and similarly $W_{SN} = W_{NS}$, hence: $W_m = 2(W_N + W_{SN})$.

To obtain W_N , let us firstly express dW_N related to the small ring of radius $R_e < r < R_i$ and of width dr on N-pole surface, to read:

$$dW_N = \frac{1}{2} \psi_m(r, l) \sigma_N \cdot 2\pi r dr \quad (3)$$

where $\psi_m(r, l)$ represents a contribution to the magnetic scalar potential created in any point on the N-pole surface by σ_N , only. Therefore, that part of the magnetic energy can be expressed in the form of integral of Lipschitz-Hankel type to read:

$$W_N = \frac{\pi \sigma_N^2}{2\mu_0} \int_0^\infty \left[R_e J_1(R_e u) \int_0^{R_e} J_0(ru) r dr - R_i J_1(R_i u) \int_0^{R_i} J_0(R_e u) r dr \right] u^{-1} du \quad (4)$$

It is, generally, $\sigma^2 = \sigma_N^2 = \sigma_S^2$, hence, after integration with respect to r we have:

$$W_N = \frac{\pi \sigma^2}{2\mu_0} \int_0^\infty \left[R_e^2 J_1^2(R_e u) - R_i^2 J_1^2(R_i u) \right] u^{-2} du \quad (5)$$

Similar procedure yields the mutual member W_{SN} :

$$W_{SN} = -\frac{\pi \sigma^2}{2\mu_0} \int_0^\infty \left[R_e^2 J_1^2(R_e u) - R_i^2 J_1^2(R_i u) \right] e^{-l_m u} u^{-2} du \quad (6)$$

In conclusion, the total magnetic energy can be expressed as follows:

$$W_m = \frac{\pi \sigma^2}{\mu_0} \int_0^\infty \left[R_e^2 J_1^2(R_e u) - R_i^2 J_1^2(R_i u) \right] (1 - e^{-l_m u}) u^{-2} du \quad (7)$$

The above integral of Lipschitz-Hankel type (with u power minus two) does not have its elliptical equivalence, hence, to compute the magnetic energy a special approach should be dealt with. In order to obtain the usable algorithm allowing an effective integration, the following approximation $1 - e^{-l_m u} \approx l_m u$ was suggested by Craik [3]; it leads to $W_m^{(+)} = V_m J^2 / 2\mu_0$ where $V_m = \pi(R_e^2 - R_i^2)$ represents a magnet volume and J – the magnetic polarization with supposition that it is homogeneously distributed within the magnet body. The above result does not reflect the fact that the magnet is submitted to its inherent demagnetization effect. For that reason, we could interpret the

above as an upper band of the expected magnetic energy value, rather, then its true value. A trial to improve the formula by taking into account the next terms of the series $1 - e^{-l_m u} \approx l_m u - \frac{1}{2}(l_m u)^2 \pm \dots$ characterized by permuted signs, indeed, seems to be disappointed because it results in the successive members, the values of which tend to infinity.

Use of a hypergeometric series

We would like to show that a direct use the hypergeometric series ${}_2F_1(\alpha, \beta, \gamma, \zeta)$ leads really to an effective benefit in computation of such Lipschitz-Hankel integrals as they occur in (7). The hypergeometric series is generally defined as a series of an infinite number of terms:

$${}_2F_1 = 1 + \frac{\alpha \beta}{1! \gamma} \zeta + \frac{\alpha(\alpha+1)\beta(\beta+1)}{2! \gamma(\gamma+1)} \zeta^2 + \dots \quad (8)$$

For α or β being negative integers, the series breaks off. We can employ that fact to compute the integrals of Lipschitz-Hankel type within the Bessel functions of kind 0 or 1 and with any negative power of the internal variable u . Let us firstly consider that term of integral (7) that is deprived of an exponential term. Generally, we have

$$I_1 = \int_0^{\infty} J_m(Ru) J_n(Ru) u^{-\delta} du \quad (9)$$

where m, n, δ are positive integers fulfilling, for positive R , the following inequality: $m+n+1 > \delta$. In the case when R is common within the arguments of both Bessel functions the relevant hypergeometric series has an implicit value. Thus, the integral I_1 can be expressed, see [8] 4.415.2, by means of the error functions of a half integer argument $\Gamma(p/2)$ and of a factorial, to be equal to:

$$I_1 = \frac{R^{\delta-1} \Gamma(p_1/2) (\delta-1)!}{2^{\delta} \Gamma(p_2/2) \Gamma(p_3/2) \Gamma(p_4/2)} \quad (10)$$

where $p_1 = m+n-\delta+1$; $p_2 = -m+n+\delta+1$; $p_3 = m+n+\delta+1$; $p_4 = m-n+\delta+1$. In relation to formula (10) we have for related integrals, e.g. for that depending on R_e , the following value:

$$\int_0^{\infty} J_1^2(R_e u) u^{-2} du = \frac{R_e \sqrt{\pi} \Gamma(2)}{4 \Gamma(5/2) \Gamma(3/2) \Gamma(3/2)} \quad (11)$$

that is g exactly equal to $4R_e/3\pi$.

Let us pass now to the second term of integral of (7). It means we consider now the term containing the exponent multiplier of the argument $-l_m u$. We would like to refer to the general formula, given by Bateman [7], modified here suitably to a particular Bessel functions of a real kind. For the following Lipschitz-Hankel integral:

$$I_2 = \int_0^{\infty} J_m(R_1 u) J_n(R_2 u) e^{-l_m u} u^{-2} du \quad (12)$$

In particular, we have:

$$I_2 = C \sum_k E_k \cdot {}_2F_1(-k, -(m+k), (n+1), \zeta^2) \cdot G_k \quad (13)$$

The constants occurring in the above expression contain same number of factorials, in particular:

$$C = \frac{R_1^m R_2^n}{2^{m+n} \zeta^{m+n+\delta+1} n!}; \quad E_k = \frac{(m+n+\delta+2k)!}{(m+k)! k!} \quad \text{and} \quad \zeta = (R_2/R_1)^2; \quad G_k = \left[-(R_1/2l_m)^2 \right]^k.$$

The specialised software has been developed by the author in order to compute I_2 . The tests performed with the use of that test software showed that a satisfactory convergence of $(E_k \cdot 2F_1)$ can be easily reached, at least for $R \leq l_m$.

To summarise the above, we can establish that the following expression for the magnetic energy, defined by (2), of a ring-shape permanent magnet holds:

$$W_m = \frac{\pi \sigma^2}{\mu_0} \left[R_e^2 (I_{1e} - I_{2e}) - R_i^2 (I_{1i} - I_{2i}) \right] \quad (14)$$

The integrals I_{1e} and I_{1i} are given by (11). The integrals I_{2e} and I_{2i} should be computed on the basis of (13). In the case of disc magnets, one put $R_i = 0$ and the same procedure holds.

The magnetic energy W_m given by (14) allows such interpretation that it is stored within the whole space, a magnet piece included. A separation of the energy on two parts, one stored within the magnet piece and other outside of it, seems to be very difficult. It is because of fact that the distribution of the magnetic quantities created by a yoke-less magnet is analytically expressed by elliptic functions not allowing an explicit integration.

Examples

Consider the modern rare-earth Schramberg's disc magnet Neodymium Iron Boron 240/95 w. It is characterised by the following average material data related to the temperature +20°C:

- energy product $(BH)_{\max} = 265 \text{ kJ/m}^3$,
- remanence $B_r = 1,200 \text{ T}$,
- coercivity $H_{cB} = 890 \text{ kA/m}$,
- magnetic susceptibility $\chi = 0,072$.

We choose the size 11-6004001:

- diameter $2R = 10 \text{ mm}$,
- length $l_m = 10 \text{ mm}$,
- volume $V_m = 785,4 \text{ mm}^3$.

Magnet in free space

The magnetic state of the above magnet was recognized by the use of the author's test-software¹ The program determines values of the magnetic quantities when the magnet is set in free space and is not influenced by external fields. In the software, a homogeneous distribution of the magnetic polarization is assumed. Its value is determined on the basis of the algorithms published in [4]. For the magnetic state of the considered magnet being set in free space, we obtained:

- magnetic polarization $J = 1,180 \text{ T}$,
- average value of the magnetic flux density on the central cross-section $B = 0,906 \text{ T}$,
- average value of the magnetic field strength (corresponding to the above value of the magnetic flux density) $H = -221 \text{ kA/m}$.

The upper band of the magnetic energy is $W_m^+ = 435 \text{ mJ}$. The volume magnetic energy equal to $W_m^+/V = 554 \text{ kJ/m}^3$ corresponds directly to that value. We can doubt on practical importance of the upper band W_m^+ . Nevertheless, the formula is widely quoted by many authors.

Let us make rather use on expression (14). We put $R_e = 0,005 \text{ m}$, $R_i = 0$ and $\sigma = J = 1,18 \text{ T}$. We obtain:

- $I_{1e} = 2,122 \cdot 10^{-3} \text{ m}$, by formula (11),
- $I_{1e} = 0,564 \cdot 10^{-3} \text{ m}$, by the author's test software².

¹ Test software packet FLAT_CYLMAG2, developed in 2001, not published.

² Specialized computer program HYPER_GEOM recently developed, not published.

Formula (14) gives the magnetic energy: $W_m = 136$ mJ, and a quotient of the magnetic energy by the magnet volume: $W_m/V_m = 172$ kJ/m³, that we can hardly interpret it as a volume energy density.

Magnet within the magnetic circuit

Let us examine yet the same magnet placed within a super-permeable magnetic circuit with an air gap. We choose its size being equal to $h_\delta = 0,0046$ m. That value of h_δ is chosen in such a way that the total magnetic energy be quite the same as in the previously examined case, i.e. when the magnet was deprived of a magnetic circuit. For the considered example, the magnetic quantities can be simply calculated. We obtain the following values of them:

- magnetic polarization $J = 1,173$ T,
- average value of the magnetic flux density on the central cross-section $B = 0,804$ T,
- magnetic field strength inside the magnet piece $H = -294,2$ kA/m,
- magnetic field strength in the air gap $H_\delta = 639,6$ kA/m.

The calculation of the magnetic energies gives the following values:

- the magnetic energy stored in the air gap $W_{m\delta} = 92,8$ mJ,
- magnetic energy within the magnet piece $W_{mm} = 45,8$ mJ,
- total magnetic energy $W_m = 138,6$ mJ.

Ring magnets in free space

Let us present yet on figures 1 and 2 the calculation results pertaining to ring magnet pieces imaginably reconstructed from the disc magnet considered in previous sub-sections. Keeping the external radius unchanged, we assume four various internal radii equal consecutively from one to four resulting in the relevant ring breadths. The previously mentioned author's test software is used.

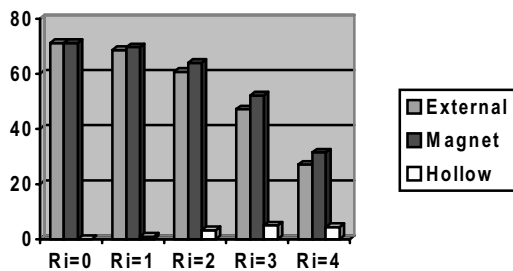


Fig. 1. Disc magnet & four ring magnets: magnetic flux [μ Wb] throughout: an external space, cross-section and hollow tube.

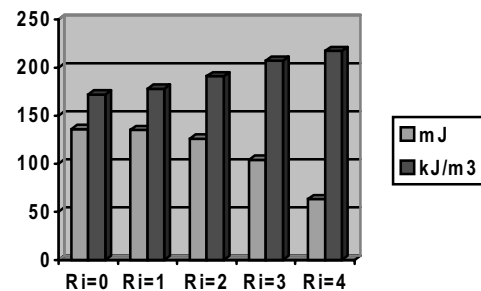


Fig. 2. Disc magnet & four ring magnets: magnetic energy [mJ], magnetic energy by the volume [kJ/m^3], $R_e = 5$ mm, R_i given [mm].

Conclusions

Generally, the boundary integral model seems to be a good tool for numerical examination of the magnetic field created by yoke-less permanent magnets when set in free space. When disc or ring magnets are under consideration the static magnetic field can be handled by means of the Lipschitz-Hankel integrals. They offer facilities in performing various differential and integral operations. Due to the main feature of those integrals to have equivalence forms to some algebraic expressions containing the complete elliptic integrals (of the first, second and of third kind) effective computer programs can be performed. In order to compute the magnetic energy stored by those magnets the approach using the elliptic integrals is inappropriate. It is shown in the paper that the magnetic energy may be calculated by means of direct computation of the hypergeometric series.

The specialized computer software was performed. It can be applied to compute as well the magnetic field quantities as the magnetic energy of the yoke-less permanent magnet structures characterized by axial symmetry. It is worth to point, that the algorithms used in the programs are in fact in their most part analytical ones and then accurate (in frame of the supposed idea). They offer, too, a good tool to improve other professional and universal programs covering (among other things) the calculations of the magnetic fields created by permanent magnet structures.

Acknowledgement

The author is very grateful to the Electrotechnical Institute for financial support of that research.

References

- [1] K. Pawluk, "3-D magnetic field of coils with an open metallic core in boundary-integral approach"; Boundary Element Technology VIII, ed. H. Pina and C.A. Brebbia, Comp. Mech. Pub., Southampton, Boston, 1993, pp. 147-156.
- [2] M. Kucharska, K. Pawluk, "On the bi-scalar boundary-integral approach to boundary-integral handling of the electromagnetic field problems", Journal of Technical Physics, Vol., 3-4, 1998, pp. 557-568.
- [3] D. Craik, "Magnetism, principles and applications", J. Wiley & Sons, Chichester, New York, Toronto.
- [4] K. Pawluk, "Algorithms based on integrals of Lipschitz-Hankel type for modelling permanent magnet field", Bulletin of the Polish Academy of Sciences, Technical Sciences, Vol. 49, No. 4, 2001, pp. 567-579.
- [5] K. Pawluk, Energetic equivalence of polar and lateral quantities on permanent magnet boundaries, Prace Instytutu Elektrotechniki, vol. 211, 2002, pp.23-35.
- [6] P.F. Byrd, M.D. Friedman, *Handbook of elliptic integrals for engineers and scientists*, Springer-Verlag Berlin, Heidelberg, New York, 1971.
- [7] H. Bateman., Higher transcendental functions, Mc Graw-Hill Book Company, Inc. New York, 1953.
- [8] I.M. Ryshik, I.S Gradstein, Tables of series, products and int-egrals, VEB Deutscher Verlag der Wissenschaften, Berlin, 1957.
- [9] K. Pawluk, "Magnetostatic fields drawn up by means of integrals of Lipschitz-Hankel type" Electromagnetic fields in electrical engineering, ISEF'01, IOS Press, Amsterdam, pp126-131.

I-14. COMPARISON OF THE GENERAL LOAD LINE METHOD WITH THE FINITE ELEMENT METHOD

R.I. Román B.¹, A. Konrad¹ and J.F. Brudny²

¹Edward S. Rogers Sr. Dept. of Electrical & Computer Eng., University of Toronto, 10 King's College Road,
Toronto, Ontario, Canada M5S 3G4 E-mail: rosa@ele.utoronto.ca and konrad@ecf.utoronto.ca

²Electrical Engineering Dept. (L.S.E.E.), University of Artois, Technoparc Futura, Bethune, France 62400, E-mail: brudny@univ-artois.fr

Abstract – The paper describes the application of the general load line method to a magnetic circuit problem with series and parallel branches of uniform cross sections consisting of the same homogeneous ferromagnetic core material, and presents a comparison with finite element analysis results.

Introduction

The operating point of the homogeneous core of a series magnetic circuit with uniform cross section and an air gap with negligible fringing can be found by a graphical method called the *load line method* (LLM) [1] provided that the B-H magnetization curve of the core material is known. Unfortunately, the operating point of a series magnetic circuit with an inhomogeneous and/or non-uniform core material cannot be calculated by the LLM because each region has its own B-H magnetization curve and/or B is multi-valued. However, the *general load line method* (GLLM) described in [2] is applicable to magnetic circuits with both inhomogeneous and non-uniform magnetic cores. Each homogeneous section of the core has its own B-H curve. The solution of this type of magnetic circuit problem by the GLLM requires the transformation of B-H curves into core flux versus core mmf curves (or ϕ_c - \mathfrak{S}_c curves). The GLLM can be applied to both series and parallel magnetic circuits with non-uniform, inhomogeneous magnetic cores.

In this paper, the application of the GLLM to a magnetic circuit problem with series and parallel branches is described. For simplicity, the branches have uniform cross sections and consist of the same homogeneous ferromagnetic core material. The equivalent ϕ_c - \mathfrak{S}_c curve for the core as a whole can be found by graphically summing all the mmf_i-s, where the subscript i refers to the i-th core section of mean length ℓ_i [2]. The operating point of the core is given by the intersection of the non-linear equivalent ϕ_c - \mathfrak{S}_c curve and the load line expressed as [2]

$$\phi_c = -\left(\frac{\mu_0 A_g}{\ell_g}\right) \mathfrak{S}_c + \left(\frac{\mu_0 A_g NI}{\ell_g}\right) \quad \text{or} \quad \phi_c = -\left(\frac{1}{\mathfrak{R}_g}\right) \mathfrak{S}_c + \left(\frac{NI}{\mathfrak{R}_g}\right) \quad (1)$$

Here ϕ_c is the core magnetic flux, \mathfrak{S}_c is the core mmf, A_g is the air gap effective cross-sectional area, ℓ_g is the air gap mean length, NI is the total mmf, μ_0 is free space permeability, and \mathfrak{R}_g is the air gap reluctance. For the solution of these problems the equivalent ϕ_c - \mathfrak{S}_c curve is obtained by graphically summing the mmf's for series elements and the fluxes for parallel elements.

Magnetic Circuit Problem

Fig.1 shows the geometry of a series-parallel magnetic circuit of uniform cross-section with an air gap, which is used for the GLLM and finite element method (FEM) examples. The magnetic core has a winding of 600 turns in which a current of 10A is applied. The magnetic core consists of two parallel branches in series with the center element of the core and the air gap. In Fig.1, ϕ_c represents the total magnetic flux of the core, ϕ_{c2} and ϕ_{c3} the magnetic fluxes in the parallel elements 1 and 2, N the number of turns, I the total current and A_c the cross-sectional area of the magnetic core. Fig.2 shows a plot of the B-H data for the core material.

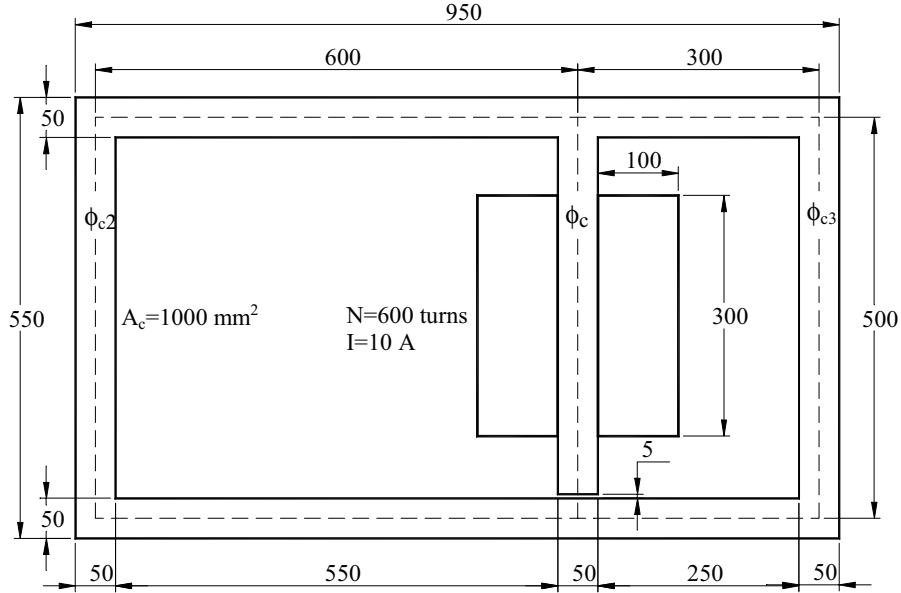


Fig. 1. Geometry of the series-parallel magnetic circuit. Dimensions are given in millimeters.

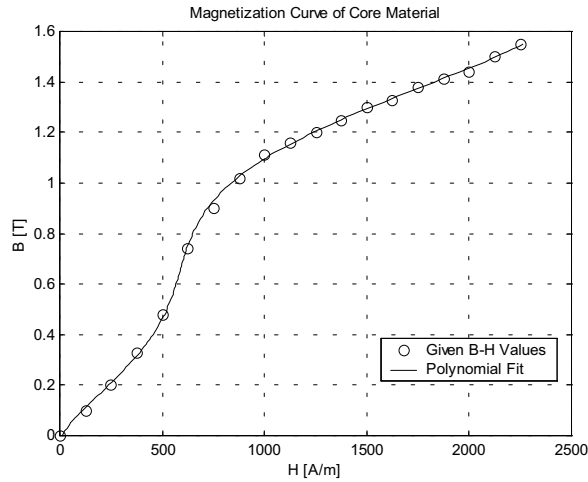


Fig. 2. Matlab[®] plot of the B-H data for the core material.

GLLM Solution

To find the operating point of the magnetic circuit shown in Fig.1, the B-H magnetization curve of Fig.2 is transformed into an equivalent ϕ_c - \mathfrak{F}_c curve by making use of the following relations [2]:

$$\phi_{ci} = B_{ci} A_{ci} \quad (2)$$

$$\mathfrak{F}_{ci} = H_{ci} \ell_{ci} \quad (3)$$

where the subscript i refers to the i -th section of the core of length ℓ_{ci} and cross-sectional area A_{ci} . Table I summarizes the known quantities.

Table I. Given data for the magnetic circuit of Fig.1.

Quantity	Notation	Value
Number of winding turns	N	600 turns
Excitation current	I	10 A
Length of series element	ℓ_{c1}	0.495 m
Length of parallel branch 1	ℓ_{c2}	1.7 m
Length of parallel branch 2	ℓ_{c3}	1.1 m
Air gap length	ℓ_g	0.005 m
Core cross-sectional area	$A_{c1} = A_{c2} = A_{c3} = A_c$	0.001 m ²

The series and parallel elements have their own ϕ_c - \mathfrak{S}_c curves. Equations (2) and (3) yield the equivalent flux-mmf values of these elements as given in Table II. *Columns 2 and 3* of Table II show the 19 measured values of the B-H magnetization curve of the core. The corresponding magnetic flux values, ϕ_{c1} , which are the same for all the elements because the cross-sectional areas are equal, are shown in *column 4*. *Column 5* shows the values of the mmf of the series element, \mathfrak{S}_{c1} , of length $\ell_{c1} = 0.495$ m. *Column 6* shows the values of the mmf, \mathfrak{S}_{c2} , of parallel branch 1 of length $\ell_{c2} = 1.7$ m. Parallel branch 2, with a length given by $\ell_{c3} = 1.1$ m, has mmf values, \mathfrak{S}_{c3} , given in *column 7*.

Table II. Magnetization curve data

Column	2	3	4	5	6	7
Row	B [T]	H [A-t/m]	$\phi_{c1} = B A_{c1}$ [μ Wb]	$\mathfrak{S}_{c1} = H\ell_{c1}$ [A-t]	$\mathfrak{S}_{c2} = H\ell_{c2}$ [A-t]	$\mathfrak{S}_{c3} = H\ell_{c3}$ [A-t]
1	0.00	0	0	0	0.0	0.0
2	0.10	125	100	61.9	212.5	137.5
3	0.20	250	200	123.8	425.0	275.0
4	0.33	375	330	185.6	637.5	412.5
5	0.48	500	480	247.5	850.0	550.0
6	0.74	625	740	309.4	1062.5	687.5
7	0.90	750	900	371.3	1275.0	825.0
8	1.02	875	1020	433.1	1487.5	962.5
9	1.11	1000	1110	495.0	1700.0	1100.0
10	1.16	1125	1160	556.9	1912.5	1237.5
11	1.20	1250	1200	618.8	2125.0	1375.0
12	1.25	1375	1250	680.6	2337.5	1512.5
13	1.30	1500	1300	742.5	2550.0	1650.0
14	1.33	1625	1330	804.4	2762.5	1787.5
15	1.38	1750	1380	866.3	2975.0	1925.0
16	1.41	1875	1410	928.1	3187.5	2062.5
17	1.44	2000	1440	990.0	3400.0	2200.0
18	1.50	2125	1500	1051.9	3612.5	2337.5
19	1.55	2250	1550	1113.8	3825.0	2475.0

In a parallel circuit, the mmf is the same for each parallel element. The equivalent ϕ_c - \mathfrak{S}_c curve of the parallel elements results from the summation of the magnetic flux of each element for common values of the mmf (similar to current summation in a parallel electric circuit). The equivalent ϕ_c - \mathfrak{S}_c values of the parallel sections of the magnetic circuit are given in Table III, where the values of magnetic flux for the common values of the mmf were obtained by interpolation. *Column 2* shows \mathfrak{S}_{cp} , the common values of the mmf. The values of the interpolated magnetic flux, ϕ_{c2} , are shown in *column 3* and the interpolated values of ϕ_{c3} in *column 4*. The total magnetic flux of the parallel section of the core, ϕ_{cp} , is obtained by summing ϕ_{c2} and ϕ_{c3} (see *column 5*). Fig.3 shows the ϕ_c - \mathfrak{S}_c curves of the parallel elements and the equivalent ϕ_c - \mathfrak{S}_c curve of the parallel section of the core using the values of *columns 2 and 5* of Table III. The equivalent parallel section of the core is in series with the section of the core with the winding and air gap. Fig.4 shows the ϕ_c - \mathfrak{S}_c curves of the equivalent parallel section and the section of the core with the winding. The equivalent ϕ_c - \mathfrak{S}_c curve of the core is obtained by summing the mmf-s of the series elements of the core $\mathfrak{S}_{c1} + \mathfrak{S}_{cp}$ for common values of the magnetic flux consisting of values of ϕ_{c1} and ϕ_{cp} . The values of ϕ_c and $\mathfrak{S}_{c1} + \mathfrak{S}_{cp}$ represent the equivalent ϕ_c - \mathfrak{S}_c curve of the core. With ϕ_c given in Wb and \mathfrak{S}_c given in A-t, the load line is obtained from (1) as

$$\phi_c = -(8.00\pi \times 10^{-8})\mathfrak{S}_c + (4.800\pi \times 10^{-4}) \quad \text{for no fringing at the air gap} \quad (4a)$$

$$\phi_c = -(11.60\pi \times 10^{-8})\mathfrak{S}_c + (6.960\pi \times 10^{-4}) \quad \text{for 45% fringing at the air gap} \quad (4b)$$

$$\phi_c = -(12.32\pi \times 10^{-8})\mathfrak{S}_c + (7.392\pi \times 10^{-4}) \quad \text{for 54% fringing at the air gap} \quad (4c)$$

Column 10 of Table III shows the \mathfrak{S}_c values for no fringing. Fig.5 shows the plot of the equivalent ϕ_c - \mathfrak{S}_c curve of the core and the three load lines. The operating point of the core is obtained from the intersection of the ϕ_c - \mathfrak{S}_c curve of the core and a load line. For no fringing, the solution is $\phi_c \cong 1178 \mu\text{Wb}$ and $\mathfrak{S}_c \cong 1311 \text{ A-t}$.

Table III. Combined magnetization curve data and load line. Interpolated values are printed in bold.

Column	Parallel section of the core (Fig.3)				Series combination of the core (Fig.4)				Load line
	2	3	4	5	6	7	8	9	10
Row	$\mathfrak{S}_{cp} = \mathfrak{S}_{c2} \& \mathfrak{S}_{c3}$ [A-t]	ϕ_{c2} [μWb]	ϕ_{c3} [μWb]	$\phi_{cp} = \phi_{c2} + \phi_{c3}$ [μWb]	$\phi_c = \phi_{c1} \& \phi_{cp}$ [μWb]	\mathfrak{S}_{c1} [A-t]	\mathfrak{S}_{cp} [A-t]	$\mathfrak{S}_{c1} + \mathfrak{S}_{cp}$ [A-t]	\mathfrak{S}_c [A-t]
	common values				common values				
1	0.0	0.0	0.0	0.0	0.0	0.0	0.0	0.0	6000.000
2	137.5	64.7	100.0	164.7	100.0	61.9	83.5	145.4	5602.113
3	212.5	100.0	154.5	254.5	164.7	101.9	137.5	239.4	5344.656
4	275.0	129.4	200.0	329.4	200.0	123.8	167.0	290.7	5204.225
5	412.5	194.1	330.0	524.1	254.5	128.9	212.5	341.4	4987.560
6	425.0	200.0	343.6	543.6	329.4	136.1	275.0	411.1	4689.311
7	550.0	276.5	480.0	756.5	330.0	136.1	275.1	411.2	4686.972
8	637.5	330.0	645.5	975.5	480.0	247.5	309.6	557.1	4090.141
9	687.5	365.3	740.0	1105.3	524.1	258.0	412.5	670.5	3914.601
10	825.0	462.4	900.0	1362.4	543.6	262.6	425.0	687.6	3836.941
11	850.0	480.0	921.8	1401.8	740.0	309.4	462.0	771.4	3055.634
12	962.5	617.6	1020.0	1637.6	756.5	315.7	550.0	865.7	2990.098
13	1062.5	740.0	1085.5	1825.5	900.0	371.3	575.3	946.5	2419.014
14	1100.0	768.2	1110.0	1878.2	975.5	410.2	637.5	1047.7	2118.788
15	1237.5	871.8	1160.0	2031.8	1020.0	433.1	656.3	1089.4	1941.549
16	1275.0	900.0	1170.9	2070.9	1105.3	491.8	687.5	1179.3	1602.191
17	1375.0	956.5	1200.0	2156.5	1110.0	495.0	690.0	1185.0	1583.450
18	1487.5	1020.0	1240.9	2260.9	1160.0	556.9	716.8	1273.6	1384.507
19	1512.5	1030.6	1250.0	2280.6	1200.0	618.8	738.2	1356.9	1225.352
20	1650.0	1088.8	1300.0	2388.8	1250.0	680.6	764.9	1445.5	1026.408
21	1700.0	1110.0	1310.9	2420.9	1300.0	742.5	791.6	1534.1	827.464
22	1787.5	1130.6	1330.0	2460.6	1330.0	804.4	807.7	1612.1	708.098
23	1912.5	1160.0	1375.5	2535.5	1362.4	844.4	825.0	1669.4	579.370
24	1925.0	1162.4	1380.0	2542.4	1380.0	866.3	832.8	1699.0	509.154
25	2062.5	1188.2	1410.0	2598.2	1401.8	911.3	850.0	1761.3	422.343
26	2125.0	1200.0	1423.6	2623.6	1410.0	928.1	853.9	1782.0	389.788
27	2200.0	1217.6	1440.0	2657.6	1440.0	990.0	868.2	1858.2	270.422
28	2337.5	1250.0	1500.0	2750.0	1500.0	1051.9	896.8	1948.7	31.690
29	2475.0	1282.4	1550.0	2832.4	1550.0	1113.8	920.7	2034.4	-167.254

Comparison with FEM Solutions

The FEM, implemented in commercially available computer programs, has been in use for many years [3] and offers an alternative way to solve this type of problem. Two commercially available computer packages called PC-Opera[®] and FLUX2D[®] were used for the finite element (FE) simulation of the magnetic circuit shown in Fig.1. Fig.6 shows the magnetic flux distribution in the core obtained with PC-Opera. The corresponding PC-Opera FE value of ϕ_c is 1547 μWb . With FLUX2D the value of ϕ_c is 1488 μWb . These values are in sharp contrast with the GLLM solution of $\phi_c \cong 1178.4 \mu\text{Wb}$ when there is no fringing. However, with fringing corresponding to an air gap effective area of $A_g = 1.45A_c$ the GLLM solution of 1487 μWb matches the FLUX2D FE solution. Similarly, with fringing corresponding to an air gap effective area of $A_g = 1.54A_c$ the solution of 1543 μWb matches the FLUX2D FE solution. Clearly, fringing cannot be neglected in this example.

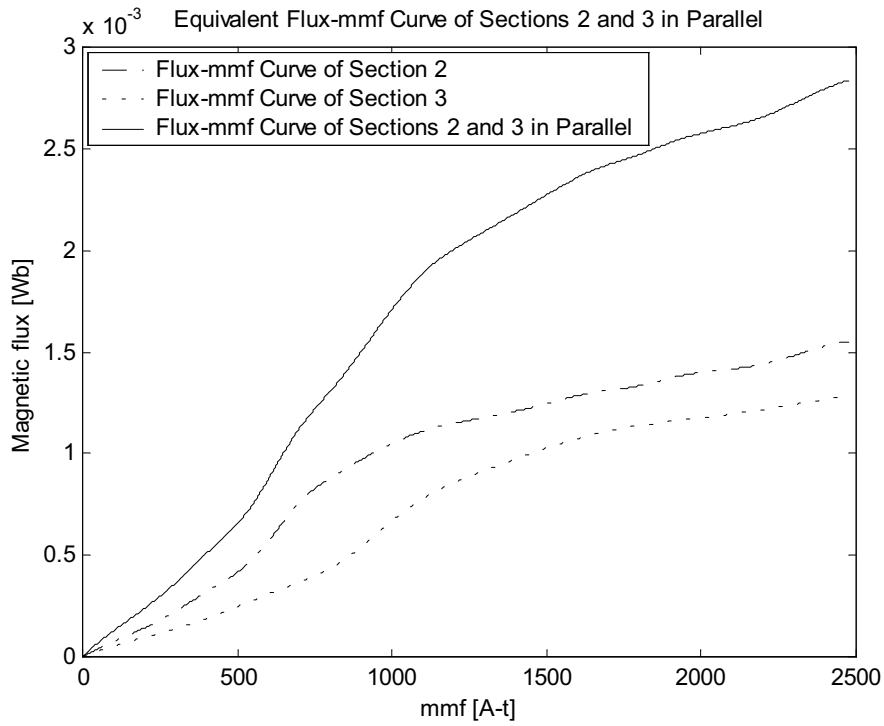


Fig. 3. Equivalent ϕ_c - \mathfrak{F}_c curve of the parallel section of the core.

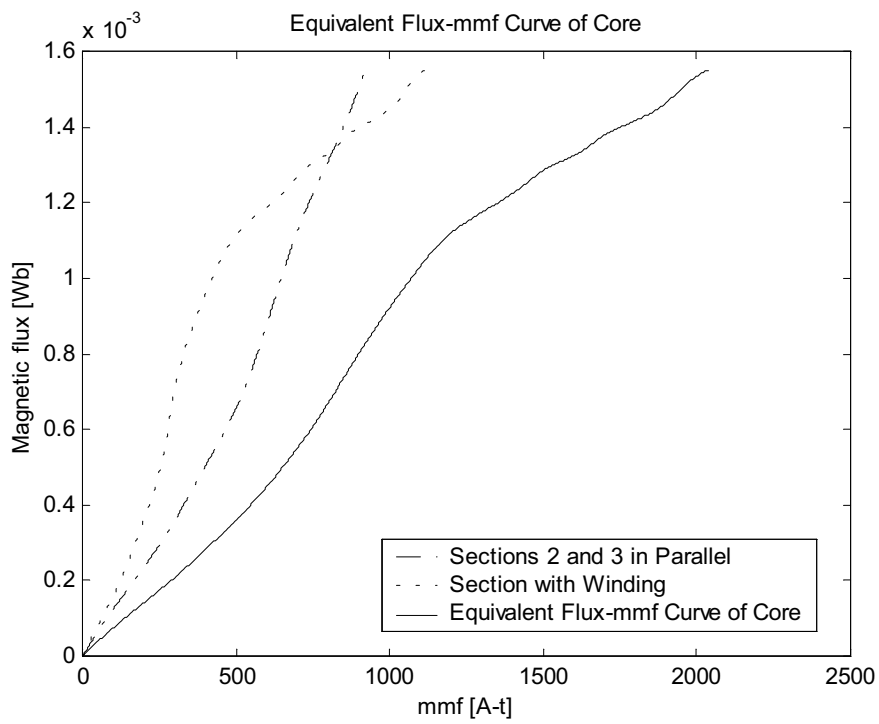


Fig. 4. Equivalent ϕ_c - \mathfrak{F}_c curve of the series combination of the core.

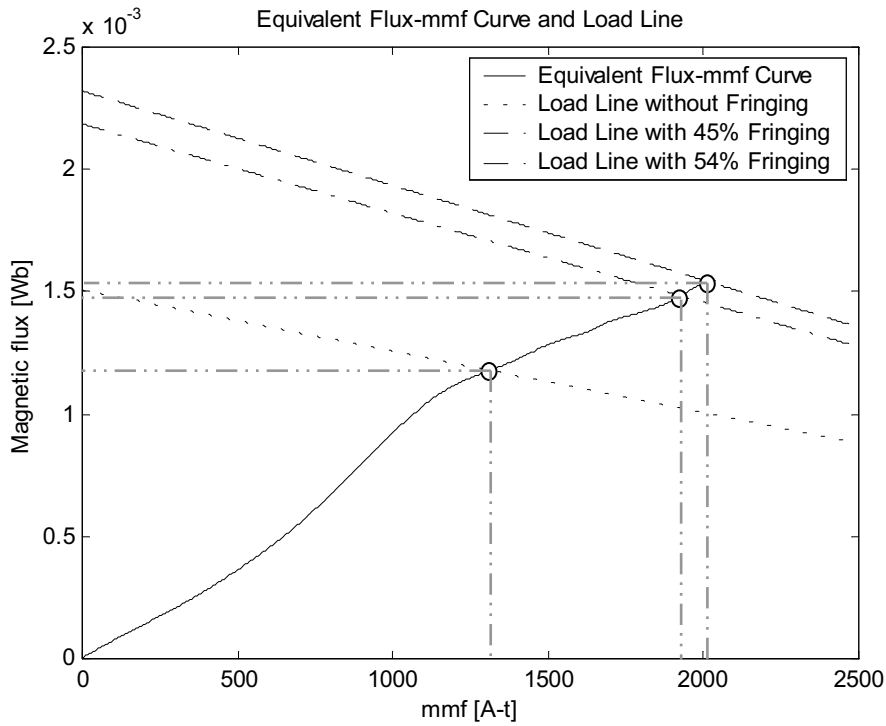


Fig. 5. Equivalent ϕ_c - \mathcal{F}_c curve of the core, three load lines, and the corresponding operating points.

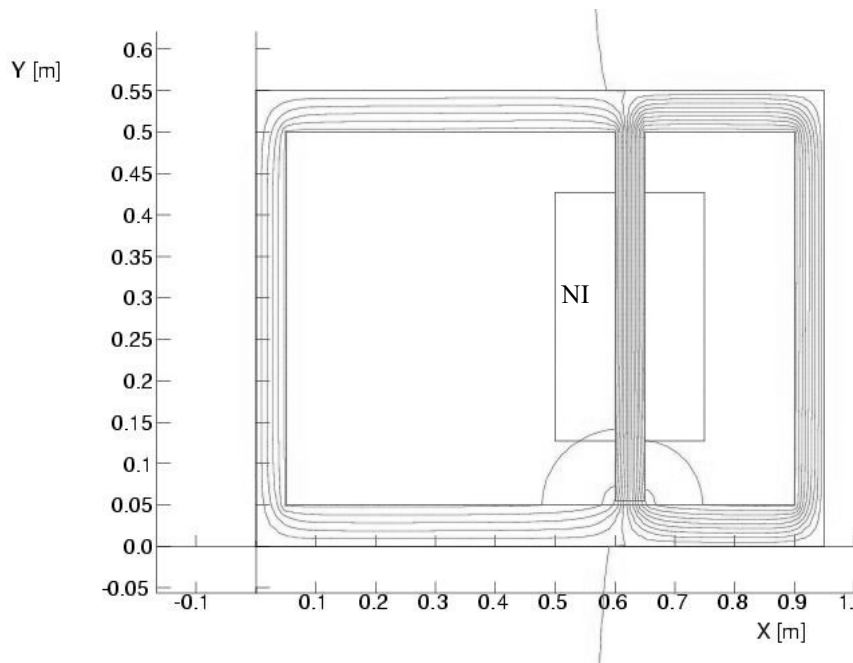


Fig. 6. Magnetic flux distribution (PC-Opera[®] FEM solution) clearly showing fringing at the air gap.

References

- [1] J.J. Cathey, *Electric Machines Analysis and Design Applying Matlab[®]*, Boston, MA: McGraw-Hill, 2001.
- [2] A. Konrad, "Extension of the load line method to series magnetic circuits of non-uniform cross-section," in *Electromagnetic Fields in Electrical Engineering*, A. Krawczyk and S. Wiak (Editors), Amsterdam, The Netherlands: IOS Press, 2002, pp.98-103.
- [3] D.A. Lowther and P.P. Silvester, *Computer-Aided Design in Magnetics*, New York, NY: Springer-Verlag, 1986.

I-15. OPTIMIZATION FOR HIGH VOLTAGE COMPOSITE INSULATORS USING EXPERIMENTAL DESIGN THEORY

Imre Sebestyén

Department of Electromagnetic Theory, BUTE – Budapest University of Technology and Economics
Egry J. u. 18. H-1521 Budapest, Hungary, E-mail: si@evtsz1.evt.bme.hu

Abstract – In the paper a method for optimizing parameters of HV composite insulators is presented. The optimal values of design parameters are determined by multivariable optimization procedure using theory of experimental designs. For repetitive calculation of the electric field strength the finite element method is used with domain decomposition. This method gives fast working software with accurate results to examine a very complex geometry without extra high computational effort.

Introduction

Composite insulators are being increasingly used to replace porcelain and glass insulators because of their advantageous features [1]. Main components of them are the fiberglass rod, the sheath and the weather sheds on the rod and the metal end fittings (Fig. 1). The sheath and sheds are made of polymeric materials (silicon rubber, ethylene propylene copolymer etc.). Controlling of the electric field strength around polymeric HV insulators is very important. Mainly because of, that, polymers are more sensitive to degradation initiated by surface discharges.

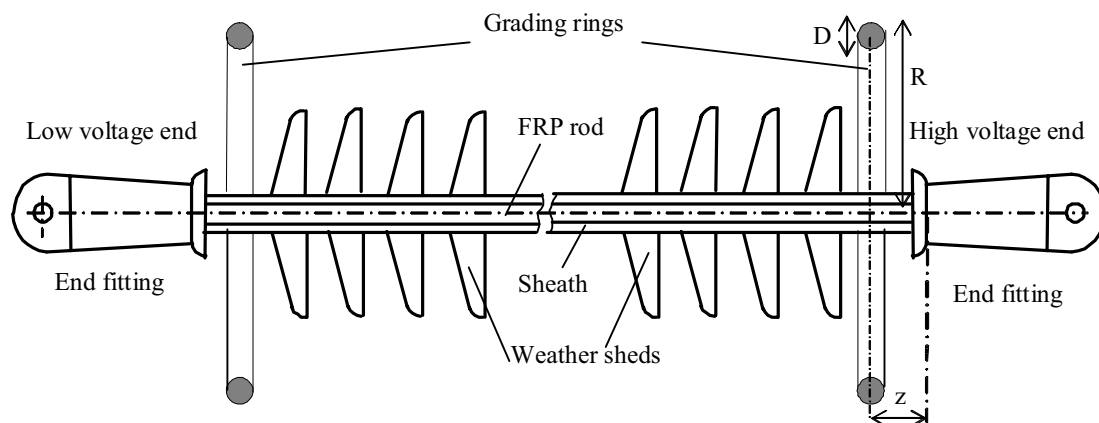


Fig.1. Main parts of HV composite insulators

Pollution and wetting related to hydrophobic surfaces may lead to the formation of small polluted water droplets which can initiate discharges due to field enhancement if the background field is high enough [2]. Possible other negative consequences of high level of electric field are additional losses, electromagnetic pollution and premature aging of insulation. To decrease the high electric field strength, manufacturers provide special grading rings attached near the ends of insulators (grading rings). In this paper a method is presented for obtaining the optimal design of and the grading ring at the high voltage end of the insulator.

Method of optimization

Objective of the optimization is the minimization of the overall electric field strength along the surface of the insulator at the high voltage end. For the electric field analysis the finite element method (FEM) is used. However, FEM-analyses for a complex 3-dimensional problem are very time consuming, which results very long run-time in case of iterative optimization. To decrease the computation time we have developed a fast FEM solver for electric field analysis [3] and instead of iterative optimization we used the method of experimental designs [4].

A) FEM using domain decomposition

Considering the specific conditions for the application of the insulators (towers, line conductors of 3-phase system and the ground conductors) a model with very complex geometry is resulted. To determine the accurate value of the electric field strength a very fast field solver is needed. For this purpose we apply a modified domain decomposition method presented in [3]. This method applies iterative solutions on two overlapped sub-domains (global and local domain) of the problem resulted in effective decrease of the time of FEM computation. We assume that the model of the structure in domain $D_1 \cup D_{12}$ is the large-scale model of the whole problem (*global domain*), see Fig. 2. In the domain $D_2 \cup D_{12}$ only the sub-problem is modeled, where the exact field distribution is required (*local domain*). These domains are overlapped along D_{12} (*mortar domain*). The finite element meshes generally are *not adjacent* at the boundaries Γ_{1b} and Γ_{2b} .

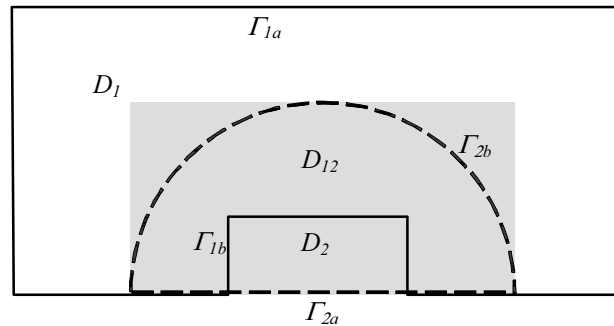


Fig. 2. Computational model partitioned into global and local domains.

The iterative procedure starts with the solution of the boundary value problem for the entire analyzed domain $D_a = D_1 \cup D_{12} \cup D_2$, using an initial adjacent mesh for the local domain, but the structure is simplified significantly inside of it. This step is used to get the initial boundary conditions for Γ_{1b} and Γ_{2b} instead of arbitrary chosen values. After the initialization, the boundary value problem is solved repeatedly with two different meshes in the sub-domains. This method ensures that embedding the full-scale 3D model of the insulators into the real 3D environment of the power transmission lines can be analyzed without extreme high demands of computer memory and CPU time also.

B) Optimization using experimental design theory

Using method of experimental designs instead of repeatedly analyzing the structure and subsequently updating the design variables, several structures chosen a priori analyzed. The FEM calculation of a chosen structure is termed as “experiment” and the set of appropriate structures to be analyzed as “experimental design”. In order to run the experiment, different values, so-called levels, have to be chosen for each design variable. The space spanned by the design variables forms the design space, and a point of the design space is mapped to result of that experiment. The discretization of the design space, by assigning a certain number of levels to each design variable, results in a set of candidate points. The number of them is denoted by n_c . Analyzing all candidate points in the design space is

expensive and inefficient. Therefore the restriction of the experiments to a subset of candidates is advisable. The experimental design theory provides optimality criteria and algorithms by means of them optimal experimental designs can be generated. In this work we apply the algorithm DETMAX developed by Mitchell [5]. On base of experiments the regression equation of the model is created (simple polynomial function), which are used as the problem function of the optimization.

Application

The above outlined method is applied for grading rings of composite insulators on power transmission line with 400 kV nominal voltage. The transmission line has doubled three-phase systems with bundle of conductors. In case of the FEM analysis with domain decomposition, the solution domain of the global problem includes the transmission line tower together with the phase- and ground conductors as well as the simplified insulators. The local domain is bounded by a cylindrical surface coaxial to the investigated insulator (Fig.3). In the local domain, the investigated insulator was modeled by the exact

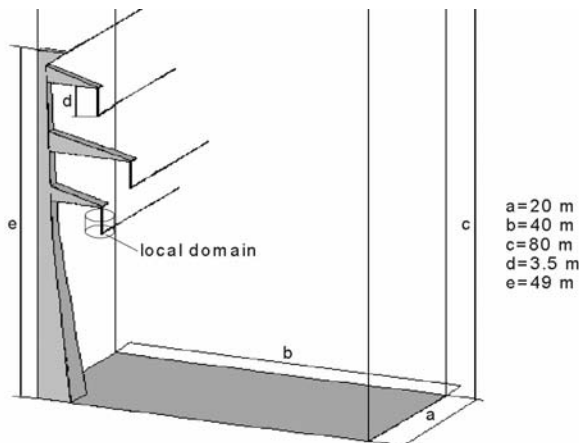


Fig. 3. View of the global model with the power line tower.

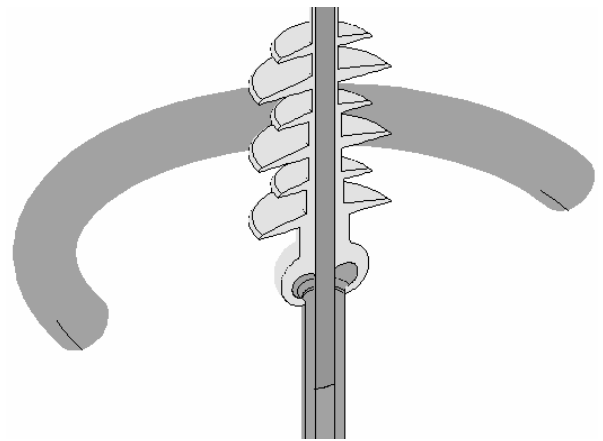


Fig. 4. The view of the high voltage end of the insulator with grading ring.

geometry together with the metal end-caps and the shedding. This structure is presented in Fig. 4, where the cross-sectional view of the high voltage end of the investigated insulator is shown.

Design parameters are the mean radius R , the thickness diameter D and the axial disposition z of the grading ring (see Fig. 1). The design variables are constrained to the intervals: $0 \leq z \leq 60$ [mm], $185 \leq R \leq 245$ [mm] and $36 \leq D \leq 60$ [mm]. Design variable z is varied on four equidistant levels, while R and D are varied on three equidistant levels, so we have $n_c=4 \times 3 \times 3=36$ candidate experiments. For regression model we apply the function

$$E_{\max} = c_1 + c_2 z + c_3 r + c_4 d + c_5 z^2 + c_6 r^2 + c_7 d^2 + c_8 zr + c_9 rd + c_{10} dz, \quad (1)$$

where $r = R - R_0$, with $R_0 = 215$ mm and $d = D - D_0$, with $D_0 = 48$ mm notations are used. The model (1) contains 10 unknowns; we apply in three cycles 10, 11 and 15 experiments for model building. Finally, with help of function LSQCURVEFIT of the MATLAB Optimization Toolbox, we have obtained parameters of the model listed in Table I.

Table I. Values of the model parameters

c_1	1.0238	c_6	-13.2061
c_2	-5.6688	c_7	-9.1739
c_3	2.9372	c_8	-4.2806
c_4	-8.0279	c_9	-42.7284
c_5	75.5481	c_{10}	-38.8339

Due to its simple shape, the minimization of the second order model function (1) can be performed either graphically or analytically.

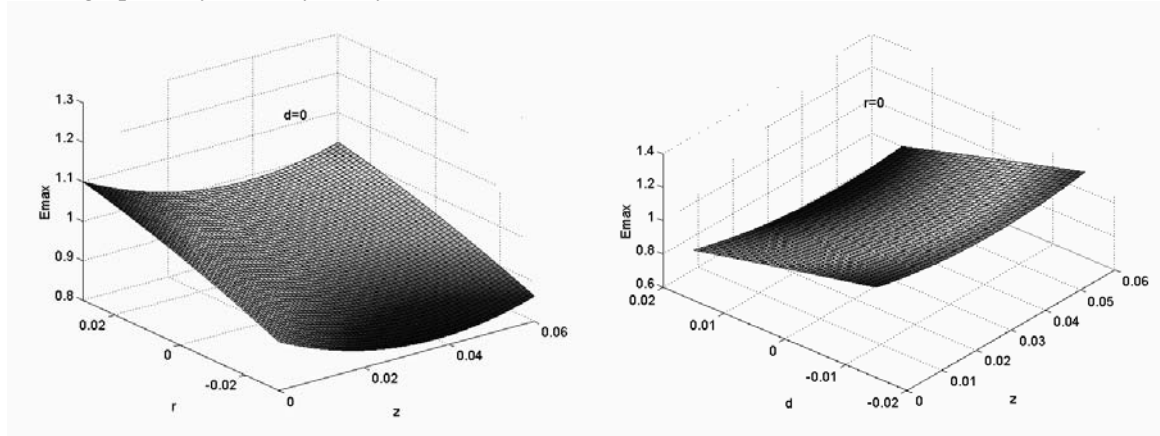


Fig. 5. Views of the model functions

In Fig. 5 the model function is displayed, where the value of E_{max} practically monotonously varies with variables r and d . Thus the $\frac{\partial E_{max}}{\partial z} = 0$ condition serves the optimal values for the disposition of the grading ring. As an analytical result of the optimization we have obtained $z=39.75$ mm for disposition with $r=-30$ mm and $d=12$ mm, and the overall electric field intensity is $E_{max}=0.7221$ kV/mm. Graphical solution gives practically the same results: $z=40$ mm with the same r and d values, and the maximum of the field intensity is 0.721 kV/mm. This means that the overall field is reduced to approximately 70% comparing to the original arrangement. Validating this result we have performed a FEM analysis of the model using the optimal value of the grading ring that is: $z=40$ mm, $r=-30$ mm and $d=12$ mm. The maximum of the overall electric field intensity by this analysis is 0.7041 kV/mm, that is the relative difference is 2.5%, so the presented procedure of optimization gives very good results.

References

- [1] H.M. Schneider, J.F. Hall, G. Karady, and J. Rendowden, "Nonceramic Insulators for Transmission Lines," *IEEE Trans. on Power Delivery*, vol. 4, No. 4, pp. 2214-2221, Oct. 1989.
- [2] A.J. Phillips, D.J. Childs, H.M. Schneider, "Aging of Non-Ceramic Insulators due to Corona from Water Drops," *IEEE Trans. on Power Delivery*, vol. 14, No. 3, pp. 1081-1089, July 1999.
- [3] I. Sebestyén, "Electric Field Calculation for HV Insulators Using Domain Decomposition Method," *IEEE Trans. on Magnetics*, vol. 38, No. 2, pp. 1213-1216, March, 2002.
- [4] D.H. van Campen, R. Nagtegaal, A.J.G. Schoofs, "Approximation Methods in Structural Optimization Using Experimental Designs for Multiple Responses," in *Multicriteria Design Optimization* (Ed. H. Eschenauer, J. Koski, A. Osyczka) Springer, 1990, pp.205-228.
- [5] T. J. Mitchell, "An algorithm for the construction of "d-optimal" experimental designs". *Technometrics*, vol. 16, No. 2, pp. 203-210, May 1974.

I-16. MODELLING AND OPTIMISATION OF INTELLIGENT ELECTROSTATIC COMB ACCELEROMETER

Sławomir Wiak*, Krzysztof Smółka*, Marek Rudnicki**

* Institute of Mechatronics and Information Systems

** Institute of Computer Science

Technical University of Lodz, ul. Stefanowskiego 18/22, 90-924 Lodz, Poland

e-mail: wiakslaw@p.lodz.pl

Abstract – This paper describes the field and circuit modelling of 2D/3D structure of surface micromachined (MEMS) accelerometers. This comb structure has been able to move only within the plane (two-axes movement). The main goal of investigation is to exploit the field method to extract equivalent capacitance characteristics to be treated as the background for equivalent circuit analysis and optimisation process.

Introduction

Actually, the task of the designer is complicated by the evidence that different energy domains, in general being mutually coupled, are involved when modeling micro-electro-mechanical devices (MEMD), in the frame of more general micro-electro-mechanical systems (MEMS). Moreover, the designer has to take into account the constraints imposed by the process technology, that limit the feasibility of innovative devices.

MicroElectromechanical Systems (MEMS) technology has generated a significant interest of academic, research and business sectors. The above is caused by very promising technology market and as well cost reduction connected with microscale devices fabricated by use of silicon technology. Due to rapid grow of this market, year after year, the market is just segmented. This is also true in the reference to accelerometer market. Efficiency of the device development is also due to design flexibility, developing of simulation tools and CAD systems, integration of microdevices and microelectronics, etc. In general, multi-layer surface microactuator fabrication process is enough flexible to produce advanced device structures. MEMS structure development requires reliable fabrication processes and flexible CAD/(analysis and optimal design) tools. We could treat mask layout tools as complementary to CAD/(analysis and optimal design) tools. The device geometry is, in general, defined in the mask layout tool, then transferred to integrated circuit layout package, while specific surface micromachining process has been employed. Some specific codes based on Finite Element Method could be successfully applied to MEMS designing while microdomain physics are also taken into account. Such a sophisticated software could allow creating 3D structure of the device, full model analysis (structural mechanics, electrostatics, fluid flow, vibration, etc.). The strongest impulse to the development of such advanced tools should come mainly from industrial companies; in fact, virtual prototyping of optimal devices would determine a twofold benefit: decreasing the total time lasting from the device ideation to its implementation as a marketable product; reducing the number of fabrication experiments on real prototypes; identifying the device of minimum cost, given the performance or, conversely, the device of maximum performance, given the cost; increasing the global quality of the industrial product.

Accelerometer Design – Planar structure

Accelerometers are important devices in the range of variety applications such as air bag actuation (by Analog and Sandia), microrobots, etc (see Fig. 1). The accelerometers available on the market are

capable of measuring high values of accelerations. The electrostatic comb accelerometer is fabricated by use of different techniques like CDV, RIE, wet etching, etc. The relationship between input voltage and output displacement has been widely analysed experimentally and theoretically in the literature [1]. The accelerometer consists of a moving comb teeth, suspended by spring beams on both sides, and fixed teeth. The suspension is designed to be compliant in the x direction of motion and to be stiff in the orthogonal direction (y) to keep the comb fingers aligned. The applied voltages on the force unit causes a net electrostatic force to pull the movable part in the desired direction.

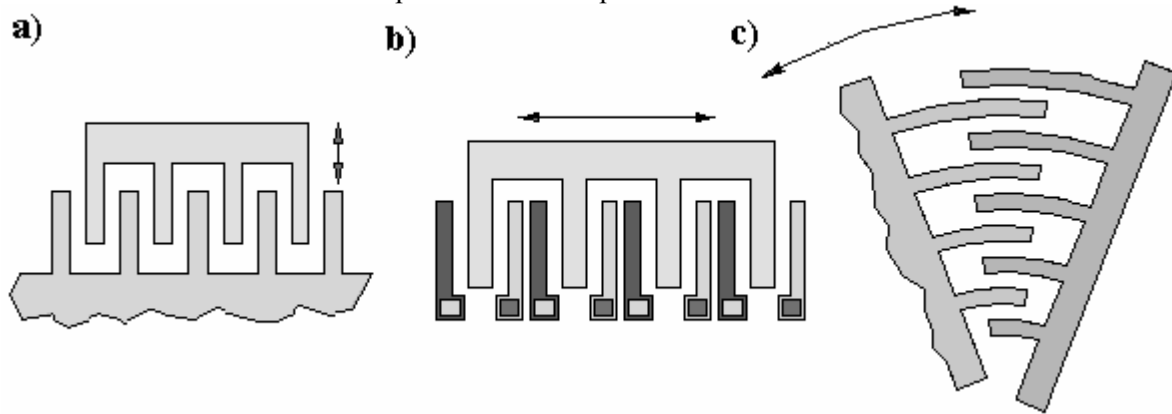


Fig. 1. Selected comb accelerometer structures

Equivalent Circuit Model

Energy stored in the device is defined as follows:

$$W = \frac{1}{2}CU^2 \quad (1)$$

A simplified scheme of a capacitive microaccelerometer is shown in Fig. 2. For the capacitive sensing approach, the displacement is detected by measuring the capacitance change (see formula 2), expressed as a function of displacement of moving comb teeth against fixed comb teeth (see Fig.3).

$$C_p = \varepsilon \frac{a(z-h+y)}{p+x} \quad C_m = \varepsilon \frac{a(z-h+y)}{m-x} \quad C_g = \varepsilon \frac{a \cdot d}{h+y} \quad (2)$$

Total accelerometer capacitance, defined as the symmetrical structure (both symmetrical and unsymmetrical structures are analysed), is the sum of three following terms: C_p , C_m and C_g :

$$C_s = (n-2)C_p + (n-1)C_m + (2n-3)C_g \quad (3)$$

Circuit method has been applied to capacitance calculations of the comb accelerometer with the following data: tooth width $d = 2 \mu\text{m}$, tooth length $z = 30 \mu\text{m}$, tooth height $a = 8 \mu\text{m}$, number of teeth $n = 10$, tooth distance of base plane $h = 1 \mu\text{m}$, distance between teeth $p = 4 \mu\text{m}$, symmetrical structure, applied voltage 10V, relative permittivity $\varepsilon = 1$. We consider as first step of capacitance computation the planar comb structure to extract the shape of each equivalent capacitance components and its influence on accelerometer drag force.

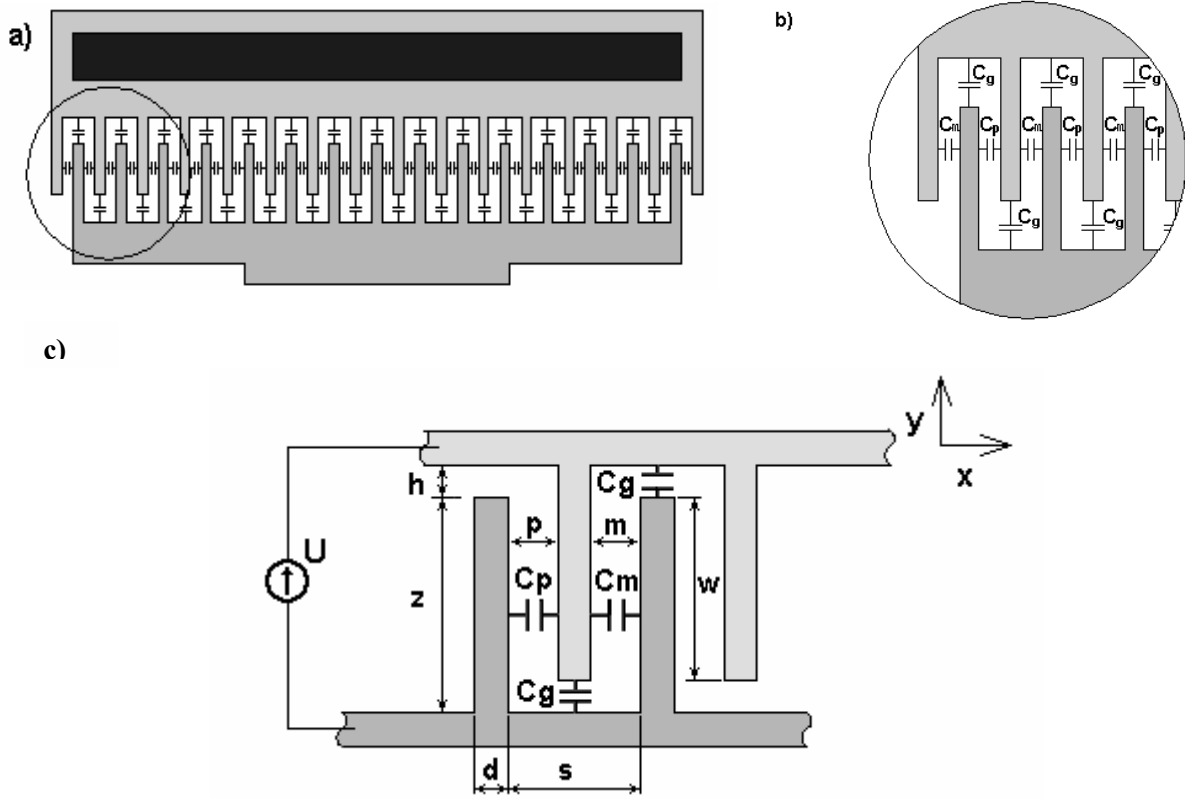


Fig. 2. Analysed comb accelerometer structure with main dimensions: a) general view of structure, B) zoom view, c) the main capacitances and dimensions

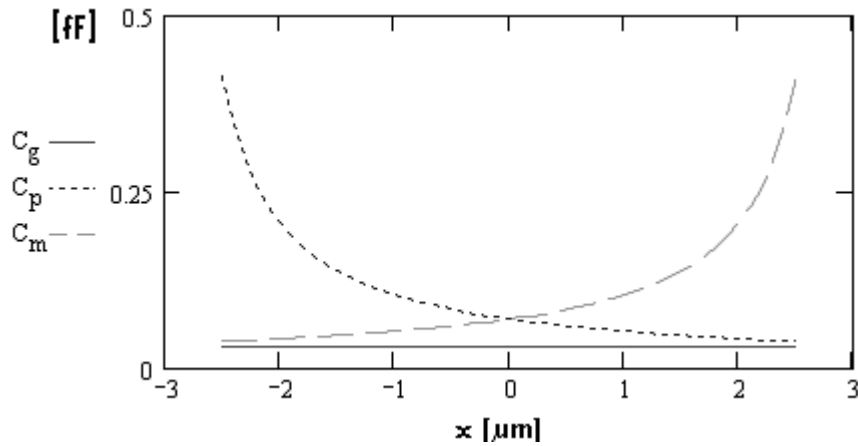


Fig. 3. Capacitance curves versus x displacement ($d=2\mu\text{m}$, $s=8\mu\text{m}$, $z=15\mu\text{m}$, $m=p=(s-d)/2$, $a=5\mu\text{m}$)

Sensitivity of the circuit model along X and Y we could express as follows:

$$s_y = \frac{\partial C}{\partial y} \quad s_x = \frac{\partial C}{\partial x} \quad (4)$$

Basing on the stored energy evaluation (see expression 1) the acting force in Y and X direction are expressed by the following formulas:

$$F_y = -\frac{\partial W}{\partial y} = \frac{1}{2} U^2 \frac{\partial C}{\partial y} \quad (5)$$

and finally (s-symmetrical structure):

$$F_{y,s} = \frac{1}{2} \varepsilon U^2 \left[(n-2) \left(\frac{1}{p+x} \right) + (n-1) \left(\frac{1}{m-x} \right) + 2(n-3) \frac{d}{(h+y)^2} \right] \quad (6)$$

Acting force along X axis is expressed as follows:

$$F_x = - \frac{\partial W}{\partial x} = \frac{1}{2} U^2 \frac{\partial C}{\partial x} \quad (7)$$

and finally (s-symmetrical structure):

$$F_{x,s} = \frac{1}{2} \varepsilon (z-h+y) U^2 \left[(n-1) \left(\frac{1}{(m-x)^2} \right) - (n-2) \left(\frac{1}{(p+x)^2} \right) \right] \quad (8)$$

Having derived formulas for the set of capacitances and drag force for each direction (x and y) we could perform the force computations (see Fig. 4).

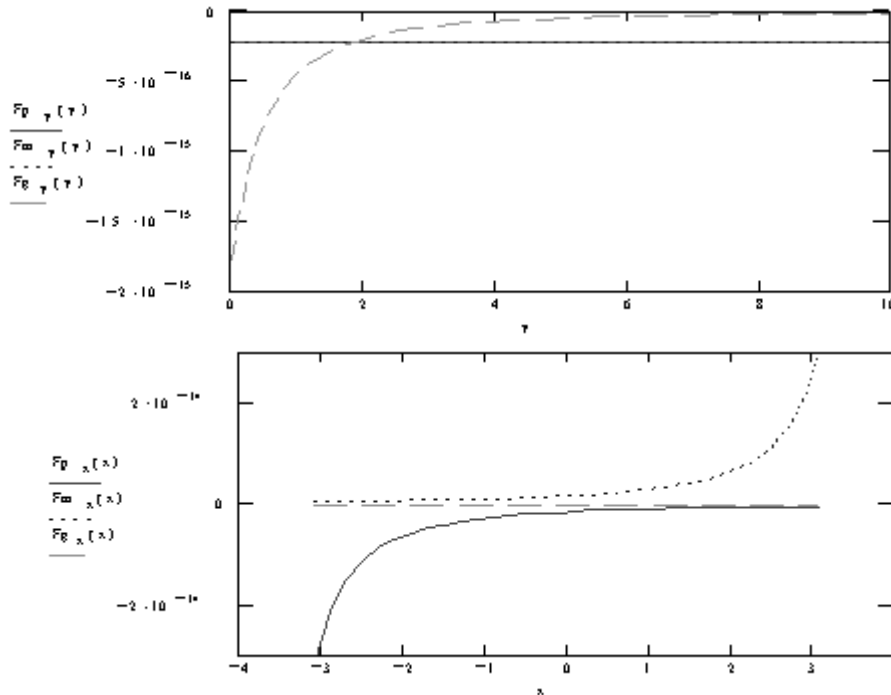


Fig. 4. Accelerometer drag forces in x and y axes corresponding to equivalent capacitance components

Comparative Study by Field Model

The analysed comb drive structures, in the literature, by means of circuit models are generally two-dimensional models. Moreover these models are rather intuitive equivalent circuit “proposals” than precisely defined structures. Therefore, in authors’ opinion, only the field approach is the base knowledge of exact computation of equivalent capacitance characteristics. This leads to next step of sophisticated method of capacitance calculations, namely field approach. It is recommended to go on with two streams of capacitance calculations; first - circuit approach than to be verified by second approach - exact field method.

Since most of the analytical solutions (models) neglect fringing fields, they cannot predict accurately the dependence of the drive force on the moving comb teeth. In order to better determine this dependence, numerical three-dimensional finite-element method (FEM) for electric field simulations in are used. A static FEM computation of electric potential, based on tetrahedron elements was carried out (see Fig. 5). Fixed potential boundary conditions were assumed. The stored electrical co-energy was computed as a function of the movable part position. In particular, detailed field analyses can be developed for investigating local effects in the steady state operation of the device.

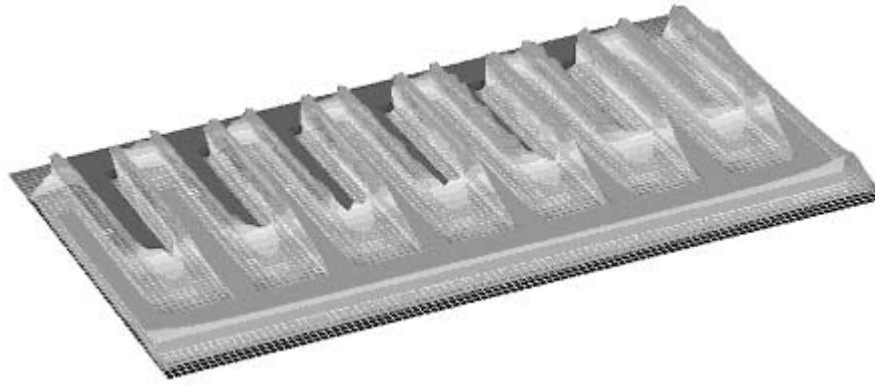


Fig. 5. Emod distribution of 3-D comb accelerometer structure

The comparative study performed for equivalent circuit method and field method allows making some improvements in final equivalent capacitance formulas. Therefore, the discrepancy between both values obtained by means field and circuit methods are negligibly small (see Fig. 6).

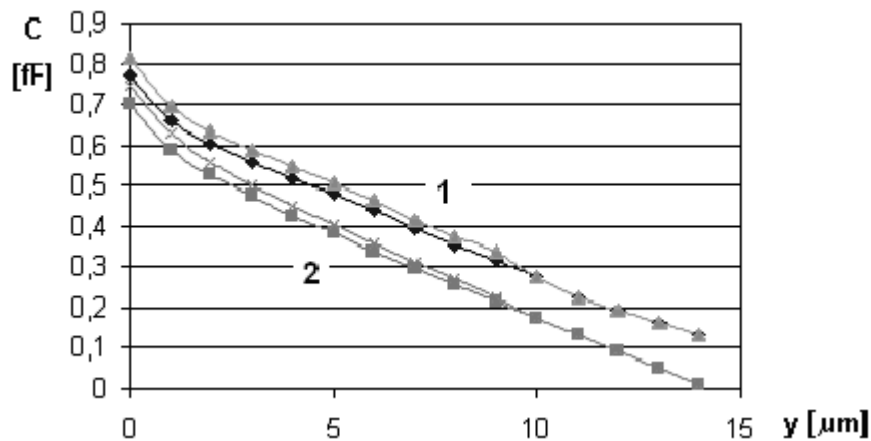


Fig. 6 Capacitance curves versus y displacement ($d=2\mu\text{m}$, $s=8\mu\text{m}$, $z=1.5\mu\text{m}$, $m=p=(s-d)/2$, $a=5\mu\text{m}$)
 (◆, ■ - symmetrical structure, ×, ▲ - unsymmetrical structure; 1-field method, 2-circuit method)

Single criterion problem and multiobjective shape design of comb accelerometer

In a design problem from real-life engineering, the presence of a single design criterion is rather an exception than a rule; often, the designer has to cope with the minimization of two or more conflictual criteria. It is reasonable to state that design – or inverse - problems are multiobjective problems by their very nature and imply the simultaneous minimization of a number of objectives being in mutual conflict. Traditionally, multicriteria problems are reduced to single criterion problems, for instance by means of one of the following procedures: i) the use of a penalty function composed of the various criteria; ii) the separate solutions of single criterion problems and their trade-off; iii) the solution of a single criterion problem, taking the other criteria as constraints. This approach leads to classical methods of multiobjective optimization and gives a solution which is supposed to be the optimum. A much more satisfactory way to tackle the problem of multicriteria optimisation consists of applying the Pareto optima theory in connection with a suitable minimization algorithm. These improved analytical formulas are in the next step of accelerometer design introduced to optimal design procedure. Authors have defined the following optimisation criteria being partially conflictual criteria: 1) Maximum of accelerometer drag force, 2) Maximum of accelerometer force sensitivity, 3) Minimum stress response. As the test problem optimisation, while two criteria are defined (1 and 2 as separate criteria), the comb drive with movement in one direction (y) is taken. The dedicated software is with gradient methods has been elaborated to carry out optimisation process. The list of accelerometer basic

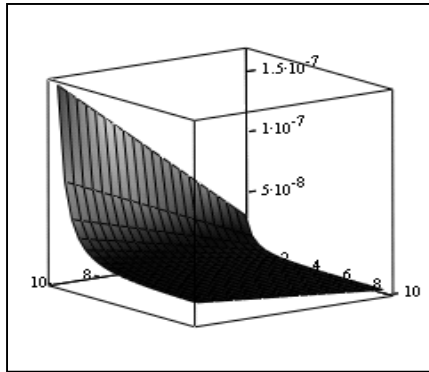
variables to be introduced into optimisation algorithm for selected: pole configurations, air gap length and geometric parameter variations are as follows: $a_{\min}=1\mu\text{m}$; $a_{\max}=10\mu\text{m}$; $p_{\min}=2\mu\text{m}$; $p_{\max}=5\mu\text{m}$; $d_{\min}=1\mu\text{m}$; $d_{\max}=5\mu\text{m}$; $h_{\min}=1\mu\text{m}$; $h_{\max}=10\mu\text{m}$; $z_{\min}=10\mu\text{m}$; $z_{\max}=50\mu\text{m}$; $n_{\min}=10$; $n_{\max}=15$.

Improved circuit formulas, verified by field method, leads to the following expressions, than to be treated as the basic two optimisation criteria:

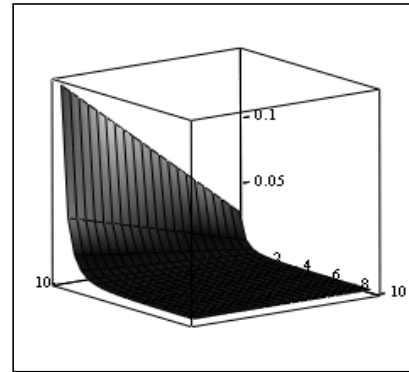
$$\text{➤ Max sensitivity } S_s(y) := -\frac{d}{d y} F_s(x_0, y) \quad S_{s_opt}(a, h, d, n, y) := \frac{\varepsilon \cdot a \cdot U^2}{2} \cdot \left[(2n-3) \cdot \frac{d}{(h+y)^3} \right]$$

$$\text{➤ Max force } F_{s_optd}(a, p, h, d, n, x, y) := \sqrt{F_{xs_opt}(a, p, h, d, n, x, y)^2 + F_{ys_opt}(a, p, h, d, n, x, y)^2}$$

The preliminary results are displayed in Figure 7 confirming that both first and second criterion are not in conflict, moreover the maximum values (optimisation criterion) are for almost the same accelerometer structure.



$$F_{ah}(a, h) := F_{s_opt}(a, p, h, d, n, x_0, y_0)$$



$$S_{ah}(a, h) := S_{s_opt}(a, h, d, n, y_0)$$

Fig. 7. Force and sensitivity curves in y axis corresponding to geometry constraints (d, n, p) and variables (a, h).

References

- [1] Di Barba P., Savini A., and Wiak S. (1994) 2-D numerical simulation of electrostatic micromotor torque, IEE Second International Conference on Computation in Electromagnetics, Nottingham, UK
- [2] Price R.H., Wood J.E., and Jacobsen S.C. (1989) Modelling considerations for electrostatic forces in electrostatic microactuators, *Sensors and Actuators*, 20, 107-114.
- [3] Trimmer W. and Jebens R. (1989) Harmonic electrostatic motors. *Sensors and Actuators*, 20, 17-24.
- [4] Wiak S., "Optimal Design of Silicon Micromotors by Use of Field/Circuit Modeling", *COMPUMAG*, PE1-13, vol. III, pp.38-39, Evian, July 2-5, 2001.
- [5] C. W. Tang. "Electrostatic Comb Drive Levitation and Control Method", *Journal of Micromechanical Systems*, 1992, vol.1, no. 4, December .
- [6] Julian W Gardner, Vijay K. Varadan, and O. Osama Awadelkarim, "Microsensor MEMS and Smart Devices", J. Wiley, UK, 2001

I-17. THE OPTIMAL DESIGN OF PASSIVE SHIMMING ELEMENTS FOR HIGH HOMOGENEOUS PERMANENT MAGNETS UTILIZING SENSITIVITY ANALYSIS

Yingying Yao, Chang Seop Koh^{*}, Guangzheng Ni, Shiyong Yang, and Dexin Xie^{}**

College of Electrical Engineering, Zhejiang University, Hangzhou, Zhejiang 310027, P.R.China
yaoying62@hotmail.com

^{*}School of Electrical and Computer Engineering, Chungbuk National University, Chungbuk 361-763, Korea.
kohcs@chungbuk.ac.kr.

^{**} School of Electrical Engineering, Shenyang University of Technology

Abstract–This paper presents a useful and simple method to design the passive shimming system for homogeneous permanent magnets based on numerical optimization. To simulate the effects of manufacturing and assembling tolerances, the actual geometrical parameter of the magnet with a derivation is suggested. Then, the optimal design model of a passive shim system is set up to correct the derivative of field homogeneity. The numbers, sizes and locations of the passive shims are optimized by steepest descent algorithm combined with design sensitivity analysis. Two implementations show the proposed method can achieve required homogeneity of the field with the minimum quantity of ferromagnetics.

Introduction

The MRI (Magnetic Resonance Imaging) requires very high homogeneous static magnetic field. In order to produce high-resolution images, the magnetic field inhomogeneity produced in high performance MRI scanner must be maintained to the order of several ppm. However, the initial static magnetic field built by virgin magnets is usually less uniform than that required to image successfully because of manufacturing tolerance. Especially with permanent magnet, the initial inhomogeneity is higher than the order of 10^{-3} . After manufacturing, thus, the magnet must be adjusted in some points to produce a more uniform field by making small mechanical and/or electrical adjustments to the overall field. This process is known as shimming. The mechanical adjustments, which add small pieces of iron or magnetized materials, are typically called passive shimming, while the electrical adjustments, which use extra exciting currents, are known as active shimming [1]. The active shimming can be easily achieved by adjusting the physical and electrical parameters of the exciting coils. But there are numerous drawbacks associated with it. For example, the electric current in the shim coil may be unstable, which causes “ghosting” in the MR images, and the shim coils are temperature sensitive, which results in image artifacts and, furthermore, it is very complicated and expensive. The passive shimming, however, can overcome the disadvantages of the active shimming although it needs a lot of iron pieces of which the sizes and locations are concerned with the experience of the designer.

The shimming system can be designed in two ways: analytic and numerical methods. The analytic method uses special-shaped and composed shimming coils or permanent magnetic elements to compensate the harmonic fields of each order. In fact, the harmonic fields above the fifth order can't be compensated by using the analytical method, because it is very difficult to design the higher order shimming [1]. Especially with permanent magnets, the field error caused by the harmonics of higher orders may be so large that the homogeneity of the field cannot reach a satisfactory uniformity. By using numerical method, the design directly sets the total field error rather than each harmonic field as the objective of correction. Therefore it is simpler and more effective than the analytic design method.

In this paper, an intelligent design method of the passive shimming system is presented. The size of shim is determined by using sensitivity analysis combined with the steepest descent method. The proper homogeneity of the magnetic field is also achieved with the minimum quantity of ferromagnetics.

Description of the Proposed Method

The proposed method is composed of four steps: 1) acquisition of original magnetic data, 2) expansion of the magnetic field in orthonormal basis set, 3) design of pre-shim or initial shim system, and 4) calibration of shim sensitivity and calculation of shim size needed to get the desired homogeneity.

The first step is the preparation of field data for shim design. The basic magnetic field data may be measured for a MRI system. But, in the design stage the measured data can not be available, and therefore, the construction tolerances in manufacturing and assembling are simulated. The field data can be obtained by computing the magnetic field of the magnet under deviation. For example, the permanent magnet system shown in Fig. 1(a) consists of 64 Nd-Fe-B permanent magnet bars in length of 0.8m with the directions of magnetization as follows:

$$\beta_i = (i-1) * 5.625^\circ + 2.8125^\circ \quad (1)$$

where, i is the number of permanent magnet bar, and β_i is the angle from symmetrical axial of each bar. Fig. 1(b) shows the magnetized direction in a block. To simulate a magnetic field with manufacturing tolerance in the direction of magnetization, the direction of magnetization of each permanent magnet bars with little deviation is assumed as:

$$\beta_i = (i-1) * 5.6^\circ + 2.8125^\circ. \quad (2)$$

After computing the magnetic field by using F.E. method, the initial field data are obtained.

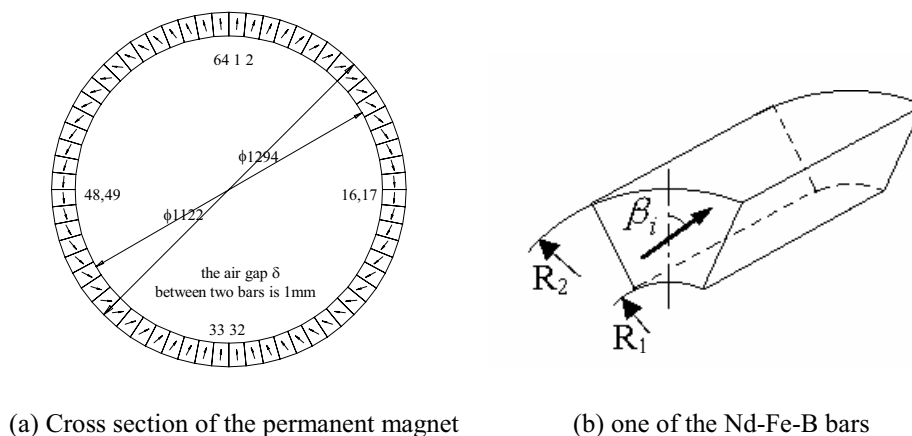


Fig. 1. A test example of the permanent magnet

The next step is to expand the original magnetic field data in the form of a polynomial expansion having a predetermined number of harmonic terms. It is necessary for two reasons. The first, if the original magnetic field is serious inhomogeneous, a special pre-shim should be made by examining the harmonic terms, determining which harmonic term of the polynomial expansion should be modified in order to change the homogeneity. The second, it is helpful for the design of initial shim system, which is the initial of an optimization process. The initial size and position can be determined by the harmonic analysis result.

Supposing the magnetic field of the permanent magnet is along the z direction in a magnetically homogeneous region, the dominant component B_z can be expressed in a spherical harmonics series as follows:

$$B_z = B_0 + \sum_{n=1}^{\infty} \sum_{m=0}^n r^n P_n^m(\cos\theta)(A_n^m \cos m\alpha + B_n^m \sin m\alpha) \quad (3)$$

where, B_0 and (A_n^m, B_n^m) are the homogenous magnetic field value and the amplitudes of harmonic components in the volume of interest. Using the magnetic field data, the amplitudes of harmonic series can be best determined by solving the following equation:

$$\text{Minimize } \sum_{i=1}^{N_{\text{measured}}} (B_{z_i} - \tilde{B}_z)^2 \quad (4)$$

where, B_{z_i} is the i th magnetic field value of known data set, \tilde{B}_z is assumed to be adequately represented by a finite number of terms of (3).

Based on the dominant terms of the harmonics, we can design the preshim or initial passive shim system. This step is usually for open type MRI magnet because its initial inhomogeneity is higher than 10^{-3} order. The preshim is to improve the homogeneity by modifying the shape of pole piece[2], or by using iron element having specified physical dimensions, such as rings, arcuate segments and blocks[3]. The initial passive shim system is composed of the shim element having a predetermined size. Each dominant term of the harmonics should be compensated by shim elements with proper location[3].

The next step is the optimal design of passive shim system by using small magnetized pieces. Our purpose is to design a passive shimming system to compensate the high order of harmonic field and obtain a highest homogeneous magnetic field.

With the pre-shim or initial shim, the inhomogeneity of initial field may be less than 10^{-3} , and the shimming elements should be very small. Here we utilize small magnetized pieces, such as magnetic dipole, to improve the field homogeneity. A magnetic dipole located at (x_s, y_s, z_s) will produce magnetic field at point (x, y, z) as:

$$\mathbf{B} = \frac{\mu_0}{4\pi r^3} \left[\frac{3}{r^2} (\mathbf{M} \cdot \mathbf{r}) \mathbf{r} - \mathbf{M} \right] \quad (5)$$

where $\mathbf{M} = V\mathbf{m}$; \mathbf{m} is magnetizing intensity and only in the direction of main magnetic field, that is $\mathbf{m} = m_z \mathbf{k}$; V is the volume of shim piece; $\mathbf{r} = (x_s - x)\mathbf{i} + (y_s - y)\mathbf{j} + (z_s - z)\mathbf{k}$; (x_s, y_s, z_s) is the coordinates of shim located. The optimization model is

$$\begin{cases} \text{Min. } F = \sum_{p=1}^N \left(B_p - B_0 - \sum_{k=1}^{N_s} B_{p,k} \right)^2 + \alpha \sum_{k=1}^{N_s} V_k^2 \\ \text{Sub. } 0 \leq V_k \leq V_{\max} \end{cases} \quad (6)$$

where $k = 1, \dots, N_s$ is for shimming blocks, $p = 1, \dots, N$ for testing points, B_p is the initial field at each testing point, and the magnetic field $B_{p,k} = A_{p,k} V_k m_z$ produced by shimming pieces is calculated by (5), and α is a weighting factor to dictate the relative minimization of the total volume of shim and the field inhomogeneity. For example, $\alpha = 0$ indicates that the aim is to minimize the field inhomogeneity and to neglect the total volume of shim. For the solution of (6), the gradient search method based on design sensitivity analysis is used. The design sensitivity of the objective function with respect to the design variables can be written as follows:

$$\frac{\partial F}{\partial V_k} = -2 \sum_{p=1}^N \left(B_p - B_0 - \sum_{k=1}^{N_s} B_{p,k} \right) A_{p,k} m_z + 2\alpha V_k \quad (7)$$

The new design variables are obtained according to modified one dimensional line search as follows:

$$[V]_{q+1} = [V]_q + \alpha [s]_q \quad (8)$$

$$[s]_q = -\nabla f_q + \beta_q [s]_{q-1} \quad (8-1)$$

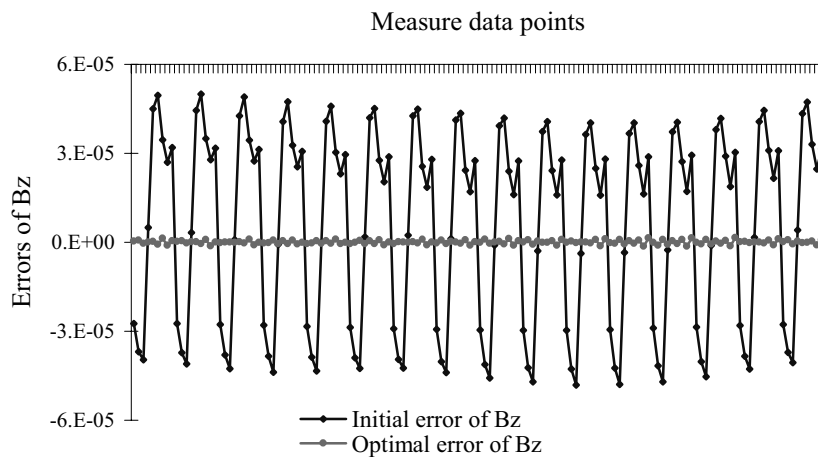
$$\nabla f_q = F(V) \frac{dF}{d[V]} / \left\| \frac{dF}{d[V]} \right\|^2 \quad (8-2)$$

$$\beta_q = \frac{(\nabla f_q - \nabla f_{q-1})^T \cdot \nabla f_q}{\nabla f_{q-1}^T \cdot [s]_{q-1}} \tag{8-3}$$

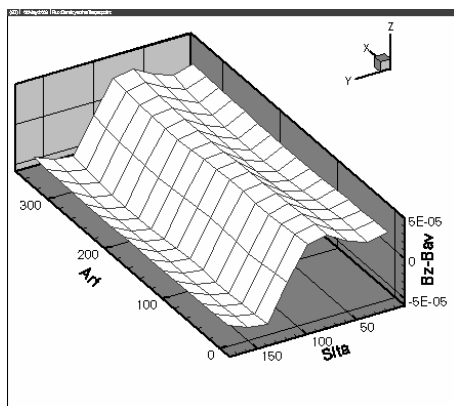
Numerical Application and Results

A. Example 1: Passive shim for a superconducting magnet

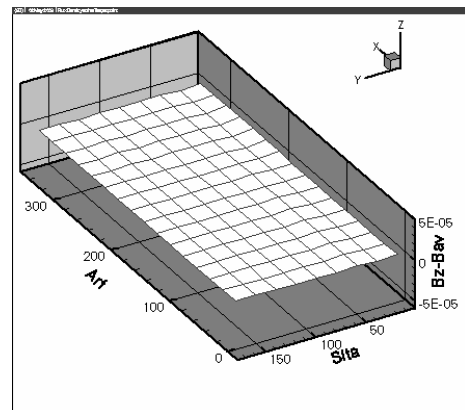
The original magnetic field data come from a superconducting magnet, which is the first superconductive NMR imaging magnet produced in China[4]. There are two sets of measured data from 50cm DSV surface. The coordinates Arf and $Sita$ in Fig.2 and Fig.3 indicate the α and θ angle in spherical coordinate respectively. By using the proposed optimization method, 900 magnetic dipoles are located on a tube like surface with radius of 0.485m and $|z| < 0.6m$. For the first set of measured data, the inhomogeneity can be improved from 162.437ppm to 4.172ppm. For the second data set, the initial and optimum inhomogeneity are 98.022ppm and 5.78ppm respectively.



(a) The error of Bz

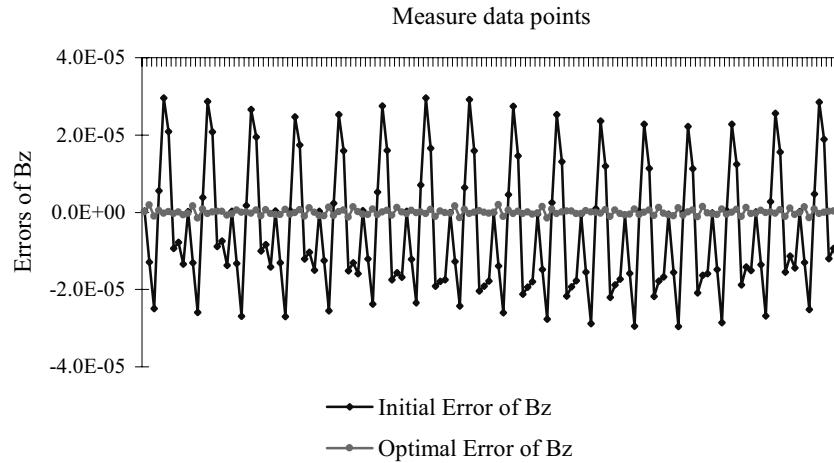


(b) initial case

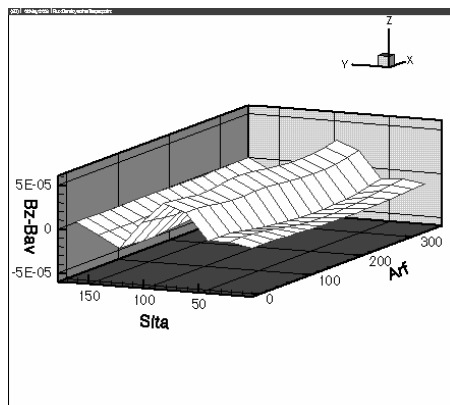


(c) optimal case

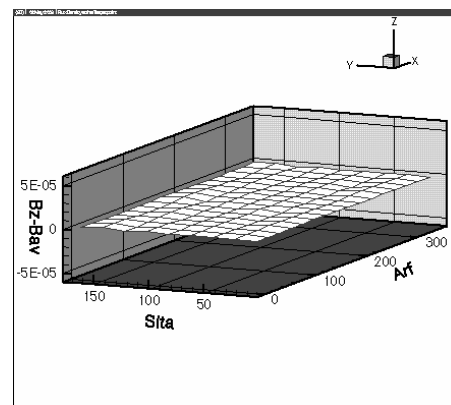
Fig. 2. The field error in the initial and optimal case based on the first set of measured data set



(a) The error of Bz



(b) initial case



(c) optimal case

Fig. 3. The field error in the initial and optimal case based on the second set of measured data

B. Example 2: Shim design of a permanent magnet with manufacturing tolerance

For the permanent magnet geometry, shown in Fig. 1, each permanent magnet bar should be magnetized in the direction of specified in (1). However, in the numerical simulation, it is supposed as in (2) to take into account of the deviations in manufacturing. The inhomogeneity of the magnetic field is 56649.82ppm. Fig. 4 shows the magnetic flux distribution. Expanding the original field data in the spherical harmonic form of 2nd order and arranging the pre-shim by using iron rings and bars, the inhomogeneity is increased to 9704.89ppm. Then, 255 test points are arranged in the region of a 0.7m DSV. Passive shims are located on a cylinder of diameter 1.12m and length 0.8m. The position of shims and the interesting region DSV are shown in Fig. 4(b). After the optimal design of the shimming elements, the homogeneity of the field is improved to 256.43ppm. Fig. 5 compares the error distribution of initial and optimal field. The final flux distribution, shown in Fig. 6, is acceptable.

Conclusions

A passive shim design method is presented, in this paper, based on numerical optimization. By using sensitivity analysis, the size of shims with the minimum volume of ferromagnetics can be determined intelligently. The numerical implementations reveal that the proposed method can effectively improve the homogeneity even when the initial fields have different inhomogeneity levels.

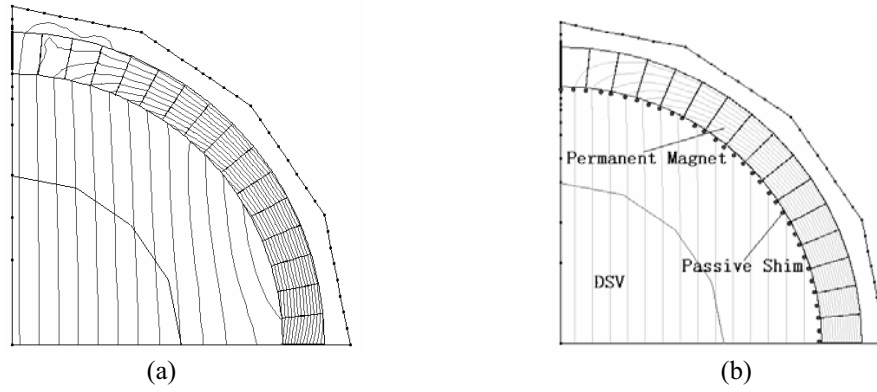
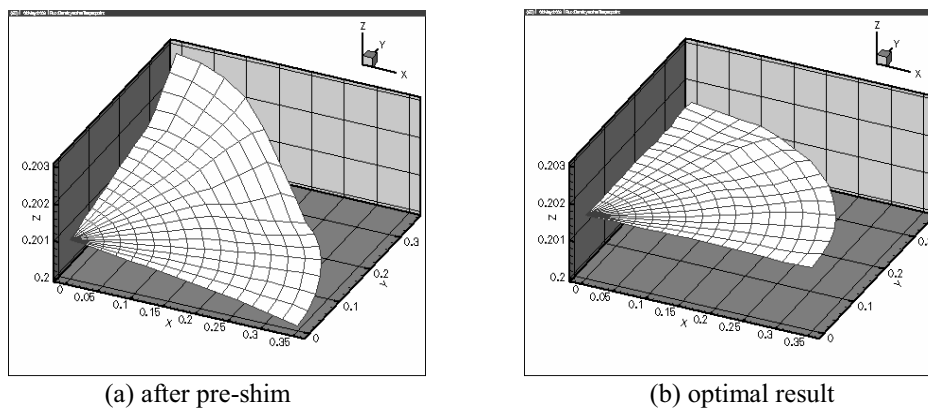


Fig. 4. A permanent magnet with some defaults and the sketch figure of shims
 (a) The field distribution of a permanent magnet with some defaults
 (b) The sketch figure of shims and interesting region.



(a) after pre-shim (b) optimal result
 Fig. 5. The field error distributed in the interesting region

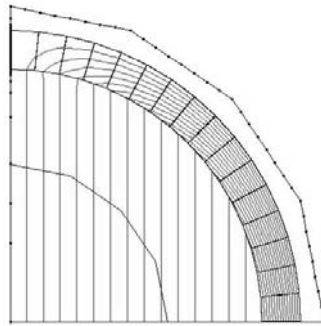


Fig. 6. The field distribution after correction with passive shimming.

References

- [1] X.H. Jiang, S. Han, Effective of passive shimming on MRI superconducting and permanent magnets, 1997, Proceedings of the International Conference MT-15, 867-869
- [2] Dong-Hun Kim, et. al., 3D optimal shape design of ferromagnetic pole in MRI magnet of open permanent-magnet type, IEEE Trans. on Applied Superconductivity, vol.12, No.1, pp.1467-1470, 2000
- [3] Pastislav Vadovic, Magnetic field correction using magnetized shims, IEEE Trans. on Magnetics, vol.25, No.4, pp.3133-3139, July 1989
- [4] X.H. Jiang, S. Han, Optimization problem in the passive shimming of superconducting NMR imaging magnets, 1992, Proceedings of the International Conference ICEF'92, 337-339

I-18. RECONSTRUCTION OF THE INTERFACE BETWEEN TWO CONDUCTING FLUIDS WITH MODIFIED GENETIC ALGORITHMS

Marek Ziolkowski^{1,2}, Hartmut Brauer¹, Milko Kuilekov¹
Christian Resagk¹, Shouqiang Men¹

¹ Technische Universität Ilmenau, Helmholtzplatz 2, D-98684 Ilmenau, Germany

² Technical University of Szczecin, Sikorskiego 37, PL-70313 Szczecin, Poland

e-mail: marek.ziolkowski@tu-ilmenau.de

Abstract – In magnetic fluid dynamics appears the problem of reconstruction of free boundary between conducting fluids. The reconstruction problem of the interface between two conducting fluids with different conductivities using external magnetic field measurements in the case of a highly simplified model of an aluminium electrolysis cell has been investigated. In the paper, the comparison of two reconstruction procedures based on modified and simple genetic algorithms has been presented.

Introduction

There are a variety of problems in material processing where it would be useful to know the time-dependent distribution of the electrical conductivity of a single fluid or a multiphase flow. For instance, the knowledge of the position of the interface between highly conducting molten aluminium and poorly conducting electrolyte (cryolite) is important to prevent unwelcome instabilities in aluminium reduction cells [1]. In the previous work [2], it has been demonstrated that concepts of *Magnetic Field Tomography (MFT)* can be successfully used for detection of interfaces between current carrying fluids of different electrical conductivity. We have demonstrated that the external magnetic field generated by the electrical current flowing in a highly simplified model of an aluminium reduction cell provides sufficient information to reconstruct the unknown interface shape. In the reconstruction process we have applied a simple genetic algorithm (GA). Genetic algorithms (GAs) – search techniques based on the mechanism of natural evolution and genetics – are particularly effective when the goal is to find an approximate global maximum (or minimum) in a multimodal function domain. In genetic algorithms a population of potential solutions evolve toward a global optimal solution as a result of pressure exerted by a weighted selection process and exploration of the solution space. That is accomplished by recombination and mutation of existing characteristics represented in the current population. In the present work, we study different versions of GAs applied to *magnetic fluid dynamics (MFD)*. The basic idea of our research is to exploit different GAs and their parameters in order to obtain precise solution and efficiency of the computation process.

Inverse Field Problem in Magnetic Fluid Dynamics

If we consider typical figures of aluminium electrolysis cells it must be noticed that the cross section has a length of about $L = 10$ m, whereas the interface displacement η is very small compared to the lateral extent of the system. Industrial practice shows that already such small interface displacement can perturb significantly the operation of the cell [4]. Consequently, our physical model is characterized by a very small ratio η/L . The considered problem is shown in Fig. 1. Two fluids with different electrical conductivities σ_1 (*up*) and σ_2 (*down*), are situated in a long cylinder with the radius R . The cylinder walls are non-conducting. Along the length axis of the cylinder a homogeneous electrical current density \mathbf{J}_0 is applied.

The complete interface perturbation can be found solving the Euler equation and the mass conservation law as

$$\eta(r, \alpha) = A \sum_{m=-M}^M \sum_{n=1}^N \eta_{mn} J_m(k_{mn} r) e^{jm\alpha} \quad (1)$$

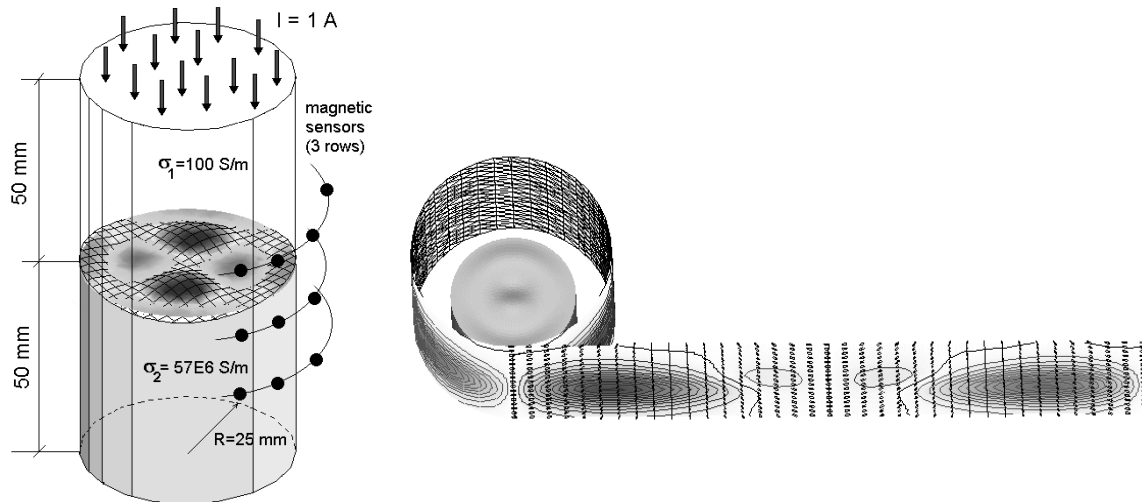


Fig.1. Highly simplified aluminium electrolysis cell model with a non-axisymmetric interface (*left*). Sample distribution of the magnetic flux density (B_r component) around cylinder and on the enveloped cylindrical surface for 36x17 sensors (*right*).

The value n is called the *radial* mode number and the value m the *azimuthal* mode number. Although the quantity of modes is usually unlimited, the highest modes have the smallest amplitudes and can be neglected. The abbreviation η_{mn} is used for the description of the interface shape as it is shown in Fig.2. The validity of the above interface representation is limited by the amplitude of the interface oscillations. We consider only small interface oscillations because the larger interface oscillations lead to instabilities due to drop formation.

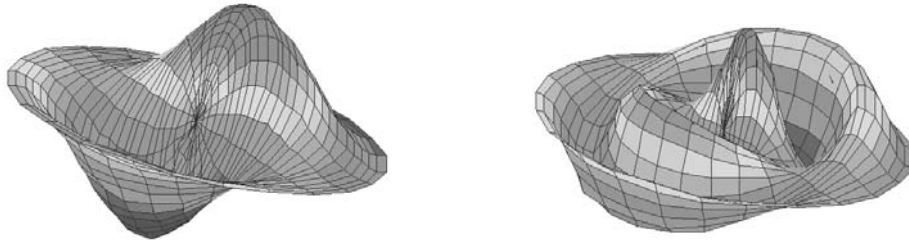


Fig. 2. Sample interface modes: η_{12} (*left*) and η_{14} (*right*).

If the interface between fluids is flat, the current density \mathbf{J} is homogeneous everywhere in the cylinder. As soon as the interface deviates from its flat shape due to interfacial waves or an external forcing, the current density \mathbf{J} will become inhomogeneous near the interface. The inhomogeneity of \mathbf{J} can be represented by the perturbation current density \mathbf{j} . If the perturbation of the fluid interface is non-axisymmetric, it leads to a perturbation of the r - and z -components of the magnetic field outside the cylinder.

To model the magnetic field we have to calculate first the current density distribution in the cylinder. This can be done by applying finite element method (program FEM3D). Having the distribution of the current density \mathbf{j} in the cylinder volume, the magnetic flux density around the cylinder (at the sensors positions) is calculated using the Biot-Savart law:

$$\mathbf{B}(\mathbf{r}) = \frac{\mu}{4\pi} \int_V \frac{\mathbf{j} \times (\mathbf{r} - \mathbf{r}')}{|\mathbf{r} - \mathbf{r}'|^3} dV' \quad (2)$$

The inverse problem is formulated as follows: having the magnetic field flux density distribution (B_r , B_z components) in the sensors positions around the cylinder we would like to reconstruct the interface shape described by (1).

The flowchart of the procedure for the interface reconstruction is shown in Fig. 3. In the current state it enables to identify the modes of the interface between two conducting fluids on the basis of simulated data. It consists of two basic parts: simulation and reconstruction. In the first part for the chosen mode, e.g. mode η_{13} , the magnetic

flux density distribution at the sensors positions is calculated using the finite element method. To simulate more realistically the problem, the magnetic field is modified by adding some white noise to the calculated values and reducing the number of sensors.

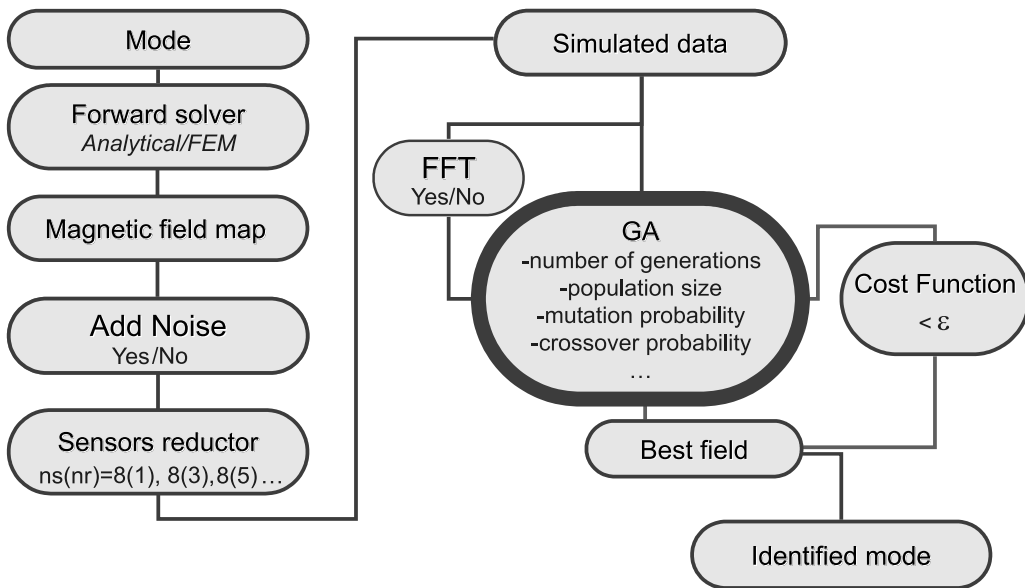


Fig.3. Flowchart of the mode identification procedure with the genetic algorithms.

Fig. 4 shows the flowchart of the modified genetic algorithm. The goal of the modification is to eliminate the problem of the premature convergence which has been observed in the case of the simple genetic algorithm. We have applied a multiple optimization loop accompanied by a scaling block which enables to rescale the initial vector of each simple GA run. In that sense starting point for each run is the same but the parameter vectors are scaled to the best solution from the previous step.

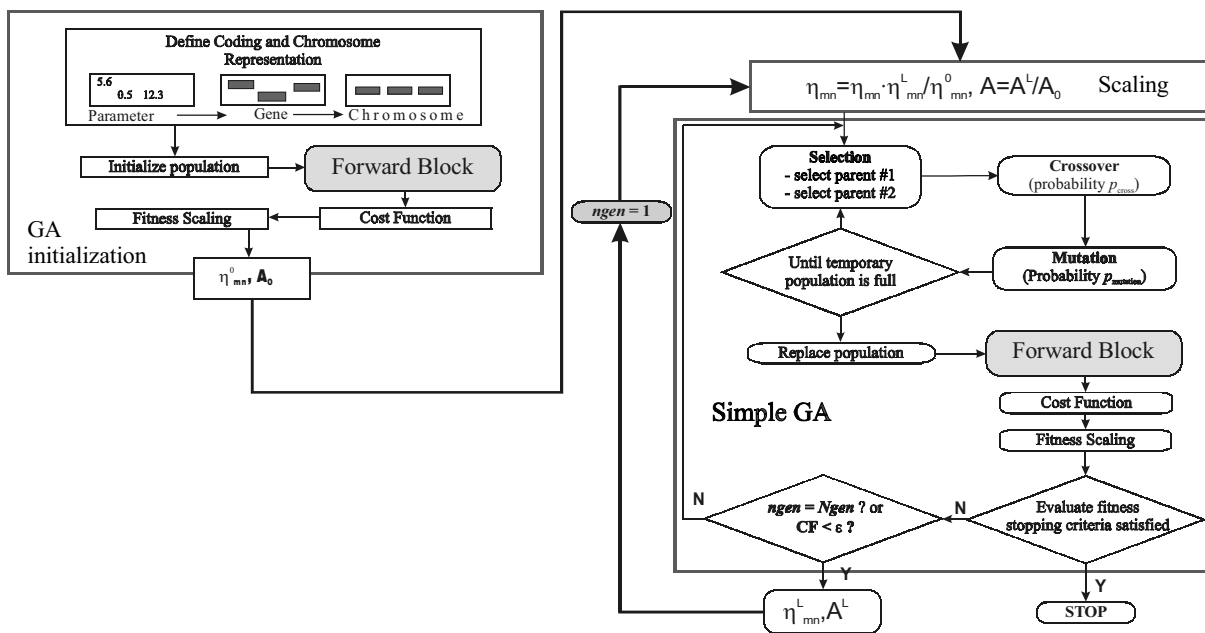


Fig.4. Flowchart of modified genetic algorithm.

Results of simulations

To test the presented procedure we have applied it to reconstruction of the interface surface described by the mode η_{13} . We have restricted the search space to 12 parameters consisting of amplitudes of the interface perturbation given by (1). The simulated magnetic field has been calculated for one row of equally distributed B_r sensors located at the radius 35 mm (Fig.5).

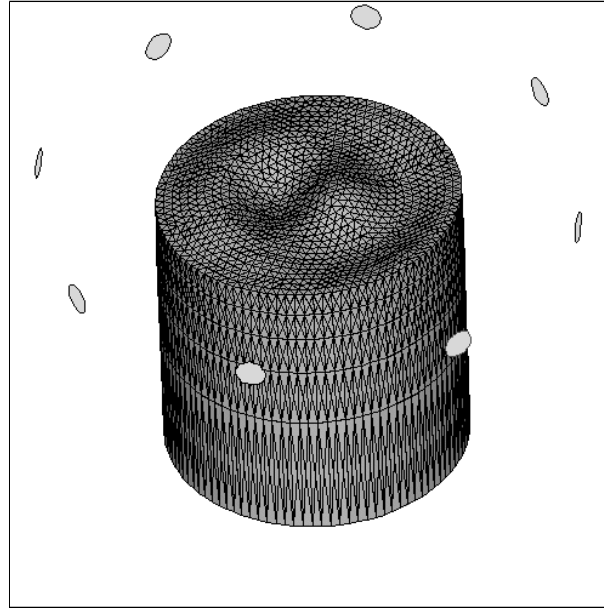


Fig.5. FE mesh ($N_P=60090$, $N_E=270760$) of bottom part of analyzed model (mode η_{13}) with 8 B_r sensors.

In our simulations we have assumed that the oscillating interface is in a steady state, i.e. we record the signal from the sensors and then we choose the time instant in which the signal reached the maximum. That time moment corresponds to the maximum of the amplitude of the interface which is identified with the presented procedure.

In the modified reconstruction procedure, we have used a C++ library of genetic algorithm components (GAlib) developed at the M.I.T. [5] with non-overlapping populations (size 30), the optional elitism (i.e. the best individual from the previous generation is copied to the next generation) and the roulette-wheel selection scheme. We have applied the 16 bit binary-to-decimal genome (which converts binary strings to decimal values) and the values of one-point crossover p_{cross} and mutation p_{mut} probabilities equal 0.95 and 0.01 respectively. The cost function has been defined as

$$CF = \sqrt{\sum_{i=1}^{Ns} (B_{ri} - B_{ro})^2 + (B_{zi} - B_{zo})^2}, \quad (3)$$

where Ns denotes the number of sensors, and B_i , B_o are the values of the magnetic flux density for the current generation and the simulated input data, respectively. For evaluation of the cost function in the GA, the finite element method (program FEM3D) has been used. Additionally, we have defined the quality of the reconstruction (eta standard deviation) using the following formula

$$\eta_{SD} = \sqrt{\frac{\sum_{i=0}^M \sum_{j=1}^N (\tilde{\eta}_{ij} - \eta_{ij}^0)^2}{\sum_{i=0}^M \sum_{j=1}^N (\eta_{ij}^0)^2}} 100\%, \quad (4)$$

where M , N are the numbers of Bessel's functions and radial modes used in the reconstruction process, $\tilde{\eta}_{ij}$, η_{ij}^0 are the amplitudes (1) defining the reconstructed and the original surface, respectively.

Fig.6 shows the reconstructed interface shape for the mode η_{13} after 75 generations together with the original interface shape in the case when only the information from 8 B_r sensors is available. Both reconstruction procedures have found correctly the positions of extremes but the modified algorithm have circumscribed more precisely the shape of the interface.

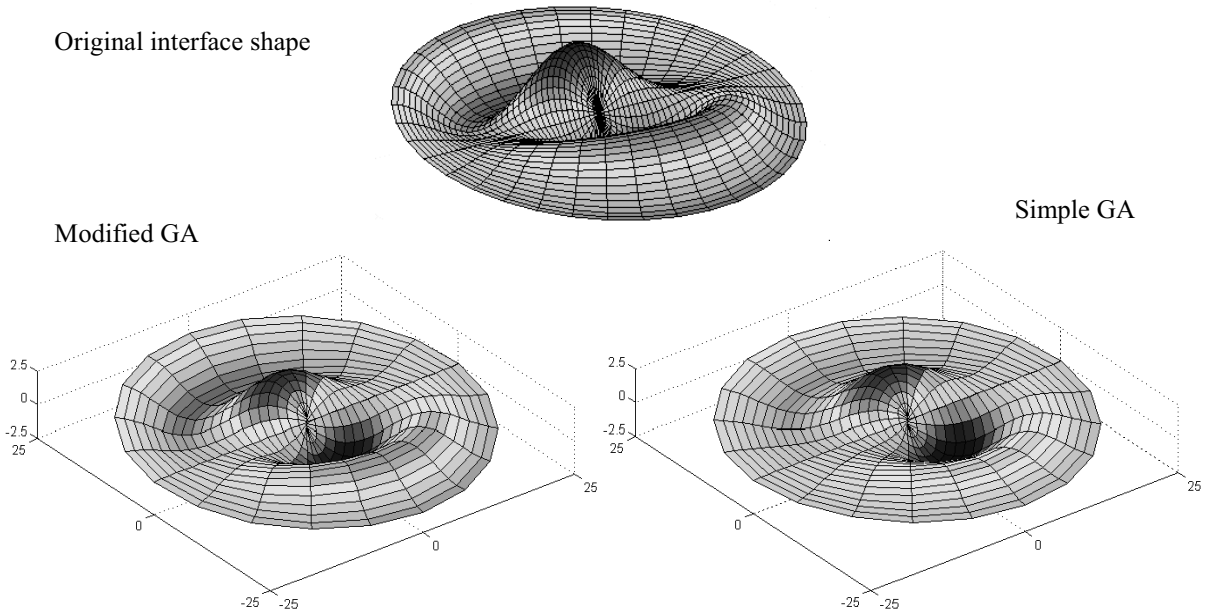


Fig. 6. Reconstructed interface shape of mode η_{13} : modified GA (left), simple GA (right).

In Fig.7, the cost function (3) is plotted versus number of generations. After 75 generations, the simple GA has found the solution with the value of CF equals 1.1 nT whereas the modified version stopped with 0.35 nT conforming the qualitative conclusion given above.

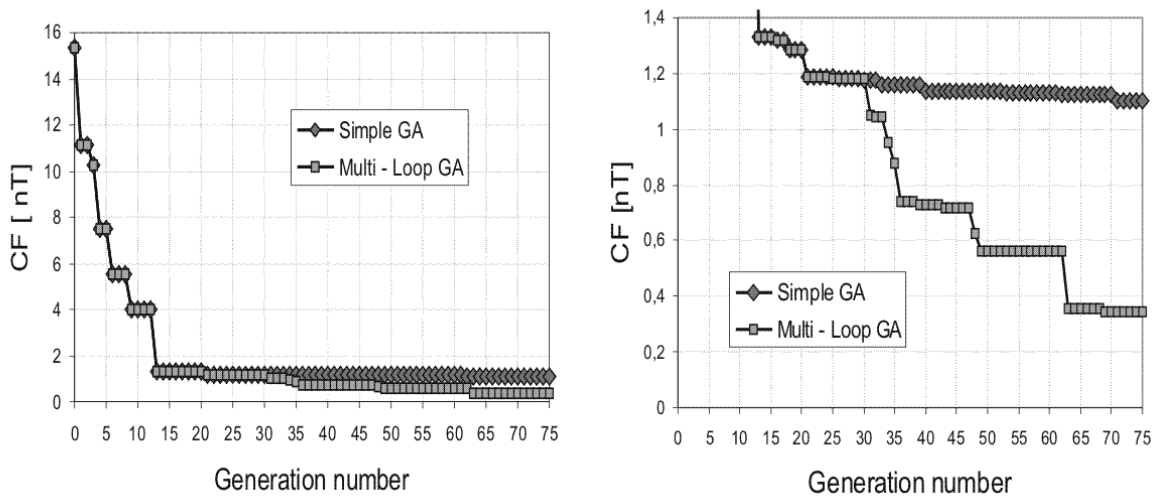


Fig. 7. Comparison of cost function values versus generation number for modified and simple GA.

To compare how close the reconstructed interface shapes are to the original mode, the goodness parameter SD (4) has been also calculated and plotted versus the number of generations (Fig.8). It can be observed that in the presented case, the solution found by modified algorithm is over 4 times better ($SD=10\%$) than in the simple GA ($SD=43\%$). In Fig. 8 it is also presented the distribution of B_r component corresponding to the reconstructed interface (modified GA).

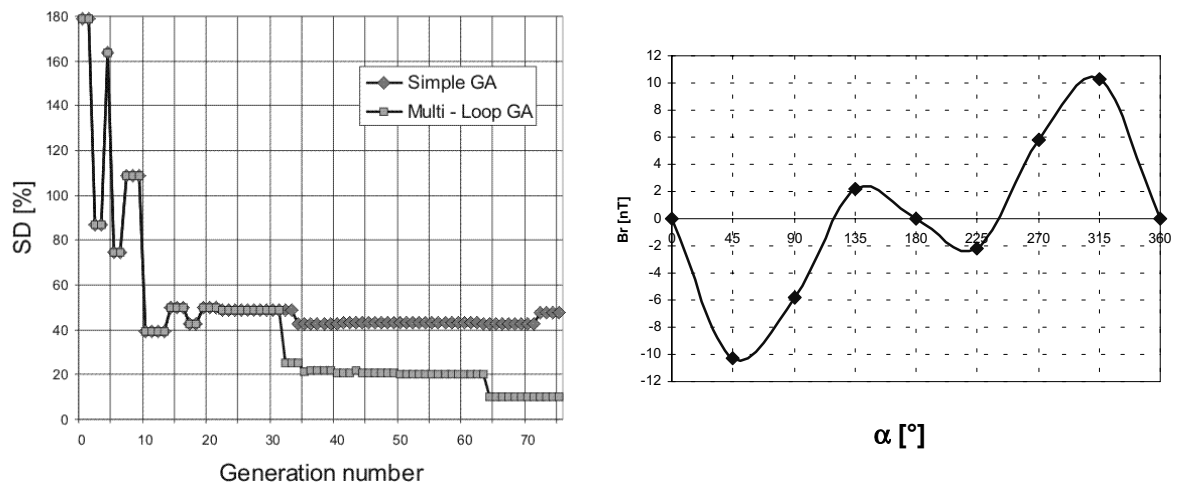


Fig. 8. Eta standard deviation (SD) versus generation number and distribution of B_r component for one row of 8 sensors equally distributed around cylinder located at $z=H/2$.

We have also performed the simulations for various values of GA parameters (crossover p_{cross} and mutation p_{mut}) and with the greater number of generations but all those experiments confirmed the results presented above i.e. modified version of GA has given always better solution than simple GA.

Conclusions

We have shown that it is possible to reconstruct the shape of the interface between two conducting fluids on the basis of magnetic flux density simulations with a good quality using genetic algorithms. The new implementation of the reconstruction procedure (modified GA version) gives better results than the simple GA due to avoiding premature saturation of the cost function. Further tests of the algorithm have to be performed to assure proper reconstruction results also in the case of measured data.

References

- [1] P.A.Davidson, "Magnetohydrodynamics in material processing," *Annu. Rev. Fluid Mech.*, vol. 31, pp. 273-300, 1999.
- [2] M. Ziolkowski, H.Brauer, M. Kuilekov, "Interface Reconstruction Between Two Conducting Fluids Applying Genetic Algorithms," COMPUMAG 2003, July 13-17, 2003, Saratoga Springs, USA
- [3] Z. Michalewicz, *Genetic Algorithms + Data Structures = Evolution Programs*, 3rd ed., Springer Verlag, Berlin, Heidelberg, New York, 1996.
- [4] J. Miles, and D. Henderson, "Parametrically forced surface waves," *Annu. Rev. Fluid Mech.*, vol. 22, pp. 143-165, 1990.
- [5] M. Wall, "GAlib: A C++ Library of Genetic Algorithm Components". V2.4, 1996, <http://lancet.mit.edu/ga/>

SECTION II ELECTROMAGNETIC ENGINEERING

Introductory Remarks

The second section is devoted to classical applications of computational techniques. As has already been mentioned in the Preface, the classical applications are a little bit out of date but there is still some need to consider them. It is obvious that electrical devices are more and more complex, and so their analysis becomes more and more complex too. And it works inversely too: more and more complex methods of calculation mean that more complex devices can be designed and manufactured. In the past, electrical devices (motors, generators, transformers, reactors and the like) were designed by using electric circuit schemes and led to evaluation of bulk parameters, such as reactance, resistance and capacitance. This gave good designs, but probably far from optimum. The advent of the computer era has totally changed the philosophy of designing electric devices. The main attention is nowadays focused on electromagnetic field calculation which allows a deepening of the design process and to be close to an optimum design. However, the numerical techniques again have to be more complex and must possess some new optimizing tools, like these discussed in the previous section. In this section, theory of numerical modeling meets its practical use.

Unlike the previous section, this one is completely heterogeneous as concerns the variety of subjects considered. Thus, it seems to be difficult to find any good way to classify the papers. One can divide them *grosso modo* into two subgroups:

- numerical analysis of electric devices,
- computer analysis and design of electric drive systems.

The above distinction is of essential meaning, as there is a difference in looking at an electric machine as the machine itself and as an element of a drive system. And there are different approaches which are being applied in both cases.

Needless to say, the first subgroup dominates at the ISEF conference, as the conference is of computational electromagnetics priority. Again, one can meet a large variety of machines. And thus the papers deal with: a doubly slotted machine (II-3), an instrument transformer (II-5), a power transformer (II-7, II-14, II-20), an induction motor (II-4, II-9, II-12), a disc-type brushless DC motor (II-10, II-19, II-21), a fractional slot wound PM motor (II-17), and an electromagnetic drum-type separator (II-22). In fact, almost each particular paper concerns one device.

We encourage all readers to look at the papers carefully, just in order to find some inspiration for solving one's own problem. It is, indeed, a good area of interest for all people who are more involved in practical problems.

Many fewer papers are devoted to modeling of drive systems. The reader who wants to find more papers from this area is advised to look into the proceedings and post-conference material from electrical machine conferences, e.g. ICEM.

The papers from this subgroup deal mainly with an electric machine model (II-1, II-2, II-12), an inverter fed machine (II-13), and the characteristics of skeleton type PM motors (II-8). Again, the readers are requested to find the papers they need by themselves.

Summing up the section on electromagnetic engineering, one has to say that careful reading of the papers strengthens the common feeling that the more attractive areas of adopting computer models lie in the novel applications. This is the theme of the next section.

II-1. ON THE USE OF THE CURRENT AND FLUX STATE VARIABLES IN THE DYNAMIC ANALYSIS OF MAGNETOELECTRIC NETWORKS

°Andrea G. Beccuti, *Sonia Leva, *Adriano P. Morando,

°Department of Electrotechnics and Information Engineering ETH Zurich, Physikstrasse 3, Zurich, Switzerland
e-mail: beccuti@control.ee.ethz.ch

*Dipartimento di Elettrotecnica, Politecnico di Milano, Piazza Leonardo da Vinci 32, Milano, Italy
e-mail: sonia.leva@polimi.it, adriano.morando@polimi.it

Abstract – The goal of the present paper is to analyse the comparative implications related to the use of the current and flux state variables in the dynamic analysis of a magnetolectric network. This analysis is made from both the energetic and system theory viewpoint. The paper also defines criteria on the basis of which the topological identification and the consequential formalization of the solving equations in terms of the flux variables can be carried out directly by inspection. Finally it defines, the topological properties that a network must satisfy in order to consent the analysis in terms of the current variables.

Introduction

The dynamic analysis of magnetolectric networks usually assumes voltage v as the input, current i as the output and the flux $\psi = N\phi$ as state variable. This value however is internal to the system: it is thus of some interest, when this is possible, to be able to substitute it with the current, as the latter is a port value and is therefore directly measurable (Fig 1).

In the case of a single winding ($n=1$), if the $b(h)$ constituent relation is non linear, this choice may not be advantageous. This is because it implies the calculation of the differential inductance $L_d(i) = d\psi(i)/di$ from the $b(h)$ relation which is only given empirically. Similarly, the presence of time dependence, which causes the separation of the derivative $d\psi/dt$ in the two motional $\dot{\xi} \partial\psi/\partial\xi$ and variational $\partial\psi/\partial t$ terms, increases the formal complexity of the model.

In the more general case of $n \geq 2$ windings the use of the current variables is constrained by even more binding conditions, which lead to the constituent relation in terms of non-linearity and time dependence. To these one must then add considerations related to the topology of the network. Concerning the former the evaluation of the differential inductance would be equivalent to that of a Jacobian matrix $\left[\frac{\partial\psi_i(i_1, \dots, i_n)}{\partial i_j} \right]$ performed by

considering a one-dimensional $b(h)$ relation. Concerning the latter, if the current state variable were employed, matrix notation would lead to the following relation $[L] \frac{d}{dt} [i] + [R][i] = [v]$.

The integrability of such a model cannot be assumed *a priori*: it depends on the fact that the matrix $[L]$ be non-singular.

This paper gains insight into the comparative implications related to the use of the current and flux state variables, from both the energetic and system theory viewpoint. It also defines criteria on the basis of which the topological identification and the consequential formalization of the solving equations in terms of the flux variables can be done directly by inspection. Finally, it analyses the conditions of integrability of the state model based on the current variables $[i]$ in the formal and topological aspects.

Conditions for equivalence of the flux-current state variables: the energetic point of view

In Circuit Theory variables may either be intensive or extensive. The former, known as network variables, are such that their product yields a power term. The latter, classified as state variables, are the time integrals of the former. In the case of an inductor such a distinction gives a twofold interpretation related to the two distinct

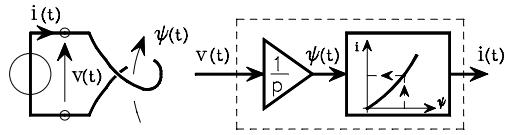


Fig. 1. The role of voltage, flux and current in the dynamic analysis of magnetolectric networks.

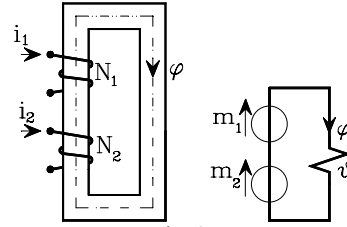


Fig. 2.

electrical and magnetic ports of the component. In terms of the energetic balance one has the following two exact differentials:

$$dW_{\mu} = \begin{cases} m(\varphi) d\varphi \\ i(\psi) d\psi \end{cases} \quad (1)$$

respectively associated to the magnetic and electric constituent relations $m(\varphi)$ and $i(\psi)$. In both cases the extensive flux variable appears as a differential: it is therefore and without exception the state variable representative of the energy accumulation and of the dynamics of the inductor. The current variable is present as an integrand: it is an intensive and therefore “auxiliary” variable. Consequentially the order of the mathematical model depends exclusively on the flux φ and not on the current i . In the case of Fig. 2 for example, since energy is expressed by:

$$W = \int_0^{\varphi} \left(\sum_{k=1}^2 m_k \right) d\varphi = \int_0^{\varphi} (N_1 i_1 + N_2 i_2) d\varphi \quad (2)$$

the model, related to the flux φ , is of the first order. The currents instead are two and independent as they are not bound by any electrical connections.

The use of the intensive current variables, whenever possible and/or advantageous, must be done in such a way so as to preserve the specific dynamical behaviour of the mathematical model. It must thus be carried out in an indirect fashion, starting from the original flux state model and subsequently implementing the appropriate flux-current change of variable. The employment of the current variables is foreign to any energetic implication, which pertains uniquely to extensive variables, and assumes as such a solely formal function. It is strictly subordinate: indeed, during integration of a set of equations the change of variables implies that there be a bijective correspondence between those same variables.

In the multi-dimensional case of n perfectly coupled inductors, the magnetic analysis is still possible, without any exceptions. However, two distinct aspects, both specifically associated to multi-dimensional functional expressions, condition the electrical equivalent. The first is related to the presence of non-linearity in the constituent relations [1]. The second, which will be thoroughly examined in the following, is linked to the network topology and to the constraints that it implies in terms of the bijective flux-current correspondence.

Conditions for the use of the flux state variables

By extending to magnetic planar networks the properties of graph theory usually employed for electrical networks, the magnetic state variables are the loop fluxes ϕ .

With reference to the case of a linear and planar magnetic network consisting of n windings not electrically interconnected, ℓ edges with one winding at the most per edge and a loops, by employing the number of windings diagonal matrix $[N]$ and the restricted edge-loop incidence matrix of the magnetic graph $[M_m]$, this approach leads to the definition of the following linkage matrix¹:

$$[N_C]_{a,\ell} = [M_m]_{a,\ell} \cdot [N]_{\ell,\ell} = [M_m]_{a,\ell} \cdot \begin{bmatrix} [N^*]_{n,n} & [0]_{n,\ell-n} \\ [0]_{\ell-n,n} & [0]_{\ell-n,\ell-n} \end{bmatrix}_{\ell,\ell} = \begin{bmatrix} [N^*]_{a,n} & [0]_{a,\ell-n} \end{bmatrix}_{a,\ell} \quad (3)$$

which is generally rectangular. The following relations consequently hold:

¹ The magnetic edges are enumerated starting from the active ones, i.e. from those which feature a winding. It is furthermore assumed that for the case $n=a$ there is a winding for each loop a . If that were not the case, that is in the presence of passive meshes, these must be preventively eliminated.

$$\begin{cases} [m]_{a,1} = [N_C]_{a,\ell} \cdot [i]_{\ell,1} = [N_C^*]_{a,n} \cdot [i^*]_{n,1} \\ [\psi]_{n,1} = [N_C^*]^T [\phi]_{a,1} \end{cases} \quad (4)$$

and describe the correlation respectively existing between the loop mmfs (magneto motive force) and the edge currents and the linkage fluxes and the loop fluxes. The magnetic loop analysis and the Ohm equation formulation for each solenoid implies the following equation set²:

$$\begin{cases} [\mathcal{G}]_{a,a} \cdot [\phi]_{a,1} = [m]_{a,1} \\ [R]_{n,n} \cdot [i^*]_{n,1} + \frac{d}{dt} [\psi]_{n,1} = [v]_{n,1} \Rightarrow [R]_{n,n} \cdot [i^*]_{n,1} + [N_C^*]^T \cdot \frac{d}{dt} [\phi]_{a,1} = [v]_{n,1} \end{cases} \quad (5)$$

where $[\vartheta]$ is the reluctance matrix of the magnetic network and $[R]$ is the edge resistance matrix. The magnetic approach implies the removal of the $[i]$ vector. This entails, starting from the second expression in (5), the preventive use of the following relation:

$$[i^*] = [R]^{-1} \cdot \left\{ [v] - [N_C^*]^T \cdot \frac{d}{dt} [\phi] \right\} \quad (6)$$

This calculation is binding for the magnetic analysis and depends on the existence of $[R]^{-1}$. Since the $[R]$ matrix is always non-singular, it can always be performed. This would not be the case had $[i]$ been inferred from the first of (5). As $[N_C^*]$ is generally rectangular, its inverse matrix is not even defined *a priori*. By substituting (6) in the first of (5), having defined:

$$\begin{cases} [F]_{a,a} = - \left\{ [N_C^*] \cdot [R]^{-1} \cdot [N_C^*]^T \right\}^{-1} [\mathcal{G}] \\ [G]_{a,\ell} = \left\{ [N_C^*] \cdot [R]^{-1} \cdot [N_C^*]^T \right\}^{-1} \cdot [N_C^*] \cdot [R]^{-1} \end{cases} \quad (7)$$

one has the following normal form:

$$\begin{cases} \frac{d}{dt} [\phi] = [F] \cdot [\phi] + [G] \cdot [v] \\ [\phi(t_o)] = [\phi_o] \end{cases} \quad (8)$$

The correctness of this procedure is subordinated to the non-singularity of the matrix:

$$[D]_{a,a} = \left\{ [N_C^*]_{a,n} \cdot [R]_{n,n}^{-1} \cdot [N_C^*]^T_{n,a} \right\} \quad (9)$$

To this regard, having observed that (9) may be expressed as:

$$[D]_{a,a} = [M_m] \cdot \begin{bmatrix} [N^*]_{n,n} \\ [0]_{\ell-n,n} \end{bmatrix} \cdot [1/R] \cdot \begin{bmatrix} [N^*]_{n,n} \\ [0]_{\ell-n,n} \end{bmatrix}^T \cdot [M_m]^T = [M_m] \cdot [N^2/R] \cdot [M_m]^T \quad (10)$$

one can deduce that (10) assumes the typical structure of the loop matrix of classical theory. It can be obtained by inspection in the following way: the terms D_{kk} on the leading diagonal are equal to the sum of the terms N^2/R pertaining to loop k ; the terms D_{kh} not belonging to the leading diagonal are equal to the opposite of the sum of the terms N^2/R pertaining to the common windings of the loops k and h [3].

By observing the analogies with circuit theory one can deduce that this matrix is invertible if $n \geq a$. In case $n < a$ ³, that is when there are passive magnetic meshes, one can still bring oneself to the preceding case by preventively eliminating these meshes.

Solving (8), and taking (6) into account, having set:

² The electrical network connected to the winding is represented by its Thevenin equivalent.

³ This case corresponds to the case featuring shortcircuited edges in the electrical network in the classical loop analysis.

$$\begin{cases} [H] = [R]^{-1} \{ [I] - [N_C]^T \cdot [G] \} \\ [K] = [R]^{-1} \cdot [N_C]^T \cdot [F] \end{cases} \quad (11)$$

the currents, algebraically become:

$$[i] = [H] \cdot [v] - [K] \cdot [\phi] \quad (12)$$

The loop fluxes always lead to the formulation of the state equations for the study of the dynamics of the magnetolectric network, for which there always exists a solution.

Equations (8) may also be written by means of inspection by applying the well known rules of electrical circuit theory [3].

Conditions for the use of the current state variable

The substitution, in the state model, of the loop flux extensive variable ϕ with the intensive current variable i is carried out by solving the first of (5) with regards to the loop flux, in a form such as the following:

$$[\phi]_{a,1} = ([\mathcal{G}]^{-1})_{a,a} \cdot [m]_{a,1} = [\Lambda]_{a,a} \cdot [N_C]_{a,\ell} \cdot [i]_{\ell,1} = [T]_{a,\ell} \cdot [i]_{\ell,1} \quad (13)$$

Expression (13) must be a bijective relation between the variables i and ϕ since it represents a change of variables. This requires that the matrix $[T]$ be square and non-singular.

The first requirement implies that the number of rows a , equal to the number of magnetic loops, be greater or equal than the number of solenoids n . Indeed, in terms of matrices of matrices:

$$[\phi]_{a,1} = [\Lambda]_{a,a} \cdot \begin{bmatrix} [N_C^*]_{a,n} & [0]_{a,\ell-n} \end{bmatrix}_{a,\ell} \cdot \begin{bmatrix} [i^*]_{n,1} \\ [0]_{\ell-n,1} \end{bmatrix} \quad (14)$$

from which by eliminating the last $\ell - a$ rows/columns one obtains:

$$[\phi]_{a,1} = [\Lambda]_{a,a} \cdot \begin{bmatrix} [N_C^*]_{a,n} & [0]_{a,a-n} \end{bmatrix}_{a,a} \cdot \begin{bmatrix} [i^*]_{n,1} \\ [0]_{a-n,1} \end{bmatrix} \quad (15)$$

This turns out to be non-singular in the case $n=a$. In this case the two factors $[\Lambda]_{a,a}$ and $[N_C^*]_{a,a}$ are each in turn non singular without exception: the first is the matrix of the magnetic loops; the second is the restricted incidence matrix of the magnetic network and therefore consists of linearly independent rows/columns and for $n=a$ it is also square.

By substituting (13) in the second of (5) one obtains the following equation in the current state variables.

$$[R]_{n,n} \cdot [i^*]_{n,1} + [N_C^*]_{n,a}^T \cdot [\Lambda]_{a,a} \cdot [N_C^*]_{a,n} \cdot \frac{d}{dt} [i^*]_{n,1} = [v]_{n,1} \quad (16)$$

whose solution leads to, in a form such as the following:

$$\frac{d}{dt} [i] = -[\Gamma] \cdot [R] \cdot [i] + [\Gamma] \cdot [v] \quad (17)$$

to the electric state model. This is always valid as long as the elastance matrix $[\Gamma] = [[L]_{n,n}]^{-1} = [[N_C^*]_{n,a}^T \cdot [\Lambda]_{a,a} \cdot [N_C^*]_{a,n}]^{-1}$ is defined, that is when $\det[L] \neq 0$. The inductance matrix:

$$[L]_{n,n} = [N_C^*]_{n,a}^T \cdot [\Lambda]_{a,a} \cdot [N_C^*]_{a,n} \quad (18)$$

Table I. State variables that may be used for the dynamic analysis of a magneto-electric network

	$[D]$	$[L]$	$[T]$	State variable
$a < n$	Square and invertible	Square and not invertible	Rectangular	ϕ
$a = n$	Square and invertible	Square and invertible	Square and invertible	ϕ, i
$a > n$	Square and not invertible, can be reduced to invertible	Square and invertible	Square and not invertible, can be reduced to invertible	i, ϕ

for the same reasons as for matrix $[T]$, turns out to be non-singular when $n=a$.

The following topological properties can be deduced. In a magnetolectric network the analysis in terms of the currents requires that the n solenoids – at most one per edge – be equal, in a network with no passive meshes, to the number a of magnetic loops. In this case there will be a one to one correspondence between the flux and current variables. In the case $a < n$ it will not be possible to employ the current variable because the inductance matrix $[L]$ is not invertible. In the case $a > n$, that is in the presence of passive meshes, it is possible to use both variables by preventively reducing the magnetic network, whereas the current variable is of immediate use.

Table I shows which state variables may be used, as a function of a and n , and the characteristics of the matrices representative of the system state equations.

Example

In the following an example will be considered as an application of the preceding statements. The analysis of this network shall be carried out with reference to the three cases n greater, equal and less than a .

Consider for example, the planar magnetolectric network of Fig. 3a. The magnetic network equivalent, Fig. 3b, has $\ell=3$ magnetic edges, $a=2$ magnetic loops and $n=3$ windings, as can be seen from Fig. 3c, representing its topological graph.

In this case one has:

$$[M_m] = \begin{bmatrix} 1 & 0 & 1 \\ 0 & -1 & -1 \end{bmatrix} \quad [N] = \begin{bmatrix} N_1 & 0 & 0 \\ 0 & N_2 & 0 \\ 0 & 0 & N_3 \end{bmatrix} \quad [R] = \begin{bmatrix} R_1 & 0 & 0 \\ 0 & R_2 & 0 \\ 0 & 0 & R_3 \end{bmatrix}$$

$$[N_C] = [M_m] \cdot [N] = \begin{bmatrix} N_1 & 0 & N_3 \\ 0 & -N_2 & -N_3 \end{bmatrix} = [N_C^*] \quad [\vartheta] = \begin{bmatrix} \vartheta_1 + \vartheta_3 & -\vartheta_3 \\ -\vartheta_3 & \vartheta_2 + \vartheta_3 \end{bmatrix}$$

from which, to the purpose of employing the flux variable, the following holds:

$$[D]_{a,a} = \left\{ [N_C^*]_{a,n} \cdot [R]_{n,n}^{-1} \cdot \left([N_C^*]^T \right)_{n,a} \right\} = \begin{bmatrix} \frac{N_1^2}{R_1} + \frac{N_3^2}{R_3} & -\frac{N_3^2}{R_3} \\ -\frac{N_3^2}{R_3} & \frac{N_2^2}{R_2} + \frac{N_3^2}{R_3} \end{bmatrix}$$

This matrix is invertible without exception. Furthermore, it can be formulated by means of the aforementioned inspection rules.

The use of the current variables entails that the following inductance matrix:

$$[L] = \begin{bmatrix} L_1 & L_{12} & L_{13} \\ L_{12} & L_2 & L_{23} \\ L_{13} & L_{23} & L_3 \end{bmatrix}$$

be invertible. Having observed that:

$$L_1 = N_1^2 \frac{\vartheta_2 + \vartheta_3}{\vartheta_1 \vartheta_2 + \vartheta_2 \vartheta_3 + \vartheta_3 \vartheta_1} \quad L_{12} = N_1 N_2 \frac{\vartheta_3}{\vartheta_1 \vartheta_2 + \vartheta_2 \vartheta_3 + \vartheta_3 \vartheta_1}$$

$$L_2 = N_2^2 \frac{\vartheta_1 + \vartheta_3}{\vartheta_1 \vartheta_2 + \vartheta_2 \vartheta_3 + \vartheta_3 \vartheta_1} \quad L_{23} = N_2 N_3 \frac{\vartheta_1}{\vartheta_1 \vartheta_2 + \vartheta_2 \vartheta_3 + \vartheta_3 \vartheta_1}$$

$$L_3 = N_3^2 \frac{\vartheta_1 + \vartheta_2}{\vartheta_1 \vartheta_2 + \vartheta_2 \vartheta_3 + \vartheta_3 \vartheta_1} \quad L_{13} = N_1 N_3 \frac{\vartheta_2}{\vartheta_1 \vartheta_2 + \vartheta_2 \vartheta_3 + \vartheta_3 \vartheta_1}$$

the following holds:

$$\det[L] = L_1 L_2 L_3 - L_1 L_{23}^2 - L_2 L_{13}^2 - L_3 L_{12}^2 - 2L_{12} L_{23} L_{13} = 0$$

The singularity of matrix $[L]$ holds $\forall \{ \vartheta_1, \vartheta_2, \vartheta_3, N_1, N_2, N_3 \}$ and is therefore due to topological reasons.

Eliminating one of the mmfs may equalize the number of independent magnetic and electric variables. In this case, for the fluxes one can have the following:

$$N_3 = 0 \Rightarrow [D]_{a,a} = \left\{ [N_C^*]_{a,a} \cdot [R]_{a,a}^{-1} \cdot \left([N_C^*]^T \right)_{a,a} \right\} = \begin{bmatrix} N_1^2/R_1 & 0 \\ 0 & N_2^2/R_2 \end{bmatrix}$$

$$N_2 = 0 \Rightarrow [D]_{a,a} = \left\{ [N_C^*]_{a,a} \cdot [R]_{a,a}^{-1} \cdot \left([N_C^*]^T \right)_{a,a} \right\} = \begin{bmatrix} \frac{N_1^2}{R_1} + \frac{N_3^2}{R_3} & -\frac{N_3^2}{R_3} \\ -\frac{N_3^2}{R_3} & \frac{N_3^2}{R_3} \end{bmatrix}$$

Both are invertible without exception.

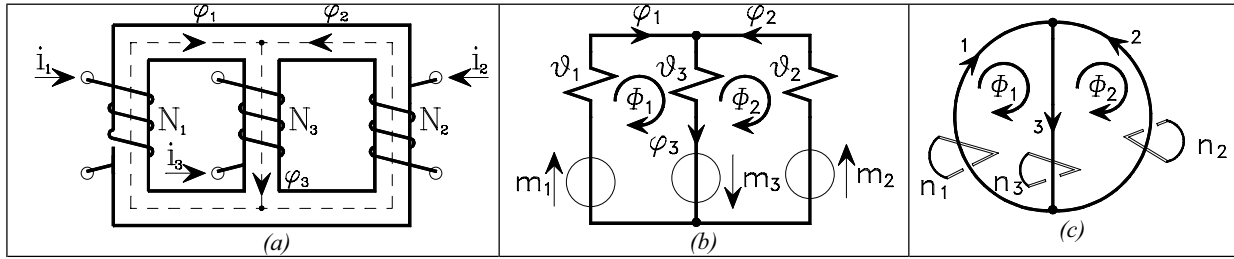


Fig. 3. Example of a magnetoelectric network

To the purpose of the employment of the current state variables one has in the two cases:

$$N_3 = 0 \Rightarrow [L] = \begin{bmatrix} \frac{N_1^2(\vartheta_2 + \vartheta_3)}{\vartheta_1\vartheta_2 + \vartheta_2\vartheta_3 + \vartheta_3\vartheta_1} & \frac{N_1N_2\vartheta_3}{\vartheta_1\vartheta_2 + \vartheta_2\vartheta_3 + \vartheta_3\vartheta_1} \\ \frac{N_1N_2\vartheta_3}{\vartheta_1\vartheta_2 + \vartheta_2\vartheta_3 + \vartheta_3\vartheta_1} & \frac{N_2^2(\vartheta_1 + \vartheta_3)}{\vartheta_1\vartheta_2 + \vartheta_2\vartheta_3 + \vartheta_3\vartheta_1} \end{bmatrix} \quad N_2 = 0 \Rightarrow [L] = \begin{bmatrix} \frac{N_1^2(\vartheta_2 + \vartheta_3)}{\vartheta_1\vartheta_2 + \vartheta_2\vartheta_3 + \vartheta_3\vartheta_1} & \frac{N_1N_3\vartheta_2}{\vartheta_1\vartheta_2 + \vartheta_2\vartheta_3 + \vartheta_3\vartheta_1} \\ \frac{N_1N_3\vartheta_2}{\vartheta_1\vartheta_2 + \vartheta_2\vartheta_3 + \vartheta_3\vartheta_1} & \frac{N_3^2(\vartheta_1 + \vartheta_2)}{\vartheta_1\vartheta_2 + \vartheta_2\vartheta_3 + \vartheta_3\vartheta_1} \end{bmatrix}$$

which are also invertible without exception.

There is consequently complete equivalence between fluxes and currents for $n=a$. The inductance matrix is therefore invertible. It is thus possible to use the current vector as state variable.

One can obtain the case $n < a$ by eliminating one of the remaining fms. In this case as well there are two different conditions. For the flux one has:

$$N_2 = N_3 = 0 \Rightarrow [D]_{a,a} = \begin{bmatrix} \frac{N_1^2}{R_1} & 0 \\ 0 & 0 \end{bmatrix} \quad N_1 = N_2 = 0 \Rightarrow [D]_{a,a} = \begin{bmatrix} \frac{N_3^2}{R_3} & -\frac{N_3^2}{R_3} \\ -\frac{N_3^2}{R_3} & \frac{N_3^2}{R_3} \end{bmatrix}$$

Matrix $[D]$ is not invertible. This is due to the presence of a passive loop and a passive mesh in the magnetic network. In this case it is therefore not possible to uniquely identify the two loop fluxes; it is thus necessary to preliminarily eliminate the passive meshes. In doing so one obtains:

$$N_2 = N_3 = 0 \Rightarrow [D]_{a,a} = \frac{N_1^2}{R_1} \quad N_1 = N_2 = 0 \Rightarrow [D]_{a,a} = \frac{N_3^2}{R_3}$$

which are evidently invertible without exception.

To the purpose of the employment of the current state variables one has in the two cases:

$$N_2 = N_3 = 0 \Rightarrow [L] = \frac{N_1^2(\vartheta_2 + \vartheta_3)}{\vartheta_1\vartheta_2 + \vartheta_2\vartheta_3 + \vartheta_3\vartheta_1} \quad N_1 = N_2 = 0 \Rightarrow [L] = \frac{N_3^2(\vartheta_1 + \vartheta_2)}{\vartheta_1\vartheta_2 + \vartheta_2\vartheta_3 + \vartheta_3\vartheta_1}$$

which, by means of the notion of self-inductance, consents the use of the current state variables.

In this last case the use of the current state variables is straightforward whereas that of the flux state variables requires some preliminary verifications.

Conclusions

Having gained insight into the different energetic significance that pertains to intensive and extensive variables, the twofold and simultaneous nature of physical and systemic variables is duly attributed to the magnetic flux extensive variables. On the other hand the current variables are intensive and therefore uniquely systemic. After having explicitly stated that models based on the use of the magnetic flux variables are invariably feasible and that those based on the current variables are only conditionally valid, appropriate criteria for the formulation of the state equations in terms of the flux variables and the topological properties that a network must possess to consent the analysis in terms of the current variables are specified (see Table I).

References

- [1] S. Leva, A.P. Morando, Topology and Dynamics of Mutual Inductors with Ferromagnetic Non-Linearity, Proc. ECCTD '99, Stresa, Italy, 1999, pp.189-192
- [2] C.A. Dosoer, E.S. Kuh, Basic Circuit Theory, New York: McGraw-Hill, V ed 1978
- [3] F. Ayres Jr, Matrices, New York: McGraw-Hill, 1974

II-2. CALCULATION OF LINEAR MOTOR PERFORMANCE USING FINITE ELEMENT METHOD

Miroslav Bugeza, Danilo Makuc, Rastko Fišer

University of Ljubljana, Faculty of Electrical Engineering, 1000 Ljubljana, Slovenia, E-mail: mirob@fe.uni-lj.si

Abstract – The paper presents calculation of linear induction motor and linear synchronous motor steady- state characteristics using finite element method. 2D non-linear magnetostatic and eddy-current solver were used for magnetic field and force calculation. A detailed insight in magnetic field distribution and produced output force is a basic step for evaluation of motor performance. Calculations were performed for different excitation currents and different air gap lengths for both types of linear motor. The results obtained from the magnetic field calculations could also be used for determination of motor parameters (e.g. inductance) useful for mathematical modelling and control system simulations.

Introduction

Linear motors are widely used in machine tools, linear tables, textile tools, saws, separators, transportation systems and many others [1]. This paper focuses on permanent magnet linear synchronous motor (PMLSM) and linear induction motor (LIM) applied as servo motor for machine tools. For optimal operation of the motor a detailed insight into a steady-state and dynamic performance characteristics is very important [2,3,4].

Both types of linear motors are installed in our laboratory and a lot of measurements have already been performed. In spite of that there is a problem of analysing steady-state operating conditions since the available moving range is short, the system is highly dynamic and during operation there are almost no steady states. Furthermore all measurements of electrical and mechanical quantities are very demanding. In Table 1 basic parameters of the linear motors are stated.

Table 1. Basic constructional and rated parameters of the motors

	Number of pole pairs	Length of primary part (mm)	Length of secondary part (mm)	Rated force (N)	Rated current (A)	Rated speed (m/s)
LIM	2	390	3000	1000	19	1
PMLSM	4	390	3000	1500	17	2.5

Analyses of Motors Using FEM

For analyses of both motors a 2D FEM software was used. The force produced by the motor was calculated using a method of virtual work. For linear induction motor analyses the eddy current solver was used. Magnetic field was described by equation (1)

$$\bar{\nabla} \times \left(\frac{1}{\mu} \cdot \bar{\nabla} \times \bar{A} \right) = \sigma \cdot \bar{\nabla} \phi - \sigma \cdot \frac{\partial \bar{A}}{\partial t} \quad (1)$$

where μ is permeability, \bar{A} is magnetic vector potential, σ is conductivity and ϕ is electric scalar potential.

The fluxes in primary and secondary part have different frequencies for all operating states except for a locked primary condition. Equation (1) describes electromagnetic conditions only at one frequency. To solve that problem the frequency of primary excitation current corresponds to instantaneous slip

value at chosen steady-state operating point [5]. With sweeping the excitation frequency from rated value down to zero the complete steady-state force characteristic can be obtained.

For analyses of linear synchronous motor a magnetostatic field solver was used and the result was derived from equation (2)

$$\bar{\nabla} \times \left(\frac{1}{\mu} \cdot \bar{\nabla} \times \bar{A} \right) = \bar{J} \quad (2)$$

where \bar{J} is current density which consists of exciting current and equivalent magnetizing current of permanent magnets. Force was calculated for different displacement of primary part and different air gap lengths.

Magnetic Field Distribution

Figure 1 shows the magnetic field distribution at maximal force of (a) linear induction motor at slip 0.12 and (b) linear synchronous motor at displacement of 12.5 mm. The primary part has a two-layer winding with half-filled end slots, which is typical topology for linear motors [1]. Because of this constructional particularity the number of poles is odd. Contrary to the magnetic field in rotational motors, which is always symmetrically distributed along air gap the magnetic conditions in linear motors are regularly asymmetrical. Besides that the holes of the water-cooling system are placed in the yoke of the linear synchronous motor primary core (Fig. 1b). They obviously have an additional influence to asymmetrical magnetic flux distribution. The linear induction motor also has a water-cooling system but the aluminium unit is mounted above the primary part and has no influence on the magnetic field.

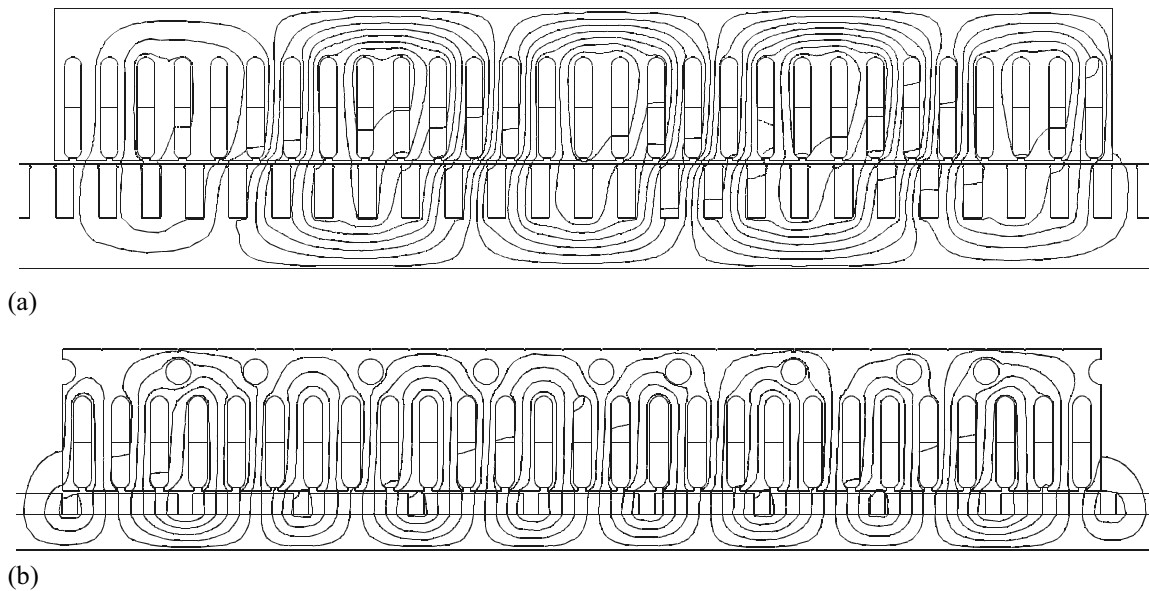


Fig.1. Magnetic field distribution of (a) linear induction motor and (b) linear synchronous motor

Steady-state Force Characteristics

For both motors a propulsion force (F_x) characteristics were calculated at different excitation currents. Figure 2 shows those steady-state force characteristics of (a) linear induction motor and (b) linear synchronous motor. There is obvious influence of detent force in linear synchronous motor characteristics, which could be reduced in a design phase with an appropriate choice of secondary configuration and permanent magnet length [8]. As it was expected two times greater current is required in the linear induction motor to get the same propulsion force as in linear synchronous motor.

Characteristic of attractive force (F_y) between primary and secondary part is shown in Fig. 3 for (a) linear induction motor and (b) linear synchronous motor. At same excitation current the ratio of maximal attractive to propulsion force is about 10 for linear induction motor and just 4 for linear synchronous motor.

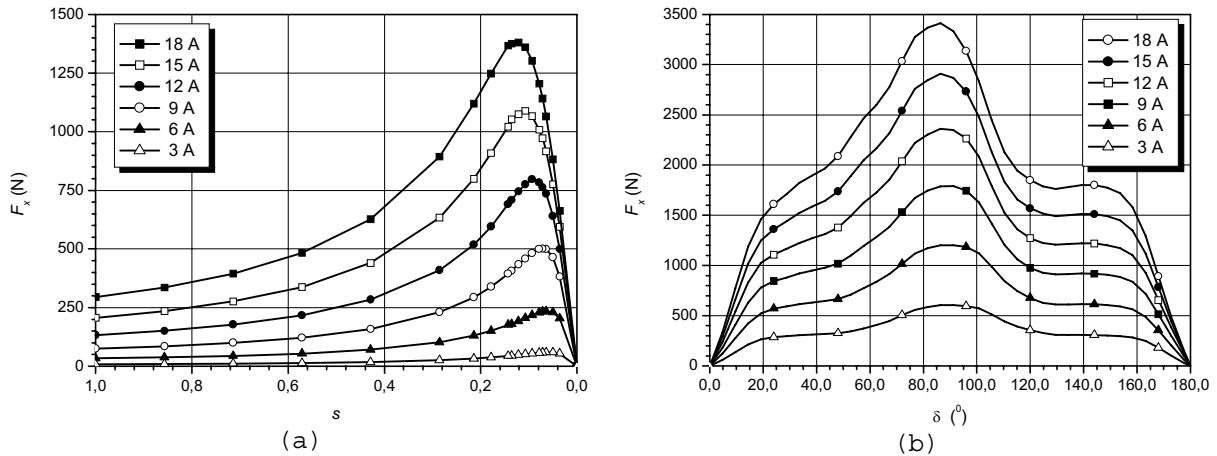


Fig. 2. Propulsion force characteristics at different excitation currents of (a) linear induction motor and (b) linear synchronous motor

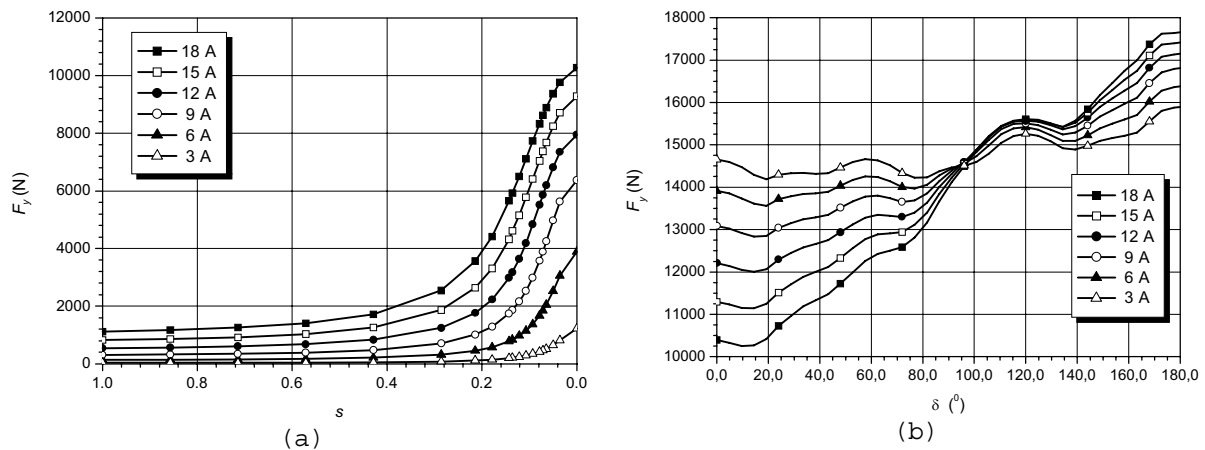


Fig. 3. Attraction force characteristics at different excitation currents of (a) linear induction motor and (b) linear synchronous motor

Since the linear synchronous motor produces the same propulsion force at just half of the current of linear induction motor, the force characteristics for different air gap lengths had to be calculated at different exciting currents: 18 A for induction motor and 9 A for synchronous motor. Comparison of the characteristics is shown in Fig. 4. Decreasing of the propulsion force while the air gap was changing from 0.4 mm to 1.2 mm was relatively small: 18.8 % for induction motor and 12.8 % for synchronous motor.

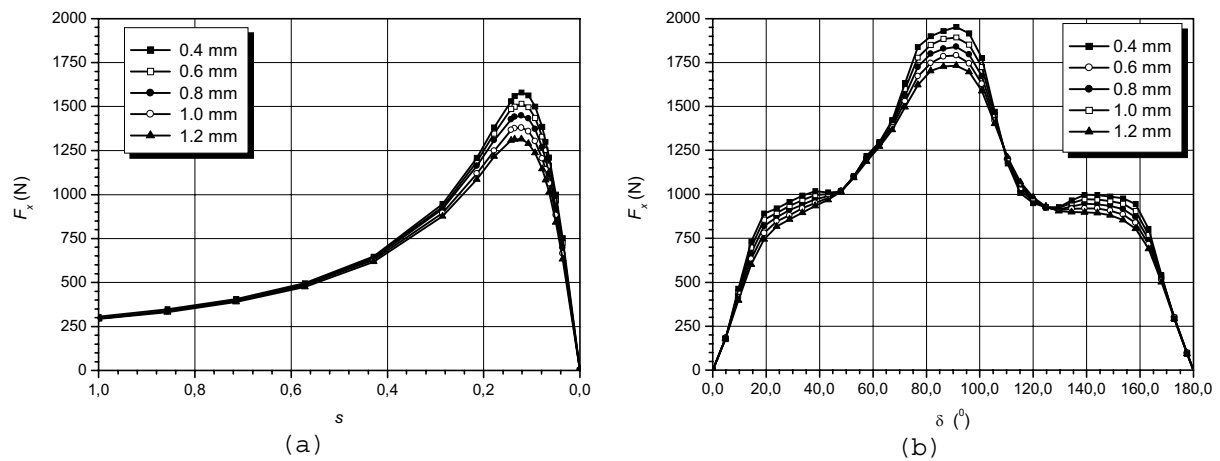


Fig. 4. Propulsion force characteristics for different air gap lengths of (a) linear induction motor and (b) linear synchronous motor

Conclusions

Magnetic field calculation results enable simulation of many steady-state and dynamic characteristics. Obtained parameters of linear motors are very useful in the process of inverter control design of servo drives with linear motors.

Comparison of linear induction motor and linear synchronous motor reveals as expected, that synchronous motor has the same performance at much lower currents than induction motor. Due to application of permanent magnets the dimensions of linear synchronous motor are smaller, thus more appropriate for servo drives. Linear induction motor still has the advantage in lower price and simpler construction.

References

- [1] I. Boldea, S.A. Nasar, *Linear Motion Electromagnetic Devices*, Taylor Francis, 2001.
- [2] J.F. Gieras, *Linear Induction Drives*, Oxford, Clarendon Press, 1994.
- [3] J.F. Gieras, *Linear Synchronous Motor: Transportation and Automation Systems*, London, CRC Press, 2000.
- [4] M. Poloujadoff, *The Theory of Linear Induction Machinery*, Oxford, Clarendon Press, 1980.
- [5] R. Fišer, Application of a Finite Element Method to Predict Damaged Induction Motor Performance, *IEEE Transaction on Magnetics*, Vol. 37, No. 5, September 2001.
- [6] J.K. Sykulski, *Computational Magnetics*, Chapman&Hall, 1995.
- [7] T. Utsumi, I. Yamaguchi, Parameter-Value Evaluation of 3-phase Equivalent Circuit of Linear Induction Motor, Record of the 1999 IEEE International Symposium on Diagnostic of Electrical Machines, Power Electronics and Drives, pp 275-280, Gijon, Spain, September 1999.
- [8] S.M. Jang, S.H. Lee, I.K. Yoon, Design Criteria for Detent Force Reduction of Permanent-Magnet Linear Synchronous Motors With Halbach Array, *IEEE Transactions on Magnetics*, Vol. 38, No. 5, September 2002.

II-3. ANALYTICAL MODEL OF THE MAGNETIC FIELD IN DOUBLY SLOTTED ELECTRICAL MACHINES WITH DISTRIBUTED WINDINGS AND EVALUATION OF E.M.F. AND TORQUE

Antonino Di Gerlando, Gian Maria Foglia, Roberto Perini

Dipartimento di Elettrotecnica - Politecnico di Milano, Piazza Leonardo da Vinci 32, 20133 Milano, Italy

E-Mails: antonino.digerlando, gianmaria.foglia, roberto.perini@polimi.it

Abstract – The quantities of interest in an electrical machine (e.m.f. and torque) can be evaluated once known the air-gap flux density. The paper shows how to analytically model this flux density distribution, as a function of time and of the rotor position, considering the actual disposition of slots and conductors and the geometrical characteristics of the air-gap periphery. The winding m.m.f. is evaluated by summing suited step functions; as regards the slots, specific field notch functions are obtained, by analytical field solutions and applying suited superposition techniques. The method is applied to constant air-gap machines, neglecting magnetic saturation. Some e.m.f. and torque evaluations are shown and discussed.

Basic step model of the m.m.f.

The winding m.m.f. is obtained by adding the contributions of the various coils.

At first, sharp step functions will be employed, subsequently showing how to smooth the field near the coil sides.

In the following, x is the generic linear coordinate, measured along the air-gap periphery.

M.m.f. of integer pitch coil windings

The m.m.f. space distribution of an integer pitch coil of a winding with a generic N° of poles N_p is expressed by:

$$M_{c\sigma}(x) = \sigma[\cos(\pi \cdot x/\tau)] - 1/2, \quad (1)$$

where $\tau = \pi D/N_p$ is the pole pitch, D the air-gap diameter and $\sigma(x)$ is the step function:

$$\sigma(x) = 1 \text{ for } x \geq 0, \quad \sigma(x) = 0 \text{ for } x < 0. \quad (2)$$

Called $I_t(t) = N_t i(t)/a$ the coil total current ($N_t = N^\circ$ of turns/coil; $i(t)$ = phase current; $a = N^\circ$ of parallel paths), the coil m.m.f. becomes:

$$m_c(x,t) = M_{c\sigma}(x) \cdot I_t(t) = M_{c\sigma}(x) \cdot (N_t/a) \cdot i(t) = \{\sigma[\cos(\pi \cdot x/\tau)] - 1/2\} \cdot (N_t/a) \cdot i(t). \quad (3)$$

In case of uniformly distributed phase coils, called q the number of coils/(pole-phase) and τ_s the slot pitch, the phase m.m.f. space distribution can be obtained by adding q terms like (1); by adopting a displacement equal to $(q-1) \cdot \tau_s/2$ in order to obtain a phase m.m.f. centred along the phase axis, the following expression follows:

$$M_{f\sigma}(x) = \sum_{k=1}^q \left\{ \sigma \left[\cos \left\{ \left(\frac{\pi}{\tau} \right) \cdot \left[x - (k-1) \cdot \tau_s + (q-1) \cdot \tau_s/2 \right] \right\} \right] - 1/2 \right\}. \quad (4)$$

Called $i_p(t)$ the instantaneous current of the phase p ($p = 1, 2, 3$), the three-phase m.m.f. equals:

$$m_{3f}(x,t) = M_{f\sigma}(x) \cdot (N_t/a) \cdot i_1(t) + M_{f\sigma}(x - 2 \cdot \tau/3) \cdot (N_t/a) \cdot i_2(t) + M_{f\sigma}(x - 4 \cdot \tau/3) \cdot (N_t/a) \cdot i_3(t); \quad (5)$$

In case of balanced, three-phase, sinusoidal currents, we have: $i_p(t) = \sqrt{2} \cdot I \cdot \cos[\omega t - (p-1) \cdot 2\pi/3]$.

In a similar manner it is possible to obtain corresponding expressions for the m.m.f.s in case of two layer windings, both with integer and shorted pitch coils [7].

Field functions and their superposition

The basic analytical approach employs the method of the conformal transformations. As known, a classical example is the problem of a surface with one indefinitely-deep single slot, separated from a faced smoothed surface throughout a constant air-gap g ; among the surfaces, a constant scalar magnetic potential difference (m.p.d.) U is applied. This problem, studied by Carter for unsaturated magnetic cores [1], leads to express the position $p(w)$ within the air-gap and the corresponding flux density $B_1(w)$ as a function of an auxiliary complex parameter w . To our aims, we are interested in analysing B_1 just along the smoothed surface ($p(w) \equiv x(w)$): thus,

a more suitable expression can be obtained by substituting the parametric formulation with a function $B_1(x)$, interpolating a suited N° of points along x axis (e.g. by means of a cubic spline); $B_1(x)$ is a real function of a real variable (in fact, the flux density vector, always orthogonal to the smoothed surface, has just one component). Called $B_i = \mu_0 \cdot U/g$ “ideal” flux density (as it exists between two smoothed faced surfaces), we define “lost” flux density $B_L(x)$ the difference among B_i and any actual flux density $B(x)$, and call “field function” $\beta(x)$ the ratio among $B(x)$ and B_i ; $\beta(x)$ is so named as it describes the field behaviour by means of a p.u. function. For example, the field functions related to $B_1(x)$, and to the lost flux density $B_{L1}(x)$, and the corresponding relations are:

$$\beta_1(x) = B_1(x)/B_i, \quad \beta_{L1}(x) = B_{L1}(x)/B_i, \quad (6)$$

$$B_{L1}(x) = B_i - B_1(x) = B_i \cdot (1 - \beta_1(x)) = B_i \cdot \beta_{L1}(x). \quad (7)$$

The problem is how to combine simple field functions like (6), in order to model the actual geometrical structures, in which several slots are disposed along one surface (for now the other surface is maintained smoothed): to this aim, the Principle of Superposition of the Lost Flux Density (PSLB) must be introduced.

The PSLB declares the possibility to sum the lost flux densities of the single slots: the actual lost flux density of a multi-slot structure equals the sum of the lost flux densities due to each slot, as if it were the only existing slot; thus, the actual flux density equals the difference among the ideal flux density and the global lost flux density:

$$B_L(x) = \sum_j B_{L1}(x - j \cdot \tau_s), \quad B(x) = 1 - B_L(x) \Rightarrow \beta_L(x) = \sum_j \beta_{L1}(x - j \cdot \tau_s), \quad \beta(x) = 1 - \beta_L(x), \quad (8)$$

with j extended to all the slots. The PSLB is valid also in case of intersecting lost flux density curves, due to very near adjacent slots, and it can be applied also to other geometrical “disturbances”, as the interpolar zones.

The PSLB has not been demonstrated yet, but several FEM tests have shown its correctness [3, 4, 5, 6].

Air-gap flux density distribution

The analysis is aimed to obtain the air-gap flux density distribution among two toothed surfaces, with any disposition of the currents in the slots: to this aim, some simple, basic situations must be progressively analysed. Called x and y the linear peripheral coordinates along the stator and rotor surfaces respectively, and called z the position of the rotor origin with respect to the stator origin, it follows:

$$x = y + z. \quad (9)$$

Two slotted surfaces, between which a constant m.p.d. U is applied

The following functions should be defined (subscripts S, R, L indicate: Stator, Rotor, Lost):

– $B_S(x)$ and $B_{LS}(x)$: flux density and lost flux density due to a slotted stator surface faced to a smoothed rotor one, evaluated along the rotor smoothed surface ($\beta_S(x)$ and $\beta_{LS}(x) = 1 - \beta_S(x)$ are the related field functions);

– $B_R(y)$ and $B_{LR}(y)$: flux density and lost flux density due to a slotted rotor surface faced to a smoothed stator one, evaluated along the stator smoothed surface ($\beta_R(y)$ and $\beta_{LR}(y) = 1 - \beta_R(y)$ are the related field functions);

– $B(x,y)$ and $B_L(x,y)$: resultant flux density and lost flux density, in case of both slotted surfaces, assumed as purely radial, considered at half air-gap width ($\beta(x,y)$ and $\beta_L(x,y) = 1 - \beta(x,y)$ are the related field functions).

The field functions $\beta_{LS}(x)$ and $\beta_{LR}(y)$ could be obtained by the previously described analytical procedure, and applying the PSLB: indeed, once operated the superposition (8), it is more suited to employ an interpolating function. Good results have been achieved by using exponential periodic functions.

For the stator field function, called τ_{sS} the slot pitch, the following equation was used:

$$\beta_{LS}(x) = \beta_{LS0} \cdot \exp \left\{ - \left[v_S \cdot \sin^2 \left(\pi \cdot x / \tau_{sS} \right) \right]^{\lambda_S} \right\}, \quad (10)$$

where β_{LS0} , v_S , and λ_S can be evaluated by parameter identification, from analytical or FEM solution results.

As regards $\beta_{LR}(y)$, an expression like (10) can be similarly obtained only if the rotor is uniformly slotted (as in the induction motors). In case of an isotropic synchronous machine, this condition is not verified, and a different global slotting model must be developed: after performing the superposition (8), the function $\beta_{LR1}(y)$ should be considered, interpolating the field just within one rotor slot pitch; then, the slotting repetition is obtained by summations, at first extended within one pole ($\beta_{LRp}(y)$), subsequently all along the overall periphery ($\beta_{LR}(y)$):

$$\beta_{LR1}(y) = \beta_{LR0} \cdot \exp \left\{ - \left[v_R \cdot \left(\left(y - \frac{\tau}{2} \right) / \tau_{sR} \right)^2 \right]^{\lambda_R} \right\}, \quad \beta_{LRp}(y) = \sum_{j_r=0}^{c_{pR}-1} \beta_{LR1} \left(y - \left(\frac{c_{pR}-1}{2} - j_r \right) \cdot \tau_{sR} \right), \quad (11)$$

$$\beta_{LR}(y) = \sum_{j_p} \beta_{LRp}(y - j_p \cdot \tau), \quad j_p = 0, \dots, N_p - 1, \quad \text{where} \quad (12)$$

$c_{pR} = N^\circ$ of rotor slots/pole, $\tau_{sR} =$ slot pitch, $N_p = N^\circ$ of poles, β_{LR0} , v_R , and λ_R to be evaluated as for the stator. As regards the functions $B(x, y)$ and $\beta(x, y)$, y must be explicitly expressed by eq. (9): in fact, while the rotor

Of course, even if applied to the m.m.f., in principle $\alpha(x)$ is a flux density correction function.

The application of $\alpha(x)$ to the basic situation of a coil with an integer pitch shows that the product among $\alpha(x)$ and the step square-wave waveform (1) can be conveniently substituted by the following expression:

$$M_m(x) = (1/2) \cdot \tanh[k_{m\tau} \cdot \cos(\pi \cdot x/\tau)] \quad ; \quad (19)$$

$k_{m\tau}$ is a coefficient set to the value that correctly reproduces the slope of $\alpha(x)$ at the zero crossing; it is always sufficiently high (usually higher than 10) to saturate the tanh value to ± 1 when the cosine function tends to unity. In case of a shorted pitch coil, called τ_c the coil pitch, the smoothed slope m.m.f. expression is:

$$M_{m.sh}(x) = (1/2) \cdot \left\{ \tanh \left[k_{m\tau} \cdot \left(\cos(\pi \cdot x/\tau) - \cos \left[\pi \cdot \tau_c / (2 \cdot \tau) \right] \right) \right] \right\} + (\tau - \tau_c) / (2 \cdot \tau). \quad (20)$$

As concerns eq.s (3), (4), (5), they remain unvaried, but in them (19) and (20) should substitute (1).

Doubly slotted synchronous machine with three-phase stator winding and distributed field rotor winding

Consider an isotropic synchronous machine having a generic three-phase stator winding (one or two layers; integer or shorted pitch) with q slots/(pole-phase), a rotor winding with c_p slots/pole and N_f turns/(field coil), and stator and rotor slot pitches equal to τ_{sS} and τ_{sR} .

Called $M_{fS}(x)$ and $M_{fR}(y)$ the m.m.f. space distributions of one phase stator winding and of the field winding respectively, and indicated with $i_f(t)$ the instantaneous current in the field winding, the following stator, rotor and resultant instantaneous m.m.f.s. can be written:

$$m_S(x, t) = (N_t/a) \cdot \sum_{p=1,2,3} M_{fS} \left[x - (p-1) \cdot 2\tau/3 \right] \cdot i_p(t) \quad ; \quad m_R(y, t) = M_{fR}(y) \cdot N_f \cdot i_f(t) \quad , \quad (21)$$

$$m(x, y, t) = m_S(x, t) + m_R(y, t) \quad \Rightarrow \quad m(x, x-z, t) = m_S(x, t) + m_R(x-z, t) \quad . \quad (22)$$

The second formulation of the instantaneous distribution of the total m.m.f. points out that the m.m.f. acting in each point x measured along the stator periphery depends on time (as concerns the current time waveforms) and on rotor position z (that can vary as a time dependent variable too).

Finally, the instantaneous distribution of the air-gap flux density is described by this compact expression:

$$b(x, y, t) = (\mu_0/g) \cdot m(x, y, t) \cdot \beta_S(x) \cdot \beta_R(y) \quad \Rightarrow \quad b(x, x-z, t) = (\mu_0/g) \cdot m(x, x-z, t) \cdot \beta_S(x) \cdot \beta_R(x-z), \quad (23)$$

where $\beta_S(x)$ and $\beta_R(x-z)$ are the ‘‘notch’’ field functions taking into account the stator and rotor slotting effects, while the interpolar field effects are modelled directly by the tanh zero crossing shape of the m.m.f. terms.

As an example of m.m.f. space distributions, in case of single-layer, integer pitch stator windings, the stator and rotor coil m.m.f. expressions can be written as follows:

$$M_{cS}(x) = (1/2) \cdot \tanh[k_{mS} \cdot \cos(\pi \cdot x/\tau)] \quad ; \quad M_{cR}(y) = (1/2) \cdot \tanh[k_{mR} \cdot \cos(\pi \cdot y/\tau)], \quad (24)$$

while the corresponding phase and field winding expressions are given by:

$$M_{fS}(x) = \sum_{j_S=1}^q M_{cS} \left[x - \left(\frac{q-1}{2} - (j_S - 1) \right) \cdot \tau_{sS} \right] \quad ; \quad M_{fR}(y) = \sum_{j_R=1}^{c_p} M_{cR} \left[y - \left(\frac{c_p-1}{2} - (j_R - 1) \right) \cdot \tau_{sR} \right]. \quad (25)$$

Validation of the field analytical model by FEM comparison

A lot of global and local tests have been done, performing FEM simulations [6] and analytical evaluations of different geometrical and operating conditions: in the following, just one example is shown, aimed to show the soundness of the adopted approach. Reference is made to a constant air-gap synchronous machine (see Table 1). Fig.3 shows the flux density distribution as a function of the angle θ along the stator bore. Since the analytical model assumes a purely radial flux density, in the FEM simulations only radial components at half air-gap width have been considered. As can be noted, the field distributions are very close, confirming the model soundness. As regards the method accuracy also in case of partial overlapping of faced slots, several comparisons with FEM simulations have confirmed the correctness of the field evaluation [7], both in waveforms and values.

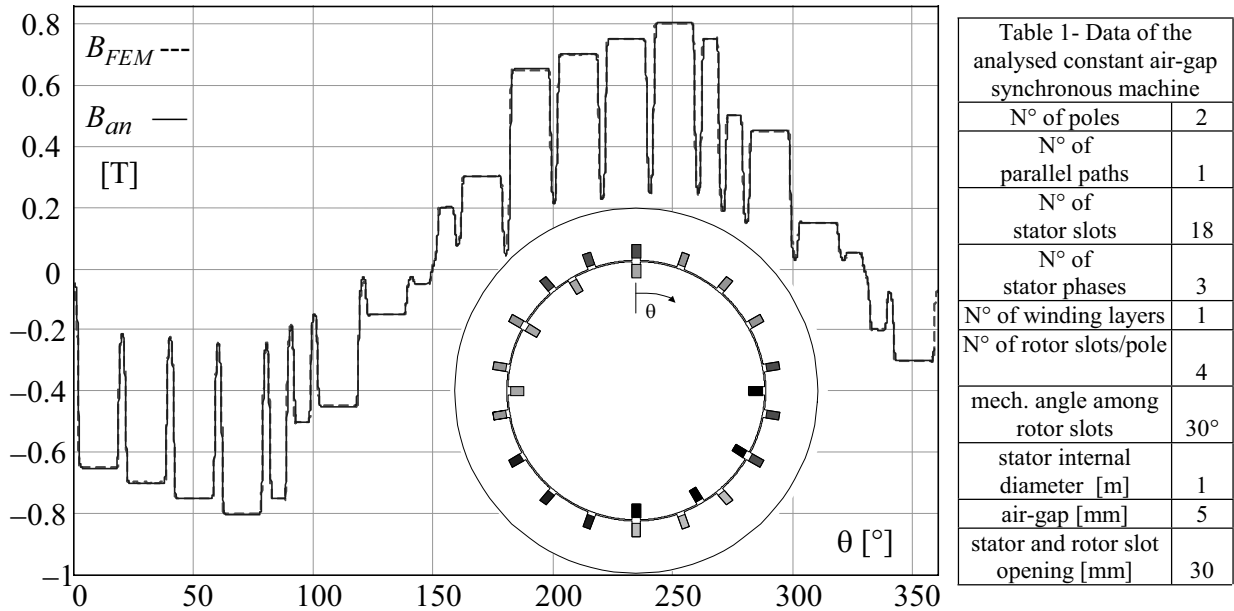


Fig.3 - Flux density distribution as a function of the angle θ along the stator bore, for the shown rotor position; B_{an} = analytical method; B_{FEM} = FEM calculations (radial component, evaluated at half air-gap width); machine data of Table 1; operating conditions: field slot tot. current = $I_{ff} = 1000$ A; sinus. stator currents: peak phase slot tot. current = $I_{tphM} = 400$ A.

Analytical evaluation of the winding e.m.f.

Called y_c the coil pitch (expressed in N° of slot pitches), and x_{ip1} the position of the initial active side of the first stator coil of the p -th phase; the initial and final active side positions of the k -th coil of the same p -th phase are:

$$x_{ipk} = x_{ip1} + (k-1) \cdot \tau_{sS} ; \quad x_{fpk} = x_{ipk} + y_c \cdot \tau_{sS} \quad , \quad (26)$$

For an unskewed machine of stack axial length ℓ and stator internal diameter D , the flux linkage of a group of q series connected coils under each pole (obtainable from (22), (23)) and the corresponding e.m.f. e_p are given by:

$$\Psi_p(z, t) = \sum_{k=1}^q \Psi_{pk}(z, t) = (\mu_0/g) \cdot \ell \cdot N_t \cdot \sum_{k=1}^q \left\{ \int_{x_{ipk}}^{x_{fpk}} \beta_S(x) \cdot \beta_R(x-z) \cdot [m_S(x, t) + m_R(x-z, t)] \cdot dx \right\} \quad . \quad (27)$$

$$e_p(t) = \frac{d\Psi_p(z(t), t)}{dt} = \frac{\partial \Psi_p(z, t)}{\partial z} \cdot \frac{dz}{dt} + \frac{\partial \Psi_p(z, t)}{\partial t} = e_{pm}(t) + e_{pt}(t) \quad . \quad (28)$$

Being $\Omega = \Omega(t)$ the rotational speed and $k_m = \mu_0 \cdot \ell \cdot D \cdot N_t / (2 \cdot g)$, by performing the z -derivative under the integral operator, observing that $\partial f(x-z)/\partial z = -\partial f(x-z)/\partial x$, and performing a “per part” integration, e_{pm} becomes [8]:

$$e_{pm}(t, z(t)) = -k_m \cdot \Omega \cdot \sum_{k=1}^q \left\{ \int_{x_{ipk}}^{x_{fpk}} \left\{ \frac{\partial \beta_R(x-z)}{\partial x} \cdot \beta_S(x) \cdot m_S(x, t) - \frac{d\beta_S(x)}{dx} \cdot \beta_R(x-z) \cdot m_R(x-z, t) \right\} dx + \left[\beta_S(x) \cdot \beta_R(x-z) \cdot m_R(x-z, t) \right]_{x_{ipk}}^{x_{fpk}} \right\} \quad (29)$$

As regards the transformer e.m.f. e_{pt} of a group, by time derivating under the space integral operator, it becomes:

$$e_{pt}(t, z(t)) = (\mu_0/g) \cdot \ell \cdot N_t \cdot \sum_{k=1}^q \left\{ \int_{x_{ipk}}^{x_{fpk}} \beta_S(x) \cdot \beta_R(x-z) \cdot \left[\frac{\partial m_S(x, t)}{\partial t} + \frac{\partial m_R(x-z, t)}{\partial t} \right] \cdot dx \right\} \quad . \quad (30)$$

The calculation of the eq.s (29) and (30) appears cumbersome, mainly because of the presence of time dependent quantities under the space integral operators; on the other hand, it is possible to extract these time dependent factors out of the integrals, leaving inside just the space dependent terms:

$$e_{pm}(t, z(t)) = -k_m \cdot \Omega \cdot (N_t/a) \cdot \{ J_1(z(t)) \cdot i_1(t) + J_2(z(t)) \cdot i_2(t) + J_3(z(t)) \cdot i_3(t) \} + k_m \cdot \Omega \cdot \left\{ J_f(z(t)) - \sum_{k=1}^q \left[\beta_S(x) \cdot \beta_R(x-z) \cdot M_{fR}(x-z) \right]_{x_{ipk}}^{x_{fpk}} \right\} \cdot N_f \cdot i_f(t) \quad , \quad (31)$$

$$e_{pt}(t, z(t)) = \sum_{u=1,2,3} L_{pu}(z) \cdot di_u/dt + L_{pf}(z) \cdot di_f/dt, \quad p = 1, 2, 3, \quad \text{with} \quad (32)$$

$$J_p(z) = \sum_{k=1}^q \left\{ \int_{x_{ipk}}^{x_{fpk}} \left[\frac{\partial \beta_R(x-z)}{\partial x} \cdot \beta_S(x) \cdot M_{fS}[x-(p-1) \cdot 2\tau/3] \right] dx \right\}, \quad p = 1, 2, 3, \quad (33)$$

$$J_f(z) = \sum_{k=1}^q \left\{ \int_{x_{ipk}}^{x_{fpk}} \left[\frac{d\beta_S(x)}{dx} \cdot \beta_R(x-z) \cdot M_{fR}(x-z) \right] dx \right\}; \quad (34)$$

$$L_{pu}(z) = (\mu_0/g) \cdot \ell \cdot \left(N_t^2/a \right) \cdot \sum_{k=1}^q \left\{ \int_{x_{ipk}}^{x_{fpk}} \beta_S(x) \cdot \beta_R(x-z) \cdot M_{fS}[x-(u-1) \cdot 2\tau/3] \cdot dx \right\}, \quad p, u = 1, 2, 3, \quad (35)$$

$$L_{pf}(z) = (\mu_0/g) \cdot \ell \cdot N_t \cdot N_f \cdot \sum_{k=1}^q \left\{ \int_{x_{ipk}}^{x_{fpk}} \beta_S(x) \cdot \beta_R(x-z) \cdot M_{fR}(x-z) \cdot dx \right\}, \quad p = 1, 2, 3. \quad (36)$$

Equations (31)-(36) suggest that the functions $J_p(z)$, $J_f(z)$, $L_{pu}(z)$, $L_{pf}(z)$ ($p, u = 1, 2, 3$) can be evaluated off line just once, subsequently taking into account the time dependent functions.

In the particular case of the steady-state, no-load, operation, just the motional e.m.f. e_{pm} exists; considering the q series connected coils of the group under one pole of the phase p , its e.m.f. is given by (see eq.s (31), (34)):

$$e_0(t, z(t)) = k_m \cdot \Omega \cdot \left\{ \begin{array}{l} \sum_{k=1}^q \left\{ \int_{x_{ipk}}^{x_{fpk}} \left[\frac{d\beta_S(x)}{dx} \cdot \beta_R(x-z) \cdot M_{fR}(x-z) \right] dx \right\} + \\ - \sum_{k=1}^q \left[\beta_S(x) \cdot \beta_R(x-z) \cdot M_{fR}(x-z) \right]_{x_{ipk}}^{x_{fpk}} \end{array} \right\} \cdot N_f \cdot I_f. \quad (37)$$

Fig.4 shows the comparison among the no-load phase-to-neutral e.m.f. evaluated analytically (by means of eq. (37), multiplied by the N° of poles $N_p = 2$), and by a transient FEM simulation (machine geometry in Table I).

The following remarks can be made:

- the analytical and FEM results are very close, confirming the correctness of the developed model;
- the waveform disturbances due to the stator and rotor slotting effects are very important: they correspond to the classical, well known e.m.f. tooth harmonics, whose amplitude can be reduced by using skewing only (not considered here, just with the aim to show and estimate the evaluation accuracy of this effect).

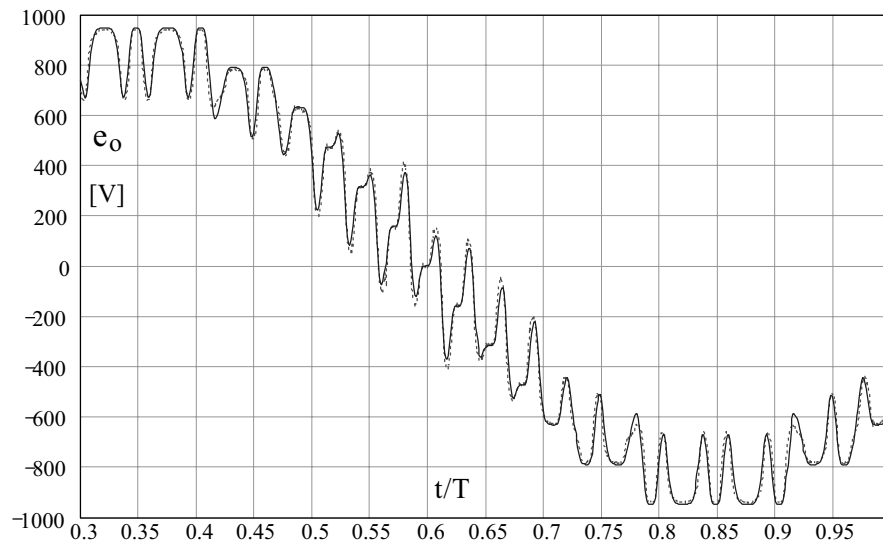


Fig.4 – No-load e.m.f. simulated waveforms for the machine whose data are given in Table I: solid line = analytically evaluated waveform (see eq. (37)); dotted line = FEM transient simulation waveform. Time is expressed in p.u., referred to the waveform period T.

Analytical evaluation of the electromagnetic torque

As known, the torque evaluation is based on the rotor position derivative of the co-energy W_c , performed at constant currents: adopting the hypothesis of zero ferromagnetic voltage drops, the magnetic energy W equals W_c : thus, W will be directly considered in the following, performing its position derivative at constant currents. The stored energy should be expressed as a function of the flux density distribution (see eq.s (22), (23)), but this distribution does not allow to obtain an accurate torque evaluation; in fact:

– it does not model the tangential components of the flux density and its radial variation;
 – it does not consider the flux paths in slots, near the slot openings, that give some torque contribution.
 Thus, in order to improve the energy and torque calculation, equation (23) has been modified, by substituting the functions $\beta_S(x)$ and $\beta_R(x-z)$ with suited “effective” notch field functions $\beta_{eS}(x)$ and $\beta_{eR}(x-z)$:

$$b_e(x, x-z, t) = (\mu_0/g) \cdot \beta_{eS}(x) \cdot \beta_{eR}(x-z) \cdot [m_S(x, t) + m_R(x-z, t)] ; \quad (38)$$

b_e is the equivalent flux density, whose b_e^2/μ_0 volume integral in the machine gives the correct stored energy.

As regards $\beta_{eS}(x)$ and $\beta_{eR}(x-z)$, starting from the lost flux densities $\beta_{LS}(x)$, $\beta_{LR}(x-z)$, they are defined as:

$$\beta_{eS}(x) = (1 - \eta_{\beta S} \cdot \beta_{LS}(x)) ; \quad \beta_{eR}(x-z) = (1 - \eta_{\beta R} \cdot \beta_{LR}(x-z)) , \quad (39)$$

in which $\eta_{\beta S}$ and $\eta_{\beta R}$ are field constants (for their evaluation, based on an energetic approach, see [9]).

On the basis of eq. (38), called ℓ the stack length and ζ the rotor angular position, carrying the $\partial/\partial z$ operator under the integral $\int(\cdot)dx$, and observing that $\partial f(x-z)/\partial z = -\partial f(x-z)/\partial x$, the torque expression becomes [9]:

$$T(z, t) = \frac{D}{2} \cdot \ell \cdot g \cdot \frac{\partial}{\partial z} \left[\int_0^{\pi \cdot D} \left(\frac{b_e^2(x, x-z, t)}{2 \cdot \mu_0} \right) \cdot dx \right] = -\frac{D \cdot \ell \cdot g}{2 \cdot \mu_0} \cdot \int_0^{\pi \cdot D} \left[b_e(x, x-z, t) \cdot \frac{\partial b_e(x, x-z, t)}{\partial x} \right] \cdot dx . \quad (40)$$

Called $\Lambda_g = \mu_0 \cdot \ell \cdot (D/2)/g$, by developing eq. (40), and putting $\partial(\cdot)/\partial x = D_x(\cdot)$, the following terms follow:

– mutual torque, due to the simultaneous existence of stator and rotor m.m.f.s:

$$T_m(z, t) = -\Lambda_g \cdot \int_0^{\pi \cdot D} \left\{ m_S(x, t) \cdot \beta_{eS}^2(x) \cdot \beta_{eR}(x-z) \cdot \left[2 \cdot m_R(x-z, t) \cdot D_x \beta_{eR}(x-z) + \beta_{eR}(x-z) \cdot D_x m_R(x-z, t) \right] \right\} \cdot dx ; \quad (41)$$

– stator slotting reluctance torque, to which the torque reduces in case of zero rotor m.m.f.:

$$T_S(z, t) = -\Lambda_g \cdot \int_0^{\pi \cdot D} \left\{ m_S^2(x, t) \cdot \beta_{eS}^2(x) \cdot \beta_{eR}(x-z) \cdot D_x \beta_{eR}(x-z) \right\} \cdot dx ; \quad (42)$$

– rotor slotting reluctance torque, to which the torque reduces in case of zero stator m.m.f.:

$$T_R(z, t) = -\Lambda_g \cdot \int_0^{\pi \cdot D} \left\{ m_R(x-z, t) \cdot \beta_{eS}^2(x) \cdot \beta_{eR}(x-z) \cdot \left[m_R(x-z, t) \cdot D_x \beta_{eR}(x-z) + \beta_{eR}(x-z) \cdot D_x m_R(x-z, t) \right] \right\} \cdot dx . \quad (43)$$

The integration of eq.s (41)-(43) appears cumbersome; as before, we can separate space and time dependence:

$$T_m(z, t) = -\Lambda_g \cdot (N_t/a) \cdot N_f \cdot i_f(t) \cdot \sum_{p=1,2,3} i_p(t) \cdot Y_{mp}(z) , \quad \text{with} \quad (44)$$

$$Y_{mp}(z) = \int_0^{\pi \cdot D} \left\{ M_{fS} \left[x - (p-1) \cdot 2 \cdot \tau/3 \right] \cdot \beta_{eS}^2(x) \cdot \beta_{eR}(x-z) \cdot \left[2 \cdot M_{fR}(x-z) \cdot D_x \beta_{eR}(x-z) + \beta_{eR}(x-z) \cdot D_x M_{fR}(x-z) \right] \right\} \cdot dx ; \quad (45)$$

$$T_S(z, t) = -\Lambda_g \cdot (N_t/a)^2 \cdot \sum_{p,u=1,2,3} i_p(t) \cdot i_u(t) \cdot Y_{Spu}(z) , \quad \text{with} \quad (46)$$

$$Y_{Spu}(z) = \int_0^{\pi \cdot D} \left\{ M_{fS} \left[x - (p-1) \cdot \frac{2\tau}{3} \right] \cdot M_{fS} \left[x - (u-1) \cdot \frac{2\tau}{3} \right] \cdot \beta_{eS}^2(x) \cdot \beta_{eR}(x-z) \cdot D_x \beta_{eR}(x-z) \right\} \cdot dx ; \quad (47)$$

$$T_R(z, t) = -\Lambda_g \cdot N_f^2 \cdot i_f^2(t) \cdot Y_R(z) , \quad \text{with} \quad (48)$$

$$Y_R(z) = \int_0^{\pi \cdot D} \left\{ M_{fR}(x-z) \cdot \beta_{eS}^2(x) \cdot \beta_{eR}(x-z) \cdot \left[M_{fR}(x-z) \cdot D_x \beta_{eR}(x-z) + \beta_{eR}(x-z) \cdot D_x M_{fR}(x-z) \right] \right\} \cdot dx . \quad (49)$$

As an example, consider the holding torque, at constant stator currents I_1, I_2, I_3 and at constant field current I_f : to this aim, the stator currents are assumed as evaluated in a chosen instant t_0 ($I_1 = i_1(t_0), I_2 = i_2(t_0), I_3 = i_3(t_0)$):

$$T_h(z) = T_m(z, t_0) + T_S(z, t_0) + T_R(z, t_0) = -\Lambda_g \cdot \left[\frac{N_t}{a} N_f I_f \cdot \sum_{p=1,2,3} i_p(t_0) \cdot Y_{mp}(z) + N_f^2 \cdot I_f^2 \cdot Y_R(z) + (N_t/a)^2 \cdot \sum_{p,u=1,2,3} i_p(t_0) \cdot i_u(t_0) \cdot Y_{Spu}(z) \right] . \quad (50)$$

Fig.5 shows the comparison among the holding torque evaluated analytically by means of (50) (solid line), and by a transient FEM simulation (dotted line), as a function of the rotor angular position θ , performed for the same machine geometry described in Table I (field constants: $\eta_{\beta S} = \eta_{\beta R} = 0.66$): a fair similarity can be observed.

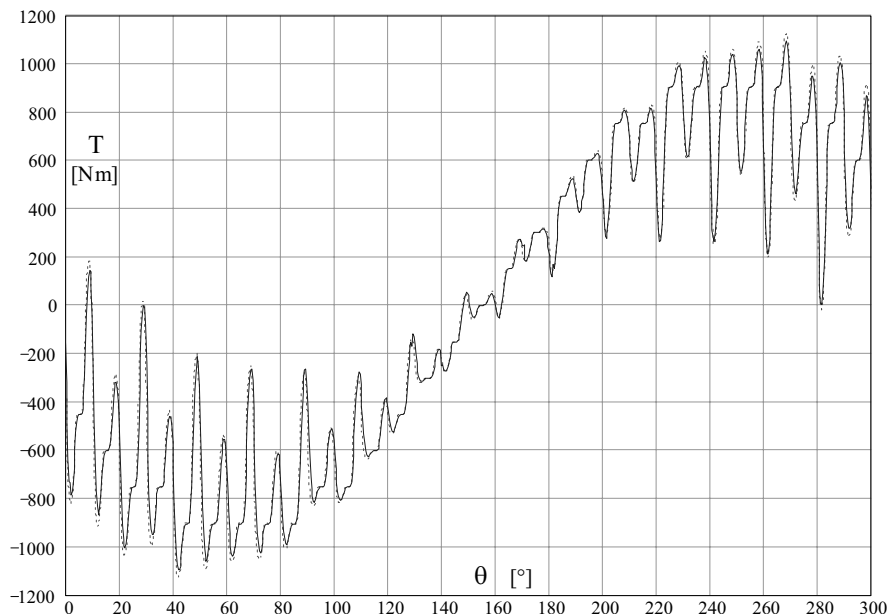


Fig.5 – Holding torque simulated waveforms, as a function of the angular rotor position θ ; machine data of Table I; solid line = analytical evaluated waveform (see eq.(50)); dotted line = FEM transient simulation waveform.

Conclusion

An analytical method for the evaluation of the flux density distribution at the air-gap, taking into account the stator and rotor slotting effects and the actual distribution of the instantaneous currents, has been described. It is well suited to the analytical, accurate, evaluation of e.m.f. and torque waveforms, of great interest in many modelling and design problems concerning slotted electrical machines. The good level of accuracy of the method has been verified considering a test case, concerning an isotropic synchronous machine.

References

- [1] W. J. Gibbs, *Conformal Transformation in Electrical Engineering*, Chapman & Hall, 1958, pp. 96-123.
- [2] D. Ginsberg, A. L. Jokl, L. M. Blum, *Calculation of No-Load Wave Shape of Salient-Pole A-C Generators*, AIEE Trans., 72, p.974, 1953.
- [3] A. Di Gerlando, G. Foglia, "Improved Analytical Evaluation of Air Gap Fluxes and Forces of Ferromagnetic Smoothed and Toothed Structures and Pole Shoes", in ISEF'99 Conference Proceedings, Pavia, Italy, September 1999, and in International Journal COMPEL, n° 19, 2000.
- [4] F. Castelli Dezza, A. Di Gerlando, G. Foglia, "Field-Circuit Integrated Methodologies for Design and Modelling of Permanent Magnet Levitation Devices for Maglev Transportation Systems", *ibidem*.
- [5] G. Foglia, "Theoretical and Experimental Analysis of Excitation and Levitation Devices in EMS Maglev Systems", Ph.D Thesis (in Italian), Politecnico di Milano, Milano, Italy, February 2001.
- [6] Maxwell 2D FEM code, 8.0.27 Version, Ansoft Corporation, Pittsburgh, PA.
- [7] A. Di Gerlando, G. M. Foglia, R. Perini: "Analytical Model of Air-Gap Magnetic Field in Doubly Slotted Electrical Machines with Distributed Windings, ISEF 2003 Conference Proc., Maribor, Slovenia, 18-20 Sept. 2003, pp.67-72.
- [8] A. Di Gerlando, G. M. Foglia, R. Perini: "Analytical Evaluation of E.M.F.s in Doubly Slotted Synchronous Machines with Distributed Windings, *ibidem*, pp.405-410.
- [9] A. Di Gerlando, G. M. Foglia, R. Perini: "Analytical Computation of the Electromagnetic Torque in Doubly Slotted Synchronous Machines with Distributed Windings, *ibidem*, pp.399-404.

II-4. THE 3D-ANALYSIS OF THE FIELD DISTRIBUTION OF FRACTIONAL POWER INDUCTION MOTOR

Krzysztof Komeza, Maria Dems, Paweł Jastrząbek

Institute of Mechatronics and Information Systems, Technical University of Lodz,

ul. Stefanowskiego 18/22, 90-924 Lodz, Poland

e-mail: komeza@p.lodz.pl, mdems@p.lodz.pl, pjastrza@pf.pl

Abstract – In the paper, three-dimensional analyses of the electromagnetic field of a fractional power induction motor are presented. The results of these analyses for different discretizations were compared with 2D analyses to determine the proper discretization. The skewing effect of the rotor slots was taken into account using solid modelling of the motor.

Introduction

Induction motors are usually investigated using 2D method according to the proportions of the outer motor diameter and core length. For the fractional power motors this proportion is not large, hence a more interesting 3D analysis, especially that the skewing effect of the rotor bars can be described properly only using 3D analysis. This problem was analysed using 2D method in [2] but this analysis takes into account only a multi-sliced model with straight slots in each section. The 3D or 2D models of the motor are always the results of approximations of real field distributions with the finite element shape function so neither of them are error free. It is very important from the practical point of view to observe the differences between both solutions for different discretization densities. In the paper the results of 2D and 3D are compared.

Mathematical model.

Despite the growing possibilities of modern computers the solution of the equation systems created by 3D analysis is still very time consuming. Therefore the optimal description of three-dimensional electromagnetic field of induction motor needs the application of methods, which use the smallest number of variables. The use of scalar description is always less expensive than the vector one. The magnetic scalar potential can be used to describe the magnetic field in non-conducting materials.

$$-\operatorname{div}(\mu \operatorname{grad} \Psi) = 0$$

$$\operatorname{grad} \Psi \cdot \operatorname{grad} \mu + \mu \nabla^2 \Psi = 0 \quad . \quad (1)$$

The disadvantage of magnetic scalar is well known. Because of this,

$$\operatorname{rot}(\operatorname{grad} \Psi) = 0 \quad (2)$$

this description can only be used in current-less areas. Furthermore by applying the integral Ampere's law, the integral of the tangential component of the magnetic field strength along any closed contour, in an area described with scalar potential, must be zero.

Application of reduced magnetic scalar potential Φ provides a basis for accounting the presence of the forced currents of known distribution in non-conducting areas. The magnetic field strength can be expressed as the sum of three components

$$\mathbf{H} = \mathbf{H}_s + \mathbf{H}_m + \mathbf{H}_e \quad (3)$$

from the first \mathbf{H}_s is the magnetic field strength obtained as a result of the source's current flow in the air ($\mu=\mu_0$), the second \mathbf{H}_m is a result of the existence of a ferromagnetic material in the surroundings and the last \mathbf{H}_e is a result of the existence of some conducting material in the surroundings.

Using the Biot-Savart law the formula for the first component becomes:

$$\mathbf{H}_s = \frac{1}{\mu_0} \mathbf{B} = \int_V \frac{\mathbf{J} \times \mathbf{1}_r}{4\pi r^2} dv \quad (4)$$

The last two components can be described using the mentioned reduced magnetic scalar potential Φ .

$$\mathbf{H}_m + \mathbf{H}_e = -\text{grad } \Phi \quad (5)$$

Resultant magnetic field strength takes the form:

$$\mathbf{H} = \int_V \frac{\mathbf{J} \times \mathbf{1}_r}{4\pi r^3} dv - \text{grad } \Phi \quad (6)$$

The magnetic vector potential can describe the electromagnetic field in the conducting area. The magnetic vector potential is defined by the expression

$$\mathbf{B} = \text{rot } \mathbf{A} \quad (7)$$

and leads into the equations

$$\begin{aligned} \text{rot} \left(\frac{1}{\mu} \text{rot } \mathbf{A} \right) - \text{grad} \left(\frac{1}{\mu} \text{div} \mathbf{A} \right) &= -\gamma \left(\frac{\partial \mathbf{A}}{\partial t} + \text{grad} V \right) \\ \text{div}(\gamma \text{grad} V) + \text{div} \left(\gamma \frac{\partial \mathbf{A}}{\partial t} \right) &= 0 \end{aligned} \quad (8)$$

with an unambiguous solution for the Coulomb condition

$$\text{div } \mathbf{A} = 0 \quad (9)$$

In quasi-static problems field solutions are obtained in complex form. The real-time fields \mathbf{E} and \mathbf{H} are related to their complex forms

$$\mathbf{E}(x, y, z, t) = \text{Re} \left[\underline{\mathbf{E}}(x, y, z) e^{j\omega t} \right] \quad (10)$$

Hence the complex Maxwell's equations

$$\nabla \times \underline{\mathbf{E}} = -j\omega \mu \underline{\mathbf{H}} \quad (11)$$

With this assumption the equations (8) become

$$\begin{aligned} \text{rot} \left(\frac{1}{\mu} \text{rot } \underline{\mathbf{A}} \right) - \text{grad} \left(\frac{1}{\mu} \text{div} \underline{\mathbf{A}} \right) &= -\gamma (j\omega \underline{\mathbf{A}} + \text{grad} \underline{V}) \\ \text{div}(\gamma \text{grad} \underline{V}) + j\omega \gamma \text{div} \underline{\mathbf{A}} &= 0 \end{aligned} \quad (12)$$

For obtaining the unambiguous solution of the equations (1, 8 and 12) in the whole area, the above equations have to be completed by taking into account the equations of conditions of continuity of solution at borders of areas described by different potentials.

Application of Ψ - Φ - \mathbf{A} - V method is difficult because of the necessity of correctly describing the area where scalar potential is used. It requires a high precision in determination of the topology of the object and the introduction of properly oriented cuts to the areas described by the magnetic scalar potential Ψ . It is possible to model non-linear materials using a quasi non-linear model. The assumption is that \mathbf{B} and \mathbf{H} are both in phase. The magnitude of the field is used to determine the value of the permeability. The Galerkin procedure and the weighted residual method are used to transform the partial differential equation to a discretized set of non-linear algebraic equations. Boundary conditions and interface conditions will also be embedded in these equations.

Analysis

The object of investigation was the three-phase induction squirrel-cage motor of 380 V (star connected) with rated output power 0,37 kW. Table 1 shows the specification of the motor.

Table 1. Specification of analysed motor

Diameter of Rotor and Stator	60,5 mm, 106 mm
Air gap length	0,25 mm
Core Length	56 mm
Number of phase and poles	3 phases, 4 poles
Primary Winding Resistance	21 Ω
Primary Winding Pitch	Single layer, 5/6 short pitch
Number of series turns in stator winding	612
Rotor winding	Aluminium Cage
Number of stator and rotor slots	24, 18
Depth of Secondary Slot	10,56 mm

The presented motor was used to study the influence of the discretization on the results and to compare the results of 2D and 3D analyses. For this study the 2D model shown in Fig. 1 was taken. Because the real winding produces some extra effects connected with coil-ends two simplified models for 3D calculation were taken into account. The first, shown in Fig. 1, consist of two long, straight conductors going out of the modelled space and the second consist of one coil of the winding only.

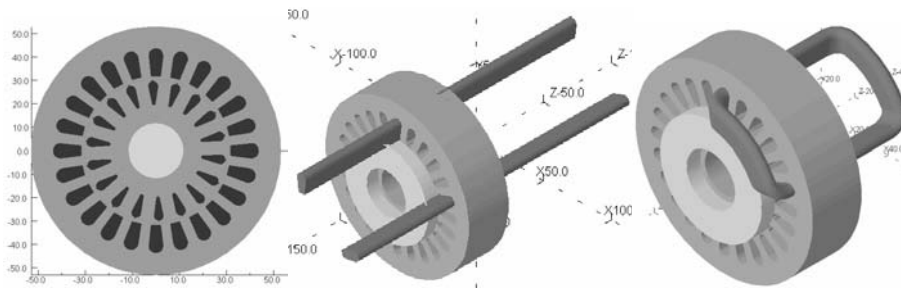


Fig. 1. The 2D model and simplified 3D models of the investigated motor

In Fig. 2 the complete model of the motor is shown. The stator windings overlap each other at the coil-ends because the real shape of the winding's outhangs is very complicated. Nevertheless the amount of currents in the coil-ends region is equal to the real one. To take advantage of motor symmetry only half of the motor was investigated.

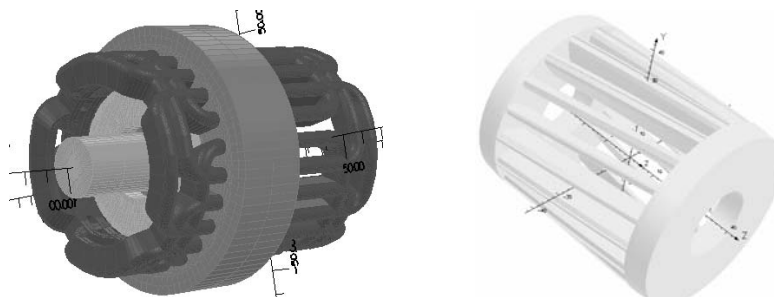


Fig. 2. The complete 3D model of the investigated motor and the 3D model of the motor with skewed slots

The software package OPERA-3D includes the possibility of building models in terms of brick (hexahedral) elements as well as tetrahedral elements. It is a feature of the two types of finite element that, for the same number of nodes, hexahedral can give greater accuracy than tetrahedral. Complex geometric shapes make modelling in terms of hexahedral elements very time consuming and sometimes impossible. The skewed slots in the rotor are a good example. It is possible to create a model with straight slots and then rotate points on each level to create a skew effect but the elements in the air gap between the stator and the rotor will be unacceptably distorted or they overlap the rotor elements. For this reason only the model without skewing was analysed using tetrahedral elements and

compared with the 2D model. The created model makes it possible to analyse different meshing and grade of elements.

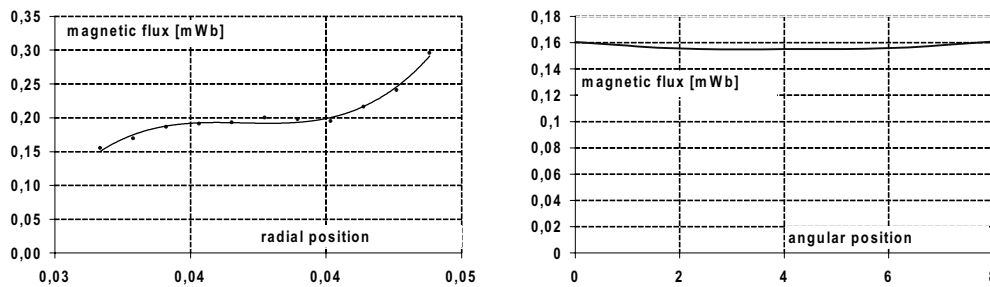


Fig. 3. The change of the flux linkage with the coil versus the radial and angular positions of the patch.

The flux linkage with the coil may be calculated using a suitable patch and the expression for a normal component of the flux density vector is $\Phi = \int_S (B_x N_x + B_y N_y + B_z N_z)$ where N is the vector normal to the surface at any point. When the solution is obtained in complex form the real and imaginary part of flux can be calculated using the proper real or imaginary part of the flux density vector respectively. An additional problem is the choice of the appropriate patch on which the flux will be integrated. In multi-strand coils each separate wire can be placed in any position within the coil. The integration patch has to be as close as possible to the real coil placement. Therefore the influence of the patch position was investigated. In Figure 3 we can observe the change of the flux linkage versus the radial and angular positions of the patch. Despite the small dimension of the motor, the radial change is significant for starting conditions. The process of flux calculation consists of performing separate calculations for different patch radial positions and then producing a weight sum of all of this taking into account the width of the coil.

In the Modeller, the user is able to construct the model using primitive volumes, swept surfaces and Boolean operations. Surfaces of volumes (cells) are initially discretised into triangles. Defining a maximum element size on vertices, edges, facets or cells within a model can control element size.

Using Modeller function is possible to create only sliced models of the skewed rotor. Therefore we try to use another solid modelling package, which also uses the SAT format, to collect data of objects. The Solid Edge package from Electronic Data Systems gives us the possibility to create a real skewed bar, which is then used, by Boolean operations, to create a model of the skewed rotor. In order to avoid the existence of multi-valued scalar potential in the stator and rotor core volumes the air gap was divided into two layers of equal width. The layer that touches the stator surface consists of reduced scalar volumes and the layer touching the rotor surface consists of vector potential volumes. Due to the very small width of the air gap (0,25 mm) it is quite impossible to place extra layers with total scalar potential in the middle of the air gap.

Results of computation

In order to compare 2D and 3D computation results the starting conditions were taken into account with the starting current equal to 3,7 rated currents. The current distribution in the stator windings was assumed. For this current excitation the current induced in rotor bars and magnetic flux linkage with stator coil was investigated.

Table 1 and 2 shows the comparison of the results for different, in terms of discretization, models built with hexahedral elements. The basis for this calculation was the simplified model with one stator coil only. In Table 1 the values of maximal current induced in the nearest rotor bar and in Table 2 the values of magnetic flux linkage with the stator coil are presented. For comparison results for 2D calculations were also presented. Analysis of the models with and without end parts shows very little influence of the coils outhangs on the induced current in the rotor bars. Summarizing the results from Tables 1 and 2, the integral values like bar's current or flux linkage with coil are not very sensitive to discretization density and the basic division produces adequate results.

Table 1. The comparison of rotor bar induced currents for different discretization and element type for:

a) 3D calculations

Number of equations	Element type	Induced current [A]
164 000	linear	713,1
203000	linear	712,7
441000	quadratic	698,8
546000	linear	712,0

b) 2D calculations

Number of equations	Element type	Induced current [A]
4763	linear	817,2
64000	linear	811,0
256000	linear	808,4
570000	linear	808,2

Table 2. The comparison of the magnetic flux linkage with the stator coil for different discretization and element type for 3D calculation

a) 3D calculations

Number of equations	Element type	Magnetic flux [mWb]	Number of equations	Element type	Magnetic flux [mWb]
164 000	linear	0,612	4763	linear	0,624
203000	linear	0,611	64000	linear	0,674
441000	quadratic	0,619	256000	linear	0,674
546000	linear	0,615	570000	linear	0,675

b) 2D calculations

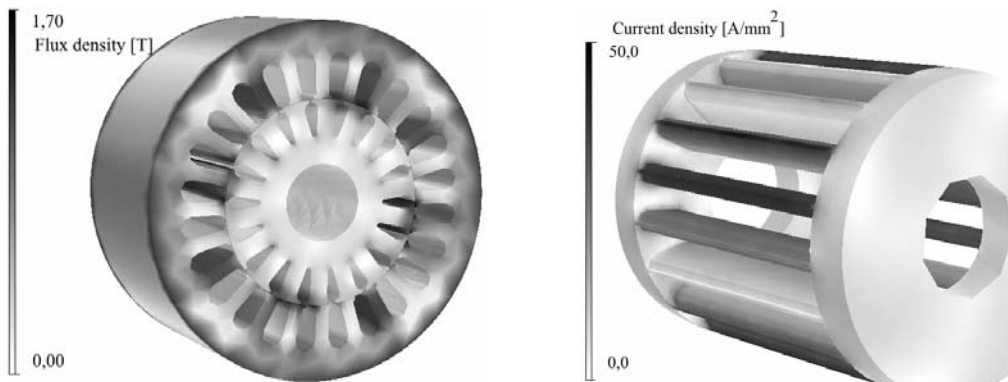


Fig. 4. The flux density and current density on the surface of the model with straight rotor bars

In Figures 4 and 5 the distributions of flux density and current density for models with straight and skewed rotor bars are shown. As can be seen from Fig. 5 the skewing of the rotor bars reduces the value of the rotor bars' currents. The starting torque is also about 4% lower than for straight bars. Additionally, in a skewed cage induction motor the interbar currents, related to imperfect insulation of the rotor bar from the iron, can be an important component of the stray load losses. This effect was analysed in [2] using 2D multislice models. The authors' own 3D model can be used for modelling the interbar current problem with the use of anisotropic conductivity with zero component along the motor length. In Fig. 6 the effect of interbar current on the rotor surface can be observed. The power losses due to interbar currents are nearly 3% of rotor power. To ensure that these currents really flow between the rotor bars the calculation without rotor bars was also performed showing no presence of the currents in this case.

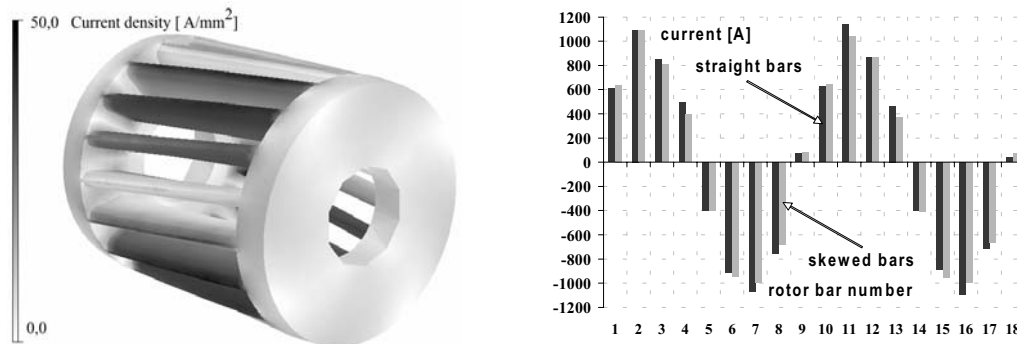


Fig. 5. The current density on the surface of the model with skewed rotor bars and the comparison of bars current for straight and skewed rotor bars.

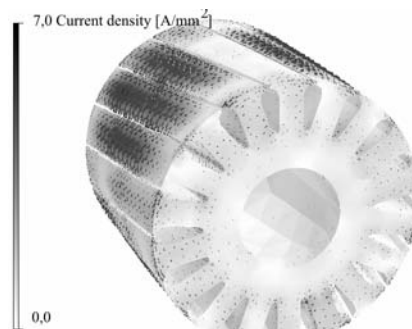


Fig. 6. The interbar current density on the surface of the rotor core

Conclusion

The obtained results of using 3D modelling of fractional power induction motors shows the possibility of efficient investigation of analysed objects especially at starting and no-load conditions. The solid modelling technique allows modelling of the rotor with skewed slots. This creates the possibility to investigate currents flowing between rotor bars through rotor sheets. Many authors suggest the great influence of these currents on the additional losses especially for die-cast aluminium rotor cages. The comparison of results for different discretization creates a basis for estimation of errors and possible accuracy limits, which can be obtained using numerical methods.

Acknowledgements

Polish National Committee for Scientific Research KBN Project 8 T10A 033 20 sponsors the work.

References

- [1] Carlson R., da Silva C.A., Sadowski N., Lefevre Y., Lajoie-Mazenc M.: Effect of the stator-slot opening on the interbar currents of skewed cage induction motor, *IEEE Trans. Magn.*, vol. 38, pp. 1285-1288, 2002
- [2] Dems M., Leśniewska E., Komeza K., Wiak S.: Finite-element method accuracy in three-dimensional field analysis of induction motors, *Electromotion*, vol.5, no.3, 1998, pp.103-106.
- [3] Komeza K., Dems M., Podzorski P.: The 3D-analysis of the field distribution and leakage reactances of induction motor with increased slip, *Proc. XVII Symposium EPNC'2002, Liege. Belgium, 2002*, pp. 95-99
- [4] Wiak S., Komeza K.: Field/Torque modelling of Electromagnetic Devices by Use of Opera-3D Code. *International Workshop on Electric Machines, Prague, 8-9 September 1999*, pp. 12-24
- [5] Yamazaki K.: An efficient procedure to calculate equivalent circuit parameter of induction motor using 3-D nonlinear time-stepping finite-element method, *IEEE Trans. Magn.*, vol. 38, pp. 1281-1284, 2002
- [6] PC OPERA-2D and OPERA-3D– version 8.7, Software for electromagnetic design from VECTOR FIELDS

II-5. IMPROVEMENT OF THE ELECTRIC STRENGTH OF AN INSULATION SYSTEM OF A MEDIUM VOLTAGE INSTRUMENT TRANSFORMER USING FIELD ANALYSIS

Elżbieta Leśniewska

Department of Applied Electrical Engineering & Instrument Transformers, Technical University of Łódź
90-924 Łódź, ul. Stefanowskiego 18/22, Poland, e-mail:elalesni@ck-sg.p.lodz.pl

Abstract – In this paper, the methods of improvement of an insulation system of a voltage transformer are considered. Computations, carried out based on the finite element numerical method, make it possible to find the locations of high electric field strength values. The electric field distributions for several different versions of insulation systems are compared. The design process was continued until the permissible electric field strength was not exceeded in any part of the insulation system and the homogeneity of the electric field was maintained. Conclusions concerning constructional modifications are also given.

Introduction

The subject of analysis is a voltage transformer with two insulated voltage terminals and a transformation ratio of 15kV/100V. The aim of redesigning the voltage transformer was the achievement of a greater rated power at the same accuracy class and greater electric strength in the same dimensions. This modernisation considered the shape of its core and windings. The main assumption was the same external dimensions of both versions. Greater rated power requires an increase in the cross sectional area of the core, causing a decrease in the thickness of the insulation layer and in consequence lowers the electric strength of the whole insulation system of the voltage transformer.

In order to determine the value of the electric field strength the computations for some variants of the insulation system were performed. Computations were carried out based on the finite element numerical method. The commercial software OPERA was used to compute field distributions in insulation systems.

The two versions of a voltage transformer 15kV/100V before and after redesign (the last version) are shown scaled in Fig.1.

The Mathematical Model

The electric field in an insulation system (after introducing the scalar electric potential $\mathbf{E} = -\nabla V$ where \mathbf{E} is the electric field strength) is described by the Laplace's equation

$$\nabla^2 V = 0 \quad (1)$$

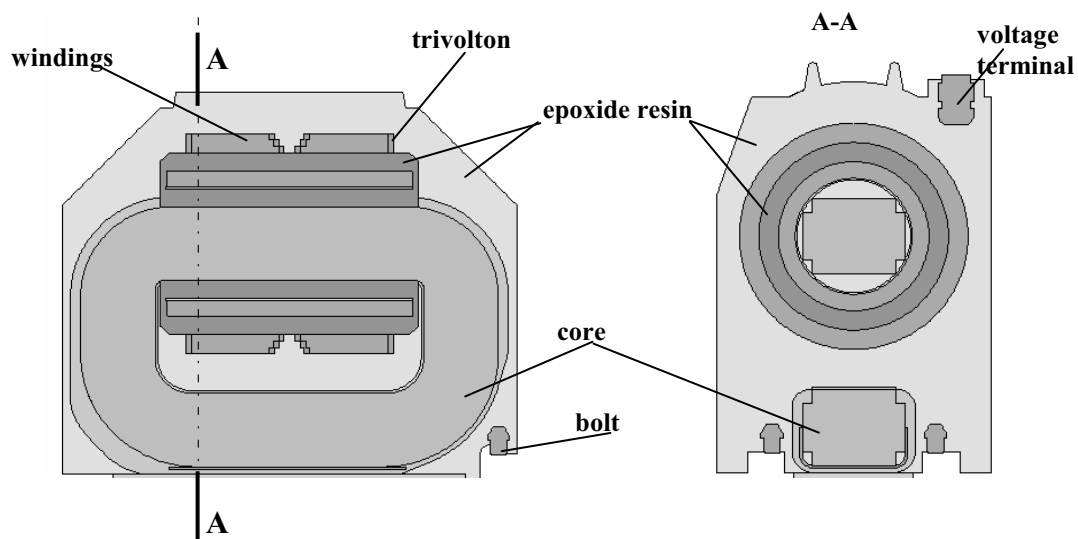
with Neuman's and Dirichlet's boundary conditions. Applying the numerical finite element method can solve this equation. The electric field analysis allows the estimation of the field distribution in the system and makes it possible to determine the maximum electric field strength in insulation.

The insulation system contains some materials of different permittivity (epoxide resin $\epsilon'=4$, trivoltlon $\epsilon'=4,2$, pressboard $\epsilon'=3$ and the other elements. $\epsilon'=1$). The computation was performed in a 2D system for two perpendicular cross-sections of the voltage transformer. Accuracy of the field distribution requires the model of the physical device to be a precise reproduction of the device. Two conditions were taken into consideration: the voltage test and the operating state of the voltage transformer.

The electric field strength obtains maximum value in time when test voltage obtains amplitude $38\sqrt{2}$ kV. The boundary conditions for the test are: values of potential (Dirichlet's) of the grounded bottom, bolts, secondary windings and core all at 0kV, of the voltage terminals and the outermost layers of the both parts of the primary coil at test voltage $38\sqrt{2}$ kV, the innermost layers of the primary coil wound on the electrostatic shield at $19\sqrt{2}$ kV, and the condition of the tangential electric field strength (Neuman's) at the boundary of the whole system with the surrounding air.

During rated operation the worst condition is when the voltage at one terminal will be $15\sqrt{2}$ kV and at the second terminal $-7.5\sqrt{2}$ kV. The boundary conditions for this state are: values of potential (Dirichlet's) of the grounded bottom, bolts, secondary windings and core all at 0kV, of the voltage terminal and the outermost layer of one part of the primary coil at $15\sqrt{2}$ kV, the terminal and the outermost layer of the second part at $-7.5\sqrt{2}$ kV, the innermost layers of the primary coil wound on the electrostatic shield at 0kV, and the condition of the tangential electric field strength (Neuman's) at the boundary of the whole system with the surrounding air.

a)



b)

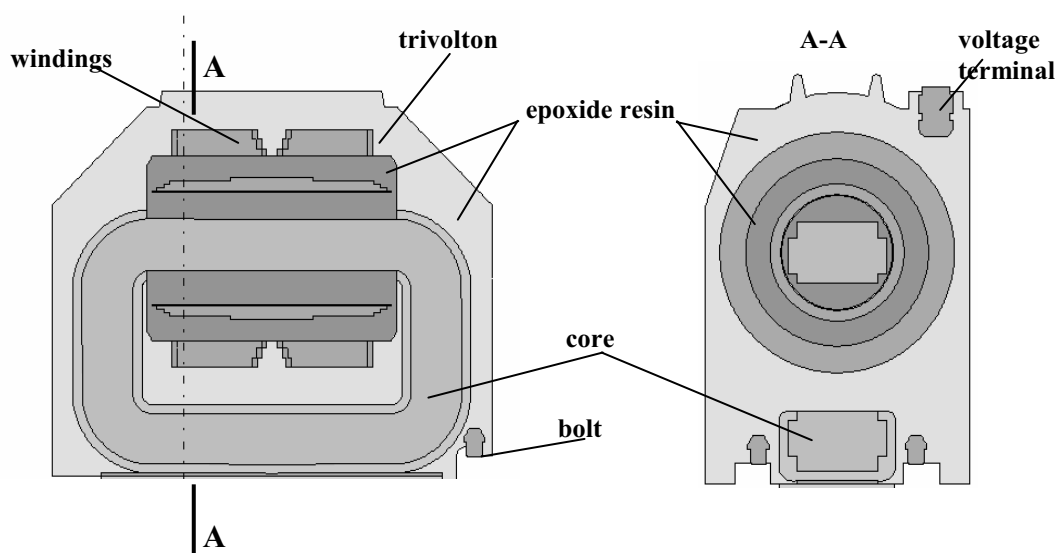


Fig. 1. Two constructional variants of the same external dimensions of the voltage transformer 15kV/100V
 a) before redesign
 b) after redesign

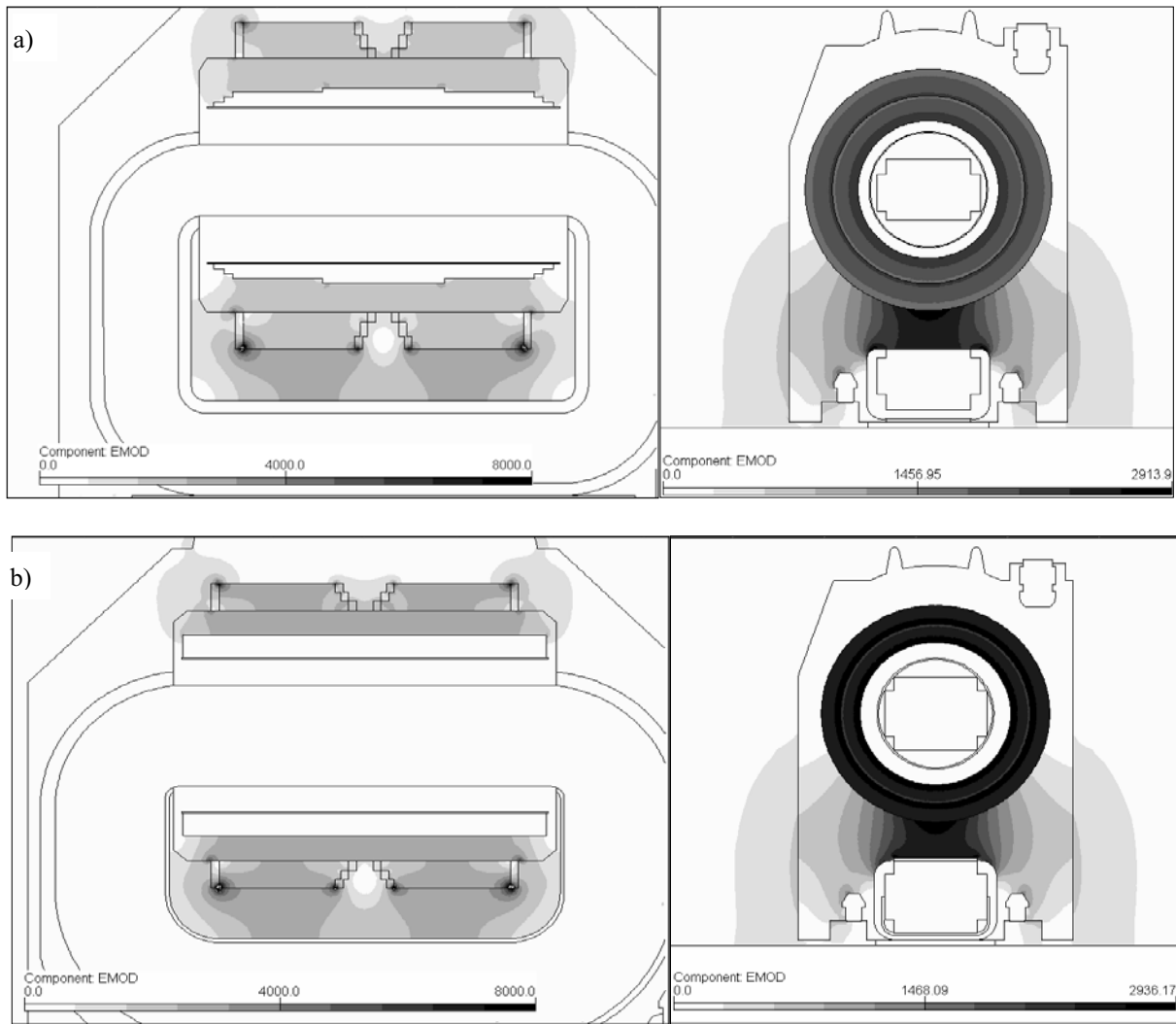


Fig.4. Distribution of the electric field strength [V/mm] in the area of the voltage transformer under the test condition (38kV-1 minute)

a) before redesign (version 1)

b) after redesign (version 2)

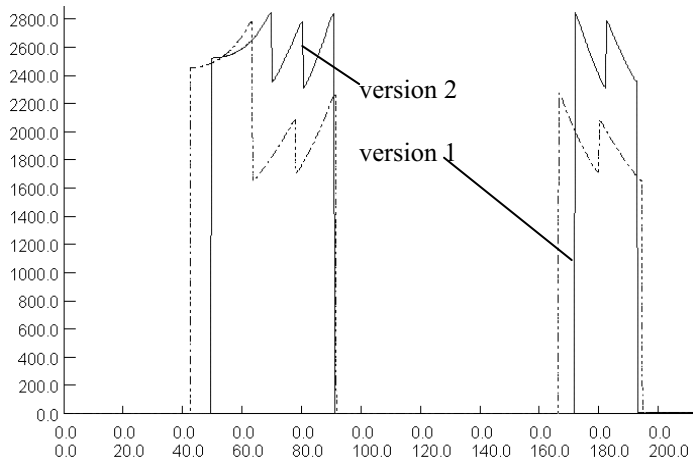


Fig.5. The comparison of the distributions of the electric field strength [V/mm] along the symmetry axis in the insulation system of two constructional variants of the voltage transformer at the test voltage 38kV (1 minute)

The computation done for the final version of the voltage transformer at the operating state shows the level of electric field strength to be 3kV/mm and the peak values in trivolton, near the edges of the primary coil, to be 6.4kV/mm. The potential distribution and electric field strength distribution during operation are presented in Fig.6 and 7.

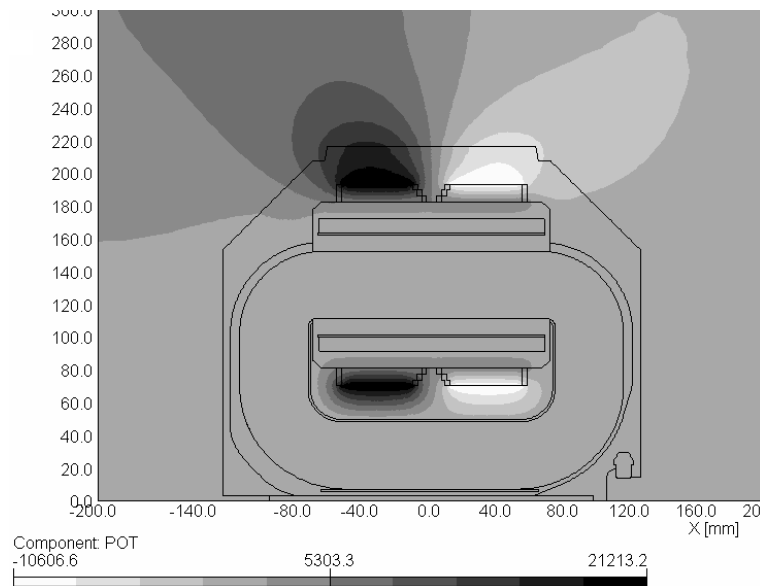


Fig. 6. Distribution of electric potential [V] at the surface passing through the centre of the voltage transformer after redesign under operating conditions

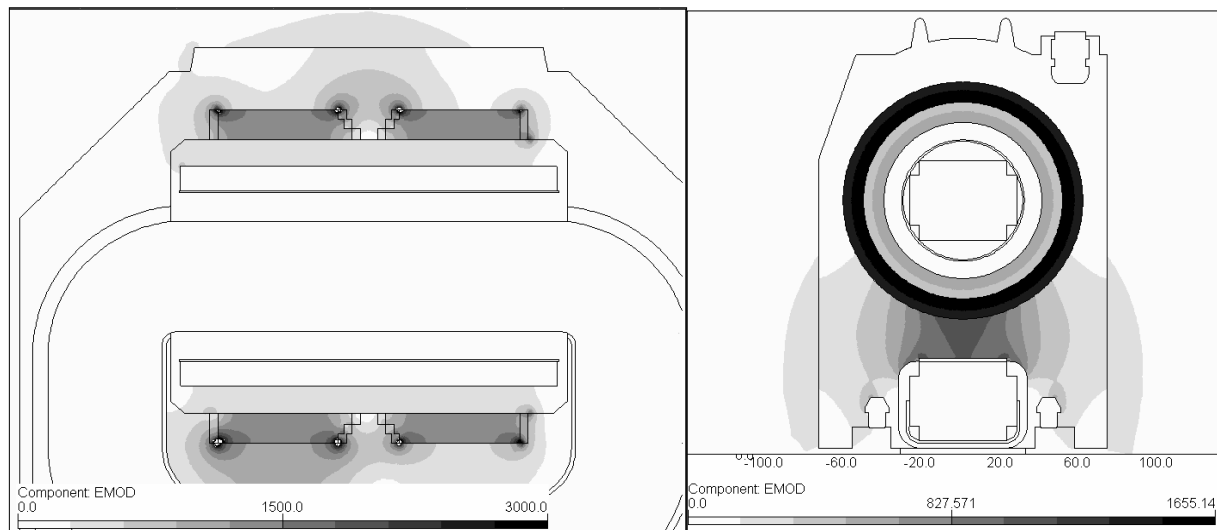


Fig.7. Distribution of the electric field strength [V/mm] in the area of the voltage transformer after redesign under operating conditions

The electric strength of epoxide resin as well as trivolton is higher than the level of the values of the electric field strength in the insulation of the voltage transformer and there are no dangers of breakdowns of insulation or partial discharges neither at voltage test nor at rated operating state.

Compatibility of the computed field distributions with distributions in real-life models depends on very accurate mapping of the real-life model. The dividing meshes, which were used in the computation, had respectively 50985 and 41371 nodes for two perpendicular cross-sections. The division was the result of the accuracy analysis and further mesh refinement does not change this solution.

Conclusions

Computations of the electric field distributions for several different versions of insulation systems are compared. The electric strength of an insulation system during the design process was achieved using an iterative approach. The design process was continued until the permissible electric field strength had not been exceeded in any part of the insulation system and the homogeneity of the electric field was maintained. The results of computations and tests were compared.

Every construction improvement is carried out in order to obtain better devices. For the voltage transformer it means achieving a greater rated power at the same accuracy class and greater electric strength at the assumption of the same external dimensions. The author has presented the results of the use of numerical methods in the design process. The numerical analysis of the electric field distribution shows that the final constructional version of the voltage transformer is better than the starting version. The test results are a confirmation of the results of the numerical analysis.

References

- [1] E. Leśniewska, The Use of 3D Electric Field Analysis and the Analytical Approach for Improvement of a Combined Instrument Transformer Insulation System, IEEE Transaction on Magnetics, vol.38, no 2, March 2002, pp. 1233-1236
- [2] E. Leśniewska, Application of 3D Field Analysis for Modelling the Electric Field Distribution in Ceramic Insulator of HV Combined Instrument Transformer, ELSEVIER, Journal of Electrostatics, vol. 51-52, 2001, pp. 610-617
- [3] E. Leśniewska, Application of Electromagnetic Field Simulations in the Design Process of Instrument Transformer, Zeszyty Naukowe PŁ, nr 766, Rozprawy Naukowe z.236, 1997 (in Polish)
- [4] A. Koszmider, J. Olak, Z. Piotrowski, Current Transformers, WNT, Warsaw, 1985 (in Polish).
- [5] Leśniewska E., Komezka K.: Problems with the Creation of 3D Models of Real-Life Electrical Systems for Fields Computation, ACTA MOSIS No. 82, Ostrava, Czech Republic 2000, pp. 185-194
- [6] E. Leśniewska, Z. Kowalski, Designing Voltage Transformer Insulation System with SF6 - Insulations Using CAD, Archiv für Elektrotechnik, 74 (1991), pp. 427-432.

II-6. A METHOD FOR REDUCTION OF COGGING TORQUE IN PM MACHINES USING STEPPED MAGNETS

M. Łukaniszyn, R. Wróbel, M. Jagiela

Department of Electrical Engineering and Automatic Control,
Technical University of Opole, Poland
PL 45-245 Opole, ul. Luboszycka 7
E-mail: {luk, mjagiela, rwrobel, lata}@po.opole.pl

Abstract: The paper presents a general approach to minimization of the cogging torque in electrical machines using surface-mounted magnets with discrete skew angle. Two types of pole shapes, namely monotonic skewing as well as herringbone-shaped magnets are proposed for the purpose of reducing the cogging torque. The elaborated algorithm is validated against the 3D finite element model as well as experimental data obtained from physical model of the motor. The presented cost-effective method leads to a great reduction of cogging torque with only slight decrease of overall electromagnetic torque.

Introduction

Some applications like servodrives or hdd micromotors do not tolerate cogging torque of any level [1-3]. Among various approaches, skewing is known to be the most effective method for reducing of cogging torque in PM machines [2-4]. There are two alternative solutions, in which skewing of either the stator sheet pack (laminated core) or the rotor permanent magnets can be applied. The latter method is a cost-effective solution recommended for the machines with short stack length [3]. This paper demonstrates how the cogging torque can be reduced when replacing continuous skewing of permanent magnets with discrete one along the machine length (see Fig. 1). Such a construction of magnetic circuit leads to a great reduction of the cogging torque and its optimisation procedure is less complicated than that for the magnets with continuous skew angle.

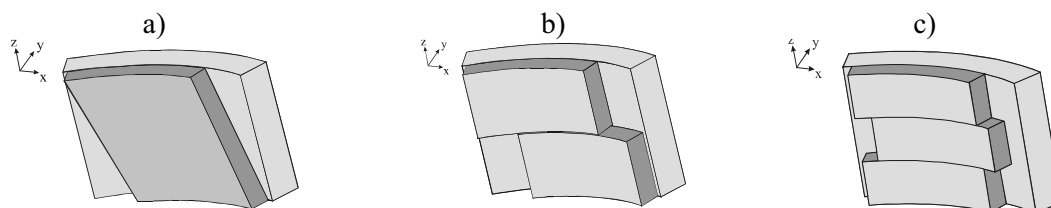


Fig. 1. Three alternative solutions for skewing of the magnets: a) continuous, b) simple monotonic two-segment stepped skewing, c) simple three-segment stepped herring-bone-shaped magnet

Field model

The skewed magnets need to be analysed using 3D field models. In this paper the simplified approach, only partially supported by the three-dimensional finite element model is presented. To describe the optimisation procedure using the proposed model, introduce the symbols shown in Fig. 2.

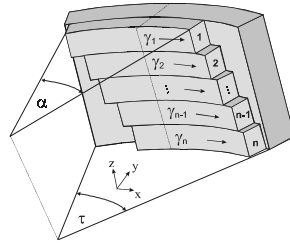


Fig. 2. Symbols

The design variables are as follows:

- number of PM segments (slices) per single pole k ,
- slice width α ,
- pole shape expressed by the vector of consecutive dislocations of PM pole-slices $\Gamma=(\gamma_1, \gamma_2, \dots, \gamma_{k-1}, \gamma_k)$.

The optimisation procedure for the stepped magnets contains the following stages:

1. The permanent magnet is divided into k symmetric slices. Because the torque is not constant along the machine length, each n -th among all k slices contributes to the production of cogging torque in accordance to the following formula:

$$T_n(\Theta) = \frac{f_n}{f} \cdot T(\Theta) \quad , \quad (1)$$

where:

f_n – area under n -th segment of the torque curve (see Fig. 3),

f – total area under the torque curve (see Fig. 3),

$T(\Theta)$ – angular variation of the cogging torque (see Fig. 4).

The above functions are determined from the 3D finite element model, using Maxwell stress tensor. To obtain the variation of torque along machine length, the Maxwell stresses are integrated over each pole slice (see Fig. 3).

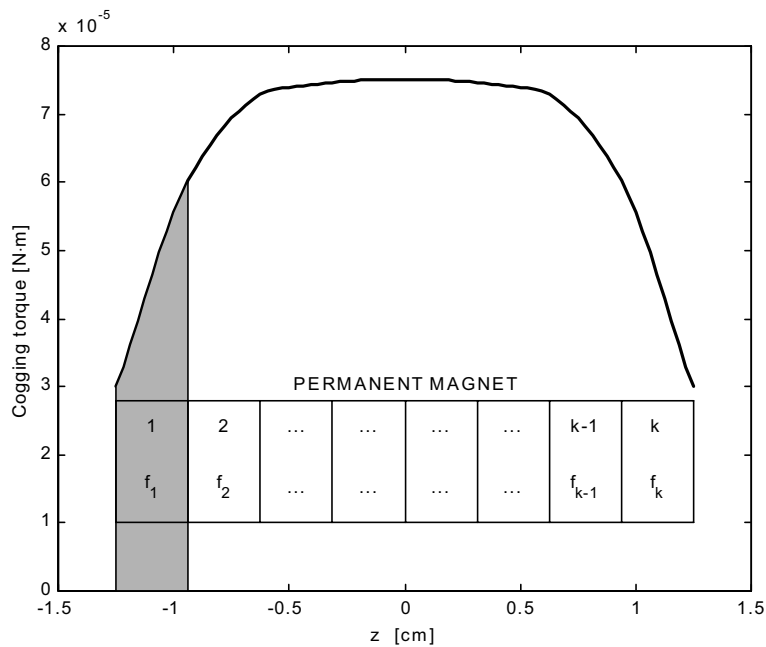


Fig. 3. Variation of cogging torque along machine length for a specific rotor position

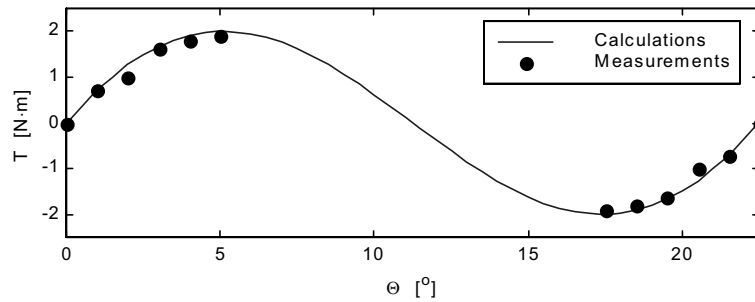


Fig. 4. Angular variation of cogging torque determined from the 3D field model

2. The specific optimisation procedure is started when each of k segments is shifted over the rotor surface until the optimum configuration is arranged. The total torque is composed overall torques produced by each pole segment. The optimum configuration is achieved when the standard deviation of the cogging torque from zero does not exceed the assumed error level.

Calculation results

To demonstrate the effectiveness of the method presented above, the new outer-rotor brushless DC motor for an electric fan is considered (see Fig. 5). The machine specifications are as follows: two-phase, 150 Watt, 1500 rpm. The outer diameter is 112 mm and total length is 25 mm. Large armature saliency and high-energy permanent magnets contribute to generation of considerable cogging torque, which produces vibrations transmitted to the whole construction of the drive. So, the reduction of the cogging torque is of great importance in this type of motor.

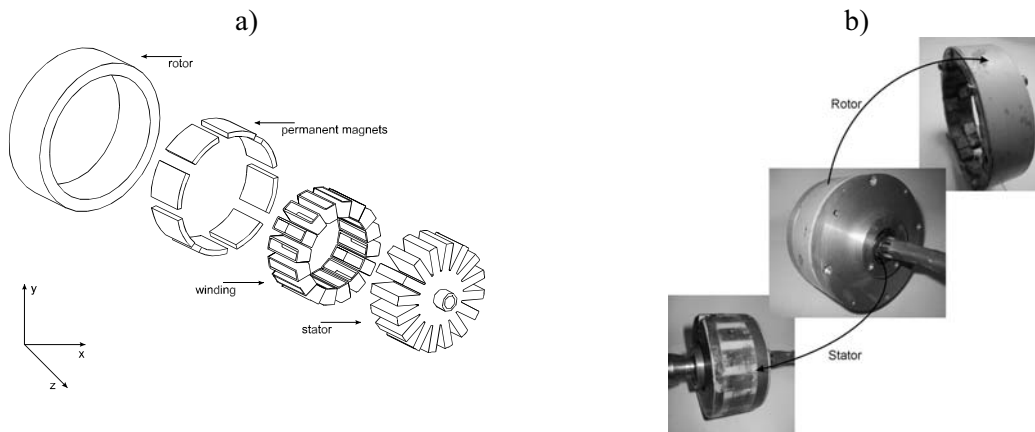


Fig. 5. Cross section of two-phase brushless dc motor a) and its physical model b)

The design procedure was performed for the radially-magnetized stepped poles. In general, a number of slices can vary from 3 to 8 what assumed to be a reasonable maximum of slices for the motor under considerations. With higher number of slices and various possible angular dislocations of slices, the size of the optimisation problem makes it prohibitive to attack the problem by any other but just the simplified method.

The optimisation calculations are carried out for width of the PM pole $\alpha/\tau = 33/45$ and different numbers of possibly dislocated PM slices. In Fig. 6, values of the objective function versus a number of the PM slices are shown. For monotonically skewed magnets, the minimum of the objective function is obtained for the four-slice PM ($n=4$). And in case of herringbone-shaped ones the highest reduction of the cogging torque is obtained for the seven-slice PM ($n=7$), what is shown in Fig. 7. Figure 8 compares angular variations of the cogging torque for optimised PM shapes. The 3D FEM

solution was assumed as a reference. Taking into account the practical application of the motor, the electromagnetic torque must be analysed together with the torque pulsation. In electrical machines excited by the surface-mounted PMs and supplied without switch-overs, the electromagnetic torque includes two components: cogging torque and mutual torque [1]. Such a statement is correct for the rare earth permanent magnets which are characterized by relative magnetic permeability approximately equal to one. In this case, the reluctance torque can be omitted [5].

In Table 1 computational results for the torques are summarized. The electromagnetic torque calculations were carried out for a single-phase supply without switch-overs ($I = 20A$). The torque pulsation factor for the electromagnetic torque (without switch-overs) is defined as $\lambda = (T_{e\ max} - T_{e\ min}) / 2 \cdot T_{e\ av}$ where $T_{e\ max}$, $T_{e\ min}$ and $T_{e\ av}$ are, respectively, the maximum, minimum and average values of the electromagnetic torque determined for a half of the period.

It is interesting to note that the motor versions II and III are more useful as they ensure the average torque comparable to the motor version I (single-slice PM). We can also observe that, for the motor versions II and III, the torque pulsation factor is about 2.5 –times lower, which is a significant advantage. Figure 9 shows the angular variations of the electromagnetic torque.

Additionally in Figures 10 and 11 angular variations of the axial force and back EMF, obtained for optimised permanent magnets shapes, are presented. It is worth noticing that for herringbone-shaped poles the axial unbalance does not occur. We can also observe that for the optimised magnets the back EMF waveform is less distorted from the trapezoidal shape (see Fig. 11).

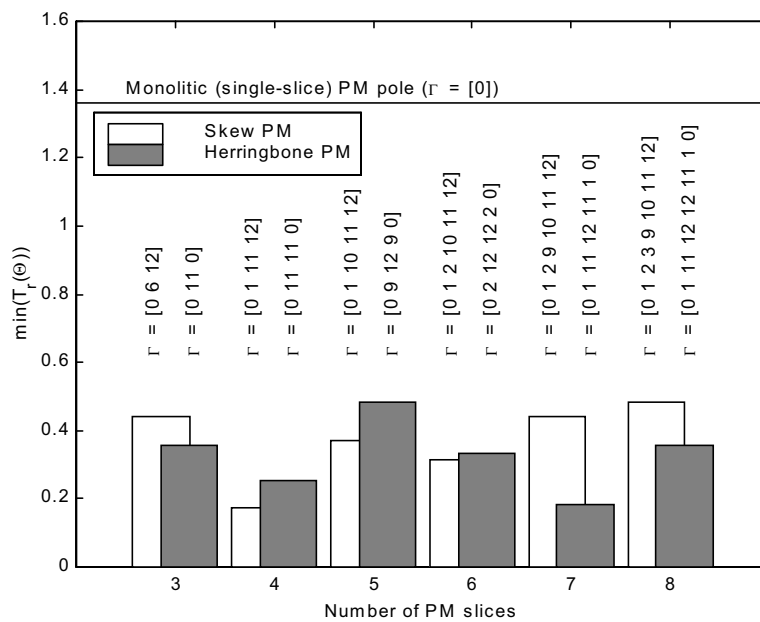


Fig. 6. Variation of the maximum cogging torque vs. number of PM slices

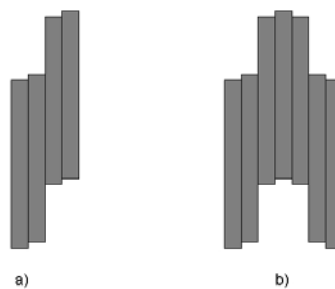


Fig. 7. Optimised magnets configurations, a) monotonically skewed, b) herringbone-shaped

Table 1. Quantities of the motor for optimised PM shapes (one-phase supply without switch-overs, $I = 20$ A)

Motor version	$T_{r\ max}$ [N·m]	$T_{e\ max}$ [N·m]	T_{av} [N·m]	$F_{z\ av}$ [N]	λ
I Monolithic PM			0.54	0	5.16
II Skew PM			0.50		2.10
III Herringbone PM			0.52	0	2.12

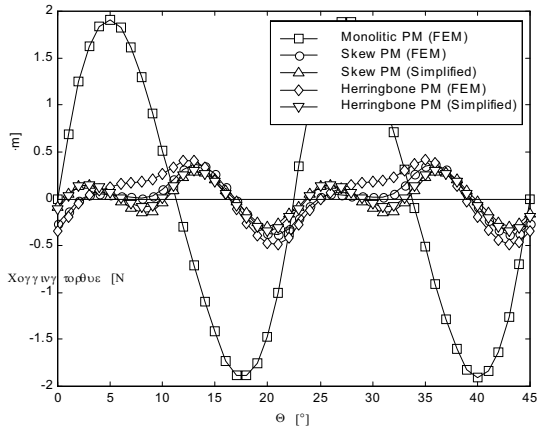


Fig. 8. Angular variation of cogging torque for optimised PM shapes

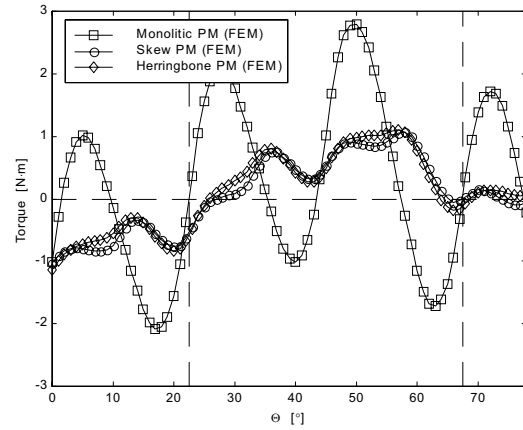


Fig. 9. Angular variation of the torque developed by the motor for single-phase supply without switch-overs ($I = 20$ A)

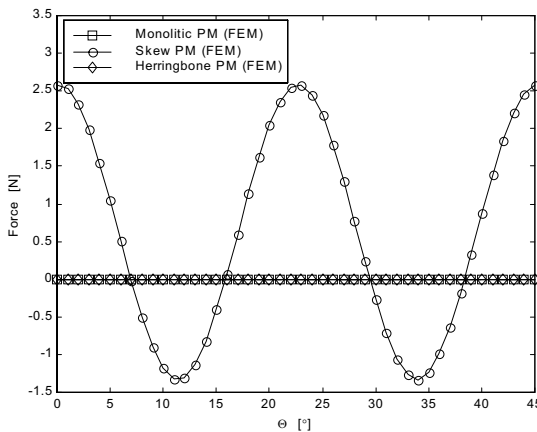


Fig. 10. Angular variation of axial force

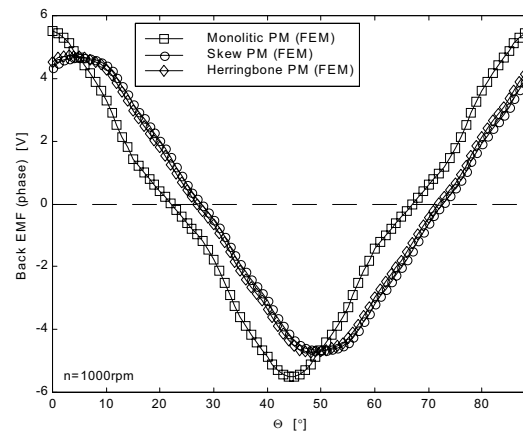


Fig. 11. Angular variation of back EMF

Conclusions

The presented method for reduction of the cogging torque in permanent magnet motors can be applied in almost all types of electrical machines with the surface-mounted magnets. The reduction of cogging torque is substantial, and the torque drop can be considered negligible.

The monotonic skewing cause the rotor unbalance which does not occur for the second type of the magnets considered.

The magnetization distribution for optimized magnets shapes can be obtained either the arrangement of PM pole-slices or specific shape of magnetizing devices.

Acknowledgements

The authors are grateful to the Foundation for Polish Science, Warsaw, Poland for support of their research.

References

- [1] T.M. Jahns, W.L. Soong: Pulsating torque minimization techniques for permanent magnet AC motor drives - a re-view, *IEEE Trans. on Industrial Electronics*, Vol.43, No.2, 1996, pp. 321-330.
- [2] G.H. Jang, J.W. Yoon, K.C. Ro, N.Y. Park, S.M. Jang: Performance of a brushless DC motor due to the axial geometry of the permanent magnet, *IEEE Trans. on Magnetics*, Vol.33, No.5, 1997, pp. 4101-4103.
- [3] M. Łukaniszyn, M. Jagieła, R. Wróbel: A disc-type motor with co-axial flux in the stator; - influence of magnetic circuit parameters on the torque, *Archives of Electrical Engineering*, Vol. 84, No. 2, 2002, pp. 91-100.
- [4] M. Łukaniszyn, R. Wróbel, M. Jagieła.: Reduction of the Torque Ripple in a Brushless DC Torus Motor, *International Conference on Electrical Machines*, In proc. of ICEM'2002, Brugge, 2002
- [5] Y.D. Yao et al.: Simulation study of the reduction of cogging torque in permanent magnet mo-tors, *IEEE Trans. on Magnetics*, Vol.33, No.5, 1997, pp. 4095-4097.

II-7. ELECTRIC FIELD ANALYSIS OF THE INSULATION STRUCTURE OF POWER TRANSFORMER

Danilo Makuc¹, Juso Ikanović², Konrad Lenasi¹

¹University of Ljubljana, Faculty of Electrical Engineering, Tržaška 25, 1000 Ljubljana, Slovenia

²ETRA 33 d.d. Power Transformers, Šlandrova 10, 1000 Ljubljana, Slovenia

E-mail: danilo.makuc@fe.uni-lj.si

Abstract – Electric field and dielectric conditions were analysed in an oil immersed power transformer. The particularity of the transformer's design we are dealing with is an attempt to eliminate the stress-control ring above the low voltage (LV) winding. Using the finite element method (FEM) we analysed the steady state electric field that suited conditions during dielectric test with a separate AC source. In the paper is also discussed the evaluation and analyses of other possibilities to form an adequate electric field with simple constructional elements at the ends of the windings. Therefore we evaluated the influence that the radius of conductors, thickness of paper insulation, and additional insulation elements have on electric field strength in the critical places.

Introduction

Transformer's insulation system must be designed to withstand not only the operating voltages with some allowance of small overvoltages, but also high overvoltages produced by lightning or switching operations. To prove the correct design of the insulation structure every transformer has to be tested before installation and operation. During the standard test with a separate AC source the insulation structure of the transformer must remain intact, which can be assured with a correct insulation coordination. Design of the insulation structure is mainly based on a known potential distribution in the transformer. Various methods for the calculation of electric field can be used for that purpose, but it seems that only FEM is suitable for complex geometries. In our case we used a 2D magnetostatic solver and we analysed the dielectrical conditions in a high voltage (HV) oil immersed power transformer during the test with the AC voltage (140 kV). The old design includes stress-control rings above both windings in contrast to the new one, which has only HV ring. It is difficult to define an exact value of the electric field strength (E) which should not be exceeded in a particular insulation material. Despite that we fixed the maximal E in the oil to 10 kV/mm. It has to be stressed that the voltage and the electric field strength mentioned in the paper are given in RMS values.

Finite element model

Modelling of the complete transformer structure to analyse the electric field in just a specific region of the transformer is a complex and a time-consuming procedure. In fact such a procedure is really not needed since we can get satisfactory results also with the analyses of so called sub-models of the transformer. In our case the research region was limited to the upper part of the LV and HV windings. Consequently using appropriate boundary and excitation conditions our model included only the outlined region shown in Fig. 1. To calculate the electric field in the mentioned region a 2D magnetostatic solver was used. Since analyzing of the fields in transformer structure is a true 3D problem, some simplifications and modifications of the model were necessary. To come as much as possible near to actual conditions an axi-symmetric model was used to represent the problem in two dimensions. Unfortunately such a model is adequate only for a circular limb and the windings but not for a transformer's yoke and other constructional part. We had to consider this fact in choosing appropriate boundary conditions, especially at the upper and right border of the model (Fig. 2).

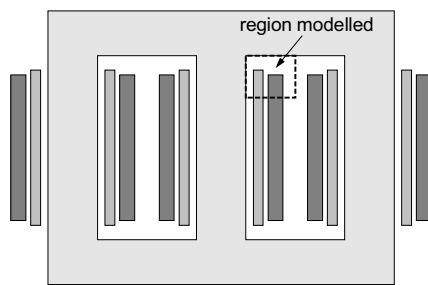


Fig. 1. Cross section of a three phase transformer with marked region which was analysed using FEM.

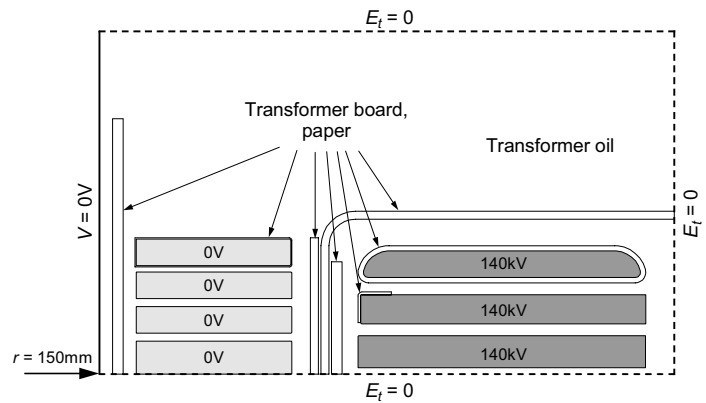


Fig. 2. Geometry, materials and boundary conditions of the FEM model.

Boundary conditions of FEM model

The calculated electric field in the transformer should in any case represent the worst conditions for the insulation structure. Therefore the chosen boundary conditions might or could not describe the problem exactly as it is in real transformer. The Dirichlet boundary condition ($V = 0V$, Fig. 3a) would better describe the conditions under the yoke but to assure the highest electric field strength at the top of LV windings Neumann boundary condition ($\partial V / \partial n = 0$, Fig. 3b) was chosen. Same boundary condition was used on the right boundary of the model as the electric field is symmetrical to the mid-plane between the HV windings. Again, also that boundary could be given a Dirichlet condition if we have in mind a tank of transformer, which is also held at zero potential.

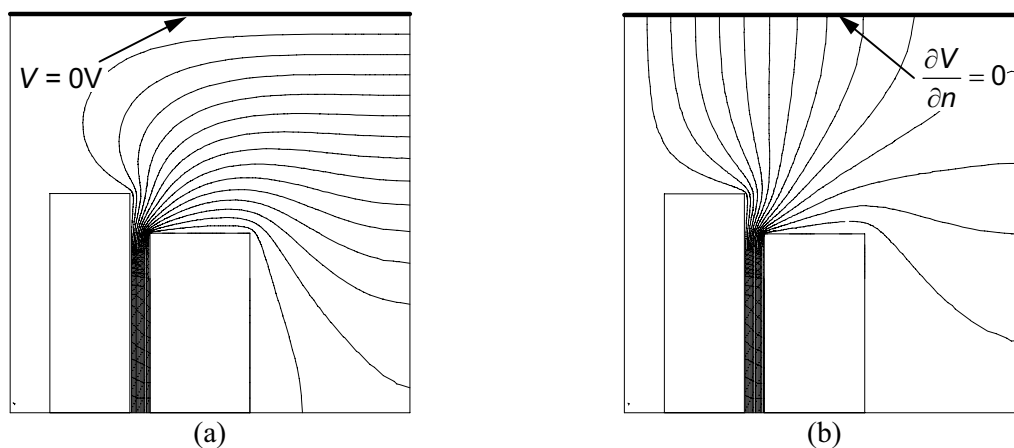


Fig. 3. Different boundary condition at the top of the model: a) Dirichlet and b) Neumann boundary condition.

Determination of maximal electric field strength

When the electric field in a model is calculated the magnitude of the E can easily be presented in a form of a 2D field with a colour map. Such presentation is suitable in case that we would like to investigate the conditions in a given structure, but very inappropriate if we would like to compare the effects of some structural changes. Therefore we have to define paths or lines and draw a diagram of E along those lines. Mostly there is no dilemma where to start the line but problem appears how to continue the line, how to define the line course. Since we would like to observe the regions with the highest electric field strength we simply followed the direction of the vectors E (Fig. 4).

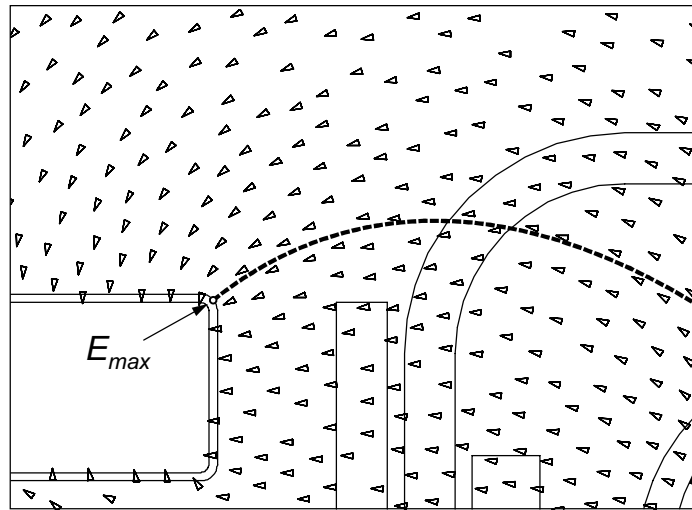


Fig. 4. Determination of a line course using the directions of E .

Conditions at present insulation structure with LV and HV stress-control rings

Just for comparison of the conditions in old and new insulation structure without LV stress-control ring we analysed the electric field at present conditions where both windings have stress-control rings. In Fig. 5 a potential distribution is shown and Fig. 6 shows electric field strength distribution along marked line 1. The maximal E in oil at the top of the LV winding is 6.9 kV/mm and safely below the limit of 10 kV/mm.

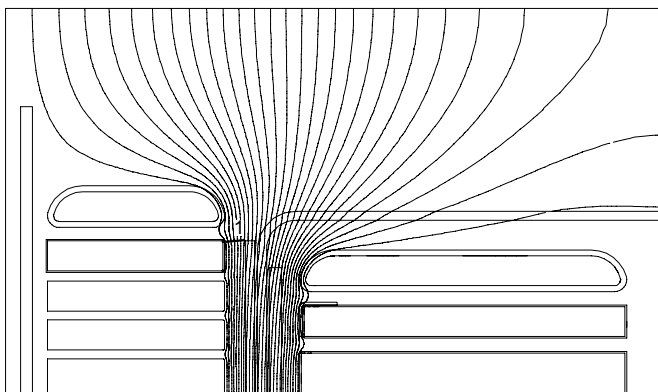


Fig. 5. Potential distribution at present insulation structure.

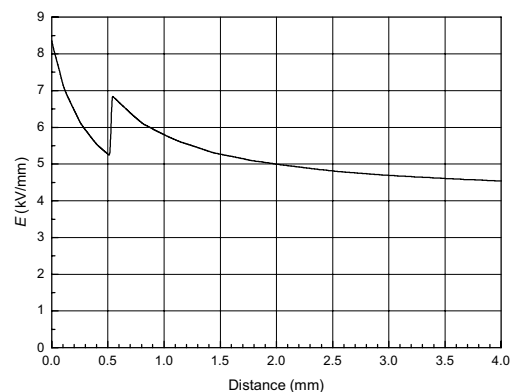


Fig. 6. Electric field strength along line 1.

Electric field in a configuration without LV stress-control ring

To estimate E in a dielectrically most stressed region of the transformer we defined lines along which the E was observed. As expected the maximal E appears along line 1 on the outer corner of LV winding. That winding has no stress-control ring and the radius of the conductor corner is relatively small (0.5 mm). Additional paper insulation (0.5 mm) of upper layer successfully decreases the maximal E in oil to 9.7 kV/mm. The electric field strength is also very high at the outer conductors of LV winding near radial cooling ducts whose height is 3 mm (line 2 in Fig. 7), where E is even higher than 10 kV/mm. Due to the relatively high radial cooling duct above HV winding (4.5 mm) the function of the stress-control ring is diminished or in a some way lost. The maximal E in the oil near paper insulation is 8.8 kV/mm and still below the limit.

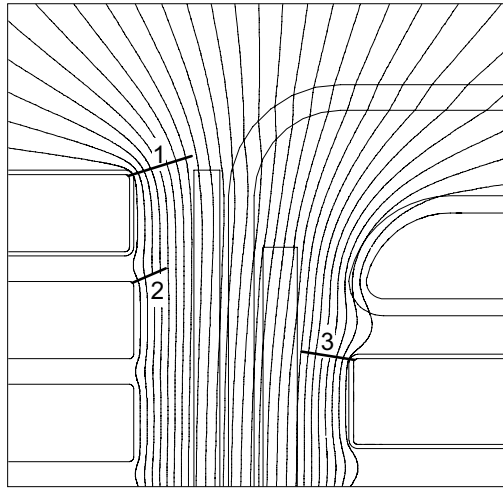


Fig. 7. Potential distribution and lines along which the electric field strength was observed.

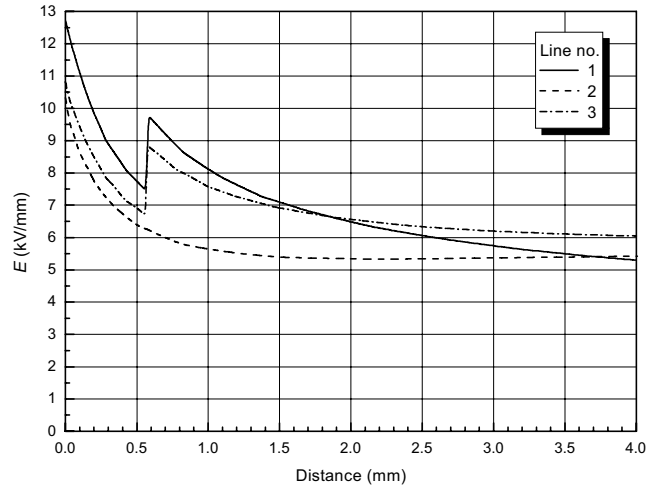


Fig. 8. Electrical field strength along defined lines.

Electric field strength at different radius of conductor's rounded edge

As it was expected and can be seen in Fig. 8, the electric field strength had a maximal value just at the outer conductor at the top of LV winding. Since the increase of the conductor's radius is an effective and quite simple way to decrease the electric field to an appropriate level we analysed the conditions for different radius of conductor's round edge. The thickness of the paper insulation (0.5 mm) and the other geometry of the model remained the same. In Fig. 9 a family of curves for different radius is shown.

Using the values of electric field strength at the distance of 0 mm (Fig. 9) a new diagram was made (Fig. 10). It presents the dependence of the E_{max} on conductor's radius. Those values were used to find an approximative function $E_{max}(r)$:

$$E_{max} = \frac{9.92}{r^{0.326}} \tag{1}$$

where r is radius in mm and the result is E_{max} in kV/mm. We have to stress that this approximation suits just for the used model configuration and it enables the comparison of the results with analytical equations for simpler geometries.

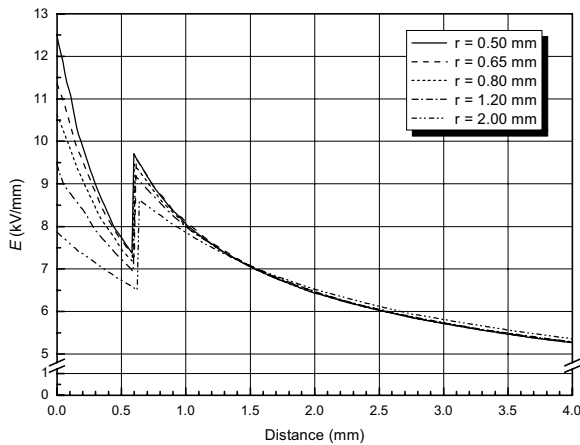


Fig. 9. Electric field strength along line 1 for different radius of conductor's rounded edge.

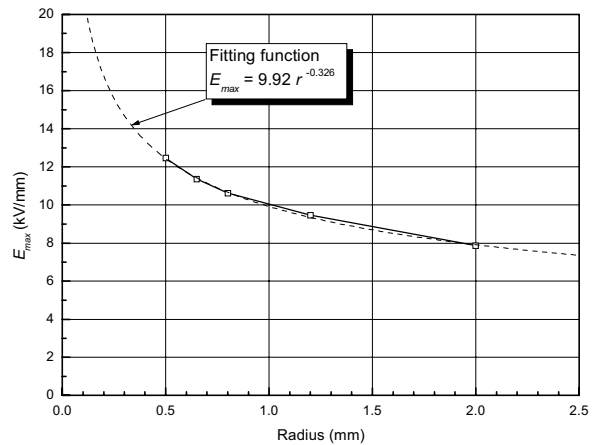


Fig. 10. Maximal electric field strength in dependence of radius.

Electric field at the top of HV winding

Stress-control rings above and below the HV winding have two functions: because of larger radius they reduce the electric field strength at the end of the winding and the other function is that as equipotential surfaces influence to the initial voltage distribution at impulse test of the transformer. Due to better cooling of thermally most stressed top turns the stress-control ring is raised over the top of the winding. That radial duct with the height of 4.5 mm and the fact that the conductive screen of the stress-control ring is shifted out from the inner corner of the HV winding are reasons for increase of E in that region (Fig. 11). On the basis of the calculated electric field strength along line 3 we can establish that it is quite high (Fig. 12). In the FEM model the paper insulation of HV conductors was also taken into consideration (thickness of the paper insulation is about 0.5 mm).

The possibility of using an additional insulating angle ring at that corner was also investigated. The angle ring of the thickness 1 mm was placed at the inner corner of the HV winding and a new distribution of electric field strength was calculated along the line 3. The comparison of the results is shown in Fig. 12. As we already state in the case of different insulation thickness of LV conductors the electric field strength near the conductor remained almost the same but it decreased in the oil. Due to the fitting of the angle ring the lower layer of the conductors is more exposed. In Fig. 12 is also shown the comparison of the electric field strength distribution along lines 3 and 4.

Electric field in the radial cooling ducts of LV winding

In Fig. 13 we can see that the potential lines at the radial cooling ducts of LV winding are not straight vertical but slightly curved into the ducts. We were interested in how the height of such duct influences to the maximal electric field strength at the conductors' corner. The calculated E_{max} for different duct's height (1, 2, 3 and 4 mm) are shown in Fig. 14. Unfortunately we have to consider the fact that in the FEM model the paper insulation of conductors (0.1 mm) was not included. Relatively thin layer of insulation would namely considerable increase the mesh density.

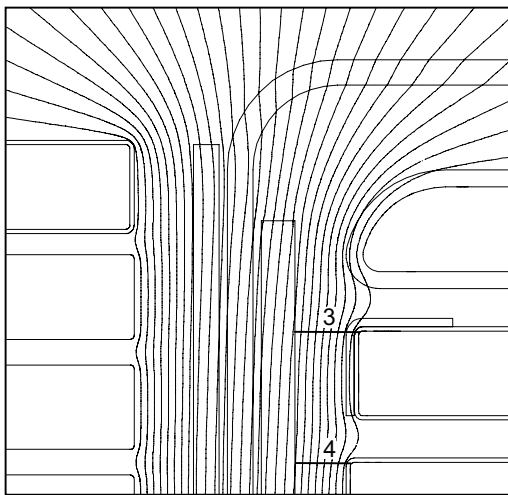


Fig. 11. Potential lines at the top of the HV winding with angle ring.

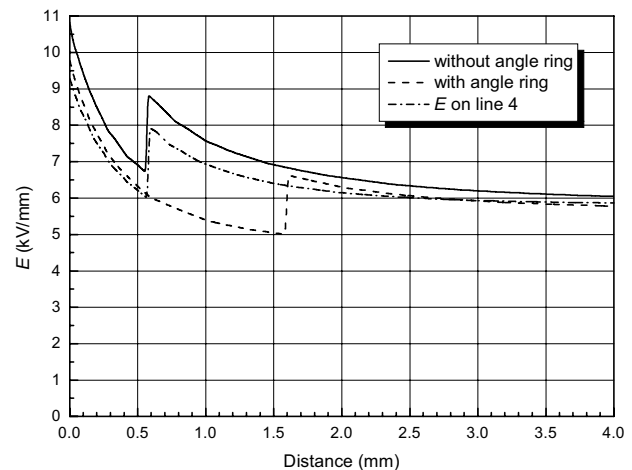


Fig. 12. Electric field strength along line 3 at the inner corner of HV winding with and without angle ring.

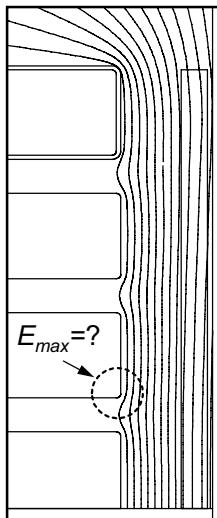


Fig. 13. Electrical field strength at radial ducts

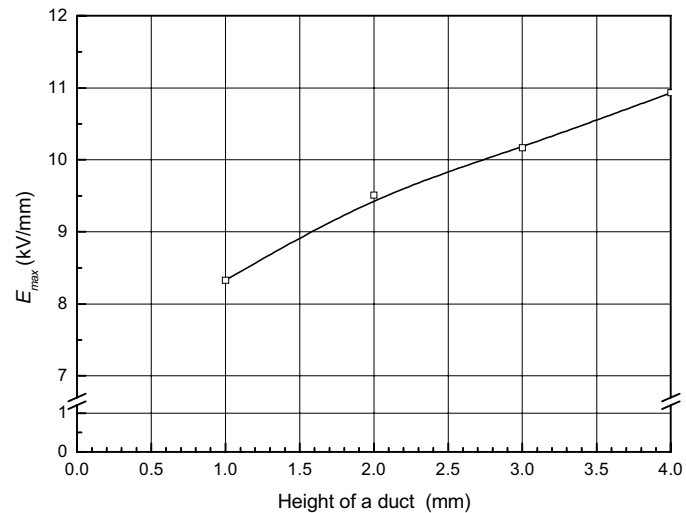


Fig. 14. Dependence of E_{max} at the corner of the conductors on the height of axial cooling duct.

Conclusions

With a careful choice of boundary condition even complex transformer structures can easily be analysed using 2D FEM. Especially parametric solutions give valuable results which are indispensable in the process of transformer design. The insulation coordination is certainly one of the processes we can hardly imagine it without numerical analyses like those presented. With an automated FEM software for electric field analyses, which is our goal, this process can be even faster and simpler.

References

- [1] A. B. J. Reece, T. W. Preston, Finite Element Methods in Electrical Power Engineering, Oxford University Press, New York, 2000.
- [2] Robert M., Del Vecchio, Transformer Design Principles, Gordon and Breach Science Publishers, 2001.
- [3] K. Karsai, D. Kerényi, L. Kiss, Large Power Transformers, Akadémiai Kiadó, Budapest, 1987.
- [4] M. J., Heathcote, J&P Transformer Book, Newnes, Oxford, 1998.
- [5] J. J., Winders, Jr., Power Transformers - Principles and Applications, Marcel Dekker, Inc., New York, 2002.

II-8. A STUDY ON IMPROVEMENT IN ENERGY EFFICIENCY OF SKELETON TYPE SINGLE-PHASE PM MOTOR USING FINITE ELEMENT METHOD

Tatsuya Masuda*, Yoshiharu Takashima*, Masataka Murase*,
Yoshihiro Kawase**, Tadashi Yamaguchi** and Toshinori Okouchi**

*Aichi Electric Co.,Ltd., 1, Aichi-cho, Kasugai, Aichi Pref., 486-8666, Japan

E-mail: masuda.tatsuya@adkk.co.jp

**Department of Information Science, Gifu University, 1-1, Yanagido, Gifu, 501-1193, Japan

E-mail: kawase@info.gifu-u.ac.jp

Abstract – Recently, it is necessary to improve the higher energy efficiency for various motors. A skeleton type single-phase permanent magnet motor is analyzed using the finite element method, and the effects of the stator in different shapes and the rotation direction on the energy efficiency are clarified. In addition, the validity of our method is confirmed by measurements.

Introduction

Recently, it is necessary to improve the higher energy efficiency for various motors. A skeleton type single-phase permanent magnet (PM) motor has a simple structure and is composed of the stator, which has a single-phase winding, and the rotor, which has a permanent magnet. Especially, these motors can be replaced for shaded-pole type induction motors because the shapes of these motors are similar each other. Moreover, skeleton type single-phase PM motors are more efficient than shaded-pole type induction motors. However, it is necessary to improve the higher energy efficiency. In this paper, a skeleton type single-phase PM motor is analyzed using the finite element method, and the effects of the stator in different shapes and the rotation direction on the energy efficiency are clarified. In addition, the validity of our method is confirmed by measurements.

Method of Analysis

The fundamental equation of the magnetic field using the finite element method can be written using the magnetic vector potential A as follows [1]:

$$\text{rot}(\nu \text{ rot } A) = J_0 + \nu_0 \text{ rot } M \quad (1)$$

where ν is the reluctivity, ν_0 is the reluctivity of the vacuum, J_0 is the current density and M is the magnetization of the permanent magnet.

When the current is unknown, the magnetic field should be calculated by coupling the equation of the electric circuit. The equation of the electric circuit connected to the coil is given as follows [2]:

$$E = V_0 - RI_0 - L \frac{dI_0}{dt} - \frac{d\Psi}{dt} = 0 \quad (2)$$

where V_0 is the applied voltage, R the resistance, I_0 is the current, L is the additional inductance of the analyzed region and Ψ is the interlinkage flux of the coil.

The torque at each position of the rotor is calculated using the Maxwell stress tensor method.

The average torque T obtained with this method is composed of output torque T_{out} and torque of mechanical loss T_m :

$$T = T_{out} + T_m \quad (3)$$

Especially, no-load torque can be written as follows:

$$T = T_m \quad (4)$$

Generally, T_m can be written as follows:

$$T_m = k\omega \quad (5)$$

where ω is the angular velocity and k is the constant. From (3), (4) and (5), it is obtained the speed-output torque characteristics to measure no-load speed.

The energy efficiency η is obtained as follows:

$$\eta = \frac{P_{out}}{P_{in}} \times 100 = \frac{T_{out}\omega}{\frac{1}{\tau} \int_0^{\tau} V_0 I_0 dt} \times 100 [\%] \quad (6)$$

where, τ is the period of the applied voltage.

Analyzed Model and Conditions

Fig.1 shows an analyzed model of skeleton type single-phase PM motors. In this paper, three patterns of the model are analyzed. Models B and C have cut notches. Model C can be seen that the rotation direction is opposite of model B, though the shapes of the two models are exactly the same. Table 1 shows the motor conditions. Fig. 2 shows the finite element meshes. Fig. 3 shows the applied voltage of each model. These graphs are energization patterns when each energy efficiency is maximum.

It is desired to analyze the 2-D method to reduce the CPU time, but it is impossible to consider the end-coil effects. Fig. 4 shows the current waveform of model B. It is found that the results calculated by the 3-D analysis agree well with the measurements. The calculated results by the 2-D analysis also agree well with the measurements only if L is considered. Therefore, in this paper, these models are analyzed with the 2-D method with L , which is considered to be 19.5mH.

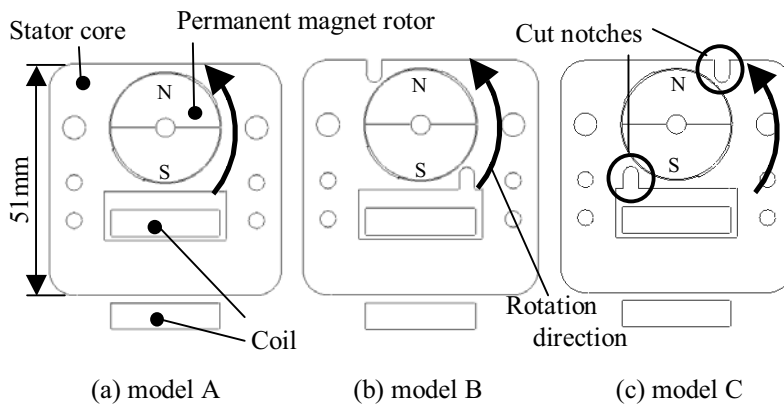


Fig. 1. Analyzed model.

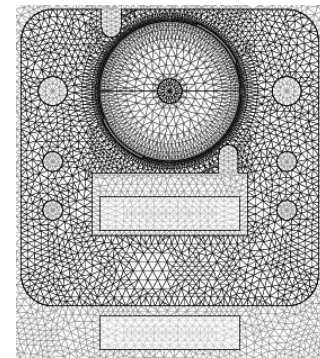


Fig. 2. meshes.

Table 1. Motor conditions

Axial length of the armature	15mm
Air gap	0.3mm
Turn of winding	350turn
Resistance of winding	5.32Ω
Magnetization of permanent magnet	0.295T

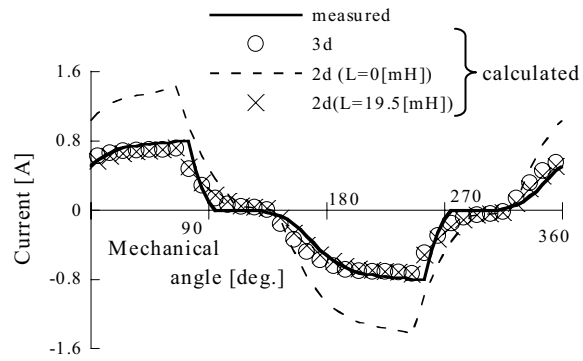


Fig. 4. Current waveform (model B).

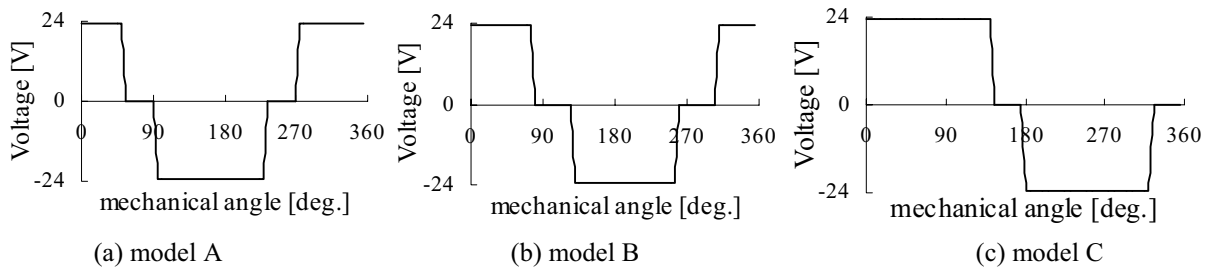


Fig. 3. Applied voltage.

Results and Discussion

Fig.5 shows the magnetic flux distributions when the momentary torque reaches maximum and the rotor speed is 4,000 rpm. In model B, saturation areas can be seen only near the notches. Therefore, it is found that the input power of model B is used as more effective magnetic flux for the torque than those of other models.

Fig.6 shows the speed-current characteristics. It is found that the calculated results agree very well with the measurements. Fig.7 shows the speed-output torque characteristics. It is found that the results agree well with each other. It is also found that the speed of models B and C is higher than that of model A when the torque is low. It is because that the interlinkage flux from permanent magnet of model A is less than other models, for this model has not cut notches. Fig.8 shows the output torque-current characteristics. It is found that the results agree well with each other, but the calculated torque is smaller than the measurement when the current is high. One reason for the differences is that the heat generation of the coil is not considered in these analyses. It is also found that the efficiency of model B is the highest and that of model C is the lowest of the three models.

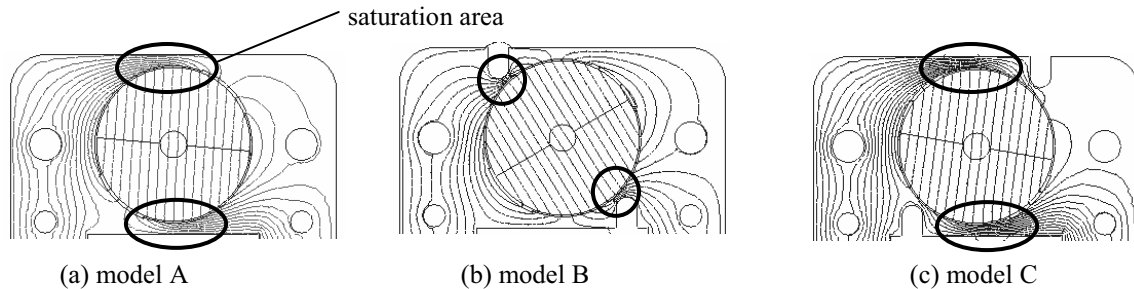


Fig. 5. Magnetic flux distributions.

Fig.9 shows the energy efficiency-output torque characteristics. In both the calculation and the measurement, it is found that the energy efficiency of model C is higher than that of model A, and that of model B is the highest of them. It is estimated that the efficiency of the measurement at high torque is smaller than that of calculation because of the heat generation of the coil.

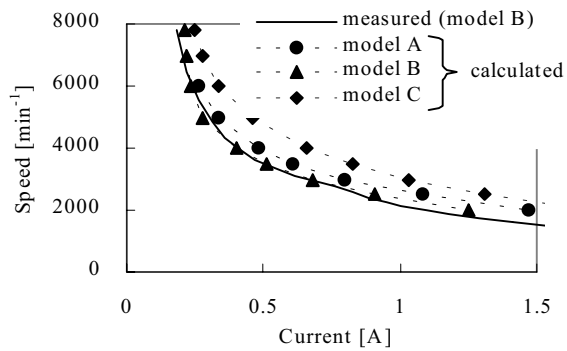


Fig. 6. Speed-current characteristics.

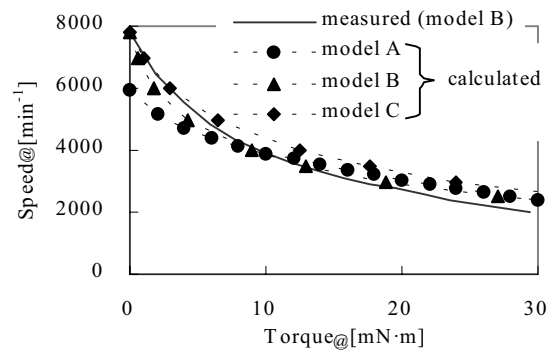


Fig. 7. Speed-output torque characteristics.

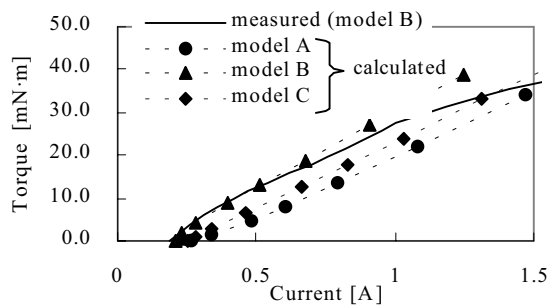


Fig. 8. Output torque-current characteristics.

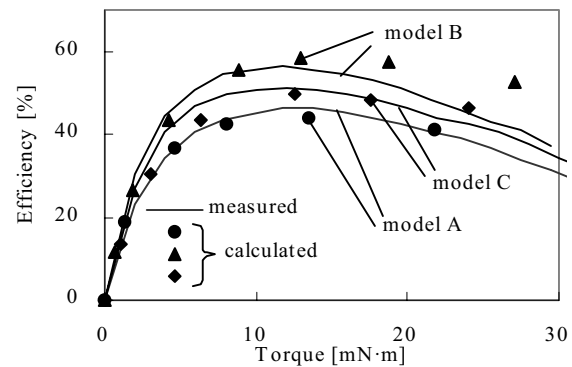


Fig. 9. Energy efficiency-output torque characteristics.

Conclusions

In this paper, a skeleton type single-phase PM motor is analyzed using the finite element method. The method to calculate the energy efficiency of this motor is investigated. In these models, cut notches in the stator core can make the energy efficiency higher. The effects of the rotation direction on the energy efficiency are also clarified. The results of these calculations are very useful for the optimum design of skeleton type single-phase PM motors. It is also clarified that our method is confirmed with the measurement.

References

- [1] S. Ito and Y. Kawase, "Computer Aided Engineering of Electric and Electronic Apparatus Using Finite Element Method", Morikita Publishing Co., 2000.
- [2] Y. Kawase, K. Suwa and H. Sekino, "3-D Dynamic Transient Analysis of Stepping Motor for Wristwatch by Finite Element Method", IEEE Transactions on Magnetics, Vol.34, No.5, pp. 3130-3133,1998.

II-9. ANALYSIS OF CHARACTERISTICS OF INDUCTION MOTOR BY THREE-DIMENSIONAL AXI-SYMMETRIC FINITE ELEMENT METHOD

T. Matsusaka, K. Harada, Y. Ishihara, T. Todaka, S. Kitamura^{*}, and T. Shimomura^{*}

Department of Electric Engineering, Doshisha University, Kyotanabe, Kyoto, 610-0321, Japan

^{*}Department of Development, Kusatsu Electric Co.,Ltd., Kusatsu, Shiga, 525-8501, Japan

E-mail : yishihar@mail.doshisha.ac.jp

Abstract – This paper proposes the magnetic field analysis method of an induction motor using Three-Dimensional Axi-symmetric Finite Element Method (3D-ASFEM). The part of analysis that cannot be dealt with the two-dimensional magnetic field analysis is made by 3D-ASFEM. The induced voltage of the end ring is calculated by using the vector potentials obtained from 3D-ASFEM. Then, the circuit equations considering the induced voltage and the electromagnetic equation are solved simultaneously by using Two-Dimensional Finite Element Method (2D-FEM). The calculated characteristics of induction motor are in good agreement with the measured ones.

Introduction

Recently, the numerical analysis by finite element method is widely used for design and development of induction motor. But, in the magnetic field analysis by Two-Dimensional Finite Element Method (2D-FEM), it is difficult to consider the induced voltage of the end ring in order to handle the infinity current for the cross section in the two-dimensional field. This becomes one of the causes of the analysis error. In the magnetic field analysis by 3D-FEM, enormous calculation time and memory for the analysis are required. Therefore, it has not reached the stage which the designers of the induction motor can analyze easily.

To avoid these drawbacks and difficulties, the Three-Dimensional Axi-symmetric Finite Element Method (3D-ASFEM) together with 2D-FEM is proposed. These two approaches are complementary in the analysis of the magnetic field in induction motor. The improvement in the analysis accuracy of induction motor is examined.

The analysis method of induction motor

The magnetic field analysis cannot be carried out by 2D-FEM in the part of the end ring which is a parallel cross section in rotating shaft of induction motor. Therefore, at this part, the magnetic field analysis by 3D-ASFEM is employed. The induced voltage is then calculated from the vector potentials obtained from 3D-ASFEM. The flow chart of magnetic field analysis is shown in Fig.1.

Consideration method of the end ring

The current flowing in the end ring between the rotor bars is obtained from two-dimensional magnetic field analysis of induction motor. The current in the end ring calculated by 2D-FEM is handled as an input of 3D-ASFEM. The vector potentials of the end ring are obtained from the magnetic field analysis by 3D-ASFEM. The induced voltage of the end ring is calculated.

After the calculation, induced voltage of each end ring is added in the conventional circuit equation of rotor-bar conductor. Then, the new circuit equations are made. The equivalent circuit in converting cage rotor which has the skewed slot into electric circuit is shown in Fig.2. The circuit equation applying the Kirchhoff's second law to electric circuit shown in Fig.2 is as follows:

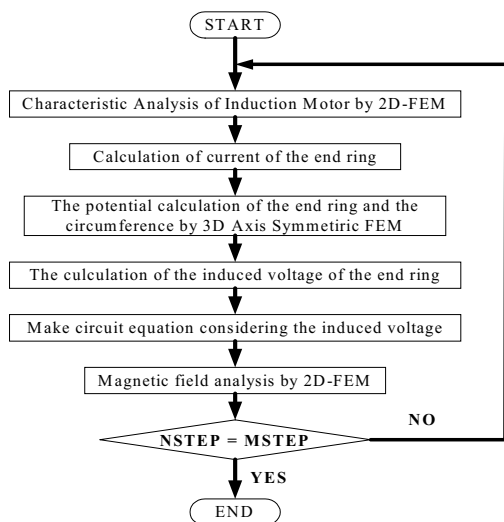
$$2(R_e + R_b)I_n - R_b(I_{n-1} + I_{n+1}) = \frac{1}{2}(V_{r(n+1)} - V_{r(n-1)}) + (V_{e(n)} + V_{e(n+1)}) \tag{1}$$

where : R_b, R_e - the resistances of rotor bar and end ring, respectively,

I_n - the current flowing in respect of the end ring of the n number,

$V_{r(n)}, V_{e(n)}$ - the induced voltages of the rotor bar and end ring of the n number.

Therefore, the simple three-dimensional analysis of induction motor can be carried out by calculating Eq. (1) and electromagnetic equation simultaneously.



MSTEP : All analysis number of step

NSTEP : Present analysis number of step

Fig. 1. The flow chart of magnetic field analysis.

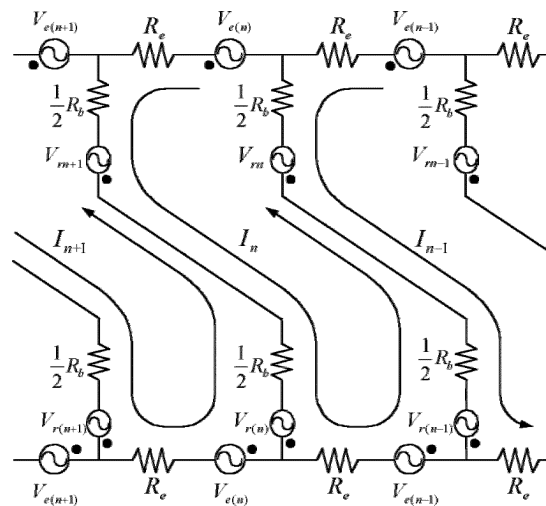


Fig. 2. The equivalent circuit of rotor-bar conductor.

Consideration method of the lamination factor

In the magnetic field analysis of 3D-ASFEM, the parallel cross section in rotating shaft becomes an object of analysis. Since this part is stacking direction of magnetic steel sheet, iron core part of the induction motor is handled as anisotropic magnetic steel sheet. Then, the magnetic resistance considering the lamination factor of magnetic steel sheet is calculated. It is assumed that the magnetic steel sheet is piled up, as it is shown in Fig.3 (a).

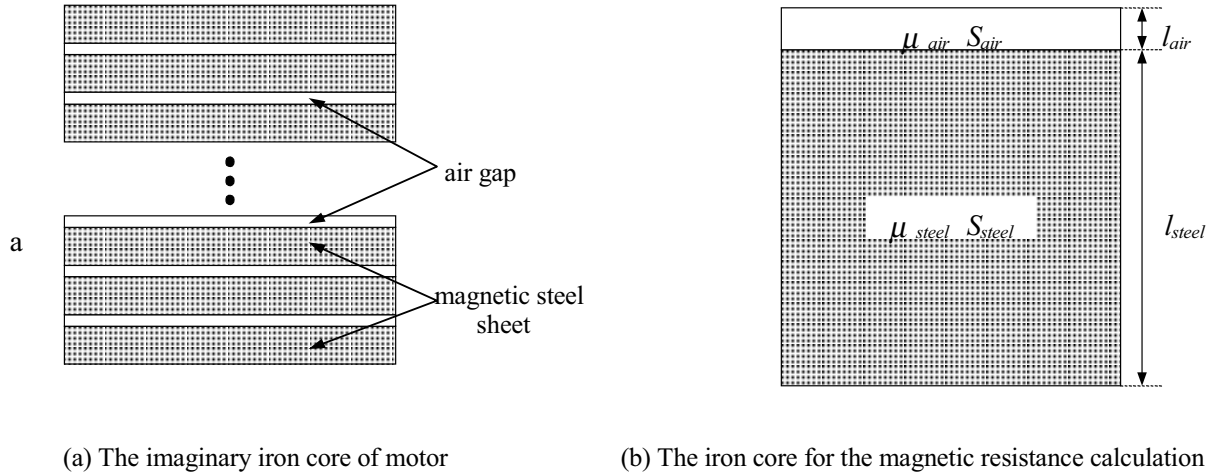


Fig. 3. The handling of the anisotropic magnetic steel sheet.

It seems to connect for the series of the magnetic resistances of magnetic steel sheets and air gaps between them, as it is shown in Fig.3 (a). Therefore, iron core part of induction motor is shown as Fig.3 (b), and equations of the magnetic resistance of each material are as follows:

$$R_{air} = \frac{l_{air}}{\mu_{air} S_{air}}$$

$$R_{steel} = \frac{l_{steel}}{\mu_{steel} S_{steel}} \quad (2)$$

$$R_{mag} = R_{air} + R_{steel}$$

By considering Eq. (2), it is possible to carry out the magnetic field analysis considering lamination factor.

Analytical model

The model for two-dimensional analysis is shown in Fig.4 (a). The model for three-dimensional axi- symmetric analysis is shown in Fig.4 (b). The analytical model is 3-phase 6-pole squirrel-cage induction motor with stator (36 slots) and rotor (44 slots). The material of the iron core is non-oriented magnetic steel sheet 50A1000. The thickness is the 55 mm, The width of gap between stator and rotor is the 0.2 mm, and lamination factor is 98.5%. The magnetization characteristic of magnetic material 50A1000 is shown in Fig.5. In the magnetic field analysis of 3D-ASFEM, magnetization characteristic shown in Fig.5 (b) is handled.

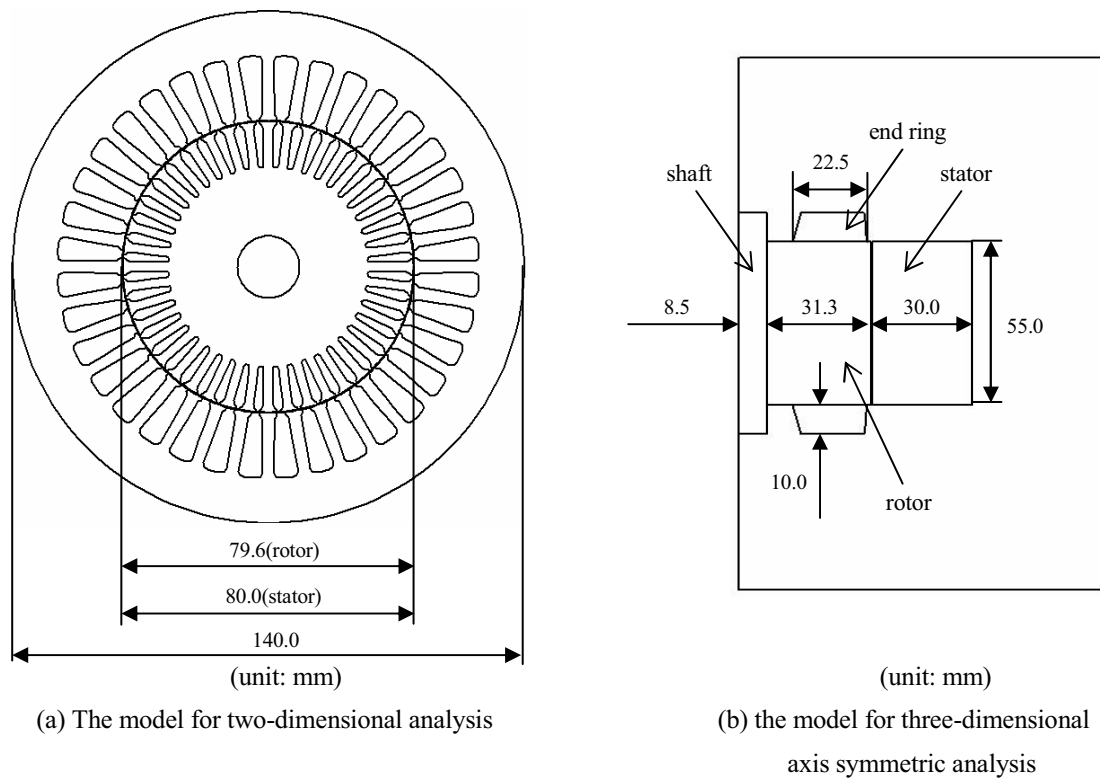


Fig. 4. The analytical model.

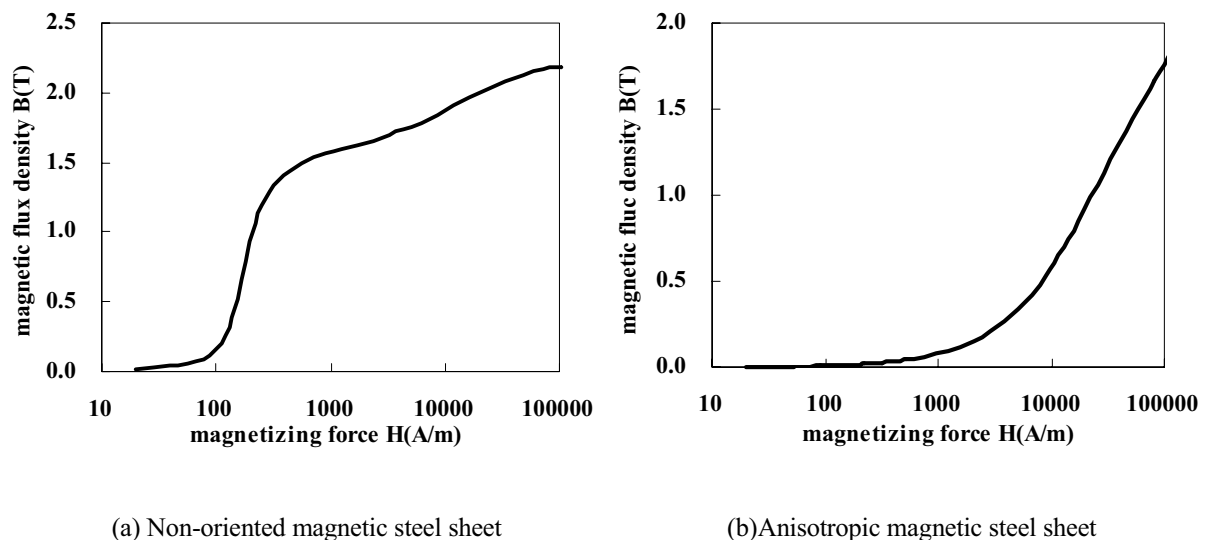


Fig. 5. 50A1000 magnetization characteristic.

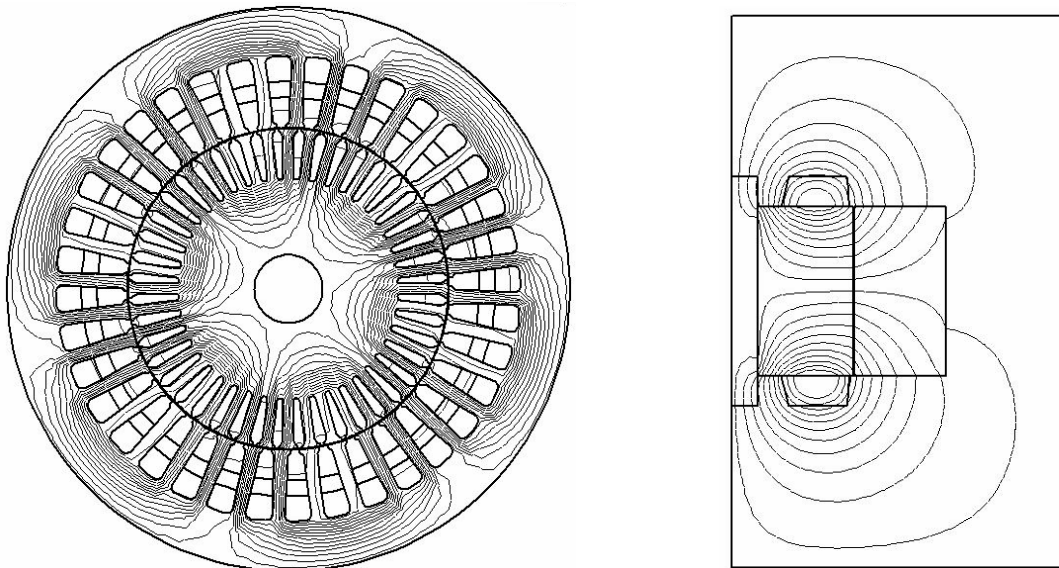
Two coils have been inserted on a stator slot, however, these have deviated by the one slot pitch, and the structure does not show the symmetry. Therefore, the analysis region was made to be the 360 degrees. They are the 56 turns per one coil. Coil resistance of the stator is 12.1Ω , resistance of rotor bar is $58.0 \mu\Omega$, and resistance of end ring is $0.518 \mu\Omega$. The magnetic field analysis was carried out under two kinds of conditions: frequency: 50 Hz, applied voltage: 200 V and frequency: 60 Hz, applied voltage: 200 V.

Results

The magnetic flux distribution is shown in Fig.6, and the characteristics of speed-torque and speed-current are shown in Fig.7 when the slip is 0.1 at 50Hz.

Since the current of rotor-bar conductor is small, it is proven that the disturbance from the stator side decreases on the magnetic flux in Fig.6 (a). The axial iron core is magnetic steel sheet considering air gap, as it is shown in Fig.6 (b), and the permeability is smaller than the non-oriented magnetic steel sheet. Therefore, it is proven that the magnetic flux is difficult to pass further than the radial direction.

It is cleared that the characteristic of speed-torque approaches the measured value by considering the induced voltage of end ring in Fig.7 (a). With the decrease of the slip, the correction by the induced voltage of end ring is difficult to work because the current in the rotor-bar conductor decreases. It is also cleared that there are no difference between proposal technique and conventional one. However, the characteristic of speed-current is approximate to the measured one without consideration of the induced voltage of end ring, as it is shown in Fig.7 (b). As a cause, it is mentioned that the induced voltage of stator windings which cannot be considered in two-dimensional magnetic field analysis, mechanical loss and core loss of an induction motor are not considered.



(a) Two-dimensional analysis

(b) Three-dimensional axis symmetric analysis

Fig. 6. Magnetic flux distribution. (50Hz, slip=0.1)

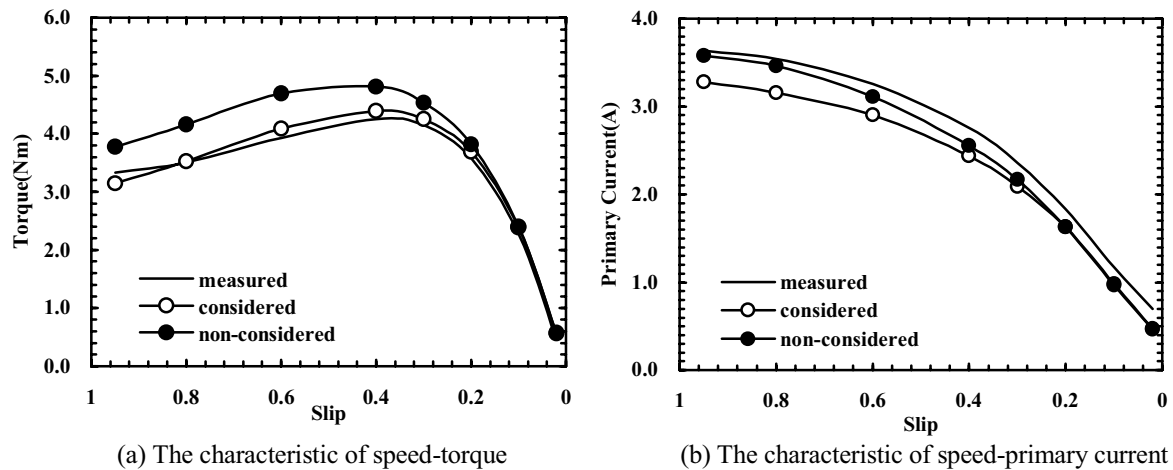


Fig. 7. The characteristics of induction motor.

Conclusions

The magnetic field analysis method of induction motor using 3D-ASFEM and 2D-FEM was proposed. By considering lamination factor of iron core and the induced voltage of end ring which cannot be considered in two-dimensional magnetic field analysis, the characteristic of speed-torque reached the measured one, and the accuracy of analysis of an induction motor can be improved by proposal technique to a great extent.

In the future, the characteristic of speed-current will be improved too, and the magnetic field analysis of induction motor considering the induced voltage of stator windings will be carried out.

References

- [1] Y. Koba, S. Kitamura, T. Matsubara, Y. Ishihara, T. Todaka, and Y. Inoue : "Analysis of Condenser Motor Characteristics Considering Skewed Slot", The Papers of Technical Meeting on Rotating Machinery, IEE Japan, 1997, RM-97-32, pp51-56
- [2] T. Nakata, and N. Takahashi : "The Finite Element Method of Electrical Engineering second edition", Morikita Publication, 1986, pp7-19
- [3] Application technology survey expert committee of the rotating machine electromagnetic field analysis software : "Application technology of the rotating machine electromagnetic field analysis software", Technical Report, IEE, Japan, 1994, No.486
- [4] K. Yamazaki : "Approximated Modeling of End-Rings for Electromagnetic Field Analysis of Induction motors", T. IEE, Japan, 2001, Vol.121-D, No.2, pp184-195
- [5] S. Yoshida, Y. Matsumoto, Y. Mitani, Y. Ishihara, and T. Todaka : "Analysis of Three-phase Four-Limb Transformer Core with V-Connection by Using the Finite Element Method", The Papers of Technical Meeting on Magnetics, IEE Japan, 1997, RM-97-32, pp51-56

II-10. AN INFLUENCE OF PERMANENT MAGNET SHAPE ON THE TORQUE RIPPLE OF DISC-TYPE BRUSHLESS DC MOTORS

E. A. Mendrela

Louisiana State University, Department of Electrical and
Computer Engineering, Baton Rouge, LA 70803, USA,
e-mail: ermen@ece.lsu.edu

M. Jagieła and R. Wróbel

Technical University of Opole, Department of
Electrical Engineering and Automatic Control
PL 45036, ul. Luboszycka 7, Opole, Poland

Abstract – An analysis of the torque developed by two types of the disc-type permanent magnet (PM), brushless DC motors: slotted torus motor and motor with stator salient poles is presented. The calculations were performed using three-dimensional finite element method (FEM). Two shapes of PMs are analyzed: trapezoidal and rectangular. The results show that application of rectangular shaped PMs provides significant reduction of the torque ripple in both considered motors.

Introduction

Among the disc-type PM electrical machines a few types of them can be distinguished. In that number are the torus, and axial-flux stator salient pole motors (see Figs. 1 and 2) [1, 2]. The torus motor is usually built as a slotless machine. In order to increase its torque density the space between the adjacent coils of the motor winding can be filled with the ferromagnetic material. However, such a modification of the magnetic circuit contributes increasing of the torque ripple.

There are several different methods for minimization of the torque ripple [6, 7]. In this paper the author proposed modification of PM shape. Two alternative shapes of PM are proposed: trapezoidal and rectangular. In both cases, volume of PM material is the same. The analysis of the torque developed by the motors is carried out in 3D space using the finite element method.

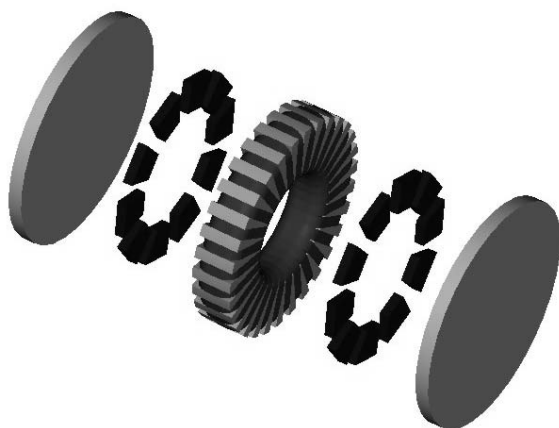


Fig.1. Structure of a slotted torus-type motor

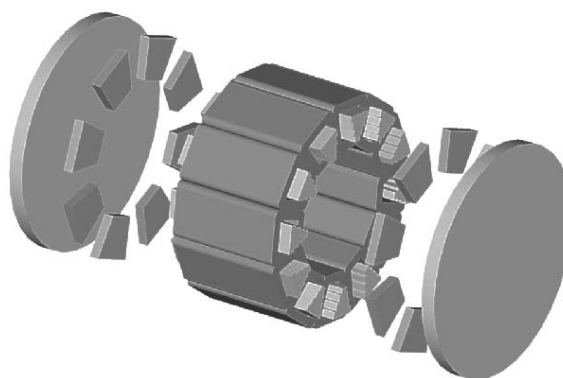


Fig.2. Structure of a disc motor with salient pole stator

This work was supported in part by the National Science Foundation, project No.: ECS-0217308, and partly by the Foundation for Polish Science.

Torus-Type Motor

The slotless version of the torus-type motor was designed for gearless drive of light electric scooter, as it is described in [3]. Its design parameters are as follows:

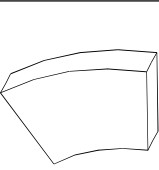
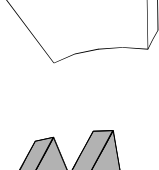
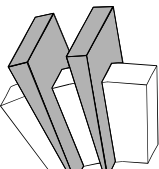
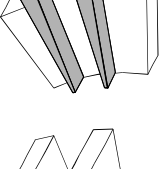
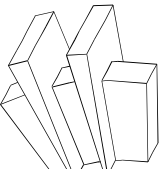
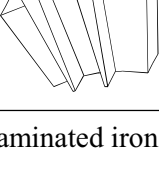
- outer stator core diameter	$D_{out} = 140$ mm,
- inner stator core diameter	$D_{in} = 90$ mm,
- stator core thickness	$d_c = 10$ mm,
- 3-phase winding with the number of coils per pole per phase	$q = 1$,
- number of coils	$N_c = 30$,
- number of turns per coil	$N_t = 36$,
- air-gap length	$g = 0.4$ mm,
- number of rotor poles	$2p = 10$
- thickness of rotor discs	$d_r = 10$ mm.

A toroidal core of the stator is made of laminated iron, and the rotor discs are made of soft magnetic iron. As an excitation of the motor the neodymium ($\text{Nd}_2\text{Fe}_4\text{B}$) PMs are employed ($B_r = 1.21\text{T}$ and $H_c = -950$ kA/m).

Two other modified versions of the torus motor are considered. The slotless stator core (motor version I) was replaced by slotted one with composite and laminated iron teeth (motor versions II and III respectively). The composite parts of magnetic circuit are made of ferromagnetic powder and synthetic resin. The magnetic permeability of the ferromagnetic composite is equal to 5.

Table 1 presents the calculation results for all considered versions of the torus-type motor.

Table 1. Torques of the torus-type motor versions due to variation of PM shape for $I = 8\text{A}$

Motor version		T_{max} [N·m]	T_{min} [N·m]	T_{av} [N·m]	ϵ [%]
I a		6.91	5.74	6.50	17.99
I b		6.91	5.71	6.49	18.39
II a		11.15	7.77	9.63	35.10
II b		12.76	7.51	9.60	54.67
III a		18.28	6.55	12.81	91.56
III b		20.38	3.49	12.60	134.10

Laminated iron

Composite, ($\mu_r = 5$)


Square PM


Trapezoidal PM

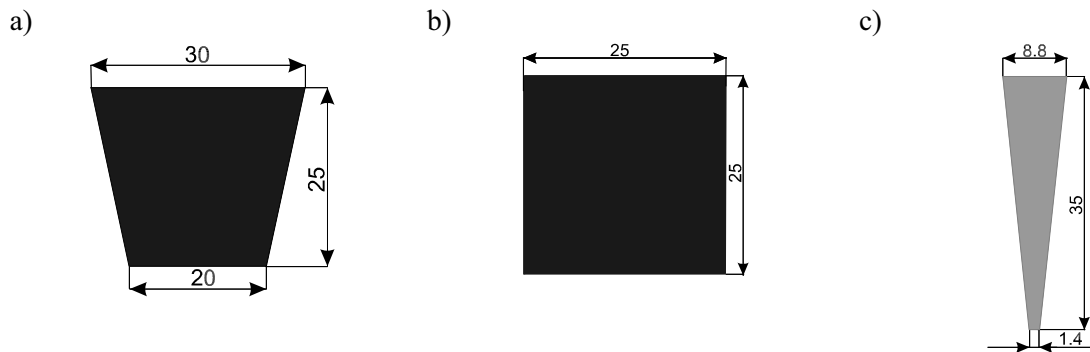


Fig.3. Dimensions of: a) trapezoidal magnets, b) rectangular magnets, c) stator teeth of the torus motor

The calculations of the torque were carried out for rectangular current-wave and current $I = 8A$. Figs. 4 and 5 illustrate angular variation of the electromagnetic and cogging torque, determined for the slotted motor versions. The results show significant reduction of the ripple torque for the slotted motor versions with the rectangular shaped PMs. It is worthy to note that the resultant torque developed by the motors is the same as for the motor with a trapezoidal shape of PM.

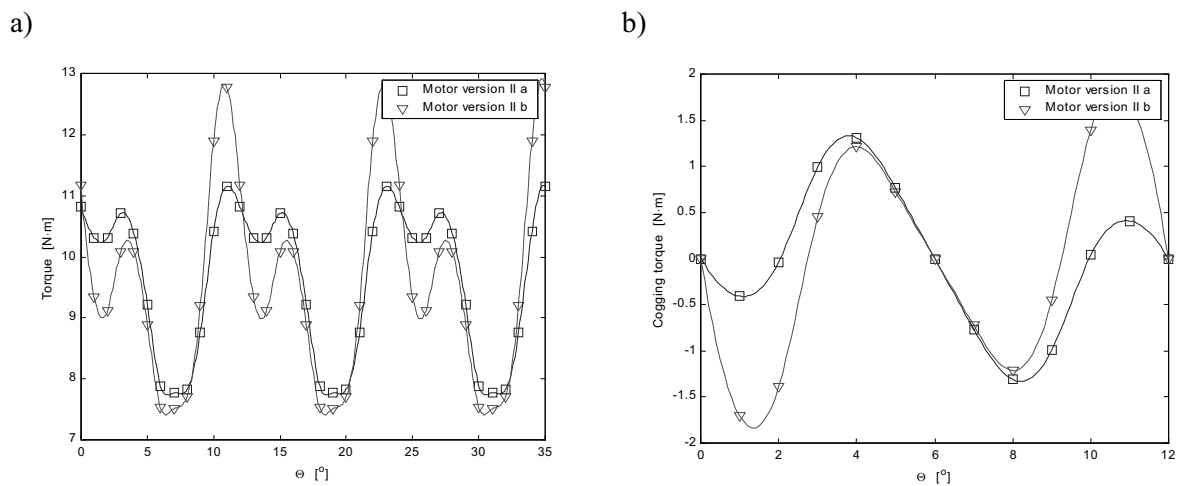


Fig.4. Torque vs. rotational angle (θ) characteristics of motor version II: a) resultant torque, b) cogging torque

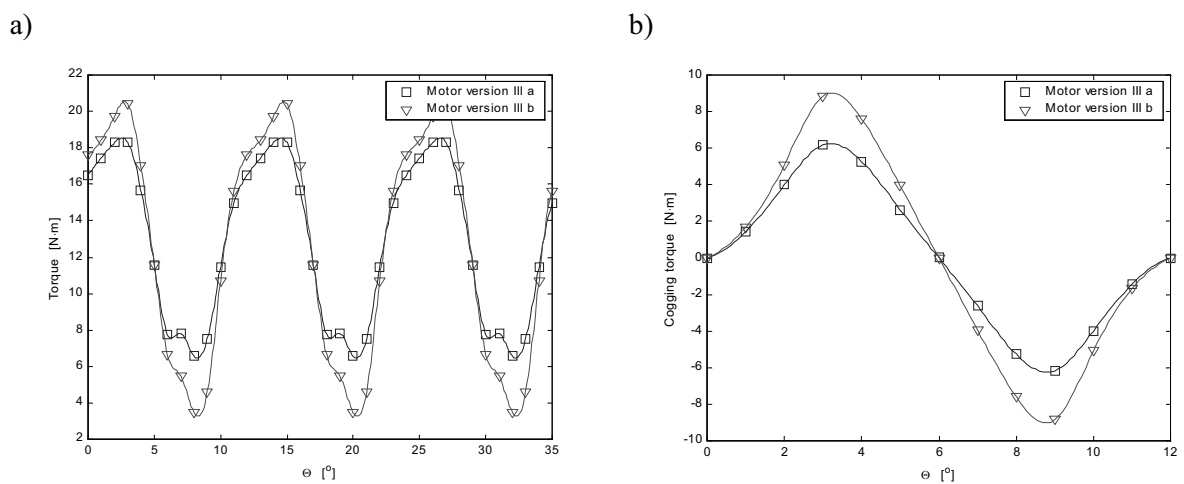


Fig.5. Torque vs. rotational angle (θ) characteristics of motor version III: a) resultant torque, b) cogging torque

In order to define value of the torque pulsation, the torque ripple factor ε was defined [5]:

$$\varepsilon = \frac{T_{\max} - T_{\min}}{T_{\text{mean}}} \cdot 100 \% , \quad (1)$$

where: T_{\max} , T_{\min} and T_{mean} are the maximum, minimum and mean values of the torque respectively.

The main component of the torque ripple is the cogging torque, which is caused by the interaction of permanent magnets' field and angular variation of the stator reluctance. The influence of the cogging torque is particularly shown for the slotted motor with laminated iron teeth (see Fig. 5).

Disc Motor with Salient Pole Stator

The second of the considered motors was designed as a small capacity water pump with a wet rotor (rotor operates in the water environment) [6,8]. The design specifications are as follows:

- external diameter of the stator core	$D_{ex} = 80 \text{ mm}$,
- internal diameter of the stator core	$D_{in} = 50 \text{ mm}$,
- number of stator poles	$N_c = 12$,
- number of turns per coil	$Z_c = 16$,
- air gap length	$g = 0.8 \text{ mm}$,
- number of rotor poles	$2p = 8$,
- thickness of rotor discs	$d_r = 6 \text{ mm}$,
- total length of motor	$l_r = 76 \text{ mm}$.

The characteristics of the materials used for the stator core poles, rotor discs and permanent magnets are respectively the same as for the torus motor. The dimensions of the trapezoidal magnets, which were used, are shown in Fig. 6.

The calculations of the torque were carried out for rectangular current-wave and current $I = 23 \text{ A}$. The results show that the modification of PMs shape in this case does not affect the resultant torque in terms of cogging torque reduction (see Fig. 7a).

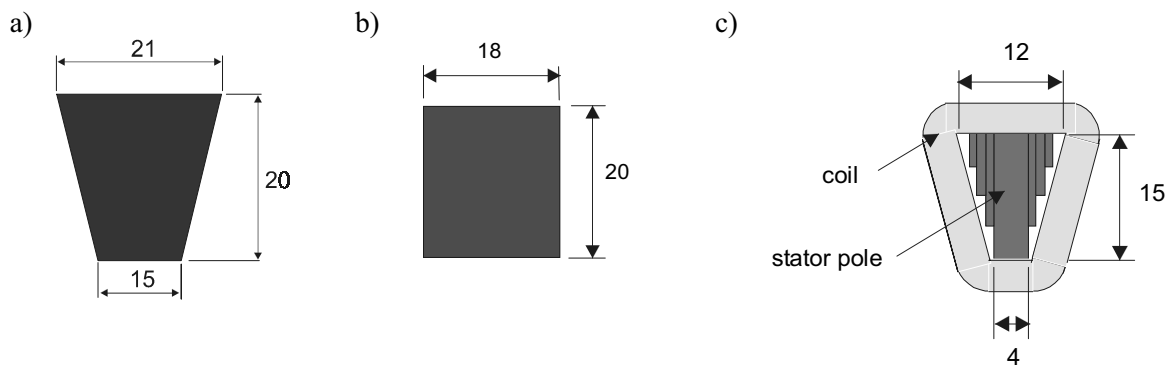


Fig.6. Dimensions of: a) trapezoidal magnets, b) rectangular magnets, c) stator pole-pieces

The above mentioned conclusion that the PMs shape does not influence the torque ripple is in reference to the motor whose stator pole cores have the same cross-section along the entire stator length as does the prototype motor.

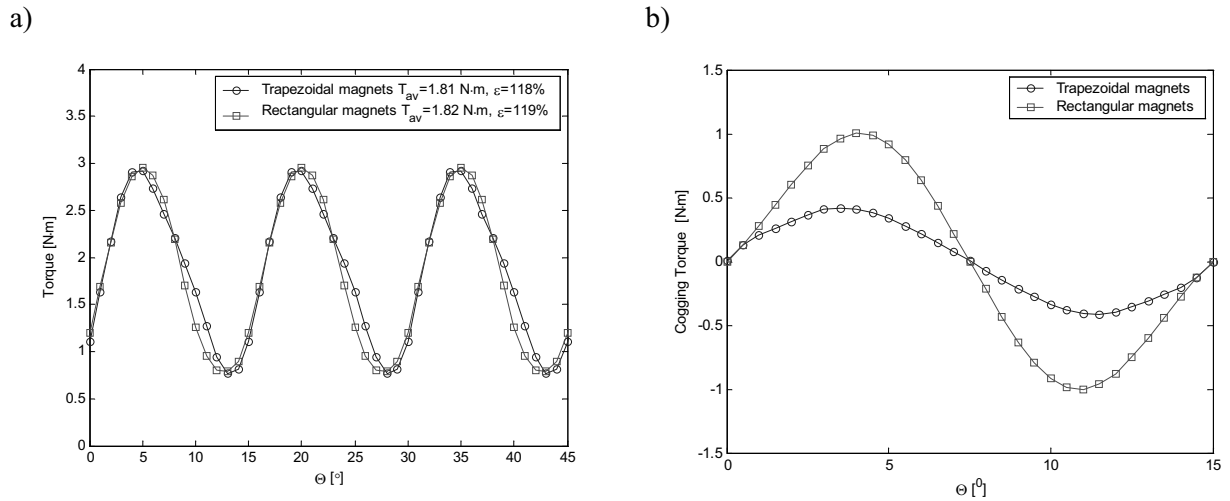


Fig.7. Torque vs. rotational angle (θ) characteristics: a) resultant torque, b) cogging torque

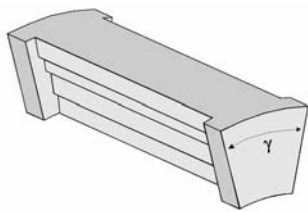


Fig.8. Shape of stator pole piece of disc motor with salient pole stator

To examine whether the width of the stator pole shoe influences the torque waveform, the calculations were repeated for different widths of stator pole shoe γ (see Fig.8). Fig.9 illustrates angular variation of the resultant torque for different γ . It is assumed that the γ/τ factor relates the angular length of the stator pole shoe to the angular length of the rotor pole pitch. For the prototype motor $\gamma/\tau = 0.20$. The results show that the width of the stator pole shoe has small influence on the resultant torque on the trapezoidally-shaped PMs (see Fig.9a). In case of the rectangular shaped PMs there is significant influence of γ/τ factor on the results (see

Fig.9b). The increase of the angular length of the stator pole shoe causes the decrease of the torque ripple. However, it should be added that from the technological point of view it is easier to manufacture the stator pole shoe of the same angular length along the entire stator length (as for the prototype motor) than apply a different dimension of the pole shoe.

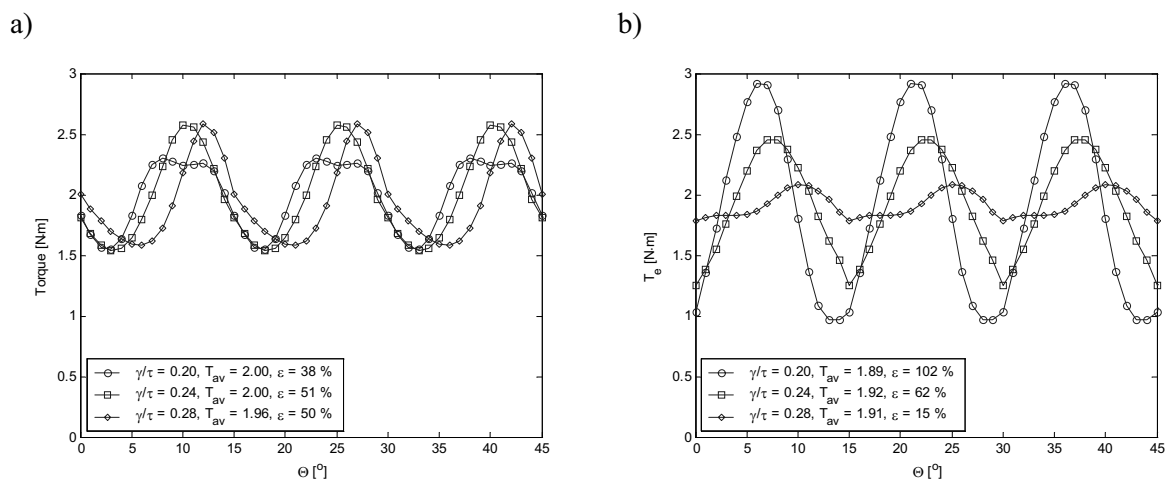


Fig.9. Torque-rotational angle characteristics determined for various angular length (γ) of stator pole pieces: a) motor with trapezoidal magnets, b) motor with rectangular magnets

Conclusions

The objective of the analysis carried out in this paper was to diminish the torque ripple in two types of disc motors: torus motor and salient stator pole motor. To minimize torque pulsation the shape of the permanent magnets was changed from trapezoidal to rectangular. This approach refers to some extent to the skew of stator teeth with respect to the permanent magnets in cylindrical motors, similarly as it is in cylindrical structures. The application of the rectangular shaped PMs diminishes the torque ripple whereas the average torque remains the same. In cylindrical motors the skew angle of teeth, with respect to the magnets, influences the torque pulsation. In disc motors this was examined on salient stator pole motor that the mutual relation between the angular length of the stator pole shoe and permanent magnet strongly influences the torque ripple. The calculation results were partially verified on the physical models for the trapezoidally-shaped PMs [3].

References

- [1] F. Caricchi, F. Crescimbin, E. Fedeli, G. Noia: Design and construction of a wheel-directly-coupled axial-flux PM motor prototype for EVs, *IEEE Trans. on Ind. Appl.*, Vol.1, pp. 254-261, 1994.
- [2] E. Mendrela, J. Moch and P. Paduch: Performance of disc-type brushless DC motor with single-phase winding, *Archives of Electrical Engineering*, No 2, pp. 145-153, 2001.
- [3] E. A. Mendrela, R. Beniak, and R. Wrobel: Influence of Stator Structure on Electromechanical Parameters of Torus-Type Brushless DC Motor, *IEEE Trans. on Energy Conversion*, Vol. 18, NO. 2, June 2003.
- [4] Opera Version 7.1 User Guide, Vector Fields, 1999.
- [5] T. Nakata, N. Takahashi, K. Uehara.: Analysis of magnetic characteristic of brushless DC motor taking into account the distribution of magnetization, *IEEE Trans. on Magnetics*, Vol. 22, No.5, pp. 1084 – 1086, 1986.
- [6] M. Jagiela: Analysis of the operation of a disc-type brushless motor with co-axial magnetic flux in the stator (*Analiza pracy trojasmowego bezszczotkowego silnika tarczowego prądu stałego ze strumieniem osiowym w stojanie*) – in Polish, Ph.D. Dissertation, Technical University of Opole, 2002.
- [7] T. M. Jahns, W. L. Soong: Pulsating torque Minimization Techniques for Permanent Magnet AC Motor Drives – A Review, *IEEE Trans. on Ind. Elect.*, Vol. 43, No. 2 , pp. 321-330, 1996.
- [8] Łukaniszyn M., Jagiela M., Wróbel R.: Electromechanical Properties of A Disc-type Salient-pole Brushless DC Motor with Different Pole Numbers, *International Journal in Computations in Mathematics and Electrical Engineering COMPEL*, Emerald Press, 2003, Vol. 22, No. 2, 2003, pp. 285-303.

II-11. ANALYSIS OF MAGNETIZATION CHARACTERISTICS OF HTS BULK ROTOR IN A ROTATING MAGNETIC FIELD

Taketsune Nakamura, Hun-June Jung, Nobuyoshi Tanaka, Itsuya Muta and Kentaro Fukui

Department of Electrical Engineering, Graduate School of Engineering, Kyoto University,
Yoshida-Honmachi, Sakyo, Kyoto 606-8501, JAPAN, E-mail: tk_naka@kuee.kyoto-u.ac.jp

Abstract – Magnetization characteristics of Bi-2223 superconducting bulk disk in a rotating magnetic field are analyzed with the use of 3-D finite element method. The disk is utilized as a rotor for an axial-type superconducting motor. Power-law approximation as well as Kim model is introduced in order to express the constitutive relation between electric field vs. current density for the analysis. It is shown that the analysis results of the hysteresis loops agree semi-quantitatively with the measurements. The dependency of the applied field amplitude upon the magnetization characteristics and its relation to the standstill torque will also be discussed based on the analysis.

Introduction

High temperature superconducting (HTS) materials have potentials to the improvement of power density as well as efficiency in power devices. Especially, ‘‘bulk’’ shaped HTS has an advantage with respect to the fabrication of flexible shapes compared to other structures such as tape and film. Therefore, intensive and extensive studies on HTS bulk power application systems have been carried out worldwide. HTS bulk motor is surely one of such applications, and various types of HTS bulk motor have been fabricated and tested successfully [1-5]. Precise estimation of electromagnetic characteristics, on the other hand, is crucial for the design of the HTS power application systems. However, current density, J , vs. electric field, E , (J - E) property in HTS is varied non-linearly as a function of operating temperature and applied magnetic field vector, and then this relation induces the hysteretic behaviour of the magnetization curves in a rotating magnetic field.

In this study, magnetization characteristics of Bi-2223 superconducting disk, which is utilized for an axial-type motor, is analyzed in a rotating magnetic field based on the 3-D finite element method (3-D FEM). Power-law approximation (so-called n -value model) and Kim model are introduced for the J - E constitutive relations. Standstill torque is also calculated based on the 3-D FEM. Analysis results are to be compared with the experiments and discussed.

Analysis Method

Analysis Model and Governing Equation

The magnetic hysteresis curves of the Bi-2223 bulk rotor have been measured by using the fabricated motor system [6]. This means that the magnetic characteristics of the bulk, experienced as a

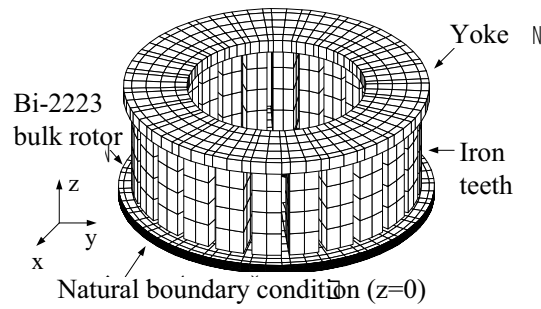


Fig. 1. 3D-FEM analysis model. Upper half of an axial-type motor system is modelled for symmetry, and natural boundary condition is set at the plane $z=0$, i.e., half of the thickness of Bi-2223 rotor.

solid rotor, can exactly be obtained. Then, the axial-type Bi-2223 bulk motor system is directly modelled for 3D-FEM analysis as shown in Fig. 1. This system consists of disk shaped Bi-2223 bulk rotor (120 mm in diameter and 7 mm in thickness), and the stator (116.4 mm in outer diameter, 71.4 mm in inner diameter and 41.4 mm in height) that has iron teeth with the number of 24. Iron yoke is also connected to the teeth in order to make magnetic path. The Bi-2223 rotor is sandwiched in between two stators that are connected in parallel each other. In this study, upper half of the system is only modelled because of the symmetry of the electromagnetic characteristics (see Fig. 1), and then natural boundary condition is set at the plane $z=0$, i.e., half of the thickness of Bi-2223 bulk rotor. The armature has 3-phase and 4-pole windings, and the corresponding rotating speed of magnetic field at 60 Hz is 1800 rpm in the experimental system. Instead of this winding, however, the forced magnetic flux density is applied to the iron teeth with phase difference at 30° for each of adjacent teeth in order to reproduce the same rotating field in the analysis. The relative permeability and conductivity of the iron are, respectively, set to be 1000 and $1 \times 10^5 \text{ Sm}^{-1}$ (effect of magnetic saturation is ignored).

The governing equation with respect to vector potential, \mathbf{A} , is expressed by assuming $\phi=0$ (ϕ : scalar potential) as follows:

$$\sigma \frac{\partial \mathbf{A}}{\partial t} + \nabla \times \left(\frac{1}{\mu_0} \nabla \times \mathbf{A} - \mathbf{M} \right) = 0 \quad (1)$$

where, σ and μ_0 denote the conductivity and permeability in vacuum, respectively. \mathbf{M} is magnetization. Eq. (1) is solved by commercialized FEM software (PHOTO series: MOTION, PHOTON Co., Ltd., Japan). Derivation of σ for HTS is explained in the following section.

Current Density vs. Electric field Relation

Constitutive J - E relation in HTS are generally non-linear and complicated in function depending on the operational conditions such as external magnetic field, and then the following power-law approximation (so-called n -value model) is introduced as follows:

$$|\mathbf{E}|(|\mathbf{J}|) = E_c \left(\frac{|\mathbf{J}|}{J_c} \right)^n, \text{ if } |\mathbf{E}| \neq 0 \quad (2)$$

$$\frac{\partial \mathbf{J}}{\partial t} = 0, \text{ if } |\mathbf{E}| = 0 \quad (3)$$

where, J_C is the critical current density defined with the electric field criterion of E_C . Parameter n denotes a power-law index describing the sharpness of the take-off of the J - E curves. Further, the magnetic field dependency of J_C is considered by Kim model as,

$$J_C(|\mathbf{B}|) = \frac{J_C(0)}{1 + \frac{|\mathbf{B}|}{B_0}} \quad (4)$$

A parameter B_0 denotes the effectiveness of the magnetic field dependency of J_C . By combining eqs. (2) and (4), magnetic field dependency of J - E curves can be expressed [7]. With the assumption that the direction of \mathbf{J} coincides with that of \mathbf{E} , J - E relation can be expressed as $\mathbf{J} = \sigma \mathbf{E}$ with the aid of conductivity, σ . Then, σ in HTS is derived by using eqs. (2) and (4) as follows:

$$\sigma = J_C(|\mathbf{B}|) \left[\frac{|\mathbf{E}|}{E_C} \right]^{\frac{1}{n}} \frac{1}{|\mathbf{E}|} \quad (5)$$

Results and Discussion

Hysteresis Loops in a Rotating Magnetic Field

In this section, all magnetization characteristics are estimated at the surface of the Bi-2223 bulk rotor. Fig. 2 shows the analysis results of the hysteresis loops in a rotating magnetic field at the speed of 1800 rpm. Operating temperature is 77.3 K, i.e., temperature of atmospheric liquid nitrogen. The

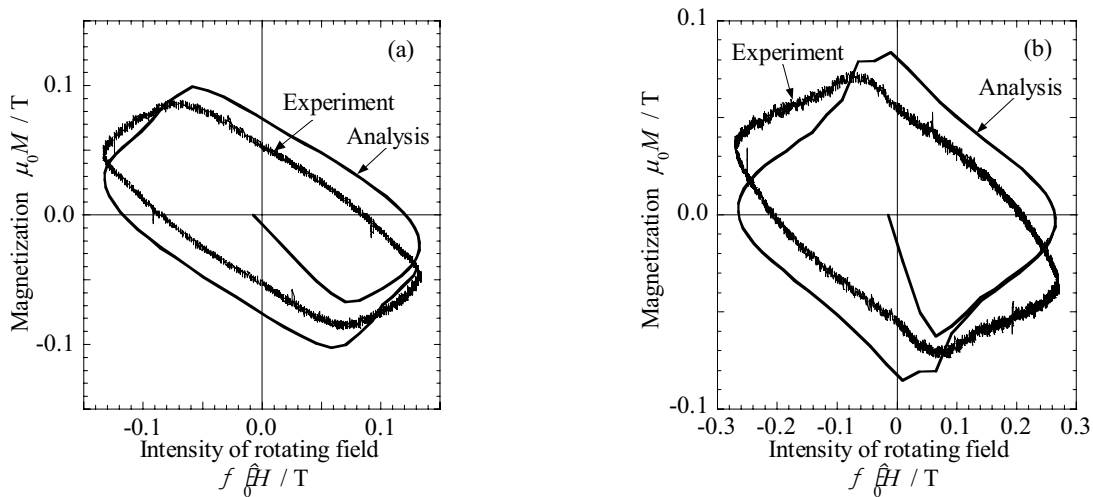


Fig. 2. Hysteresis loops at the surface of the Bi-2223 bulk rotor in a rotating magnetic field at 1800 rpm. The operating temperature is 77.3 K. The peak value of $\mu_0 H$, $\mu_0 H_{\text{peak}}$, are (a) 0.13 T and (b) 0.25 T, respectively.

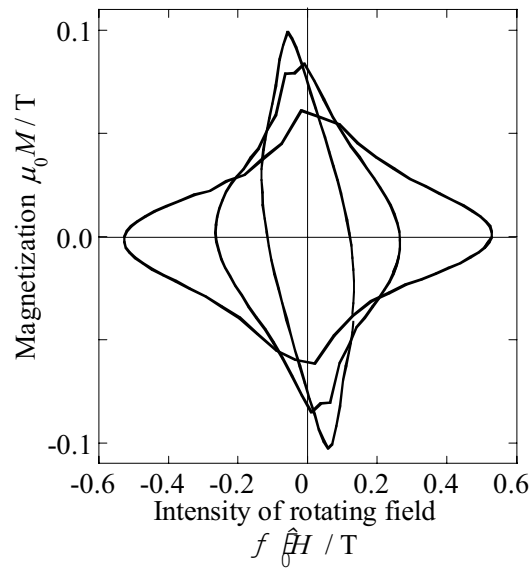
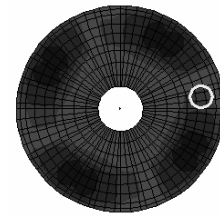
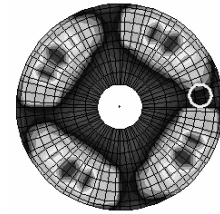


Fig. 3. Analysis results of the magnetization, $\mu_0 M$, for different amplitude of rotating magnetic field. Rotating speed of the field and the temperature are, respectively, 1800 rpm and 77.3 K.



(a) $\mu_0 H_{\text{peak}} = 0.13$ T



(b) $\mu_0 H_{\text{peak}} = 0.50$ T

Fig. 4. Contour plots of magnetic flux density at the surface of Bi-2223 bulk rotor obtained by 3-D FEM. The white areas denote the invasion of large magnetic flux. The circle shows the measured point of Fig. 3.

parameters in eqs. (2) and (4) are, respectively, $n = 5$, $J_C(0) = 4 \times 10^6 \text{ Am}^{-2}$, $E_C = 10^{-4} \text{ Vm}^{-1}$ and $B_0 = 0.02$ T, which are determined by fitting the measured data. As can be seen, shapes of the hysteresis loops vary complicatedly depending on the amplitude of the rotating magnetic field due to the non-linear J - E properties in Bi-2223 bulk rotor. The experimental results with the same conditions of analysis are also shown in the figures for comparison. In the experiments, the magnetization, $\mu_0 M (= B - \mu_0 H)$, is measured by transverse-type hall sensor that is directly installed in the air-gap of the motor system [6]. As shown, the analysis results agree semi-quantitatively with the experiments for both peak values of $\mu_0 H$, i.e., $\mu_0 H_{\text{peak}} =$ (a) 0.13 T and (b) 0.25 T.

Fig. 3 shows the magnetic field dependency of M at 77.3 K obtained by the analysis. It can be clearly seen in this figure that the peak value of $\mu_0 M$ is suppressed as the amplitude of the field increases. This peak reduction is often discussed by the joule heating in the Bi-2223 bulk, i.e., the superconducting properties are weakened by the application of the high magnetic field [8]. In this analysis, however, the thermal process is not considered. Namely, another explanation will be possible for the peak reduction of the hysteresis curves. Fig. 4 shows the contour plots of the magnetic flux density at the surface of the Bi-2223 bulk rotor. As shown, large fluxes (white areas) invade into the bulk rotor at higher magnetic field (Fig. 4 (b)). Then, the corresponding shielding current path is suppressed, and this leads to the peak reduction of hysteresis loops. As will be discussed in the following section, the area of the hysteresis loop is in proportion to the value of the standstill torque of the motor. Therefore, high magnetic field application results in the reduction of the torque generation.

Relationship Between Torque Generation and Hysteresis Curves

The standstill torque is calculated from the analysis results by using Maxwell's stress tensor. Fig. 5 (a) shows the calculated results that are plotted with double-logarithmic scale at 77.3 K. The areas of

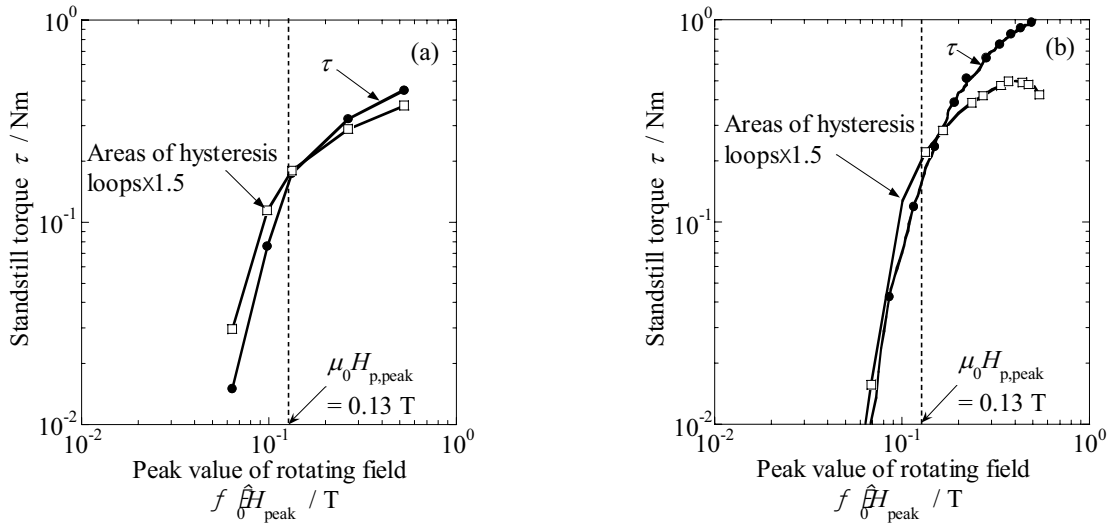


Fig. 5. Standstill torque, τ , vs. peak value of rotating magnetic field, $\mu_0 H_{p,peak}$, characteristics at 77.3 K. The areas of the hysteresis curves $\times 1.5$, are also plotted for comparison. (a) Analysis results, (b) Experimental results.

hysteresis loops $\times 1.5$ are also plotted in the same figure. As can be seen, the tendencies of both curves agree each other, and it can be deduced that the standstill torque is generated as a hysteresis one. It is interesting to note that the curvature of both curves changes at around $\mu_0 H_{p,peak} = 0.13$ T. The reason for this curvature variation can be explained as follows. That is, Fig. 6 shows the ratio of magnetic flux density between middle point, B_m , and surface, B_s , of the bulk rotor. These points for the calculation are schematically illustrated in the inset. When the Bi-2223 bulk is in the normal conducting state, the ratio B_m/B_s is a constant value without magnetic field amplitude dependency. The bulk is in the superconducting state, on the other hand, the ratio is almost zero at lower magnetic field due to the shielding effect of the Bi-2223 bulk rotor. However, even in case of the superconducting state, the magnetic flux is beginning to penetrate into the bulk by increasing the field, and finally fully invades at around $\mu_0 H_{p,peak} = 0.13$ T. Therefore, the value of $\mu_0 H_{p,peak}$ is called full penetration field, and is consistent with the point that the curvature of τ changes (see Fig. 5). The reason for the value that is less than 1 in the normal conducting state is due to the difference of the measuring points between B_m

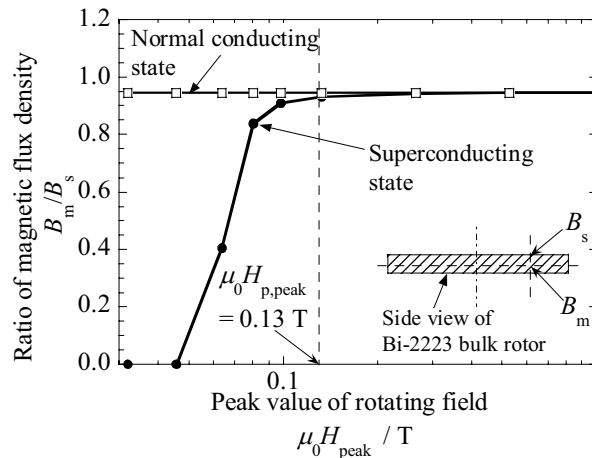


Fig. 6. Ratio of magnetic flux density between middle point, B_m , and surface, B_s , of the bulk rotor at normal conducting and superconducting state, respectively. Inset: Schematic illustration of measuring points.

and B_s . Experimental results with the same condition of Fig. 5 (a) are also shown in Fig. 5 (b). One can see that the agreement between the analysis and the experiment is fairly good, and the torque characteristics is possible to be explained by the aforementioned discussion.

Conclusion

In this paper, magnetization characteristics of superconducting Bi-2223 bulk, which was utilized for a solid rotor of an axial-type motor, were studied based on the 3-D finite element method (3-D FEM) taking into account the non-linear properties of J - E curves. It was shown that the analysis results of the hysteresis loops agreed semi-quantitatively with the experiments. It was also confirmed by the analysis that the mechanism of the torque generation was hysteresis properties of the bulk, which was induced by the shielding current. Furthermore, the peak reduction of the hysteresis curves by increasing the amplitude of the rotating magnetic field was due to the suppression of the shielding current path in the Bi-2223 bulk rotor, and this leads to the reduction of the torque generation.

Acknowledgements

This work has been supported by Fundamental Research Developing Association for Shipbuilding and Offshore (REDAS), the Ube foundation and Grant-in-Aid for Scientific Research (No. 13450113) from the Ministry of Education, Culture, Sports, Science and Technology in Japan. This work has also been carried out as a project of the 21st Century COE Program (No. 14213201) in Japan.

References

- [1] M.D. McCulloch, K. Jim, K. Kawai and D. Dew-Hughes, Prospects for brushless AC machines with HTS rotors, *Inst. Phys. Conf. Ser.*, No.158, pp 1519-1522, 1997
- [2] L.K. Kovalev, K.V. Ilushin, V.T. Penkin, K.L. Kovalev, S.M.-A Koneev, V.N. Poltavets, A.E. Larionoff, K.A. Modestov, S.A. Larionoff, W. Gawalek, T. Habisreuther, B. Oswald, K.-J Best and T. Straßer, Hysteresis and reluctance electric machines with bulk HTS elements. Recent results and future development, *Superconductor Science and Technology*, Vol.13, pp 498-502, 2000
- [3] I. Muta, H. J. Jung, T. Nakamura and T. Hoshino, Performance of axial-type motor with Bi-2223 HTS bulk rotor, *Physica C*, Vol. 372-375, pp 1535-1538, 2002
- [4] B. Oswald, M. Krone, T. Straßer, K.-J. Best, M. Söll, W. Gawalek, H.-J. Gutt, L. Kovalev, L. Fisher, G. Fuchs, G. Krabbes and H.C. Freyhardt, Design of HTS reluctance motors up to several hundred kW, *Physica C*, Vol. 372-376, pp 1513-1516, 2002
- [5] M. Hirakawa, S. Inadama, K. Kikukawa, E. Suzuki and T. Nakasima, Developments of superconducting motor with YBCO bulk magnets, *Physica C*, in press
- [6] T. Nakamura, H.J. Jung, K. Fukui, I. Muta and T. Hoshino, Electromagnetic characteristics of Bi-2223 disk in a rotating magnetic field, *Physica C*, in press
- [7] E.H. Brandt, Superconductor disks and cylinders in an axial magnetic field. I. Flux penetration and magnetization curves, *Physical Review B*, Vol. 58, No. 10, pp 6506-6522, 1998
- [8] J. Ogawa, M. Iwamoto, K. Yamagishi, O. Tsukamoto, M. Murakami and M. Tomita, Influence of AC external magnetic field perturbation on trapped magnetic field in HTS bulk, *Physica C*, Vol. 386, pp 26-30, 2003

II-12. EQUIVALENT CIRCUIT ANALYSIS OF POLE-CHANGE SINGLE-PHASE INDUCTION MOTOR CONSIDERING HARMONIC COMPONENTS

Hyuk Nam, Seung-Kyu Jung, and Jung-Pyo Hong, Senior Member, *IEEE*
Dept. of Electrical Eng., Changwon Nat'l Univ., Changwon, Gyeongnam, 641-773, Korea
haeggee@korea.com, namhyuk3@empal.com, jphong@sarim.changwon.ac.kr

Abstract – This paper deals with the characteristic analysis of a pole-change single-phase induction motor using equivalent circuit considering harmonic components, of the magnetic flux density in the air gap. The harmonics can have a significant detrimental effect on the characteristics of the machine such as crawling. Therefore, it is very important to analyze the accurate motor characteristics considering harmonics for many aspects related to the machine design and the performance. In this paper, the magnetic flux density distribution is analyzed by analytical method and Finite Element Method. Discrete Fourier Transform is used to analyze the harmonics and the characteristics are calculated from the equivalent circuit considering the harmonic components. Finally, The characteristic analysis results by the presented method is compared with the experimental results.

Introduction

Capacitor-run single-phase induction motors (SPIMs) are widely used in household appliances. The major reason is that the motors are fed directly from the commercial single-phase source without any control devices [1]. A pole-change SPIM in this paper is the capacitor-run SPIM that has two kinds of poles, 4-pole and 2-pole. Therefore, this motor is capable of variable speed operation and can expand the constant torque range using the pole change technique. In addition, it is maintenance-free and cheap in comparison with the motors such as 3-phase inverter motors and brushless DC motors, because it uses a pole change switch to change the speed without inverters or drives. Moreover, when the pole-change SPIM, which can have two outputs and speeds at the same torque using the commercial frequency, is used for the compressor of household appliances, it can improve the system efficiency of the compressor even though the efficiency of the motor itself is a little low. Therefore, the household appliances using the pole change SPIM is expected to be able to have more competitive power in cost and efficiency aspects than that using capacitor-run SPIMs and inverter-type motors.

The pole change SPIM in this paper is composed of a main winding, an auxiliary winding and a compensation winding. The main winding is used at both 4-pole and 2-pole. The auxiliary winding is used only for 4-pole, because it is started at 4-pole. When 4-pole is changed into 2-pole, the main winding is connected with the voltage source but the auxiliary winding is disconnected. At this time, the magnetic flux density distribution by only the main winding can result in severe distortion caused by harmonic components. The existence of harmonics is well known to have a significant detrimental effect on the characteristics of the machine such as crawling [2]. Therefore, to compensate both the magnetic flux density and the torque such as negative torque, the compensation winding is connected in parallel with the main winding at 2-pole operation. However, in spite of the compensation winding, speed-torque curve can be distorted by harmonic components, especially, the third and the fifth harmonics. Therefore, it is very important to calculate the magnetic flux density distribution in the air gap and analyze the characteristics of the pole change SPIM considering the harmonic components for many aspects related to the machine design and the performance.

This paper deals with the characteristic analysis of the pole-change SPIM using equivalent circuit considering harmonic components of the magnetic flux density in the air gap. The magnetic flux density distribution is analyzed by analytical method and Finite Element Method (FEM). Discrete

Fourier Transformation (DFT) is used to analyze the harmonics in the magnetic flux density distribution and the harmonics are applied to calculate the characteristics using the equivalent circuit. Finally, the characteristic analysis results by the presented method are compared with the experimental results.

Pole-Change Technique

Fig. 1 shows the winding patterns at 4-pole and 2-pole operations. When pole is changed from 4-pole to 2-pole, pole N' and pole S' of the main winding in Fig. 1(a) are changed into pole S'' and pole N'' in Fig 1(b), respectively. The auxiliary winding is disconnected and the compensation winding is connected in parallel with the main winding instead of the auxiliary winding as shown in Fig. 1(c).

Fig. 2 shows the magnetic flux density distribution by FEM, DFT of the magnetic flux density distribution and the speed-torque curves, which are obtained from the experimental results according to the existence of the compensation winding. 90 deg. of rotor position in Fig. 2(a) corresponds to the pole center at 2-pole.

In Fig. 2(a) and (b), the unbalanced 6-pole of N-S-N-S-N-S occurs due to the harmonic components such as the third and the fifth order at 2-pole operation with only the main winding. As the result, the third harmonic component synchronizes the speed near 1,200 rpm, and the speed-torque curve is distorted and generates the negative torque, which is larger than the positive torque as shown in Fig. 2(c). Thus, the compensation winding is wound to compensate both the magnetic flux density distribution and torques such as the negative torque and the maximum torque at 2-pole.

As shown in Fig. 2, the magnetic flux density distribution of 6-pole is changed into that of 2-pole by the compensation winding, and the harmonic components as well as the negative torque are reduced. However, in spite of the compensation winding, the distortion of the speed-torque curve can be still produced. Therefore, it is very important to calculate the magnetic flux density distribution in the air gap and analyze the characteristics of the pole change SPIM considering the harmonic components.

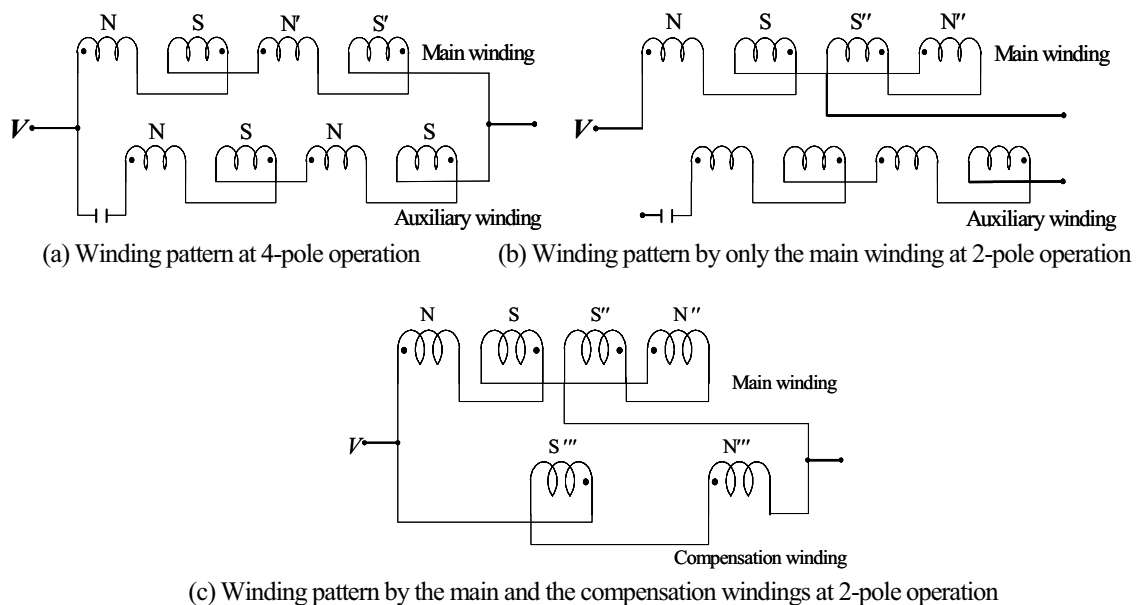


Fig. 1. Winding pattern according to the pole number

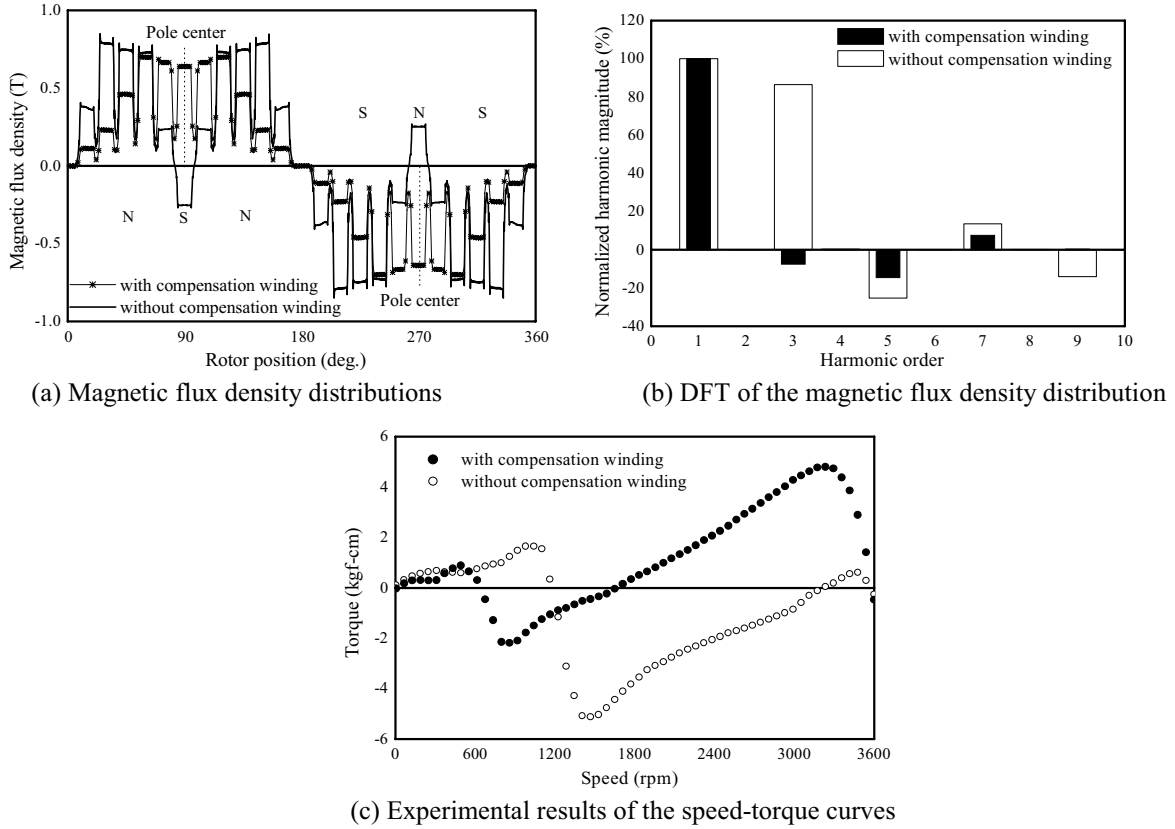


Fig. 2. Characteristics according to the compensation winding at 2-pole operation

Analysis Methods

Magnetic Flux Density in the Air Gap and DFT

The magnetic flux density distribution by analytical method is calculated as follows. To avoid unnecessary mathematical complexity, certain simplifying assumption is made. The main simplifying condition is the assumption of the infinite relative permeability of iron ($\mu_r = \infty$). It is assumed that the motor consists of two smooth coaxial cylinders made of a magnetic material and the cylinders are separated by the air gap in Fig. 3.

The magnetic flux density produced by an arbitrary system of conductors in the air gap is obtained by the superposition of the field densities of the individual conductors. The magnetic flux density $B(\alpha)$ of the individual turns at any point P having the coordinate α is obtained by using equation (1) [3].

$$B(\alpha) = \frac{\mu_0 C_\theta i}{\pi \delta} \sum_{n=1}^{\infty} \frac{1}{n} \sin n(\alpha - \theta) \quad (1)$$

where n is the harmonic order, C_θ is the number of conductors that are placed at the position θ and δ is the magnetic air gap.

DFT for the harmonic analysis of the magnetic flux density distribution can be expressed as equation (2).

$$a_n = \frac{2}{Num} \sum_{i=0}^{Num} b_i \sin \left(\frac{2\pi ni}{Num} \right) \quad (2)$$

where a_n is the n-th harmonic magnitude of the magnetic flux density, Num is the number of data and b_i is the magnetic flux density magnitude at each data. The ratio of the fundamental magnitude to the harmonic magnitude a_n/a_1 is used to obtain magnetizing reactances and secondary parameters of the n-th harmonic [4].

Characteristic Analysis Methods

The pole change SPIM at 4-pole operation is analyzed from the equivalent circuit by the symmetrical-coordinate system, as shown in Fig. 4, in order to consider the elliptical magnetic field. The main and the auxiliary windings are designed for 4-pole and there are few harmonics in the magnetic flux density distribution. Thus, the equivalent circuit is composed of the fundamental component.

On the other hand, the harmonics should be considered at 2-pole, because the 2-pole characteristics affected by the harmonic.

Fig. 5, as suggested by Alger and others, shows the equivalent circuit considering the harmonic components for the characteristic analysis at 2-pole operation [5]. It is a useful concept to visualize the electromagnetic behavior of the various space harmonic as being similar to the behavior of separate motors, with a common stator winding and a common shaft, but with magnetizing reactances and secondary impedances corresponding respectively to the air gap flux wave of each specific harmonic. Therefore, the effect of the various harmonic torques on the fundamental speed-torque curves can be evaluated from the equivalent circuit. The phase quantities V_1, R_1, R_2, X_2 and X_M of the circuit are identical to those of the standard equivalent circuit, such as that shown in Fig. 5. The magnetizing reactance of each of the harmonics, such as X_{M-5} , is based on the component of air gap flux of that particular harmonic. In addition, the slip function of R_{2-n} for each harmonic is set up for the rotor slip for that particular harmonic and is dependent on the order of the harmonic and on whether the harmonic field is positive (or forward) rotating or negative (or backward) rotating.

Thus, the n-th slip function can be expressed as equation (3) if it is a forward rotating field and it can be expressed as equation (4) if it is a backward rotating field [5].

$$s_{pn} = 1 - n(1 - s) \tag{3}$$

$$s_{nn} = 1 + n(1 - s) \tag{4}$$

where n is the order of the harmonic, s is the slip of the fundamental component. Considering the fundamental component as a harmonic of the first order, the harmonic order of the pole change SPIM consists of odd terms only.

Fig. 6 shows the flow chart for the characteristic analysis at 2-pole operation. The phases of the main and the compensation windings are same. Therefore, the mutual effect on the two windings should be considered. Moreover, the characteristics of each winding are calculated by using the equivalent circuit of Fig. 6, respectively. The total torque can be obtained from superposition of the torques by the main and the compensation windings according to slip.

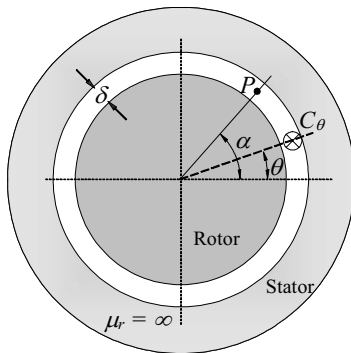


Fig. 3. Illustration relating to the calculation of the field of conductors

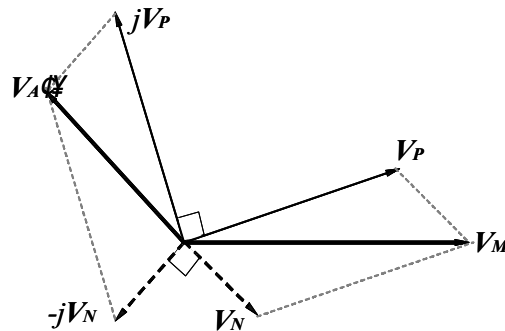


Fig. 4. Symmetrical-coordinate system

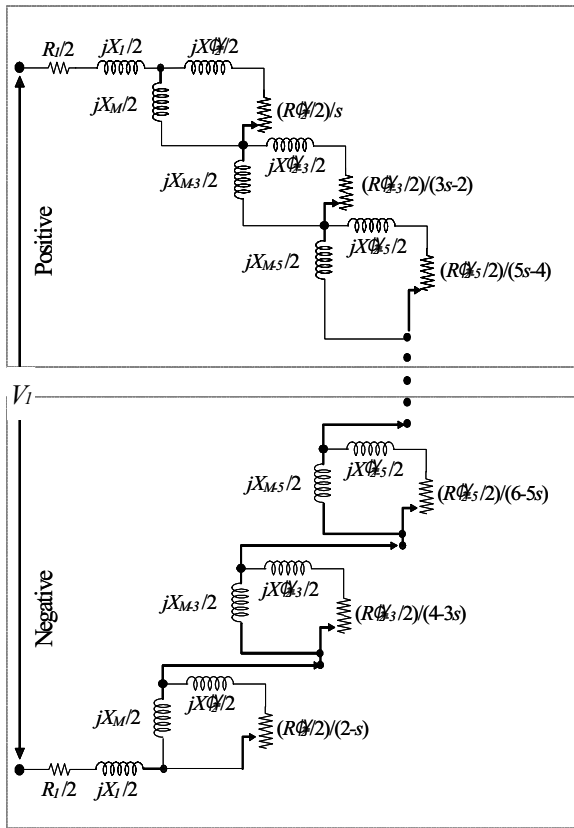


Fig. 5. Equivalent circuit considering the harmonics

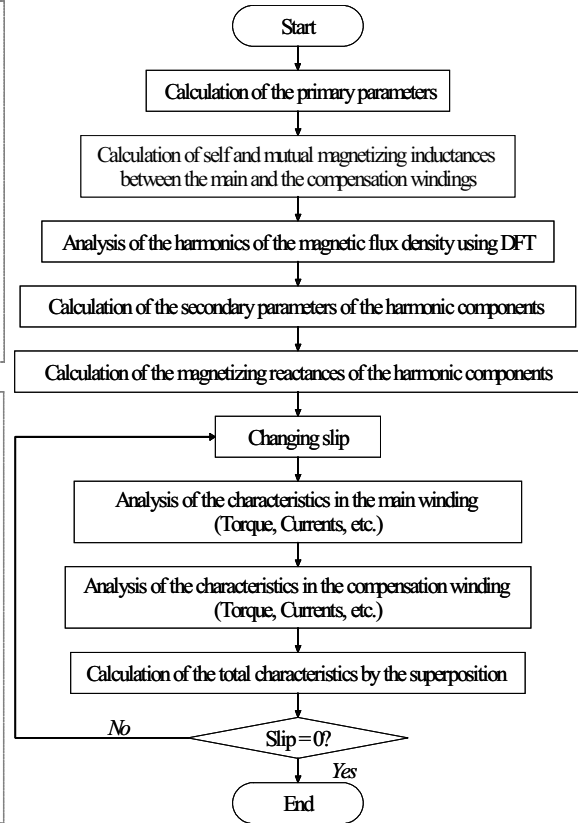


Fig. 6. Flow chart for the characteristic analysis

Analysis and Experimental Results

To verify the presented analysis method in this paper, the characteristics are analyzed using the analysis model of which the specifications is input voltage of 220 V, frequency of 60 Hz and rated torque of 4.4 kgf-cm. While output power and synchronous speed are 160 W and 3,600 rpm at 2-pole operation, those of 4-pole operation are 80 W and 1,800 rpm, respectively.

Fig. 7(a) shows the magnetic flux density distribution in the air gap using the analytical method in comparison with the FEM. The effect on the saturation can be considered by the FEM, but not by the analytical method. Therefore, the difference between the harmonic analysis results by two methods occurs as shown in Table. 1. As the results, the speed-torque curve of the analysis model by the experimental result is affected by the fifth order harmonic component, while that of the analysis model by the simulation result is more affected by the third order harmonic component than the fifth order harmonic component as shown in Fig 7(b). Even though the speed-torque curve of the analysis result differs from that of the experimental result, the analysis results by the presented method show the effect of the harmonics and the important torques such as the pole change torque and the maximum torque at 2-pole can be estimated. Thus, this presented method is used for the characteristic analysis.

Table 1. Harmonic analysis results

Harmonic order	Analytical method (%)	FEM (%)
1	100.0	100.0
3	-17.6	-7.5
5	-7.3	-14.5
7	4.0	7.5

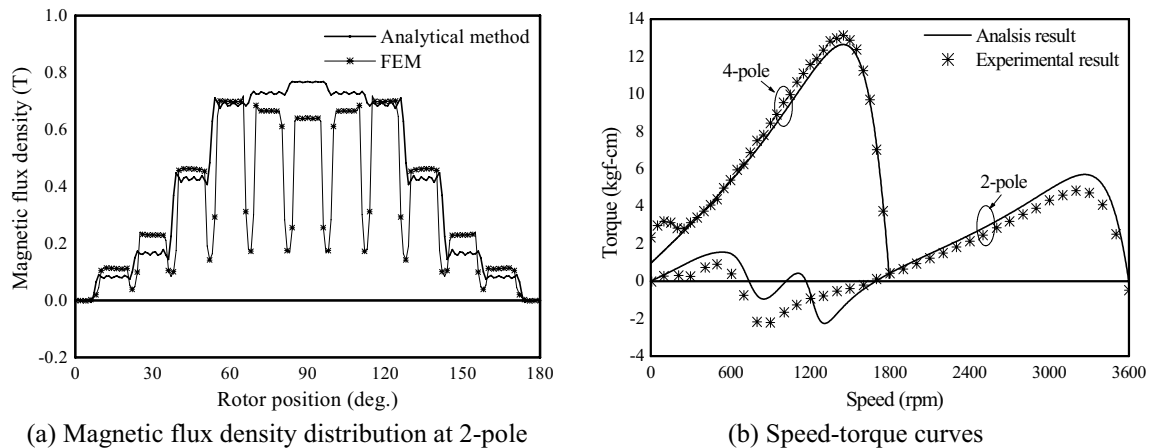


Fig. 7. Characteristic analysis results of the analysis model

Conclusion

This paper presents the characteristic analysis using the equivalent circuit considering the harmonic components of the pole change SPIM. The harmonic analysis results of the magnetic flux density distribution in the air gap are used to calculate the parameters of the harmonic equivalent circuit. The analysis results by the presented analysis method are compared with the experimental results. From the characteristic analysis results, it is confirmed that the speed-torque curve is distorted by the harmonic components, especially, the third and the fifth harmonics, contained in the magnetic flux density distribution. Therefore, there is need to design the windings in order to reduce the harmonics and obtain torques such as pole change torque and breakdown torque at 2-pole operation.

References

- [1] H. Nam, K. H. Ha, J. J. Lee, J. P. Hong, and G. H. Kang, "A study on iron loss analysis method considering the harmonics of the flux density waveform using iron loss curves tested on Epstein samples," *IEEE Trans. Magn.*, Vol. 39, No. 3, pp. 1472-1475, May 2003.
- [2] H.A. Toliyat, and N. Sargolzaei, "A Comprehensive Method for Transient Modeling of Single Phase Induction Motors Including the Space Harmonics," *Journal of Electric Machines and Power Systems*, Vol. 26, No. 3, pp. 221-234, 1998.
- [3] B. Heller and V. Hamata, *Harmonic Field Effects in Induction Machines*, Academia, Publishing House of the Czechoslovak Academy of Sciences, 1977.
- [4] C. G. Veinott, *Theory and Design of Small Induction Motors*, McGRAW HILL, 1959.
- [5] P. L. Cochran, *Polyphase Induction Motors, Analysis, Design, and Application*, Marcel Dekker, Inc., 1989.

II-13. THE 3D DYNAMIC SIMULATION OF THE INVERTER FED ELECTROMECHANICAL ACTUATORS INCLUDING EDDY CURRENTS

Lech Nowak

Poznań University of Technology, Institute of Industrial electrical Engineering
ul. Piotrowo 3a, 60-965 Poznań, Poland, lech.nowak@put.poznan.pl

Abstract – The paper deals with a transient and dynamic simulation of the linear actuator supplied with the three-phase inverter. The 3D field model of the device has been applied. In order to solve three-dimensional eddy current problem a formulation based on two vector potentials \mathbf{A} and \mathbf{T} has been proposed. The equations describing transient electromagnetic field have been coupled to the Kirchhoff's equations of the electric circuits of the device and to the equations of the supply system. The movement of the conducting non-ferromagnetic parts has been taken into account.

Introduction

The inverters are often used for the electromechanical three-phase converters supply. The inverter switching on and switching off processes cause permanently transient states. Consequently, the time-variations of the exciting currents in the windings are not known in advance. Thus, the equations describing transient electromagnetic field must be coupled to the Kirchhoff's equations of the device and the feed system. During the dynamic operation, the equation of the motion must be also included.

If the electromagnetic device contains solid conducting parts, then its equivalent resistances and inductances vary during the transient states. Additionally, when the movement is considered, then the time-varying electromotive force E is generated. The behaviour of the system strongly depends on the relations between the actual values of the parameters $R(t)$, $L(t)$, $E(t)$. These parameters have significant influence on the backward diode conduction angles and consequently they determine the shape and value of the output inverter voltage waveforms. Thus, the accuracy of determination of the parameters R , L , E is very important. Therefore, the **three-dimensional** field model is required.

3D Eddy Current Formulation

Different approaches are used to describe the 3D electromagnetic field in conducting regions [1,2,3,6]. The most commonly used formulations are $\mathbf{A}-V$ or $\mathbf{T}-\Omega$ formulations, where \mathbf{A} and \mathbf{T} are the magnetic and electric vector potentials, respectively, Ω and V are the magnetic and electric scalar potentials. Unfortunately, the pairs of potentials \mathbf{A}, V and \mathbf{T}, Ω are not described uniquely [1,2]. This is the essential disadvantage of these formulations. Therefore, in this paper a formulation based on two vector potentials \mathbf{A} and \mathbf{T} has been proposed [3,4]. The *magnetic* field is described in terms of the magnetic vector potential in the whole considered region D . The *electric* vector potential \mathbf{T} is computed only in conducting area D_e , which usually is relatively small in comparison to D .

The magnetic vector potential \mathbf{A} and electric vector potential \mathbf{T} are introduced by putting $\mathbf{B} = \text{curl } \mathbf{A}$ and $\mathbf{J} = \text{curl } \mathbf{T}$. Taking the constitutive properties: $\mathbf{H} = \nu \mathbf{B}$, $\mathbf{J} = \sigma \mathbf{E}$, the Ampere's law $\text{curl } \mathbf{H} = \mathbf{J}$ and Faraday's law $\text{curl } \mathbf{E} = -\partial \mathbf{B} / \partial t$ may be written in the following form:

$$\text{curl } \nu \text{ curl } \mathbf{A} = \text{curl } \mathbf{T} \quad (1)$$

$$\text{curl } \sigma^{-1} \text{ curl } \mathbf{T} = -\text{d}(\text{curl } \mathbf{A})/\text{d}t \quad (2)$$

where: ν, σ are the reluctivity and conductivity, respectively.

The A - T approach is very advantageous in movement modelling. In case of non-ferromagnetic moving bodies, the matrix of the FEM equations describing the distribution of magnetic potential \mathbf{A} , which is the largest one, remains unchanged during the successive time steps.

The Combined Field-Circuit Model

Numerical implementation of the algorithm is based on the finite element method. The FEM representation of (1) and (2) for the conducting solid area can be represented in the form [4]:

$$\mathbf{S}_\nu \mathbf{A} = \mathbf{Q} \mathbf{T} \quad (3)$$

$$\mathbf{S}_\sigma \mathbf{T} = \mathbf{Q}^T d\mathbf{A}/dt \quad (4)$$

In order to solve transient problem, the time-stepping Crank-Nicholson algorithm has been applied. After including field sources due to the filamentary coil, the global system of the FEM equations for the n -th time step may be written in the following matrix form [4]

$$\begin{bmatrix} \mathbf{S}_\nu & -\mathbf{Q} \\ -\mathbf{Q}^T & -0.5\Delta t \mathbf{S}_\sigma \end{bmatrix} \cdot \begin{bmatrix} \mathbf{A}_n \\ \mathbf{T}_n \end{bmatrix} = \begin{bmatrix} \mathbf{V}_c N_c i_n \\ -\mathbf{Q}^T \tilde{\mathbf{A}}_{n-1} \end{bmatrix}, \quad (5)$$

where: i is the coil current, N_c is the coil "turn density", \mathbf{V}_c is the vector of elementary volume cells within the coil, $\tilde{\mathbf{A}}_{n-1} = \mathbf{A}_{n-1} + 0.5\Delta t (d\mathbf{A}/dt)_{n-1}$.

The flux linked with a winding composed of filaments can be written in the form: $\psi = N_c \mathbf{V}_c^T \mathbf{A}$. If number of windings $n_c > 1$, then the vector \mathbf{V}_c should be replaced with matrix \mathbf{V} composed of n_c columns \mathbf{V}_c . Then, the system of Kirchhoff's equations takes the form

$$2\mathbf{N}^T \mathbf{V}^T (\mathbf{A}_n - \tilde{\mathbf{A}}_{n-1}) / \Delta t + \mathbf{R} \mathbf{i}_n = \mathbf{u}_n \quad (6)$$

where \mathbf{N} is the diagonal matrix composed of winding turn densities, $\mathbf{i}_n, \mathbf{u}_n$ are the vectors of currents and voltages, respectively.

After branch connection into n_l independent circuit loops, a system of n_l equations is obtained

$$2\mathbf{K}^T \mathbf{N}^T \mathbf{V}^T (\mathbf{A}_n - \tilde{\mathbf{A}}_{n-1}) / \Delta t + \mathbf{K}^T \mathbf{R} \mathbf{K} \mathbf{i}_l = \mathbf{u}_l \quad (7)$$

where: $\mathbf{i}_l, \mathbf{u}_l$ are the loop currents and voltages respectively and \mathbf{K} is the incidence matrix describing the connections of branches, such that $\mathbf{i} = \mathbf{K} \mathbf{i}_l$; $\mathbf{u}_l = \mathbf{K}^T \mathbf{u}$.

The global system of the field-circuit equations for the n -th time step can be written as follows

$$\begin{bmatrix} \mathbf{S}_\nu & -\mathbf{Q} & -\mathbf{V} \mathbf{N} \mathbf{K} \\ -\mathbf{Q}^T & -0.5\Delta t \mathbf{S}_\sigma & \mathbf{0} \\ \mathbf{K}^T \mathbf{V}^T \mathbf{N}^T & \mathbf{0} & 0.5\Delta t \mathbf{R}' \end{bmatrix} \cdot \begin{bmatrix} \mathbf{A}_n \\ \mathbf{T}_n \\ \mathbf{i}_l \end{bmatrix} = \begin{bmatrix} \mathbf{0} \\ -\mathbf{Q}^T \tilde{\mathbf{A}}_{n-1} \\ \mathbf{F}_n \end{bmatrix} \quad (8)$$

where $\mathbf{R}' = \mathbf{K}^T \mathbf{R} \mathbf{K}$, $\mathbf{F}_n = 0.5\Delta t \mathbf{K}^T \mathbf{u}_l + \mathbf{K}^T \mathbf{N}^T \mathbf{V}^T \tilde{\mathbf{A}}_{n-1}$.

The Movement Modelling

The electromagnetic field in conducting *moving* medium may be described in term of potentials A and T as follows [5]:

$$\text{curl } \nu \text{ curl } \mathbf{A} = \text{rot } \mathbf{T} \quad (9)$$

$$\text{curl } \sigma^{-1} \text{ curl } \mathbf{T} = -\text{curl}(\partial \mathbf{A} / \partial t) + \text{curl}(\mathbf{v} \times \text{curl } \mathbf{A}) \quad (10)$$

In equation (10) additional term proportional to the velocity \mathbf{v} occurs. If the converter has only one degree of mechanical freedom, the velocity can be considered as a scalar quantity. Let $\mathbf{v} = \mathbf{1}_x v_x$. Then the system of the FEM equations corresponding to (10) may be written in the form [5]:

$$\mathbf{S}_\sigma \mathbf{T} = \mathbf{Q}^T \frac{d\mathbf{A}}{dt} + v_x \mathbf{C}\mathbf{A} \quad (11)$$

In case of non-ferromagnetic moving body, the matrix \mathbf{S}_v in (3) remains unchanged in successive time steps. This is the most important advantage of the \mathbf{A} - \mathbf{T} formulation.

A special procedure for the moving problem has been elaborated [5]. It is proposed to calculate the derivative $d\mathbf{A}/dt$ in a fixed point $Q_i = Q_i(x_i, y_i, z_i)$ of the moving region D_e according to the formula:

$$\left. \frac{d\mathbf{A}}{dt} \right|_{Q_i, t_n} \cong \frac{\mathbf{A}_n(x_i, y_i, z_i) - \mathbf{A}_{n-1}(x_i - \Delta\xi_n, y_i, z_i)}{\Delta t} \quad (12)$$

where $\Delta\xi_n$ is the displacement during the period $\Delta t = t_n - t_{n-1}$.

The point $(x_i - \Delta\xi_n, y_i, z_i)$ determines the previous position of the moving body volume cell, which at the n -th time-step overlaps the node (x_i, y_i, z_i) . Expression (12) includes, at the same time, both terms occurring in the right-hand side of (10).

According to (12), system (5) of the FEM equations of the \mathbf{A} - \mathbf{T} formulation can be written as:

$$\begin{bmatrix} \mathbf{S} & -\mathbf{Q} \\ -\mathbf{Q}^T & -\Delta t \mathbf{S}_\sigma \end{bmatrix} \cdot \begin{bmatrix} \mathbf{A}_n \\ \mathbf{T}_n \end{bmatrix} = \begin{bmatrix} N_c \mathbf{V}_c i_n \\ -\mathbf{Q}^T \mathbf{\Gamma} \mathbf{A}_{n-1} \end{bmatrix} \quad (13)$$

The matrix $\mathbf{\Gamma}$ in (13) enables linear interpolation of function $A(x)$ between two nodes. It is necessary because the point $(x_i - \Delta\xi_n, y_i, z_i)$ in (12) usually does not overlap any node.

The dynamic response of the linear induction motor, after the application of ac supply voltage (i.e. start-up operation) is presented in Fig. 1. The time variation of the propulsion force $F(t)$, displacement $\xi(t)$ and velocity $v_x(t)$ related to their maximum values for the initial 10 periods are given.

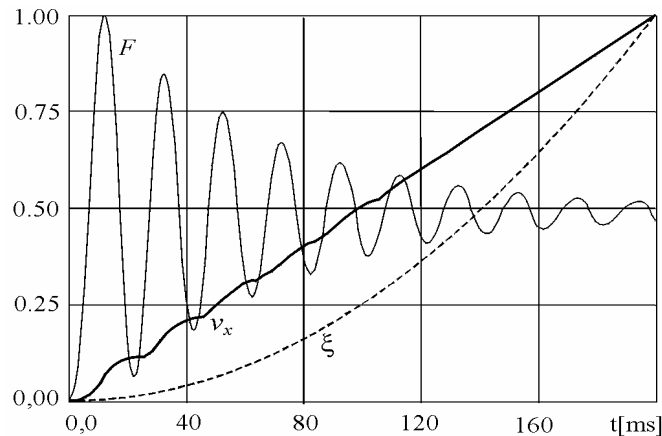


Fig. 1. The dynamic response of the linear motor

Inverter Fed Linear Motor

Inverter fed linear induction motor (Fig. 2) has been considered. The ideal characteristics of the semiconductors have been assumed, i.e. their resistances are equal to zero or are infinite and change without any delays. The incidence matrix in (8) varies: $\mathbf{K} = \mathbf{K}(s)$, where $s = 1, 2, \dots, n_s$ is the number of the inverter step. Total number of steps n_s depends on the conducting angle β . In case of $\beta = \pi$ there are 6 steps. The changes of the circuit structure may be described as follows

$$[\mathbf{U}_D \quad 0]^T = \mathbf{K}_2^T(s) [u_1 \quad u_2 \quad u_3]^T \quad (14)$$

where U_D is the d.c. supply voltage, u_1, u_2, u_3 , are the output phase voltages. Matrix \mathbf{K}_2 has 3 rows and 2 columns; its elements are equal to: -1, 0, 1. For $\beta \in (2/3\pi, \pi)$ there are 12 inverter steps. For odd steps the structure is described by (14). For even steps, the equation is: $U_D = \mathbf{K}_1^T(s)[u_1 \ u_2 \ u_3]^T$, where \mathbf{K}_1 is the one-column matrix. The computation were made for the period $t \in (0, 60 \text{ ms})$, taking $\beta = \pi$. The time variations of transient phase currents $i_1(t), i_2(t), i_3(t)$ are shown in Fig. 3. The d.c. decaying components of currents can be observed.

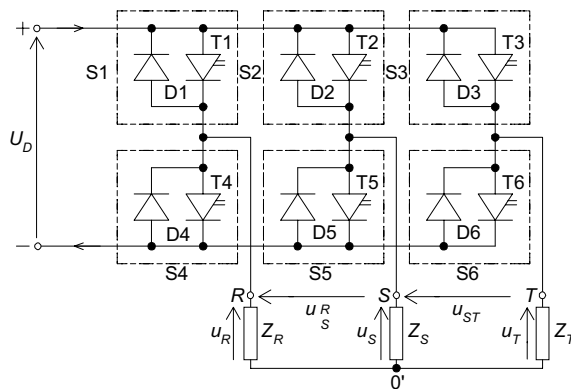


Fig. 2. Three-phase voltage inverter

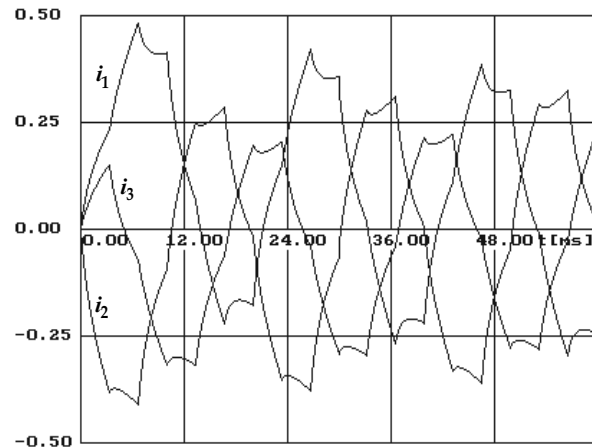


Fig.3. Time variations of phase currents (in Amperes)

References

- [1] R. Albanese, R. Rubinacci, Formulation of the eddy-current problem, IEE Proceeding, Part A, Vol. 137, No. 1, pp. 16-21, 1990.
- [2] Biro O., Preis K., Renhart W., Richter K.R., Virsk G., (1990), "Performance of different vector potential formulations in solving multiply connected 3-dimensional eddy current problems", IEEE Transactions on Magnetics, Vol. 26, No. 2, pp. 438-441.
- [3] Henneberger G., Dappen S., Albertz D., (1996), "Calculation of the 3D non-linear eddy current field in moving conductors and its application to braking systems", IEEE Trans. Magn., Vol. 32, No. 3, pp. 768-771.
- [4] Nowak L. The iterative procedure for 3D eddy current transient problem, COMPEL, MCB University Press, Vol.19, No.2, 2000, s.317-322.
- [5] Nowak L. Demenko A. The 3D Coupled Field-Circuit Simulation of Transients in converters with conducting solid parts, IEEE Transactions on Magnetics, Vol.36, No.4, July 2000, s.1412-1415.
- [6] Trowbridge C.W., (1988), "Status of 3D Electromagnetic Field Computation", Proc. BISEF'88, pp. 3-8, 1988.

II-14. AN OPTIMAL DETERMINATION OF STRANDED WIRES USED IN WINDINGS OF SWITCHED MODE POWER TRANSFORMERS

France Pavlovčič¹, Konrad Lenasi², Janez Nastran²

¹ Ministry of Environment, Spatial Planning and Energy, Environmental Agency of Slovenia, Vojkova 1b, SI-1000 Ljubljana, Slovenia, france.pavlovic@gov.si

² University of Ljubljana, Faculty of Electrical Engineering, Tržaška 25, SI-1000 Ljubljana, Slovenia, konrad.lenasi@fe.uni-lj.si, janko.nastran@fe.uni-lj.si

Abstract – The paper deals with the optimisation method of the winding conductors considering the designed transformer parameters, the skin and proximity effect and the usage of the rounded enamelled copper wires in stranded structure, as well as in the filled cross-section structure. On the principles of this optimisation method the software for designing switched mode power transformers up to 1 kW on ferrite cores operating on frequencies of 10 to 300 kHz is also made, to be running on the personal computer.

Introduction

Switched mode power transformers are designed according to their further usage in various types of switched mode power supplies. Mains operated switched mode power supplies are AC/DC converters operating in a feed forward or a fly back mode. The feed forward converters could be single phase, push-pull or bridge converters. The fly back converters are single phase only [1]. The selected type of a converter, the designed transformer would be built in, is a basic datum in a designing process of the transformer. A permitted overheating temperature due to a maximal operating ambient temperature and a thermal resistance between transformer and external medium under operating condition defines a dissipating power and therefore a continuous transferring power of the transformer [2]. The dissipating power must be balance over windings and a ferrite core [3,4]. In this way basic parameters of the transformer are achieved. The parameters of our further concern are real components of impedances due to power losses in copper of windings at a maximal operating temperature, which is a sum of the overheating temperature and the maximal operating ambient temperature. These real components are the maximal allowable values of AC resistances at an operating frequency, and not merely DC resistances. This means that the increasing parts of the resistances due to the skin and the proximity effect are included. According to technical data of ferrite materials, cores and accessories [2,5,6] there was created database and appropriate software to optimise the AC resistances of the designed transformer.

The skin and the proximity effect

It is impossible to distinct between influences of the skin effect and those of the proximity effect, because the windings are current loops with extremely small distances between conductors [7]. But it is proper to take into account two types of windings, when researching quantification problem of the skin and the proximity effect, and these types are one layer and multilayer windings. The research has been carried out on the windings of one layer of rounded enamelled copper wires. Taking into account an exponential distribution [8] of a current density over a cross-section of the conductor, we calculate an effective depth of a penetration of the current into the conductor.

Measurements of the resistances of various windings, having one layer of a rounded enamelled copper wire of various dimensions, have been carried out over the frequency interval from 10 kHz to 1 MHz, and the results have been statistically analysed, and the effective depths have been calculated. The ef-

fective depth (δ) is dependent upon the operating frequency (f), but is not a function of dimensions of the cross-section of the conductor and for copper it is (eq. 1):

$$\delta = \frac{2.05}{f^{0.65}} \quad (1)$$

There are very small deviations of values of the effective depth using the experimental equation (eq. 1), comparing to the values using the equation stated in literature [8].

Windings of filled rounded copper wires

Further on the influence of the skin and the proximity effect on the increasing resistance is quantified by a coefficient of the AC resistance, which is obtained by a mathematical analysis of measured data as a quotient of the AC resistance and the DC resistance of a respective winding:

$$k_f = \frac{R_{ac}}{R_{dc}} = \frac{0.5 \cdot \left(\frac{d}{2 \cdot \delta}\right)^2}{\frac{d}{2 \cdot \delta} - \left(1 - e^{-\frac{d}{2 \cdot \delta}}\right)} \quad (2)$$

This coefficient of the AC resistance is a very powerful tool in designing the transformer and it is dependent on the operating frequency (eq. 1) and on the conductor dimensions (eq. 2: d means the diameter of the wire copper cross-section), cross-section shape and structure. The AC resistance is calculated as a product of this coefficient and the DC resistance of the filled rounded copper wires, which could be simply determined by the diameters of their conductor and the coil they are wound on, and so defining their length (fig. 1).

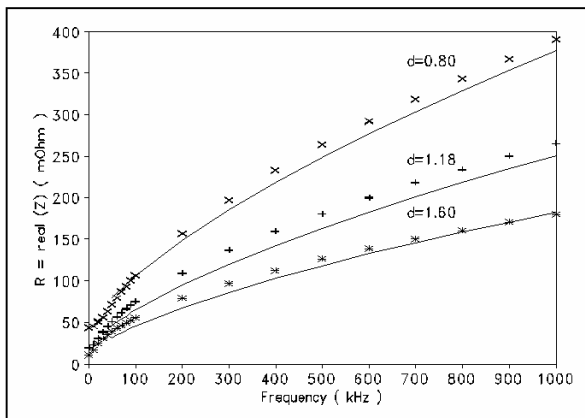


Fig. 1: The real component of resistance of filled rounded wires of the same length depending on the frequency at several diameters of conductors.

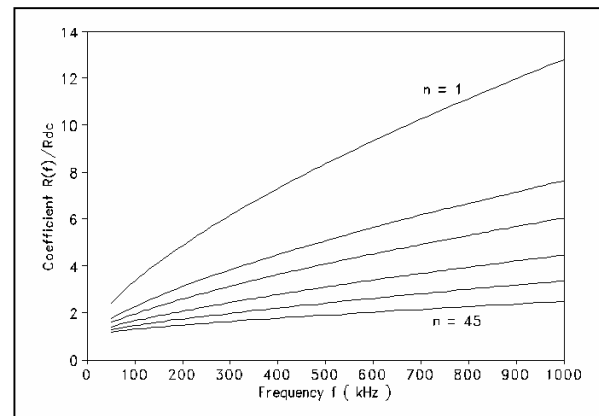


Fig. 2: The coefficient of resistance of stranded rounded wires depending on the frequency at several numbers of stranded wires.

The measured data are also on this figure, represented by points, so that the comparison between calculated and measured values could be made.

Windings of stranded rounded copper wires

When using stranded wires [9,10,11] the influence of the skin and the proximity effect is diminished. The reduction of the AC resistance is seen on diagrams of the coefficient of the AC resistance as a function of the frequency (fig. 2), and further on as a function of a number of wires in the strand (fig. 3).

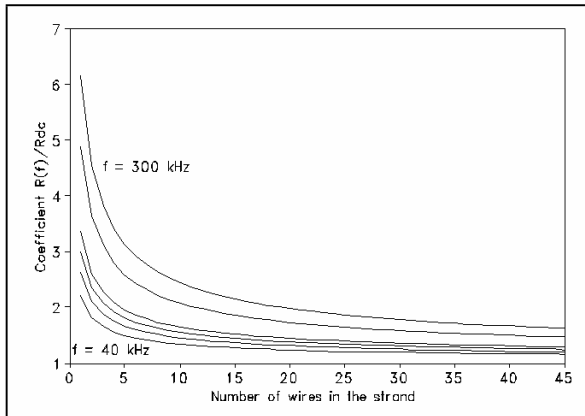


Fig. 3: The coefficient of resistance depending on the number of stranded wires at several values of frequency.

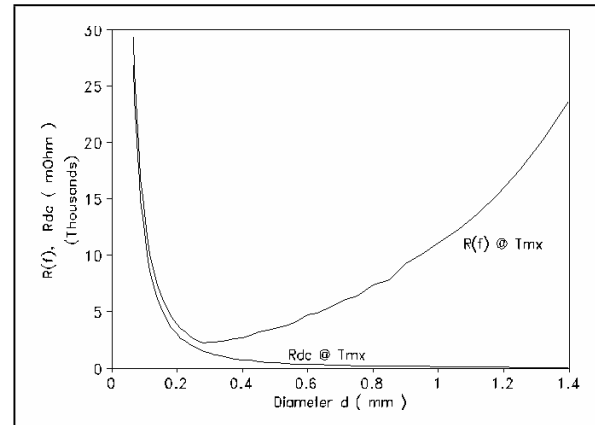


Fig. 4: Resistance depending on diameter at the frequency 100 kHz, the maximal temperature 120°C, the coil ETD 44.

On the basis of this research a mathematical model and optimisation software have been made to be running on the personal computer. Analysing a function of the AC resistance dependent upon a diameter of the filled wire (fig. 4), it is evident, that the function has its minimum. The minimal AC resistance determine the optimal diameter of the wire.

The same function is also valid for a single wire out of the strand and therefore the same optimal diameter of the single wire is achieved, but calculating the AC resistance a number of wires in the whole strand of wires has been taken into consideration.

Conclusions

The mathematical model made by experimental and research work of the authors takes into consideration the filled and stranded enamelled copper wires, and with appropriate coefficient [7,12] the multilayer windings have been taken into account. This multilayer coefficient is not significant in an interval very near to the minimal value of AC resistance, and therefore has minimal influence on the optimisation of the diameter of the wire. The software has been evaluated in practical designs and prototypes of switched mode power transformers.

A mains operated feed forward switched mode power transformer of 400 W at 100 kHz, using the core ETD 44, made of the ferrite material N67 by Siemens, has been used in the evaluating process of this method. The optimal calculated values of some parameters of the transformer compared with their measured values are seen in table 1.

Comparison of the calculated characteristics and the measured ones under the same conditions in table 1 shows, that the algorithm of the optimal determination of the stranded rounded copper wire is suitable and quite accurate in the design of the switched mode power transformers.

Parameter	Primary winding	Secondary winding
No. of turns in the windings	71	35
No. of stranded wires	105	180
Diameter of one wire (mm)	0.071	0.071
R_{dc} calc. @ 22°C	194	76
R_{dc} meas. @ 22°C	208	83
$R(f)$ calc. @ 22°C	226	85
$R(f)$ meas. @ 22°C	240	125
ΔT calc. (°C)	70	
ΔT meas. (°C)	64	

Legend:

R_{dc} (m Ω) ... DC resistance,
 $R(f)$ (m Ω) ... AC resistance $f = 100$ kHz,
 ΔT ... overheating temperature,
 P_{Cu} ... joule losses in copper,
 P_{Fe} ... joule losses in ferrite,
max. ... maximal value,
calc. ... calculated value,
meas. ... measured value.

Table 1: The optimal values of parameters compared with measured values.

References

- [1] Siemens: Switched Mode Power Supplies (SMPS) - Technology and Components - Application Note, Muenchen 1985.
- [2] Siemens Matsushita Components, Ferrites and Accessories, Soft Magnetic Siferit Material, Data Book 1991/92.
- [3] Colonel Wm.T. McLyman: Transformer and Inductor Design Handbook, Marcel Dekker, INC. - New York and Basel 1988.
- [4] Colonel Wm.T. McLyman: Magnetic Core Selection for Transformers and Inductors, Marcel Dekker, INC. - New York and Basel 1982.
- [7] E.C. Snelling: Soft Ferrites, Properties and Applications, Butterworths - London 1988.
- [8] Yavorsky and A. Detlaf: Handbook of Physics, Mir publisher - Moscow 1975.
- [9] IEC 317-0-1: Specifications for particular types of winding wires, Part 0: General requirements, Section 1 - Enamelled round copper wire - 1990.
- [10] DIN 46447 Teil 1: Wickeldraehete, Runddraehete, isoliert, umspinnene Hochfrequenz - Litzen aus Kupferlackdraeheten, Masse - 1979.
- [11] Rudolf Pack GmbH & Co. - Feindraehete, Katalog 1986.
- [12] Philips Components: Symposium Schaltnetzeile, Philips GmbH Forschungslabor Aachen - 1990.

II-15. CHART AND EXPRESSIONS FOR EDDY CURRENT LOSSES CALCULATION IN STEEL LAMINATIONS DERIVED FROM FINITE ELEMENT NUMERICAL RESULTS IN 2D

Paulo G. Pereirinha^{1,2}, Carlos F. R. Lemos Antunes¹

E-mail: ppereiri@isec.pt, lemos.antunes@deec.uc.pt

¹ ISR - Lab. CAD/CAE,

Univ. of Coimbra, 3030-290 Coimbra - Portugal

² Instituto Superior de Engenharia de Coimbra

Rua Pedro Nunes, 3030-199 Coimbra - Portugal

Abstract – A chart and a set of expressions obtained from 2D Finite Element solutions are presented. These allow the 2D eddy current losses calculation for any steel lamination considering skin effect, thickness and width, in the linear zone of the magnetization curve. A comparison between the numerical results and the obtained by the proposed expressions shows a very good agreement.

I. Introduction

There is a growing demand of electrical machines with power electronic drives and of miniaturized inductive devices in all sorts of applications, both associated with the increase of frequency operation and magnetic losses. As the importance of the eddy current losses, regarding the hysteresis and excess losses, increases with the frequency f , there is a need to predict those with great accuracy. Accordingly, this paper deals only with the eddy current losses calculation.

The use of analytical expressions has always been preferable for the designer use, due to the quickness and easy manipulation of data, at least during the design and optimization stage of the device, leaving the numeric field analysis and simulation techniques, as the finite element (FE) method, only for the last level of the design to confirm or improve the results. Analytical expressions for 1-D eddy current losses accommodating the skin effect have been published before [1][2]. However these are not applicable when the ratio between the width w and the thickness d of the lamination is such that $w \gg d$ is not true, even taking the skin depth δ into account. In former work [3] a 2-D eddy current FE analysis was carried out in a steel lamination in order to determine the relation P_J/P_{ref} for different values of d/δ (0.14-7.93, corresponding to 12 different frequencies from 25 Hz to 10 kHz), and w/d (2-17.14). P_J is the 2-D FE eddy current losses and P_{ref} the analytical 1-D reference value of the eddy current losses in (1).

Following the work in [3], three main purposes were now pursued: decrease the numerical errors by using a some more refined mesh, analyse the P_J/P_{ref} values for a different magnetic steel lamination material, and extend the study to a wider and higher frequency range ($d/\delta=[0.05-30]$).

II. Formulation for Eddy Current Losses Calculation

1-D analytical eddy current losses with skin effect

For high frequencies the skin effect due to the eddy currents has to be taken into account. Considering B_a as the average value of the peak flux density over the lamination thickness, the 1-D analytical reference eddy current losses P_{ref} (W/m³) is given by

$$P_{ref} = \frac{\sigma \pi^2 d^2 f^2 B_a^2}{6} F_{sk}, \quad (1)$$

where σ is the electrical conductivity, for B_a it was considered a reference value of the B (i.e. $B_a=B_{ref}$)

and the skin effect is considered by the dimensionless term F_{sk} [1][3], function of λ and δ (where μ is the magnetic permeability) all given by

$$F_{sk} = \frac{3}{\lambda} \frac{\sinh \lambda - \sin \lambda}{\cosh \lambda - \cos \lambda}, \quad \lambda = \frac{d}{\delta}, \quad \delta = \sqrt{\frac{1}{\pi f \sigma \mu}}. \quad (2)$$

FE eddy current losses calculation

Using a diffusion processor of CADDyMAG, a 1st order FE package developed at our CAD/CAE Lab., the 2-D harmonic diffusion equation (3) expressed in terms of the z component of the magnetic field strength H_z [3] was numerically solved

$$\nabla^2 H_z - j\omega\mu\sigma H_z = 0. \quad (3)$$

The Dirichlet complex values of H_s , i.e. the boundary condition H_s (A/m), to apply to the lamination boundaries are given [2][4] by

$$H_s = \frac{B_a}{\tilde{\mu}_e} = \frac{B_{ref}}{\tilde{\mu}_e}, \quad (4)$$

in order to impose the same B_a as used in (1). To calculate H_s it is used a complex equivalent permeability $\tilde{\mu}_e$ (H/m), that expressed in the form $|\tilde{\mu}_e| \angle \phi$, is given by

$$|\tilde{\mu}_e| = \mu \frac{\sqrt{2}}{\lambda} \left(\frac{\cosh \lambda - \cos \lambda}{\cosh \lambda + \cos \lambda} \right)^{1/2}, \quad \tan \phi = \frac{\sin \lambda - \sinh \lambda}{\sinh \lambda + \sin \lambda}. \quad (5)$$

1) 1-D FE eddy current losses

The exact analytical solution for 2-D eddy current losses is not known. In order to access the errors associated with the new finite element meshes (related to the first objective of this work), it was used 1-D numerical models as in [3]. The complex boundary condition in (4), was applied only to the horizontal boundaries (“ w side”) to impose a 1-D problem. This 1-D numerical solution can be compared with the corresponding analytical one P_{ref} given by (1) that can be accepted only when $w \gg d$.

The eddy current density \tilde{J} was calculated applying the rotational operator to both the real and imaginary parts of H_z . The average eddy current losses resulting from the Joule effect over one period $T = 1/f$, were computed in W/m^3 for sinusoidal eddy currents by

$$P_J = \frac{1}{S} \iint_S \frac{\tilde{J}_{max}^2}{2\sigma} dS, \quad (6)$$

where $S = w \cdot d$, and \tilde{J}_{max} is the maximum value (over the period) of the complex eddy current density in each “point” (i.e. FE).

2) 2-D FE eddy current losses

To force the eddy currents to close around the lamination, the same H_s as for the 1-D numerical problem was also applied to the 2-D numerical models, but now all over the external boundaries. However, this lead to a superposition effect that had to be taken into account, as now the B_a calculated from the FE solution differs from the intended B_{ref} value, depending on the w/d and d/δ values. So, in order to compare the numerical 2-D P_J value with P_{ref} , the P_J given by (6) (noted in (7) as P'_J) must be corrected, using a correction factor F_{cor} also function of w/d and d/δ [3]. The corrected values of the eddy current losses related to the reference values, P_J / P_{ref} , are finally given by (7)

$$P_J / P_{ref} = (P'_J / P_{ref}) F_{cor} \quad (7)$$

III. Numerical Analysis Results and Generic Chart

Application example and used FE meshes

It was considered a lamination material in the linear behavior zone of the $B(H)$ curve, with $\mu=6.667 \times 10^{-3}$ H/m ($\mu_r=5305.2$), $\sigma=4.5 \times 10^6$ S/m and it was considered a $B_a = B_{ref} = 1.2$ T (significantly different from the one used before [3], with $\sigma=2 \times 10^6$ S/m, $\mu=1 \times 10^{-3}$ H/m and $B_{ref}=1.5$ T).

The numeric results were obtained with first order FE meshes with a discretization of about 600 nodes for the $1/4$ 2-D model and 1200 nodes for the $1/2$ 1-D model. These 1-D numerical models used exactly the same corresponding meshes as the 2-D models (except that for the 1-D problem H_s is imposed only at the horizontal boundaries of the lamination), and so nearly with the same discretization and numerical errors. To adapt the skin depth it was considered 6 layers of elements near the surface boundaries.

Comparison between 1-D numerical P_J and P_{ref}

It was computed 264 different models, corresponding to 33 different values of d/δ and 8 different values of w/d . Compared with P_{ref} the error for the 1-D numerical eddy current losses P_{J1Dnum} is presented in Fig.1. It can be seen that in spite of a relatively coarse mesh the maximum error is 0.7%, with an overall error of 0.18%.

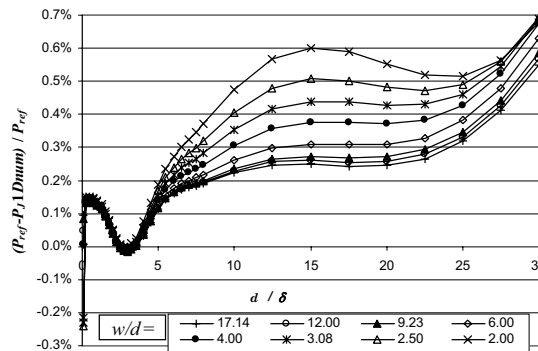


Fig.1. P_{J1Dnum} (1-D numerical P_J) errors.

Comparison between 2-D numerical P_J and P_{ref}

For the 2-D case, it was also computed 264 different models, corresponding to the same 33 d/δ and 8 w/d values. The corrected 2-D numerical P_J/P_{ref} is presented in Fig.2.

Comparing these results with the previously obtained [3] it was clearly seen that they are coincident. As this pointed that the results could be valid for other materials, the P_J/P_{ref} values were also numerically calculated for the same cases presented by other authors [1] for another different lamination material in the linear behavior zone, with $\mu=6.2832 \times 10^{-3}$ H/m ($\mu_r = 5000$), $\sigma=3 \times 10^6$ S/m (we considered $B_a = B_{ref} = 1.0$ T). In the columns I, II and III of table I it is presented a comparison between our results and the ones presented in [1], with an overall difference of 0.218%.

So, as the results presented in Fig.2 stand for any w/d and d/δ in the considered range for any considered soft magnetic steel lamination in the linear zone, the authors concluded that the results presented in Fig.2 may be considered as a generic chart. A related conclusion is that the P_J/P_{ref} values are function of w/d and d/δ , and so the same point in the abacus can be obtained with “infinite” combinations of d, f , and w .

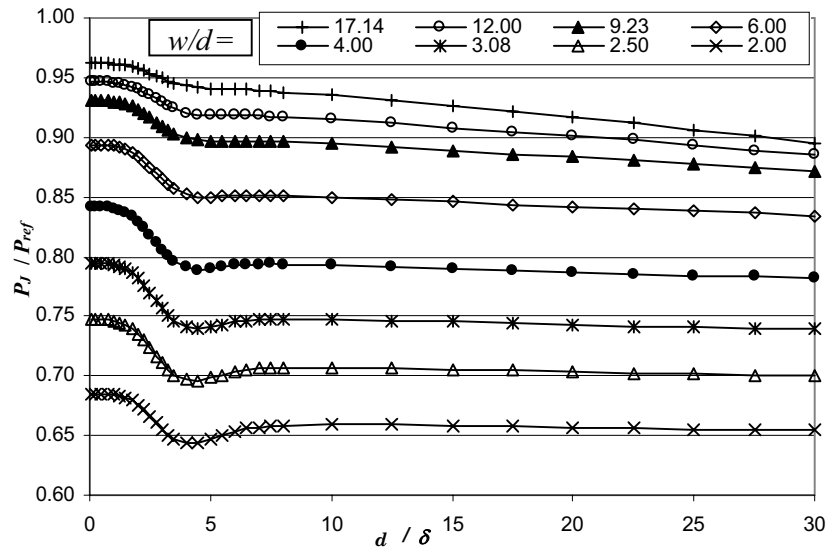


Fig.2. P_J/P_{ref} general chart for $w/d=2$ to 17.14 and $d/\delta=0.05$ to 30.

Table I: Comparison of authors numerical results (I), other authors (II), and analytical proposed model (IV)

w/d	d/δ	I: P_J/P_{ref}	II: P_J/P_{ref} in [1]	III: Diff.= (II-I)/II	IV: Diff.= (II-Analit.)/II
1	1.12	42.144%	42.200%	0.132%	13.126%
1	2.24	42.629%	42.700%	0.166%	16.650%
1	5.00	47.278%	47.500%	0.467%	15.718%
3	1.12	78.736%	78.800%	0.082%	0.311%
3	2.24	77.058%	77.200%	0.183%	-0.187%
3	5.00	73.641%	73.900%	0.350%	0.118%
5	1.12	87.142%	87.200%	0.067%	0.280%
5	2.24	85.705%	85.800%	0.111%	-0.073%
5	5.00	82.487%	82.700%	0.258%	0.160%
10	1.12	93.486%	93.600%	0.122%	0.317%
10	2.24	92.615%	92.700%	0.092%	0.221%
10	5.00	90.409%	90.600%	0.211%	0.264%
15	1.12	95.457%	95.700%	0.254%	0.245%
15	2.24	94.867%	95.100%	0.245%	0.195%
15	5.00	93.273%	93.600%	0.350%	0.204%
20	1.12	96.522%	96.800%	0.287%	0.227%
20	2.24	96.072%	96.300%	0.237%	0.025%
20	5.00	94.810%	95.100%	0.305%	0.023%
Overall difference:				0.218%	

IV. Analytical Model Derived from Numerical Results

Straight line model

As the chart in Fig.2 is valid for any magnetic steel lamination, with the expressed conditions, an analytical model was derived based on the numerical results.

In the chart (Fig.2) the authors identified four zones in d/δ , named *A*, *B*, *C* and *D*, for d/δ within $[0.05-1.5[$, $[1.5-4[$, $[4-8[$, and $[8-30]$ respectively (see “zones delimitation” in Fig.4(a)). Using straight lines in the general form $y=mx+b$, the proposed analytical model for each zone is given by

$$P_J / P_{ref} = m[(d/\delta) - (d/\delta)_0] + b \quad (8)$$

where m and b are the slope and constant term of the straight lines, and $(d/\delta)_0=(0.05, 1.5, 4$ or $8)$ is the initial value of the zone of the considered d/δ . For each w/d , m and b are constants within each zone.

Analytical expressions for determination of the straight line model coefficients, m and b

We intended to find analytical expressions allowing to calculate, for each $(d/\delta, w/d)$ pair, the values of m and b to apply in (8). So, the values of m and b obtained from fitting the numerical data, noted as “ m_{*num} ” and “ b_{*num} ” (where “ $*$ ” is the zone name: A, B, C or D) were plotted as a function of w/d , as can be seen (with continuous lines) in Fig.3. The values of m_{*num} are the straight line slopes for each w/d and zone. The values of b_{*num} are simply the P_j/P_{ref} values at the beginning of each zone (i.e. for $d/\delta=0.05, 1.5, 4$ or 8) taken from each w/d curve.

For the b_{*num} and m_{Cnum} coefficients, it was found out that a very approximated analytical value, named “ b_* ” ($b_A, b_B, b_C,$ and b_D , dot-dash lines in Fig.3(b)) and “ m_C ” (Fig.3(a)), can be calculated by $Coef$, where

$$Coef = k1 + \frac{k2}{(w/d)k3}, \tag{9}$$

with constants $k1, k2,$ and $k3$ values presented in Table II (e.g. $b_B=0.998+0.628/(w/d)^{0.99}$), calculated from the numerical data by using the Least Square Method. For “ m_{Anum} ”, “ m_{Bnum} ”, and “ m_{Dnum} ”, the analytical corresponding coefficients “ m_A ”, “ m_B ”, and “ m_D ” were calculated by $Coef'$, where

$$Coef' = m'(w/d) + b', \tag{10}$$

with m' and b' presented in Table II. These straight lines representing $Coef'$ are shown in Fig.3(a) (dot-dash lines). The values of m' and b' (slope and constant term) were obtained using the “trendline” feature of Microsoft Excel (for example it is shown in Fig.3(a) the values for m_B). In table II it is also presented the overall differences between b_* and m_* , calculated from (9) or (10), and the corresponding b_{*num} and m_{*num} , extracted from the numerical data.

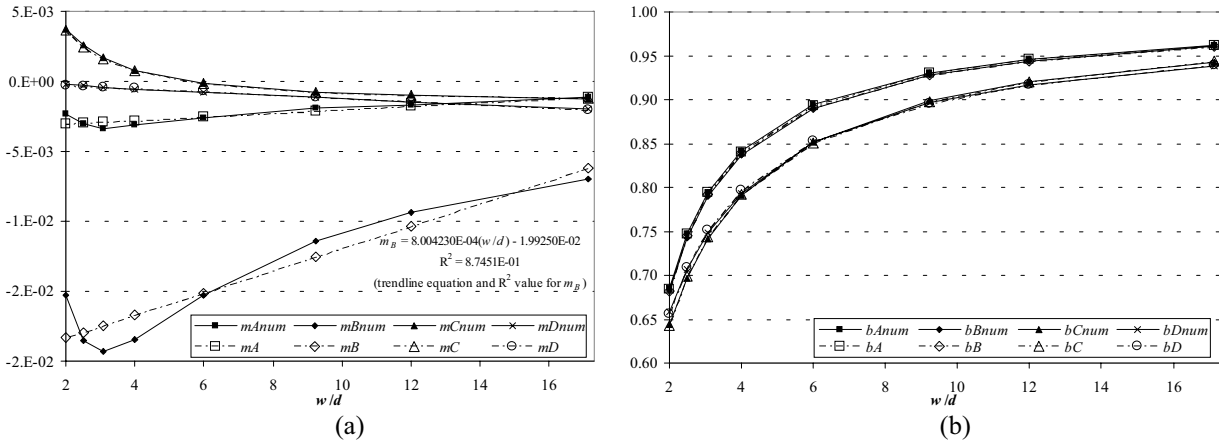


Fig.3. (a): Values of numerical m_{*num} and analytical m_* coefficients
(b): Values of numerical b_{*num} and analytical b_* coefficients.

TABLE II: Constants for the Calculation of $Coef$ and $Coef'$, and Overall Differences between b_* and m_* and the corresponding b_{*num} and m_{*num}

k1, k2 and k3 values, for $Coef$ in (9)				
$Coef$	k1	k2	k3	Overall difference
b_A	0.998	0.628	1	0.08%
b_B	0.998	0.628	0.99	0.12%
b_C	1.0305	0.593	0.717	0.19%
b_D	1.0165	0.593	0.717	0.24%
m_C	-0.0017	-0.0118	1.13	2.96%
m' and b' values, for $Coef'$ in (10)				
$Coef'$	m'	b'	Overall difference	
m_A	1.27541E-04	-3.30073E-03	10.45%	
m_B	8.00430E-04	-1.99250E-02	9.01%	
m_D	-1.14584E-04	-4.49947E-05	8.67%	

Final results

Using the proposed model, the analytical P_j/P_{ref} was calculated (dashed lines in Fig.4(a)). The numerical P_j/P_{ref} are also presented in Fig.4(a) with continuous lines). It can be seen that the analytical proposed approach produces a very good fitting to the numerical results. Their absolute differences (analytical minus numerical) are presented in Fig.4(b), and have an overall difference of 0.20%.

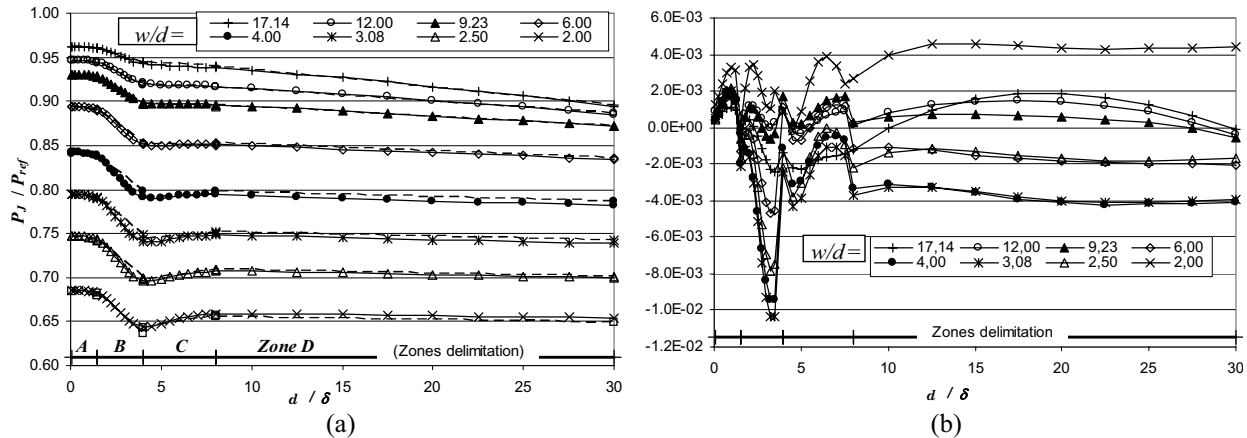


Fig.4. (a): P_j/P_{ref} from FE analysis (continuous lines) and analytical model (dashed lines).
(b): Absolute difference between P_j/P_{ref} derived from FE analysis and analytical model.

The analytical model presented also a very good concordance with the cases in [1], as can be seen by the difference shown on the column IV of Table I (values in *italics* are outside the model's range).

V. Conclusions

The authors have presented a new generic chart and an analytical model derived from finite element numerical solutions that allow an easy calculation of the eddy current losses related to the reference 1-D analytical value P_{ref} , for any considered soft magnetic isotropic and non-hysteretic steel lamination in the linear zone. Both the chart and the model are valid for any w , d , and f , in the considered range of w/d from 2 to 17.14, and d/δ from 0.05 to 30.

Further work in this area of application is being extended and is published elsewhere [5].

Acknowledgments

P. G. Pereirinha is sponsored by the PRODEP PhD Program "4/5.3/PRODEP/2000".



References

- [1] J. Gyselinck., L. Vandeveld, J. Melkebeek, P. Dular, F. Henrotte, W. Legros, Calculation of eddy currents and associated losses in electrical steel laminations, IEEE Trans. Magn., vol. 35, pp. 1191-1194, 1999.
- [2] R.L. Stoll, The Analysis of Eddy Currents, Oxford: Clarendon Press, 1974, pp. 11-15.
- [3] C.L. Antunes, P.G. Pereirinha, Finite element computation of eddy current losses in steel lamination considering the skin effect, the lamination width and thickness, Proc. of the International Conference on Electrical Machines, ICEM 2002, paper 159 (CD ROM), Bruges, Belgium, August 25-28, 2002.
- [4] P.G. Pereirinha, C.L. Antunes, "Comparison of Expressions for Calculation of Eddy Current Losses and Finite Element Solutions in Steel Laminations", Proc. of 8CLEEE, 8º Congresso Luso Espanhol de Engenharia Electrotécnica, vol. I, pp.1.119-1.124, Vilamoura, Algarve, Portugal, July 3-5, 2003.
- [5] P.G. Pereirinha, J. Gyselinck, C.L. Antunes "Study of the Local Eddy Current Loss Density near the Edges in Steel Laminations of Finite Width", Proc. of Compumag 2003, 14th Conference on the Computation of Electromagnetic Fields, Saratoga Springs, vol. IV, pp.194-195, New York, USA, July 13-17, 2003.

II-16. AC MOTOR MAGNETIC SIGNATURE: CONTRIBUTION OF STATOR LAMINATIONS

Daniel Roger, Antoine Henneton

LSEE – Université d'Artois, FSA – Technoparc Futura

62400 BETHUNE, France, tel: 33 3 21 63 72 00

e-mails: roger@univ-artois.fr ; antoine.henneton@fsa.univ-artois.fr

Abstract -- This paper presents a new theoretical approach able to understand the contribution of the motor laminated stator core for high frequency electromagnetic emissions. The proposed analytical model is based on skin effect in laminations, it shows that HF current loops in magnetic sheets have a major effect on high frequency magnetic field existing in the vicinity of a standard machine fed by a PWM inverter.

Introduction

Low level magnetic field in the vicinity of electrical motors carries information on machine behaviour and on its power supply. It can be seen as a magnetic signature. Frequencies of this signature can be cut in two ranges: low frequencies (from DC to a few kilohertz) and high frequencies (up to several megahertz). Low frequency fields correspond to slotting effects, mechanical vibrations... Physical phenomena that create high frequency magnetic signature are tied to resonances in windings due to leakage inductances and stray capacitors excited by fast fronted inverter voltages [1]. Partial discharges in insulating layers cause also high frequency magnetic radiations. The exploitation of external magnetic field measurements for predictive maintenance applications requires a good understanding of the mechanisms linking external magnetic field to the physical internal phenomenon that is at its origin. Two parts of the machine mainly influence this mechanism : the laminated magnetic core and the stator frame often made of aluminium. These two parts have a very different electromagnetic behaviour. The proposed paper focuses attention on the laminated stator.

Experimental detection of the magnetic field near an AC motor

Magnetic field measurement in the vicinity of a standard induction machine has been made using a small 10-turn coil placed near the active part of a motor. Figure 1 shows this coil used as a near field magnetic sensor. It is connected to an instrumentation amplifier fed by batteries in order to avoid unwanted couplings. There is only one coaxial cable between the amplifier output and the oscilloscope. With this magnetic field antenna, it is possible to measure low-value flux densities (down to 1nT) over wide frequencies (up to 10MHz). The amplifier gain and frequency range are adjusted to each kind of measurement. Before operations, the positions of the feeding strand and of the other power devices are slightly changed to verify that the magnetic field measured comes only from to the motor.

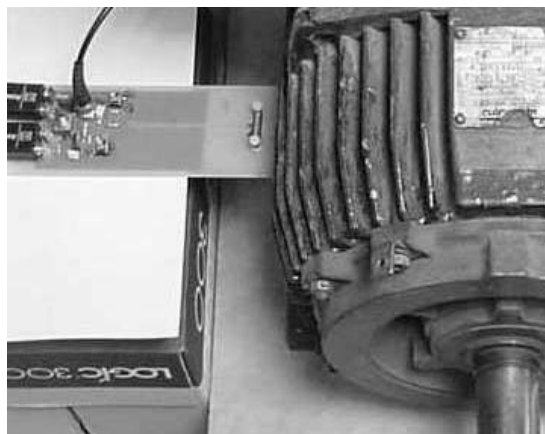


Fig. 1. Magnetic field sensor

When the motor is fed by the 50Hz power grid, the Fourier analysis of the measured field corresponds to a large 50Hz component and harmonics of the grid frequency. Spectrum lines, up to several kilohertz corresponding to slotting effects, can also be observed. Quite a lot of machine faults can be

detected (eccentricity, broken rotor bars, partial short circuits in stator windings) within this low frequency range [2].

When the machine is fed by a standard PWM inverter, its magnetic signature is very different. The spectrum contains many additional lines corresponding to the inverter switching frequency and its multiples. The Fourier analysis yields information on the PWM inverter in addition of the machine ones. This frequency domain analysis is very efficient for repetitive phenomena but it gives poor results for more complex signals such as stator winding high frequency resonances. Time domain analysis is more suitable.

Figure 2 shows the rising edge of a voltage pulse imposed by the PWM inverter, the current in a stator winding and the signal given by the magnetic antenna. This measurement is possible using a special synchronisation system able to isolate a given pulse in the PWM voltage produced by a standard inverter. The current high frequency damped oscillation is superposed to its classical wave form, which is not visible for a such fast time base (400ns/div). This waveform results from the excitation of a resonance in the stator winding by the fast fronted voltage pulse imposed by the inverter. This curve contains information on winding stray capacitors hence on the dielectric characteristics of the material used to insulate windings. A similar damped wave can be observed on the antenna signal, which can be considered as a high frequency magnetic signature of the machine insulation system. Other experiments were made with the same kind of magnetic antenna and windings fed by high voltage pulses. High frequency phenomena due to partial discharges in winding insulation can also be observed.

These experiments prove that a small near field antenna is able to catch useful information for maintenance. But for a good interpretation of the measured signals, it is necessary to understand the mechanism on transmission of information from the stator winding to the machine vicinity through the laminated stator core. Two frequency ranges have to be considered: low frequencies, up to about 5kHz, allowing the detection of mechanical failures and high frequencies used to keep an eye on the machine insulation ageing.

Transmission of information through the laminated magnetic stator

For low level high frequency signals, eddy currents cause the well known skin effect, which concentrates all the electromagnetic phenomena inside the skin depth (δ) below each lamination surface. For small signals, the magnetic steel can be considered as linear and, neglecting anisotropy, can be characterized by two parameters: its magnetic permeability (μ) and its electric conductivity (σ). With this hypothesis, the skin depth is expressed as a function of the excitation signal pulsation (ω) by:

$$\delta = \sqrt{2/(\omega\mu\sigma)} \quad (1)$$

Parameters μ and σ correspond to small signals defined around a magnetic operating point. This operating point runs on the hysteresis loop that characterizes the magnetic steel for classical large signals. Small signals measured by the antenna correspond to minor loops and parameters μ and σ have to be an approximation of these minor loops. A special method is used for their determination [3]. The permeability (μ) is much lower than usual values determined for large signals.

Low frequency considerations

For low frequencies, when the skin depth (δ) is higher than the half of a lamination thickness ($a/2$), the skin effect can be neglected and magnetic stator behavior can be studied with a classical finite element

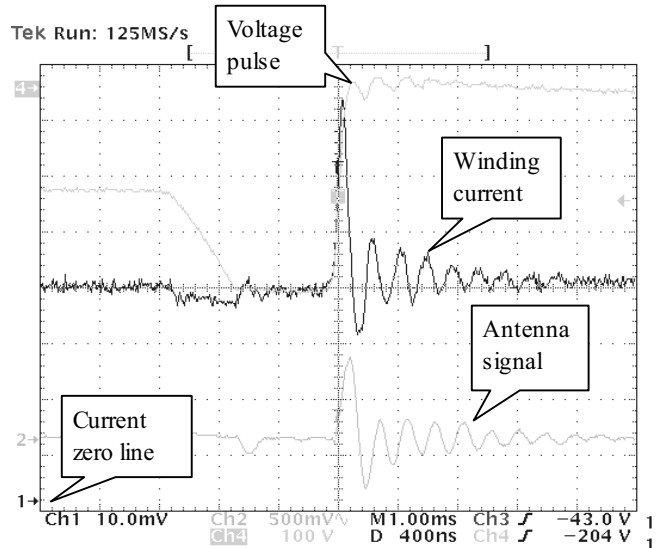


Fig. 2. Time domain signals after a pulse edge

software. Nevertheless, a special care have to be taken to compute the external field of the machine. The boundary condition at the problem external border may have a major influence on results. Special numerical methods, including an infinite boundary, can be used [4].

High frequency considerations

When the skin depth (δ) is lower than the half of a lamination thickness ($a/2$), the skin effect have to be taken into account. The analytical approach presented is valid for high frequencies when $\delta \ll a/2$.

Eddy currents form rectangular loops inside each lamination. These currents are concentrated in a small depth under lamination surfaces. A previous study shows also that only the current density component parallel to the sheet border is significant and that current density in the skin depth J is a function of magnetic field in insulating layer between sheets [5]. Figure 3 shows a

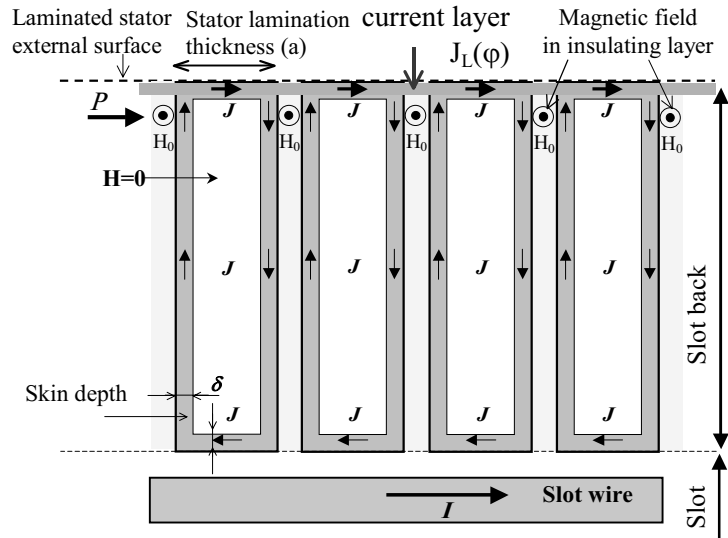


Fig. 3. Eddy current loops in the machine slot back

schematic representation of these rectangular current loops in the laminated stator zone situated on the back of a slot. On this figure, it can be seen that the small sides of each rectangular loop form a current layer flowing below the external surface of the magnetic sheet stack, which forms a radiating layer. To determine the current density in this external current layer, it is necessary to know the magnetic field tangential component magnitude H_0 existing in insulation layers between iron sheets just underneath the stator external surface. This field is produced by the machine winding coils. The study mentioned above [5] shows also that the current density per unit length, along the stator periphery, is equal to the magnetic field in the insulation layer. The point P for this calculus is considered to be on the external stator radius.

Figure 4 presents a plane situated at the center of the insulation layer between two laminations. It is also assumed that there are no high frequency currents in the rotor. In these conditions, H_0 depends only on high frequency current in stator winding.

Each slot, which contains wires carrying HF currents, is replaced by a current density in a virtual layer. The whole machine winding is assimilated to an equivalent current layer distributed on the internal periphery of the stator. This layer carries the current density $J_c(\varphi_c)$ at any point. Each current element corresponding to the elementary angle $d\varphi_c$ is written $di_c = J_c(\varphi_c)R_c d\varphi_c$ and creates at the point P the magnetic field :

$$|\overrightarrow{dh_c}| = di_c / (2\pi|PC|) \quad (2)$$

Calculus is simplified using the complex vector method. Considering a complex plane, whose axis are superposed on the rectangular ones, any vector in the (x,y) plane can be represented by a complex number. The position of the current element is defined by the complex number $\underline{z}_c = R_c e^{j\varphi_c}$ and the position of the point P by $\underline{z} = R_{ex} e^{j\varphi}$. As $\overrightarrow{dh_c}$ is normal to \overline{CP} , the complex formula has to yield the complex number traducing an unity vector perpendicular to \overline{CP} . The second part of (3), written in parenthesis, corresponds to this unity vector :

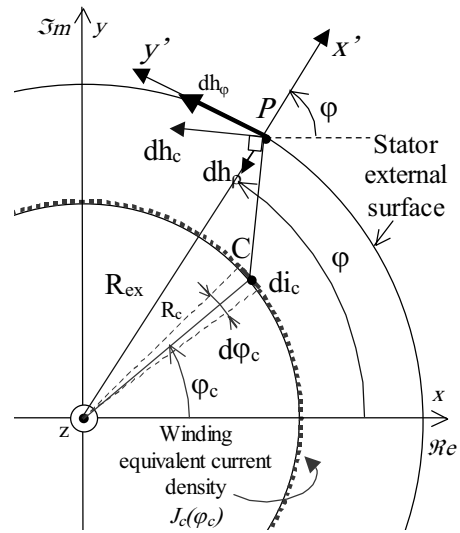


Fig. 4. Magnetic field in the insulation layer between laminations

$$\underline{dh_c(\varphi)} = \frac{J_c(\varphi_c)R_c d\varphi_c}{2\pi|z - z_c|} \cdot \left(j \frac{z - z_c}{|z - z_c|} \right) \quad (3)$$

The total magnetic field produced by all the current elements constituting the winding equivalent current density is obtained with the principle of superposition :

$$\underline{h(\varphi)} = \frac{jR_c}{2\pi} \int_0^{2\pi} J_c(\varphi_c) \frac{R_{ex} e^{j\varphi} - R_c e^{j\varphi_c}}{|R_{ex} e^{j\varphi} - R_c e^{j\varphi_c}|^2} d\varphi_c \quad (4)$$

To get the tangential component of the field at any point of the periphery, the complex vector has to be expressed in a new reference frame (x',y') defined by normal and tangential unity vectors at the point P (Fig. 4). In this reference frame the new argument value of the complex vector $\underline{h(\varphi)}$ is obtained subtracting the angle φ . Then the tangential value of the magnetic field at the point P is the imaginary part of the complex vector expressed in this new reference frame :

$$H_\varphi = \Im m \left[\underline{h(\varphi)} e^{-j\varphi} \right] = \Im m \left[\frac{jR_c}{2\pi} \int_0^{2\pi} J_c(\varphi_c) \frac{R_{ex} e^{j\varphi} - R_c e^{j\varphi_c}}{|R_{ex} e^{j\varphi} - R_c e^{j\varphi_c}|^2} d\varphi_c e^{-j\varphi} \right] \quad (5)$$

The peak value of the current density per unit length, along the stator periphery, can be determined with the same formula (5).

Considering a thin current layer $J_L(\varphi)$ on the external face of the magnetic sheet stack as shown on Figure 5, Ampere theorem allows the determination of the magnetic field tangential component. Because of skin effect, the field inside the iron sheet is zero. Considering $d\rho$ on each side of the surface, the Ampere theorem applied to the path (C) yields :

$$d\varphi(R_{ex} + d\rho) \cdot H_\varphi(R_{ex} + d\rho, \varphi) = J_L(\varphi) \cdot R_{ex} \cdot d\varphi \quad (6)$$

When $d\rho$ is very small relatively to R_{ex} , the equation (6) can be simplified as :

$$H_\varphi(R_{ex}, \varphi) = J_L(\varphi) \quad (7)$$

The magnetic field tangential component in the air near the stator periphery is directly tied to the current density flowing inside the skin depth underneath the stator surface.

The problem consists in elaborating a field map in an infinite plan with border conditions on a circle that represents the current layer jut below the stator external radius. Because of skin effect, field inside this circle is null. Magnetic field in the vicinity of the stator core is calculated using potential vector A defined by $B = \nabla \times A$. For a 2D problem, A is always perpendicular to the considered plane and vector equations reduce to a scalar one. With cylindrical coordinates (ρ, φ) and using potential vector, Maxwell equations are reduced to :

$$\frac{1}{\rho} \frac{\partial}{\partial \rho} \left(\rho \frac{\partial A}{\partial \rho} \right) + \frac{1}{\rho^2} \frac{\partial^2 A}{\partial \varphi^2} = 0 \quad (8)$$

The general solution of this equation obtained with the separation of variables method is :

$$A(\rho, \varphi) = \sum_{m=0}^{\infty} \rho^{-m} [A_m \sin(m\varphi) + B_m \cos(m\varphi)] \quad (9)$$

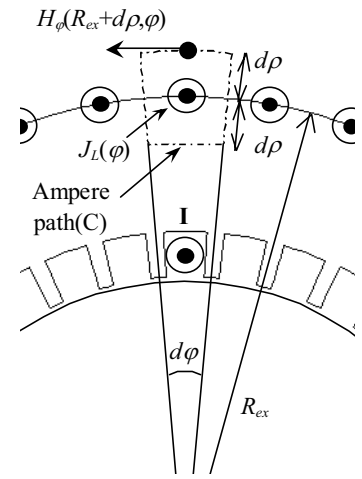


Fig. 5. Ampere path on an element of the external current layer

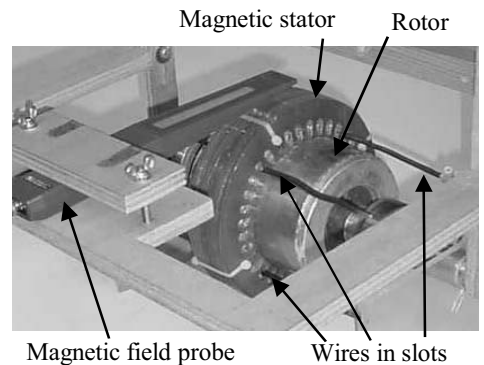


Fig. 6. Experimental testing bench

where A_m and B_m are constant coefficients calculated with boundary conditions imposed at the air-iron border. The cylindrical symmetry imposes m to be integer. Magnetic field components in the air are deduced from the potential vector using $\mathbf{B} = \nabla \times \mathbf{A}$:

$$B_\rho = \frac{1}{\rho} \frac{\partial A_z}{\partial \varphi} = \sum_{m=0}^{\infty} m \rho^{-m-1} [A_m \cos(m\varphi) - B_m \sin(m\varphi)] \quad (10)$$

$$B_\varphi = -\frac{\partial A_z}{\partial \rho} = \sum_{m=0}^{\infty} m \rho^{-m-1} [A_m \sin(m\varphi) + B_m \cos(m\varphi)] \quad (11)$$

To verify this analytical approach, an experimental testing bench was designed with a standard induction machine magnetic circuit and a simplified winding. The aluminum motor frame was removed, as shown on Figure 6, in order to measure only the effect of the magnetic stator core. The magnetic sheet stack is mounted on the rotor of the same induction machine. An insulation layer avoids contacts between stator and rotor and simulates the air-gap. Stator winding is reduced to two one-turn elementary coils placed at the center of the slots. Their opening angle is 90° to simulate a 4-pole induction machine. A sine wave generator feeds the device through a wide band amplifier. HF magnetic field components are measured using a magnetic probe connected to a spectrum analyser. Because of the symmetry of the device, probe position is changing by 90° corresponding to the pole pitch. Reference position $\varphi=0^\circ$ is in front of a slot wire. Experimental device main sizes are : $R_{ex}=96\text{mm}$, $R_c=69\text{mm}$ and $\alpha=0.65\text{mm}$.

The winding equivalent current density is written :

$$J_c(\varphi_c, t) = i(t)f(\varphi_c) \quad (12)$$

The function $f(\varphi_c)$ represented on Figure 7 takes into account the geometrical distribution of the winding in the stator slots. α is the opening angle of a slot. The Fourier expansion of the winding equivalent current density is :

$$J_c(\varphi_c, t) = \frac{2pi(t)}{\pi R_c} \sum_{k=0}^{\infty} \frac{\sin\left[(2k+1)p\frac{\alpha}{2}\right]}{(2k+1)p\frac{\alpha}{2}} \cos[(2k+1)p\varphi_c]$$

Noting I the current RMS value, the peak value of the magnetic field tangential component at the iron-air border is obtained substituting $J_c(\varphi_c)$ of equation (4) by its expression and for $i(t) = I\sqrt{2}$:

$$H_\varphi(R_{ex}, \varphi) = \Im m \left[\frac{jR_c}{2\pi} \int_0^{2\pi} \frac{2pI\sqrt{2}}{\pi R_c} \sum_{k=0}^{\infty} \frac{\sin\left[(2k+1)p\frac{\alpha}{2}\right]}{(2k+1)p\frac{\alpha}{2}} \cos[(2k+1)p\varphi_c] \frac{R_{ex}e^{j\varphi} - R_c e^{j\varphi_c}}{|R_{ex}e^{j\varphi} - R_c e^{j\varphi_c}|^2} d\varphi_c \right] \quad (13)$$

The integral, with respect of the variable φ_c , inside this expression has no analytical solution. A numerical solution has been performed and Figure 8 plots the results of (13) for the experimental device sizes and for $I=1\text{A}$. This function has been decomposed in Fourier series: using a numerical method. It is expressed as a function of a reference field arbitrary chosen as:

$$H_\varphi(R_{ex}, \varphi) = H_{\text{Ref}} \sum_{k=0}^{\infty} a_{2k+1} \cos(2k+1)p\varphi \quad (14)$$

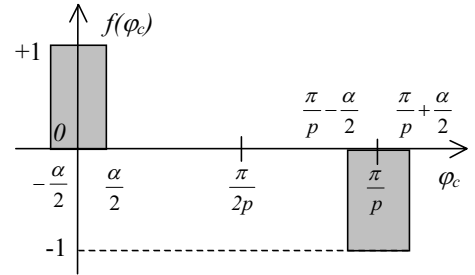


Fig. 7. Equivalent current density distribution

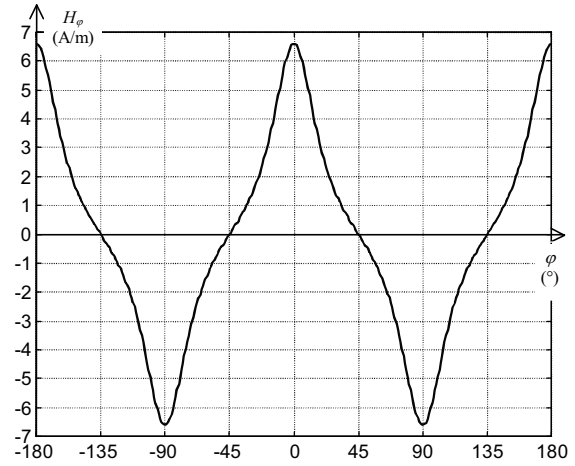


Fig. 8. Magnetic field tangential component at the iron-air border

The most significant numerical value of coefficients are : $a_1=0.58$, $a_3=0.157$, $a_5=0.0464$, $a_7=0.0116$. The identification of this expression with (10) for the iron-air border ($\rho=R_{ex}$) yields the unknown

$$\text{coefficients } m, A_m \text{ and } B_m: m=(2k+1)p, A_m=0 \text{ and } B_m = \frac{\mu_0 H_{Ref} a_{2k+1}}{(2k+1)p R_{ex}^{-(2k+1)p-1}}.$$

Figure 9 is plotted using equations (10) and (11) with the previously defined coefficients for $I=1.5A$ and $\rho=R_{ex}+2cm$. Experimental tangential and normal components of magnetic field, measured in the same conditions are given on Fig. 10; the probe gives the RMS values without sign. Despite magnetic field measurement difficulties tied to a precise probe positioning and the decoupling between components which is not perfect, it can be seen that the proposed HF model predictions agree with experimental curves.

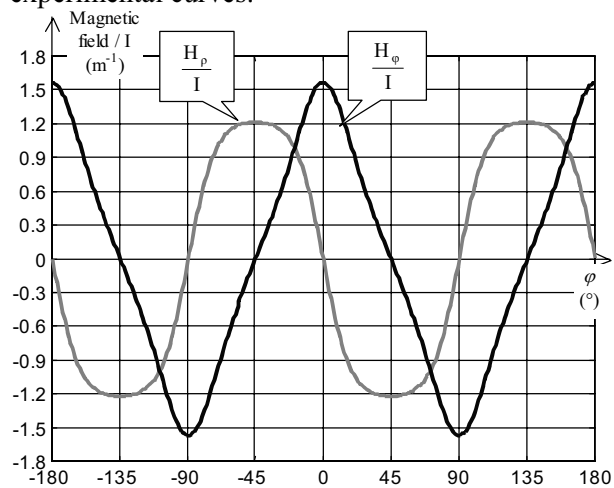


Fig. 9. Theoretical predictions

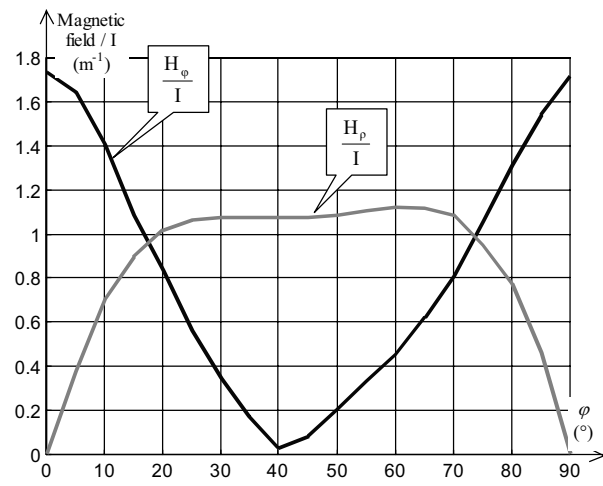


Fig. 10. Experimental measurements

Conclusion

This study shows that a high frequency magnetic field can be measured with a very simple probe in the vicinity of an inverter fed AC machine. It shows also that such measurements may give information on winding resonances tied to insulation ageing. An analytical approach of HF magnetic fields in stator laminations proposes a model describing the transmission of information from winding HF currents to external field. This model explains that, for high frequencies, a current layer due to skin effect has a major influence on electromagnetic radiations.

References

- [1] G. L. SKIBINSKI, R. J. KERKMAN « EMI Emission of Modern PWM AC drives » IEEE Trans. on Industry Applications Magazine November/December 1999, pp. 47-81.
- [2] Y. PANKOW, R. CORTON, R. ROMARY, V. AUTIER, J. F. BRUDNY “Effet de la denture des moteurs asynchrones dans le cadre du diagnostic par la mesure du champ radial”, quatrième conférence internationale sur les méthodes de surveillance et techniques de diagnostic acoustiques et vibratoires”, Université de Compiègne, 16-18 octobre 2001, pp. 283-292.
- [3] D. ROGER, O. NINET, S. DUCHESNE. “Wide Frequency Range Characterization of Rotating Machine Stator-Core Laminations”, accepted for publication in EPJ-AP.
- [4] Q. CHEN, A. KONRAD, “A Review of Finite Element Open Boundary Techniques for Static and Quasi-Static Electromagnetic Field Problems”, IEEE Trans. on Mag., Vol. 33, No 1, January 1997, pp. 663-676.
- [5] A. HENNETON, D. ROGER, E. NAPIERALSKA « Study of electromagnetic phenomena contributing to external radiation of machines » ; International Conference on Electrical Machines, ICEM 2000, 28-30 August 2000, Espoo (Finland), pp 1125-1129.

II-17. A COMPARISON BETWEEN SURFACE MAGNETS AND EMBEDDED MAGNETS IN FRACTIONAL SLOT WOUND PM MOTORS

P. Salminen, J. Pyrhönen, M. Niemelä

Lappeenranta University of Technology, Department of Electrical Engineering,
P.O. Box 20, FIN-53851 Lappeenranta, Finland
E-mail: Pia.Salminen@lut.fi

Abstract – This study compares permanent magnet motor performance with different rotor structures. The motors are equipped with concentrated fractional slot windings. The rotor structures under investigation include surface mounted magnets or embedded magnet. Because of the large amount poles and small pole pitch it is possible to increase the air-gap diameter due to the reduced space needed by the stator yoke. This increases the torque capacity of the motor. The Joule's losses in the stator windings are reduced due to the reduced length of the end winding. Therefore, the power density of these motors can be especially high. The results of different FEM calculations are given.

Introduction

In synchronous PM motors the back-EMF and current excitation waveforms are usually designed to be sinusoidal or trapezoidal. The obtained waveforms depend on the magnetic flux distribution as well as the winding distribution. In machines with fractional slot windings, the windings are not sinusoidally distributed, and the obtained air-gap flux density distribution may be far away from sinusoidal even though the resulting induced EMF may be very sinusoidal. For a machine that has q (the number of slots per pole and per phase) less than unity, the flux density distribution in the air-gap over one pole pitch can consist of just one teeth and one slot, e.g. in Fig. 1 $q = 0.3636$. The main flux can flow through one tooth from rotor to stator and return via two other teeth and the resulting air gap flux density distribution is not sinusoidal, as it is illustrated in Fig. 1. Therefore, it could be expected problems while considering the cogging torque or dynamic torque ripple, but the matter is not so simple.

Hendershot and Miller [3] have studied the choices possible for slots and poles for brush-less motors in terms of how well they will resist cogging according to pole and slot alignments. It was noticed that the minimum cogging torque was not dependent on whether the machine type is fractional-slot or integral-slot. If q is an integer every leading or lagging edge of poles line up simultaneously with stator slots – causing cogging, but in fractional slot combination fewer pole-edges line up with slots. The actual pole arc can make this situation either worse or better. The high number of poles gives some advantages as for a given stator inner diameter the mass of the motor may be reduced by using more poles, because the thickness of the stator yoke can be reduced. It is obvious that the end turns are shortest when the pitch is one or two-slots and that is why some two-layer constructions can be useful. This can reduce the stator copper losses. [1], [3].

In this paper the performance of a 24-slot 22-pole fractional wound PM machine is reported with two different rotor possibilities: the rotor with surface mounted permanent magnets and the rotor with embedded magnets. A no load solution with 2D finite element method was carried out to solve the flux created by the magnets. For surface mounted magnets it is quite simple to solve the flux produced by the magnets also analytically, but for embedded magnets it is not so straightforward. Static and dynamic computations were then carried out in order to find out the torque production capability of dif-

ferent designs. Furthermore, from dynamic computations it is possible to get a value for inductance, axis torque, phase current and induced back EMF. [1], [2].

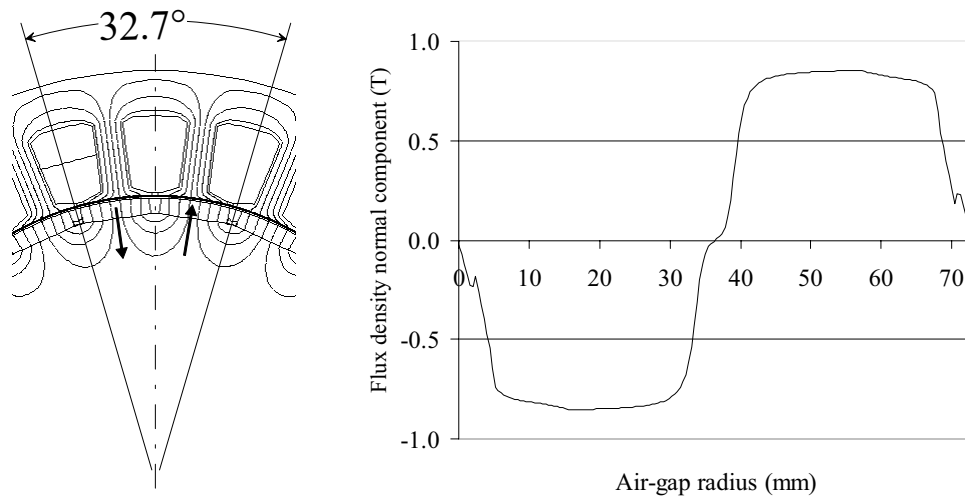


Fig. 1. a) Flux lines of a fractional slot machine with 24 slots and 22 poles machine. b) The corresponding normal component of the air gap flux density along one pole pitch arc. The length of the 32.7 degrees arc is 73 mm along the air-gap.

Surface magnet versus embedded magnet motor

Surface permanent magnets are nowadays the most commonly used construction for the PM motors. In a surface magnet motor the magnets are usually magnetized radially. The use of Nd-Fe-B rare-earth magnets cause that the synchronous inductances in the d - and q -axis may be considered to be equal which can be helpful while designing the surface magnet motor. The construction of the motor is quite cheap and simple, because the magnets can be attached to rotor surface.

The embedded magnet motor has circumferentially magnetized permanent magnets embedded in deep slots. The stator synchronous inductance in the q -axis is greater than the synchronous inductance in the d -axis. If the motor has a ferromagnetic shaft a large portion of the permanent magnet produced flux goes through the shaft. In this study the buried-magnet motor is equipped with a non-ferromagnetic shaft in order to increase the linkage flux crossing the air-gap. Another method to increase the linkage flux crossing the air-gap is to equip a non-ferromagnetic sleeve between the ferromagnetic shaft and the rotor core. [1].

Compared to embedded magnets, one important advantage of the surface mounted magnets is the smaller amount of magnet material needed in a design (in integral-slot machines). If the same power is wanted from the same machine size, the surface mounted magnet machine needs less magnet material than the corresponding machine with embedded magnets. However, several other advantages favour the use of embedded magnets: Because of the high air-gap flux density, the machine may produce more torque per rotor volume compared to the rotor with has surface mounted magnets. This, however, necessitates usually more PM-material. The danger of permanent magnet material demagnetisation remains smaller. The magnets can be rectangular and there are no fixing and bonding problems with the magnets: The magnets are easy to mount into the holes of the rotor and the danger of damaging the magnets or possible magnet-retaining belt is small. [4].

Static computation

It was studied stator windings with $q < 1$. In order to obtain a fair comparison there is the same amount of copper and magnet material (9.5 kg) in a same frame size in all motors. Also the air-gap diameter was fixed so that the stator inner diameter is 254 mm. Static FEM computations were performed for different slot/pole combinations: FEM computations were done for both surface and embedded magnets. A FEM calculation is carried out with steady currents in slots and the rotor is moving with nominal speed. The maximum slot current was 10760 A. The FEM computations were carried out for different rotor structures and the results are shown in Table I.

Table I: Results from static FEM –computations

Poles	28	26	22	20
Slots/poles/phase, q	0.285	0.3077	0.3636	0.4
Magnet position	Surface	Surface	Surface	Surface
Maximum torque (Nm)	980	910	970	960

The results given for the surface magnet motors show that the 28-pole machine generates the highest torque and the 26-pole machine the lowest. The difference between the machines is anyway small. To compare embedded magnet motors with surface magnet motors some analytical calculations of the parameters were done. One of the motors studied was $q = 0.3636$, 24 slots and 22 poles. The results of static FEM computations at no load situation are shown in Fig. 2. On the left side is the motor designed with 22 surface magnets and on the right side with 22 embedded magnets. (There are 12 flux lines going through each magnet in both pictures.)

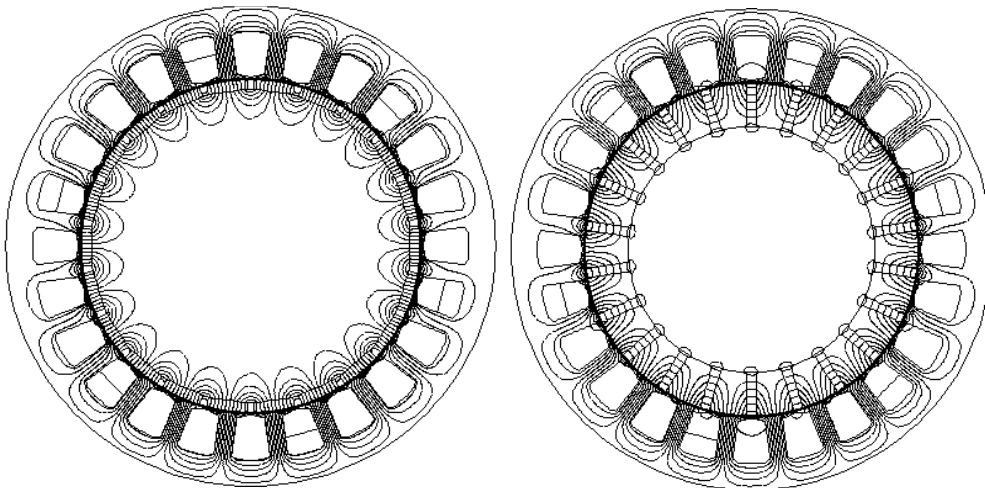


Fig. 2. A static FEM computation at no load for a $q = 0.3636$ motor of a) surface magnet motor and b) embedded magnet motor.

For the surface magnet motor the fundamental value (from the Fourier spectrum) of the flux density normal component was 1.01 T and for the embedded magnet motor 1.17 T. The r.m.s values were 0.738 T and 0.92 T. With the same amount of magnet material – 10.3 kg – the embedded magnet solution gives clearly higher flux density values at no load. Motor parameters (shown in table II) were analytically calculated to find out the values at nominal point. Some values for analytical calculations are taken from the FEM calculations, e.g. the flux created by the magnets. At the rated load 1075 Nm the power densities of the studied motors are 39 kN/m².

Table II: Motor parameters from analytical and FEM computations

	Surface magnet	Embedded magnet
Slots/poles	24 / 22	24 / 22
Stator radius inner (mm)	127	127
Winding factor	0.96	0.96
Nominal current (A)	86.4	86.1
Main voltage (V)	351	351
Winding turns per phase	104	88
Air-gap length (mm)	1.25	1.25
Phase resistance, R_{ph} (Ω)	0.1	0.07
Back EMF (V)	192.4	188
Air-gap maximum flux density (T), due to permanent magnets	1.01	1.17
Frequency (Hz)	73.33	73.33
Output power (kW)	45	45
Efficiency	0.93	0.94
Power factor	0.931	0.91
Magnets (kg)	10.3	10.3
Slot area (mm ²)	805	805
Load angle (deg)	42	48
Rated torque (Nm)	1075	1075

The effect of the magnet width to the performance of the surface magnet motor ($q = 0.3636$) was optimised. With the magnet width about 80 % from pole pitch, the maximum torque achieved was 1164 Nm and the magnet width 70 % from pole pitch 1038 Nm. In this machine the wider magnet structure gives more torque. The results of static FEM calculations for the best surface and for the best embedded magnet motors (parameters are in Table II) are shown in Fig. 3. The steady current for the surface magnet motor is now the nominal current of the motor e.g. 86.4 A, and for the embedded magnet motor 86.1 A. The maximum slot current of surface magnet motor is 12708 A, and embedded magnet motor 10715 A.

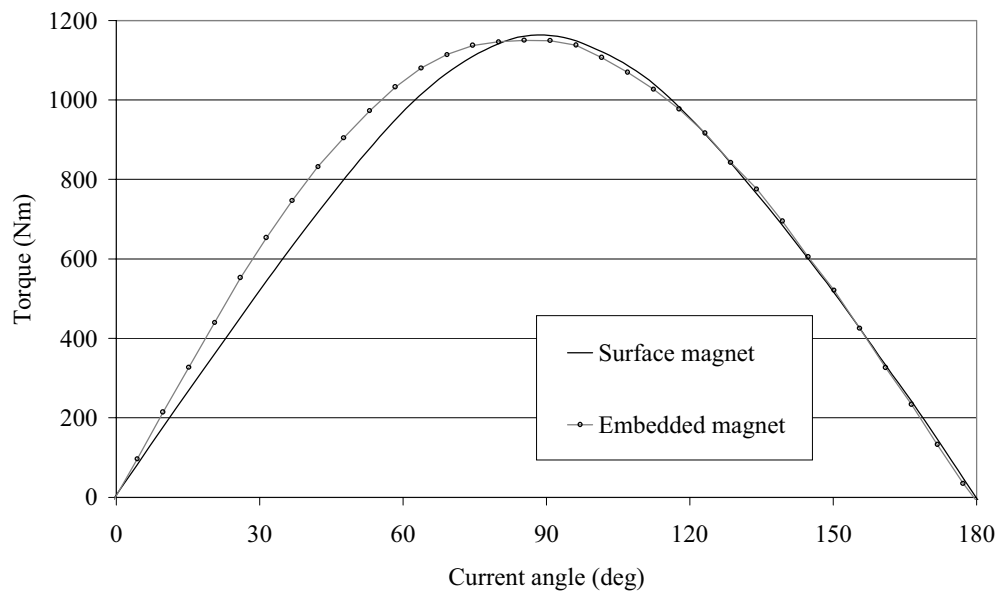


Fig. 3. The developed air-gap torque as a function of motor current angle for a surface magnet motor and for an embedded magnet motor (with constant nominal current).

The maximum value of the torque developed by the surface magnet motor is 1164 Nm and by the embedded magnet motor 1148 Nm. The shape of the torque curve of the surface magnet motor is symmetric, but the armature reaction has twisted the curve of the embedded magnet motor. (The synchronous inductance in the q -axis is greater than the synchronous inductance in the d -axis.) Because there are less winding turns in the embedded magnet motor, and the phase resistance is smaller, it is possible to make a solution for this machine using other dimensions of the stator: smaller slots, shorter yoke height and 5 mm longer air-gap radius. The maximum torque of the static FEM computation with such a motor is 1300 Nm.

The normal component of the flux density was solved along the whole air-gap for a loaded machine. The result for the surface magnet motor is shown in Fig. 4. It can be seen that the curvature of the flux density wave in the air gap is individual above each of the magnets.

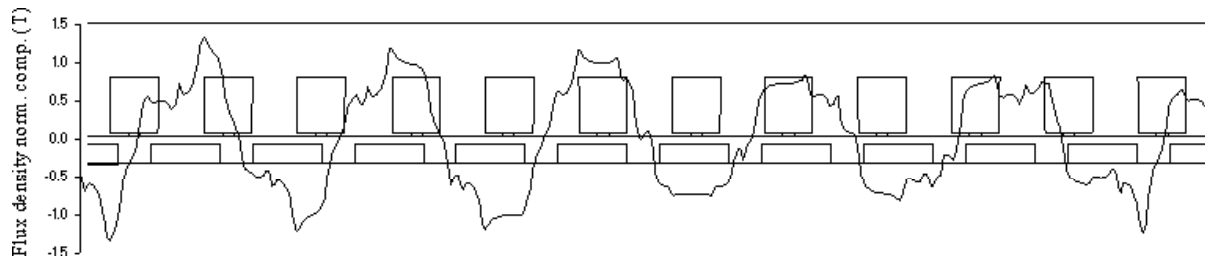


Fig. 4. The flux density normal component along the air-gap diameter. The result is from static FEM computation for a surface magnet motor $q = 0.3636$ at load situation.

Dynamic computation

A time-stepping computation with circuit coupling was carried out for the surface and embedded motors with 24 slots and 22 poles ($q = 0.3636$). The motor was connected to star and the electrical circuit consists of three voltage sources, which supplied voltage to each phase coil. The line-to-line voltage used was 351 volts. Speed was fixed to be 400 rpm. The computation results, axis torque as a function of time, are shown in the Fig. 5.

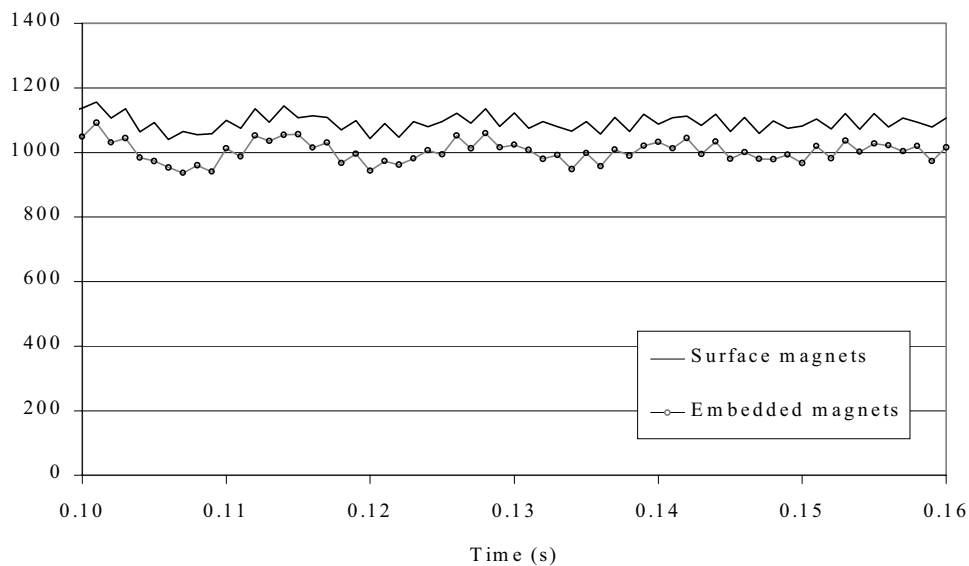


Fig. 5. Axis torque as a function of time for surface magnet motor and embedded magnet motor from dynamic FEM computation. The load angle of both machines is 42 degrees.

The axis torque of the surface magnet motor at load angle 42 degrees was 1090 Nm and embedded magnet motor 1000 Nm. The torque ripple peak-to-peak value for the surface magnet motor is 6% and for the embedded magnet motor 9%. In this case the embedded magnet motor gives less torque than the surface magnet motor at the same load angle.

Table III: Results from dynamic FEM –computation at load angle 42 degrees

	Surface magnet Motor	Embedded magnet Motor
Axis torque (Nm), T	1090	1000 Nm
Current (A), I	82.4	80 A
Power factor, $\cos\phi$	0.988	0.986
Load angle (deg), δ	42	42

A series of computations, with voltage control, was carried out for the surface magnet motor with different load angles. From the results it could be stated that the maximum torque available from this machine is 1675 Nm. The embedded magnet solution with voltage control gave a little less torque so that the maximum torque was 1545 Nm, which is 8% less than the maximum torque of surface magnet motor. Both machines exceed the given requirement and the overloading capacity is fulfilled.

Conclusion

A 24-slot 22-pole fractional wound PM machine was designed with two different rotor possibilities: surface and embedded magnet rotor. According to only static computations the embedded magnet rotor seems to give as much torque as the surface magnet rotor, but the dynamic calculation procedure showed that the embedded magnet solution gives actually a little less torque. It was shown that both magnet structures were possible to use for a low speed application. If the motor size and stator dimensions are kept the same and there is the same amount of magnet material, the better solution and the higher torque is achieved with surface magnet motor. Compared to surface mounted magnets, it was shown that the fundamental component of the air gap flux is essentially higher in a case of embedded magnets with the same air gap diameter. This can be a great advantage in some applications. Further examination will be carried out to find out the behaviour of some other fractional slot machines.

References

- [1] Gieras, F. Wing, Mitchell (1997). Permanent Magnet Motor Technology -Design and Applications. Marcel Dekker, Inc. New York, ISBN 0-8247-9794-9
- [2] K. Vogt (1996), Berechnung elektrischer Maschinen, Weinheim, VCH, ISBN 3-527-28391-9
- [3] J.R. Hendershot and The Miller, Design of Brushless permanent-magnet motors, Oxford, Magna physics publishing and Clarendon press, 1994, from 3-6 to 3-15
- [4] T. Heikkilä, Permanent magnet synchronous motor for industrial inverter applications –analysis and design, Thesis, Acta Universitatis Lappeenrantaensis 134, ISBN 951-764-699-2, Lappeenranta, 2002

II-18. EVALUATION OF NEW SURFACE MOUNTED PERMANENT MAGNET SYNCHRONOUS MACHINE WITH FINITE ELEMENT CALCULATIONS

T. Schneider, A. Binder

Department of Electrical Energy Conversion, Darmstadt University of Technology,
Landgraf-Georg-Strasse 4, 64283 Darmstadt, Germany
tschneider@ew.tu-darmstadt.de

Abstract This investigation focuses on the comparison of different surface mounted magnet rotor designs for electric vehicle applications. Using finite element calculations both base speed and maximum speed under field weakening conditions are taken into consideration. Starting from a given torque-speed specification and a maximum inverter output voltage an algorithm determines the required stator current. The algorithm reacts on the presence of saliency by slightly shifting the current phasor from q-axis to the d-axis, thus reducing the overall current for a given torque demand. The results show that iron covers on top of the magnets and magnetic shunts inside the pole gap do not cause any outstanding benefits compared to the much simpler standard surface mounted permanent magnet synchronous machine. Furthermore, it could be shown that apart from special buried magnet arrangements introducing saliency by filling the pole gap with rotor iron gives the best results in terms of high torque/current ratio both at base speed and maximum speed under field weakening conditions.

Introduction

Nowadays, electric cars and small handling vehicles are most often equipped with induction or dc machines. Fig. 1 illustrates the speed-torque requirements of such vehicle drive applications. At low speed, high torque is required to enable a heavily laden car to climb up a ramp or a curbstone. Once moving, the vehicle only needs low torque to overcome friction and to keep its speed. Usually, these restraints are met by making use of field weakening techniques. At low speed, a high magnetic flux provides a reasonable torque/current ratio, whereas the magnetic field is reduced at high rotational speeds in order to limit the stator voltage to the maximum inverter output voltage. Both induction and dc motors are well suited for field weakening applications because both machines offer easy regimes for field weakening [1].

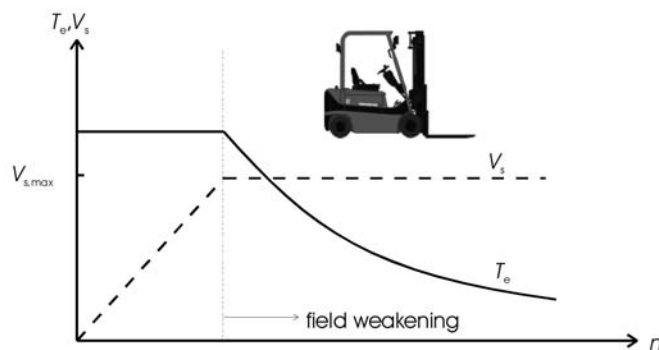


Fig. 1. Typical speed-torque requirement in an electrical drive application

Nevertheless, replacing induction or dc machines by permanent magnet synchronous machines (PMSM) would lead to some key benefits. Avoiding the brushes minimises the maintenance requirements. Furthermore, the efficiency can be increased significantly due to the permanent

excitation, thereby increasing the range of the vehicle for a given battery capacity. But replacing dc motors by permanent magnet synchronous machines also raises some challenges [1-5]. Using permanent magnet excited machines one does not have the degree of freedom to directly vary the magnitude of the air gap flux density. However, indirect field weakening is still possible by superimposing a stator excited demagnetising field to the rotor field as described in [1]. Cost effectiveness demands a simple and cheap motor construction. Therefore, surface mounted magnet machines are preferred to buried magnet rotor designs. This investigation focuses on surface mounted magnet synchronous machines, whose field weakening capability is usually rather poor. In [5] a new rotor structure with iron covered magnets and flux shunts inside the pole gap is proposed, which is announced to show a very good behaviour in case of field weakening. This rotor geometry is compared to the standard PMSM with surface mounted and inset type magnets making use of finite element calculations. The stators of all calculated 6 pole ($2p = 6$) three phase machines ($m = 3$) are identical and are based on the assumption of a 10 kW drive with a water-jacket cooled housing for an electric forklift.

Operation of standard PMSM

Based on a linear dq -model, the steady-state equations of the PMSM regarding only the fundamental harmonic can be expressed as

$$\underline{V}_s = R_s \underline{I}_s + jX_q \underline{I}_q + jX_d \underline{I}_d + \underline{E}_0, \quad (1)$$

$$\underline{E}_0 = j\omega_s \underline{\Psi}_p \quad (2)$$

and

$$T_e = \frac{mp}{\omega_s} \left[E_0 I_s \cos \gamma + \frac{I_s^2}{2} (X_q - X_d) \sin 2\gamma \right]. \quad (3)$$

V_s and I_s represent the stator voltage and current, whereas I_d , I_q and X_d , X_q stand for the d - and q -components of the current and reactances, respectively. R_s symbolises the stator resistance. The EMF E_0 is caused by the flux linkage of the stator windings with the PM rotor flux Ψ_p . The torque T_e is generated both by permanent magnets and by saliency ($X_d \neq X_q$) and depends on the angle between the current phasor and the q -axis γ . In case of a non-salient rotor ($X_d = X_q$) the current phasor must be aligned with the q -axis ($\gamma = 0$), in order to get the maximum torque output.

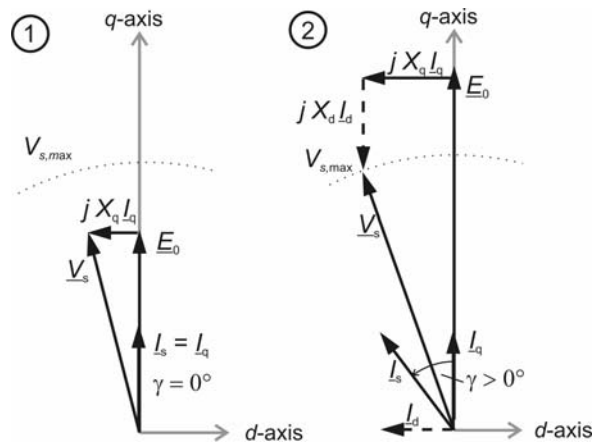


Fig. 2. Phasor diagrams of a PMSM at base speed (1) and under field weakening conditions (2)

In contrast, equation (3) indicates that a salient rotor with $X_q > X_d$ requires a current phasor slightly shifted towards the d -axis ($\gamma > 0$), to achieve maximum torque at a given current. The stator voltage V_s depends on the EMF E_0 , which is directly proportional to both flux linkage and speed. At high rotational speeds, E_0 can cause the stator voltage to exceed the maximum inverter output voltage V_{max} . In that case, flux weakening is necessary to reduce the EMF and to enable the machine to operate at

that speed. By adding a negative d -component to the current phasor, the voltage drop $jX_d I_d$ in (1) becomes negative, thus compensating the EMF excess (Fig. 2).

Performance of standard PMSM



Fig. 3. 120°-section of a 6-pole surface magnet synchronous machine (a) and calculated flux lines under no-load conditions (b)

Fig. 3 illustrates the standard permanent magnet synchronous machine as it is most commonly used in PM drive applications. The magnets are glued to the rotor surface and a non-magnetic bandage is employed to prevent the magnets from displacing at high rotational speeds. The magnets are chosen to cover 80 % of the pole pitch at a magnet height of 5 mm and the pole gap is filled with non-magnetic material. As the magnets have a relative permeability of $\mu_r \approx 1.06$, the inductances in both d - and q -axis are nearly identical if saturation of iron is neglected. Fig. 3b) shows the FE results for this rotor structure under no-load conditions, with a magnitude of the fundamental air gap flux density B_1 of 0.884 T. In order to compare the different rotor structures, a typical torque-speed demand of an electric forklift has been chosen as benchmark. Fig. 4 shows both the typical speed-torque demand of an electric forklift and the FE simulation results of the standard rotor structure. The q -component of the stator current I_q is employed to generate torque, therefore the curve progression follows the torque demand. The stator voltage V_s is limited to 18 V, representing the maximum converter output voltage. At frequencies above 80 Hz a demagnetising current component I_d is employed to limit the stator voltage. The total current, composed by the phasors I_d and I_q (Fig. 2), is first dropping due to the falling q -current. At frequencies above 100 Hz the total current is rising again, because the demagnetising current is becoming the major component of the overall current.

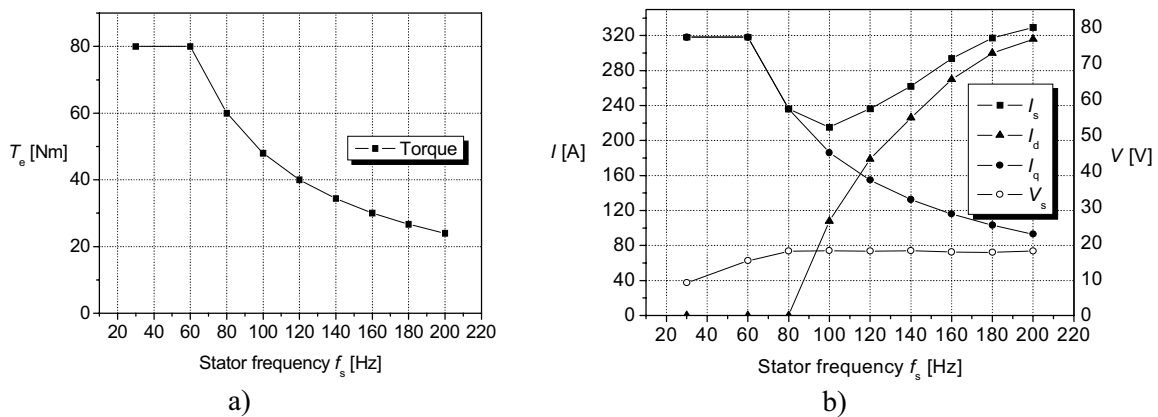


Fig. 4. Typical speed-torque requirement of an electric forklift (a) and corresponding current demand and stator voltage of standard PMSM (b)

Evaluation of a new rotor structure

In [5] a new rotor structure for a 4 pole permanent magnet synchronous machine has been introduced and very good field weakening performance has been reported. The geometry of this rotor structure has been adapted to the 6 pole motor configuration and the FE results are compared to the results discussed above.

New rotor structure

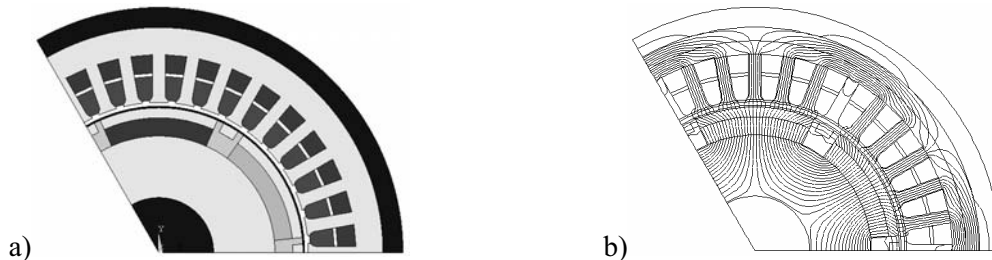


Fig. 5. Rotor structure proposed in [5] for enhanced field weakening (a) and calculated flux lines under no-load conditions (b).

Fig. 5 displays the rotor structure as it has been reported in [5]. The magnets are covered by rotor iron and inside the pole gap a magnetic shunt has been installed. This configuration can hardly be investigated analytically due to the complicated flux paths and due to saturation. FE calculations are necessary to provide detailed information about the performance of this rotor structure. In order to achieve good comparability of the different rotor structures, the total amount of magnet material is kept unchanged by increasing the magnet height from 5 mm to 5.43 mm. The iron cover on top of the magnets is 3 mm thick and the flux barrier from the magnet to the flux shunt amounts to 2 mm. As seen in Fig. 5, some of the flux lines are shunted under no-load conditions, therefore the magnitude of the air gap flux density is reduced to $B_1 = 0.733$ T. The idea of this very sophisticated structure is illustrated in Fig. 6. While running idle, only a few flux lines are shunted, but as seen in Fig. 6(b) a demagnetising d -current does not need to superimpose a second field to the rotor magnet flux, but the flux lines of the rotor can be bent inside the iron covers and flux shunts. A considerable amount of magnet flux can be forced into the flux shunts and is prevented from crossing the air gap. According to [5] this flux weakening approach is very effective and the magnets are well protected against permanent demagnetisation.



Fig. 6. Rotor 2 under no load conditions (a) and with field weakening current (b)

Fig. 7 shows the comparison of the FE results of both rotors. In case of field weakening, the new rotor structure requires far less current compared to the standard PMSM. Unfortunately, at base speed the current demand is considerably increased, so the benefit at field weakening speed is balanced. According to (1) and (3), the reduced current at field weakening speed and the increased current demand at base speed can both be explained by the reduced magnitude of the air gap flux density under no-load conditions. In case of field weakening less magnetic flux needs to be compensated, hence less demagnetising current is required. At base speed, a reduced magnetic field yields an increased current requirement to generate a given torque.

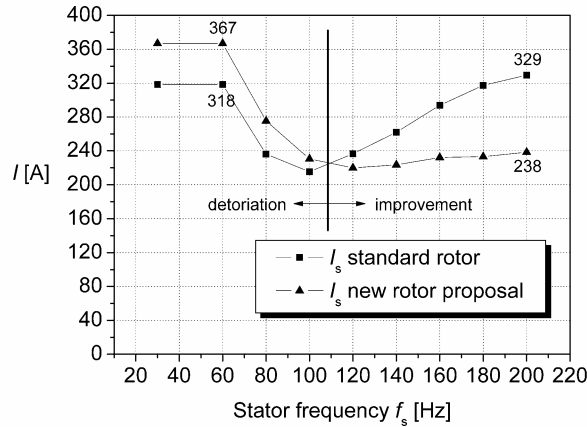


Fig. 7. Comparison of current demand of standard PMSM and new proposal [5]

Revised structure

Increasing the magnitude of the flux density to a value comparable to that of the standard PMSM would reveal if the new structure is still beneficial at field weakening speed, even if the current demand at base speed is similar to that of a standard PMSM. Therefore, the magnet height is increased to 7 mm, the height of the iron covers is reduced to 1.5 mm and the flux barrier is set to 2.5 mm. That way, the magnets are enlarged by 31.4 % and the magnitude of the air gap flux density is increased to $B_1 = 0.825$ T. Fig. 8 shows that in case of an increased flux density the current/frequency characteristics of the new rotor proposal approaches the standard PMSM current characteristics. The flux density is still slightly lower than at the standard PMSM structure, so at base speed, more current needs to be employed, whereas at field weakening the stator current is slightly reduced. In total, the beneficial behaviour reported in [5] can not be verified in case of this 6-pole PMSM arrangement.

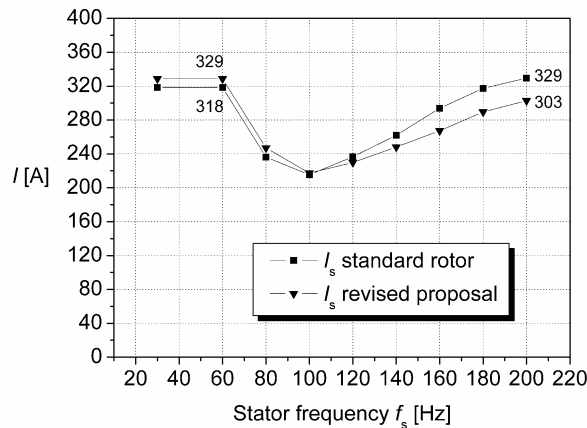


Fig. 8. Comparison of performance of standard rotor and revised new rotor proposal

Enhancing the PMSM by introducing saliency

According to (3), both the interaction of rotor flux with the stator currents and saliency ($X_d \neq X_q$) contribute to torque generation. Therefore, introducing saliency can be expected to be advantageous in order to reduce the total current at a given torque. In Fig. 9 saliency is achieved by filling the pole gap with rotor iron. The flux distribution under no-load conditions shows that some of the flux lines are shunted inside the pole gap. The magnitude of the air gap flux density is 0.857 T. The results of the FE analysis show that this reduced flux is beneficial in case of field weakening, because less flux needs to be compensated at high rotational speed (Fig. 10). At base speed, an increased current demand could be expected, as seen in Fig. 7. But in contrast, the stator current can be further reduced compared to

the standard PMSM. The lower magnetic flux can be fully compensated by making use of reluctance torque due to saliency. In both operating regions, at base speed as well as at field weakening speed, the total stator current can be reduced slightly.

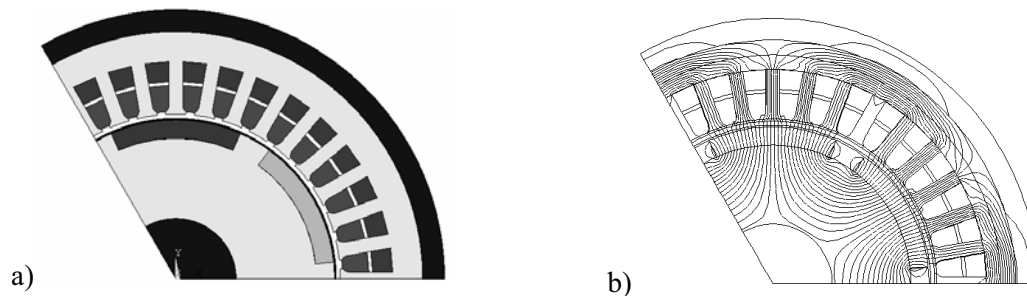


Fig. 9. Salient PMSM (a) and calculated no-load flux distribution (b)

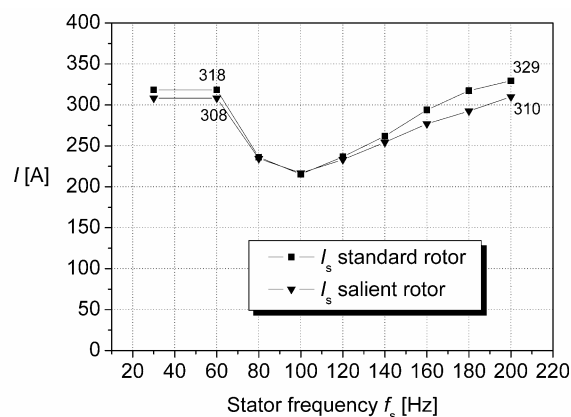


Fig. 10. Comparison of standard rotor structure with salient rotor

Conclusion

With the speed-torque demand of an electric forklift application, three different rotor arrangements of permanent magnet synchronous machines have been investigated. The positive behaviour of a new rotor structure announced in [5] could not be confirmed in the case of 6-pole machines. Especially the enlarged magnets of about 31 % due to enhanced stray flux and the very complicated mechanical configuration causing increased manufacturing effort are major disadvantages. Compared to the standard, non-salient permanent magnet synchronous machine a salient rotor structure, obtained by filling the pole gap with rotor iron, is found to show the highest torque/current ratio both at base and field weakening speed without increasing material or manufacturing costs.

References

- [1] Binder, A., Greubel, K., Piepenbreier, B., Tölle, H.-J.: "Permanent-Magnet Synchronous Drive with Wide Field Weakening Range", *ETEP* Vol. 8, No. 3, pp.157-166, May/June 1998
- [2] Ionel, D.M., Eastham, J.F., Miller, T.J.E., Demeter, E.: "Design considerations for permanent magnet synchronous motors for flux weakening applications", *IEE Proc. Electr. Power Appl.*, Vol. 145, No. 5, pp. 435-440, September 1998
- [3] Bianchi, N., Bolognani, S., Zigliotto, M.: "Design and Development of a PM Synchronous Motor Drive for an Electrical Scooter", pp. 1295-1299, *ICEM 2000*
- [4] Wen L. Soong, Nesimi Ertugul, "Field –Weakening Performance of Interior Permanent-Magnet Motors", *IEEE Transactions on Industry Applications*, Vol. 38, No. 5, 2002
- [5] Xu, L., Ye, L., Zhen, L., El-Antably, A.: "A New Design Concept of Permanent Magnet Machine for Flux Weakening Operation", *IEEE Transactions on Industry Applications*, pp. 373-378, 1995

II-19. NUMERICAL ANALYSIS OF THE BRUSHLESS MOTOR MAGNETIC FIELD AND TORQUE

Igor Tičar, Andrej Stermecki, Ivan Zagradišnik

Faculty of Electrical Engineering and Computer Science, Maribor, Slovenia, ticar@uni-mb.si

Abstract - The purpose of this research was to determine the magnetic field distribution and torque of the brushless electric motor. Different construction varieties are considered for decreasing a cogging torque component. 2D and 3D motor models were built with great attention to the finite element mesh, so that the meshes of different models are directly comparable. Final comparison of the described models, the numerical formulations and the measurement results offer a variety of answers and evaluations from different numerical approaches. All numerical analyses were performed by a research version of the ANSYS 6.1 (EMAG) computer program.

Introduction

The object of this analysis was the 12 pole brushless PM motor with a nominal power of 800 W. The permanent magnets used were standard ferrites with a remanent flux-density of $B_r=0.39$ T and coercive force of $H_c=310000$ A/m. The motor winding was a standard 3-phase winding with star-connected phase windings. These properties and the power supply system characteristics correspond to *square-wave PM brushless motor drive*. Detailed characteristics for these types of brushless motors can be found in literature [1].

The study of cogging torque reduction methods for this motor was analyzed from different points of view. The first aspect was the study of different construction variations for decreasing the cogging torque, consecutively improving motor performance. Furthermore, different numerical modeling approaches and formulations were compared to evaluate these approaches from the input/benefit ratio perspective. A lot of time can be saved by the optional use of simpler 2D models, but it is crucial to be aware of the limitations that are inevitable using 2D numerical analyses. Different modeling approaches often require different numerical formulations. The numerical formulations used in this study were the *Magnetic Vector Potential (MVP)* for a 2D model, the *Reduced Scalar Potential (RSP)* for a 3D model and the *Difference Scalar Potential (DSP)* for a 3D model that includes current sources.

Cogging torque minimization techniques

Brushless PM machine designing requires discontinuance of the stator and rotor structures. This leads to dissimilar reluctance values when observed in different angular directions. This is mainly caused by the openings of stator slots towards the air-gap area resulting from the technological restrictions of the winding process. A tangential component of magnetic attraction between the rotor-mounted permanent magnets and the stator teeth is produced due to dissimilar reluctance values. This attraction, the cogging torque, is an undesirable effect that causes additional irregularities in the torque characteristic of the brushless PM machine. Such irregularities can cause problems when starting the motor, difficulties in motor speed/torque control, additional noise, vibrations et al. All cogging torque minimization techniques are derived from the basic definition of cogging torque production described above. This can also be interpreted using the following equation:

$$T_{\text{cog}} = \sum_1^p \left(-\frac{1}{2} \Phi_g^2 \frac{dR_m}{d\Theta} \right) \quad (1)$$

where p stands for the number of poles, Φ_g for magnetic flux in the air gap, R_m for the reluctance and Θ for the rotor position in radians. Consequently, most methods for cogging torque minimization are based on reducing the reluctance change rate with respect to rotor position, which can be achieved in several ways. The combination of different minimization techniques provides a greater number of possibilities that can only be completely investigated with the help of numerical analysis.

Numerical modeling

There are two symmetries present in the construction of electrical machines – geometric symmetry and electro/magnetic symmetry. As the nature of the cogging torque is a strong interaction with the model's symmetries, it is also absolutely necessary that the finite element mesh strictly follows the same symmetries as the model itself. Automated mesh generation is, therefore, not recommended, and, therefore, the so-called mapped mesh generation was used for analysis. Such fixed mesh is certainly necessary, because small modifications in the geometry should not result in drastic mesh changes, which is often the case for automated mesh generation. The conclusion can be drawn from experience of the presented work, that the appropriate mesh with emphasis on symmetric distribution of the elements is crucial for correct analysis.

Additionally the symmetry of the motor cross-section was taken into consideration. Solving time was essentially reduced by analyzing only the portion of the motor cross-section. Symmetric boundary conditions were assured by coupling the appropriate degrees of corresponding node freedom on both symmetry planes.

Two different approaches were applied and compared for the consideration of relative motion. The first method is based on rotor rotation over a fixed angular distance which is accordant with the node distribution in the air gap. The nodes in the air gap layer are merged after each rotation step. This method can be applied to 2D and 3D models without skewed rotor or stator. The second method is based on coupling the neighboring nodes in the air gap using constraint equations. Constraint equations tie together two layers of non-coincident nodes with respect to the element shape function. Therefore, the final result is virtually disconnected mesh, but the layers of slip surface are tied up by the mentioned equations. This method is very convenient and substantially speeds up modeling process. The described method with constraint equations is inevitably followed by a numerical error. It can be concluded from the presented research, that the numerical error derived by this method can be neglected when the mesh is sufficiently dense.

Results

Firstly the results for the 2D models are presented. These models were programmed using MVP numerical formulation. All calculations were firstly tested on the whole motor cross-section and later compared to the results obtained from the symmetric portion of the model. Comparisons were also performed between different approaches when considering relative motion. The modeling of only a symmetric portion of the motor, and the use of constraint equations for movement consideration were applied to the 3D models on the basis of these 2D model findings.

Basic model: In the picture below (Fig.1) the basic 2D model of the brushless permanent motor is shown. In this model no strategies were implemented for cogging torque minimization. The model cross-section contains 36 stator slots and 12 radially magnetized permanent magnets.

Fig.3 shows the cogging torque versus rotor position. The peak value of cogging torque is 0.8 Nm. High cogging torque values caused irregularities in the total torque characteristic that are evident from Fig.2 where the curve does not run smoothly.

Model with closed stator slots: As a cogging torque is mainly produced by the openings of stator slots towards the air gap area, the prime solution for this problem seemed obvious – closed stator slots. This was easy to simulate in numerical analysis but is much harder to realize in production. These types of motors can indeed be found on the market but for a rather high price and are, therefore, meant for special electrical drives. Consequently, the purpose of a numerical analysis of the motor with closed stator slots, shown here, is not to present yet another cogging torque minimization technique, but rather to serve as a later comparison with other (substantially less expensive) methods.

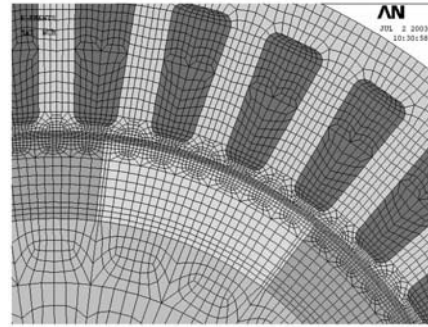


Fig.1. A closer view of the mesh (mesh contains 25344 elements)

Cogging torque (Fig.3) and its influence on torque (Fig.2) in the model with closed stator slots is practically negligible. Therefore, the torque characteristic (Fig.2) is almost completely equivalent to the theoretically predicted torque characteristic of the idealized brushless square-wave motor model [1].

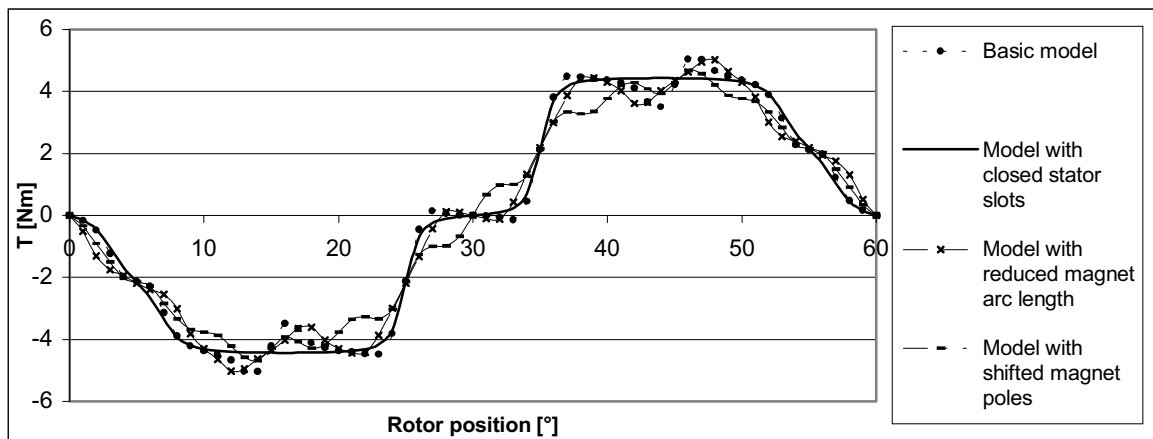


Fig.2. Numerically calculated torque values versus rotor position obtained by 2D models

Model with reduced magnet arc length: Cogging torque is produced when the magnetic flux from the edge of a permanent magnet enters a stator slot. Varying the lengths of the magnet arcs, therefore, affects the cogging torque. As reduction in magnet arc length also eliminates some technological problems when placing (gluing) permanent magnets on the rotor, this method is often combined with other torque minimization methods. Here a model is presented with the lengths of all magnet arcs shortened by 2 mechanical degrees compared to the basic model. The cogging torque peak value was reduced by 0.1 Nm (12.5%) (Fig.3), using this method.

Model with shifted magnetic poles: It is possible to shift the magnet poles in such a way, that the cogging torque producing tangential forces are partially mutually cancelled. This procedure is very delicate – namely, by shifting the magnet poles the total torque can be substantially reduced. To obtain the desired results, the shifting angle should be very carefully chosen and the search for its optimal value should be approached by numerical analysis.

The presented results for this method were obtained using a model with the magnetic poles shifted by 5 degrees compared to the basic model. This method proved to be highly efficient. The peak value of cogging torque was under 0.4 Nm which represents a reduction of more than 50 % compared to the basic model. Especially significant with this approach is that the total torque characteristic was

considerably less affected by cogging torque when the peak value of the total torque remained unchanged.

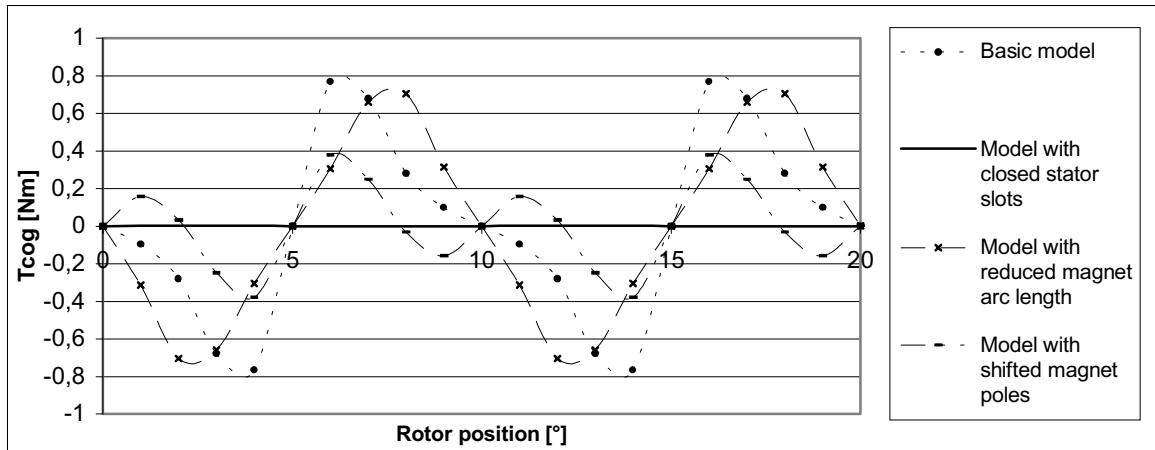


Fig.3. Numerically calculated cogging torque values versus rotor position obtained by 2D models

Model with shifted magnetic poles and skewed magnetizing direction of permanent magnets: A 3D model was built to investigate the effects of skewing on cogging torque and total torque characteristics. The cogging torque was determined by analysis where no current was assigned to the stator winding and, therefore, RSP numerical formulation was used. On the other hand, the total torque

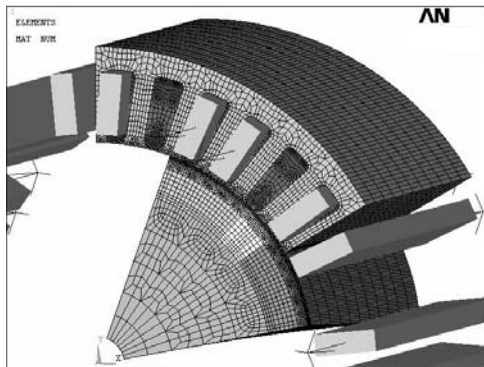


Fig.4. 3D model with skewed magnetizing direction of permanent magnets

was calculated by DSP numerical formulation which considers the effects of the stator current using the Biot-Savart principle. A model of only a symmetric portion of the whole motor cross-section was built to speed up the solving process. Winding was modeled to its full extent because of being one of the basic requirements for DSP numerical formulation. The two layers of the slip surface in the air gap were tied together with constraint equations for movement consideration. The geometry and the mesh of the 3D model were derived from the 2D model with shifted magnetic poles. The basic 3D geometry is presented in Fig.4.

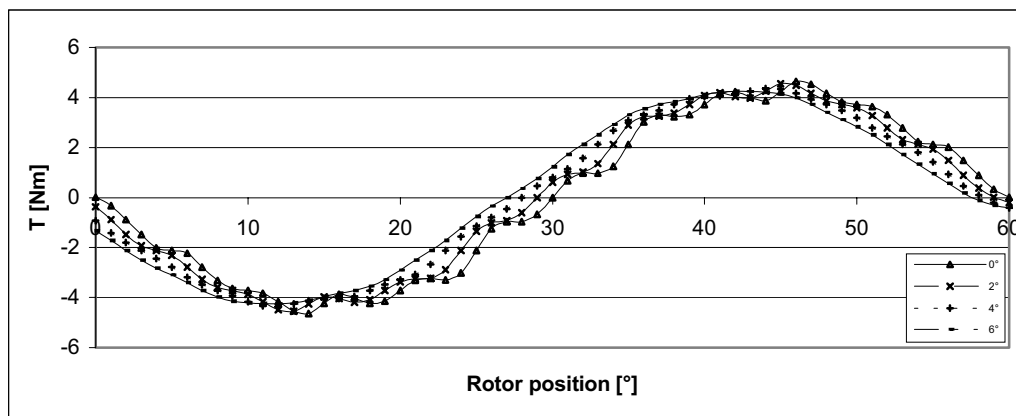


Fig.5. Numerically calculated torque values versus rotor position for different skewing angular values

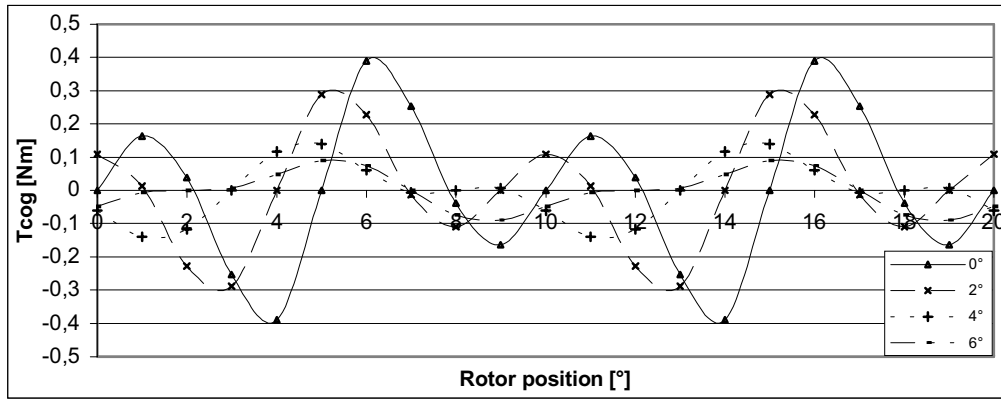


Fig.6. Numerically calculated cogging torque values versus rotor position for different skewing angular values

Comparison between 2D model and 3D model results

When no skewing was applied to the 3D model, this model displayed similar electro-magnetic conditions as the 2D model with shifted magnetic poles. There were, however, major differences in numerical formulations and approaches between these two models:

- The 2D model was built for the whole motor cross-section. Only its symmetric portion was considered in the 3D model.
- The layers in the air gap in the 3D model were tied together by constraint equations which was not the case in the 2D model.
- RSP and DSP numerical formulations were used in the 3D model, whilst MVP numerical formulation was applied in the 2D model.
- Numerical formulation for the 2D model enabled the assigning of current density to the real geometry of the conductors. In the 3D model, conductors were modeled using the basic block shape elements needed for Biot-Savart calculation.

The deviation between the results of the 2D model and 3D model without skewing being applied proved to be less than 0.1 %. Furthermore, this comparison also shows equivalence among the results of different numerical formulations. This assertion is very significant as the 3D model was built with simplifications that essentially speeded up the process of modeling and solution.

Predicting the torque characteristic of the 3D skewed model on the basis of the 2D model results

The torque characteristic of a skewed 3D model can be predicted on the basis of the 2D model by

using following equation:

$$T = \sum_{i=1}^N \frac{(T_i)}{N} \quad (2)$$

where T_i stands for the torque at rotor position i and N stands for the number of positions taken into account. Better results are expected, if more positions N are considered. This means that a 2D analysis should be performed at as many rotor positions as possible (in the presented case at each mechanical degree). In picture (Fig.7) such a prediction is presented for the model with a skewing angle of 6° .

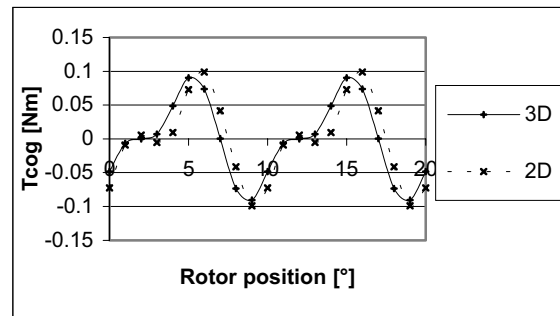


Fig.7. Cogging torque characteristic predicted on the basis of the 2D model compared to the 3D model results

Conclusions

The presented research shows that the torque characteristic of a model with closed stator slots is actually the closest approximation to the desired torque characteristic. Efforts should be made because of the high price to reach a cogging torque minimization using less expensive methods. In the performed analyses the best results were obtained from the combination of two different methods – skewing the magnetizing direction combined with shifting the magnetic poles. In this way the cogging torque was reduced by over 85 % and, consequently, most of the total torque characteristic irregularities disappeared without significantly lowering the total torque peak value.

These simplified 3D modeling approaches ensured results with no considerable deviations compared to the results of more exact modeling techniques. Modeling and solving the problem on only a symmetric portion of the motor cross-section substantially lessened the solution time. The use of constraint equations for movement consideration in the 3D model proved to be a very effective method for simplifying the modeling process.

Comparisons among the results of different numerical formulations showed their equivalence. The torque results obtained from the 3D model corresponded to the results obtained from the 2D model with MVP formulation despite the fact that the basic shape elements used for 3D winding modeling at DSP numerical formulation did not outline the winding geometry in details. Therefore, using the presented 3D modeling approach, a lot of modeling and solving time can be saved. On the other hand, it should always be considered carefully as to whether 3D modeling should be undertaken at all. Namely, as shown in the article, a lot of typical 3D problems (i.e. skewing) can be adequately investigated by 2D analysis.

References

- [1] T. J. E. Miller, *Brushless Permanent-Magnet and Reluctance Motor Drives*, Oxford: Clarendon Press, 1989
- [2] ANSYS 6.1 documentation, ANSYS, Inc. Theory Reference
- [3] A. Keyhani, C. B. Studer, T. Sebastian, S. K. Murthy, *Study of Cogging Torque in Permanent Magnet Machines*, *Electric Machines and Power Systems*, Vol. 27 (7), pp 665-678, 1999
- [4] O. Biro, K.R. Richter, *CAD in Electromagnetism*, Graz: Institute for Fundamentals and Theory in Electrical Engineering, Graz University of Technology, 1996

II-20. MAGNETIC FIELD AND SHORT-CIRCUIT REACTANCE CALCULATION OF THE 3-PHASE TRANSFORMER WITH SYMMETRICAL AMORPHOUS CORE

B. Tomczuk^{*}, K. Zakrzewski^{}, D. Koterak^{*}**

^{*} Technical University of Opole, Dep. of Electr. Eng. and Automatic Control,
ul. Luboszycka 7, 45-036 Opole, Poland, e-mail: tomczuk@po.opole.pl

^{**} Technical University of Lodz, Institute of Mechatronics and Information Systems
ul. Stefanowskiego 18/22, 90-924 Lodz, Poland, e-mail: zakrzew@po.lodz.pl

Abstract – Magnetically symmetric, 3- phase transformer has been analysed. For the two variants of the windings, the calculation results have been compared with the measured ones. Magnetic flux density components were calculated in and out of the core. The flux distribution and short-circuit reactance have been verified experimentally and a good agreement has been obtained.

Introduction

All manufacturers and users of transformers capitalize the core loss while considering the total costs of a transformer. In amorphous-metal transformer cores, the losses are quite low [3]. They are several times lower than the losses in some grain silicon steel sheets [5]. Therefore, the 3-D computations of the flux distribution in the transformers may ignore the eddy currents in its core.

The earliest amorphous-metal transformers contained simple, continuous, spiral wrapped cores. It was necessary to assemble the coils by winding insulated wire through the center and around the legs of the closed core. However, in most distribution transformer manufacturing operations, the core and the coils are produced independently. That is why the core can be “opened”.

Several technologies were developed which allowed amorphous metal to be used in transformer manufacturing in a manner similar to silicon steel. One of them is the modular technology where the columns are assembled with several parts. In this work the magnetically symmetrical core, which is assembled with the modular technique, has been considered. Thus, due to the symmetry the magnitudes of the no-load currents in the 3-phase transformer are even.

Description of the object

The magnetic field distribution and leakage reactance for the 3-phase transformer with magnetically symmetric core have been calculated (Fig. 1). The magnetic circuit is composed of hollow cylinders made of amorphous material. Two circular plate-form yokes are joined with three limbs (columns). The internal and external diameters of the limbs are $d_1=1.3\text{cm}$ and $d_2=10\text{cm}$ respectively. Their height is $h_c=19.7\text{cm}$, while the depth of the yokes is much smaller ($h=3.6\text{cm}$). Each limb is provided with inner and outer concentric coils which height is $h_w=18\text{cm}$ (Fig. 1). The rated power of the physical object is $S=10\text{kVA}$, and the nominal currents are $I_{1N}=15.9\text{A}$, $I_{2N}=26.2\text{A}$.

To obtain a small value of the short-circuit reactance, the primary and secondary cylindrical windings are separated by a thin insulating sleeve. The numbers of their turns are $N_1=191$, and $N_2=116$, respectively.

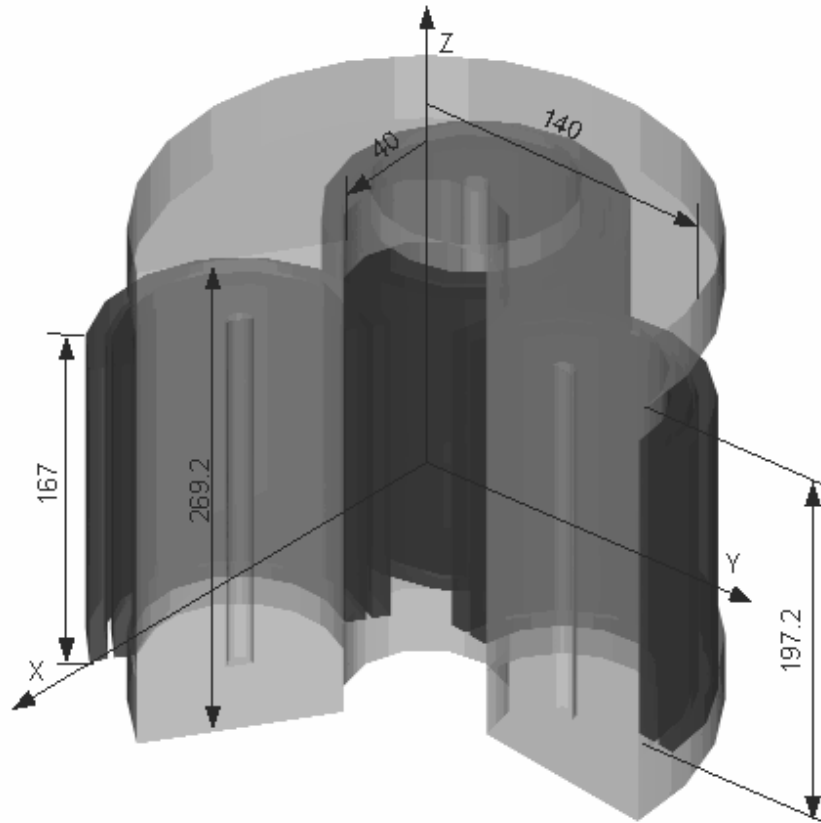


Fig 1. Main dimensions of the analyzed object

We have considered two systems of coils. They are with complete layers and incomplete ones as well. For the second case, the incomplete layers cling to the insulating sleeve. Thus, for the arrangement, the manufacturer obtained uniform and level surface of the external coil.

Calculation model

The Finite Element (FE) method is used for the field analysis in the 3-D leakage region of the transformer [1], [2]. As the device has a symmetrical structure (Fig. 1), and to keep the calculations within the limit of elements [2], the calculation model has been halved along the z-axis (Fig. 1). The FE grid consists of tetrahedral elements [5], [6].

For the leakage reactance calculation, the state of symmetrical short-circuit of the transformer is considered. A few simplifications have been made. Due to the short-circuit state, we included the compensation of primary and secondary ampere-turns. The flux in the core is relatively low, and the saturation effect of the core is negligible. Thus, including the nonlinear characteristic does not influence leakage reactance X of each phase. Moreover, the conductivity of the core material is low, and the amorphous ribbon is very thin. Thus, under power frequency the core losses can be neglected in the field model for the leakage reactance calculation.

The combination of two scalar potentials is used for the evaluation of the 3-D leakage field [1]. The first one, called total potential ψ , satisfies the Laplace's equation in the current-free regions

$$\nabla \cdot (\mu \nabla \psi) = 0. \quad (1)$$

In the conductors, the equation for the so-called reduced potential Φ is obligatory

$$\nabla \cdot (\mu \nabla \Phi) - \nabla \cdot (\mu \vec{H}_s) = 0 \quad (2)$$

The field intensity \vec{H}_s arises from the current carrying conductors.

Results of the calculations and measured verification

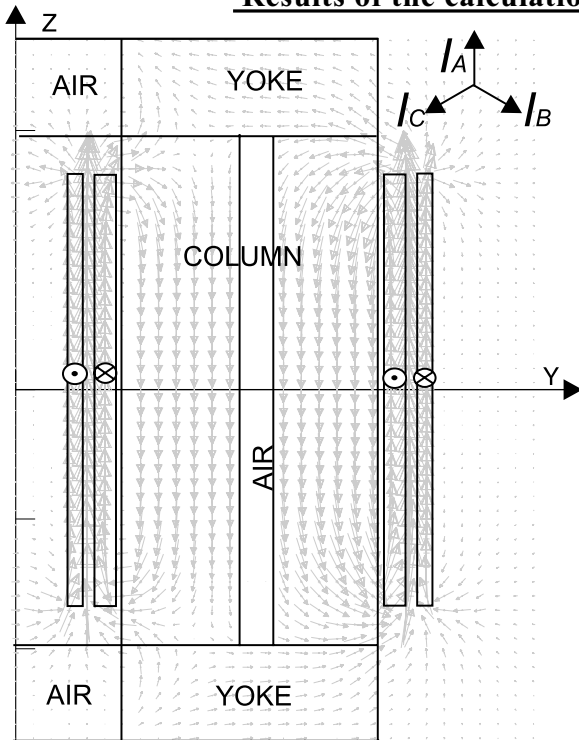


Fig. 2. Magnetic flux density in uniform coils (phase A)

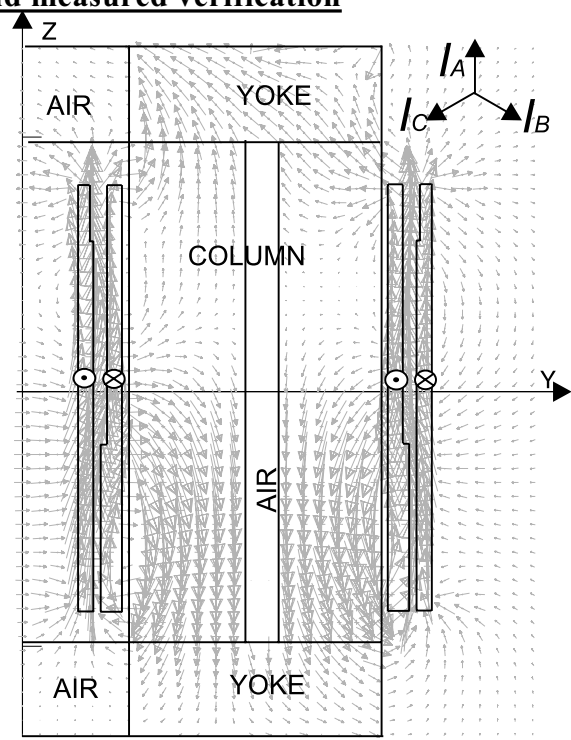


Fig. 3. Magnetic flux density for incomplete layers (phase A)

The B distributions in axial cross-section of the leg (for the two systems of coils) are presented in Figs. 2 and 3. The values were calculated for the depicted current arrangements. Obviously, for the short-circuit condition, the maximum values are in the air gap between the primary and secondary coils. The field in the gap is nonuniform (Fig.3). First and foremost, for the nonuniform coils the distribution is not symmetrical in relation to the XY plane (Fig. 1).

The obtained values of the flux density influenced short-circuit reactance naturally. The flux linkage can be found as a sum of the magnetic flux Φ_k linked with each wire. Knowing the flux linkage and frequency f of the current I , we obtained the leakage reactance X per one phase [4]

$$X = \sum_{k=1}^N \Phi_k \frac{2\pi f}{I}, \quad (3)$$

where N is number of turns. The calculated values were compared with the measured ones. For the two studied arrangements of the windings, they are given in Tab. 1. For the transformer with incomplete turns on the outskirts of the coils, the reactance is slightly more than for the uniform windings.

In Fig. 4 we show a comparison between FE model results and measured values of the B_z component. The values concern the points near the end of the uniform coils $Z=8.6\text{cm}$. Due to the ampere-turns compensation, they are relatively low ($B < 5\text{mT}$). The B_z values were also compared for the nonuniform windings, which are not presented here.

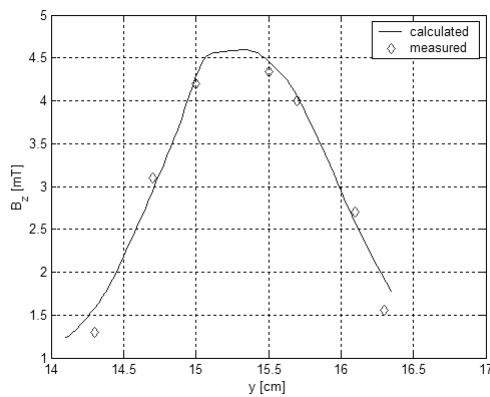


Fig. 4. B_z component over the ends of the uniform windings.

Table 1. The values of the leakage reactance X per phase (in Ω)

coils	calculated	measured
uniform coils	0.251	0.254
nonuniform coils	0.285	0.282

Conclusions

A new construction of the magnetic core for a 3-phase transformer has been studied with the Finite Element Method. The grid of tetrahedral elements has been used.

To determine the leakage reactance, the 3-D magnetic field analysis was carried out under short-circuit condition. Finite element computations were run for two constructions of the cylindrical windings. The coils with uncompleted layers as well as uniform windings were examined. The calculations confirm that the arrangement of incomplete layers has not a considerable effect on distribution of the leakage field and the short-circuit reactance (Table 1). Thank to modular technique the described structure is convenient to build.

This work was partially supported by The Scientific Research Committee under grant No. 1154/T10/2003/24

References

- [1] K.J. Binns, P.J. Lawrenson, C.W. Trowbridge, *The Analytical and Numerical Solution of Electric and Magnetic Fields*, Chichester, John Wiley & Sons LTD, 1992.
- [2] OPERA3D- Users Manual, Vector Fields, London, 1995.
- [3] S. Sieradzki, R. Rygał, M. Soinski, Apparent core losses and core losses in five-limb amorphous transformer of 160 kVA, *IEEE Trans. on Magn.*, USA, Vol. 34, No. 4, 1998, pp. 1184-1191.
- [4] B. Tomczuk, Three-dimensional leakage reactance calculation and magnetic field analysis for unbounded problems, *IEEE Trans. on Magn.*, USA, Vol. 28, No. 4, 1992, pp. 1935-1940.
- [5] K. Zakrzewski., B. Tomczuk, Finite element (FE) calculations of 3-d fields in the autotransformer windings under short-circuit by electric arc, *Proc. of the International Symposium on Electromagnetic Fields in Electrical Engineering, ISEF'2001, Cracow, Poland, September. 20-22, 2001*, pp. 331-334.
- [6] K. Zakrzewski., B. Tomczuk, D. Koterias, Simulation of forces and 3-d field arising during power autotransformer fault due to electric arc in HV winding, *IEEE Trans. on Magn.*, New York, USA, Vol. 38, No. 2, March 2002, pp. 1153-1156.

II-21. ANALYSIS OF INSTANTANEOUS VOLTAGE DISTRIBUTION IN PERMANENT MAGNET BRUSHLESS GENERATOR

Beata Wawrzyniak, Pawel Witczak

Institute of Mechatronics and Information Systems, Technical University of Lodz
18/22 Stefanowskiego St., 90-924 Lodz, Poland, pwitczak@p.lodz.pl

Abstract – The paper presents the connection of the classical rotational fields approach with the numerical modeling obtained by means of the finite element method. Results of numerical calculations are inserted directly into analytical formulae. The proposed method does not require the sinusoidal shape of the flux density, both in time and space and also does not use the concept of the magnetic inductance. The application of this approach is shown for the exemplary permanent magnet synchronous machine; however, it can be easily applied for any other kind of rotating magnetic device.

Introduction

Permanent magnet machines must have some regions being magnetically over-saturated. In most of cases it causes additional deformations of time and space distributions of quantities like air-gap flux density or induced voltage. Simultaneously, these machines cannot be modeled in classic way by means of the single inductance representation only, because of significant influence of the magnetic nonlinearity causing the spatial distribution of the flux density wave to be far from the sine function. The example of such a machine it is the synchronous generator connected with the rectifier, most often named as Permanent Magnet Brushless Generator (PMBG). The finite element approach together with the time-stepping technique enables the solution of the transient distribution of the magnetic flux density and usually required integral quantities like induced voltage or magnetic torque. However, the computing efforts are still too high for many practical needs, like in control applications. Therefore, the mixed approach inserting directly the outputs of the finite element (FE) model into the lumped circuit of the machine may be interesting for some further developments. The general idea of this work is to replace the sinusoidal in space shape of the magnetic field in the air gap used extensively from many years [1][2] by another functions being much closer to the reality.

Approximation of flux density in air gap

Initial assumptions for further considerations are:

- The spatial distribution of the radial component of the flux density vector in the air gap is constant in time, when observed in the coordinate system $d\beta$ rotating with the same velocity and direction as the magnetic field patterns. It means that effects of stator slotting are not properly taken into account, however, for these cases when high time harmonics are not investigated it is reasonable. It will be shown later that it causes some changes in frequency spectrum but the overall RMS value is not much affected.
- The mechanical angular velocity remains constant. It may be accepted, when the moment of inertia of the system is sufficiently high to neglect the fluctuations of the velocity caused by the torque ripples. It is fulfilled for the majority of electric machines.
- The magnetic energy stored in the air gap can be evaluated on the basis of the one – dimensional distribution of the radial component of the flux density. The correctness of this statement, or more precisely, the limited amount of error results from FE insertion into analysis.

- Analyzed machine is axially symmetric – the rotor eccentricity is not investigated.

Any distribution of the flux density along the air gap $B(\beta)$ may be represented by the sum

$$B(\beta) = \sum_m b_m \vartheta_m(\beta) \tag{1}$$

where $\{\vartheta_m\}$ is the set of basis functions of the arbitrary functional space. The mostly popular choice of that space it is the Fourier series of trigonometric sine and cosine functions. Their slow convergence is the major disadvantage of that representation. One may extend the definition of used functional space into periodic odd $\{\vartheta_{Om}\}$ and periodic even $\{\vartheta_{Em}\}$ functions. Their important properties are:

- the operator of derivation converts the odd function into the even one and reciprocally

$$\frac{d\vartheta_{Om}}{d\beta} \in \{\vartheta_{Em}\} \tag{2}$$

$$\frac{d\vartheta_{Em}}{d\beta} \in \{\vartheta_{Om}\}$$

- the scalar product of arbitrary odd and even periodic functions (having the same fundamental period) is always equal to zero

$$(\vartheta_{Ek}, \vartheta_{Om}) = \int_{-\pi}^{\pi} \vartheta_{Ek}(\beta) \vartheta_{Om}(\beta) d\beta \equiv 0 \tag{3}$$

Examples of orthogonal set of basis functions for the model of PMBG sketched in fig.1a are presented in fig.1b.

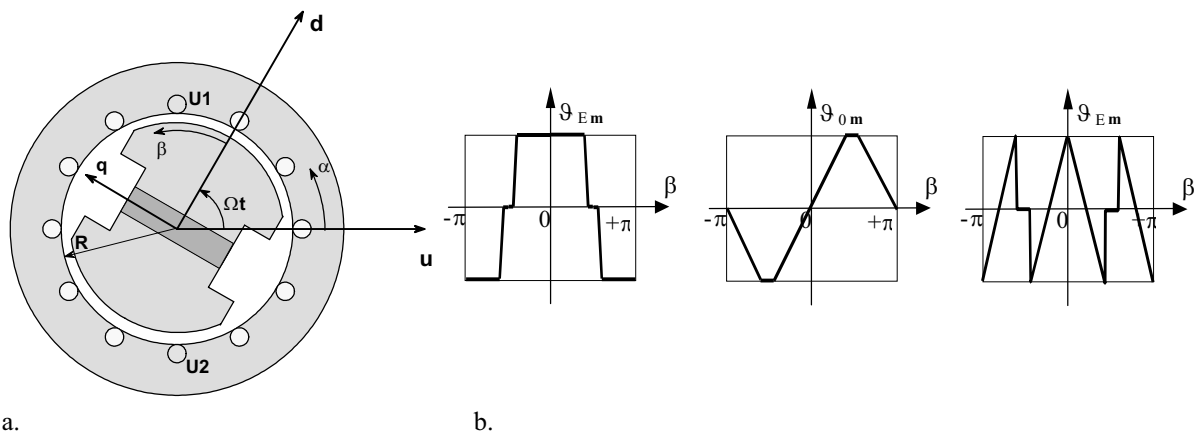


Fig.1. a. Placement of co-ordinate systems in PMBG ($d\beta$ - rotor oriented, $d\alpha$ - stator oriented)
 b. Examples of orthogonal basis functions ϑ_m available for the analysis.

The number of basis functions depends on required accuracy, the minimum amount seems be equal to three – the first one represents magnetic field at no-load state B_0 , the next two should show the armature reactions in quadrature B_q and direct B_d axes. It can be written in the following form

$$B_0(\beta) = b_0 \vartheta_0(\beta) \tag{4}$$

$$B_d(\beta, I_d) = b_{d0}(I_d) \vartheta_0(\beta) + b_{d1}(I_d) \vartheta_1(\beta) \tag{5}$$

$$B_q(\beta, I_q) = b_{q0}(I_q) \vartheta_0(\beta) + b_{q1}(I_q) \vartheta_1(\beta) + b_{q2}(I_q) \vartheta_2(\beta) \tag{6}$$

The magnitudes of particular components are given by

$$\begin{aligned}
 b_0 &= \|B_0\| \\
 b_{d0} &= (B_d, \vartheta_0) & b_{d1} &= (B_d, \vartheta_1) \\
 b_{q0} &= (B_q, \vartheta_0) & b_{q1} &= (B_q, \vartheta_1) & b_{q2} &= (B_q, \vartheta_2)
 \end{aligned} \tag{7}$$

The relations (7) require the explicit forms of ϑ_m . They can be obtained using the standard orthonormalisation algorithm

$$\begin{aligned}
 \vartheta_0(\beta) &= \frac{1}{\|B_0\|} B_0(\beta) \\
 \vartheta_k(\beta) &= \vartheta_0(\beta) - \sum_{j=1}^{k-1} (B_k, B_j) \vartheta_j(\beta) \\
 \vartheta_k(\beta) &= \frac{1}{\|\vartheta_k\|} \vartheta_k(\beta)
 \end{aligned} \tag{8}$$

where $k = 1, 2$ and $B_k = B_d, B_q$, respectively.

The coefficients b given by equation (7) are dependent on current and load angle ψ (between negative rotor \mathbf{d} and resultant stator \mathbf{s} axes). For symmetrical three-phase load they are

$$\begin{aligned}
 b_{d0}(I, \psi) &= (b_{d0} - b_0) \frac{I}{I_R} \cos \psi & b_{dk}(I, \psi) &= b_{dk} \frac{I}{I_R} \cos \psi \\
 b_{q0}(I, \psi) &= (b_{q0} - b_0) \frac{I}{I_R} \sin \psi & b_{qk}(I, \psi) &= b_{qk} \frac{I}{I_R} \sin \psi
 \end{aligned} \tag{9}$$

where I_R is the current RMS value, at which the distributions $B_d(\beta)$ and $B_q(\beta)$ were obtained. When the generator is connected with the rectifier, the trigonometric functions in (9) should be replaced by trapezoidal shapes. The detailed explanation of this item is beyond the scope of the paper due to its limited size.

Induced phase voltages

Having the flux density distribution obtained in rotor co-ordinate system $\mathbf{d}\beta$ it is easy to convert it into the EMF induced in stator phase winding. Following the Faraday law one obtains for single coil U1U2 shown in fig. 1a

$$e_U(t) = -n_s L_i R \frac{d}{dt} \left(\int_{\alpha_2}^{\alpha_1} B(\alpha, t) d\alpha \right) \tag{10}$$

where n_s – coil turn number, L_i – length of core, α_1, α_2 – angular co-ordinates of the coil
 R – air gap mean radius.

Exchanging the derivation with integration operator and introducing the rotor co-ordinates it holds

$$e_U(t) = -n_s L_i R \left(\int_{\alpha_2}^{\alpha_1} \frac{\partial B(\alpha, t)}{\partial \alpha} \frac{d\alpha}{dt} d\alpha \right) = -n_s L_i R \Omega [B(\beta = \alpha_1 - \Omega t) - B(\beta = \alpha_2 - \Omega t)] \tag{11}$$

where Ω is the field angular velocity.

Finally, for not shortened coils the phase EMF e_{ph} amounts to

$$e_{ph}(t) = -2c_{ph}n_s\xi_c H_{med}(\beta)L_i R \Omega B(\beta = \alpha_1 - \Omega t) \tag{12}$$

where c_{ph} – number of coils connected in series, ξ_c – winding factor, H_{med} – running median filter. Introduction of median filter (of slot pitch width) results from stator slotting, which without this factor would create fictitious time harmonics. Unfortunately, it also cancels the real harmonics introduced by proximity effects between stator and rotor permeance jumps.

Example of analysis

The FE model of PMBG has been constructed in 3D space. Application of anty-periodic boundary conditions enabled to limit the size of the model to one pole pitch. The basic geometric and material data are: $R=0.12$ m, $L_i=0.2$ m, magnets made of bonded NdFeB. Geometry of the model and flux density distribution for the case, when the armature reaction is all directed along the rotor q axis are shown in fig.2.

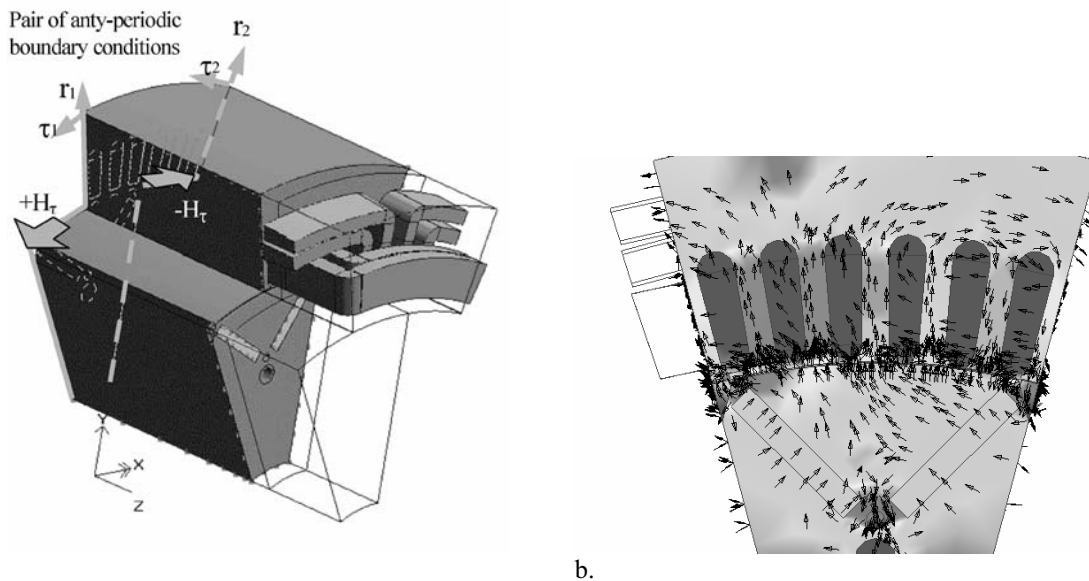


Fig.2. Finite element model of permanent magnet brushless generator.
 a. Geometry and boundary conditions applied,
 b. Flux density distribution for stator reaction in q axis.

As expected, the end effects along z axis are quite small, the difference in energy stored between 2D and 3D solutions is of size, say, 3-5%. Therefore, the assumption of the flat field in the air gap is acceptable. Details are given in [3]. The distributions of radial component of the flux density in the plane of the machine's symmetry along the air gap are plotted in fig.3.

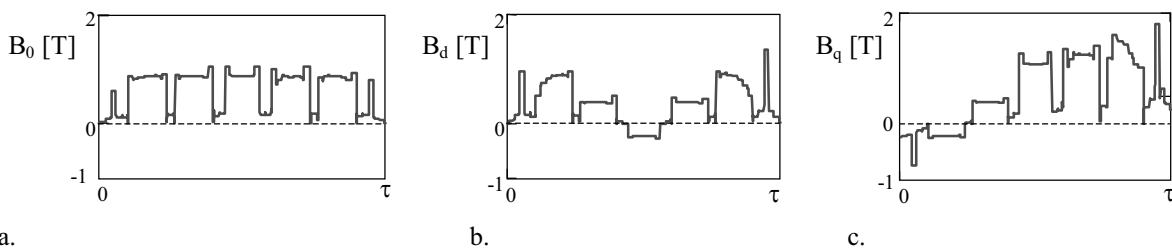


Fig.3. Distributions of radial component of flux density in the middle of air gap for three load conditions.
 a. no-load state,
 b. armature reaction in d axis,
 c. armature reaction in q axis.

Following the method described above the set of three ortho-normal functions $\{\vartheta_m\}$ was obtained. They are presented in fig.4. (for one pole pitch only)

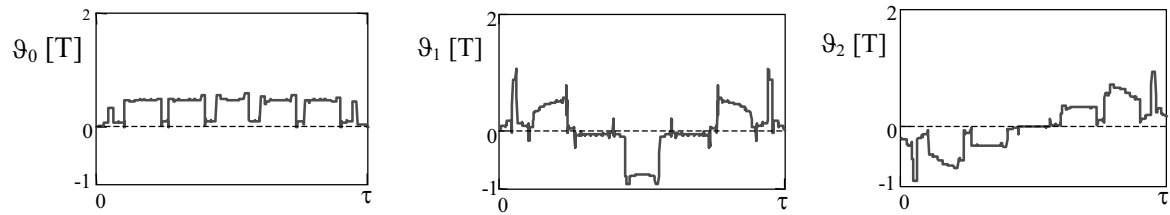


Fig.4. Distributions of basis functions $\{\vartheta_m\}$ - halves of their periods only.

Now the magnetic flux density can be calculated for any load. The examples of results for the chosen load angles and constant phase current (kept by inverter in DC line) are presented in table 1 and fig.5.

Table 1. Amplitudes of modified basis functions for chosen loads at the same stator current

Load angle, [deg]	b_0 , [T]	b_{d0} , [T]	b_{q0} , [T]	b_{d1} , [T]	b_{q1} , [T]	b_{q2} , [T]
60	1.82	-0.61	-0.16	0.62	-0.24	0.92
75	1.82	-0.22	-0.21	0.23	-0.32	1.26

The negative values of b_{d0} mean that armature d-axis reaction is demagnetizing, the small negative b_{q0} values show the demagnetizing effect of q-axis reaction due to local saturation, the increase of b_{q2} is caused by the torque increase.

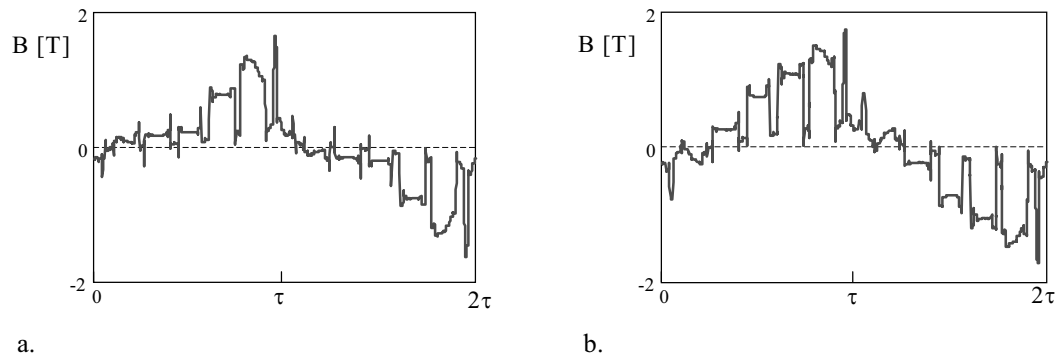


Fig.5. Flux density distribution along the double pole pitch at different load angles
 a. $\psi = 45$ deg b. $\psi = 75$ deg

The induced phase voltage calculated by (11) with $H_{med}=1$ looks like in fig.5, with rescaled values on both axes. However, stator slotting cannot produce the higher time harmonics in stator winding. After the median averaging filter the EMF induced in the phase winding at 60 r.p.m. has the form shown in fig.6.

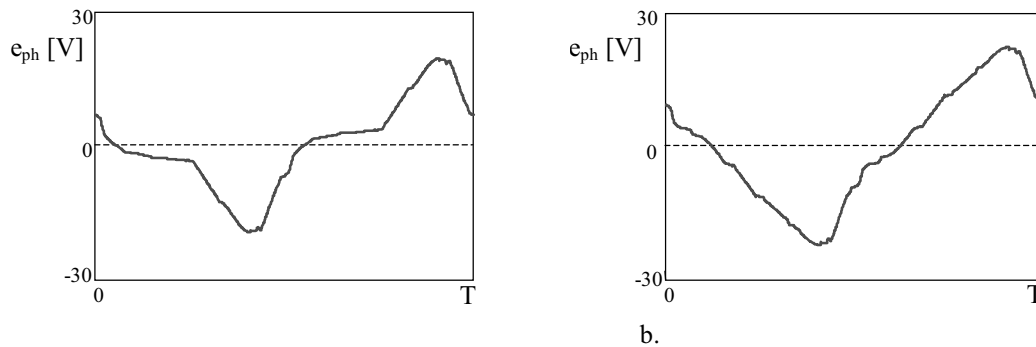


Fig.6. Phase voltage distribution within time period T at different load angles
 a. $\psi = 45$ deg b. $\psi = 75$ deg

Comparing the voltages in all stator windings one may extract their envelope and the rectified voltage afterwards. The time distributions of DC component are presented below, the period of the fundamental component of AC voltage in phase winding is denoted by T .

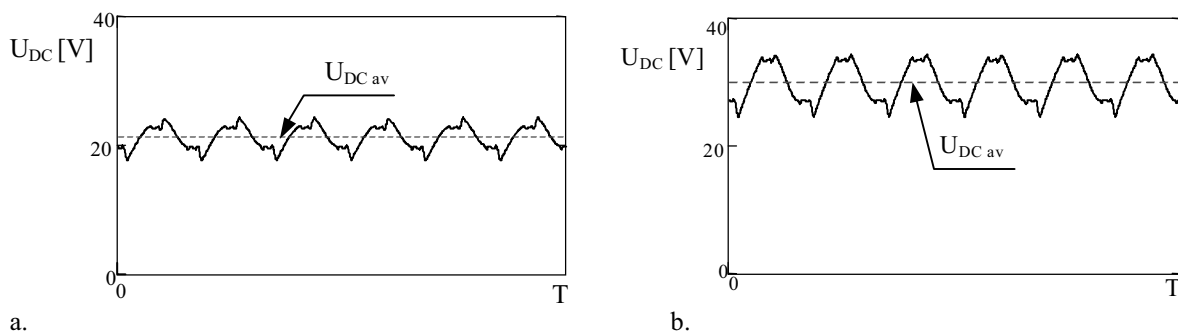


Fig.7. Distribution in time of rectified voltage of PMBG at different load angles
a. $\psi = 45$ deg b. $\psi = 75$ deg

Conclusions

The approach presented in this paper extends the existing methods towards the more accurate analysis of non-sinusoidal, both in time and space, signals generated by electric machines connected with static converters. The main advantage of proposed algorithm is to solve the quasi-steady state without the time consuming analysis of transients starting from no-supply conditions. It is worth of mentioning that magnetic over-saturation effects resulted from the presence of permanent magnet embedded in the rotor are included by means of the introduction of results from nonlinear FE analysis. The method described above should be supplemented with more precise model of the commutation in the diode bridge (the resistance and leakage reactance of the phase winding were omitted here) and also with the incorporation of not uniform rotational velocity of the stator field caused by the presence of the rectifier in the model. It is possible in presented approach, but it simultaneously requires the analysis of the magnetic torque generated in the machine. The limited extent of this work forced to skip these problems.

References

- [1] Heller B., Hamata V.: „*Harmonic field effects in induction machines*”, Academia, Prague 1977
- [2] Vas P.: „*Electrical machines and drives*”, Clarendon Press, Oxford 1992
- [3] B. Wawrzyniak, P. Witzak, “*3D Finite Element Modelling of Permanent Magnet Brushless Generator*”, XXXVIII Int. Conf. on Electric Machines, Kielce, 2002, pp.181-190

II-22. DEVELOPMENT OF MATHEMATICAL MODEL AND COMPUTATION OF ELECTROMAGNETIC DRUM-TYPE SEPARATOR BY BOUNDARY ELEMENT METHOD

Mykhaylo V. Zagirnyak*, Oleg S. Akimov**

*Kremenchuk State Polytechnical University, ul. Pershotravneva 20, Kremenchuk 39614, Ukraine,
e-mail: mzagirn@polytech.poltava.ua

**Kaf. electromechaniki, Dal East Ukrainian National University, kv. Molodejhnij 20a,
Lugansk 91034, Ukraine, e-mail: akimov@snu.edu.ua

Abstract The technique for modeling and computation of three-dimensional magnetic fields of electromagnetic separators is presented. The example of electromagnetic drum-type separator computation by boundary element method is given.

Introduction

A number of difficulties occur in the practice of designing electromagnetic separators magnetic systems. They are related with the computation of magnetic fields in the working area open space. The field has clear three-dimensional character as the size of interpole gaps are often comparable to the size of magnetic system.

Similar problems may be solved and they are really solved by numerical methods. The finite element method (FEM) and the boundary element method (BEM) are most widespread among them.

At present there are many program packages for FEM and BEM implementation to make the computation of the magnetic field. However, most of them are intended for magnetic field computation in particular conditions, so they comprise limited mathematical functions, that makes impossible optimization and magnetic system parameters varying in a required range.

Therefore till now there are no technique for complete computation and optimization of the magnetic system of electromagnetic separators with variable in a rather wide range geometrical parameters. Hence, the development of the technique using current-technology computing facilities is an actual problem.

Prior experience shows that the most acceptable package for electromagnetic separators magnetic systems computation is that one, which implements FEM or BEM, has internal programming language and possibility to solve problems of analysis and optimization. The system of Wolfram Research Company and the integrable module Radia® is such a package [1,2].

The system Mathematica® has a set of functions, which makes possible to pose and solve many mathematic problems using the internal programming language Mathlink® [1]. The module Radia® realizes BEM. Complex of module functions adds functions of system Mathematica® by functions for magnetic fields computation and applies the internal programming language Mathlink® for connection with package Mathematica® interface.

From foregoing, the task to develop the mathematical model of electromagnetic drum-type separator magnetic system (Fig. 1) and to make the magnetic system computation using the system Mathematica® and the integrable module Radia® was posed.

Development of mathematical model

The magnetic circuit of drum-type electromagnetic separator physical model (Fig. 1) consists of the yoke 1, poles 2, 3, 4 with pole pieces 5, 6, 7, 8. Magnetizing coils 9, 10 are placed on the central pole 3.

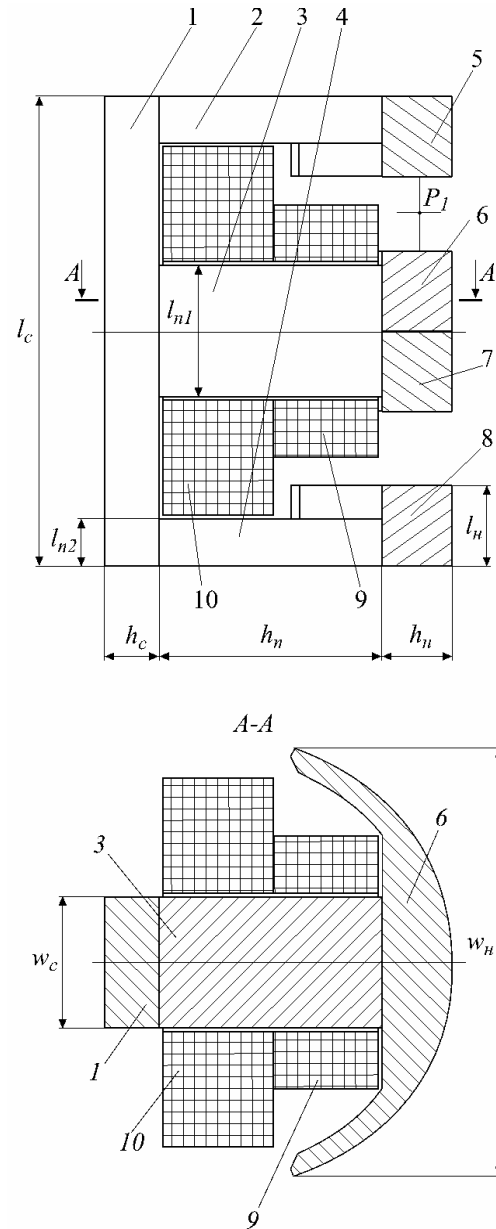


Fig. 1. Outline of electromagnetic drum-type separator physical model:
 1 – yoke; 2, 3, 4 - poles; 5, 6, 7, 8 – pole pieces;
 9, 10 – magnetizing coils

The problem of mathematical model development in the system Mathematica® is proper dividing the separator electromagnetic system into constructive geometrical parts; for each of them mathematical description is made. Separate parts described mathematically are combined into common model. The division into elements, i.e. elementary geometrical figures, is made for each part of the model.

Taking into account magnetic system symmetry and recommendations of the package Radia® makers [2], the half of magnetic circuit (Fig. 2) was taken up for modeling.

The magnetic circuit yoke was divided into three parts 5, 6, 7 (Fig. 2) representing three parallelepipeds.

The pole piece is a complex geometric figure, so its model was made up of some simple figures. Prisms of the same height with triangular bases placed on one plane (Fig. 3) were used as simplified figures.

Magnetic circuit model parts were divided into elements. Computation accuracy and computer memory used are dependant on proper dividing into elements [2].

Since separator magnetic circuit geometry is complex, the division of different parts of the magnetic circuit is various.

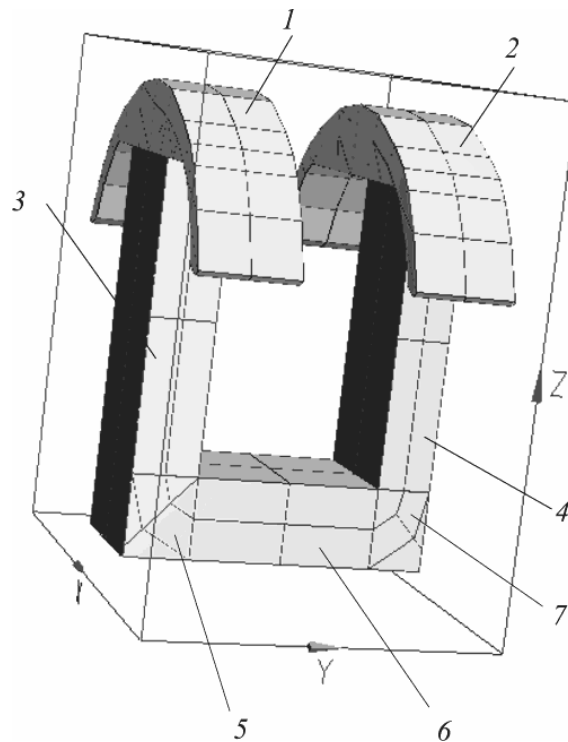


Fig. 2. Fragment of magnetic circuit of electromagnetic system model of drum-type separator divided into elements: 1, 2 – pole pieces; 3, 4 – poles; 5, 7 – yoke end parts (elliptic dividing used); 6 – yoke central part

Model dividing into elements was made separately for each part [2] and realized by planes with equal step for n_x elements in the direction of Cartesian axis x , for n_y and n_z elements in the direction of axes y and z , correspondingly.

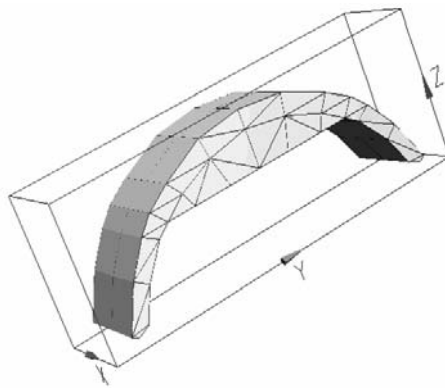


Fig. 3. Pole piece model

The pole piece model was divided into elements in the direction of the axis y only, since it was primarily divided into group of elementary models – prisms, and it was not required to divide it into elements by other axes.

End parts 5, 7 (Fig. 2) of the magnetic circuit yoke were divided into elements by functions of elliptic dividing. It is stipulated by that fact that the main flux changes its direction in those parts of the magnetic circuit, so using standard function for dividing into elements results in reducing computation accuracy [2].

Geometrical functions (*Field Sources*) of the package Radia® was applied for describing magnetic circuit parts models.

Parts, described in this manner, were moved in space with the help of transformation functions (*Space Transformation*) by specifying geometric layout in the magnetic system. After that, models of poles, yoke and pole pieces were combined into magnetic circuit group (*Container*).

Magnetizing coils models (Fig. 4) were described by special function determining coils shape and size. Current density for magnetizing coils was specified additionally.

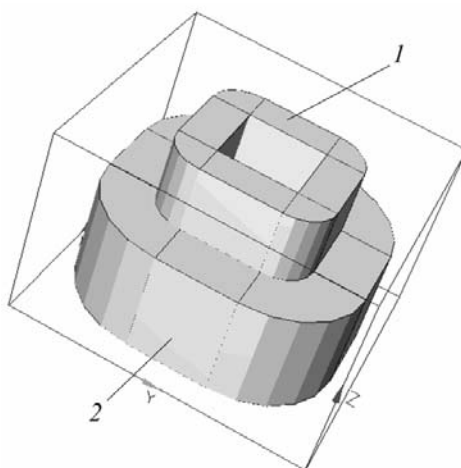


Fig. 4. Model of separator magnetizing coils:
1- small coil; 2 – large coil

The dependence describing magnetization curve for the steel, which the magnetic circuit of the modeled separator is made of, was specified in magnetic properties of magnetic circuit elements by functions of magnetic materials (*Magnetic Materials*) of the module Radia®. Magnetizing curve represented the dependence of magnetic inductance B on given magnetic field strength H .

Magnetic circuit elements and magnetizing coils, combined into a group, represent the mathematical model of a quarter of separator electromagnetic system. Complete model of separator electromagnetic system (Fig. 5) was made using functions of symmetry.

Computation example and evaluation of computation errors

Computation of the magnetic system mathematical model was made by functions of field computation (*Field Computation*), controlling parameters and specifying computation requirements. Maximum number N of iterations, to make the computation, and computation accuracy σ were the parameters limiting and specifying computation accuracy. If specified accuracy of the computation was not reach for given number of iterations, the computation was stopped and its results were considered inauthentic.

Computation of the physical model of the electromagnetic drum-type separator magnetic system was made as an example. Its dimensions were as follows.

Poles height $h_n = 130$ mm, poles and magnetic circuit yoke width $w_c = 60$ mm, end poles length $l_{n2} = 25$ mm, central pole length $l_{n1} = 60$ mm, yoke height $h_c = 35$ mm, yoke length $l_c = 280$ mm, pole piece main part height $h_u = 30$ mm, pole piece length $l_u = 40$ mm, pole piece width $w_u = 186$ mm.

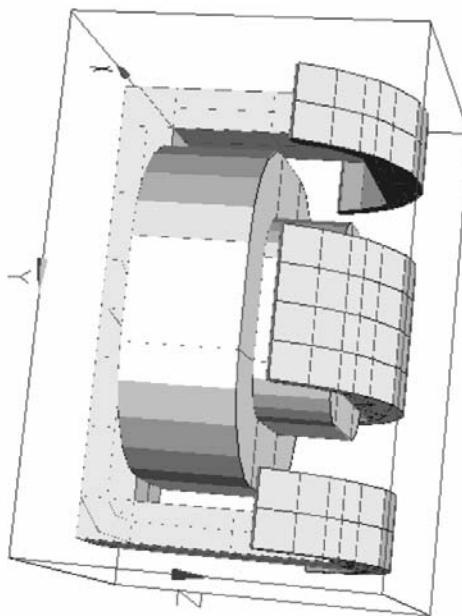


Fig. 5. Complete model of electromagnetic drum-type separator magnetic system

In magnetic properties of magnetic circuit material the curve of steel (grade 15 JI) magnetizing was specified as analytical dependence $H = 4\pi 10^{-7} \cdot 102B(9,95 + B^8)$ [2, 3], where H - reduced magnetic field strength in T, B - magnetic field inductance in T.

Current density in magnetizing coils $J = 0,009$ A/mm², coils magnetomotive force (EMF) was determined by $F = JS$, where S - coil sectional area.

The number of iterations $N = 1000$. Computation accuracy $\sigma = 0,000001$.

Coefficients determining the magnetic circuit dividing into elements were specified by $n_x = 2$, $n_y = 2$, $n_z = 2$ for all parts of the model.

Computation of the magnetic system model of the electromagnetic drum-type separator was made on PC with processor AMD Athlon (processor clock speed 1HHz), on-line memory 128 Mb, hard disc Caviar (Western Digital) with 20 Gb.

The evaluation of computation accuracy was made by comparison of the axial component of the vector of magnetic inductance in point P1 (Fig. 1), placed in the center of the air gap, with the induction obtained analytically according to the law of full current for magnetic circuit without taking into account declining magnetic potential drop in steel. The magnetic inductance in P1 according to the law of full current $B_{P1} = \frac{\mu_0 F}{\delta} = 0,00148$ T, where $\mu_0 = 4\pi 10^{-7}$ H/m. The magnetic inductance obtained by separator model computation by package Mathematica® and Radia® $B_M = 0,00147$ T. Relative error of the computation $\Delta = 0,675\%$, correspondingly the computation accuracy is 99,325%.

Conclusions

From computation results it is evidently that the relative error of computation is less than 1%. Common time for computation of drum-type separator magnetic system mathematical model is less than 5 minutes.

Obtained results of the computation of drum-type separator magnetic mathematical model system show that application of the package Mathematica® and the integrable module Radia® is expedient.

Hence, the package Mathematica® and the integrable module Radia® can be used for optimization of guard magnets and separators magnetic systems.

References

- [1] V. Diakonov, Mathematica 4: a training course, St.Petersburg: Piter, 2001, 656 p.
- [2] http://www.esrf.fr/machine/groups/insertion_devices/Codes/Radia (Radia documentation. Reference Guides and samples.)
- [3] M.V. Zagirnyak, V.M. Usatyuk, Working Magnetic Field Calculation for Separator with Prism Polar Pieces. – Electromagnetic Field in Electrical Engineering. Edited by A. Krawczyk and S. Wiak. – Oxford: IOS Press, 2002, pp. 537 – 542.

SECTION III SPECIAL APPLICATIONS

Introductory Remarks

The third section of papers is collected under the title: Special Applications. It does mean that the reader may find here a very wide spectrum of problems and devices. In the section we move from medical application, through the analysis of material features, to power HV lines. Indeed, the spectrum is wide but the real consistency is very close to that of electrical machines and apparatus. Although people show modeling of biological tissue or magnetic material structure or dielectric material structure, they use the same, or a little modified, mathematical description. On the other hand, problems connected with materials in general are much more difficult since parameters of continuous structures are not well-evaluated. It is especially seen when considering biological material (tissue) – its electromagnetic parameters change by object as well as they may change in time in one object. Anyway, the parameters are somehow averaged, just in order to make computer simulation possible.

All the papers in the section can be divided into four groups:

- bioelectromagnetic interactions,
- magnetic material modeling,
- electromagnetic and thermal coupling,
- electromagnetic and mechanical coupling.

The first group consists of three papers. Paper III-20 deals with the problem of the possible hazard evoked by base stations for wireless communication and describes this problem from all aspects, but not very deeply. Paper III-3 is devoted to the analysis of the SAR coefficient, the parameter which estimates the hazard. And paper III-18 presents a positive usage of electromagnetic field, namely the technique of hyperthermia.

The papers of the next group consider problems which are strongly connected with electromagnetism, namely magnetic material features. Paper III-23 shows the method of magnetic diagnosis of structural materials. It deals strongly with experiments and, therefore, is of practical meaning. Conversely, paper III-1 is very computational and shows the procedure of calculation of losses in magnetic materials. It is also of practical meaning, as it gives formulae which allow one to estimate the components of power losses in ferromagnetic material. These two papers are two ends of a spectrum in which we have the papers presenting the calculation of magnetic circuits, particularly occurring in a variable reluctance PM motors (III-16, III-17), a brushless motor (III-12), a special motor with oscillatory starting (III-15), a motor with broken bar (III-14), an axial permanent magnet motor (III-18), and at the end of this sequence one meets a micro-relay (III-19). Besides, in this group one can find papers which are devoted to measurement of magnetic circuit (III-8, III-10). Magnetic material problems are also considered in the paper where a magnetic circuit with hysteresis is simulated electrically (III-4).

The group of papers concerning the problems of thermal coupling has two subgroups. The first one is connected with superconductivity and one meets here a paper dealing with a superconducting magnet with a ferromagnetic core (III-5), and a paper (III-21) which presents the analysis of high temperature superconducting synchronous machines. The second subgroup is a little wider and one can find here considerations on coupled electromagnetic fields and temperature fields to analyze the voltage-fluctuate of a synchronous generator (III-22), the classical technical problem of surface electroheating (III-13), and the classical computational problem of modelling of temperature-dependent effective impedance of massive conductor (III-6).

The last group of papers is concentrated on mechanical problems linked with electromagnetic phenomena. And thus, one finds here paper III-7 which models a magnetic noise of a DC motor (the noise includes electromagnetic, mechanical and acoustic phenomena) and paper III-11 which investigates DC electromagnets and their attractive force by 3-D Finite Element Analysis.

A little distant from the above papers is paper III-2 which discusses the problem of grounding and distribution of current in ground.

It is worth saying that the section we have presented above is very heterogeneous and readers are again requested to find by themselves the topics in which they are particularly interested.

III-1. THE ROTATIONAL POWER LOSS CALCULATION IN THE SQUARE SAMPLE

Jan Anuszczyk, Zbigniew Gmyrek

Technical University of Lodz, Institute of Mechatronics and Information Systems,
90-924 Lodz, ul. Stefanowskiego 18/22, POLAND
e-mail: gmyrek@p.lodz.pl

Abstract - A special problem is the calculation of power loss in the core of rotating electrical machines because the magnetic fields occurring in the core are neither unidirectional nor sinusoidal. This paper discusses the calculation of rotational power losses. Several methods have been proposed for this purpose. Among these, the method based on calculation of the field quantities B_x and B_y is described. In this method the rotational power losses are calculated employing empirical approach directly from these quantities. The main point of presented method is creating of calculation model to calculate components of the flux density vector (module and argument) in every elements of the mesh representing the magnetic circuit of tested material. Beside this, the excess losses are calculated using statistical theory proposed by Bertotti.

Introduction

A special problem is the calculation of power loss in the core of rotating electrical machines because the magnetic fields occurring in the core are neither unidirectional nor sinusoidal. In order to define the power loss increase (that takes place as a result of rotational magnetization of a given magnetic material), can be used the so called RSST testers. Principles and results of measurements with use of above mentioned equipment were described by many authors [1,2,3]. This paper discusses the rotational power loss calculation method. Till now several methods have been proposed for this purpose. Among these, the method based on calculation of the field quantities B_x and B_y is described. In this method the rotational power losses are calculated employing empirical approach directly from these quantities. But when we use computational models we must also take so-called excess power losses into account. In this paper the excess losses are calculated using theory proposed by Bertotti. The main point of presented method is creating of calculation model to calculate components of the flux density vector (module and argument) in every elements of the mesh representing the magnetic circuit. These values should be calculated for successive moments. At defined moment a simple element of the mesh is accepted as isotropic, thus magnetic permeability determined for components of the flux density is the same as for resultant vector B . The magnetic circuit has been investigated in two alternative versions:

- made of siliconless steel sheet LOSIL 19 – practically isotropic material,
- made of transformer steel sheet UNISIL 56 – anisotropic material.

The proposed method of rotational power loss calculation (p_r) uses for eddy current loss (p_e) the Poyting's model with two components of magnetic field and for hysteresis loss (p_h) a special model of rotational hysteresis. Calculated in this way power losses are known as classical losses. The excess losses are calculated also, using statistical theory proposed by Bertotti.

Calculation of rotational power losses

The mathematical description of the model

The method used to define rotational losses, is based on analytical formulae, which take the ellipticity of field vector hodograph and the change of speed of field vector rotation into consideration. The proposed method uses the Poynting's model with two components of magnetic field for eddy - current losses and a special model of rotational hysteresis for hysteresis losses. In the considered case, the vectors of magnetic field strength $H(\phi)$ and flux density $B(\phi)$ have different directions and hysteresis angle between them is Θ_B . Poynting vector representing power density penetrated the steel sheet from opposite surfaces, neutralised each other in the central part of the sheet. In every moment, rotational field components H_x and H_y are known in each elementary region and the components of flux density B_x and B_y are known as well. The instantaneous value of eddy current power loss in an elementary layer dz

$$p_e' = \frac{1}{\gamma} \left[\left(\frac{\partial H_y}{\partial z} \right)^2 + \left(\frac{\partial H_x}{\partial z} \right)^2 \right] \quad (1)$$

After realisation indispensable transformations the average power losses in the unity volume (within the limits of the sheet thickness) are

$$p_e = \sqrt{\frac{\pi f \mu}{\gamma}} \frac{1}{d} (H_{ox}^2 + H_{oy}^2) \frac{\text{shkd} - \text{sinkd}}{\text{chkd} + \text{coskd}} \quad (2)$$

where

f - frequency of rotation, $k = f(f, \mu, \gamma)$ - special function of coefficient of amplitudes wave attenuation,

$\mu = B_x / H_x = B_y / H_y$ - magnetic permeability in considered elementary region, γ - electrical conductivity, d - thickness of sheet.

It can be stressed that in the accepted procedure for the full cycle of the rotational magnetization we get an average value of local power losses which were obtained on the basis of power loss values in each phase of cycle $p_e = p_e(\phi)$. Hence

$$p_{eav} = \frac{1}{2\pi} \int_0^{2\pi} p_e(\phi) d\phi \quad (3)$$

A hysteresis power loss analysis under the rotational field condition gives consideration to delay of vector B in relation to vector H . The hysteresis angle Θ_B is the measure of it. In other words, to the calculation of the hysteresis power loss under rotational field, it is necessary to take hysteresis loop and also the hysteresis angle between B and H vectors resulting from it into account. Remembering that B , H and Θ_B quantities depend on the turn angle ϕ , we get the hysteresis loss energy expression under rotational magnetization within the limits of turn angle ϕ . After conversion if the full cycle of rotational magnetization is taken into consideration

$$w_h = \int_0^{2\pi} \left[H \cos \Theta_B \frac{\partial(\mu H)}{\partial \phi} + \mu H^2 \sin \Theta_B \left(1 - \frac{\partial \Theta_B}{\partial \phi} \right) \right] d\phi \quad (4)$$

Average values of the hysteresis power loss under rotational magnetisation come from instantaneous energy values integral over cycle

$$p_{hav} = \frac{1}{T} \int_0^{2\pi} w_h(\phi) d\phi \tag{5}$$

where: T - rotational magnetization cycle period.

So, according to (4) when the hodograph going ahead and going back (for example in case of PWM supply) then we must use the following formula

$$w_h = H(\phi) \cos \Theta_B \frac{\partial B(\phi)}{|\partial \phi|} + H(\phi) B(\phi) \sin \Theta_B - H(\phi) B(\phi) \sin \Theta_B \frac{\partial \Theta_B}{|\partial \phi|} \tag{6}$$

The absolute value of angle $\Delta\phi$ was used because the increase of power losses occurs both of direction of vector B turn.

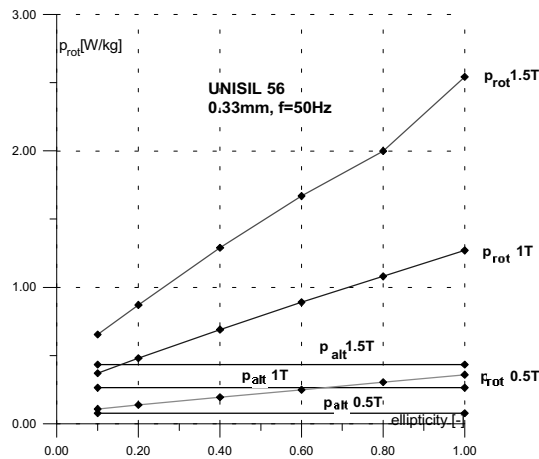


Fig.1. The classical rotational power losses for transformer steel sheet UNISIL 56 (p_{alt} – power losses in case of alternating magnetization).

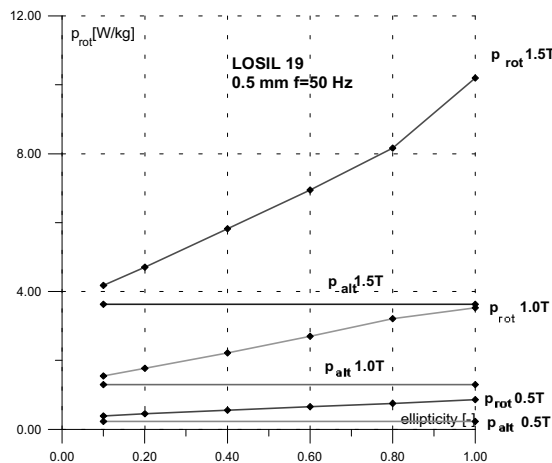


Fig.2. The classical rotational power losses for steel sheet LOSIL 19 (p_{alt} – the specific power losses in case of alternating magnetization).

Note that specific power losses (in case of alternating magnetization for material UNISIL 56) were calculated for angle 0° with respect to rolling direction. The calculations of rotational power losses include different material characteristics for other angles.

Calculation of the excess losses

According to the statistical theory of eddy current losses proposed by Bertotti a few years ago, the basic physical mechanism governing excess losses in soft materials is identified with the competition between the external magnetic field and highly inhomogeneous local counterfields due to eddy currents and microstructural interactions. The theory leads to the conclusion that the large-scale behavior of magnetic domains can be described in terms of the dynamics of n statistically independent magnetic objects. In this way the loss problem reduces to the investigation of the physical properties of n as a function of product f and B_{\max} (f – frequency, B_{\max} – maximum value of flux density). Bertotti propose the simple law for several soft ferromagnetic materials.

$$n = n_0 + \frac{H_{\text{exc}}}{V_0} \quad (7)$$

where

n_0 – the number of simultaneously active magnetic object approximated for $H_{\text{exc}} = 0$,

V_0 – factor identified with the quasi-static coercive field,

H_{exc} – the so called excess dynamic field acting on magnetic objects.

The simple law (7) leads to following equation

$$P_{\text{exc}} \propto \sqrt{V_0 n} (B_{\max} f)^{3/2} \quad (8)$$

It should be stressed that parameter n depends on frequency and maximum flux density level. That parameter depends also on the microstructural properties of the material. To calculate values of parameters V and n we should execute a lot of measurements and calculations in range of frequency about several Hz to several hundred Hz. The measuring system consists of two ring cores, a high frequency power supplier and two amplifiers. It is presented in Fig.3. There are two exciting windings and additional measuring winding. The first one is connected to the AC supply source (this is the power amplifier with frequency of the output voltage changing in a wide range e.g. from 5 to 500 Hz). The second winding can be supplied (if it is necessary) from the another AC supply (50 Hz). In the measuring system, current in the primary winding and voltage in measuring one were observed and stored. Executed measurements created a base for calculations of the power losses in the sample (in case of alternating magnetization). Beside this, using above mentioned measuring system were calculated coefficients needed to calculate the excess losses P_{exc} according to theory proposed by Bertotti [8].

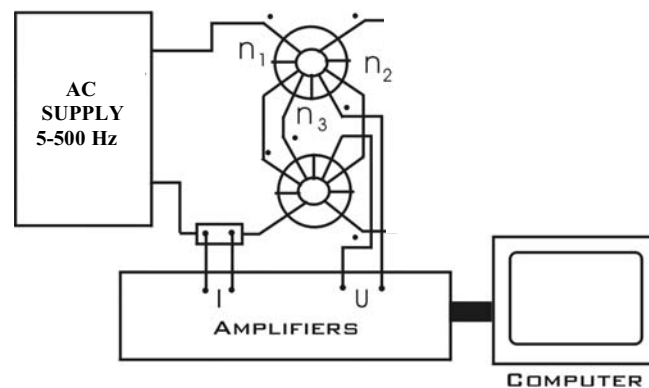


Fig.3. A measuring system built to determine the power loss increase in case of alternating magnetization.

Many authors report that for many kinds of non-oriented three-percent SiFe materials is obligatory simple dependence $n=H_{exc}/V_o$ (it is right for wide range of flux density and frequency up to several hundred Hz). In case of grain oriented 3% SiFe materials obligatory is simple law (see equation 7) but the starting value n_o can depends on the value of flux density – smaller value for lower flux densities. It should be stressed that for non-oriented three-percent SiFe materials value n_o (see eq.7) equals 1 but for grain oriented 3% SiFe value n_o is greater.

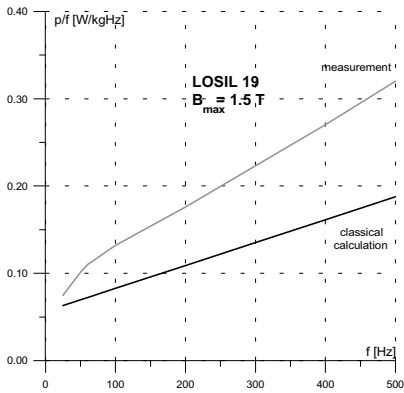


Fig.4. Differences between results of measurements and classical calculations for LOSIL 19 (in case of alternating magnetization).

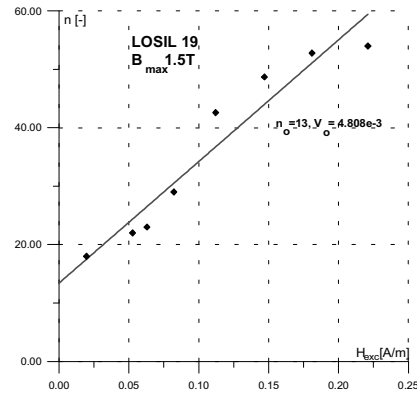


Fig.5. The calculation points and their approximation (this is the base to determination of coefficients in eq.7).

Basing on differences between measured and calculated values of power losses (in range of frequency from 10 to 100 Hz), the H_{exc} values were reached. With each value of H_{exc} corresponds value of n (number of independent magnetic objects those produce additional power losses called excess power loss). The course of magnetic objects number versus H_{exc} is presented in Fig.5. It should be stressed that proposed approximation was done in range of frequency suitable for investigated conditions. It is known that for non-oriented steel sheet, the number of magnetic objects (when H_{exc} equals 0) should be one. It is possible when we delete first point of curve (see Fig.5 - $H_{exc} = 0.02$). But then the last point (related with higher frequency) should not be taken into account. Arrangement of points can suggest that changed configuration of magnetic domains.

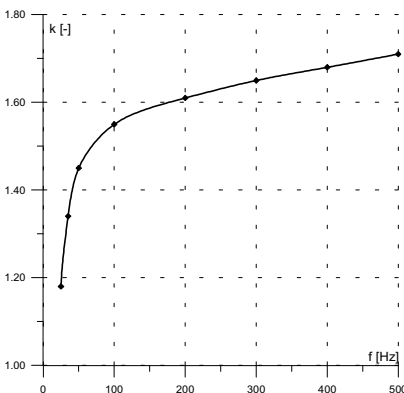


Fig.6. The excess power loss coefficient k .

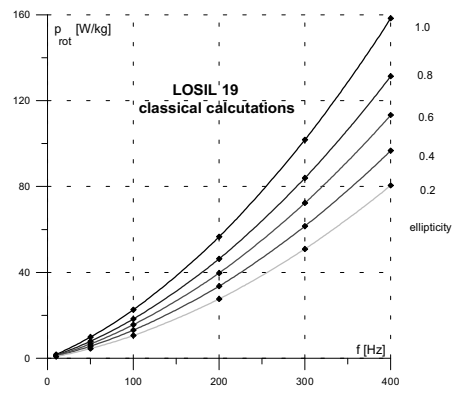


Fig.8. The values of rotational power losses determined for LOSIL 19 vs. frequency (calculations were carried out for major axis 1.5 T).

Using calculated in classical manner power losses (in alternating conditions of magnetization) and specified before excess losses, the total power losses in non-oriented steel sheet LOSIL 19 and oriented steel sheet UNISIL 56 were marked. If we relate the total power loss to the so called classical power loss we reach the excess power loss coefficient k (see Fig. 6).

Authors suggest that determined coefficients k_{rot} fixed with the excess power loss coefficient k can be helpful in calculation of rotational power loss. Authors assume that coefficient k is the same for alternating and rotational magnetization.

Table 1. The Specific power losses in the isotropic and anisotropic magnetic Materials ($B_{max}=1.5$ T for long axis).

Kind of sheet		Ellipticity					
		1.0	0.8	0.6	0.4	0.2	0.1
LOSIL 19	P_{rot} W/kg	10.20	8.167	6.949	5.824	4.707	4.175
	P_{alt} W/kg	3.624	3.624	3.624	3.624	3.624	3.624
UNISIL 56	P_{rot} W/kg	2.543	2.000	1.670	1.290	0.871	0.654
	P_{alt} W/kg	0.433	0.433	0.433	0.433	0.433	0.433

P_{rot} – the specific rotational power losses,
 P_{alt} – the specific alternating power losses.

Conclusions

The total power losses under rotational magnetization in the core of induction motor exceed the loss values for the unidirectional magnetization. This increase depends on the ellipticity of the flux density hodographs, on the level of the saturation and on the spectrum of harmonics in the flux. Practically, it depends also on the kind of the magnetic material. The percentage fraction of eddy - current power loss and hysteresis power loss in the total rotational losses corresponds to their fraction under axial magnetization. The excess losses were estimated according to theory proposed by Bertotti. Basing on the proposed study, it is possible for most designing purposes, to estimate the increase of specific core loss under the rotating field which has the direct influence on the fundamental core losses in electrical machines. For example, for induction motors with tangential flux density level in the stator yoke in the neighborhood 1.5 T, the increase of core losses due to rotational magnetization is about 40 %.

References

- [1] M. Enkizono, T. Suzuki, J. Sievert, J. Xu, "Rotational power loss of silicon steel sheet", *IEEE Transactions on Magnetics*, No 5, September 1990,
- [2] R. D. Findlay, D. K. MacKay, "Losses due to rotational flux in three phase induction motor", *IEEE Transactions on Energy Conversion*, No 3, September 1994,
- [3] J. Anuszczyk, Z. Gmyrek, "Rotational magnetization in the core of an induction motor supplied from the PWM inverter", *Proceedings of ICEM*, Finland, 2000,
- [4] J. Anuszczyk, *Analyse of magnetic field distribution and power losses under rotational magnetization in magnetic circuit of electrical machines*. Elektryka nr 629, Dissertation, Technical University of Lodz, 1991 (in Polish).
- [5] J. Anuszczyk, Z. Gmyrek, "Calculation of field distribution and rotational power loss in three phase induction motor", *Proceedings of 8th International IGTE Symposium*, Graz Austria, 1998,
- [6] C. Ragusa, M. Repetto, "Anisotropic vector Preisach model and magnetic field solution", *Proceedings of 8th International IGTE Symposium*, Graz Austria, 1998,
- [7] J. Gyselinek, L. Dupre, L. Vandeveldel, J. Melkebeck, "Calculation of iron losses in electrical machines using the Preisach model", *Proceedings of 3rd International Workshop on Electric and magnetic Fields*, Liege Belgium, 1996,
- [8] G. Bertotti, "General properties of power losses in soft ferromagnetic materials", *IEEE Transactions on Magnetics*, No 1, January 1988.

III-2. A METHOD FOR STUDYING THE CURRENT FIELD GENERATED BY INTERCONNECTED GROUNDING SYSTEMS

M. Bronzini, G. Delvecchio, N. Mitaritonna, P. Pugliese, M. Sylos Labini

Department of Electrotechnics and Electronics - Polytechnic of Bari

Via E. Orabona 4 - 70125 Bari (Italy)

phone: +39 080 5963256, fax: +39 080 5963410, e-mail: sylos@poliba.it

Abstract - In this paper the Authors propose a method for analyzing the current field generated by interconnected grounding systems, with any shape and extension. The method is absolutely general and allows to study the field both in the event of a single line to ground fault (LGF) in one of the interconnected grounding systems and in case of simultaneous line to ground faults in different grounding systems, interconnected to each other. Moreover, this method allows to analyze the grounding systems connected to each other by leaking conductors, as well as to analyze the effects of the faults on metal structures in contact with the soil, such as water pipelines or railway tracks.

Introduction

At present, long leaking conductors are employed in the grounding systems of MV/LV transformation stations (secondary substations), these conductors being used as auxiliary grounding electrodes and being buried in parallel with low-voltage and high-voltage cables. This technical solution allows to greatly reduce the current leaked by the grounding system of the secondary substation where the fault occurs and, consequently, allows to reduce the cost of the grounding system of this substation. Obviously, in this case, the study of the current field becomes more complex, since it is necessary to take into account the current leaked by the auxiliary conductors, too.

Another problem is due to the fact that in the subsoil there are a lot of metal elements having considerable longitudinal dimension; some of them are in close contact with the soil such as, for example, water or gas pipelines; other elements such as, for example, the telecommunications cables are insulated from the soil but magnetically coupled with the leaked currents. Each leaking conductor generates voltages on the adjacent metal elements, and this can determine both a danger to human beings and conditions of inadmissible interference with electronic and electrical equipment. Similar problems occur in the electric traction systems, since the currents which return to the feeding sub-stations, partly by rails and partly by the soil, give rise to various effects on the metal elements buried close to them.

The method proposed by the Authors allows the study of the current field in all the above-mentioned cases. It is an extension of the method given in [1], since it considers the current leakage due not only to the real grounding systems but also to all the conductors which are in close contact with the soil.

The Method Proposed

The study of a grounding system leaking a known fault current is usually performed by the Maxwell's subareas method [2], [5]. Briefly, it lies in dividing the grounding systems under examination into an appropriate number of subareas, in imposing the equipotentiality of this system, and in calculating the subcurrents leaked by each subarea. These subcurrents allow us to determine the voltages in any point P of the soil surface.

J. M. Nahman in [1] and P. Buccheri et al. in [4] have generalized very well the above-mentioned method.

The procedure suggested by [1] for the calculation of the current field generated by grounding systems interconnected to each other in a very general way is briefly explained in Appendix (see Fig. 9).

An example of study by the Nahman's method is given in Fig. 1: it concerns two grounding systems connected to each other by a ground wire supported by five towers. Fig. 1 shows the two grounding systems and the grounding systems of the five towers. In this case the Nahman's method can be applied, taking into account that the grounding systems are seven in number and are interconnected only by the ground wire. The voltages on the soil surface are given in Fig. 3.

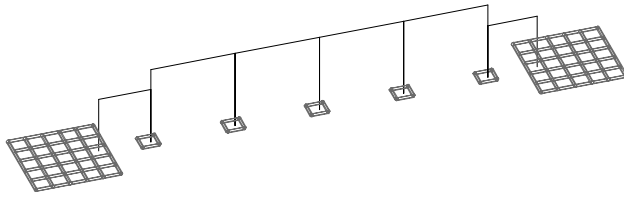


Fig. 1. - An example of study by the Nahman's method: two grounding systems connected to each other by a ground wire supported by five towers; of these towers only the grounding systems are represented

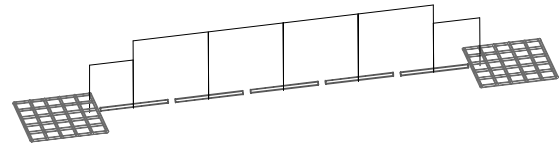


Fig. 2. - An example of study by the new method: two grounding systems connected to each other by an uninsulated buried conductor; the study can be brought back to electrodes similar to those of Fig. 1

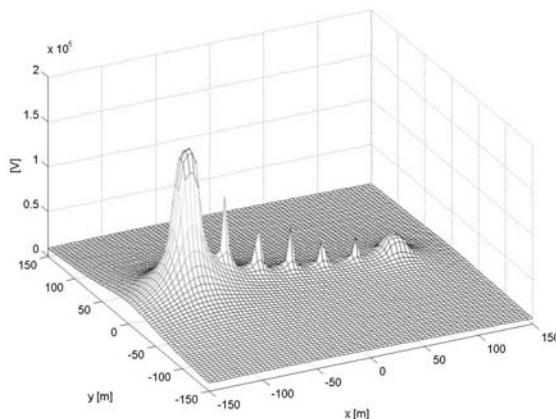


Fig. 3. - Voltages on the soil surface generated by the grounding systems of Fig. 1 (fault in the ground system on the left)

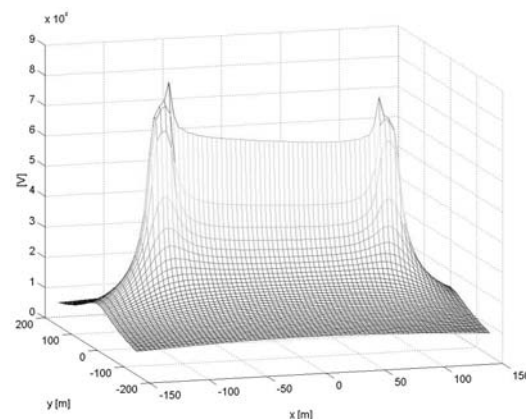


Fig. 4. - Voltages on the soil surface generated by the grounding systems of Fig. 2 (fault in the ground system on the left)

It is important to point out that the Nahman's method can be applied to grounding systems which are connected to each other only by insulated conductors (ground wire and/or insulated cables). Thus the Authors have re-examined this method and made it able to consider also the conductors not-insulated from the soil, such as the conductors coming out of the substations and the conductors interconnecting the various grounding systems. That's not all, they have also made the new method able to consider other metal elements put close to leaking systems.

The new method lies in subdividing also the leaking conductors, as well as the passive metal elements, into subareas, and in considering each leaking conductor and each metal element as a separate grounding electrode, active or passive, according to whether it leaks current or not. Obviously, in this way the Nahman's method is still valid.

Some examples of application of the new method are here given.

Grounding systems connected to each other by leaking conductors

An example of study by the method proposed by the Authors is shown in Fig. 2 with regard to the case of two grounding systems connected to each other by an uninsulated buried conductor: the study can be brought back to grounding electrodes similar to those of Fig. 1 in the following way.

The conductor is subdivided into many parts (or trunks), and each of them is considered as a separate grounding electrode. Moreover, each trunk is considered as being connected to the elements that are put immediately before and after it by means of the admittance of each trunk; this admittance con-

nects the barycenter of two successive trunks. In this way, if we increase the number of subdivisions, our model is very close to reality. In fact, the new algorithm is always based on the Maxwell's subareas method and so it calculates the voltage in the barycenter of each trunk and then imposes it to the whole trunk [5]; that's why the shorter the trunk is the more accurate the model is. If we use this model the trunks take voltages which gradually decrease beginning from the grounding system where the fault occurs up to the other grounding system. In this way we can study the field on the soil surface near the buried conductor. This field decreases along the same conductor (see Fig. 4).

Interference between grounding systems and passive metal tubes

The algorithm proposed allows also the evaluation, by the matrices \mathbf{R} , \mathbf{T} and \mathbf{Y} in Eq. (9), of the interferences between grounding systems and metal tubes, even if they are not connected to each other from the galvanic point of view.

The method has been applied to three interference cases between a horizontal grounding electrode and a passive metal tube. This horizontal electrode is made up of a copper conductor having a cross-section of 35 mm^2 , is buried to a depth of 1 m in a soil whose resistivity is $\rho=100 \text{ }\Omega\text{m}$. Near this electrode there is a passive metal tube, with a diameter of 10 cm, a length of 1 km, buried to a depth of 2 m and placed at a distance of 1 m from the electrode. Let's examine the three cases individually.

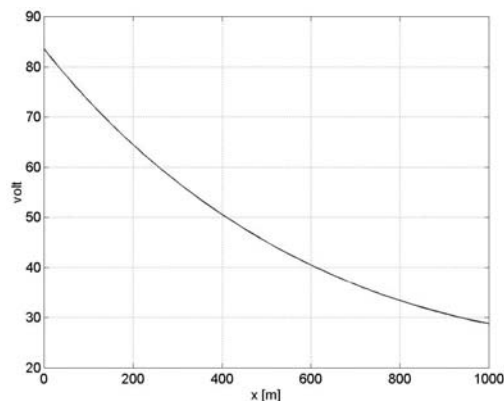


Fig. 5. - Case 1: Voltage profiles along a horizontal leaking electrode (1 km long) crossing a passive metal tube (1 km long)

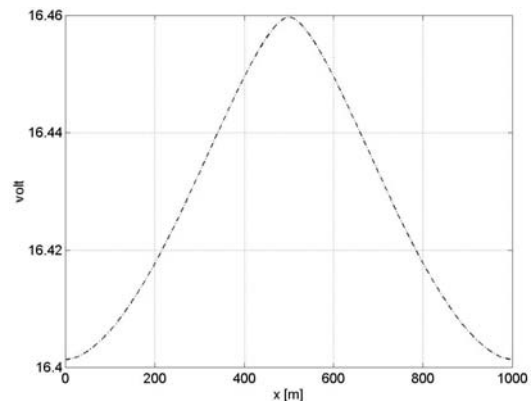


Fig. 6. - Case 1: Voltage profiles along a passive metal tube (1 km long) crossing a horizontal leaking electrode (1 km long)

Case 1

In this case, the horizontal grounding electrode has a length of 1 km and a current $I=200 \text{ A}$ is injected at its center; the electrode is connected with a grounding system and we assume that it transfers 30 A to this grounding system and leaks 170 A in the soil. The passive metal tube crosses this electrode.

The voltage profiles along the horizontal electrode and the tube are given in Fig. 5 and 6, respectively, and are equal to the voltages found in [3]. Fig. 6 shows that, on the basis of the voltages indicated on the axis of ordinates, the tube is almost equipotential.

Case 2

Also in this case, the horizontal grounding electrode has a length of 1 km and a current $I=200 \text{ A}$ is injected at its center; the electrode is connected with a grounding system and we assume that it transfers 30 A to this grounding system and leaks 170 A in the soil. The metal tube is parallel to this electrode.

The voltage profiles along the tube and the horizontal electrode are given in Fig. 7, and are equal to the voltages found in [3]. The figure points out that the voltage drop along the electrode, which is equal to about 65%, is considerably higher compared to that of the tube, which is equal to about 20%.

Moreover, the average value of the voltage induced on the tube is equal to about 60% of the average value of the voltage on the electrode; this points out that there can be a state of danger for human beings when the soil resistivity and the current leaked are higher. Moreover, the comparison between Fig. 7 and Fig. 5 shows that the tube has a little influence on the behaviour of the electrode.

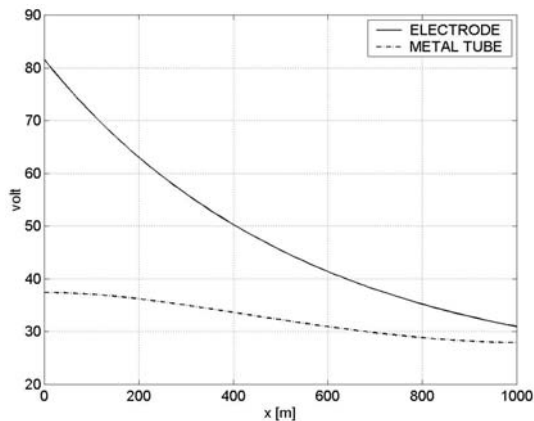


Fig. 7. - Case 2: Voltage profiles along a horizontal leaking electrode (1 km long) and a passive metal tube (1 km long) which are in parallel with each other

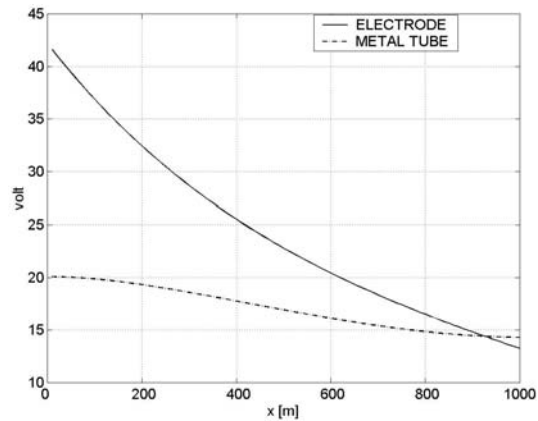


Fig. 8. - Case 3: Voltage profiles along a horizontal leaking electrode (11 km long) and a passive metal tube (1 km long) which are in parallel with each other

Case 3

In this case the horizontal grounding electrode has a length of 11 km. The metal tube is in parallel with this electrode. A current $I=200$ A is injected at the start of the horizontal electrode. The voltage profiles, both along the tube and the horizontal electrode, are given in Fig. 8.

The study shows that the voltages on the tube, in its last part, are greater than the voltages on the active electrode, and are similar to the voltages found in [3].

Obviously, if we choose higher values for ρ and I , some dangerous voltages on the tube may occur even if the electrode has a non-dangerous voltage.

Conclusions

The Authors have proposed a method for studying the voltages occurring in areas which are interested by the current field produced by the fault, and are very distant from the point where a ground fault takes place. The method is absolutely general and allows to take into account also the currents leaked by uninsulated buried conductors connecting various grounding systems, as well as the presence of passive metal elements put near the leaking systems.

The examples here given, besides showing the potentialities of the method proposed, prove the reliability of the same method since the same results got by means of another model given in literature are obtained.

References

- [1] J. M. Nahman, Analysis of interconnected earthing systems, Archiv für Elektrotechnik, No. 63, pp. 261-265, 1981
- [2] P. Pugliese, P. Settanni, M. Sylos Labini, Una procedura per determinare rapidamente la resistenza di terra di dispersori di forma usuale in terreni non omogenei, L'Energia Elettrica, No. 11, pp. 467-475, 1987
- [3] G. Ala, P. Buccheri, A. Campoccia, Interferenza tra elettrodi interrati rettilinei a caduta di tensione longitudinale non trascurabile. Analisi dell'accoppiamento conduttivo, L'Energia Elettrica, No. 10, pp. 405-413, 1992

- [4] P. Buccheri, S. Mangione, R. Miceli, Drenaggio della corrente di guasto a terra da parte di funi di guardia e guaine metalliche di cavi, L'Energia Elettrica, No. 7/8, pp. 325-331, 1993
- [5] M. Sylos Labini, A. Covitti, G. Delvecchio, C. Marzano, A Study for Optimizing the Number of Subareas in the Maxwell's Method, IEEE Transaction on Magnetics, Vol. 39, No. 3, pp.1159-1162, May 2003

APPENDIX

The calculation of the current field generated by interconnected grounding systems

[1]

Nomenclature

- Remote earth:* is made up of all the points in which the voltage can be considered to be equal to zero;
- J_{sk} current flowing from the power system to the node k ;
- Y_{kj} value of the admittance between the grounding systems k and j ;
- Y_k admittance between the node k and the remote earth. This admittance takes into account the current which passes through the interconnection links and is partly drained into the ground also by the capacitive effects;
- U_k earthing voltage of the grounding system k ;
- E_{kj} electromotive force induced in the interconnection conductors between the grounding systems k and j , this electromotive force being due to the fault currents circulating in the power system.

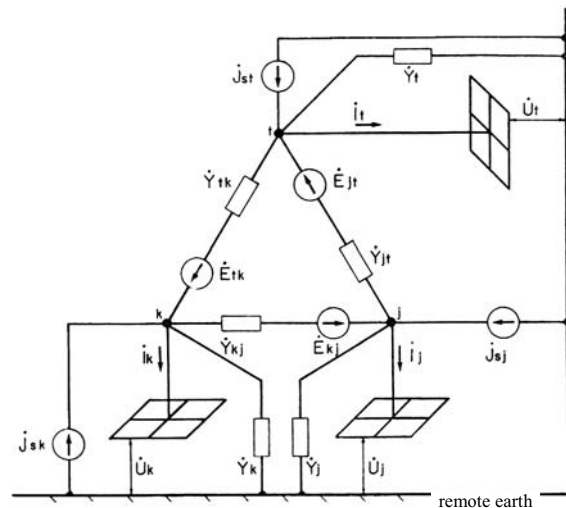


Fig. 9. - Electrical system consisting of the interconnection of three grounding systems

The calculation method

Fig. 9 shows a system made up of various grounding systems interconnected to each other in a very general way. For the sake of brevity this system will be called "total system". We intend to determine the voltages in all the points of the soil surface, these voltages being generated by a fault current occurring in a grounding system or also generated by more fault currents taking place simultaneously in various grounding systems. The method proposed by [1] is an extension of the Maxwell's subareas method, the latter referring to only one grounding system which leaks a known fault current. On the contrary, in the case under examination, the fault currents which are still known by assumption can be more than one and concern the various grounding systems interconnected to each other. The classic Maxwell's subareas method implies that we must subdivide each grounding system into elements (or subareas) and set a system of linear equations like (3). This system allows us to determine the vector i of the subcurrents leaked by the subareas, on the basis of the vector u of voltages of the various subareas.

While in the case of only one grounding system the vector u can be easily determined since it is made up of terms which are all equal to the earthing voltage U_E of the equipotential system under examination [2], [5], in the case of the "total system" the vector u is unknown. So, it is necessary to impose the LKC in all the nodes of the "total system" to determine all the electrical quantities of this system, especially the vector u that appears in (3).

Let N be the number of grounding systems, each having a voltage U_k and let N_s be the total number of subareas into which the N grounding systems of the "total system" have been subdivided ($N_s > N$).

The N voltages U_k (or earthing voltages) and the N_s subcurrents i_k leaked by the single subareas of the “total system” are, for the time being, unknown quantities.

If we apply the LKC to the node k , we obtain:

$$J_{sk} + J_{induced} = Y_k U_k + \sum_{\substack{j=1 \\ j \neq k}}^N Y_{kj} (U_k - U_j) + I_k \quad (1)$$

where the induced currents, $J_{induced}$, can be easily calculated as a function of both the admittances Y_{kj} and the electromotive forces E_{kj} [1]. The Eq. (1) can be easily put in the following matrix form [1]:

$$\mathbf{J} = \mathbf{Y} \mathbf{U} + \mathbf{I} \quad (2)$$

In (2) the vector \mathbf{J} of the currents injected into the nodes is known and depends on the kind of faults assumed, while both the vector \mathbf{U} of the earthing voltages of the various grounding systems and the vector \mathbf{I} of the currents going from each grounding system towards the remote earth are unknown.

Let's now apply the Maxwell's subareas method [5] and set the following system

$$\mathbf{u} = \mathbf{R} \mathbf{i} \quad (3)$$

where: \mathbf{R} is the matrix of the voltage coefficients (symmetrical matrix of size N_s); \mathbf{u} and \mathbf{i} are the unknown vectors of the voltages and subcurrents of N_s subareas of the “total system”.

It is now useful to introduce an appropriate connection matrix \mathbf{T} , (size $N \times N_s$), a matrix consisting only of 0 and 1. It allows us to determine the total current leaked by each grounding system on the basis of the subcurrents leaked by the N_s subareas:

$$\mathbf{I} = \mathbf{T} \mathbf{i} \quad (4)$$

and also to determine the voltages of the N_s subareas on the basis of the earthing voltages of the grounding systems:

$$\mathbf{u} = \mathbf{T}' \mathbf{U} \quad (5)$$

where \mathbf{T}' is the transpose of the matrix \mathbf{T} . Having said this, from (3) we obtain:

$$\mathbf{i} = \mathbf{R}^{-1} \mathbf{u} \quad (6)$$

and taking (5) into account we have:

$$\mathbf{i} = \mathbf{R}^{-1} \mathbf{T}' \mathbf{U} \quad (7)$$

As a consequence, (4) becomes:

$$\mathbf{I} = \mathbf{T} \mathbf{R}^{-1} \mathbf{T}' \mathbf{U} \quad (8)$$

If we substitute \mathbf{I} in (2), we obtain:

$$\mathbf{J} = [\mathbf{Y} + \mathbf{T} \mathbf{R}^{-1} \mathbf{T}'] \mathbf{U} \quad (9)$$

Equation (9) allows us to determine the vector \mathbf{U} . Once \mathbf{U} is known it is possible to determine the vector \mathbf{u} of the voltages of the subareas by (5). Having done this, we can determine the vector of the subcurrents \mathbf{i} by (6). Once the subcurrents of the various subareas are known the classic Maxwell's method allows us to determine the voltages in each point of the soil surface, these voltages being generated by all the grounding systems constituting the “total system” of Fig. 9, [5].

III-3. THE COMPARISON OF PHANTOM MODEL AND SIMULATION RESULTS IN SAR ANALYSIS

Katarzyna Ciosk¹, Andrzej Krawczyk², Hacer Oztura³, Roman Kubacki⁴

1) Technical University of Kielce, Kielce, Poland, kciosk@tu.kielce.pl

2) Electrotechnical Institute, Warsaw, Poland, krawczyk@iel.waw.pl

3) Eylul Dokuz University, Izmir, Turkey, hacer.oztura@deu.edu.tr

4) Military Institute of Hygiene and Epidemiology, Warsaw, Poland, kubacki@wihe.waw.pl

Abstract – The *Specific Absorption Rate* (SAR) is the coefficient which determines the thermal effect on the biological tissue subjected to the electromagnetic field. Thermal effect is especially important when the radio-frequency electromagnetic field is considered. The paper presents the analytical method for computational SAR analysis. The biological model is prolate spheroid. The illumination is a uniform plane wave with the magnetic field vector polarized along the z axis. The simulation results are compared with the measurement carried out on the phantom.

Introduction

The analysis of SAR (specific absorption rate) distribution in biological tissue has gained the researchers' interest recently [1]. It is to some extent the result of the proposal of EU standards which introduce the limits for SAR coefficients. The distribution of SAR can be achieved by computational technique or by experiment made on phantom. Both are very approximate solutions as they introduce very strict assumptions. Firstly, the analyzed object is mostly assumed as homogeneous and secondly, the geometry of the object is rather simple and distant from reality. These simplicities are accepted for evaluating possible hazards. Thus, the model for comparison is simple enough to employ analytical method for computational analysis. As to the phantom, there are two types of phantom: the one shows the distribution of the field and the second which measures the total energy absorbed. Here the second one was approached. The SAR is the coefficient which determines the thermal effect on the biological tissue subjected to the electromagnetic field and is expressed by:

$$\text{SAR} = \frac{\gamma E^2}{\rho} \quad (1)$$

where γ is conductivity, ρ is the mass density and E is the electric field strength.

Mathematical model

The biological model is a prolate spheroid with major axis l , minor axis a and the interfocal distance d as shown in Fig.1. The spheroid is an isotropic lossy dielectric. The external medium is assumed to be free space. We consider time-harmonic fields and the time-dependence $e^{j\omega t}$ are suppressed. The illumination is a uniform plane wave with the magnetic field vector polarized along the z axis. The primary magnetic field is given by

$$\mathbf{H}_0 = \hat{z}H_{0z} \quad (2)$$

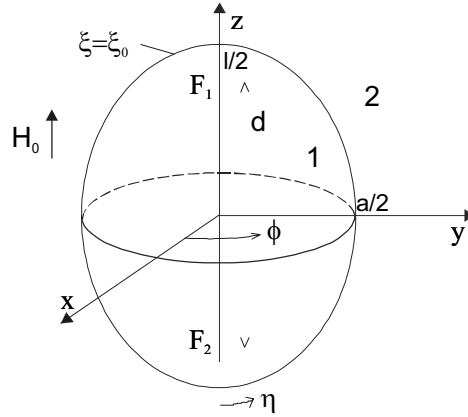


Fig. 1. Schematic diagram of spheroidal model

In order to describe the electromagnetic fields for spheroidal body, the prolate spheroidal coordinates ξ, η, ϕ are introduced:

$$\begin{cases} x = \frac{d}{2} \left[(1-\eta^2)(\xi^2-1) \right]^{\frac{1}{2}} \cos \phi \\ y = \frac{d}{2} \left[(1-\eta^2)(\xi^2-1) \right]^{\frac{1}{2}} \sin \phi \\ z = \frac{d}{2} \eta \xi \end{cases} \quad (3)$$

for the ranges of $-1 \leq \eta \leq 1, 1 \leq \xi \leq \infty$ and $0 \leq \phi \leq 2\pi$.

In view of the rotational symmetry of the configuration the electric field strength has one component

$$\mathbf{E} = \hat{\phi} E_{\phi}(\eta, \xi) \quad (4)$$

and has been selected as the unknown field. The electromagnetic field is described by the Maxwell's equations, which reduce to Helmholtz's equation

$$\nabla^2(E_{\phi}) + k^2 E_{\phi} = 0 \quad (5)$$

where $k^2 = \omega \mu_0 (\omega \epsilon - j\gamma)$. Equation (5) in terms of spheroidal coordinates can be written as

$$\frac{\partial}{\partial \xi} \left((\xi^2 - 1) \frac{\partial}{\partial \xi} E_{i\phi} \right) + \frac{\partial}{\partial \eta} \left((1 - \eta^2) \frac{\partial}{\partial \eta} E_{i\phi} \right) + \left(c_i^2 (\xi^2 - \eta^2) + \frac{1}{\xi^2 - 1} - \frac{1}{1 - \eta^2} \right) E_{i\phi} = 0 \quad (6)$$

where: $c_i = k_i \frac{d}{2}, i=1, 2$.

In region 2 outside the spheroid the electric field can be expressed in terms of associated Legendre functions of the first and second kind [3]

$$E_{2\phi}(\eta, \xi) = H_{0z} i \omega \mu \frac{d}{2} \left[\frac{1}{2} \sqrt{\xi^2 - 1} P_1^1(\eta) + \sum_{n=1}^{\infty} B_n Q_n^1(\xi) P_n^1(\eta) \right] \quad (7)$$

The magnetic field strength \mathbf{H} has two components and they outside the spheroid are given by

$$H_{2\eta}(\eta, \xi) = \frac{H_{0z}}{\sqrt{\xi^2 - \eta^2}} \left[\xi P_1^1(\eta) + \sum_{n=1}^{\infty} B_n U_{1n}(\xi) P_n^1(\eta) \right] \quad (8)$$

$$H_{2\xi}(\eta, \xi) = -\frac{H_{0z}}{\sqrt{\xi^2 - \eta^2}} \left[\frac{1}{2} \sqrt{\xi^2 - 1} V_{11}(\eta) + \sum_{n=1}^{\infty} B_n Q_n^1(\xi) V_{1n}(\eta) \right] \quad (9)$$

where

$$U_{mn}(\xi) = \frac{d}{d\xi} \left[\sqrt{\xi^2 - 1} Q_n^m(\xi) \right] \quad (10)$$

$$V_{mn}(\eta) = \frac{d}{d\eta} \left[\sqrt{1 - \eta^2} P_n^m(\eta) \right] \quad (11)$$

In region 1 inside spheroid the electric field is considered in the expression [5]

$$E_{1\phi}(\eta, \xi) \approx E_{2\phi}(\eta, \xi_0) e^{-ik_1 \int_{\xi_0}^{\xi} d\xi' h_{\xi}(\eta, \xi')} \quad (12)$$

where

$$h_{\xi}(\eta, \xi) = \frac{d}{2} \sqrt{\frac{\xi^2 - \eta^2}{\xi^2 - 1}} \quad (13)$$

For magnetic field yields

$$H_{1\eta}(\eta, \xi) \approx \frac{2}{i\omega\mu_1 d} \left[\frac{\xi}{\sqrt{(\xi^2 - \eta^2)(\xi^2 - 1)}} - ic_1 \right] E_{1\phi}(\eta, \xi) \quad (14)$$

The unknown coefficients B in equation (7) are determined by boundary condition on tangential magnetic field and can be obtain from equations:

$$B_{2m-1} \left[U_{1(2m-1)}(\xi_0) - \frac{\xi_0}{\sqrt{\xi_0^2 - 1}} Q_{2m-1}^1(\xi_0) \right] + jc_1 \sum_{n=1}^{\infty} B_{2n-1} Q_{2n-1}^1(\xi_0) \Pi_{(2m-1)(2n-1)}(\xi_0) =$$

$$= -\frac{ic_1}{2} \sqrt{\xi_0^2 - 1} \Pi_{(2m-1)1}(\xi_0) \quad (15)$$

$$\Pi_{mn}(\xi) = \frac{2m+1}{2m(m+1)} \int_{-1}^1 d\eta \sqrt{\xi^2 - \eta^2} P_m^1(\eta) P_n^1(\eta) \quad (16)$$

Measurements

The experiment was made for the spheroidal object filled up the phantom, corresponding to biological tissues in accordance with European standard CENELEC for phantoms subjected to the gsm-frequency electromagnetic radiation. The illumination was a uniform plane wave with the magnetic field vector polarized along the z axis. The frequency range was from 800 MHz to 1800 MHz. Measurement procedure depended on the measurement the total energy absorbed. The object was placed in a waveguide. The difference between input and output energy determines the energy lost in the object. This measurement is believed to be as exact as the measurement of high frequency field energy is. The results of measurements and calculation shown Fig.2. A relatively small discrepancies between measured and calculated values was obtain.

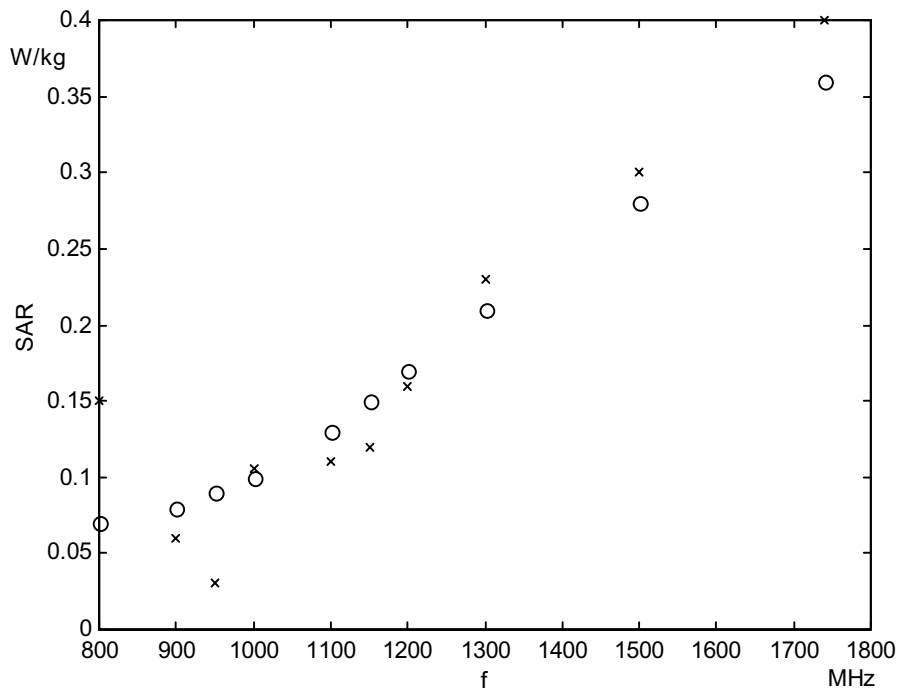


Fig. 2. The SAR distribution: x – measurement, o - calculations

Conclusions

The paper is aimed at constructing an analytical model of RF electromagnetic field in lossy dielectric materials, i.e. in biological tissues. In this approach the relationship between SAR and model parameters (conductivities and dimensions) can be calculated which may create the standardised procedure for SAR evaluation. The simple and fast procedure can be obtained for dosimetry [4] while the second one has methodological aspect – for testing numerical models. The simulation results are compared with the results of experiment. A relatively good agreement was obtain

References

- [1] C.H.Durney, D.A Christensen: Basic Introduction to Bioelectromagnetics, , CRC Press 2000
- [2] P. Moon, D.E. Spencer: Field Theory for Engineers, D. Van Nostrand Company, Inc., 1961
- [3] C. Flammer: Spheroidal Wave Functions. Stanford, CA: Stanford Univ. Press, 1957
- [4] M. Zenczak: The proposal of dosimetry of the electromagnetic field, in: Electromagnetic influences on biological objects, INB ZTUREK, Warszawa, 2001 (in Polish)
- [5] H. Braunisch, C. O. Ao. K. O'Neill, J. Kong: Magnetoquastatic Response of Conducting and Permeable Prolate Spheroid Under Axial Exitation. IEEE trans. On Geoscience and Remote Sensing, Vol 39, No 12, 2001

III-4. ELECTRIC CIRCUIT REPRESENTATION OF A MAGNETIC CIRCUIT WITH HYSTERESIS

Loredana Cristaldi, Sonia Leva, Adriano P. Morando

Dipartimento di Elettrotecnica, Politecnico di Milano, Piazza Leonardo da Vinci, 32, Milano, Italy

E-mail: loredana.cristaldi@polimi.it, sonia.leva@polimi.it, adriano.morando@polimi.it

Abstract – The goal of the present work is to formulate a method that permits, in presence of hysteresis cycle, the association of circuit elements with the graph, preserving energy equivalence. In this way for each branch of the circuit, these elements represent both storage and dissipation phenomena. The proposed method allows to represent, unambiguously and with energy equivalence, the initial system with hysteresis losses by a conductance-susceptance network which can be experimentally deduced by measuring RMS current, RMS voltage and iron losses. At the end an experimental validation is proposed.

Introduction

The topological properties of the graph associated with a magnetic circuit do not depend on the type of the constitutive relation (linear or not-linear, single- or multiple-value) imposed by the magnetic relation characterising its branch. In the absence of iron-losses, the ferromagnetic cores are represented by reluctances, which become inductances in dual electric terms. The latter can be regarded as current-dependent in cases affected by non-linearity, but still as loss-less components, independent of the waveforms considered.

In the presence of dynamic hysteresis losses, the graph remains unchanged. However, the associated circuit elements, representing hysteresis losses, are expressed in functional form, dependent on the entire function handled and not only on its actual value. The graph thus remains unchanged, but the circuit elements values associated with it change during operation and thus do not possess an intrinsic character. Similarly, from the energy point of view, the identification of the lossless component of the difference representing the energy absorbed does not lead to a single answer.

The goal of the present work is to formulate a method that allows to associate the circuit elements with the graph, preserving energy equivalence. For each branch of the circuit, these elements represent both storage and dissipation phenomena.

This analysis will be carried out according to the following guidelines:

- In order to define a unified approach and being able to employ phasor calculus in line with classical analysis, an effective ellipse of equal area for all operating conditions replaces the real hysteresis cycle.
- The circuit parameters (conductance G , inductance L) belonging to the electric circuit corresponding to the initial magnetic circuit including iron losses due to hysteresis are deduced using the rule of magnetic/electric circuit duality and the concept of the equivalent ellipse.
- Once an effective method as above is adopted, an experimental analysis follows immediately. Starting with the measurements of RMS voltages and currents and the active power and then using the concept of an elliptic hysteresis cycle, it is possible to determine the parameters of conductance and inductance which characterise the electric circuit under the operating condition.

Theoretical background

A linear time-invariant magnetic circuit can be represented, in terms of an equivalent electric circuit, by an inductance L associated with the flux-current relationship constituting the magnetic circuit itself.

In the presence of non-linearity, the inductance (expressed in differential form $L_d = Nd\varphi / di = L_d(i)$), becomes a single-value function of the actual value i of the current. The corresponding energy balance is:

$$\delta L_\mu = i(\psi) d\psi = L_d(i) idi = dW_\mu \quad (1)$$

which belongs to a conservative phenomenon – in fact $\oint L_d(i) idi = 0$ – and is expressed by an exact differential of the status function.

In the presence of hysteresis, the flux-current relation becomes multi-value and it can be represented implicitly by a functional $f(i, \varphi_{fe}) = 0$. The induced EMF can be formally expressed as:

$$e_f = -Np\varphi_{fe} = -N \frac{d\varphi_{fe}}{di} pi = N^2 \left(\frac{\partial f}{\partial h} / \frac{\partial f}{\partial b} \right) \frac{A}{\ell} pi = N^2 \mu_d \frac{A}{\ell} pi = L_d[i(t)] pi \quad (2)$$

In this case, using the differential permeability $\mu_d(i, \varphi_{fe})$, the above expression identifies a *multi-value inductance* depending on the entire function $i(t)$ and not only, as in the conservative case, on its actual value i . Given the multi-value nature of the constitutive relation, the energy balance is dissipative and is accordingly expressed by an differential relationship as follows:

$$\delta L_\mu = i[\psi(t)] d\psi = L_d[i(t)] idi = dW_\mu + \delta Q_\mu \quad (3)$$

Its integral over the cycle, equal to the area of the cycle itself, shows a loss expressed as follows:

$$L_\mu = Q_\mu = \oint i[\psi(t)] d\psi = \oint L_d[i(t)] idi \quad (4)$$

The equivalent electric circuit, topologically unchanged with respect to the conservative case, includes the complex functional inductance $L_d[i(t)]$ which allows for the presence of both storage and dissipation. In detail, the division of the total power $\delta L_\mu/dt = e(t)i(t)$ into its two parts: the conservative dW_μ/dt and dissipative $\delta Q_\mu/dt$ produces a double path in the circuit. However, this division has a purely formal character. As it is linked to the definition of the conservative part of the approximate derivative δL_μ , it has, in general, no unambiguous value.

Use of the equivalent sinusoid: elliptic constitutive relation

In the case of a real constitutive relation, a non-linearity leads to a deformed current waveform flowing when a sinusoidal voltage is applied and vice versa. When the constitutive relation is complex, as in the presence of hysteresis losses, the current absorbed is not just deformed, but also shifted in phase with respect to the applied voltage (Fig.1a). This statement is completely general: it applies to all types of time-varying waveforms.

It these cases becomes useful to employ equivalent sinusoidal concepts. In fact, under those conditions, the deformed current/voltage quantities can be replaced by sinusoidal quantities of equivalent energy, characterised by having the same frequency as the starting quantities. This procedure is equivalent to replacing formally the “real” hysteresis cycle with an equivalent elliptic loop of the same area [1], [2].

Let us consider a magnetic circuit with hysteresis fed with any periodic voltage and carrying a current of the same frequency. The equivalent sinusoidal voltage applied to the magnetic circuit can be expressed as follows:

$$v(t) = \sqrt{2}V \sin(\omega t) = \frac{d}{dt} \psi(t) = NA_{fe} \frac{d}{dt} b(t) \quad (5)$$

where ψ is the flux in the winding, N the number of turns and A_{fe} is the iron area of the magnetic circuit. The magnetic induction is then:

$$b = \frac{1}{NA_{fe}} \int v(t) dt = -\frac{\sqrt{2}V}{\omega NA_{fe}} \cos(\omega t) = \sqrt{2}B \sin\left(\omega t - \frac{\pi}{2}\right) \quad (6)$$

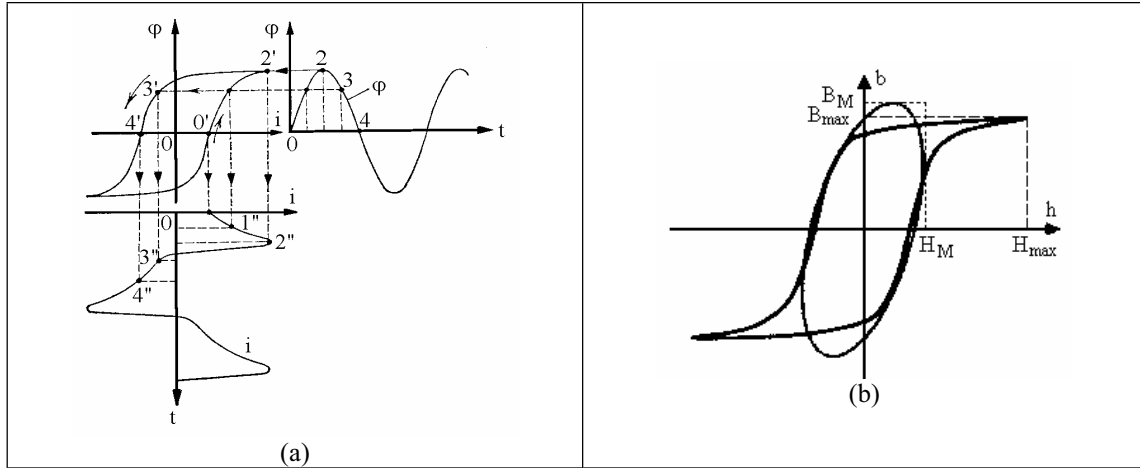


Fig.1. (a) The hysteresis cycle changes the phase of the current with respect to that of the flux.
(b) Normal hysteresis cycle and the corresponding elliptical cycle.

The equivalent sinusoidal current, shifted with respect to the voltage by the lag angle δ , is given by:

$$i(t) = \sqrt{2}I \sin(\omega t - \delta) \quad (7)$$

from which follows the magnetic force:

$$h(t) = Ni(t)/\ell_{fe} = \sqrt{2}NI \sin(\omega t - \delta)/\ell_{fe} = \sqrt{2}H \sin(\omega t - \delta) \quad (8)$$

where ℓ_{fe} is the length of the ferromagnetic circuit. The magnetic induction and the magnetic force are shifted in phase by an angle $\alpha = \pi/2 - \delta$ with respect to each other.

In the $\{b, h\}$ plane, equations (6) and (8) describe an ellipse given by the following equation:

$$\left(\frac{h}{\sqrt{2}H}\right)^2 + \left(\frac{b}{\sqrt{2}B}\right)^2 - \frac{\sin \delta}{HB} hb - \cos^2 \delta = 0 \quad (9)$$

the area of which:

$$\oint hdb = 2\pi BH \cos \delta = \pi B_M H_M \cos \delta = \pi B_M H_M \sin \alpha \quad (10)$$

is equal to that of the initial hysteresis cycle area and represents the iron losses of the magnetic circuit with hysteresis (Fig.1b). As the angle α is changed, both the position and the dimensions of the axes of the equivalent ellipse are changed. However, all the ellipses are inscribed inside a rectangle with sides $2H_M$ e $2B_M$.

In terms of integral variables, the same result can be obtained in the following manner:

$$\begin{cases} \psi(t) = \sqrt{2}\Psi \sin\left(\omega t - \frac{\pi}{2}\right) \\ i(t) = \sqrt{2}I \sin(\omega t - \delta) \end{cases} \quad \oint id\psi = \pi I_M \psi_M \sin\alpha = \pi I_M \psi_M \cos\delta \quad (11)$$

The angle α , which is complementary to the phase shift between the effective voltage and current, is called the loss angle.

Circuit representation: complex permeance

Making use of phasor algebra, the equivalent sinusoidal quantities above defined can be represented by phasors as exemplified in Fig.2a.

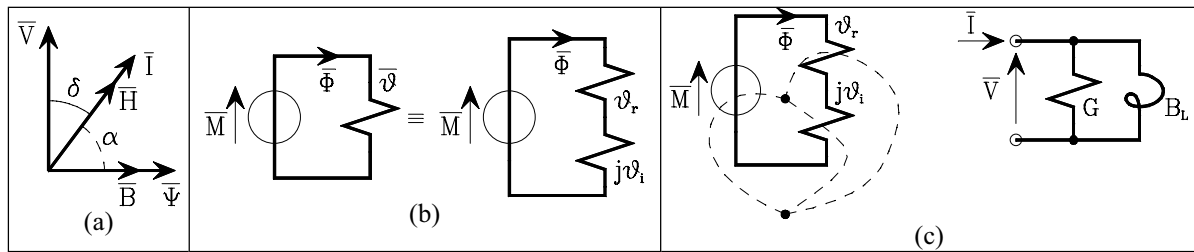


Fig.2. (a) Phasor diagram of the electric and magnetic quantities. (b) Magnetic circuit. (c) Application of the duality rule and the electric circuit deduced accordingly.

With equations (6) and (8) rewritten in phasor form, the constitutive relation of the ferromagnetic material is identified from the following complex permeability:

$$\bar{\mu} = \bar{B}/\bar{H} = B/H \cdot e^{-j\alpha} = \mu e^{-j\alpha} \quad (12)$$

From this equation, we can derive the complex reluctance:

$$\bar{\mathcal{G}} = \ell_{fe}/(A_{fe}\bar{\mu}) = \ell_{fe}(\mu_r + j\mu_i)/(A_{fe}\mu^2) = \mathcal{G}_r + j\mathcal{G}_i \quad (13)$$

and the following overall electromagnetic relationships (see Fig.2b):

$$\begin{cases} \bar{M} = N\bar{I} \\ N\bar{I} = \bar{\mathcal{G}}\bar{\Phi} \\ \bar{V} = j\omega N\bar{\Phi} \end{cases} \quad (14)$$

We can now formally extend the duality between magnetic and electric circuits to the case of circuits with complex parameters and obtain the electric network of Fig.2c by a direct topological method. In this manner, the following parameters appear in parallel form:

$$\bar{Y} = \frac{\bar{I}}{\bar{V}} = \frac{\bar{\mathcal{G}}}{j\omega N^2} = \frac{\mathcal{G}_r + j\mathcal{G}_i}{j\omega N^2} = \frac{\mathcal{G}_i}{\omega N^2} - j\frac{\mathcal{G}_r}{\omega N^2} = G - jB_L \quad (15)$$

These belong to the dual electric network. In energy terms, considering the system with an applied voltage, we have:

$$\bar{I} = \bar{V} \frac{\bar{\mathcal{G}}}{j\omega N^2} = \frac{\bar{V}}{j\omega N^2} \cdot \frac{\ell_{fe}(\mu_r + j\mu_i)}{A_{fe}\mu^2} \quad (16)$$

from which follows the power S , in terms of an energy balance, as below:

$$\bar{S} = \bar{V} \cdot \bar{I}^* = \frac{V^2}{\omega N^2} \cdot \frac{\ell_{fe} (\mu_i + j\mu_r)}{A_{fe} \mu^2} = P_\mu + jQ_\mu \tag{17}$$

The apparent power turns out to be the complex sum of a real component, representing hysteresis losses - in accordance with (4) - and an imaginary component.

In this way, the initial system with hysteresis losses is represented, unambiguously and with energy equivalence, by a conductance-susceptance network which can be experimentally deduced by measuring RMS current, RMS voltage and iron losses.

All the above has been confirmed in practice. In the case presented here, the electric circuit and its parameters have been correctly determined applying the rules of duality and not introduced to create perturbations as occurs in the classical case.

The above approach can easily be extended to the analysis of magnetic circuits with hysteresis and with residual magnetisation. In fact, if DC polarisation is present, the equivalent circuit parameters are the same as in the case of pure AC conditions and they can therefore be evaluated starting from the AC component of the voltage and current quantities. The parametric equations represent the same elliptical loop as under pure AC conditions, but the centre of the loop is shifted from the origin of the axes to a point depending on the DC component of flux and current [3, 4].

Experimental Validation

The experimental set-up shown in Fig.3 has been employed to validate the proposed method. A toroidal core with rectangular cross section, obtained with a wound ferrosilicon sheet, has been employed as a test core.

In Fig.3a Hall-effect flux probe is depicted. This device has been employed in order to have a reference value of the magnetic flux inside the test core to compare with the values provided by the proposed method with and without of a dc flux polarization [3, 4].

The algorithm developed to apply the proposed method has been implemented in a Virtual Instruments (VI) structure under LabView environment. Fig.4 shows the front panel and the block diagram of the implemented VI.

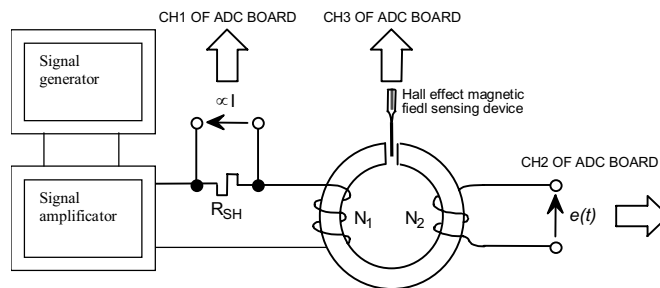


Fig.3. Schematic of circuit implemented for measurement

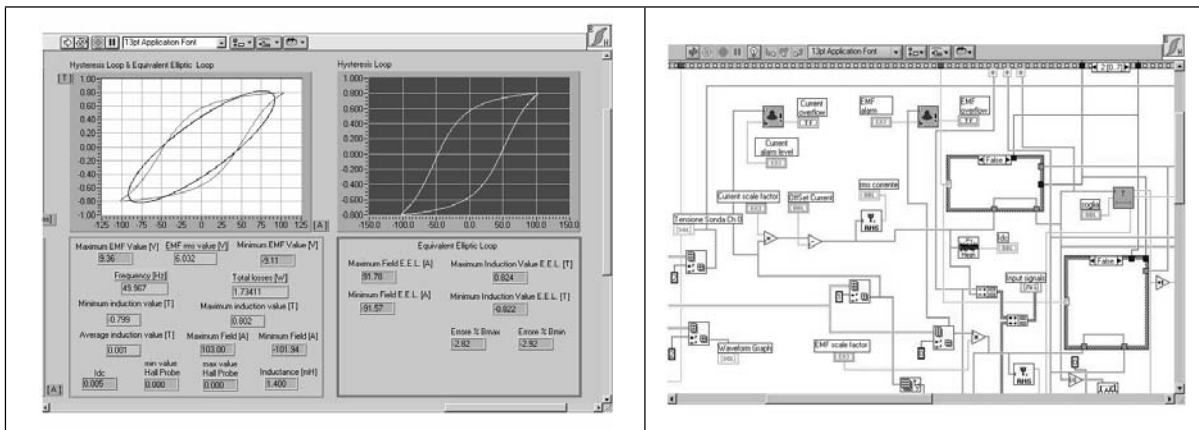


Fig.4. Front panel and Block diagram of the VI

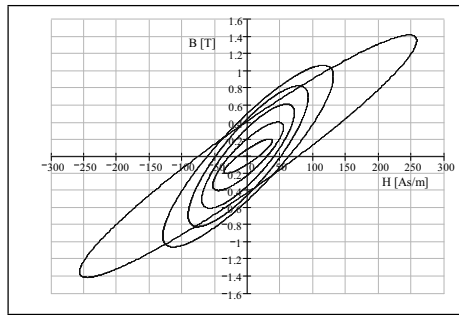


Fig.5. Equivalent ellipses evaluated at a constant frequency varying the supply voltage

The validation of the proposed model has been carried out by calculating the L - G parameters of the equivalent linear circuit of Fig.2c under two different conditions: at a constant frequency ($f=50\text{Hz}$) varying the supply voltage, and at a constant supply voltage, varying the frequency between 5Hz and 250Hz.

In the first case, starting with the equivalent ellipses of Fig.5, the data shown in Table I have been obtained. It can be seen that the loss angle α increases with an increase of the magnetic field until the effects of saturation become apparent. The inclination of the principal axis of the ellipse grows as the strength of field B is increased, until saturation is reached.

The results obtained when the frequency is varied are shown in Table II. It can be seen that, after an initial transient, the loss angle tends to stabilise itself. Consequently, the elliptical hysteresis cycles are concentric, but with different areas.

TABLE I.

B_M [T]	G [S]	L [mH]	α
0.099	1.775	0.554	0.3
0.203	1.914	0.794	0.445
0.302	1.838	0.992	0.52
0.399	1.741	1.152	0.562
0.503	1.64	1.28	0.538
0.601	1.573	1.361	0.592
0.802	1.47	1.4	0.574
1.002	1.426	1.216	0.499
1.200	1.307	0.754	0.3

TABLE II.

f [Hz]	G [S]	L [mH]	α
5	6.929	1.478	0.311
10	4.369	1.482	0.386
20	2.745	1.456	0.465
50	1.456	1.371	0.56
100	0.945	1.262	0.643
120	0.842	1.217	0.658
150	0.726	1.151	0.667
200	0.606	1.07	0.684
220	0.57	1.037	0.685
250	0.524	0.995	0.687

Conclusions

In this paper a method based on the energy equivalence by a real hysteresis loop and an elliptic loop with the same area, has been presented.

This approach allows using the phasors to magnetic non-ideal circuit. Moreover, its use allows extending the duality rules between the magnetic circuits and the electric circuit.

The method proved itself quite accurate and the experimental results of measurements performed under pure ac conditions and dc polarized cyclic conditions are in good agreement with the results of measurements coming from a Hall-effect flux probe.

References

- [1] S. Leva, A.P. Morando, Topological transition from magnetic networks to the electric equivalent ones when iron losses are present, Proc. 43rd IEEE Midwest Symposium On Circuit and Systems, Lansing MI (USA), August 8-11, 2000, pp.642-645
- [2] S. Leva, A.P. Morando, Dual electric and magnetic networks: extension to time-varying and hysteresis cases, Proc. 11th International Symposium on Electromagnetic Fields in Electrical Engineering (ISEF), Maribor, Slovenia, September 18-20, 2003
- [3] L. Cristaldi, A. Ferrero, M. Lazzaroni, A.P. Morando, A Sensorless Method for the Identification of Asymmetric Hysteresis loops of Ferromagnetic Materials, Proc. 11th IMEKO, Lisbon, Portugal, September 13-14, 2001
- [4] L. Cristaldi, A. Ferrero, M. Lazzaroni, A.P. Morando, Sensorless Evaluation of Asymmetric Hysteresis Loops of Ferromagnetic Materials, IEEE Trans. on Instrumentation and Measurement, Vol. 52, No. 3, June 2003, pp.846-851

III-5. SIMULATION OF END EFFECTS IN A SUPERCONDUCTIVE MAGNET WITH A FERROMAGNETIC CORE

Herbert De Gersem, Thomas Weiland

Technische Universität Darmstadt, Institut für Theorie Elektromagnetischer Felder
Schloßgartenstraße 8, D-64289 Darmstadt, Germany
Email: degersem/weiland@temf.tu-darmstadt.de

Abstract A superconductive dipole magnet is simulated by a transient 3D model discretised by the Finite Integration Technique. The eddy currents in the ferromagnetic yoke are taken into account by an anisotropic conductivity tensor. The eddy currents occurring in the superconductive cable due to the finite inter-wire resistance, are resolved by a semi-analytical magnetisation term added to the formulation. The simulation results indicate the importance of the eddy-current losses, especially at the yoke ends.

Nuclotron Dipole Magnet

To reduce operation costs, superconductive magnets are planned for the new accelerator facilities at the 'Gesellschaft für Schwerionenforschung' (GSI) in Darmstadt, Germany. The magnetic field in the aperture of the dipole Nuclotron magnet is generated by 2 sets of 8 windings of superconductive cable (Fig. 1). A homogeneous aperture field is achieved by a ferromagnetic yoke which is further optimised by a negative shimming of the pole and the introduction of an air slit [1]. During the ramping of the magnetic field, significant eddy current effects are generated in the laminated ferromagnetic yoke, especially at the ends of the magnets due to the time-varying field in the longitudinal direction generated by the end windings (Fig. 1). The longitudinal flux component also diminishes the homogeneity of the aperture field which is particularly harmful at particle beam injection [2]. The configuration is protected against quenching by implementing a wire coating with relatively low resistance such that the current can redistribute between adjacent wires. Due to this limited insulation, however, eddy currents migrate between different wires which leads to additional losses. The reduction of the losses and a guarantee for successful operation requires these phenomena to be accurately predicted during design.

3D Eddy-Current Model

For reasons of symmetry, only an eighth of the geometry has to be modelled. The formulation is based on the transient magnetodynamic partial differential equation in terms of the magnetic vector potential \mathbf{A} :

$$\nabla \times (\nu \nabla \times \mathbf{A}) + \kappa \frac{\partial \mathbf{A}}{\partial t} = \mathbf{J}_s \quad (1)$$

where ν and κ are the reluctivity and conductivity respectively, and \mathbf{J}_s is the current density applied to the superconductive coils. The partial differential equation (1) is discretised at a staggered and orthogonal grid pair using the Finite Integration Technique, yielding

$$\tilde{\mathbf{C}}\mathbf{M}_\nu\mathbf{C}\hat{\mathbf{a}} + \mathbf{M}_\kappa\frac{d\hat{\mathbf{a}}}{dt} = \hat{\mathbf{j}}_s \quad (2)$$

where \mathbf{C} and $\tilde{\mathbf{C}}$ are the discrete curl operators at the primary and dual grid respectively, $\hat{\mathbf{a}}$ is the component vector of the path integrated modified vector potentials, $\hat{\mathbf{j}}_s$ is the vector of source currents and \mathbf{M}_ν and \mathbf{M}_κ are the reluctivity and conductivity material matrices which are diagonal in the case of orthogonal grids and isotropic materials [3, 4]. The formulation (14) is integrated in time using the Galerkin linear time stepping scheme.

Eddy-Current Model for the Ferromagnetic Yoke

The laminations of the ferromagnetic yoke are perpendicular to the longitudinal axis of the magnet. Therefore, only eddy currents in the $x - y$ -plane are assumed to be important. The laminated yoke can be modelled as a massive yoke with the anisotropic conductivity tensor

$$\underline{\kappa} = \begin{bmatrix} \kappa_{yk} & 0 & 0 \\ 0 & \kappa_{yk} & 0 \\ 0 & 0 & 0 \end{bmatrix} \quad (3)$$

where κ_{yk} is the conductivity of the yoke iron [5]. Because the anisotropy is aligned with the axes of the applied tensor-product grid, the discretisation of the material relation still yields a

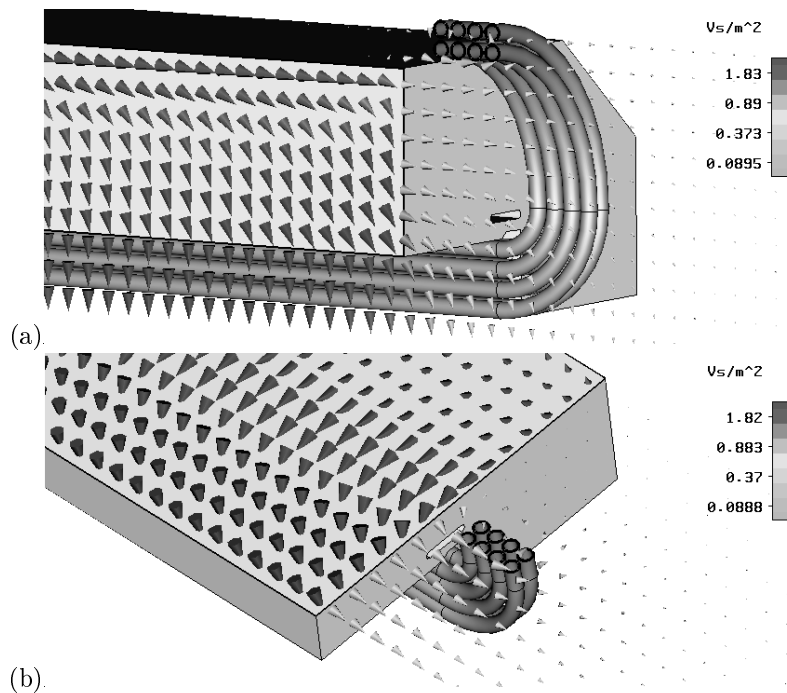


Figure 1: Magnetic flux plot at the end of the Nuclotron magnet: (a) at a vertical cross-section and (b) at a horizontal cross-section.

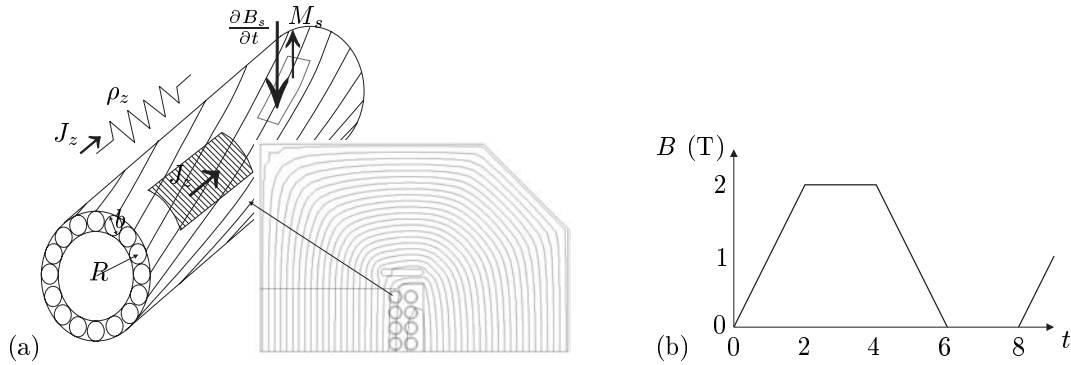


Figure 2: (a) Geometry of the Nuclotron-type cable and (b) duty cycle of the Nuclotron magnet.

diagonal conductivity matrix \mathbf{M}_κ . For locations within the yoke, \mathbf{M}_κ is given by

$$\begin{cases} \mathbf{M}_{\kappa,ii} = \frac{\tau_{\text{cable}} \tilde{A}_i}{\ell_i} & \text{for primary edges and dual facets in the } x\text{- or } y\text{-direction} \\ \mathbf{M}_{\kappa,ii} = 0 & \text{for primary edges and dual facets in the } z\text{-direction} \end{cases} \quad (4)$$

where \tilde{A}_i and ℓ_i stand for the area of the i -th dual facet and the length of the i -th primary edge respectively [6]. The induced currents and the corresponding Joule loss are computed in a post-processing step:

$$\hat{\mathbf{j}}_e = -\mathbf{M}_\kappa \frac{d}{dt} \hat{\mathbf{a}}; \quad (5)$$

$$P = -\hat{\mathbf{j}}_e^T \frac{d}{dt} \hat{\mathbf{a}}. \quad (6)$$

This formulation neglects the z -component of the eddy currents and therefore also discards all induced effects in the laminated due to the parallel magnetic flux components. More accurate formulations exist (see e.g. [7]) but are not needed to obtain a technically sufficient accuracy because of the very thin laminations considered here.

Cable Magnetisation Model

The Nuclotron-type cable consists of strands which are twisted around an iron tube (Fig. 2a). Each strand is a copper wire in which superconductive filaments are embedded. Unless the filaments are saturated or eddy currents appear, all current flows through the superconductive filaments. The configuration is protected against quenching by implementing a wire coating with relatively low resistance such that current can redistribute between adjacent wires. Due to this limited insulation, however, eddy currents migrate between different wires when the superconductive cable is submitted to an external time-varying magnetic field [8]. The insulation of the windings is of a substantially higher quality and prevents current migration between different windings.

The construction of an analytical cable eddy current model for the Nuclotron magnet configuration follows the development of the cable eddy current model for Rutherford cable as pointed out in [9]. First, the characteristic resistivity of the wire-insulation composite in the z -direction is determined (Fig 3a). Secondly, the current density and corresponding magnetisation due to an incident time-varying magnetic field is derived from an analytical model for the considered

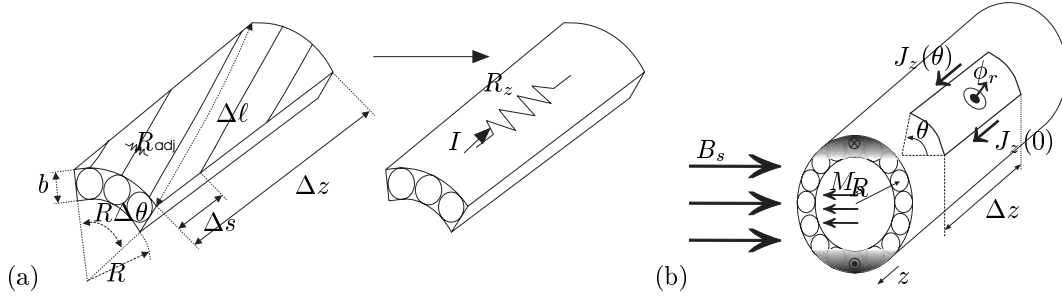


Figure 3: Nuclotron cable: (a) determination of the characteristic resistivity ρ_z and (b) current density J_z induced by a time-varying magnetic field B_s causing a magnetization M_s .

geometry (Fig. 3b). For a cable with a support of radius R and wires of diameter b , the twist factor γ_{tw} is defined by the ratio of the angular twisting to the corresponding longitudinal distance, i.e.

$$\gamma_{\text{tw}} = \frac{R\Delta\theta}{\Delta z} \quad (7)$$

From measurements, the specific inter-wire resistance r_{adj} , i.e., the resistance between two adjacent wires of unit length, is determined. The equivalent resistance ρ_z in the longitudinal direction follows a homogenisation procedure applied to this particular geometry:

$$\rho_z = \frac{\gamma_{\text{tw}}^2}{\sqrt{1 + \gamma_{\text{tw}}^2}} r_{\text{adj}}. \quad (8)$$

A time-varying magnetic flux density B_s applied in a direction \vec{e}_s perpendicular to the cable, induces a voltage drop across the wire insulation which lead to currents between different wires and which causes an additional magnetisation opposite to the direction of the incident flux. The flux through a circumferential part of the cable shell in the radial direction is $\phi_r = B_s \Delta z R \sin \theta$. The induced current density is $J_z(\theta) = -\frac{R}{\rho_z} \frac{\partial}{\partial t} B_s \sin \theta$ and gives rise to the magnetisation

$$M_s = -\tau_{\text{cable}} \frac{\partial B_s}{\partial t} \quad (9)$$

where the time constant derived from the analytical model is

$$\tau_{\text{cable}} = \frac{bR}{\nu_0 \rho_z}. \quad (10)$$

and ν_0 is the reluctivity of vacuum. From (8) and (10), it is clear that a reduction of cable magnetisation effects is possible by improving the wire insulation, applying an increased twist angle, increasing the cable support diameter and decreasing the wire diameter. The feasibility of each of these possibilities, however, is limited due to other design criteria such as quench protection and magnet size.

The cable magnetisation has only components parallel to the cross-section of the Nuclotron magnet. Hence, for implementation in the 3D Nuclotron model, the coercitive field due to the cable magnetisation is written as

$$\mathbf{H}_c = -\nu_0 \mathcal{I}_{\text{cable}} \frac{d\mathbf{B}}{dt} \quad (11)$$

with the anisotropic, but diagonal tensor

$$\mathcal{I}_{\text{cable}} = \begin{bmatrix} \tau_{\text{cable}} & 0 & 0 \\ 0 & \tau_{\text{cable}} & 0 \\ 0 & 0 & 0 \end{bmatrix}. \quad (12)$$

The time constant τ_{cable} is inserted in a material matrix \mathbf{M}_τ . The magnetic flux through the i -th facet of the primary grid is denoted by $\widehat{\mathbf{b}}_i$ whereas the coercitive field strength integrated along the i -th dual edge is denoted by $\widehat{\mathbf{h}}_{c,i}$. Since the main directions of the anisotropic tensor $\mathcal{I}_{\text{cable}}$ are aligned with the axes of the tensor-product grid, the discretisation of (11) still leads to a diagonal material operator \mathbf{M}_τ . Hence, the material relation is defined by $\widehat{\mathbf{h}}_{c,i} = \nu_0 \mathbf{M}_{\tau,ii} \frac{d}{dt} \widehat{\mathbf{b}}_i$ where

$$\begin{cases} \mathbf{M}_{\tau,ii} = \frac{\tau_{\text{cable}} \tilde{\ell}_i}{A_i} & \text{for primary facets and dual edges in the } x\text{- or } y\text{-direction} \\ \mathbf{M}_{\tau,ii} = 0 & \text{for primary facets and dual edges in the } z\text{-direction} \end{cases} \quad (13)$$

and $\tilde{\ell}_i$ and A_i denote the length of the i -th dual edge and the area of the i -th primary facet respectively. The discretised cable magnetisation model is added to the magnetodynamic model:

$$\widetilde{\mathbf{C}} \mathbf{M}_\nu \mathbf{C} \widehat{\mathbf{a}} + \mathbf{M}_\kappa \frac{d\widehat{\mathbf{a}}}{dt} + \widetilde{\mathbf{C}} \nu_0 \mathbf{M}_\tau \mathbf{C} \frac{d\widehat{\mathbf{a}}}{dt} = \widehat{\mathbf{j}}_s \quad (14)$$

which corresponds to the magnetodynamic formulation

$$\nabla \times (\nu \nabla \times \mathbf{A}) + \kappa \frac{\partial \mathbf{A}}{\partial t} + \nabla \times (\nu_0 \mathcal{I}_{\text{cable}} \nabla \times \mathbf{A}) = \mathbf{J}_s. \quad (15)$$

The introduction of a cable magnetisation model in a 2D finite element formulation is described in [10]. For the geometry of the Nuclotron cable, a reliable time constant τ_{cable} can be determined by an analytical model. For more general cable geometries, however, more sophisticated models are required [10].

Simulation Results

The duty cycle at which the Nuclotron magnet is operated, is plotted in Fig. 2b. The magnetic flux at the maximum aperture field of 2 T is depicted in Fig. 1. The currents induced in the yoke when ramping the magnet are shown in Fig. 4. The Joule loss at the end laminations reflect the shape of the neighbouring end windings (Fig. 5). The observed Joule loss amounts 213 W averaged over the entire duty cycle which corresponds to the measurements on a prototype magnet. Modifications of the design are required in order to diminish these losses. Improved designs with differently shaped end windings and with laminations with carefully located slits are under consideration.

Conclusions

The Joule losses in the ferromagnetic yoke and the superconductive cable of a dipole magnet are modelled by two anisotropic material operators added to a magnetodynamic formulation discretised by the finite integration technique.

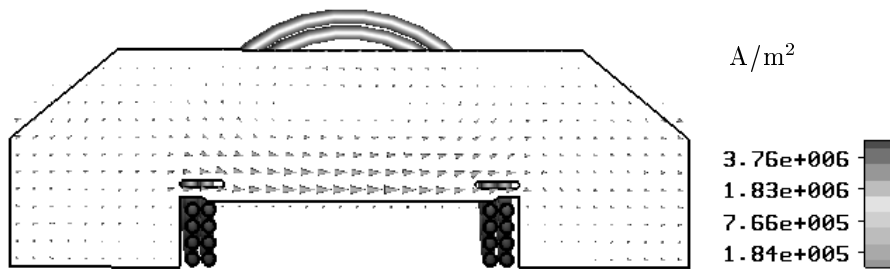


Figure 4: Eddy current distribution at the end of the Nuclotron magnet yoke.

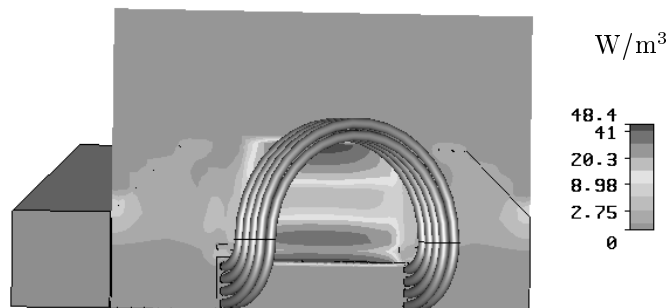


Figure 5: Joule loss distribution at the end of the Nuclotron magnet yoke.

Acknowledgement H. De Gersem is working in the cooperation project "DA-WE1 (TEMF/GSI)" with the "Gesellschaft für Schwerionenforschung (GSI)", Darmstadt.

References

- [1] A.D. Kovalenko, A. Kalimov, H.G. Khodzhbagiyani, G. Moritz, and C. Mühle, "Optimization of a superferric nuclotron type dipole for the GSI fast pulsed synchrotron," *IEEE Trans. App. Supercond.*, vol. 12, no. 1, pp. 161–165, 2002.
- [2] S. Russenschuck, "Coil end optimization for the LHC main dipole," *IEEE Trans. Magn.*, vol. 31, no. 3, pp. 1960–1963, May 1995.
- [3] T. Weiland, "A discretisation method for the solution of Maxwell's equations for six-component fields," *AEÜ*, vol. 31, pp. 116–120, 1977.
- [4] M. Clemens and T. Weiland, "Transient eddy current calculation with the FI-method," *IEEE Trans. on Magn.*, vol. 35, no. 3, pp. 1163–1166, 1999.
- [5] K. Hollaus and Oszkár Bíró, "A FEM formulation to treat 3D eddy currents in laminations," *IEEE Trans. on Magn.*, vol. 36, no. 4, pp. 1289–1292, July 2000.
- [6] H. Euler and T. Weiland, "Zur Berechnung der Wirbelströme in beliebig geformten, lamellierten, dreidimensionalen Eisenkörpern," *Archiv für Elektrotechnik*, vol. 61, pp. 103–109, 1979.
- [7] J. Gyselinck, L. Vandevelde, J. Melkebeek, P. Dular, F. Henrotte, and W. Legros, "Calculation of eddy currents and associated losses in electrical steel laminations," *IEEE Trans. on Magn.*, vol. 35, no. 3, pp. 1191–1194, May 1999.
- [8] R. Otmani, A. Devred, and P. Tixador, "Interstrand and AC-loss measurements on Rutherford-type cables for accelerator magnet applications," *IEEE Trans. App. Supercond.*, vol. 11, no. 1, Mar. 2001.
- [9] A.P. Verweij and H.H.J. ten Kate, "Coupling currents in Rutherford cables under time varying conditions," *IEEE Trans. on App. Supercond.*, vol. 3, no. 1, pp. 146–149, Mar. 1993.
- [10] H. De Gersem and T. Weiland, "Finite element models for superconductive cables with finite inter-wire resistance," *Compumag 2003*, Saratoga Springs, USA, July 13-18, 2003.

III-6. MODELLING OF TEMPERATURE-DEPENDENT EFFECTIVE IMPEDANCE OF NONFERROMAGNETIC MASSIVE CONDUCTOR

Ivo Doležel¹, Ladislav Musil¹ and Bohus Ulrych²

¹Institute of Electrical Engineering, Czech Academy of Sciences, Dolejskova 5, 182 02 Praha 8, Czech Republic, E-mail: {dolezel, musil}@iee.cas.cz

²Faculty of Electrical Engineering, University of West Bohemia, Sady Petaticratniku 14, 306 14 Plzen, Czech Republic, E-mail: ulrych@kte.zcu.cz

Abstract – Impedance of long direct massive conductors carrying time-variable currents is a complex function of time. Its evolution is affected not only by the skin effect, but also by the temperature rise. The paper presents a numerical method that allows computing the resistance and internal inductance of a nonferromagnetic conductor of any cross-section from values of the total Joule losses and magnetic energy within the conductor. The theoretical analysis based on the field approach is illustrated on a typical example, whose results are discussed.

Introduction

Simulations of fast phenomena in various electrical systems (grounding devices, windings of electrical machines etc.) often do not respect changes of the resistance and internal inductance due to the skin effect. The reason consists in a widespread opinion that the increase of the resistance leads to reduction of the surge effects while its neglecting provides results that are worse than the physical reality. And when the device is designed for less favourable parameters, its safety is higher.

In case of steep pulses or waves, however, the effective resistance of the conductor may reach values by an order higher than the DC resistance. In such a case, neglecting the skin effect can lead to quite incorrect ideas about the voltage and current phenomena in the device. The situation (particularly in fault regimes) is also affected by the temperature rise of the current-carrying parts, which brings about an additional increase of their resistances.

The complete analysis of the effect represents a coupled electromagnetic-thermal problem and the paper offers a methodology how to cope with it. We consider a surge skin effect in a direct massive nonferromagnetic conductor of a general cross-section placed in linear medium from which the produced heat is transferred by convection (which is usual, for example, at various kinds of grounders, or overhead and cable lines in power distribution systems).

Formulation of the problem

A sufficiently long direct massive conductor of constant cross-section is supplied from the current source by current $i(t)$ of general time dependence. Its material is nonferromagnetic ($\mu = \mu_0$) and temperature dependencies of its physical parameters (electrical conductivity γ , thermal conductivity λ , specific mass ρ and specific heat c) are known.

The aim of the analysis is to find the time evolution of various quantities characterising the process. Of great importance are particularly the effective resistance $R_{\text{eff}}(t)$ and internal inductance $L_{\text{eff}}(t)$ of the conductor that are generally influenced by the

- time dependence of the passing current $i(t)$,
- corresponding time-dependent distribution of the current density within its cross-section,
- consequent temperature rise due to the Joule losses in the conductor.

The task is handled as a quasi or hard-coupled problem. This means that all required quantities are calculated simultaneously.

Mathematical model

The continuous mathematical model of the problem consists of two partial differential equations describing the

- nonstationary electromagnetic field expressed by distribution of the vector potential A ,
- nonstationary temperature field in the conductor produced by the Joule losses.

The nonstationary electromagnetic field produced by current $i(t)$ within the conductor reads [1]

$$\text{rot rot } \mathbf{A} + \mu_0 \gamma \cdot \frac{\partial \mathbf{A}}{\partial t} = \mu_0 \mathbf{J}_0 \quad (1)$$

where \mathbf{J}_0 denotes the vector of the uniform current density within the conductor corresponding to external current $i(t)$ from the source. The term $\mathbf{J}_e = -\gamma \cdot \frac{\partial \mathbf{A}}{\partial t}$ expresses the eddy current density. When accepting the Cartesian co-ordinate system according to Fig. 1 (conductor of cross-section Ω_c with boundary Γ_c , Γ_a being the artificial boundary whose significance is dealt with later on), \mathbf{J}_0 has only one nonzero position-independent component $J_{0z}(t)$, \mathbf{J}_e and \mathbf{A} also one nonzero, but position-dependent component $J_{ez}(x,y,t)$, $A_z(x,y,t)$.

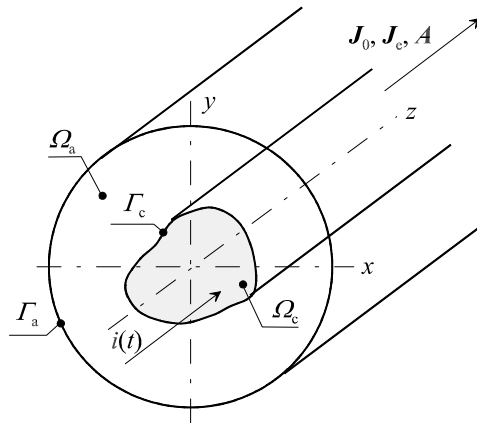


Fig. 1: The investigated arrangement

Now the equation (1) may be rewritten as

$$\frac{\partial^2 A_z}{\partial x^2} + \frac{\partial^2 A_z}{\partial y^2} - \mu_0 \gamma \cdot \frac{\partial A_z}{\partial t} = -\mu_0 J_{0z} \quad (2)$$

(other co-ordinate systems may be used, of course, as well). Uniqueness of the solution may be secured, for example, by imposing indirect boundary condition

$$\int_{\Omega} \left(J_{0z} - \gamma \cdot \frac{\partial A_z}{\partial t} \right) dS = i(t) \quad (3)$$

(parameter γ is not constant, because it is a function of temperature T that is variable within Ω_c). Practically, circular artificial boundary Γ_a placed at a sufficient distance from the conductor is characterised by a constant value of component A_z of the vector potential. Distribution of this quantity on the definition area $\Omega = \Omega_a \cup \Omega_c$ follows from (2) and (4). The initial condition reads $A_z(x, y, 0) = 0$,

because at the beginning of the process no magnetic field is supposed to affect the arrangement. The effective resistance $R'_{\text{eff}}(t)$ per unit length of the conductor calculated from distribution of the specific Joule losses is

$$R'_{\text{eff}} = \frac{\int_{\Omega_c} w_J \cdot dS}{i^2}, \quad w_J = \frac{(J_{0z} + J_{ez})^2}{\gamma} \quad (4)$$

The effective internal inductance $L'_{\text{eff}}(t)$ per unit length may be calculated from the magnetic field energy by formula

$$L'_{\text{eff}} = \frac{\int_{\Omega_c} \left(\left(\frac{\partial A_z}{\partial x} \right)^2 + \left(\frac{\partial A_z}{\partial y} \right)^2 \right) \cdot dS}{\mu_0 \cdot i^2}. \quad (5)$$

The nonstationary temperature field is described by equation [2]

$$\text{div}(\lambda \text{grad} T) = \rho c \cdot \frac{\partial T}{\partial t} - w_J, \quad (6)$$

where the temperature $T = T(x, y, t)$. In our case this equation within the conductor may be written as

$$\frac{\partial}{\partial x} \left(\lambda \cdot \frac{\partial T}{\partial x} \right) + \frac{\partial}{\partial y} \left(\lambda \cdot \frac{\partial T}{\partial y} \right) = \rho c \cdot \frac{\partial T}{\partial t} - w_J. \quad (7)$$

The boundary condition along the surface of the conductor reads

$$-\lambda \cdot \frac{\partial T}{\partial n} = \alpha_c \cdot (T - T_0) \quad \text{for } t \geq 0, \quad (8)$$

n denoting the outward normal. Radiation is (but not necessarily) neglected due to lower temperatures usually not exceeding 100–200 °C. Here α_c denotes the coefficient of the convective transfer of heat from the conductor surface into ambient medium of temperature T_0 . Finally the initial condition for the temperature reads $T(x, y, 0) = T_0$.

The algorithm of calculation of the discretised model at the $k+1$ -th time level on a grid with N nodes consists of the following steps:

- a) Iterative computation of values $A_{zi,k+1}$ from values $A_{zi,k}$, where $i = 1, \dots, N$ by means of discretised equations (2) and (3) with respecting the dependence $\gamma_{i,k} = \gamma(T_{i,k})$,
- b) Explicit determination of values $T_{i,k+1}$ from values $T_{i,k}$, where $i = 1, \dots, N$ by means of discretised equation (7) with respecting dependencies $\lambda_{i,k} = \lambda(T_{i,k})$, $\rho c_{i,k} = \rho c(T_{i,k})$,
- c) Computation of $R'_{\text{eff},k+1}$ by means of numerical approximation of (4),
- d) Computation of $L'_{\text{eff},k+1}$ by means of numerical approximation of (5).

For very short processes such as fast current pulses the heating process is practically adiabatic (convection and radiation can be neglected) and the temperature rise of the conductor may sufficiently accurately be calculated from the simple calorimetric equation. Computation of particular tasks was realised by combination of professional codes PC OPERA 7.0 and Femlab 2.3 with single-purpose user programs developed and written by the authors in Matlab 6.5.

Illustrative example

A hollow copper water-cooled conductor (Fig. 2) whose quarter is depicted in common with the discretisation mesh carries a current pulse according to Fig. 3. It is necessary to determine the time evolution of its effective resistance and internal inductance per unit length ($R'_{\text{eff}}, L'_{\text{eff}}$) as well as the temperature T (its starting value $T_0 = 20^\circ\text{C}$)

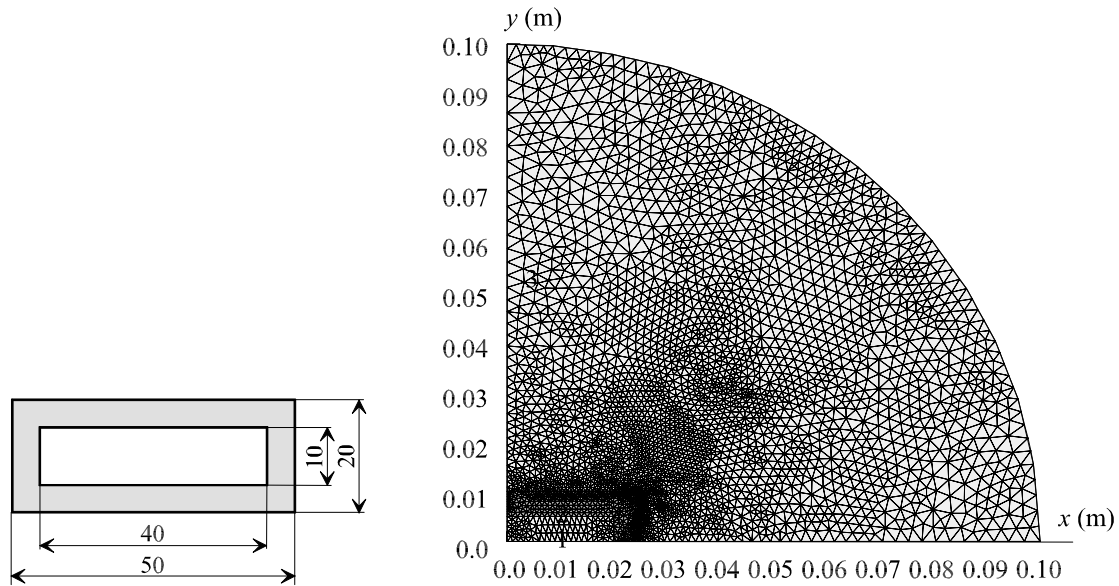


Fig. 2: The investigated conductor and meshing of the area

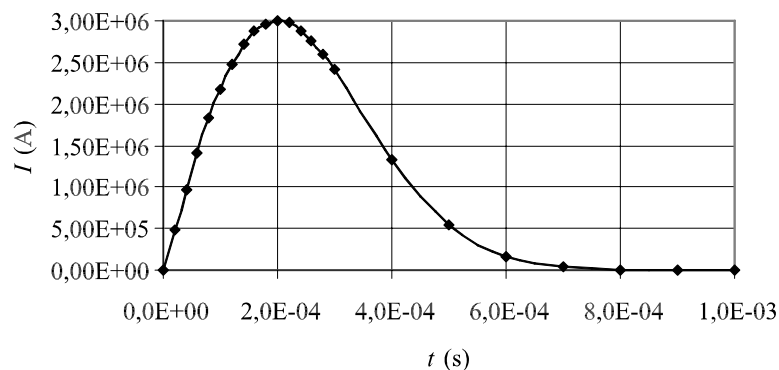


Fig. 3: Current pulse through the conductor

The temperature dependencies of the specific electrical and thermal conductivities $\gamma = \gamma(T)$ and $\lambda = \lambda(T)$ for copper are depicted in Fig. 4. An analogous dependence for $\rho c(T)$ may with a sufficient accuracy be expressed as a linear function in the form

$$\rho c(T) = 3631200 + 934.5 \cdot (T - 20) \text{ J/K m}^3.$$

These parameters are adjusted automatically during the calculation.

Computations were realised on a grid with about 6700 triangular elements (see Fig. 2), with good geometrical convergence of the results. Stability of the numerical process was secured by accepting the time step $\Delta t \leq 5 \times 10^{-6} \text{ s}$. Basic solution to the task took (according to the selected time step) several tens of minutes (PC 2.4 GHz).

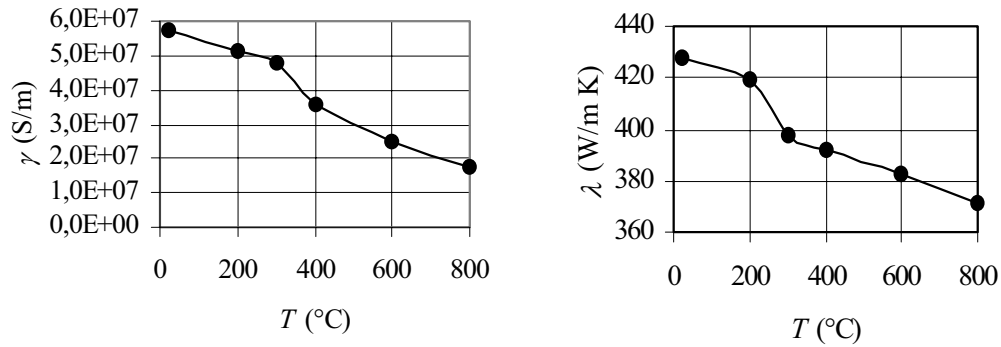


Fig. 4: Temperature dependencies $\gamma = \gamma(T)$ and $\lambda = \lambda(T)$ for copper

The most important results follow. Fig. 5 contains the time dependence of the total Joule losses $\Delta P'$ per unit length that (to some extent) copies the current pulse in Fig. 3. Its growth at the beginning of the process is, however, substantially faster due to highly expressed skin effect. This results in the time dependence of the effective resistance R'_{eff} (Fig. 6) whose maximum value is about five times higher than the direct-current value.

An analogous shape as $\Delta P'$ exhibits the magnetic field energy per unit length W'_m ; the corresponding time evolution of the effective internal inductance L'_{eff} per unit length is depicted in Fig. 7. Its minimum value is, on the other hand, about five times lower than its direct-current value. Finally, Fig. 8 contains the time evolution of the temperature. As said before, the process of heating is practically adiabatic, which was validated by solution and comparison of the corresponding equations. Cooling of the conductor can be observed only in several seconds.

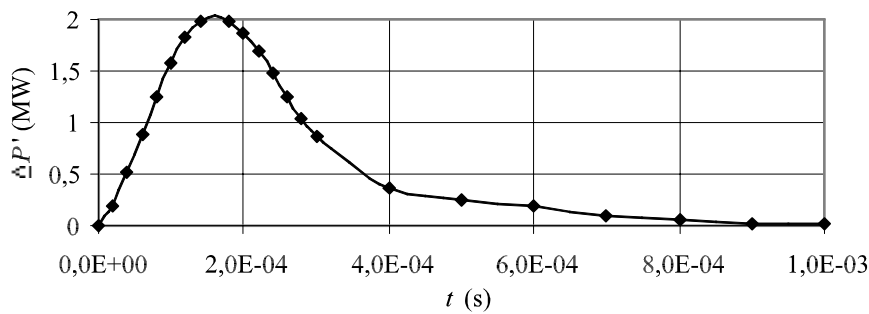


Fig. 5: Time dependence of the Joule losses $\Delta P'$ per unit length

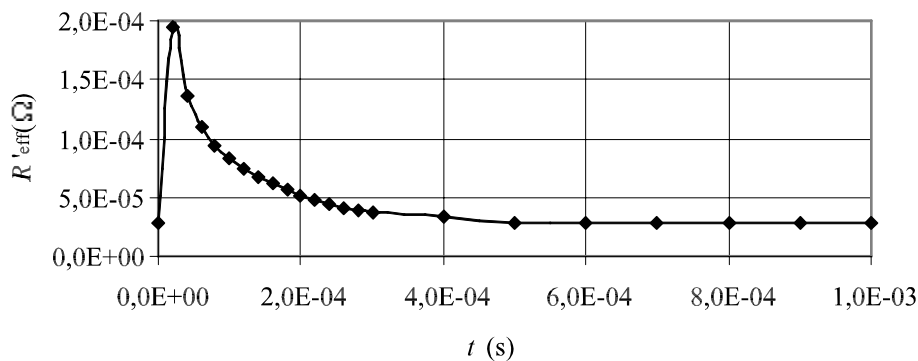


Fig. 6: Time dependence of the effective resistance R'_{eff} per unit length

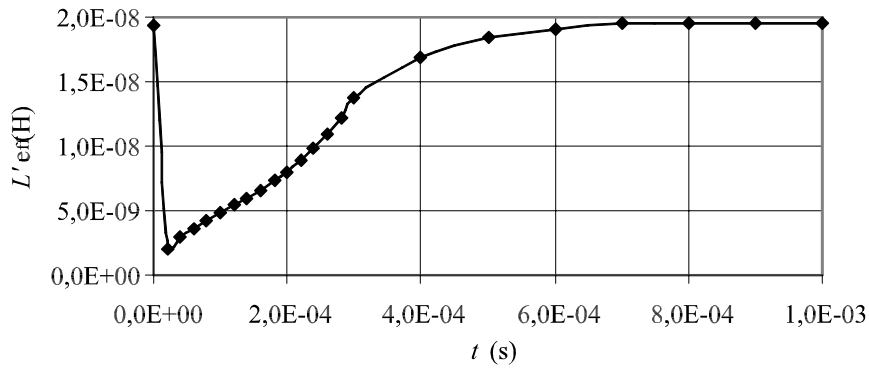


Fig. 7: Time dependence of the effective internal inductance L'_{eff} per unit length

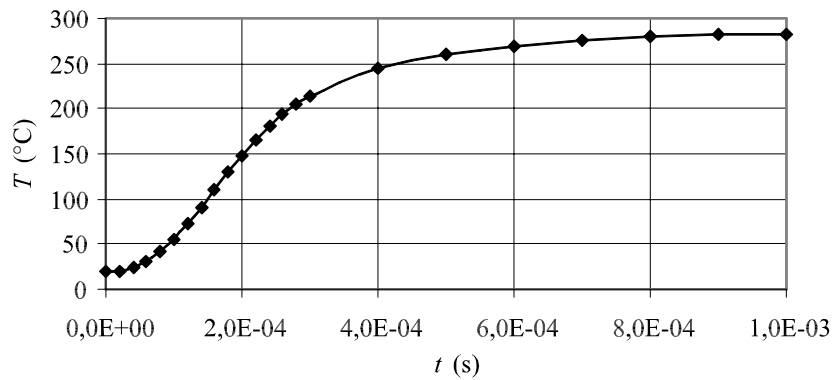


Fig. 8: Time evolution of the average temperature T of the conductor

Conclusion

The presented methodology allows solving this hard-coupled electromagnetic-thermal problem with good accuracy and reasonable time of computation. Nevertheless, problems may appear with increasing steepness of the time variations of the feeding current due to the necessity to reduce the time step in order to keep the stability of computations.

Next work in the field will be aimed at testing the integral model of the skin effect, extending the methodology by conductors fed from the voltage source (an ordinary differential circuit equation has to be added to the system), mutual influence of several near conductors (proximity effect), influence of ferromagnetic material etc.

Acknowledgement

The financial support of the Grant Agency of the Czech Republic (Project No. 102/01/1401) and Research Plan MSM 232200008 is gratefully acknowledged.

References

- [1] J. A. Stratton: Electromagnetic Theory. McGraw-Hill Book Comp., 1941.
- [2] P. J. Schneider: Conduction Heat Transfer. Addison-Wesley Pub Comp. Cambridge, Mass, 1955.

III-7. THE MAGNETIC NOISE OF A DC ELECTRIC MOTOR – MODELING OF THREE-TIMES-COUPLED ELECTROMAGNETIC, MECHANICAL AND ACOUSTIC PHENOMENA

M. Furlan¹, M. Boltežar²

¹R&D, ISKRA Avtoelektrika d.d., Polje 15, 5290 Šempeter pri Gorici, Slovenia
martin.furlan@iskra-ae.com

²University of Ljubljana, Faculty of Mechanical Engineering, Aškerčeva 6, 1000 Ljubljana, Slovenia
miha.boltezar@fs.uni-lj.si

Abstract – The sound power level of the magnetic noise radiated from a DC electric motor was numerically estimated for different loading conditions and two motor designs. Since the mechanism of the magnetic noise generation in a DC electric motor can be described as a three-times sequentially coupled problem, three linked – electromagnetic, mechanical and acoustic – numerical models were prepared. In the first phase the electromagnetic model was built to calculate the magnetic forces that excite the structure of the motor using the finite-element method (FEM). In the next phase the exciting magnetic forces were transferred to the structural model where the harmonic analysis was carried out using the FEM. The last phase was to model the acoustics, where the boundary-element method (BEM) was applied. To take account of the complexity of the investigated DC electric motor all three numerical models were three-dimensional (3-D). Finally, the numerical results from all three models were compared with the cogging torque, the vibration and the acoustic measurements, and a reasonable agreement was found.

Introduction

The need for a quiet human environment has become one of the most important environmental factors influencing almost every producer of noisy machinery, including the manufacturers of electric machines. A consequence of this is that acoustic noise defines the acceptability of electric machines for customers in a variety of industrial applications and has a major influence on their economic success. In spite of the fact that DC electric motors are being replaced by other electrical drives, the demand for noise and vibration remains a concern. For this reason it is important that the manufacturers of DC electric motors have a thorough understanding of the generation of noise and vibration.

Improved computational facilities have made it possible to provide a more quantitative description of the noise from electric machinery, especially when it is the magnetic noise that dominates [1–6]. Most research seems to be concentrated on induction machines [1–2], [5–6], where two-dimensional (2-D) models dominate; just a few papers deal with the problem of magnetic noise generation in DC electrical motors.

The aim of this paper is to demonstrate and verify a model of the magnetic noise radiated from DC electric motors. The complete analysis was performed on a permanent-magnet DC electric motor, with a rated power of 0.6kW, intended to drive an electro-hydraulic power-steering system in a car. A special emphasis is given to the investigation of different loading conditions and two design variations of the rotor skewing angle. One motor had a rotor with no skewing and the other had a rotor with a skewing of one rotor slot. The numerical results obtained with the FEM and/or the BEM are compared with the experimental data.

Magnetic Noise Modeling

Magnetic noise can be calculated from a three-times sequentially coupled electromagnetic-mechanical-acoustic numerical model [1–3], [6]. Fig. 1 shows a typical model of this kind. To calculate the magnetic forces that excite the structure of the motor, an electromagnetic model was developed. By applying the magnetic forces to the structural model we can calculate the magnitude and frequencies of the resulting vibrations. Finally, the results of the structural analysis, represented by the velocities on the exterior surface of the electric motor, are used as an input for the BEM acoustic model.

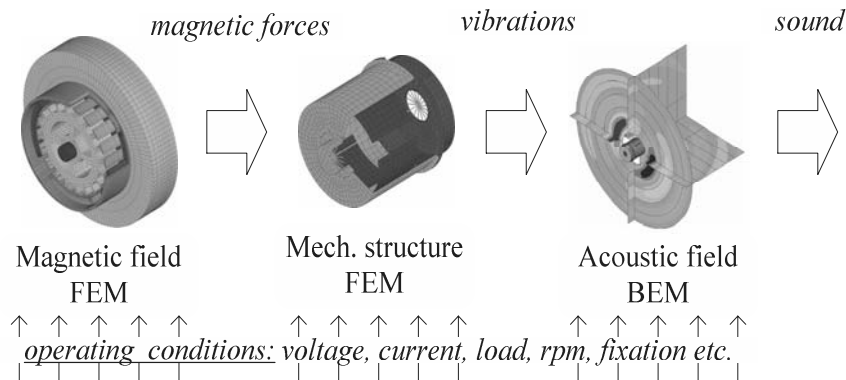


Fig. 1. Prediction of the magnetic noise in a DC electric motor

Magnetic Forces

For the magnetic-force calculation in the investigated DC electric motor, two 3-D FEM models were built; the only difference between the models was in the rotor skewing angle. Fig. 2 shows the FEM model with the magnetic forces acting on the rotors and on the stator. To estimate the current loads in the commutation zones the assumption of a linear commutation was applied.

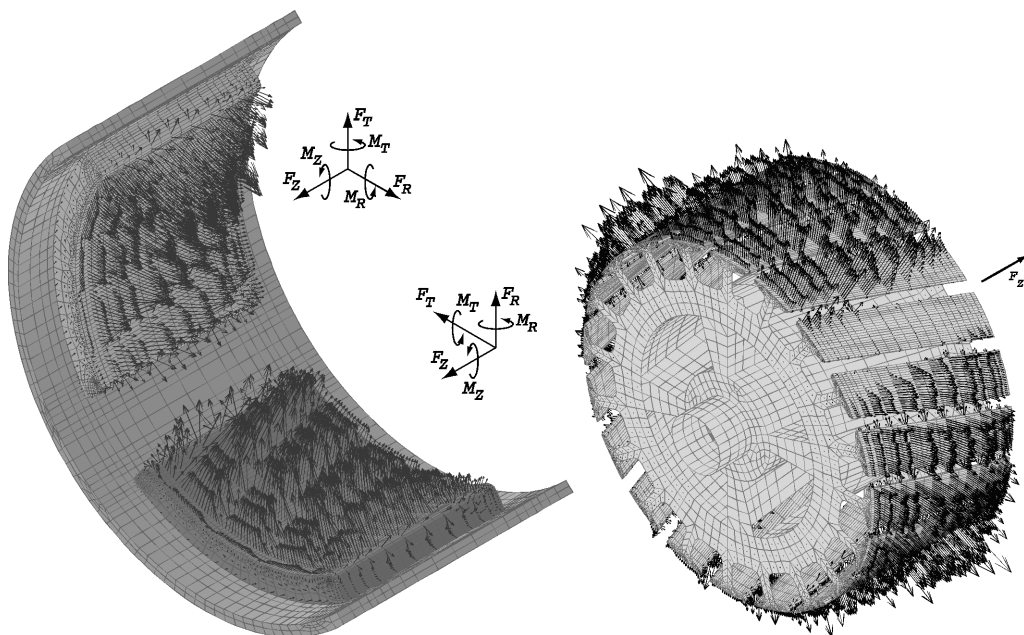


Fig. 2. 3-D FEM electromagnetic model, stator (on the left) and rotor (on the right)

By analyzing the magnetic forces acting on each magnet and on the rotor we found their amplitude and phase during the rotation for different motor currents of 0, 8, 16, 32 and 64A. Next, the variation in the resulting magnetic forces was decomposed by the discrete Fourier transform. Here, only the first five harmonics of the magnetic forces were calculated. As the rotor has twenty slots these harmonics are the 20th, 40th, 60th, 80th and 100th. Fig. 3 and Fig. 4 show the character of the most dominant component, i.e., the radial component, of the resulting magnetic force F_R , see Fig. 2, acting on the magnet for both FEM models, with the skewed and non-skewed rotor.

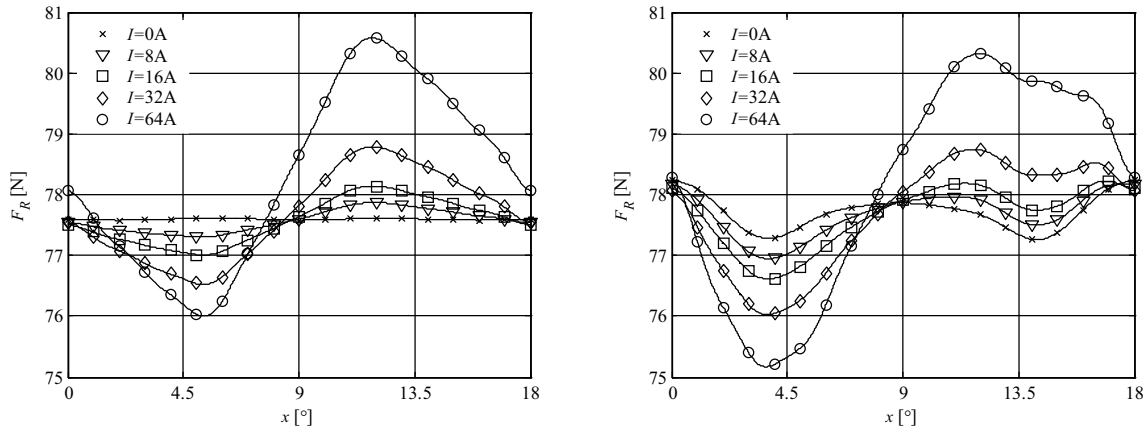


Fig. 3. The radial component of the resulting magnetic force acting on the magnet during the rotation for the FEM model with skewed rotor (on the left) and non-skewed rotor (on the right)

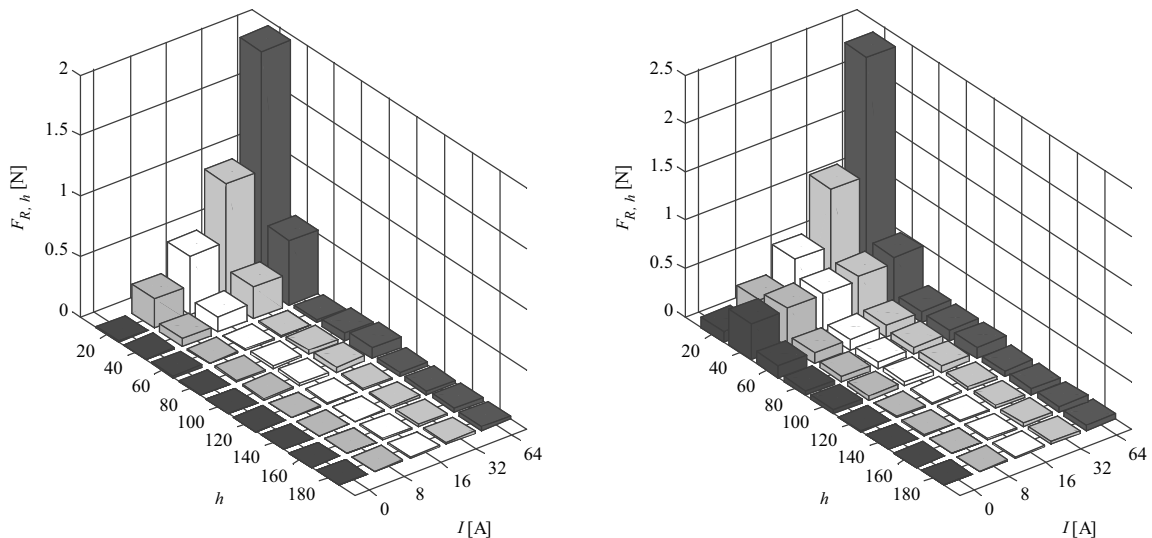


Fig. 4. The decomposed radial component of the resulting magnetic force acting on the magnet for the FEM model with skewed rotor (on the left) and non-skewed rotor (on the right)

The calculation of the magnetic forces and the electromagnetic FEM model were verified by measuring the cogging torque on the motor with the non-skewed rotor. The reason for this is that the cogging torque of the motor with the non-skewed rotor is more distinctive and therefore more practical to measure. Fig. 5 shows the comparison between the numerically calculated and the measured data of the cogging torque during the rotation. The driftage of approximately 0.075Nm that occurs in the experimentally evaluated cogging torque can be explained by the friction torque in the motor bearings, which was impossible to eliminate during the measurement. The friction torque was also measured, see Fig. 5, and a similar value to that of the driftage in the cogging torque was found. An imaginary extraction of the friction torque from the experimentally evaluated cogging torque would lead to very good agreement with the numerically calculated data.

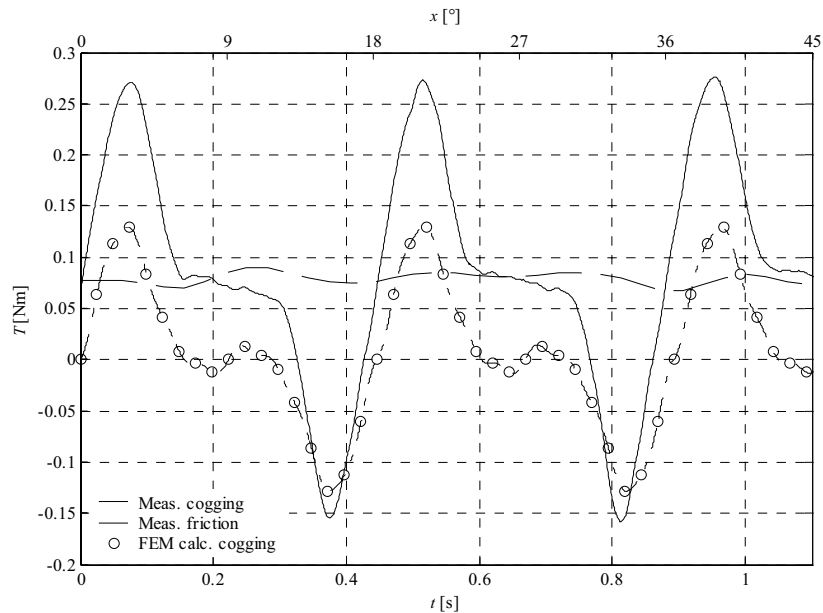


Fig. 5. The verification of the cogging torque

Vibration Response

To calculate the structural dynamic response of the investigated electric motor a 3-D FEM model was developed, see Fig. 6. For verifying the structural response of the whole model, as with the individual parts, an experimental modal analysis (EMA) was applied to the real structure. At a later stage the EMA results were used to improve the structural FEM model. The structural response of both motors was calculated using harmonic analyses, where a structural damping ratio of 2% was considered.

To make the numerical and experimental data comparable, the numerical calculation of the magnetic noise and vibrations was related to the experimental investigation. Next, the exciting magnetic forces were calculated (interpolated) for the corresponding experimental loading conditions presented in Tab. 1. The interpolated exciting magnetic forces were then transferred to the structural model as the resulting magnetic forces and moments acting on the rotor and the stator, see Fig. 6. The analysis includes the first four or five harmonics of the magnetic excitation forces, depending on the rotational speed of the motor.

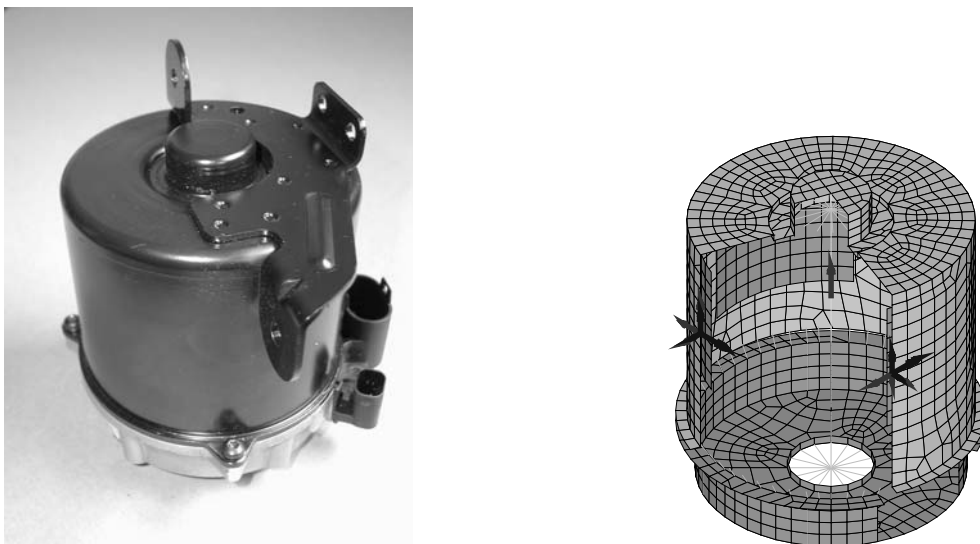


Fig. 6. The investigated DC electric motor (on the left) and its 3D structural FEM model (on the right)

Fig. 7 shows the mechanically deformed motor that is a consequence of the 20th, 40th, 60th and 80th harmonics of the magnetic forces. The results were obtained both numerically, using the FEM, and experimentally, using operation deflection analysis (ODA) – and good agreement was found. The deformed shape at a particular harmonic is almost identical for both motors, for the skewed and the non-skewed rotor, only the amplitude of the deformation is different. The important influence on the deformed shape of the motor is the excitation frequency of the magnetic forces, which is directly related to the rotational speed and indirectly related to the loading condition of the motor. This is especially evident for the deformed shapes that are a consequence of the higher harmonics, i.e., the 60th and 80th.

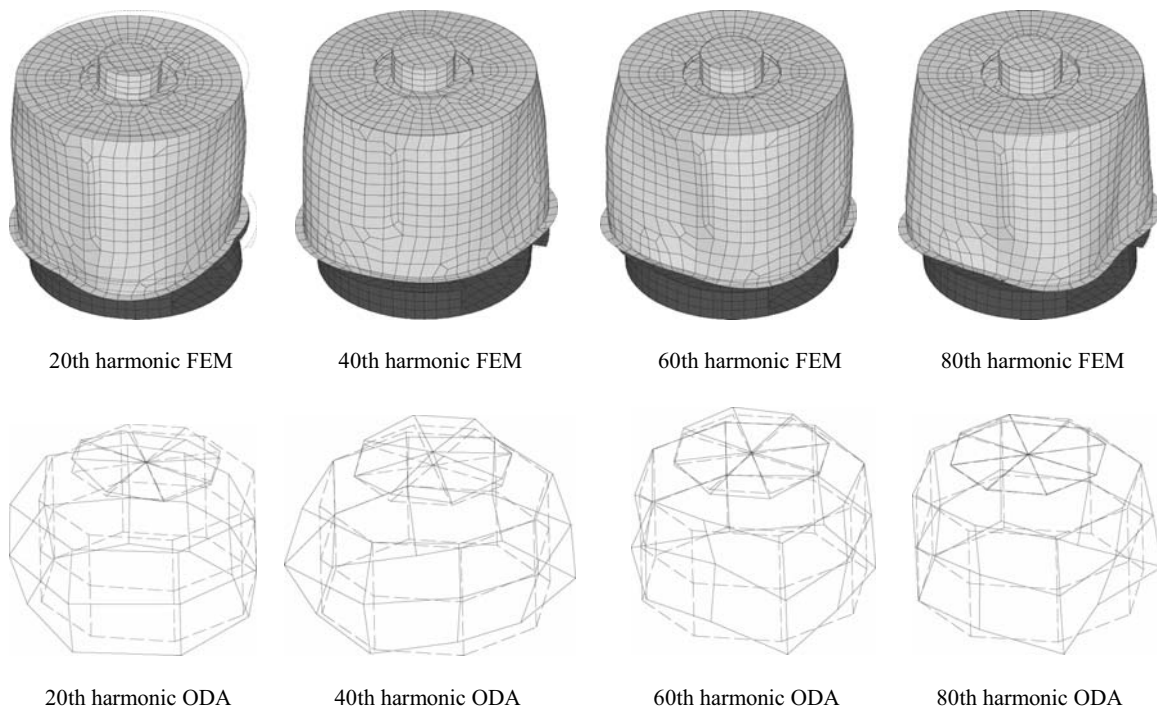


Fig. 7. Numerically calculated (on the top) and measured (on the bottom) vibration response of the motor resulting from the 20th, 40th, 60th and 80th harmonics

Acoustic Field

The acoustic field is calculated with the BEM, where the outer surface of the investigated motor is discretized. The boundary-element mesh is created over the structural shell elements sharing the same nodes. This means that the nodal velocities from the structural analysis can be easily extracted to the BEM model. To ensure the accuracy of the BEM calculation the maximum size of the element was less than one sixth of the sound wavelength at the maximum investigated frequency. Consequently, the initial mesh in the structural analysis should be considered to be fine enough for the later acoustic analysis. The exterior mesh, intended to observe the sound field in the surroundings of the motor, was built using triangular finite elements on the planar surfaces, see Fig. 8. Based on the so-prepared BEM model the sound field and the sound power level of the motor were calculated. Fig. 8 shows two acoustic parameters that describe the sound field in the surroundings of the motor and that are the result of the structural response due to the 20th harmonic component of the magnetic forces' excitation. The presented sound field radiated by the motor, due to the basic harmonic component of the magnetic forces, is similar to the acoustic dipole sound field.

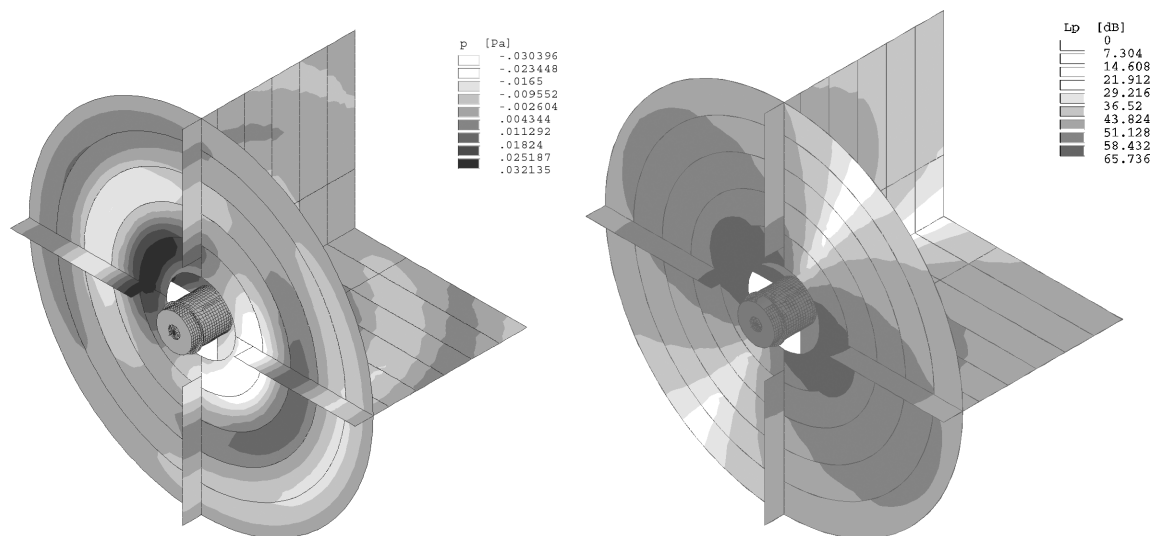


Fig. 8. Acoustic field – instantaneous pressure (on the left) and sound pressure level (on the right) due to the magnetic forces of the 20th harmonic

Fig. 10 and Fig. 11 show the comparison between the calculated and measured sound power levels for the 20th, 40th, 60th, 80th and 100th harmonics. Every graph presented in Fig. 10 and Fig. 11 has a bar on the top of it that represents the frequency range of the harmonics. Comparing the experimental and numerical data one can see that a reasonable agreement can be found for the motor with the non-skewed rotor for almost all the harmonics. A similar situation can be found for the motor with the skewed rotor, but only for the 20th harmonic. In these cases the differences between the experimentally and numerically evaluated sound power levels reach values up to 10dB. Much higher miss-agreements, up to 25dB, occur at the 40th, 60th, 80th and 100th harmonics for the motor with the skewed rotor. The explanation for this is in the character of the exciting magnetic forces. The fact is that the higher harmonic components of the magnetic forces, i.e., the 40th, 60th, 80th and 100th harmonics, are less distinctive in the motor with the skewed rotor, see Fig. 4. The consequence is that the corresponding numerically calculated sound power levels are underestimated.

A comparison between the investigated motors shows the well-known and expected situation. The motor with the skewed rotor is less noisy than the motor with the non-skewed rotor, and the differences are even bigger at higher motor loads. This is proved both numerically and experimentally.

Noise and vibration measurement

The experimental investigation of noise and vibration was conducted for a variety of loading conditions, defined by the rotational speed and the motor current. In general, the operation of the motor can be divided into free-run and loading. During free-run the motor operated at different rotational speeds between 3000 and 4000 min⁻¹ by setting the supply voltage from 8V to 13.5V. The motor current was approximately 10A for the motor with the non-skewed rotor and approximately 5A for the motor with the skewed rotor. During the loading, the motor operated at a constant voltage of 13.5V and at different loads (torques). The motor's load was defined by the motor current. Precise data that describe the loading conditions of both motors, with skewed and non-skewed rotors, are listed in Table 1 below.

To simulate the loading conditions the motor was attached to a hydraulic system that was insulated for sound. The sound power level was estimated using sound-intensity measurements at 24 points on the cylindrical surface around the motor. During the sound-intensity or/and vibration (ODA) measurement for a specific loading condition the rotation speed was kept constant.

Table 1. Loading conditions

I [A]	Loading		n [min ⁻¹]	Free-run	
	Skew. n [min ⁻¹]	No-skew. n [min ⁻¹]		Skew. I [A]	No-skew. I [A]
20	4272	4272	4000	4.5	12.5
25	4080	3936	3900	4.5	10.5
30	3648	3840	3800	4.5	10.0
35	3552	3648	3700	4.5	10.0
40	3456	3456	3600	4.0	10.0
50	3408	3360	3400	4.0	10.0
60	3116	3216	3200	3.8	10.0
65	3312	3168	3000	3.5	9.2

From the vibration spectra on the motor yoke and from the sound power-level spectra, see Fig. 9, measured for the motor with the non-skewed rotor at 4000 min⁻¹ and during free-run, peaks at the rotor-slot harmonics could be observed. This phenomenon shows that the magnetic noise, which is related to the rotor-slot harmonics, strongly dominates. A similar situation can also be found for the spectra of the motor with the skewed rotor and for different loading conditions, except that the rotor-slot harmonics' dominance is diverse.

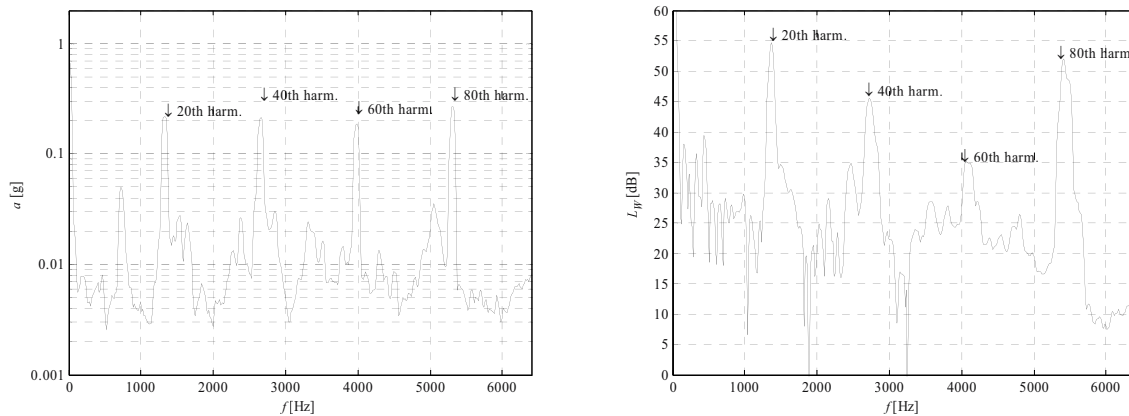


Fig. 9. Measured vibration (on the left) and sound power-level (on the right) spectra for the motor with the non-skewed rotor during the free run and at 4000 min⁻¹

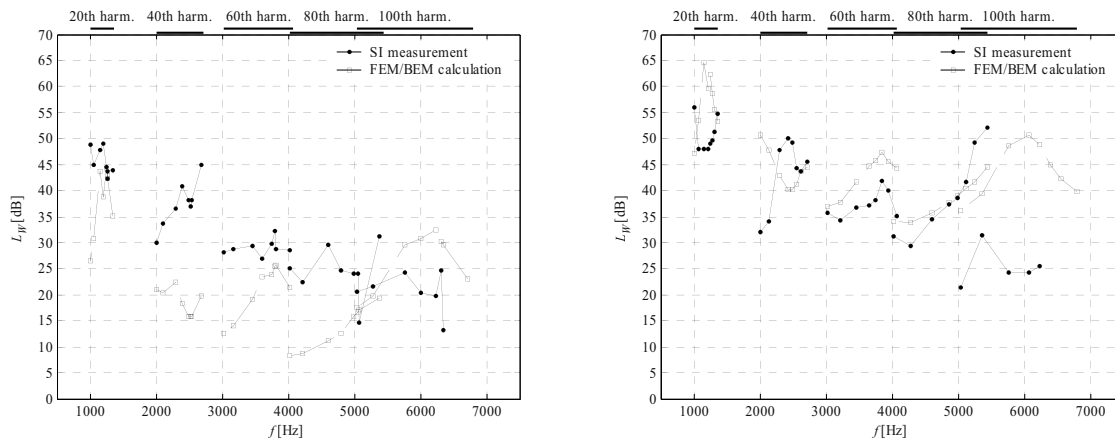


Fig. 10. Sound power level during free-run operation conditions for the motor with the skewed rotor (on the left) and for the motor with the non-skewed rotor (on the right)

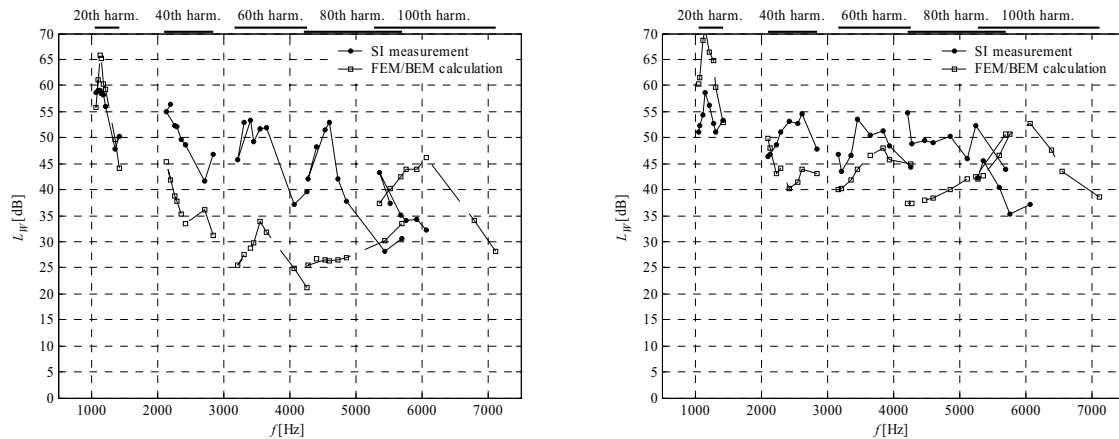


Fig. 11. Sound power level during loading operation conditions for the motor with the skewed rotor (on the left) and for the motor with the non-skewed rotor (on the right)

Conclusions

The presented investigation shows a step-by-step procedure for numerically predicting the acoustic field of a DC electric motor when the magnetic noise dominates. At each step the numerical results are verified and compared with the experimental results. The results obtained with the electromagnetic, structural and acoustic models give reasonable agreement with the measurements. Two different designs of DC electric motor were investigated, with a skewed rotor and with a non-skewed rotor, as was the impact of many different operating conditions on the evaluation of the magnetic noise. The results indicate that a numerical evaluation of the magnetic noise in a DC electric motor is more reliable in the case of more distinctive magnetic forces. For a more accurate analysis, however, improvements need to be made to the structural model.

References

- [1] C. Wang and J.C.S. Lai, Vibration analysis of an induction motor, *Journal of Sound and Vibration*, Vol. January 1999.
- [2] J.C.S. Lai and C. Wang, Prediction of noise radiated from induction motor, *Sixth International Congress on Sound and Vibration*, pp.2449-55, 1999.
- [3] D. Verdyck and R.J.M. Belmans, An acoustic model for a permanent magnet machine: modal shapes and magnetic forces, *IEEE Transactions on Industry Applications*, Vol.30, No.6, pp.1625-31, 1994.
- [4] F. Ishibashi, S. Noda and M. Mochizuki, Numerical simulation of electromagnetic vibration of small induction motors, *IEE Proceedings Electric Power Applications*, Vol.145, No.6, pp.528-34, 1998.
- [5] G.H. Jang and D.K. Lieu, The effect of magnet geometry on electric motor vibration, *IEEE Transactions on Magnetics*, Vol.27, No.6, pp.5202-4, 1991.
- [6] S. Noda and F. Ishibashi, Small induction motor acoustic noise simulation, *Proceedings, 17th International Congress on Acoustics, Italy, Rome 2001*.

III-8. MEASUREMENT OF 2-D MAGNETIC PROPERTIES OF GRAIN ORIENTED SILICON STEEL SHEET USING RRSST

Viktor Goričan, Marko Jesenik, Anton Hamler, Bojan Štumberger, Mladen Trlep
University of Maribor, Faculty of EE&CS, 2000 Maribor, Smetanova 17, Slovenia

Abstract - The round rotational single sheet tester (RRSST) is presented in order to identify its performances at higher flux densities and pure rotational flux condition in case of GO silicon steel sheets. The magnetic properties were measured in pure rotational and alternating flux condition. The difference between the rotational loss in clockwise and counter clockwise rotation of vector \mathbf{B} was considered to have a physical origin. The ability to control the vector \mathbf{B} in measuring region on GO material was considered. Additional advantages of a RRSST over square rotational single sheet tester were pointed out.

Introduction

In the past, a lot of effort was paid to the design of rotational single sheet testers [1]. Most laboratories worldwide use the square rotational single sheet tester (SRSST) with square samples. The SRSST has some drawbacks, which encourage some laboratories to use a hexagon [3] or circular samples [4-7]. One of the greatest disadvantages of SRSST is magnetizing the sample in $\pm 45^\circ$ direction, especially at higher induction levels. It seems that the sample is hard to magnetize in that direction. The real reason for that is the yoke construction itself, which yields the leakage flux in the corners of the sample at higher induction levels and therefore the higher flux densities cannot be achieved in the centre of the sample even if we have a huge power supply. That problem was overcome by using the RRSST because in the magnetic circuit of the RRSST all magnetization directions are equivalent [7,8]. In the past the conclusion has been drawn [2] that it is impossible to control the voltages in B coils (vector \mathbf{B}) at circular set-up at higher magnetic flux densities. That is may be true for some set-ups, which use a concentrate winding on the poles [5,6] or an ordinary three-phase excitation winding in the stator core of an induction motor [4].

Measurements

The measurement set-up [7] was improved by using a faster data acquisition board PCI 6110 (National Instruments), which has four simultaneously sampling input channels (Fig. 1). The yoke was improved in order to achieve a precise position of H coils and the sample (B coils). The H coil and the sample can be rotated separately by a certain angle in the centre of RRSST in order to balance the axes of B and H coils.

Two GO samples M4T27 and M0H27 were measured in RRSST [7] in order to achieve the highest induction level (up to 2T) and pure rotational magnetic flux condition (Fig. 2). The measuring area of H coils was 20 mm x 20 mm. The B coils were wound (5 turns of 0.05 mm wire) through the holes (0.8 mm) in the samples and a cross H coil was used for vector \mathbf{H} detection. The number of samples was 4000 pts/cycle for each channel and an iterative feedback control was used in order to control the induced voltages in B coils or in H coils. The vectors \mathbf{B} and \mathbf{H} and the power loss were calculated.

It can be seen, (Fig. 2) that the induced voltages in B coils can be controlled up to 2 T, that the calculated locus of vector \mathbf{B} has almost perfect circular shape. The maximal amplitude deviation (Table 1) was less than 0.8 % and the angle difference about $\pm 0.2^\circ$ for M0H27 and even better for M4T27 sample. The amplitude deviation and angular difference depend on number of iteration of the feedback loop.

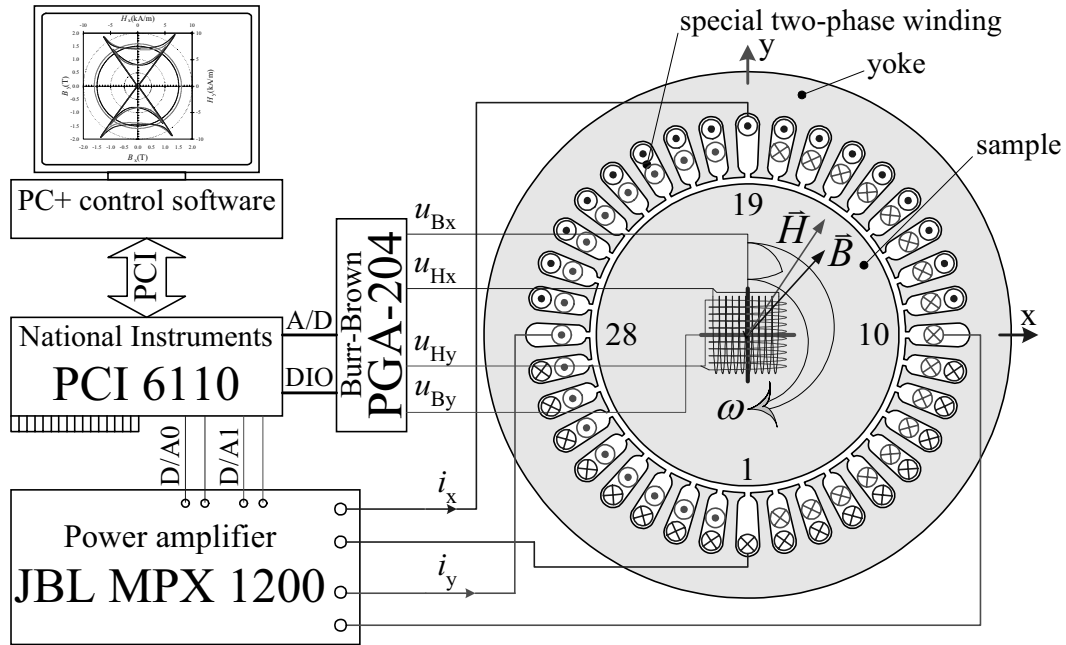
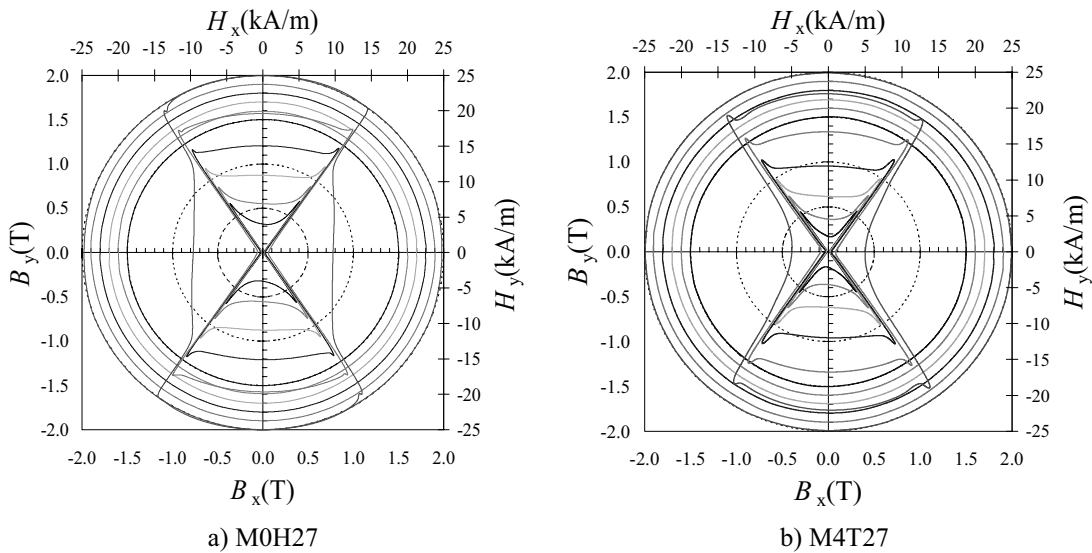


Fig. 1. The measurement set-up

Fig. 2. The locus of vectors \mathbf{B} (1.5 to 2.0 T step 0.1 T) and \mathbf{H} in M0H27 and M4T27 sample in clockwise direction (50 Hz)Table 1: Maximal deviation of the amplitude and angle difference of vector \mathbf{B} from the reference value (M0H27)

$B_{\text{ref}}(\text{T})$	0.50	1.00	1.50	1.70	1.80	1.90	2.00
$\delta B_{\text{max}}(\%)$	-0.40	-0.74	-0.10	-0.14	-0.21	-0.28	-0.22
	0.37	0.48	0.26	0.29	0.31	0.32	0.33
$\Delta\varphi_{\text{max}}(^{\circ})$	-0.65	-0.29	-0.06	-0.02	-0.19	-0.24	-0.18
	0.04	0.48	0.19	0.30	0.18	0.15	0.21

The rotational loss was measured up to 2 T (Fig. 3). Because of a great difference between the rotational loss in the clockwise (cw) and counterclockwise (ccw) rotation of vector \mathbf{B} , we turned the M0H27 sample around the y-axis. This means that the cw rotation of vector \mathbf{B} in RRSST now becomes the ccw rotation for the sample. We can see (Fig. 3) that the power loss does not change markedly, which means that the power loss at cw rotation is almost equal to the power loss at ccw rotation and turned sample ($\text{CW} \approx \text{TO CCW}$) and vice versa for ccw rotation ($\text{CCW} \approx \text{TO CW}$). The

reason for the differences in power loss in cw and ccw rotation could be the angular shift between B and H coils. To deny this assumption we shifted the signals from H coils by an angle $\Delta\phi_H$ in order to get power loss that is equal to the average value of cw and ccw power loss. The value of the shift angle is very high (Fig. 4) and it changes versus amplitude of vector B . Thus, the angular shift between of H and B coils cannot be the reason for such a difference in power loss. Obviously, there must be a physical reason in the behaviour of the material.

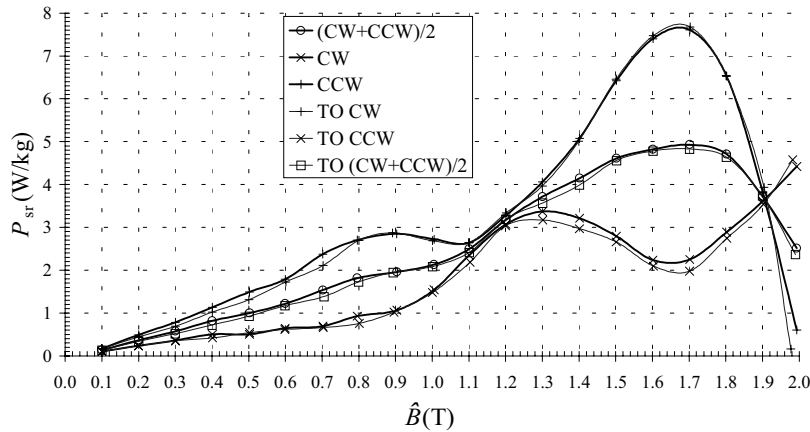


Fig. 3. Rotational loss P_{sr} measurement under cw and ccw rotation on the M0H27 sample

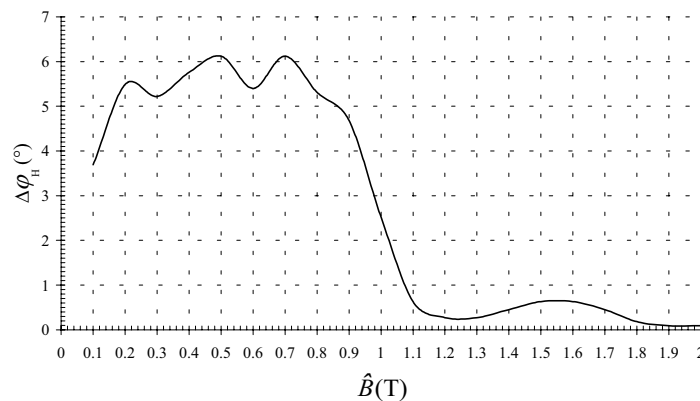


Fig. 4. The shift angle $\Delta\phi_H$ of H coil signals

In case of GO materials the following question arises: can we really control the vector B in the measuring region? The answer is no because we cannot measure the amplitude and the angle of the vector B using two perpendicularly positioned B coils (one in rolling one in transverse direction). This problem has already been pointed out for NO magnetic steel sheets and SRSST [9]. If we measure at the same time the vector B using B coils, which are displaced for 45 degrees (coils B_{x45}, B_{y45}) (Fig. 5), the results differ from those we get using B coils in the axes (coils B_{x0}, B_{y0}) (Fig. 6.). The coils give different results for the amplitude and angular speed (Table 2.) if we control the induced voltages in B (Fig. 6a.) or in H coils (Fig. 6b) even if we supply the excitation windings with sinusoidal voltages.

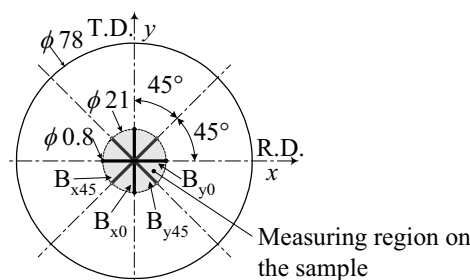


Fig. 5. The position of two pairs of B coils (B_{x0}, B_{y0} and B_{x45}, B_{y45}) wound through the holes (NC machined) on the GO sample

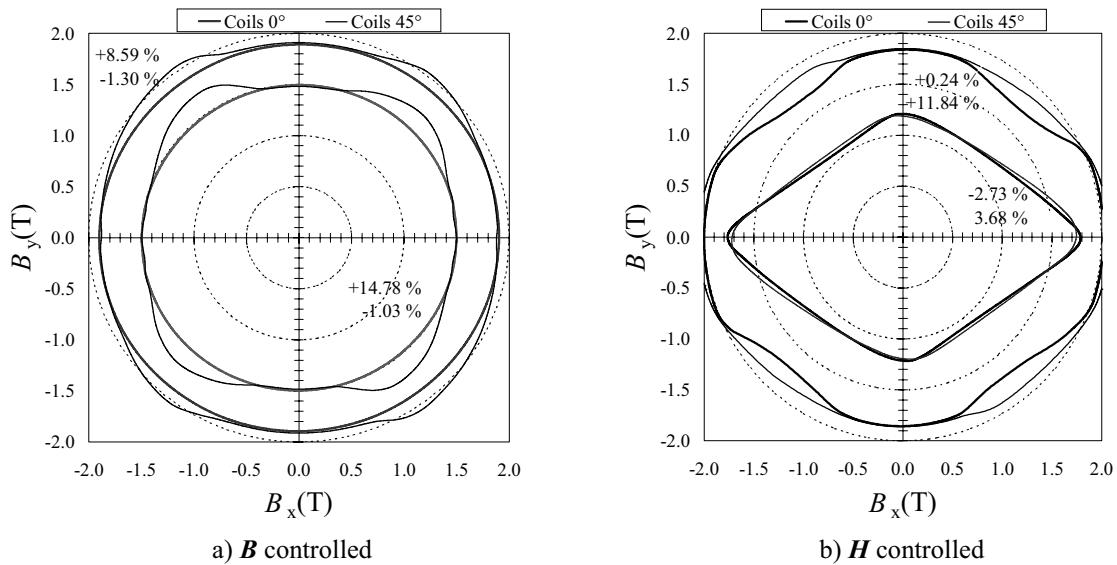


Fig. 6. The locus of vector \mathbf{B} in case we control: a) the induced voltages in B coils (1.5 and 1.9 T), b) induced voltages in H coils (500 A/m and 20 kA/m)

Table 2. The angular speed ω_B of vector \mathbf{B} , its deviation from reference value $\omega_{ref}=2\pi f$, and deviation of difference from reference ω_{ref}

circular	coil pair	$\omega_B(1/\text{rad})$		$\delta\omega_B(\%)$ $=(\omega_B-2\pi f)/(2\pi f)\cdot 100$		$\delta\omega_{B0-B45}(\%)$ $=(\omega_{B45}-\omega_{B0})/(2\pi f)\cdot 100$	
		Min	Max	Min	Max	Min	Max
1.5 T	B_{x0}, B_{y0}	286,61	337,30	-8,77	7,37		
	B_{x45}, B_{y45}	227,15	516,38	-27,70	64,37	-67,41	27,52
1.9 T	B_{x0}, B_{y0}	297,25	331,60	-5,38	5,55		
	B_{x45}, B_{y45}	256,80	386,23	-18,26	22,94	-22,86	20,08
0.5 kA/m	B_{x0}, B_{y0}	15,72	975,12	-95,00	210,39		
	B_{x45}, B_{y45}	23,75	892,98	-92,44	184,24	-35,56	47,53
20 kA/m	B_{x0}, B_{y0}	118,96	4616,14	-62,13	1369,36		
	B_{x45}, B_{y45}	117,60	3780,88	-62,57	1103,49	-140,99	288,21

The similar happens at alternating flux condition (Fig. 7). At 0° inclination angle the results from both pairs of B coils are in a pretty good agreement, therefore we can control the vector \mathbf{B} in the measuring region. On the contrary, at other inclination angles ϑ the results from both pairs of B coils are different (Table 3), that means, we cannot really control the vector \mathbf{B} in the measuring region but the induced voltages in B coils only. The locus of vector \mathbf{B} , obtained by second pair of B coils (B_{x45} and B_{y45}) at $-\vartheta$ differs from locus at $+\vartheta$ (Fig. 7b and Fig. 7d). The difference is caused by imperfect texture of the sample. The strong asymmetry of power loss (Fig. 8) may be a consequence of imperfect texture. On the other hand the sample is actually measured under different magnetic flux condition although the B coils B_{x0} and B_{y0} show a pure alternating case (Fig. 7a and Fig. 7c).

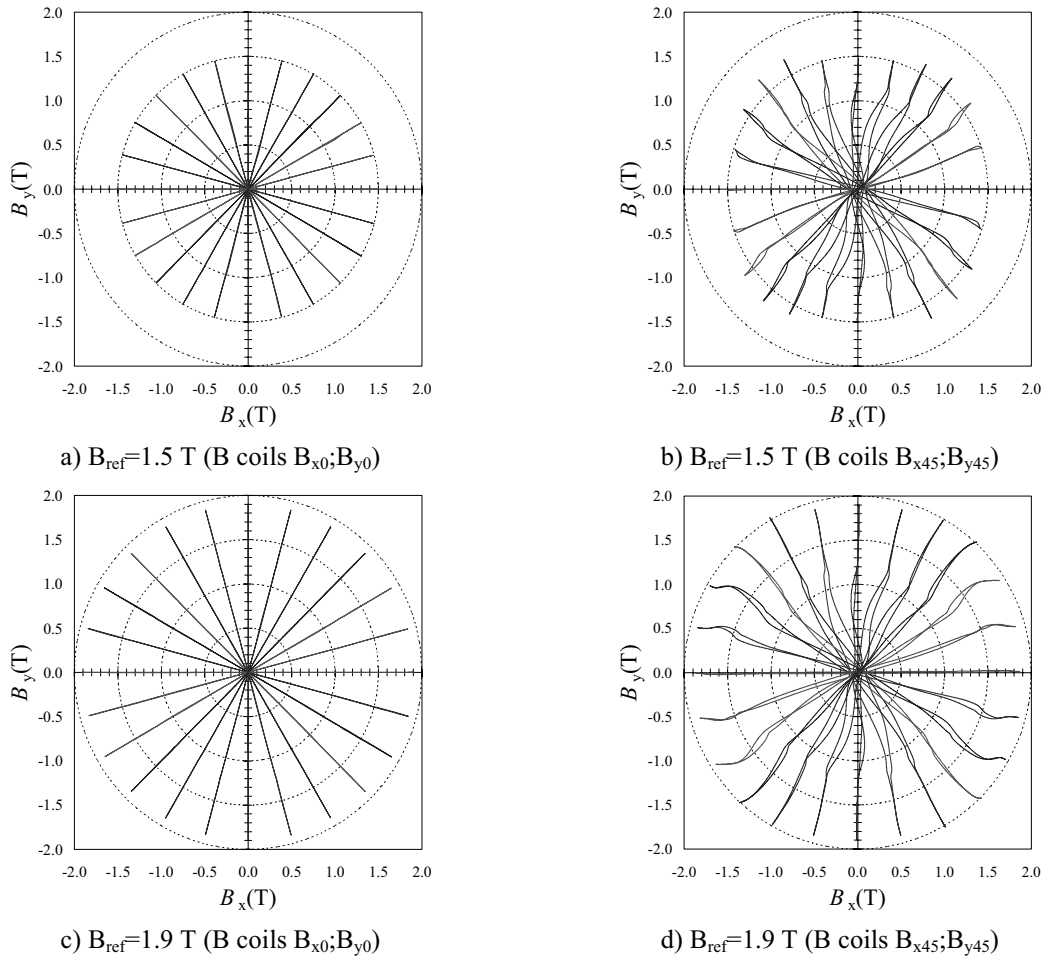


Fig. 7 The locus of vector \mathbf{B} obtained by first (B_{x0} and B_{y0}) and second (B_{x45} and B_{y45}) pair of B coils at inclination angles $\vartheta = -90^\circ$ to 75° in 15° step, measured at the same time

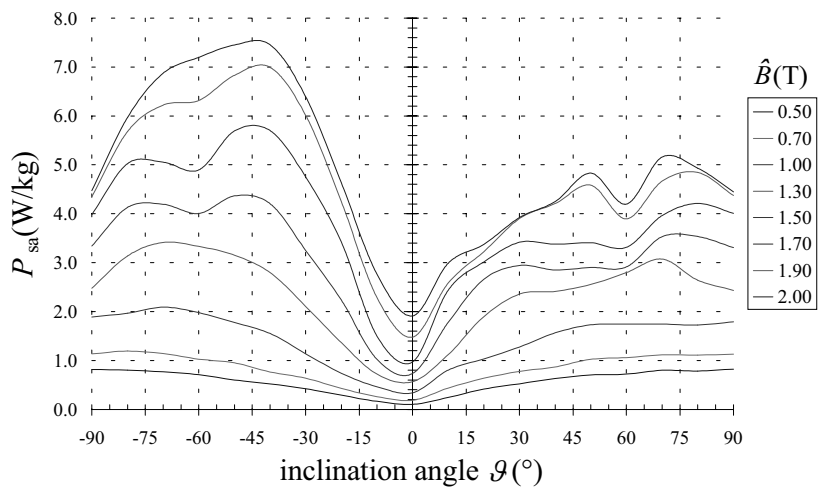


Fig. 8. The alternating power loss versus inclination angle (M0H27)

Table 3 Amplitude deviation of vector \mathbf{B} (second pair of B coils $B_{x45}; B_{y45}$) from the reference value

$B(T) \setminus \vartheta(^{\circ})$	-90	-75	-60	-45	-30	-15	0	15	30	45	60	75
1.5	-0.69	1.29	12.99	12.03	6.01	-1.23	0.39	0.70	8.53	10.99	7.16	0.37
1.9	0.47	0.64	6.65	5.76	2.97	0.62	-1.75	-0.02	1.93	5.92	4.35	0.66

Conclusion

The RRSST allows the measurement of magnetic properties of GO materials up to 2 T in “circular” or alternating flux conditions. We cannot actually control and measure the amplitude of vector \mathbf{B} and its angular speed (Fig. 6, Fig. 7) in the measuring region, which is very important for eddy current loss changes. Consequently, the power loss measurements are very questionable. (The alternating flux condition in rolling direction is an exception (Fig 7)).

There remain some questions concerning GO materials:

- Is it reasonable to control the locus of vector \mathbf{B} to make it circular or alternating in other direction than rolling?
- How can we better control and measure the vector \mathbf{B} in case of GO materials?

The RRSST has a few additional advantages over other rotational single sheet testers [7]:

- The vector \mathbf{B} rotates much better in the larger measuring region on the sample [7, 9]
- There is no waste of ampere-turns in the magnetization of the sample in the direction of $\pm 45^{\circ}$ [8]
- The flux densities achieved are higher (up to 2 T for NO and GO materials)
- The magnetic field distribution in the sample does not change versus magnetization direction because of tester itself [8]
- The eddy currents in the sample have the same path to conclude themselves at every magnetization direction [8]
- We can have a larger measuring region [8]
- Only two-phase power supply is needed
- We do not need any two to three-phase transformation
- Simplicity in making samples by turning
- Lower weight of the yoke
- Easy to get the yoke

References

- [1] J. Sievert, H. Ahlers, M. Birkfeld, B. Cornut, F. Fiorillo, K.A. Hempel, T. Kochmann, A. Kedous-Lebouc, T. Meydan, A. Moses, A.M. Rietto, European Intercomparison of Measurements of Rotational Power Loss in Electrical Sheet Steel, *J. Magn. Magn. Mater.* 160, pp. 115, 1996
- [2] J. Sievert, One and Two-Dimensional Magnetic Phenomena in Electrical Steel and Their Measurement, *Advanced Computational and Design Techniques in Applied Electromagnetic Systems*, pp. 639-642, 1995
- [3] A. Hasenzagl, B. Weiser, H. Pfützner, Novel 3-phase Excited Single Sheet Tester for Rotational Magnetization, *J. Magn. Magn. Mat.*, Vol.160, pp. 180-182, 1996
- [4] F. Fiorillo and A.M. Rietto, Extended Induction Range Analysis of Rotational Losses in Soft Magnetic Materials, *IEEE Trans. Magn.* 24, pp.1960, 1988
- [5] A. Ivanyi, *Proceedings of 2-D M*, pp. 87-95, Bad Gastein, September 2000
- [6] A. Parviainen et al., *Proceedings of 2-D M*, pp. 117-121, Bad Gastein, September 2000
- [7] V. Goričan, A. Hamler, B. Hribernik, M. Jesenik, M. Trlep, 2-D Measurements of Magnetic Properties Using a Round RSST, *Proceedings of 2-D M*, pp. 66-75, Bad Gastein, September 2000
- [8] M. Jesenik, V. Goričan, M. Trlep, A. Hamler, B. Štumberger, Field Homogeneity in 2D R.R.S.S.T. and 2D S.R.S.S.T., *Proceedings of IGTE*, pp. 375-379, Graz, 2000
- [9] V. Goričan, A. Hamler, M. Jesenik, B. Štumberger, M. Trlep, Unreliable Determination of Vector \mathbf{B} in 2-D SST, *J. Magn. Magn. Mat.*, Vol. 254-255, pp. 130-132, January 2003

III-9. THE HEAT CIRCUMSTANCES IN SWITCH BY PERMANENT LOAD

Gorazd Hrovat, Anton Hamler

University of Maribor, Faculty of Electrical Engineering and Computer Science

Smetanova 17, 2000 Maribor, Slovenia

gorazd.hrovat1@uni-mb.si

Abstract: The heating of motor protection switch (MPS), caused by Joule losses by permanent load is presented in this article. Geometry inside the switch housing was simplified, and only one pole of the three-pole switch was considered. According to the regulations, connection conductors also need to be considered by heating, so they were replaced by the appropriate boundary conditions on the connection parts. In this way we tried to approach the real heat circumstances. The calculation of Joule losses and heat circumstances was been made using the finite element method (FEM).

Introduction

Heating and cooling of the MPS is governed by various physical phenomena that affect the temperature field distribution. Besides the conduction and radiation, the physical mechanism of convection also influences the distribution greatly and it is the most difficult to define in heat analyses. It depends on the geometry along which the fluid flows and also on the fluid properties. During the fluid flow research, many studies on simple geometrical models (flat plate and cylinder) were performed, and many equations to calculate the convection coefficient were suggested.

In the MPS temperature field calculation, only one pole of the switch was considered. Connection conductors that were considered in the calculation were replaced by equivalent boundary conditions on the connection parts of the switch. This approach was used for the following reasons:

- Good quality model of connection conductors demands a large number of discretization element when using FEM. As a result, discretization and calculation time (period) is longer.
- The length of the connection conductor, which is determined by the regulation to 1 metre, is significantly longer in comparison to the switch. This proves to be inconvenient for modelling and presentation of the results.
- The software suite employed, ANSYS, is limited by a number of finite elements that must not be exceeded.

Our work is limited to the presentation of the connection conductor substitution with equivalent boundary condition.

Connection conductor model

One of the standard tests performed on the MPS is the connection part heating test. It is performed to establish whether the temperature rise exceeds the temperature rise limit, set by the EN 60947 standard. During the test, the maximum allowable current (32 A) flows through the switch. It is ensured by the power supply through the connection conductors. Their length and the cross-section are determined by a standard. The required length of the copper connection conductor is 1 m, and its required cross-section is 6 mm². The position of the switch during the measuring is also determined. The vertical position of the switch is required, and it has to be placed on a metal strip. During the measuring, connection conductors are vertical to the connection parts. After a certain length their position becomes horizontal, depending on the power supply position.

Joule losses, caused by the current flow through the conductive part of the switch, heat the conductive as well as non-conductive parts of the switch using the heat conduction. With the help of convection, there is also a heat exchange between the connection parts and connection conductor. Their final temperature is greatly affected by this heat exchange. The amount of heat transmitted from connection parts to the conductor depends on the temperature difference between these two elements.

Final temperature of the conductor is affected by the heat outflow through the isolation to ambient air, described with the convection coefficient. To determine this coefficient, we considered a standard example of long, horizontal cylinder. Many studies and tests have been performed on this example, so there are many empirically estimated dependencies. Convection coefficient is usually calculated from the average Nusselt's number, given as

$$\bar{N}_u = CR_a^n \quad (1)$$

constants C and n depend on the current mode, and R_a is a Rayleigh's number. For a laminar flow, Michejew suggests values of constants C and n , presented in Table 1 [3]. The characteristic length L is calculated by the equation (2) where r is a radius of the conductor with the insulation.

$$L = \pi r \quad (2)$$

Table 1: Values of constants C and n depending on R_a

R_a	C	n
$< 10^{-3}$	0.5	0
$10^{-3} \div 5 \cdot 10^2$	1.18	0.125
$5 \cdot 10^2 \div 2 \cdot 10^7$	0.54	0.25
$2 \cdot 10^7 \div 2 \cdot 10^{13}$	0.135	$0.\bar{3}$

All thermophysical properties of the ambient air for the calculation of the characteristic numbers (G_r , R_a in N_u) have to be taken at arithmetic mean between the average temperature of the insulation and the ambient air. If the average temperature on the surface of the conductor insulation along the whole length is 40 °C and the temperature of the ambient air is 20 °C, then the gained convection coefficient is 10.1 W/m²K.

However, we should not overlook radiation in case of natural radiation, since the radiation heat flux has the equal order of magnitude as the convection heat flux. Literature offers the following empirical formula

$$\alpha_{rad} = 0.033(T_S - T_\infty) + 5 \quad (3)$$

where α_{rad} is a radiation heat transfer and the radiation heat flux is defined analogically to the convection heat flux. The upper formula holds for the temperature differences up to 120 K. It presents a huge simplification, since α_{rad} does not depend on emissivity. Another approach is the evaluation of the radiation share, and is employed in our case. The emissivity value ε for PVC materials is 0.9 and 0.95. If the given value of ε is 0.9, we gain the convection coefficient value because of radiation, by equalising the Stefan – Boltzmann's heat radiation law and Newton's law of cooling. Thus, radiation share was substituted by a convection factor α_{rad} , which means the equal amount of conducted heat (5.7 W/m²K). Common convection factor on the conductor's surface is a sum of both (15.8 W/m²K).

Although the connection conductor's temperature decreases along with the distance from a connection part, the mechanism of heat conduction from copper to insulation and the mechanism of heat convection from conductor's insulation surface to the ambient air and convection of heat from copper to the ambient air can be joined because of radial conduction. In other words, the insulated conductor was substituted by the non-insulated, and the number of finite elements was reduced during the modelling of the conductor. To achieve that, the convection coefficient has to be changed. The circumstances are presented in Figure 1 and equations 4 and 5.

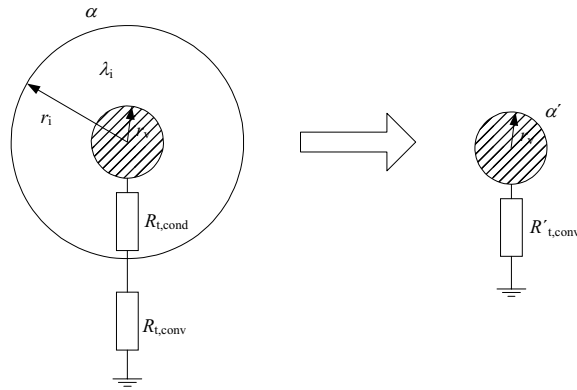


Figure 1: The substitution of conduction and convection thermal resistance for the substitute convection thermal resistance with the modified convection coefficient.

Table 2: Material properties and geometry of the connection conductor

r_v (mm)	r_i (mm)	λ_i (W/mK)	α (W/m ² K)
1.38	2.18	0.13	12.96

$$R'_{t,conv} = R_{t,cond} + R_{t,conv} \quad (4)$$

$$\frac{1}{\alpha' r_v} = \frac{\ln\left(\frac{r_i}{r_v}\right)}{\lambda_i} + \frac{1}{\alpha r_i} \quad (5)$$

where α' is gained from the equation (2), considering Table 2 its value is 22.3 W/m²K, and is directed on the surface of the non-insulated (bare) conductor. Joule losses in conductor are evaluated by the calculation of the temperature field where the difference between the potentials on the both ends of the connection conductor is such that a 32 A current flows through it. Finally, on parts where the conductor is connected to the power supply during the measuring, the ambient temperature is directed (forced).

Results

If we want to substitute the connection conductors with boundary conditions that will ensure heat circumstances equivalent to the real ones, we also have to get temperature dependence of the heat flux (for the conductor model during the calculation of temperature field). Temperature dependence can be gained in the following way: various Dirichlet's boundary conditions are placed at the conductor model's front side that contacts the connection parts. Here, we can observe the direction and magnitude of the heat flux.

Heat flow dependence on temperature is shown in Figure 3. Evidently, this dependence is linear. With temperatures lower than 37.1 °C the heat flux has the direction of connection part. In other words, the heating because of the conductor prevails over the heating because of the switch, and the conductor heats the switch. With temperatures higher than 37.1 °C the circumstances are inverse and the switch heats the conductor. The gained dependence was directed to the part of a connection conductor, as it is shown in Figure 4. On the housing of the switch, Cauchy's boundary conditions were placed, which were gained similarly as for the connection conductor. The temperature field calculation of the conductive parts of the switch is shown in Figure 5.

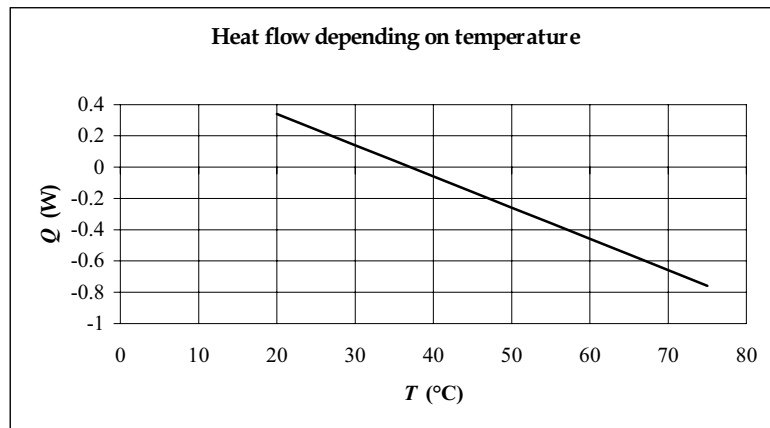


Figure 3: Conductor heat flow dependence on the temperature at the side of the connection part

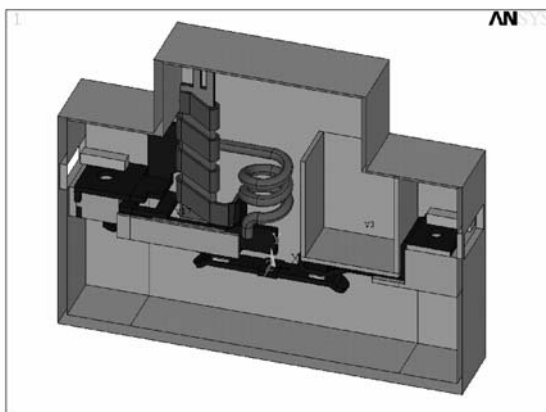


Figure 4: Model used in the analysis

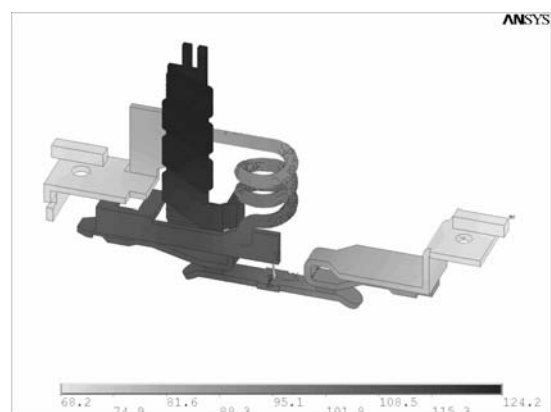


Figure 5: Temperature field distribution in the conductive parts of the switch

Conclusion

The article presents a procedure of determining the boundary condition, which substitutes the connection conductor during the MPS heating calculation. Using that we have achieved no additional modelling or discretization for the switch model. As a result, the calculation time has been reduced. When determining boundary conditions as a result of natural convection, we should not overlook the radiation, though the temperatures are relatively low.

References

- [1] C. Groth, G. Müller, FEM für Praktiker – Temperaturfelder, 2 Auflage, Technische Akademie Esslingen Weiterbildungszentrum DI Elmar Wippler, 1998.
- [2] A. Alujevič, P. Škerget, Prenos toplote, Fakulteta za strojništvo Maribor, 1990
- [3] E. Hering, R. Martin, M. Stohrer, Wärmeübertragung, Physik für Ingenieure, 6. Auflage, Springer-Verlag, Berlin, 1997

III-10. EDDY CURRENT EFFECTS IN THE SAMPLE OF 2D R.R.S.S.T. AND IN THE SAMPLE OF 2D S.R.S.S.T.

M. Jesenik, V. Goričan, M. Trlep, A. Hamler, B. Štumberger

Faculty of Electrical Engineering and Computer Science, Smetanova ul. 17, 2000 Maribor, Slovenia,
e-mail:jesenik@uni-mb.si

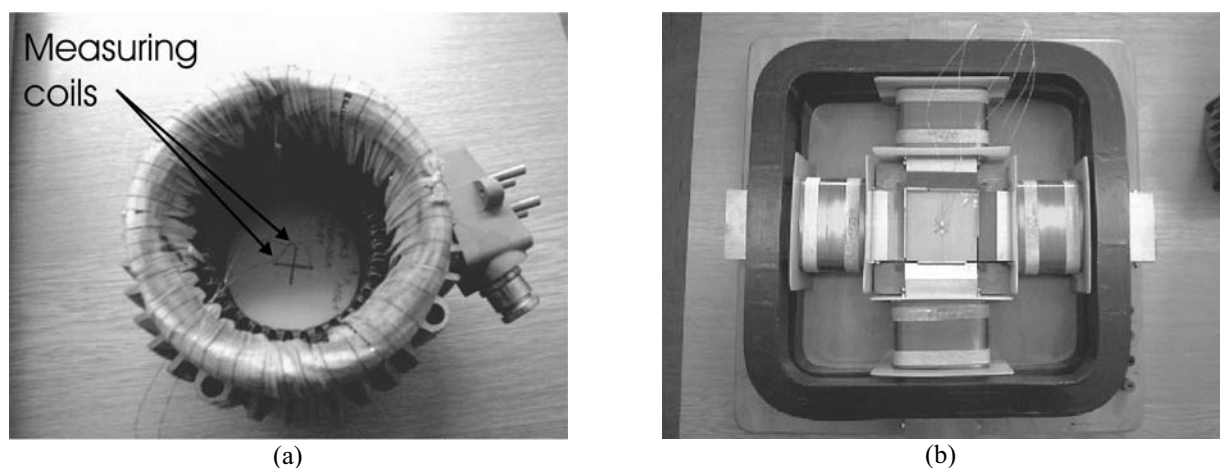
Abstract - Rotational magnetic fields in the sample of R.R.S.S.T. and in the sample of S.R.S.S.T. are calculated. The aim of the calculation is to find out which of the testers is better for the measurement of magnetic properties of magnetic materials in the rotational magnetic field. The influence of the eddy currents and influence of the magnetic density on the magnetic field homogeneity in the samples of the testers is investigated.

On the basis of the calculations and measurements some conclusion can be made. The path of eddy currents is the same for all rotational magnetisation directions for the R.R.S.S.T. and it is different for different magnetization directions for the S.R.S.S.T. The highest magnetic density B is always in the centre of the sample for the R.R.S.S.T. and the highest magnetic density for some magnetisation directions and higher amplitudes of B is at the corners of the sample for the S.R.S.S.T.

Introduction

Square rotational single sheet tester (S.R.S.S.T.) and round rotational single sheet tester (R.R.S.S.T.) are used for the measurement of magnetic properties in rotational and alternating magnetic fields [1], [2]. Rotational magnetic fields in the sample of R.R.S.S.T. and S.R.S.S.T. are calculated to find out which of them is better for the measurement of magnetic properties in rotational magnetic field. Influence of the eddy currents dependent on the frequency of the rotational field and influence of the magnetic density B amplitude on the magnetic field homogeneity in the sample of the tester is investigated. To assure a good quality of the measurement, the homogeneous area of the magnetic field has to be as big as possible. Both problems are calculated as a three dimensional nonlinear transient problems [3], [4], [5].

Photo of the R.R.S.S.T. and photo of the S.R.S.S.T. are shown in Fig. 1 (a) and Fig. 1 (b).



(a) (b)
Fig. 1 (a) Photo of the R.R.S.S.T.; (b) Photo of the S.R.S.S.T.

Influence of the frequency on the field homogeneity

Investigation was made with sinusoidal excitation currents with equal amplitudes (in both excitation coils), which are appropriate to obtain magnetic density of 1.43T in the area of the centre measuring coils (length of the centre measuring coils is 20mm). In Fig. 2(a), 2(b), 3(a) and 3(b), magnetic density \mathbf{B} is shown as arrows and eddy current is shown as shading. Results are obtained for the frequency of 500Hz. From Fig. 3(a) and from Fig. 3(b) it can be seen that the paths of eddy currents are different for different rotational magnetisation directions for the S.R.S.S.T. Even the total eddy current, obtained by the integration of the eddy current density over the area with equal direction of the eddy current density, is different.

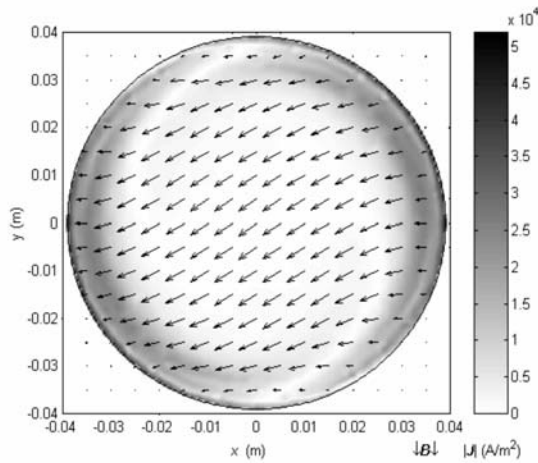


Fig. 2 (a) \mathbf{B} as arrows and \mathbf{J} as shading in the sample for rotational magnetisation direction of 225° with respect to x -axis of 500Hz T.C. for R.R.S.S.T.

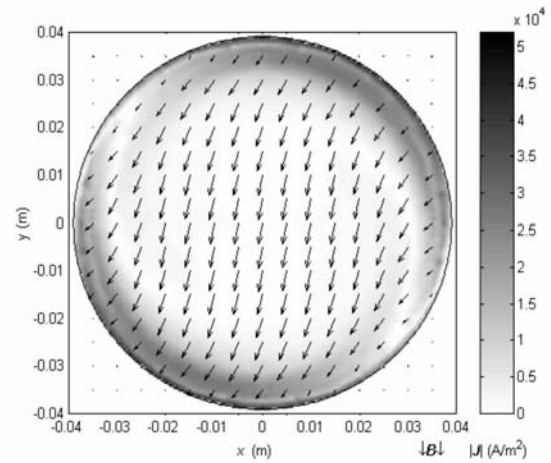


Fig. 2 (b) \mathbf{B} as arrows and \mathbf{J} as shading in the sample for rotational magnetisation direction of 270° with respect to x -axis of 500Hz T.C. for R.R.S.S.T.

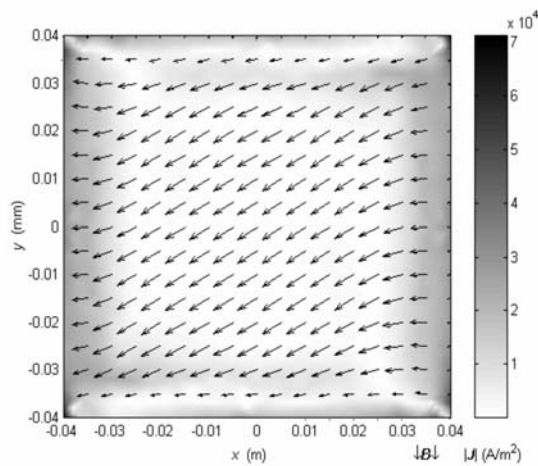


Fig. 3 (a) \mathbf{B} as arrows and \mathbf{J} as shading in the sample for rotational magnetisation direction of 225° with respect to x -axis of 500Hz T.C. for S.R.S.S.T.

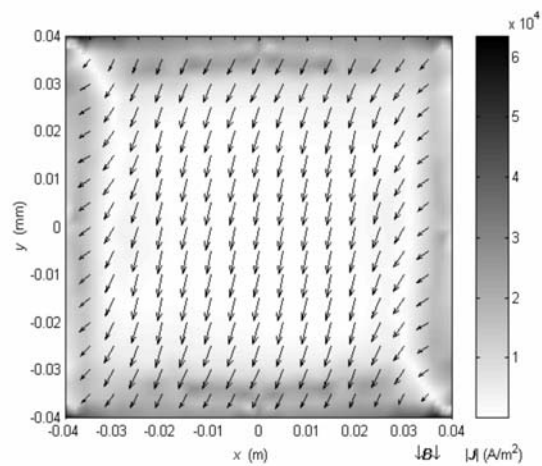


Fig. 3 (b) \mathbf{B} as arrows and \mathbf{J} as shading in the sample for rotational magnetisation direction of 270° with respect to x -axis of 500Hz T.C. for S.R.S.S.T.

Total eddy current is $I=153\text{A}$ or average current density is $\mathbf{J}=0.048\text{A}/\text{mm}^2$ for rotational magnetisation direction of 225° with respect to x -axis and total eddy current is $I=166\text{A}$ or average current density is $\mathbf{J}=0.052\text{A}/\text{mm}^2$ for rotational magnetisation direction of 270° with respect to x -axis. The deviation of total eddy current between two characteristic directions is 9%. Contrary to Fig. 3(a) and Fig. 3(b), from Fig. 2(a) and Fig. 2(b) it can be seen that the paths of eddy currents in the R.R.S.S.T. are the same for all rotational magnetisation directions.

Influence of the magnetic density amplitude on the field homogeneity

Investigation was made with sinusoidal excitation currents with equal amplitudes (in both excitation coils), which are appropriate to obtain magnetic density of 1.43T and approximately 1.6T in the area of the centre measuring coils (length of the centre measuring coils is 20mm). In Fig. 4(a) and Fig. 4(b) magnetic density $|B|$ in the sample in the centre horizontal plane for rotational magnetisation direction of 225° with respect to x -axis of 50Hz T.C. and different $|B|$ in the area of the centre measuring coils is shown for S.R.S.S.T.

From Fig. 4(b) it can be seen that in the sample of S.R.S.S.T. magnetic densities at the edges of the sample can be higher than magnetic densities in the centre of the sample for higher excitations (B in the area of the centre measuring coils of S.R.S.S.T. is 1.7T) In the case of R.R.S.S.T. for lower and higher excitations the highest value of B is obtained in the centre of the sample.

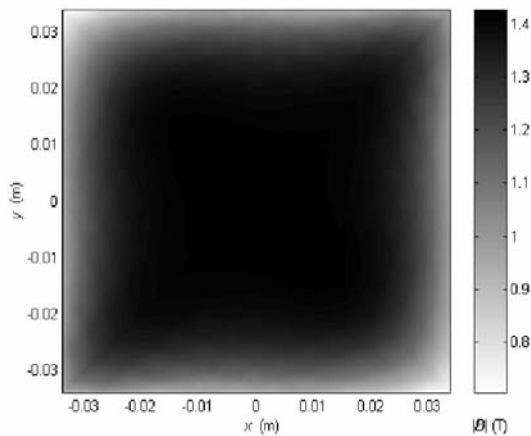


Fig. 4 (a) $|B|$ as shading in the sample for rotational magnetisation direction of 225° with respect to x -axis of 50Hz T.C. for S.R.S.S.T. ($|B|$ in the area of the centre measuring coils with length of 20mm is 1.43T). Almost the whole sample is shown.

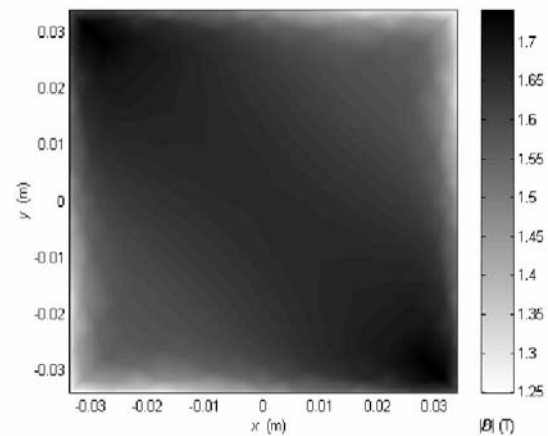


Fig. 4 (b) $|B|$ as shading in the for rotational magnetisation direction of 225° with respect to x -axis of 50Hz T.C. for S.R.S.S.T. ($|B|$ in the area of the centre measuring coils with length of 20mm is 1.6T). Almost the whole sample is shown.

Fig. 5(a) shows calculated amplitudes of B for different sinusoidal excitation currents in the case of S.R.S.S.T. and R.R.S.S.T. for magnetisation direction from 0° with respect to x -axis ($t = 0$) to magnetisation direction of 180° with respect to x -axis ($t = 0.01$) after the transient phenomenon.

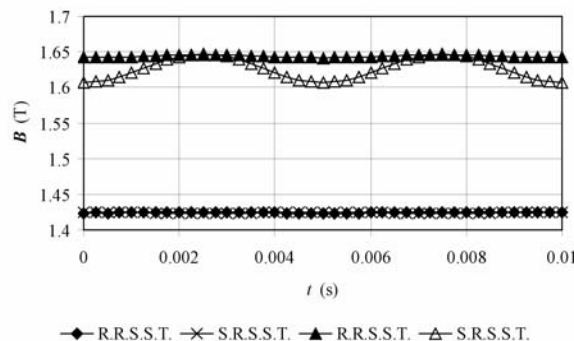


Fig. 5 (a) Amplitude of B for half period of 50Hz transient calculations of S.R.S.S.T. and of R.R.S.S.T.

The amplitude of excitation currents is the same in both phases of S.R.S.S.T and in both phases of R.R.S.S.T., but it is not the same for S.R.S.S.T. and for R.R.S.S.T. to obtain the same amplitude of B in the centre of the sample. Calculation is made for the frequency of 50Hz. For lower amplitudes (the result is shown for the amplitude of B is 1.43T at the area of the centre measuring coils) of B there is no difference of amplitude of B for both single sheet testers. From Fig. 5(a) it can be seen that in the case of higher excitations (the result is shown for the amplitude of B is 1.64T in the area of the centre measuring coils) amplitude of B of R.R.S.S.T. is constant for all magnetisation directions, which is not the case for S.R.S.S.T.

Measurements and calculation

For the verification of the results some results of the calculation are compared with measurement. Excitation currents obtained from the controlled measurement are used for the calculation. In the case of R.R.S.S.T. the deviations between the measurement and calculation are less than 9% for different frequencies and different diameters of the measuring coils. In the case of S.R.S.S.T the deviations between the measurement and calculation are less than 12%.

Conclusions

On the basis of the investigations of eddy currents influences on the magnetic field homogeneity in the sample of the S.R.S.S.T. and of the R.R.S.S.T. following conclusions can be made:

- The path of eddy currents is the same for all rotational magnetisation directions for the R.R.S.S.T. and it is different for different magnetization directions for the S.R.S.S.T. Eddy currents influence field homogeneity specially at higher frequencies.

- Total eddy current is the same for all rotational magnetisation directions for the R.R.S.S.T. and it is different for different magnetization directions for the S.R.S.S.T.

On the basis of the investigations of magnetic density amplitude influences on the magnetic field homogeneity in the sample of the S.R.S.S.T. and of the R.R.S.S.T. following conclusions can be made:

- The highest magnetic density B is always in the centre of the sample for the R.R.S.S.T. and the highest magnetic density for some magnetisation directions and higher amplitudes of B is at the corners of the sample for the S.R.S.S.T.

- In the case of sinusoidal excitation currents amplitude of B in the areas of centre measuring coils is constant also for higher excitations for R.R.S.S.T. and in the case of sinusoidal currents amplitude of B in the area of the centre measuring coils is not constant for higher excitations for S.R.S.S.T.

References

- [1] J. Sievert et. al, European intercomparison of measurements of rotational power loss in electrical sheet steel, *Journal of Magnetism and Magnetic Materials*, vol. 160, p.p. 115-118, 1996
- [2] V. Goričan, A. Hamler, B. Hribernik, M. Trlep, The Influence of Terrestrial Magnetism on Power Loss Measurement in Case of Annealed Amorphous Magnetic Material, 2-D M Proceedings, p.p. 204-206, September 2000, Bad Gastein
- [3] Jesenik Marko, Trlep Mladen, Štumberger Bojan, Hamler Anton. Transient Eddy Current Calculation with Finite Element Method, *Elektroteh. vestn.*, 2002, vol. 69, num. 2, p.p. 101-106.
- [4] O. Biro, K. Preis, On the Use of the Magnetic Vector Potential in the Finite Element Analysis of Three-Dimensional Eddy Currents, *IEEE Transaction on Magnetics*, Vol. 25, No. 4 July 1989
- [5] M. Trlep, B. Kreča, B. Hribernik, "Hybrid Finite Element – Boundary Method for Nonlinear Electromagnetic Problems", *IEEE Transaction on Magnetics*, Vol. 28. No.5. pp 2271-2273, September 1993
- [6] Goričan Viktor, Hamler Anton, Jesenik Marko, Štumberger Bojan, Trlep Mladen. Unreliable determination of vector B in 2-D SST. *J. magn. magn. mater.*, 2003, 254/255, p.p. 130-132.

III-11. 3-D FINITE ELEMENT ANALYSIS OF ATTRACTIVE FORCE BY RESIDUAL MAGNETIZATION OF DC ELECTROMAGNETS

Yoshihiro Kawase, Tadashi Yamaguchi and Kei Iwashita

Department of Information Science, Gifu University, 1-1 Yanagido, Gifu, 501-1193, Japan

E-mail: kawase@info.gifu-u.ac.jp

Abstract - In this paper, we calculate the residual attractive force characteristics and the operating characteristics of a DC electromagnet using the 3-D finite element method taking into account the residual magnetization [1][2]. Consequently, it is found that the more the residual flux density of material is, the more the residual attractive force is. The effects of the residual magnetization on the residual attractive force of the DC electromagnet are clarified quantitatively.

Introduction

It is important to obtain the effects of the residual magnetization on the attractive force of DC electromagnets, because the residual magnetization delays the operating time of electromagnets. The attractive force by the residual magnetization is affected by the B-H curve of the iron cores as well as the operating conditions. Therefore, we calculate the residual attractive force characteristics and the operating characteristics under some material conditions of the yoke, which has been magnetized, using the 3-D finite element method.

Method of Numerical analysis

The fundamental equation of the magnetic field using the 3-D finite element method can be written as follows:

$$\text{rot}(\nu \text{rot} \mathbf{A}) = \mathbf{J}_0 + \nu_0 \text{rot} \mathbf{M} \quad (1)$$

where ν is the reluctivity, \mathbf{A} is the magnetic vector potential, \mathbf{J}_0 is the magnetizing current density, ν_0 is the reluctivity of vacuum, and \mathbf{M} is the magnetization for the residual flux density calculation.

Analyzed Model

Fig. 1 shows the analyzed model of a DC electromagnet [3]. As the model is symmetric, a half of the whole region is analyzed. In the magnetizing process analysis, the DC magnetizing current is applied to the coil, which are 43.2, 86.4, 129.6, 172.8 and 216 AT. In the residual attractive force analysis, the DC magnetizing current is not applied to the coil. Fig. 2 shows the 3-D mesh of the model. Fig. 3 shows the magnetizing curves of the yoke used in the magnetizing process analysis. The demagnetizing curves used in the residual attractive force analysis and the operating process analysis are also shown in Fig. 3. From these figures, it is found that the residual flux density of material B is larger than that of material A, and the coercive force of material B is larger than that of material A.

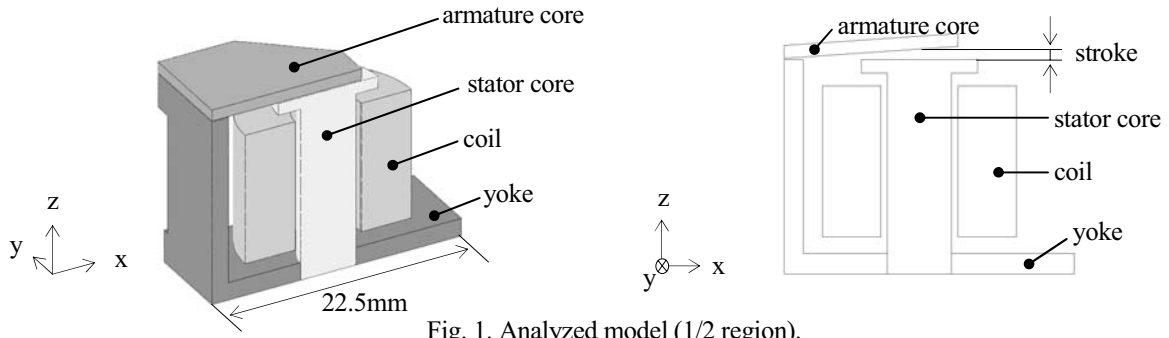


Fig. 1. Analyzed model (1/2 region).

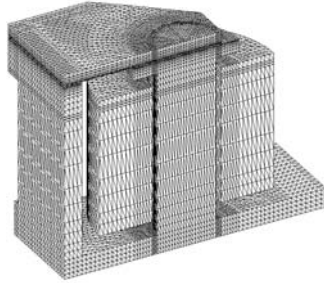


Fig. 2. 3-D mesh (except air).

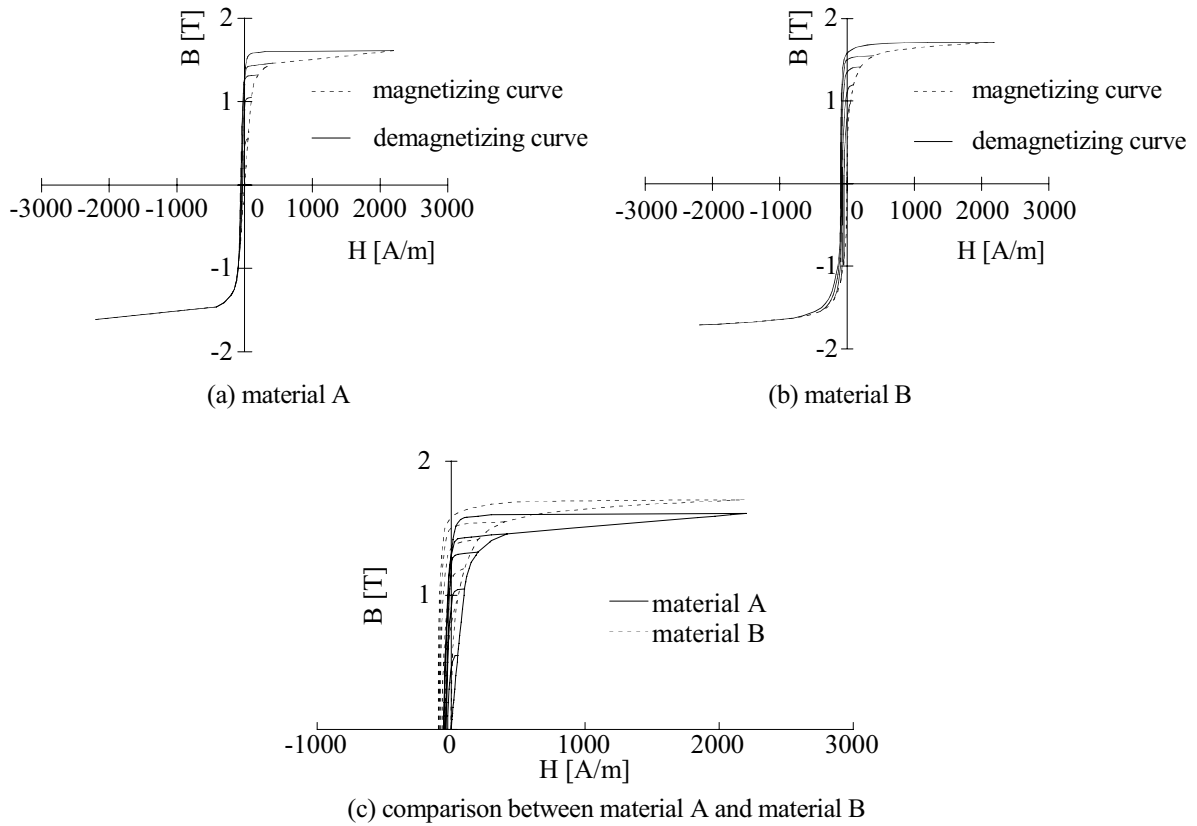


Fig. 3. B-H curves.

Results and Discussion

Attractive Force Characteristics

Fig. 4 shows the distributions of flux density vectors when the DC magnetizing current is applied to the coil, which is 216 AT. From these figures, it is found that the flux density in the yoke of material A is almost the same as that of material B. Fig. 5 shows the distributions of residual flux density vectors in the residual attractive force analysis. From these figures, it is found that the flux density in the yoke of material B is larger than that of material A. Fig. 6 shows the attractive force characteristics. From this figure, it is found that the attractive force of material A is almost the same as that of material B. Fig. 7 shows the residual attractive force characteristics. From this figure, it is found that the residual attractive force of material B is larger than that of material A, because the residual flux density of material B is larger than that of material A as shown in Fig. 3.

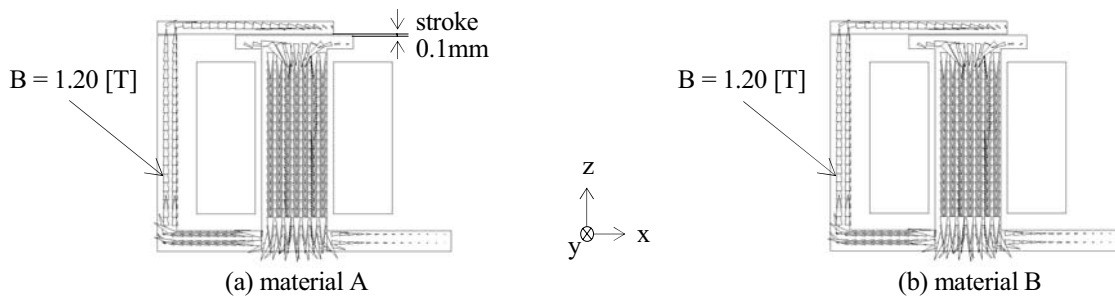


Fig. 4. Distributions of flux density vectors
(magnetizing current is 216 AT).

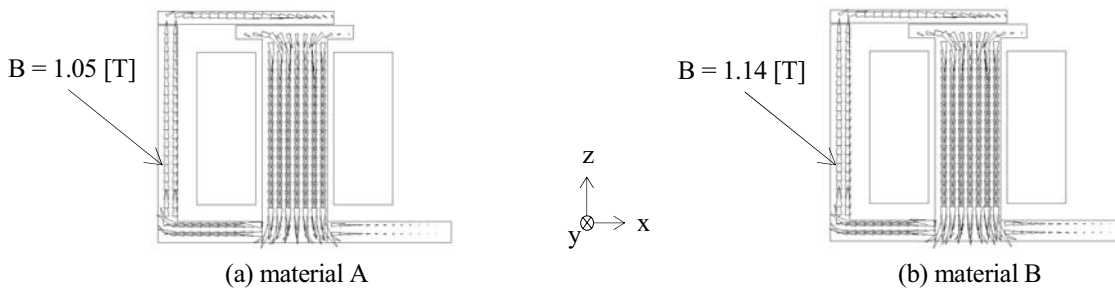


Fig. 5. Distributions of residual flux density vectors
(magnetizing current is removed).

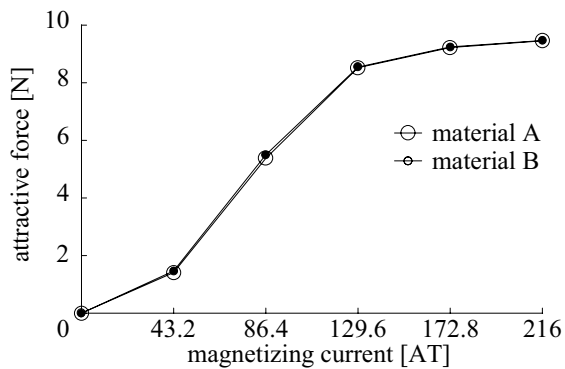


Fig. 6. Attractive force characteristics.

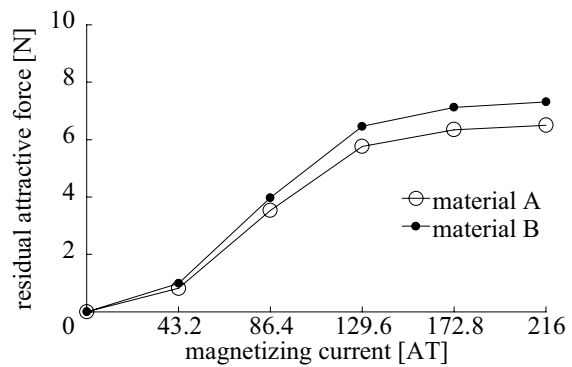


Fig. 7. Residual attractive force characteristics.

Operating Characteristics

The return spring is set in order to keep the open state (stroke = 0.72mm) when the magnetizing current is removed. Fig. 8 shows the time variations of stroke when the magnetizing current is removed. From this figure, it is found that the operating time of material B is longer than that of material A, because the residual attractive force of material B is larger than that of material A as shown in Fig. 7.

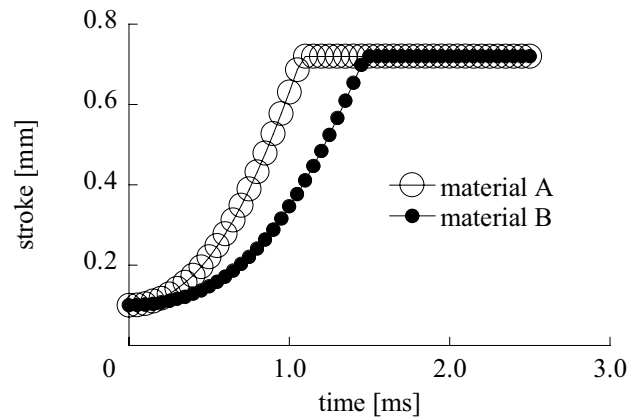


Fig. 8. Time variations of stroke.

Conclusion

In this paper, we calculated the attractive force characteristics and residual attractive force characteristics of a DC electromagnet using the 3-D finite element method. Consequently, the effects of the residual magnetization on the residual attractive force of the DC electromagnet are clarified quantitatively. It is found that material A is effective for the quick response of the electromagnetic devices by our analysis.

References

- [1] S. Ito and Y. Kawase, *Computer Aided Engineering of Electric and Electronic Apparatus Using Finite Element Method*, Morikita Publishing Co., 2000.
- [2] Y. Kawase and S. Ito, *New Practical Analysis of Electrical and Electronic Apparatus by 3-D Finite Element Method*, Morikita Publishing Co., 1997.
- [3] Y. Kawase, H. Kikuchi and S. Ito, 3-D Nonlinear Transient Analysis of Dynamic Behavior of the Clapper Type DC Electromagnet, *IEEE Transactions. on Magnetics*, Vol.27, No.5, pp.4238-4241, 1991.

III-12. CHARACTERISTIC COMPARISONS BETWEEN IRON POWDER MATERIALS AND LAMINATION CORES IN BRUSHLESS MOTORS

¹Young-Kyoun Kim, ¹Jung-Pyo Hong, Senior Member, *IEEE*,

²Kyung-Ho Ha, ³Jin Hur, and ³Ha-Kyung Sung

¹Dept. of Electrical Eng., Changwon Nat'l Univ., Changwon, Kyungnam, Korea,

²Electrical Steel Research Team of Technical Research Lab., POSCO, Gyeongbuk, Korea

³Precision Machinery Research Center of Korea Electronic Technology Institute, Korea
(email:ensigma@hitel.net, jphong@sarim.changwon.ac.kr, khha@posco.co.kr, jinhur@keti.re.kr)

Abstract – Magnetic materials are used for all kinds of electromagnetic energy-conversion devices to improve the capability of magnetic circuit. Iron Powder Materials are recently received much attention in the electric machine applications due to their advantages over lamination steels, such as low iron losses and large fill factor. This paper describes an BLDC motor with iron powder materials and its performances are compare with the Iron Powder Materials and lamination core in BLDC motor.

Introduction

Magnetic materials are used for all kinds of electromagnetic energy-conversion devices to improve the capability of magnetic circuit. Most recently, iron powder materials in new magnetic materials have been developed and electric machine designers have an interesting in applying these materials to electric machines [1]. The iron powder materials allows improvements over the lamination core with the respects of design freedom, low manufacturing cost, simple manufacturing processes, and low eddy current losses [1-2].

In this paper, the effects of magnetic properties of iron powder are investigated in the machine performances point of view in order to evaluate the application possibility and appropriate design of BLDC motors. Two different typed 300W rated BLDC motors, such as one is iron powder and the other is lamination core, are designed and manufactured to test of their properties and the comparative analysis has been performed. Moreover, practical use of tooth shape in the iron powder BLDC motor is additionally suggested to maximize the effects of end winding in the motor.

Description of the compressed iron powder material

An iron powder, Höganäs manufactured Somaloy 500, is used to produce the Soft Magnetic Composite (SMC). The iron powder materials are consisted iron powder particles insulated from each other epoxy resin and iron flakes. The magnetic properties of iron powder materials depend on shape, size content, and property of the powder particles. These iron powder materials, which are highly pure and highly compressible, ensure good soft magnetic properties. Most of all, an excellent insulation between the particles and a smaller particles size are required to reduce eddy-current losses at the higher frequency applications [1-3].

In this application, the typical particle size that is 212 micron is applied. The particles are high iron content of 99.5(%) with thin insulation layers. Moreover, the particles larger than 150 micron occupy 10 (%) and the one less than 45 micron does 20 (%) of the used metal powders. Table I shows the size of the SMC materials according to a heat treatment and pressing pressure. And Fig. 1 and Fig. 2 show experimental results of the SMC materials according to a heat treatment and pressing pressure.

Table 1. Size of the SMC materials according to a heat treatment and pressing pressure.

Density (g/cm ³)	Lindberg 275 ◻ 60min, Air				Lindberg 530 ◻ 30min, Air			
	HT (mm)		WT (mm)		HT (mm)		WT (mm)	
	Before heat treatment	After heat treatment	Before heat treatment	After heat treatment	Before heat treatment	After heat treatment	Before heat treatment	After heat treatment
6.72	7.962	7.972	21.169	21.148	8.010	8.023	21.247	21.159
6.74	7.985	7.998	21.212	21.195	8.024	8.022	21.263	21.175
6.78	7.967	7.985	21.535	21.513	8.012	8.016	21.446	21.363
6.85	8.005	8.006	21.414	21.405	8.062	8.068	21.617	21.535
7.17	8.005	-	22.655	22.617	8.014	7.988	22.654	22.547
	7.959	-	22.514	22.475	7.959	7.944	22.496	22.394
7.19	8.004	-	22.701	22.661	7.964	7.963	22.589	22.488
	7.946	-	22.525	22.489	7.947	7.93	22.535	22.435
7.23	7.989	-	22.782	22.747	8.024	8.028	22.905	22.797
	7.950	-	22.683	22.647	7.948	7.963	22.687	22.584

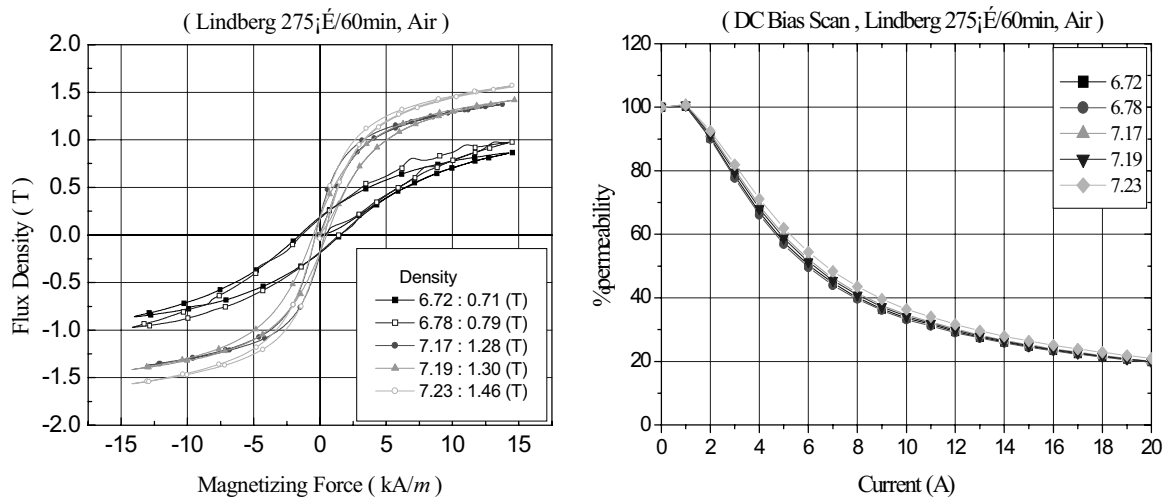


Fig. 1. Hysteresis (Magnetization) curve and Permeability according to and pressing pressure at 275 (°C).

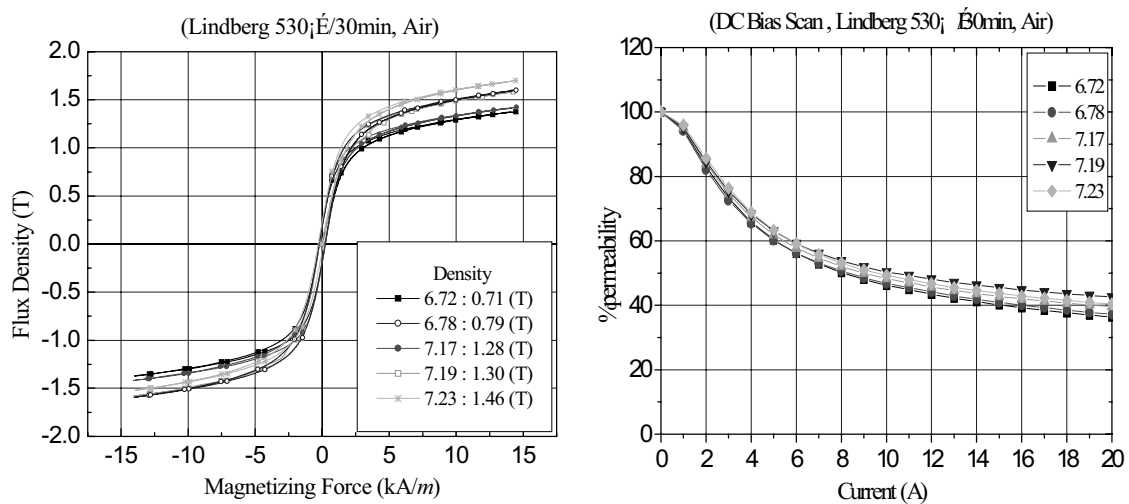


Fig. 2. Hysteresis (Magnetization) curve and Permeability according to and pressing pressure at 530 (°C).

Description of the compressed iron powder material

The applied machine is a 300W BLDC motor, and its stator has 12 slots and the rotor is built of 8 poles of radial magnetic, Ferrite magnet. In order to compare of the iron powder BLDC motor with lamination core one, two BLDC motors are applied in examin iron powder motor of the same dimension as previously designed lamination core one. Fig. 3 shows the design specification of the applied BLDC motor and the summarized procedure of its initial design.

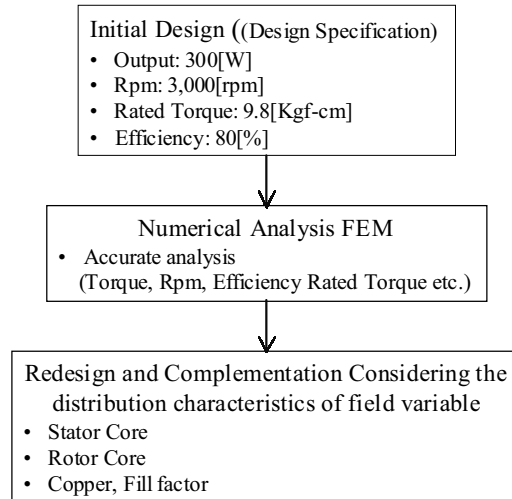


Fig. 3. Flow chart describing design of BLDC motor.

Field computation method

The magnet field within the motor is computed using the two-dimensional finite element method (2-D FEM). The analysis domain comprises an eighth model of the whole motor and periodic conditions are used as boundary conditions of analysis model. The Maxwell stress tensor is used for a resultant forces and torque calculations. Beside many advantages of the iron powder materials, it has a disadvantage of low permeability. This low permeability causes output power density to be reduced, therefore, an overhang, which covers the end winding and is shown in Fig. 4, is proposed to use the leakage component of the end winding to effective components in this paper. To analyze the effect of the overhang, 3D-EMCN [4] is introduced in this paper and its basic concept is illustrated as following.

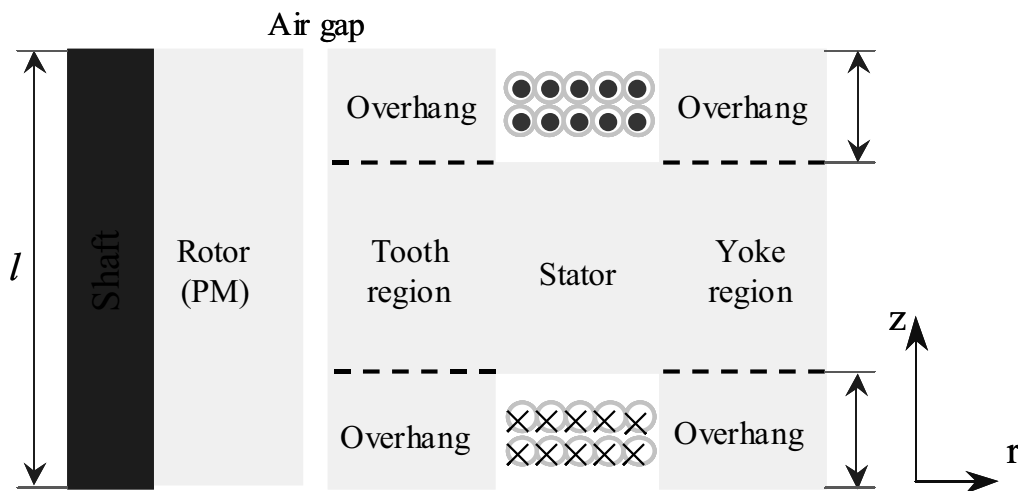


Fig. 4. Flow chart describing design of BLDC motor.

3D-EMCN is a numerical analysis method that can allow modeling of a machine in detail. Each region of the machine is divided into elementary volumes (elements) of hexahedral shape, and then 3-D equivalent magnetic circuit network is built by connecting the centroids (nodes) of adjacent elements with adjacent element's permeance.

In EMCN, Flux flow into the node (i,j,k) included in the source region, and the fundamental r -directional node equation between node (i,j,k) and node $(i,j-1,k)$ can be described by using magnetic scalar potential [4].

$$\Phi_{i,j-1,k}^r = P_{i,j-1,k}^r (U_{i,j-1,k} - U_{i,j,k} + E_{i,j-1,k}) \tag{1}$$

$$B_{i,j-1,k}^r = \Phi_{i,j-1,k}^r / S_{i,j-1,k}^r \tag{2}$$

$$E_{i,j,k} = NI/m \tag{3}$$

$$= \frac{M\{\theta(i,j,k)\}}{\int_0^{\delta} \frac{dH}{r}} r_{i,j,k} \tag{4}$$

where $\Phi_{i,j-1,k}^r$ is magnetic flux, $B_{i,j-1,k}^r$ is magnetic flux density, $P_{i,j-1,k}^r$ is permeance, $E_{i,j-1,k}$ is magneto-motive force of permanent magnet and stator current and $r_{i,j,k}$ is the magnetization depth of permanent magnet between nodes (i,j,k) and $(i,j-1,k)$. $U_{i,j,k}$ is unknown magnetic scalar potential and $M\{\theta(i,j,k)\}$ is magnetization of permanent magnet at node (i,j,k) . N is turn and m is element number of the teeth region in the r direction.

Magnetic flux continuity condition is applied at node (i, j, k) as following:

$$\sum_{p=r \neq z, q=i,j,k} \Phi_q^p = 0 \tag{5}$$

At node (i,j,k) , the node equation is calculated by substituting (1) through (4) into (5). After calculation all nodes by applying the node equation, the system matrix equation is following:

$$[\mathbf{P}]\{\mathbf{U}\} = \{\mathbf{F}\} \tag{6}$$

Result and discussion

Two different types of 300W BLDC motors are constructed in order to compare the characteristics. Fig. 5 shows teeth, which is made from the iron powder composite, their assembling stator, and lamination core stator. The stators are commonly composed of 18 slots and the rotor has 8 poles of radial ferrite magnet.

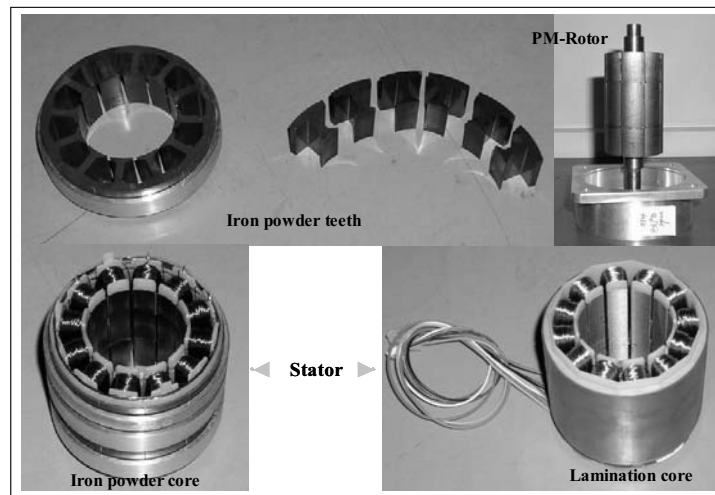
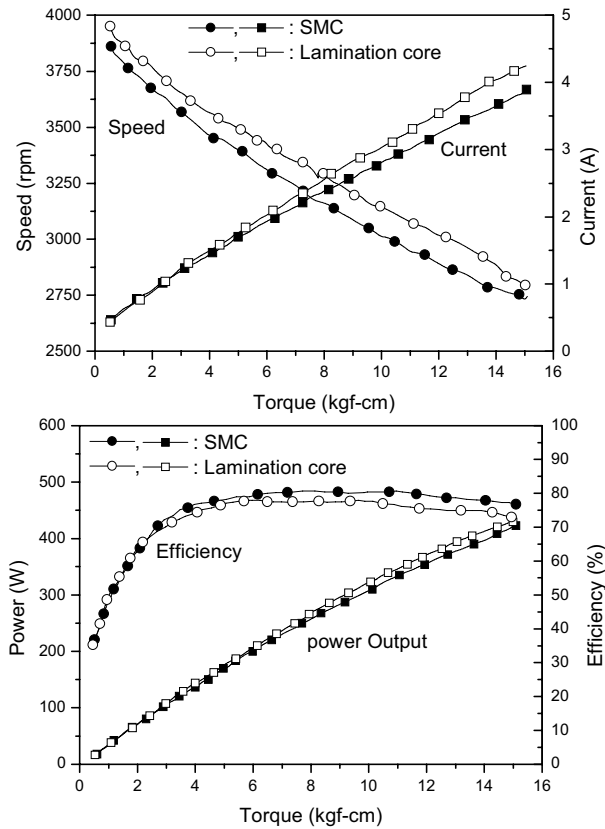


Fig. 5. Prototype of two BLDC motors.

Fig. 6 shows the experimental results of two BLDC motors. From the results, it is shown that as the torque increases, the motor with lamination core requires higher input current than the case of iron powder core. At the rated speed, the output power of the lamination core motor is 20% higher than the iron powder material motor. However, the iron powder material motor has better characteristic with the respect of efficiency than lamination core because of increasing the input current. A tooth segment, which has the overhang to cover the stator winding, is shown in Fig. 7. In order to determine the overhang length, 3D-EMCN is used to calculate the rated torque of the motor. Tables 2 shows the results of 3D-EMCN analysis according to overhang lengths. The various overhang lengths are investigated to satisfy the rated torque of lamination BLDC motor, which has 69 (mm) stack length. In this paper, the proper overhang length is selected as the 5.5 (mm) overhang length with 71 (mm) stack length of the motor.



(a) Curve of Speed and Current

(b) Curve of efficiency and power

Fig. 6. Experimental results about the SMC Motor and Lamination core motor.

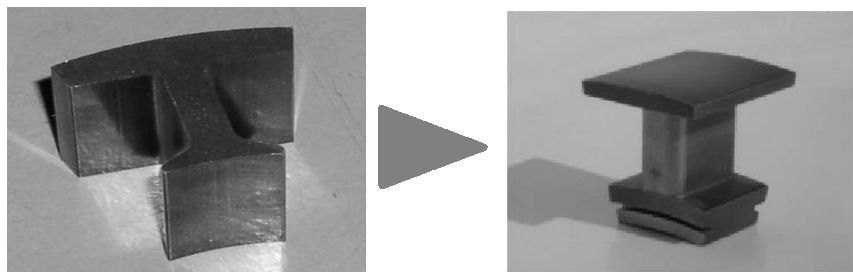


Fig. 7. Flow chart describing design of BLDC motor.

Table 2. Result of 3D Equivalent Magnetic Circuit Network (EMCN).

Stack length	Lamination core (S18)	Soft magnet composite	Overhang Length
69 (mm)	9.88 (kgf-cm)	9.11 (kgf-cm)	No overhang
69 (mm)	-	10.89 (kgf-cm)	9 (mm)
79 (mm)	-	12.36 (kgf-cm)	9 (mm)
71 (mm)	-	10.64 (kgf-cm)	5.5 (mm)

Conclusion

In order to apply the iron powder materials in BLDC motors, two different type BLDC motors with the same dimensions are investigated. One is made from the iron powder and the other is produced with lamination core. From experimental results, the torque performance of the lamination core motor is 20% higher than the iron powder material motor on the whole.

Therefore, to improve the performance of the iron powder BLDC motor over the lamination core motor, the shape of the tooth of the iron powder BLDC is introduced and it may be valuable to use its flux leakage of end winding. Additionally, the examinations of their eddy current losses and hysteresis losses according to frequency performances are required and the method of the experiment and analysis is now on the process.

References

- [1] Jack A.G., "Experience with the use of soft magnetic composites in electrical machines", *Proceeding, ICEM'98*, Istanbul, Turkey, September, pp1441-1448, 1998.
- [2] W. M. Arshad, K. C. Maliti and C. Sadarangani, "On the Use of Soft Magnetic Composite (SMC) iron Powder Materials in Induction Machines", *Proceedings of ICEET 99* Dar es Salaam, Tanzania, September 1999.
- [3] Matjaž Godec, Djordje Mandrino, Borivoj Šuštaršič, and Monika Jenko, Vasilij Prešern, "Development of Fe-Si-B Powders for Soft-Magnetic Application", *MATER. TEHNOL.*, 35(6), pp325-330, 2001.
- [4] Jin Hur, and Dong-Seok Hyun, "A Method for Reduction Cogging Torque in Brushless DC Motor Considering the distribution of magnetizing by 3DEMCM", *IEEE TRANSACTIONS ON MAGNETICS*, Vol. 34, No. 5, September 1998.

III-13. ELECTROHEATING IN SURFACE TREATMENT PROCESS

Kurek K., Dołęga D.

Silesian University of Technology, Department of Elektrotechnology,
Krasińskiego 8, 40-019 Katowice, Poland, kurekk@polsl.katowice.pl

Abstract – The paper describes the possibilities for computer forecasting of mechanical properties of elements being treated on the surface as well as the influence of electric (induction) heating parameters on the quality and mechanical properties of the products. The computer simulations using programs Flux2D, TTSteel and Metal7 have been performed basing on the suggested calculation model. The carried out experimental verification proved the usefulness of computer simulation of the product's final properties for heat treatment processes design.

Introduction

Electrical heating methods especially induction method play a big role in technology of surface heat treatment. The current level of technology and production significantly influences the requirements set on the products which are to be used for concrete often highly specific aims. The precision of execution is critical. The correctly carried out process of surface heat treatment e.g. induction hardening allows to obtain products fulfilling the highly set requirements. However it is very important to properly choose the treatment parameters. Adequate selection of heating parameters and applying the correct cooling method ensures high quality of the product obtained as a result of this process.

The computer analysis of the process enables to avoid mistakes and unnecessary costs that can arise while acting basing on experience and intuition. The paper presents the possibilities for computer forecasting of mechanical properties of the elements being treated on the surface as well as the influence of electric heating parameters on the quality and mechanical properties of the products

In order to obtain the intended simulation result it necessary to apply a proper model and tools for performing calculations. The difficulties of the hardening process analysis are associated with the electromagnetic and thermal fields coupling during the heating stage and connection of thermal field calculations with transformations of structure during heating and cooling.

The paper presents the worked out calculation model and computer simulations of the induction hardening process made on its basis allowing to determine the relations between the way the hardening process is carried out and the properties of the obtained product.

Calculation model

Induction hardening process consists of the following stages for which the calculations are performed:

- Induction heating – comprising the two-dimensional analysis of coupled electromagnetic and thermal fields which results in determination of temperature distribution in the cross-section of the hardened material,
- Quenching – comprising the analysis of transient thermal field under the influence of the applied cooling factor allowing to determine the cooling curves in cross-section of the material,
- Numerical determination of structural transformations occurring during the induction hardening process, the final hardness and mechanical properties of the process.

Induction heating

Induction heating system (Fig. 1) consists of the following areas: Ω_1 -work piece, Ω_2 - inductor, Ω_3 – air [1], [7]. Only the quarter of the considered system is analyzed because of the system's symmetry. The electromagnetic problem is limited to the Maxwell's equation solution. The following equations are in force in the particular areas :

$$\Omega_1 - \nabla \cdot \left(\frac{1}{\mu} \nabla \vec{A} \right) - j\omega\mu\gamma \vec{A} = 0 \quad (1)$$

$$\Omega_2 - \nabla^2 \vec{A} = -\mu \vec{J}_s \quad (2)$$

$$\Omega_3 - \nabla^2 \vec{A} = 0 \quad (3)$$

with boundary conditions as in Fig. 1, where: \vec{A} - magnetic vector potential, ω - angular frequency, μ - magnetic permeability, γ - conductivity, \vec{J}_s - current source density.

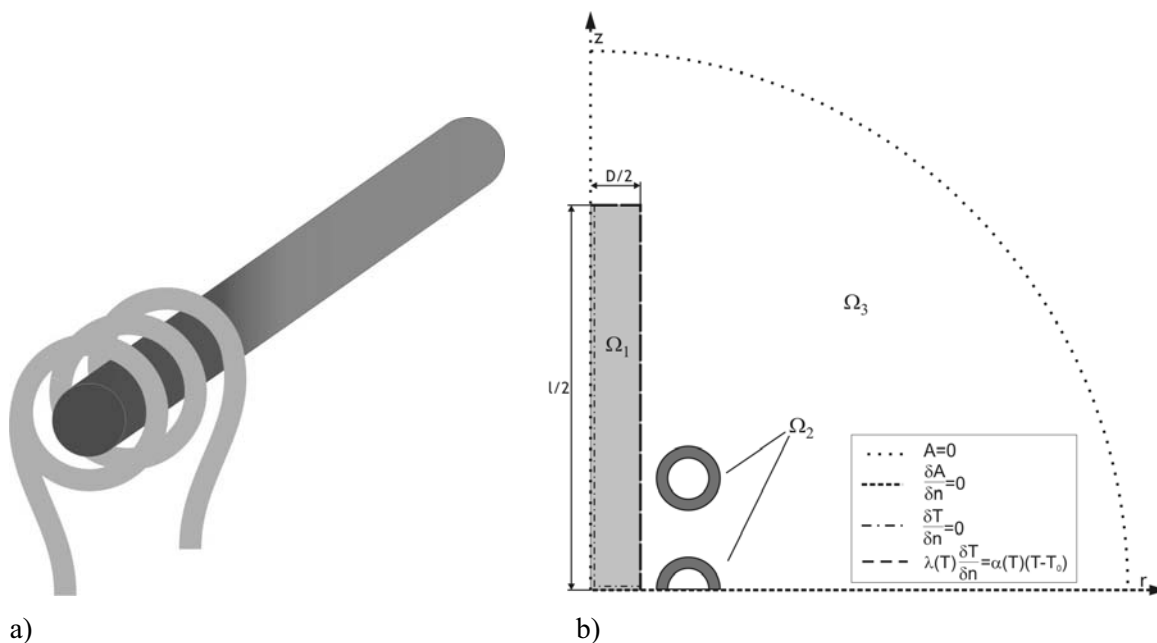


Fig.1. Induction heating system (a); calculation model with boundary conditions (b)

Thermal field analysis is connected with the solution of the Fourier-Kirchhoff's equation:

- for the Ω_1 area interior

$$\rho \cdot c \cdot \frac{\partial T}{\partial t} = \nabla \cdot (\lambda \nabla T) + Q_w \quad (4)$$

- for points on the surface Ω_1

$$\rho \cdot c \cdot \frac{\partial T}{\partial t} = \nabla \cdot (\lambda \nabla T) + Q_w - S \cdot \sigma \cdot \varepsilon (T^4 - T_o^4) - S \cdot \alpha (T - T_o) \quad (5)$$

where: ρ - charge density, c - specific heat, T - temperature, T_o - environment temperature, S - surface, α - heat exchange coefficient, σ - Stefan-Boltzman's constant, ε - emissivity coefficient, λ - heat conductivity, Q_w - density of power induced by eddy currents $Q_w = \omega^2 \gamma \underline{A} \underline{A}^*$ (6),

with the initial condition:

$$T(r, z, 0) = T_p \quad (7)$$

Cooling

The analysis of the cooling process requires the modified equation (4) ($Q_w = 0$) for the interior of the area Ω_1 and the equation for points on the surface Ω_1 :

$$\rho \cdot c \cdot \frac{\partial T}{\partial t} = \nabla \cdot (\lambda \nabla T) + S \cdot \alpha (T_w - T) \quad (8)$$

with the initial condition:

$$T(r, z, 0) = T(r, z, t) \quad (9)$$

where: T_w - water temperature, t_{kn} - time of the final calculation step during the heating process.

Structural transformations during heating and cooling

Structural transformations occur in steel during heating and quenching mainly due to temperature changes. These changes are connected with carbon diffusion (and for the most part regard formation and decomposition of austenite) or are diffusionless (austenite \rightarrow martensite). The transformation are shown by large on diagrams TTT and CCT which are worked out basing on dilatometric research. Two models are used for diffusion transformations description [2-5]:

- A mathematical model basing on the Johnson-Mehl-Avrami's formula and fiction time conception

$$y_i = y_m \left(1 - e^{-b_i \cdot (t_i^* + dt_i)^{n_i}} \right) \quad (10)$$

$$t_i^* = \sqrt[n_i]{\frac{1}{b_i} \ln \left(1 - \frac{y_{i-1}}{y_m} \right)}$$

In these exceptions time t_i in step i and the parameter y_m (max fraction of the new phase), n and b appear in an apparent way (directly). They depend on temperature, uniformity and inherent grain size of austenite microstructure. Difficulties with application of this model are connected with determination of these parameters for the analysed material.

- A model introduced by the firm PRISMECA allowing „the digitisation” of diagrams TTT [6]. The models enables to define the max fraction of the new phase, temperature T_i at the beginning of the transformation (A_{C1} for heating), temperature T_f of the transformation end (A_{C3} for heating) as a function of heating and cooling speed.

The martensite transformation model is based on the Koistinen and Marburger's formula

$$y = y_a \left(1 - e^{-a(Ms-T)} \right) \quad (11)$$

where: y_a - volume fraction of austenite in the moment of transformation, T - temperature, a -material parameter dependent on the brand of steel, Ms - temperature of the martensite transformation beginning.

The material hardness HV is calculated basing on the multiple analysis of data regression [7]:

$$HV = C_o + \sum(C_{1i} \cdot c_i \cdot Fe) + \sum(C_{2i} \cdot c_i \cdot Pe) + \sum(C_{3i} \cdot c_i \cdot Ba) + \sum(C_{4i} \cdot c_i \cdot Ma) \quad (12)$$

where: C_0, C_1, C_2, C_3, C_4 – regression coefficients, c_i - percentage of alloy add-ons, Fe, Pe, Ba, Ma - percentage of ferrite, pearlite, bainite and martensite.

The calculation of ultimate tensile strength Rm results from its direct dependence on the HV hardness:

$$Rm = f(HV) \quad (13)$$

Determination of yield point Re has been based on the following general equation:

$$Re = f(D\alpha, CR, \sum(Fe, Pe, Ba, Ma)) \quad (14)$$

where: $D\alpha$ – grain size of ferrite, CR – average cooling speed (K/s).

Simulation results

The hardening process has been analyzed using the computer simulation method. The computer program Flux2D [5] has been applied for the simulation in its part connected with heating and cooling and the programs TTSteel [4] and Metal7 [6] have been used for the metallurgical part. The calculations have been performed for three different steel brands (45, 40HM, 40H) altering the supplying (power, voltage, frequency) and cooling parameters. Temperature distribution during the final time step has been shown in Fig. 2 and temperature courses in time in selected points of the heated and cooled sample in Fig. 3.

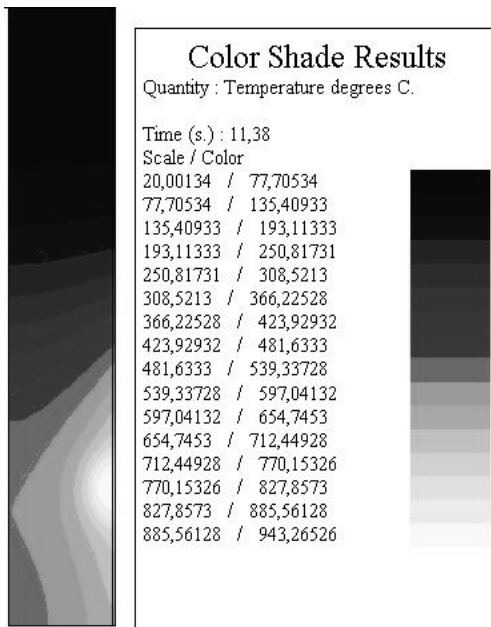


Fig.2. Temperature distribution in the cross-section of the heated sample; $f = 320$ kHz, steel 40HM

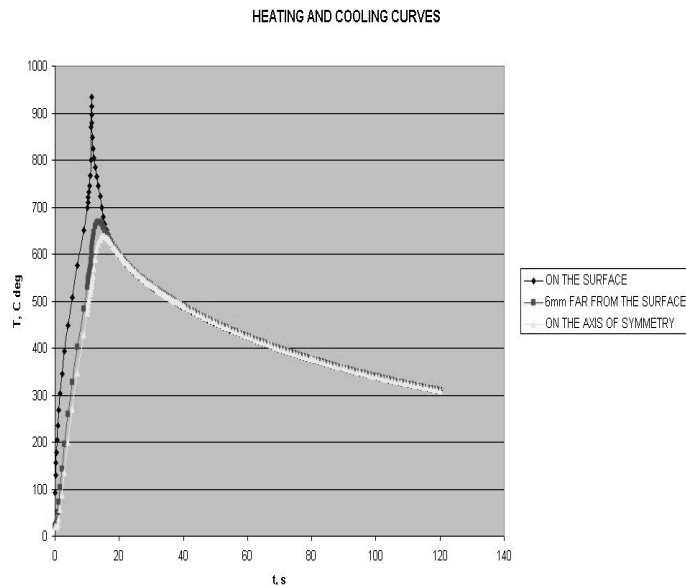


Fig.3. Temperature courses during heating and cooling in water in the selected point of the sample (steel 40HM)

The austenite forming during heating (Fig. 4) disintegrates into secondary structures: pearlite, bainite or martensite. The dominant structure by quenching is martensite (Fig. 5). The depth of the sample's hardened layer depends mainly on the supplying parameters (power, frequency) and the structure and hardness of the hardened sample is influenced for the most part by the cooling intensity (cooling curves course). The martensite is dominant by very rapid cooling which is also connected with obtaining of high values of hardness and by slower cooling the fraction of bainite and pearlite is higher and the hardness is lower.

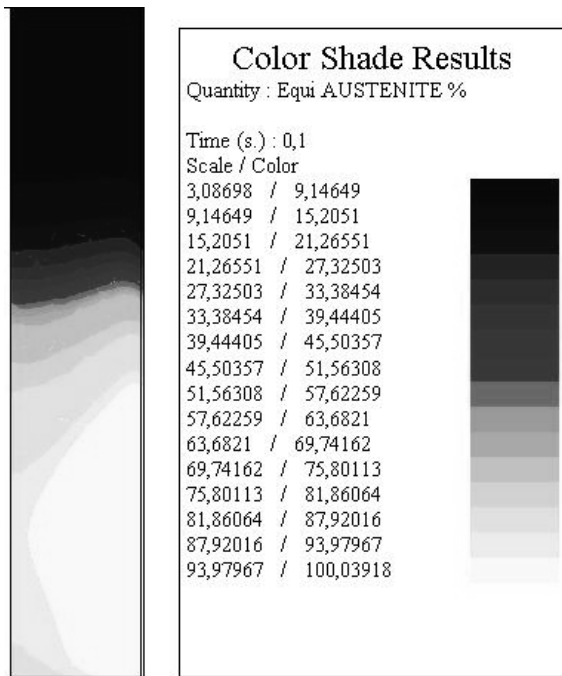


Fig. 4. Percentage of austenite at the beginning of cooling; steel 40HM

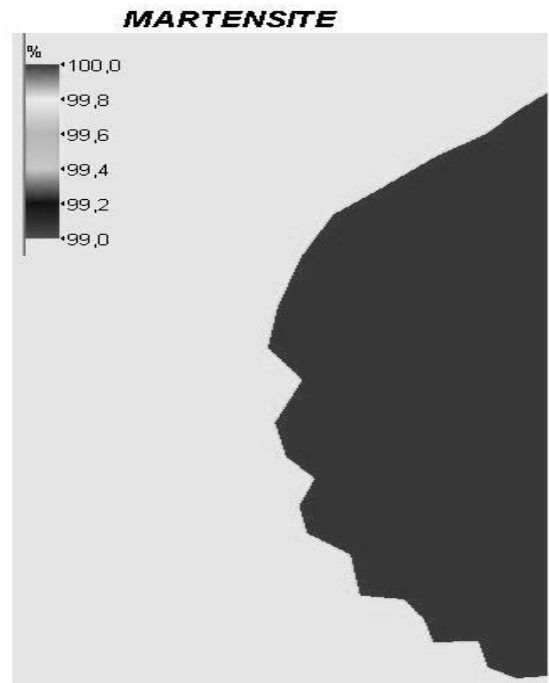


Fig. 5. Obtained martensite structure of the sample cooled in water (steel 40HM)

The essence of the hardening process is obtaining the desired final properties of the product (hardness, ultimate strength, yield point). Fig. 6 shows the obtained properties of the material using the computer simulation.

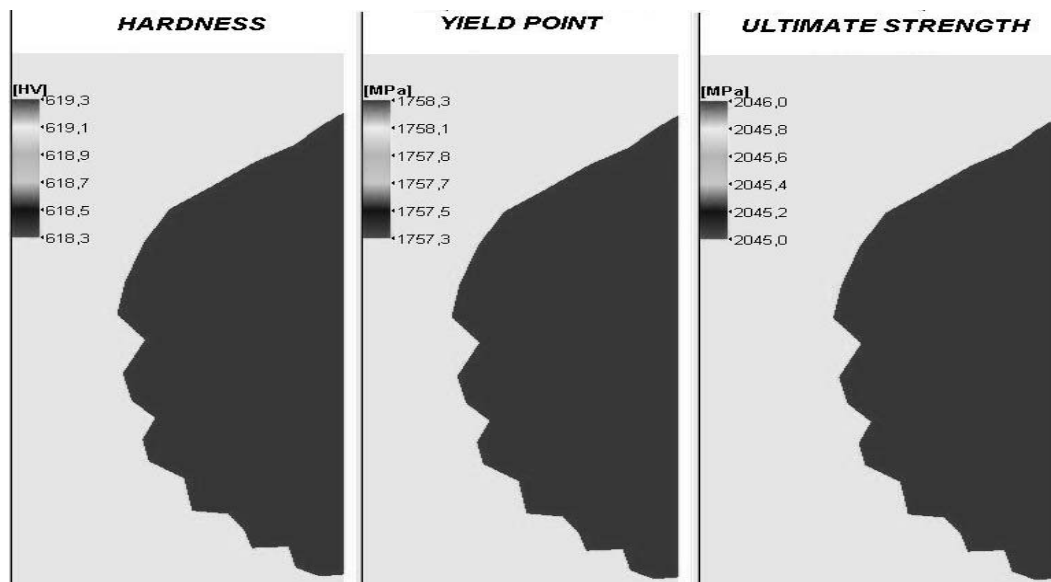


Fig. 6. Distribution of mechanical properties obtained during hardening process

Experimental verification

The results obtained using the computer simulation method have been experimentally verified. For this purpose specially prepared samples in the shape of cylinder with diameter of 25 mm, made of steel 40HM have been hardened in water by their immersion while the heating process has been carried out applying the 3-coil inductor with current of frequency $f = 320$ kHz with the average power of $P = 4,3$ kW. The experimental and calculation results during the heating and cooling stage in water are very

similar. The metallurgical calculations also show satisfactory convergence. In both cases the sample has been hardened on the surface to the depth of ca. 2 mm. Hardness obtained as a result of simulation equals 619 HV and during research 667 HV.

Conclusions

The application of the computer simulation method for forecasting of the surface induction hardening process has been show in the paper. It enables the parameters selection so that the desired final properties of the product can be achieved. The calculations are performed basing on the worked out calculation model for the particular stages of the heating process, quenching, structural transformations. The computer programs assigned for the analysis of the coupled electromagnetic and thermal fields e.g. Flux2D can be used for simulations of heating and cooling while the metallurgical calculation can be performed with the aid of the program Metal7 (made by PRISMECA) or the program TTSteel worked out in cooperation with the firm ITA (Czech Republic). The simulations described in the paper have been carried out using these very programs. The comparison of capabilities of both programs has been shown in the table below.

Comparison of TTSteel and Metal7 programs

TTSteel		Metal7	
<ul style="list-style-type: none"> - simplicity in inserting data although knowledge of exact chemical constitution of steel is needed, - assumes 100% of austenite in the heated area, - calculates structures and properties only in the area where the material has been heated up to austenitisation temperature, - simplicity in inserting the cooling curves directly from the program Flux2D, - possibility to calculate ultimate strength and yield point, - some limitations connected with the chemical constitution of steel 	<ul style="list-style-type: none"> + - - + + - 	<ul style="list-style-type: none"> - rather complicated way of creating a database in the program: required knowledge of the exact CCT_c diagram with the percentage composition of structures, - required knowledge of data concerning the hardness of austenite, martensite, bainite, pearlite and ferrite, - possibility to calculate austenite content in the heated material, - the program does not calculate structure and hardness in the whole probe, - the program does not calculate ultimate strength and yield point 	<ul style="list-style-type: none"> - - + + -

The worked out method can be used in industry for design of the surface heat treatment process (hardening, tempering or annealing).

References

- [1] T. Skoczkowski, Modelowanie i symulacja sprzężonych zjawisk polowych w urządzeniach elektrotermicznych. Warszawa, INB ZT 2000, pp.163-166
- [2] L. Quansheng, FEM Based Simulation of Induction Hardening. Worcester Polytechnic Institute, March 2002
- [3] D. Duran, D. Durban, F. Girot, Coupled phenomena and modeling of material properties in quench hardening following inductive heating of the surface. International Induction Heat Treating Symposium. Indianapolis (Indiana), September 1997, pp.855-863
- [4] Software TTSteel – Theoretical Background, ITA spol. sr.o., Ostrava 2003
- [5] Flux2D Fluid.7.6: User's guide, Cedrat, 2001, France
- [6] Metal7 Version 3.00: User's guide, PRISMECA 2001
- [7] K. Kurek, D Dołęga, Modelling of induction hardening; International Scientific Colloquium Modelling for Electromagnetic Processing; Hannover, March 24-26, 2003

III-14. MAGNETODYNAMIC PERFORMANCE IN CAGE INDUCTION MOTORS WITH A BROKEN BAR

Xose M. López-Fernandez⁽¹⁾ and Marius Piper⁽²⁾

⁽¹⁾Dept. of Electrical Engineering, Vigo University – Spain, xmlopez@ieeee.org

⁽²⁾Dept. of Electrical Engineering, Polytechnic University of Bucharest – Romania, pipermar@lmm.pub.ro

Abstract - In this work a finite element modelling approach in order to analyse the electromagnetic performance due to effects of rotor broken bars was applied. The models were used on 3-phase squirrel cage induction motors to compute the electromagnetic field distribution in the motor cross-section as well as the bar current densities due to skin effect.

Introduction

The reliability of industrial drive systems has led to concerted research and development activities around the fault conditions on bars and rings of a squirrel cage induction motor. During the last years, an important amount of methods and ways has been proposed to detect and assess such faults [1] [2]. Recently, attention is being focussed to causes which act in combination with stressing on the rotor. These stresses can be identified as due to electromagnetic, thermal, residual, dynamic, environmental and mechanical ones. We name to this stage the mechanism of the faults on squirrel cage, which provokes a cascade of failures on the rotor, what is widely assumed as a consequence of increasing in local losses. The updated works in the last mentioned line put emphasis on local core losses as a cause [3] [4]. There, efforts on measuring and obtain the thermal field under broken bar situations have also been made, in particular mentioned the paper [5], where two interesting observations were made: (1) the asymmetric distribution of adjacent bars' current depending on the direction of rotating magnetic field; (2) the temperature rise must be studied during start conditions, since the nominal steady-state does not look to offer dangerous increase. The interest for looking deep into the last observations implies to analyse the problem in terms of both thermal and electromagnetic field.

Description of the problem

Strategy of study

The work is concerned about the electromagnetic causes which condition the mechanism of propagation of faults on bars taking into account the existence of one first broken bar. Therefore, the attention was focused on the numerical assessment of the increase bar current in the adjacent bars around the faulty region, the influence of the direction of rotating magnetic field direction, and on the influence of slip to this behaviour. At the same time, the variations of the electromagnetic torque was carried out for different situations: (1) healthy rotor; (2) one broken bar – single cage, the outer broken bar and the total (inner and outer) broken bar – double cage.

Analysis assumptions

The following assumptions in the currents study were assumed:

- The starting regime is not taken into account;
- Magnetic field distribution is considered to be plane (plan-parallel symmetry);

- The end-turn leakage inductance effects are included in the external electrical circuit coupled to 2D FE portion of field model;
- Magnetic vector potential is constant (Dirichlet boundary condition) along the outside of circumferential boundary. All flux paths close within the structure of the machine;
- The effects of inter-bar currents through the rotor core laminations are not taken into account;
- No skew bars were considered in the rotor cage;
- A broken bar is modelled by a very high resistance, keeping the rotor cage circuit topology unchanged;
- The asymmetry of the rotor is strictly limited to existence of one broken bar (outer and inner with double cage);
- Non-linear behaviour of the magnetic circuit by means of B-H curve.

Field model of the induction motor

The magnetic field of the induction motor is computed using a 2D FEM and assuming an A.C. non-linear problem [6]. This approach enables to study the influence of the rotor bars conditions on the motor's operating characteristics (torque and current vs. slip). The electromagnetic field model in the magnetodynamic problems is based on the Maxwell's equations and on the concept of magnetic vector potential. As known, in 2D problems the diffusion equation (1) provides the means to calculate the induced bar currents in the rotor cage.

$$\nabla \times \left(\frac{1}{\mu} \nabla \times A \right) = -j s \omega_s \sigma A + J \quad (1)$$

Where A is the magnetic vector potential (unknown), σ is the electrical conductivity, ω_s is the angular frequency of the stator supply, s is the slip, μ is the magnetic permeability and J is the current density supplied by external voltage sources.

The natural excitation for finite element models is usually a current (or current density). In the real motor the current is normally unknown since it is supplied by an external electric circuit [5]. Therefore, the external electric circuit which supplies with voltage V must be modelled as coupled to the 2D FE model [7].

The current i in a stranded coil of the field model can be expressed as follows:

$$i = \frac{\sigma}{2N l_c} \left[S \left(V - R_{et} i + L_{et} \frac{di}{dt} \right) - S e \right] \quad (2)$$

Where R_{et} is the end-turn resistance, L_{et} is the end-turn inductance, N is the coil turns, S is the cross-sectional area where i flows, l_c is the length of the strand coil and e is the induced e.m.f. on the strand coil. This induced e.m.f. on a coil (S^+, S^-) can be expressed as follows:

$$e = \frac{l_c}{S} \left(\iint_{S^+} \frac{\partial A}{\partial t} \partial S - \iint_{S^-} \frac{\partial A}{\partial t} \partial S \right) \quad (3)$$

Geometry of the model

Two different cage geometries were considered: simple cage and double cage rotor. The existence of one broken bar causes an electromagnetic asymmetry. Therefore, symmetries were not possible to introduce in order to use reduced models, as shown Fig 1a and Fig 2a.

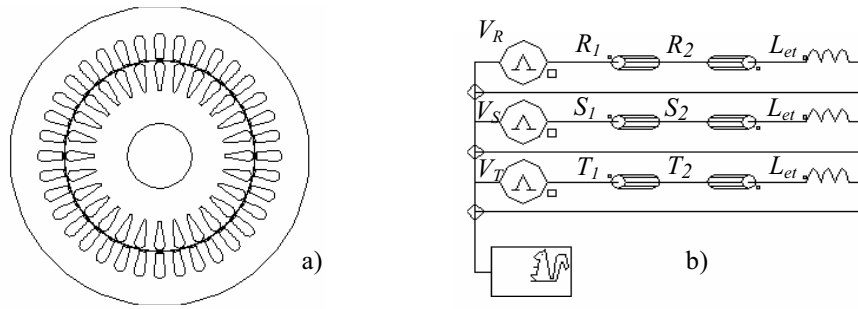


Fig.1 a) Geometry of the single squirrel cage rotor motor model and b) the Electric circuit model associated.

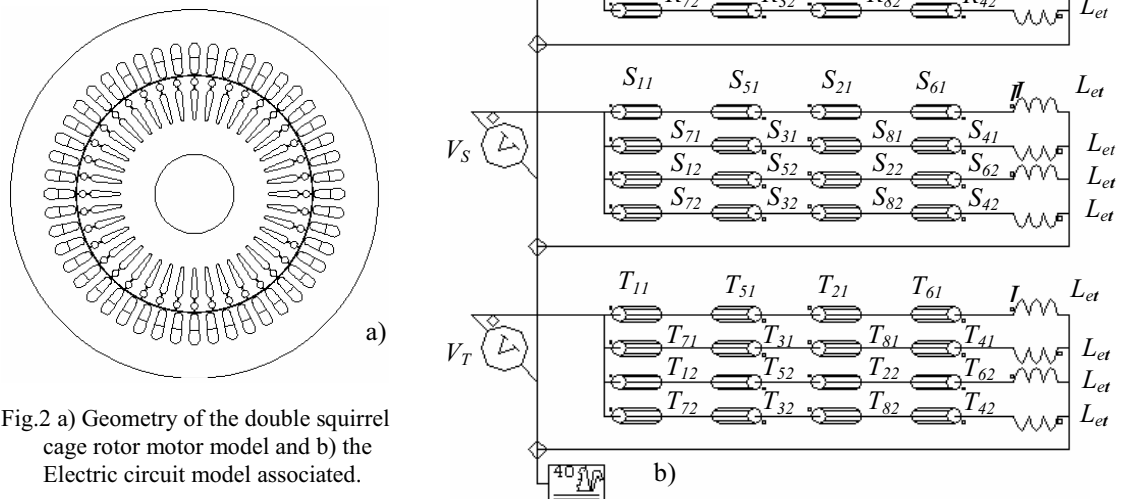


Fig.2 a) Geometry of the double squirrel cage rotor motor model and b) the Electric circuit model associated.

External electric circuit

The used electromagnetic field model considers a coupling to an external electric circuit in order to represent the external voltage sources. Fig 1b and Fig 2b show the external electrical connections used for the induction motors. Each horizontal branch represents the respective active conductors of a coil of a phase winding. These elements are modelled including winding turns and the resistance to relate with the region in the domain of finite elements. The inductance which appear in the external circuit represents the correspondent front and back end-turns of each coil, L_{et} . The related circuit shows whole electric circuit of the motor. The symbolic squirrel cage is a macro component in model including solid conductors to represent the rotor bars and the end-rings resistance and end rings inductance.

Practical application

Two different induction motors of 4 kW and 90 kW were studied: the first one, with a simple cage and the second one, with a double cage as shown Fig.1a and Fig.2a. The characteristics of these motors are presented in Table I. A summary of data of the motors are available in the next paragraph.

Summary of data of the studied Motors

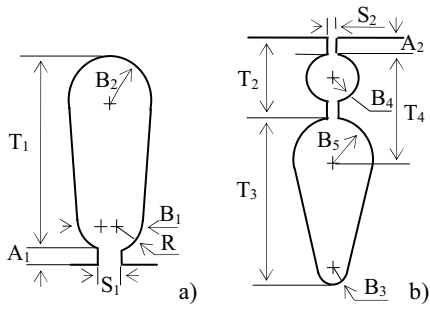


Fig.3 a) Stator slot and b) rotor bar shape of studied motors.

Table III. Motor geometrical parameters in millimetres.

Motor	ϕ stator ext.	ϕ stator interior	ϕ shaft	L			
4 kW	170	108	37	120			
90 kW	420	270	90	268			
ϕ : Diameter		L : Axial depth of magnetic body					
Motor	A ₁	A ₂	B ₁	B ₂	B ₃	B ₄	B ₅
4 kW	0.80	0.00	4.20	6.13	0.90	0.00	4.77
90 kW	1.27	2.83	11.70	6.20	1.73	4.00	4.00
Motor	R	S ₁	S ₂	T ₁	T ₂	T ₃	T ₄
4 kW	0.50	3.2	0.00	14.25	0.00	16.60	4.77
90 kW	4.60	3.10	1.10	35.30	1.73	34.69	16.47

Table IV. Motor electrical parameters.

Motor	Stator		Rotor	
	R _{conductor}	L _{et}	R _{end-ring}	L _{end-ring}
4 kW	5.90 m Ω	3.04 mH	1.84 m Ω	4.31 10 ⁻⁹ H
90 kW	1.45m Ω	0.30 mH	1.22 m Ω	7.63 10 ⁻⁹ H

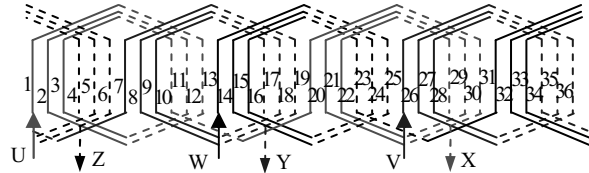


Fig.4 Single-layer, concentric winding of the 4 kW motor.

Table V. Phase/slot winding characteristics of the 90kW motor.

Phase (U-X)	R ₁₁	R ₂₁	R ₃₁	R ₄₁	R ₅₁	R ₆₁	R ₇₁	R ₈₁	R ₁₂	R ₂₂	R ₃₂	R ₄₂	R ₅₂	R ₆₂	R ₇₂	R ₈₂
Slots	1	2	37	38	11	12	2	1	25	27	13	14	35	36	23	24
	4	3	40	39	14	13	47	48	28	28	16	15	38	37	26	25
Phase (V-Y)	S ₁₁	S ₂₁	S ₃₁	S ₄₁	S ₅₁	S ₆₁	S ₇₁	S ₈₁	S ₁₂	S ₂₂	S ₃₂	S ₄₂	S ₅₂	S ₆₂	S ₇₂	S ₈₂
Slots	33	34	21	22	43	44	31	32	9	10	45	46	19	20	7	8
	36	35	24	23	46	45	34	33	12	11	48	47	22	21	10	9
Phase (W-Z)	T ₁₁	T ₂₁	T ₃₁	T ₄₁	T ₅₁	T ₆₁	T ₇₁	T ₈₁	T ₁₂	T ₂₂	T ₃₂	T ₄₂	T ₅₂	T ₆₂	T ₇₂	T ₈₂
Slots	17	18	5	6	27	28	15	16	41	42	29	30	3	4	39	40
	20	19	8	7	30	29	18	17	44	43	32	31	6	5	42	41
No. of conductors	6	5	6	5	6	5	6	5	6	5	6	5	6	5	6	5

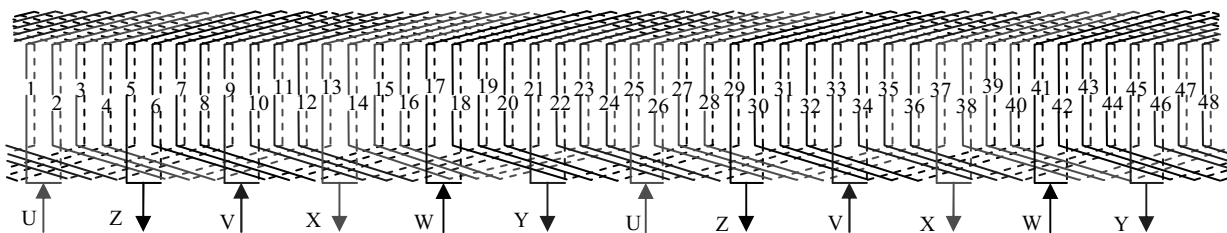


Fig.5 Double-layer, concentric winding with short pitch of the 90 kW motor.

Table I. Motor characteristics.

Motor	4 kW	90 kW
Power (kW)	4	90
Line voltage (V)	400/230	400
Line current (A)	9,2/16	168
Connection type	Y/ Δ	Y
Frequency (Hz)	50	50
Number of poles	4	4
No. of stator slots	36	48
No. of rotor bars	28	40
Efficiency	85 %	95 %
Power factor	0.83	0.83

Table II. Phase/slot winding of the 4 kW motor.

Phase (U-X)	R ₁			R ₂		
	Slot	1	2	3	10	11
	19	20	21	28	29	30
Phase (V-Y)	S ₁			S ₂		
Slot	25	26	27	34	35	36
	7	8	9	16	17	18
Phase (W-Z)	T ₁			T ₂		
Slot	13	14	15	22	23	24
	31	32	33	4	5	6
No. of conductors	27					

Results

Fig 6 and Fig 7 show the numerical results on percent increase of nominal bar current and percent decrease of electromagnetic torque vs. slip variation for the two motors. To evaluate the torque the virtual work method was used.

In the case of the 90 kW motor, the current distribution is not affected by the presence of outer broken bar (see Fig 6b). However, there are current increases in the adjacent front bar (B40) and the adjacent back bar (B2) to the broken one (B1) with respect to the rotating magnetic field direction. The same happens with the presence of the broken bar in the case of the simple cage (see Fig 7 and Fig 8). For the studied motors, with totally broken bar (B1), the front bars (B40 and B28 respectively) with respect to the rotating magnetic field direction, suffer an increase up to 18% for high values of slip. Meanwhile the current of back bar (B2) is increasing up to 50% in both studied motors. The electromagnetic torque, as it is well known, decreases in all cases as it is shown in Fig 7.

Finally, Fig. 8 and Fig. 9 show in detail the strong dependence between the flux density and the slip variation.

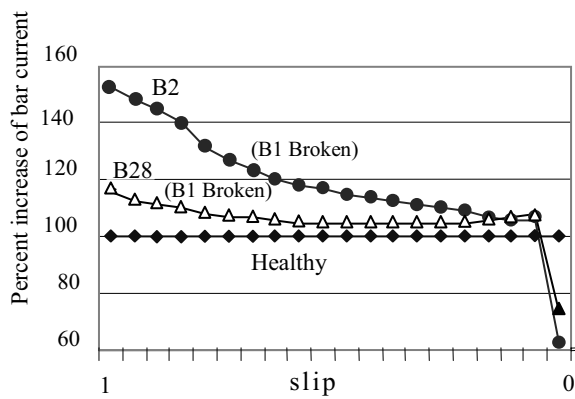


Fig.6 a) Percent bar current v.s. slip. Healthy and total broken bar. 4 kW motor.

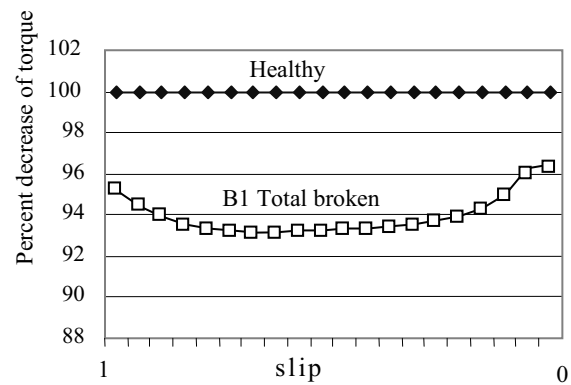


Fig.7 a) Percent torque v.s. slip. Healthy and total broken bar. 4 kW.

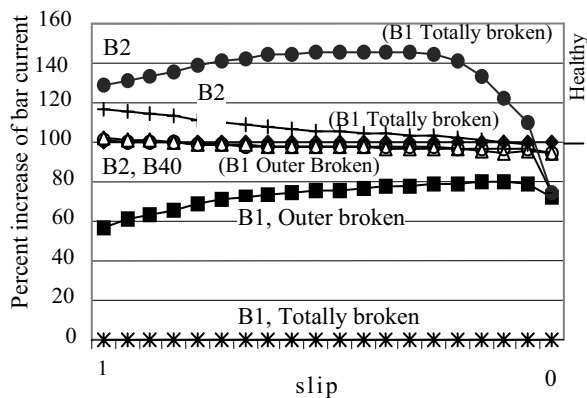


Fig.6 b) Percent bar current v.s. slip. Healthy, outer and Total broken bar. 90 kW.

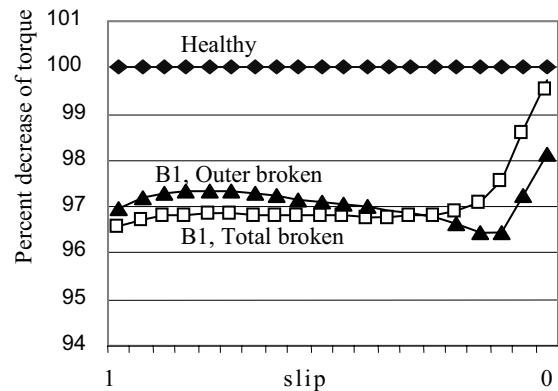


Fig.7 b) Percent torque v.s. slip. Healthy, outer and Total broken bar. 90 kW.

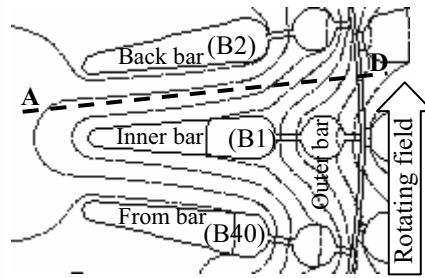
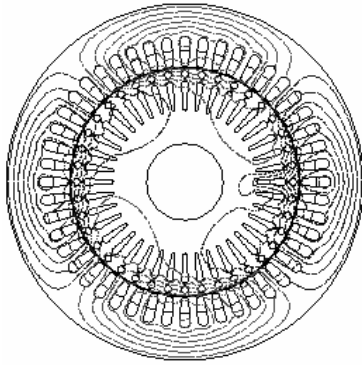


Fig. 8 a) Flux density distribution around totally broken bar at $s=1$ of motor 90 kW. b) Zoom on broken bar B1.

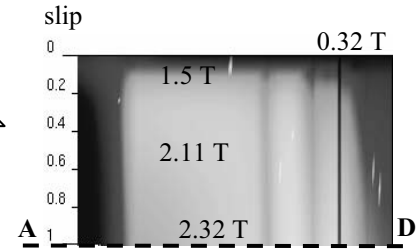


Fig. 9 Flux shade on line AD from Fig. 6 b), under totally broken v.s. slip.

Conclusions

Even if this study was made without taking into account the interbar currents, the results show that the presence of a faulty bar produces an important asymmetric increase of the bar current. These results seem to indicate the idea of that losses, which generate the thermal stress and consequently mechanic stress in bars, are mainly caused by the Joule losses more than the flux density increase, around the faulty region. This phenomenon is very important in the double-caged induction motors because the increase of current is not generated only in start conditions but also it is nearly maintained at low slip values.

The strong dependence between the increase of current and the flux density in the faulty region versus the slip variation was also shown.

Finally, it is very important to remark that with the presence of a broken bar, the bar which suffers the major increase of the current is the back bar with respect to the rotating magnetic field direction (Fig 8). Consequently, it seems to indicate the direction in which the broken bars are propagated.

References

- [1] Manolas S., Tegopoulos J. And Papadopoulos M., "Analysis of Squirrel Cage Induction Motors with Broken Rotor Bars and Rings," IEEE Trans. On Energy Conversion. Vol. 14, N° 4, December 1999.
- [2] Rastko Fiser and Stanislav Ferkolj, "Magnetic Field Analysis of induction motor with rotor faults," Int. Journal for Computation and Math. in Electrical and Electronic Eng. (COMPEL-ISEF97), vol. 17, pp. 206-211, 1998.
- [3] Bangura, J.F. and Demerdash, N.A. "Diagnosis and Characterization of Effects of Broken Bars and Connectors in Squirrel-Cage Induction Motors by Time-Stepping Couple Finite Element-State Space Modeling Approach," IEEE Trans. on Energy Conversion, vol. 14, no. 4, pp. 1167-1175, December 1999.
- [4] Demerdash, N. A., Bangura, J. F. "Comparison Between Characterization and Diagnosis of Broken Bars/End-Ring Connectors and Airgap Eccentricities of Induction Motors in ASD's Using a Coupled Finite Element-State Space Method", IEEE Transactions on Energy Conversion, Vol. 15, No. 1, March 2000.
- [5] X. M. López-Fdez, et. Al "Thermal Performance of a 3-phase Squirrel cage of an Induction Motor with a Broken Bar" Proc. Of IEEE International Symposium on Diagnostics for Electrical Machines, Power Electronics and Drives, pp. 529-533, Gijon-Spain, 1-3 September 1999.
- [6] "Computational Magnetism" Edited by J.K. Sykulski. Joint-Authors: J. Turowski, Zakrzewski, , et. al. Chapman & Hall , 1995.
- [7] Xose M. López Fernández, Vicente Aucejo Galindo, J.A. Dias Pinto, A. Paulo Coimbra. " Parametric study of rotor slot shape on cage induction motors". Studies in Applied Electromagnetics and Mechanics, vol. 22, pp. 190-195, IOS Press (ISEF01) – ISBN 1 58603 232: The Nerderland 2002.

III-15. SOFT MAGNETIC COMPOSITE IN DESIGN OF MOTOR WITH OSCILLATORY STARTING

Damijan Miljavec¹, Borivoj Šuštaršič², Željko Turk¹, Konrad Lenasi¹
¹Univerza v Ljubljani, Fakulteta za elektrotehniko, Tržaška 25, 1000 Ljubljana
²Inštitut za kovinske materiale in tehnologije, Lepi pot 11, 1000 Ljubljana
E-pošta: miljavec@fe.uni-lj.si

Abstract - The aim of proposed paper is to increase magnetostatic torque of single-phase two-pole motor with oscillatory starting. Reference values of torque are based on two basic types of motor. First is composed of laminated stator core with sintered ferrite magnet rotor and second one is made from SMC stator core with sintered ferrite magnet rotor. To reduce rotor and stator production costs the composite materials were introduced. Preparation, production, physical properties and magnetic characteristics of plastic bonded NdFeB magnet and plastic bonded ferrite magnet are examined. Also, brief description of soft magnetic composite is done. The analyze involves two new geometries. First is double layer rotor with two different plastic bonded magnets. The outer layer is made from plastic bonded NdFeB magnet and inner one is made from plastic bonded ferrite magnet. The second type of rotor is composed of these two plastic bonded magnets mixed together in proper volumetric proportions. Calculated results show the improvements in torque production for both types of rotor and stator.

Introduction

Mass production and market competition of small electric apparatus demand decrease of production costs. Meanwhile, the output characteristics have to remain the same or even increase. The use of single-phase two-pole motor with oscillatory starting is very common in such apparatus. The advantage of this motor is in its simple mechanical construction (fig. 1 and fig. 2) and relatively high efficiency at small dimensions and rated power. Classic type is composed of laminated stator core and sintered ferrite magnet rotor. The development made in permanent magnets and in soft magnetic materials have increased the interest in a design and even in re-design of such electric motors.

Basic motor theory

The motor is self-starting due to its non-uniform airgap. To obtain a starting torque, the airgap is designed as non-uniform, i.e. wider at one end of the pole shoe than at the opposite end (Fig. 1). The rest angle θ_0 of the rotor is the angle between the center axis of the stator poles and axis at the permanent magnet rotor flux. These motors are only self-starting when, with the armature current $I=0$ A, the angle $\theta_0 > 0$. The largest starting torque is achieved when the rest angle $\theta_0 = 90^\circ$. The motor construction shown in figure 1. limit the rest angle to $\theta_0 < 5..12^\circ$, which consequently results in a small starting torque [1].

With zero current in the stator winding, the rest angle $\theta_0 > 0$ as the attractive force between PM poles and the stator stack align the rotor center with the minimum airgap. After switching on the stator voltage the stator magnetic flux will push the PM rotor towards the center axis of the stator poles. The rotor oscillates with its eigenfrequency. If this frequency is close to the stator winding supply frequency, the amplitude of mechanical oscillations will increase and the motor will begin to rotate continuously. The eigenfrequency depends on inertia and torque constant of the motor, which is lower for larger motors and thus they require lower supply frequencies. It is important to now how the dynamic behavior of these motors at the design stage to ensure desired speed characteristics.

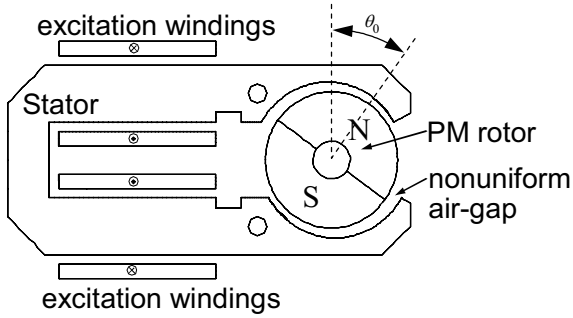


Figure 1: Cross section of motor with oscillatory starting.

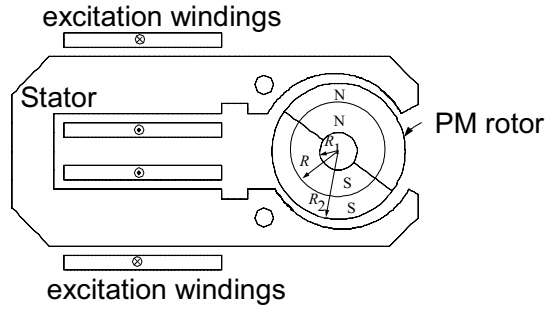


Figure 2: Cross section of motor with oscillatory starting with double layer type rotor.

The electromagnetic torque development by the motor can be found by taking the derivative of magnetic coenergy with the respect of the rotor angular position θ . If the magnetic saturation is neglected, the torque developed by the motor with $p=1$ is [2]:

$$T_d = i\psi_m \sin\theta - T_{rel} \sin[2(\theta - \theta_0)] \quad (1)$$

where electrodynamic torque is given by the first term, the reluctance torque is given by the second term, $\Psi_m = N_1 \Phi_f$ is the peak linkage flux, θ is the angle of rotation related to the main stator axis and T_{rel} is the peak value of the reluctance torque. When considering characteristic of the motor couplet to the machine to be driven, the following differential equations for electrical and mechanical balance can be written [3]:

$$V_1 \sin(\omega t + \phi_U) = i R_a + L_a \frac{di}{dt} + \frac{d\theta}{dt} \psi_m \sin\theta \quad (2)$$

$$J \frac{d^2\theta}{dt^2} = i\psi_m \sin\theta - T_{rel} \sin[2(\theta - \theta_0)] - T_{sh} \quad (3)$$

where V_m is the peak terminal voltage, ϕ_U is the voltage phase angle, i is the instantaneous stator current, R_1 is the stator winding resistance, L_1 is the stator winding inductance, J is the inertia of drive system together with the load and T_{sh} is the external load torque.

In this analyze, electromagnetic torque development of investigated types of different motor constructions and designs were carried out by software FLUX-2D [4] based on finite element method [5].

Soft magnetic composite material

The base for this composites are metallic particles (Fe, Fe-Si, Fe-Si-B, etc.), which are surrounded, at first with thin oxide layer, and then with polymer as a binding material, which has task to create a final compact product from this particles. Finally prepared mixtures are pressed in the press to form final shape.

Density of the final SMC material, the temperature, and the time of hardening, consequently, have great affect on the hardness, and magnetic features of the product [6]. In general, higher density, higher temperatures, longer time of hardening, and, at the same time, temperature processing of the material, results as the better magnetic properties of the material (higher relative permeability μ , higher magnetic induction B).

On the Fig 3 we can see microstructure of the SMC core, which was pressed out from the selected mixture. It can be seen an irregular shape of the particles and their inner porousness. Between the particles we can notice the remaining porousness and polymer isolation. Meanwhile, oxide isolation layer is too thin to perceive it at this magnification.

Plastic bonded magnets based on NdFeB and on ferrite

Magnetic phase of permanent magnets NdFeB is $\text{Nd}_2\text{Fe}_{14}\text{B}$. But these magnets “in-situ” originated composites are composed of many phases. Usually to modificate magnetic properties (higher coercivity lower magnetic remanence or vice-versa, higher Curie’s temperature, better temperature coefficient) and to improve corrosion and mechanical properties they contain other alloy supplements (Co, Cu, Zr, Ti, Cr, Ni, ...). To some other elements (C, Al, ...), which are typically for metallurgic alloy processes it is impossible to avoid. Ore deposits beside Nd contain some other rare-earth elements (La, Ce, Pr, Cy, ...), due to this, the raw stuff for NdFeB magnets production is used cheaper so-called “mish-metal”. Owing to this, the material specification is not in contain of Nd, but overall contain of rare-earth elements (TREM- total Rare Earth Metals, they have very related properties to Nd). Research show that addition of dysprosium (Dy) increase coercivity but diminish remanence, meanwhile the supplement of presidium (Pr) is more advantageous. It propitiously influence on increase of coercivity with preservation of magnetic remanence of magnets. So, general mark for these type of magnets is NdFeB, but exact mark is, for example: (Nd, Dy)-Fe-B, (Nd, Pr)-Fe-B or even $\text{Nd}_{0,09}\text{Pr}_{0,03}\text{Fe}_{0,71}\text{Co}_{0,05}\text{Zr}_{0,01}$. These subscriptions mean atomic part of elements in alloy or more exactly in composite [7].

The first and preferably used procedure to produce isotropic magnets is rapid solidification technology (RTS). Device for this technology is called melt spinner. With this device the RTS strips are produced. Their thickness is between 30-50 μm and some mm of width. The stripes are then beamed (transition from amorphous to nanocrystalline state). Finally the stripes are pulverized into chosen granulation.

NdFeB powders (MQP-B+, Magnequench. USA) were first examined with scanning electron microscope (SEM). From snap-shot (Fig. 4) it can be seen that the powder is very rough crumbed composed from sharp-edge plates irregular shapes. Between relatively rough parts are very fine particles, due to intensive crushing.

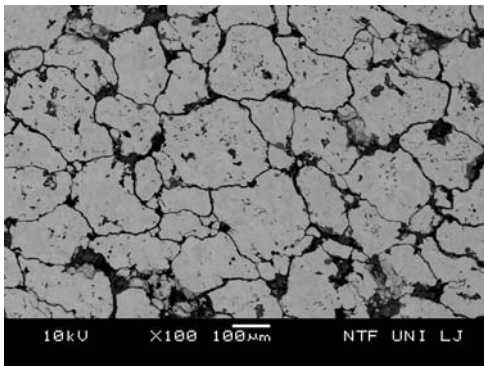


Fig. 3: SEM snap-shot of compressed SMC material

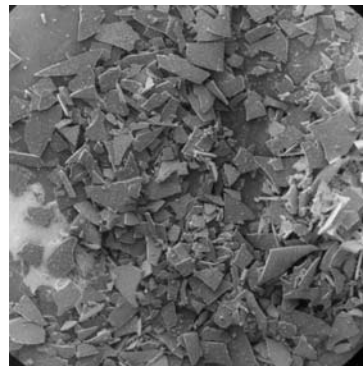


Fig 4. SEM snap-shot of MQP-B+ powder (20 times magnified)

Preparation of mixture for cold automatic one-axe pressing is with dray mixing in cylindrical mixer or in V-mixer. In these mixers the powder and araldit are mixed. Equally distributed araldit on the surface of powder is desired. In this case, the powder mix is dissolved in acetone and then mixed into uniform mixture. After that the acetone is evaporated. The mass parts are now stacked together and by pressing the mass through a strainer of convenient largeness the parts become separated from each other. The granulation is the final procedure to form final material for injection squirting. In Fig 5 the microstructure of plastic bonded NdFeB composed from MQP-B+ magnetic powder and 2.5% araldit IEVT is shown. The structure of injection squirting plastic bonded ferrite magnet powder is presented in Fig 6.

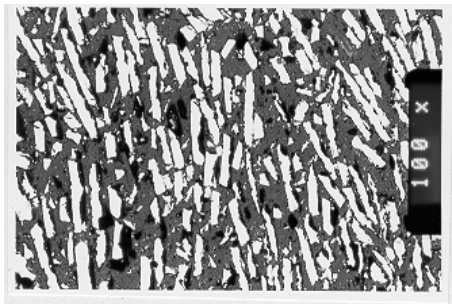


Fig. 5: Microstructure of plastic bonded NdFeB composed from MQP-B+ magnetic powder and 2.5% araldit IEVT

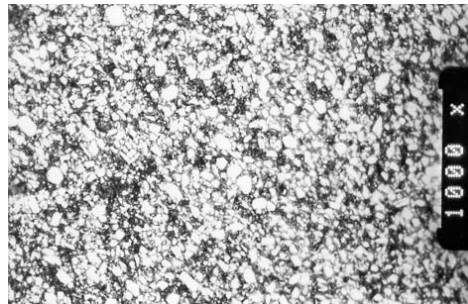


Fig. 6: Microstructure of injection squirting plastic bonded ferrite magnet powder.

Magnetic properties of injection squirted plastic bonded magnets

Typical magnetic properties of plastic bonded ferrite and NdFeB magnets are shown in Fig. 7. Also, there are presented B-H curves of classic ferrite and NdFeB magnets (Fig. 7).

Further work was in a way to produce the rotor of single-phase two-pole motor with oscillatory starting with plastic bonded magnets. In the same time the study of applying different stator materials was carried out. These materials were: laminated dynamo steel and soft magnetic composite (SMC). The goals to achieve were: new motor has to develop the same or better magnetostatic torque as reference model (laminated stator core with classic ferrite rotor), inertia has to be low as much as possible and overall price of production has to be the same or lower. Two motors were used as reference in comparison of results: Orig1 - laminated stator core with classic ferrite rotor, Orig2 - SMC stator core with classic ferrite rotor.

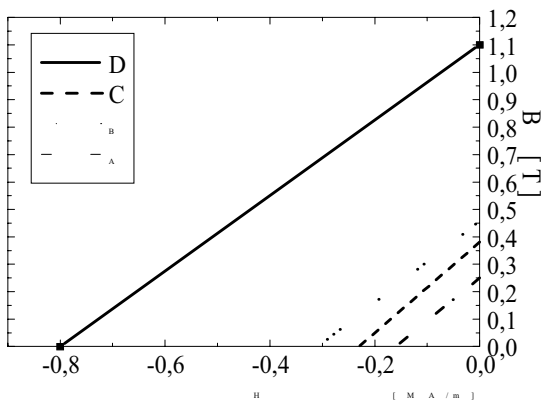


Fig. 7: B-H curves for plastic bonded ferrite (A) and plastic bonded NdFeB magnets (B) for sintered ferrite (C) and NdFeB magnets (D).

R [mm]	3	4	5	6
R_1 [mm]	1	1	1	1
R_2 [mm]	7.15	7.15	7.15	7.15
h [mm]	20	20	20	20

Table 1: Values of intermediate radius R (h – height of the rotor).

Two new rotor designs were investigated. First rotor has been a double layer type (Fig. 2). Outer layer is made from plastic bonded NdFeB magnet and inner layer from plastic bonded ferrite magnet. Magnetostatic torque calculations were made for different intermediate radius R (table 1) and for different stator materials (laminated core and SMC core). The excitation level was kept all the time at the same level. In Fig. 8 are shown the results for laminated stator core and in Fig. 9 for SMC stator core.

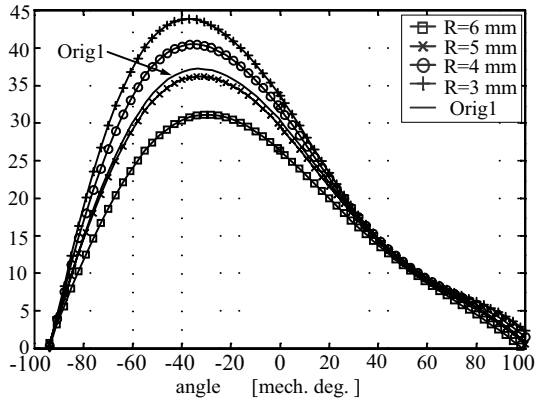


Fig. 8: Magnetostatic torque for different intermediate radius R (table 1) with laminated stator in comparison with original (Orig1).

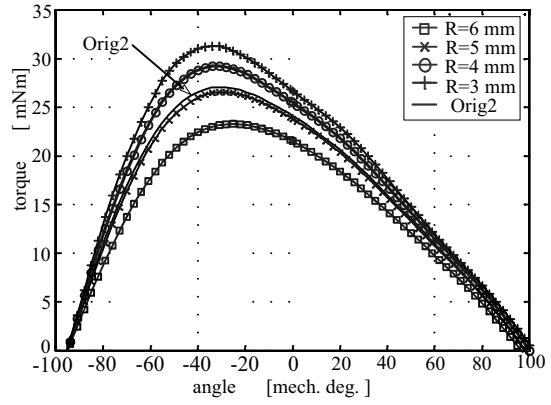


Fig. 9: Magnetostatic torque for different intermediate radius R (table 1) with SMC stator in comparison with original (Oorig2).

From Fig. 8 it is clearly that the double layer type rotor with $R < 4$ mm with laminated stator demonstrate better torque properties as original (Orig1) one. In comparison between original (Orig2) motor and SMC stator core motor with plastic bonded double layer rotor the results are also favorable to a new one for $R < 4$ mm.

Second rotor design was the same as basic one (Fig. 1), but magnet material and its properties were different. The idea was to mix (granulated ferrite with granulated NdFeB) and with injection squirting produce a new rotor. Magnetic properties of such a new magnetic material depend on contents of each basic component. The calculation of this new B-H curve was based on a volumetric proportion $V\%$ of each component. Starting point equations were:

$$(BH)_{\max,AB} = V\%_A (BH)_{\max,A} + V\%_B (BH)_{\max,B} \quad (4)$$

$$B_{r,AB} = V\%_A B_{r,A} + V\%_B B_{r,B} \quad (5)$$

$$H_{c,AB} = V\%_A H_{c,A} + V\%_B H_{c,B} \quad (6)$$

where $B_{r,A}$ (magnetic remanence), $H_{c,A}$ (coercitivity), $(BH)_{\max,A}$ (maximum energy product) are related to plastic bonded NdFeB (material A), $B_{r,B}$, $H_{c,B}$, $(BH)_{\max,A}$ to plastic bonded ferrite (material B) and $B_{r,AB}$, $H_{c,AB}$, $(BH)_{\max,AB}$ to produced mixture. In table 2 are shown typical magnetic properties of new prepared plastic bonded magnetic mixtures. The volumetric proportion was based on the volume defined by intermediate radius R (Table 1). Calculated B-H characteristics of new in different proportion mixed plastic bonded magnets are shown in Fig. 10.

name	R	V_A		V_B		$B_{r,AB}$	$H_{c,AB}$
		mm	cm ³	%	cm ³		
code3	3	2.65	84	0.5	16	0.44	292
code4	4	2.2	70	0.94	30	0.414	267
code5	5	1.64	52	1.51	48	0.37	236
code6	6	0.95	30	2.2	70	0.33	1.34

Table 2: Typical magnetic properties of new prepared plastic bonded magnetic mixtures.

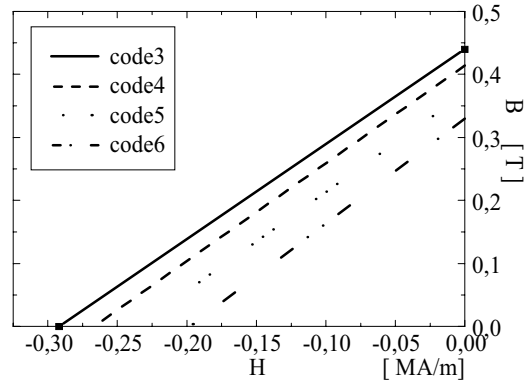


Figure 10: Calculated B-H characteristics for new in different proportion mixed plastic bonded magnets

As in the case of first type of new rotor (Fig. 2) the investigation was made for two different stator core material (laminated dynamo steel and SMC). The results of magnetostatic torque calculation are presented in Fig. 11 and Fig. 12.

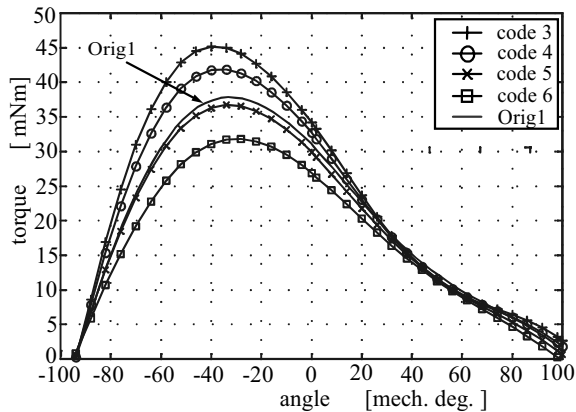


Fig. 11: Magnetostatic torque for different mixtures (table 2) with laminated stator in comparison with original (Orig1).

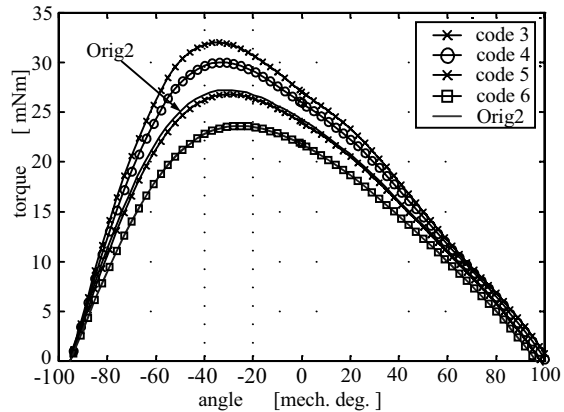


Fig. 12: Magnetostatic torque for different mixtures (table 2) with SMC stator in comparison with original (Orig2).

In Fig. 11 and in Fig. 12 can be seen the improvement in torque production in comparison with double layer rotor. Also, the manufacturing process is much simpler in the case of special magnetic mixture rotor instead of double layer rotor.

Conclusion

In the paper was presented basic theory of single-phase two-pole motor with oscillatory starting. Preparation, production, physical properties and magnetic characteristics of plastic bonded NdFeB magnet and ferrite magnet were examined and they are showing good prosperity in their further use. Also, brief description of soft magnetic composite was done. The comparison on torque capability was carried out for different combinations of stator and rotor materials. All calculations were done with finite element method with magnetostatic torque calculation. Improvement in torque production were achieved for both stator types (laminated and SMC core) with plastic bonded magnets in comparison with sintered ferrite magnet. This means with double layer rotor and with mixed plastic bonded magnets (mixture of NdFeB with ferrite). Motor with SMC stator core shows lower level of magnetostatic torque then motor with laminated stator core, regardless on rotor magnetic properties. To increase the torque different stator geometry has to be applied.

References

- [1] Jacek F. Gieras and Mitchell Wing, Permanent Magnet Motor Technology, New York, Marcel Dekker, Inc., 1997
- [2] G. Altenbernd and L. Wahner, Comparison of Fractional Horse-Power Single-Phase and Three-Phase Synchronous Motor with Permanent Magnetic Rotor, Symp. On Power Electronic, Electr. Drives, Advanced Electr. Motors SPEEDAM-92, pp.379-384, Positano, Italy (1992)
- [3] G. Altenbernd and J. Mayer, Starting of fractional Horse-Power Single-Phase Synchronous motors with Permanent Magnetic Rotor, Electr. Drives Symp., pp. 131-137, Capri, Italy (1990)
- [4] FLUX 2D, CAD package for electromagnetic and thermal analysis using finite elements, CEDRAT, October 2002.
- [5] D. Maga, R. Hartansky: "Numerické riešenia elektromechanických uloh, Trenčianska univerzita, Ludoprint Trenčín, 2001, ISBN 80-88914-29-9
- [6] B. Šuštaršič: Lastnosti kovinskih prahov, izdelanih z vodno atomizacijo, Magistrsko delo izdelano na FNT Montanistika Metalurgija, preiskovalno-tehnološka smer, mentor prof. dr. Ladislav Kosec, maj 1993
- [7] B. Šuštaršič, L. Kosec, T. Špan, M. Jelenko, M. Torkar: Instrumentirana celica za analizo obnašanja kovinskih prahov med hladnim enoosnim stiskanjem, Materiali in tehnologije, 35(2001)6.

III-16. ANALYSIS OF CORE LOSS IN VARIABLE RELUCTANCE PERMANENT-MAGNET MOTORS

Hacer Öztura

Dokuz Eylül University
Electrical and Electronics Eng. Dept.
35160 Kaynaklar Buca İzmir Turkey
hacer.oztura@deu.edu.tr

Abstract: In order to predict the motor performance more accurately, a core loss formula is derived considering the flux variation due to the magnet and the stator currents. This paper presents the result of two-dimensional finite element analysis into relationship between flux distribution and core loss in the permanent magnet motor.

Introduction

The problem of core loss calculations in electrical motors is interest for at least two reasons. First, it helps to evaluate the heat develop in the motor and secondly, motor control process take more and more sophisticated forms[1,2]. These mean needed to reduce heat and to use more powerful power electronic components.

The lack of slip rings, brushes, and field winding losses in the permanent magnet motors have always been viewed as distinct advantages over that of conventional, wound field machines[3]. Although the advantages of reduced I^2R loss in permanent-magnet motors are clear, core loss comparisons between these motors and conventional motors are cloudier. Core losses depend on numerous design and fabrication factors, such as the core form, dimensions, and material electric and magnetic properties. Steady state core loss is largely a function of the harmonic content of the core flux density.

A half portion of the motor structure used for core loss analysis in this paper is shown in Fig. 1-a. The stator of the motor has four main poles and four auxiliary poles while the rotor has four poles created by the permanent magnets. The permanent magnet material used in this machine is the Neodymium Iron Boron (NdFeB) type which is radially magnetized with 120 degrees poles in the pattern N (north) -S (south). The interpolar sections of the rotor which is the area between the permanent magnet poles are occupied by non-magnetic material represented by O[4].

The air gap flux density of the permanent magnet motor varies according to the stator current then the core loss of the permanent magnet motors is, in contrast to the induction machine, not a no-load loss [3]. So, the core loss formulation related the flux variation due to the stator windings current is required to obtain more accurate predictions. A general formulation for the core loss is used considering the flux variation in the main pole, the tooth, and the yoke due to the stator current as well as the magnet.

Electromagnetic Field Analysis

Two-dimensional Finite Element Analysis (FEA) has been performed to obtain an electromagnetic field analysis of these motors and to compute the flux density distribution on the core. FEA software used in the calculations is ANSYS.

Starting from Maxwell's equations a general formulation of the electromagnetic field for the permanent magnet machines can be expressed by in (1) [5-8]. Permanent magnets have been employed as an alternative to current carrying coils for magnetic field excitation in machines.

$$\text{Curl}(\nu \text{Curl}(\bar{A})) = \bar{J} + \bar{J}_m \quad (1)$$

Where ν is equal to $(1/\mu)$ and \bar{A} is the magnetic vector potential. \bar{J}_m is the equivalent current density corresponding to the coercive force of the permanent magnet and \bar{J} is the stator current density. The equation (1) can be used for the electromagnetic field analysis of the motor. The solution of equation (1) under load condition has provided the nodal values of magnetic vector potentials (MVP) and flux lines as given in Fig. 1-b.

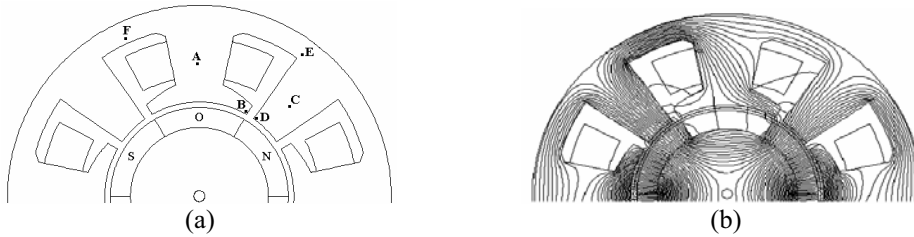


Fig.1. (a) analyzed motor geometry, (b) flux distribution of the motor

One of the most important pieces of information leading to core loss estimation is the spatial flux distribution in the iron core. Six sites were selected for the investigation of flux density variation, as shown in Fig. 1. Sites A and C are located in main and auxiliary poles and similarly F and E are located stator yoke. Sites B and D are in boundary of pole shoes. The radial and circumferential component waveforms of flux density were obtained from a sequence of finite element solutions. Fig.2 depicts the flux density distribution in selected sites.

Calculation of Core Loss

The core loss in the magnetic material occurs when the material is subjected to a time varying magnetic flux density and can be calculated from these flux densities and the rate of change of them in the stator pole and yoke. The nature of iron loss P_t can be attributed to two different components: hysteresis loss and eddy current loss [9-11].

$$P_t = P_h + P_{ed} \quad (2)$$

Hysteresis loss is due to the energy expended in the redirection of the magnetic domains of the material during every flux direction reversal. It is relatively easy to evaluate as they depend only on the peak magnetic flux density and its frequency.

$$P_h = k_h f B_m^\alpha \quad (3)$$

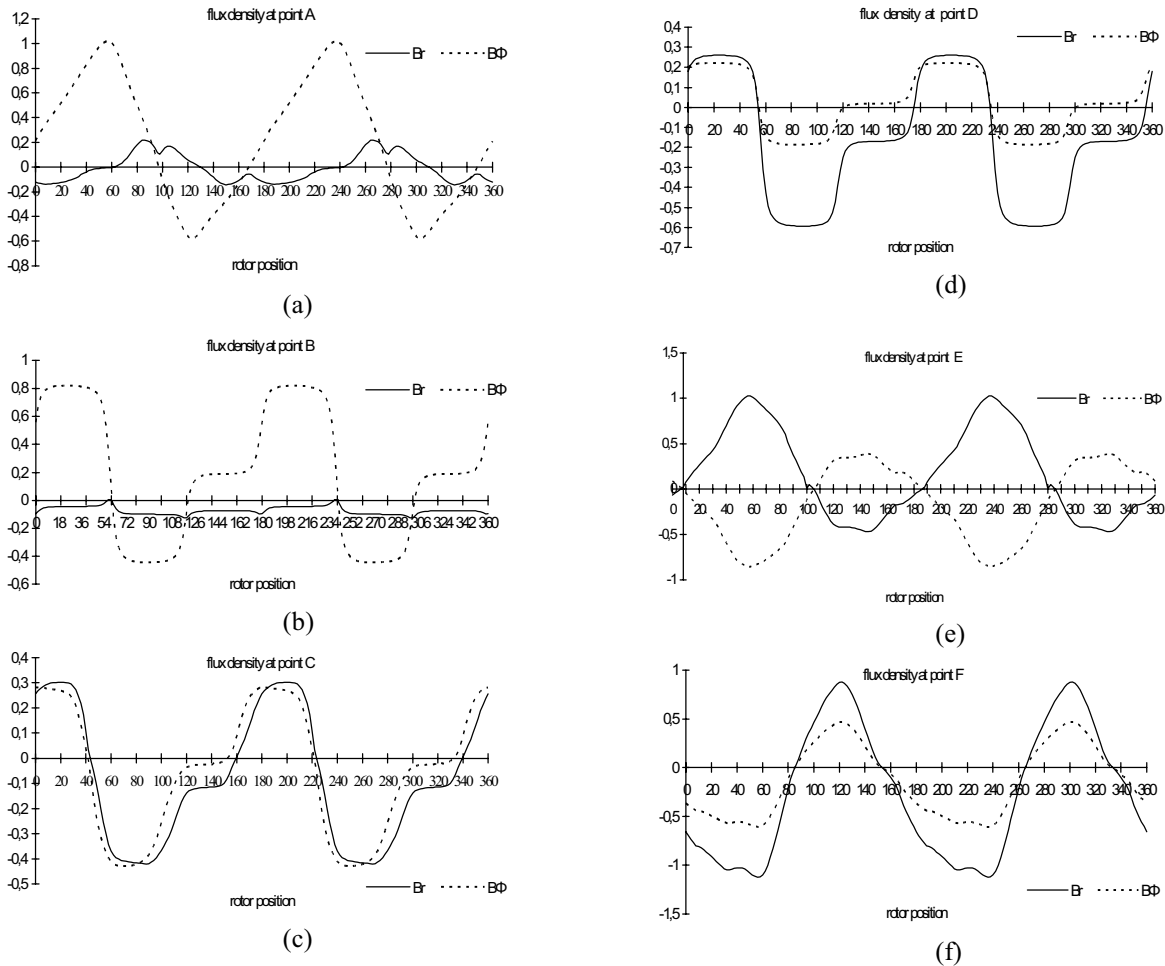


Fig. 2. Flux densities at point A, B, C, D, E, and F on the stator core

Where f and B_m are the frequency and peak value of the flux density, k_h and α are the constant determined by the manufacturer provided loss data. Eddy current losses depend also on the rate at which the magnetic flux density changes and can be expressed as two components given below [12];

$$P_{ed} = P_c + P_{exc} = \frac{\sigma d^2}{12} \frac{1}{T} \int B(t)^2 dt + \frac{k_{exc}}{T} \int |B(t)|^{1.5} dt \quad (4)$$

Where σ , d and k_{exc} are the electrical conductivity, the thickness of the lamination and the eddy current coefficient. P_c is the classical eddy current loss which is predicted on the assumption of a homogeneous flux density distribution. However, the magnetic domain structure induces eddy current concentration around moving domain walls, causing called excess loss P_{exc} . The total core losses per weight unit for a sinusoidal magnetic field are given as follows:

$$P_t = k_h f B_m^\alpha + k_e f^2 B_m^2 + k_{exc} f^{1.5} B_m^{1.5} \quad (5)$$

Fig.3 shows the calculated core loss as a function of motor speed.

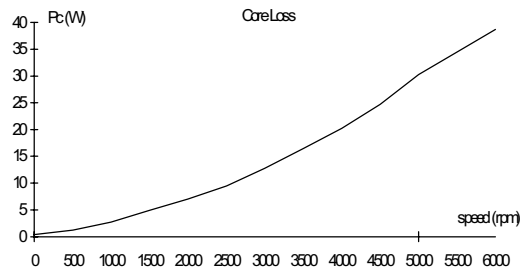


Fig.3. Calculated core loss versus motor speeds

Conclusion

A procedure has been developed to predict iron loss which is consisting of the hysteresis, eddy current and excess losses in the stator teeth and yoke, in the permanent magnet motor operating under load condition. By using two-dimensional finite element analysis, it is obtained that core losses occur mainly in the stator during the high speed operation. The finite element computation is useful in the prediction of the core losses during motor design stage before hardware prototype is built.

References

- [1] R. Rabinovici, "Eddy Current Losses of Permanent Magnet Motors", IEE Proc.-Electr. Power Appl., Vol. 141, pp 7-11, 1994
- [2] J. G. Zhu and V. S. Ramsden, "Improved Formulations for Rotational Core Losses in Rotating Electrical Machines", IEEE Trans. On Magnetics, Vol. 34, pp 2234-2242, 1998
- [3] D.H. Cho, H. K. Jung, and D. J. Sim, "Multiobjective Optimal Design of Interior Permanent Magnet Synchronous Motors Considering Improved Core Loss Formula", IEEE Tran. On Energy Con., Vol. 14, pp 1347-1345, 1999
- [4] H. Oztura and E. Akpınar, "Modelling and Analysis of a two-phase Permanent-Magnet Brushless Motor" Journal of Electric Power Component and System, Vol. 29, pp 89-104, Feb. 2001
- [5] K. J. Bins, P. J. Lawrenson, and C. W. Trowbridge "The Analytical and Numerical Solution of Electric and Magnetic Fields", John Wiley and Sons 1995
- [6] S. Chen, K. J. Binns, Z. Liu, and D. W. Shimmin, "Finite Element Analysis of the Magnetic Field in Rare-Earth Permanent Magnet Systems with Consideration of Temperature Dependence", IEEE. Tran. on Magnetics, Vol. 28, pp 1303-1306, 1992
- [7] M. Wing, & J.F. Gieras, "Calculation of the Steady State Performance for Small Commutator Permanent Magnet DC Motors: Classical and Finite Element Approaches", IEEE Tran. on Magnetics, Vol. 28, pp 2067-2071, 1992
- [8] M.A. Rahman, and P. Zhou, "Determination of Saturated Parameters of PM Motors Using Loading Magnetic Fields", IEEE Tran. on Magnetics, Vol. 27, pp 3947-3950, 1991
- [9] G. R. Slemon and X. Liu, "Core Losses in Permanent Magnet Motors", IEEE Tran. on Magnetics, Vol. 26, pp 1653-1655, 1990
- [10] F. Deng, "An Improved Iron Loss Estimation for Permanent magnet Brushless Machines", IEEE Tran. On Energy Con., Vol. 14, pp 1391-1395, 1999
- [11] R. Schiferl and T. A. Lipo, "Core Loss in Buried Permanent Magnet Synchronous Motors", IEEE Tran. On Energy Con., Vol. 4, pp 279-284, 1989
- [12] K. Atallah, Z. Q. Zhu, and D. Howe, "An Improved Method for Predicting Iron Losses in Brushless Permanent Magnet DC Drives", IEEE Tran. on Magnetics, Vol. 28, pp 2997-2999, 1992

III-17. A NOVEL AXIAL FLUX PERMANENT MAGNET MACHINE TO LABORATORY USE

A. Parviainen, M. Niemelä, J. Pyrhönen

Lappeenranta University of Technology, Department of Electrical Engineering

P.O. Box 20

FIN-53851 Lappeenranta, Finland

E-mail: asko.parviainen@lut.fi, markku.niemela@lut.fi, juha.pyrhonen@lut.fi

Abstract – The verification of the operation of any design program requires some measurement results from the actual devices. This is the situation with electrical machines also. Lappeenranta University of Technology (LUT) design and construct double-sided axial flux permanent magnet motor to the laboratory test use in order to obtain measurement results and practical experiences related to the construction of such a machine. Measurement results, obtained from the prototype machine, are used to verify the operation of analytical design program, developed for the axial flux machines by the LUT. In this paper the main features of constructed laboratory prototype machine are presented.

Introduction

In a laboratory test use, it is advantageous if there appears a possibility to use the same machine in several tests without costly and time-consuming modifications in a machine construction between the different test runs. This is especially the situation with double sided, or multi disk, axial flux machines because of the structure of the axial flux machine itself generates several interesting phenomena to be studied about. Such a phenomena are for example how uneven air gaps between the rotor disk (or disks) and stators affect to the overall performance of the machine and how the multi stator machine behaves when the machine is operating by way of one stator only. Considering the interests of electrical machine designers, the axial flux machine with two or more stators may be connected to several different electrical connections. As a result, the machine can provide measured parameter values for machine thermal- and electrical lumped parameter models verifying the calculated ones. This is advantageous for the designers working with new machine structures without previous design experiences related to similar machines. So far only few studies related to axial flux machines under this topic area are presented even though axial field PM machines have been studied with increasing interest during the last years due to their suitability to several direct drive applications such as elevators and electrical vehicles wheel motors [1]. Previously Cavagnino et. al discussed in [1] how to perform parameter identification measurements for axial field type surface mounted PM machines. Caricchi et. al introduced an interesting rotor structure and a laboratory prototype machine in [2] which is used while studying the effects of magnet skewing to the machine performance. This particular prototype machine was made purely to the laboratory test use as the one described in this paper. Braid et. al study performance of multi-disk axial flux machines with unbalanced loading [3]. Lappeenranta University of Technology build up a prototype machine to the laboratory test use in order to verify the operation of the developed design program to the design of axial field surface mounted PM machines [4]. In order to verify the operation of the design program in different situations, the prototype machine was designed such a way that a large amount of different measurement results can be obtained from the same machine without making significant modifications to the general structure of a machine. This is advantageous since it is not necessary to construct new expensive prototype machines if only small modifications are made between the tests. It is advantageous also if there appears a possibility to restore the machine to its original state after modifications. This paper discusses how the machine structure fulfilling these requirements is achieved. Furthermore, the main features of the designed machine are presented.

Prototype machine

The prototype machine is an axial flux PM machine with a configuration single rotor – two stators. Permanent magnets are Neodymium-Iron-Boron magnets and are attached on the surface of the solid iron rotor disk. Stators are operating parallel in a star connection as a default. Machine winding type is a conventional single layer winding, number of slots per pole and phase is equal to one. The main parameters of the machine are presented in Table I.

Table I. Main parameters of prototype machine.

Parameter	Definition	Value
n	Rated speed	300 rpm
T	Rated torque	159 Nm
D_{out}	External diameter of the stator	328 mm
g	Physical length of air gap per side	1.5 mm
h_m	Thickness of PM	4.0 mm

Rotor and stator structure

The rotor structure of the machine is illustrated in Fig. 1. The used rotor structure allows to change the magnets without full reinstallation of the rotor disk because of the magnets are firstly glued to additional iron plates which are then bolted to the rotor skeleton. This is a useful feature if one has to study the effects of different magnet shapes. If needed, one can change the whole rotor disk without changing the shaft because of the rotor disk is fixed into shaft via bolt joints. A non-laminated rotor disk, manufactured from magnetic iron alloy, offers possibility to run the machine as a single sided machine based to the fact that the thickness of the rotor iron is enough to keep the flux density level in rotor iron below the saturation value in a single sided operation also. Furthermore, the machine structure including deep groove ball bearings is mechanically rigid enough to handle the attractive force between the stator and rotor disk, which is 7.3 kN per stator according to performed 3D FEM analysis under load condition with nominal 1.5 mm air gap. It should be noted that in normal operation conditions the presence of another stator cancels out the attractive force between the rotor and one stator. Thus, the total axial force affecting to the rotor structure and bearings is small.

In order to align the rotor exactly between the stators, a special bearing nut arrangement was introduced. Via bearing nuts, located in both ends of shaft, it is also possible to change the rotor position inside the machine without opening the frame. Such a structure may be used when studying how the rotor misalignment affects to the performance of the machine. This structure was found to be very useful during assembling of the machine also. By the help of bearing nuts one may detach the stator and rotor if these parts snap together accidentally as it happened during the machine construction.

Two stators of the machine are manufactured from fully processed electrical steel sheet via laser cutting technique and are fixed to bearing shields via bolt joints. Each stator includes 36 slots. Due to used manufacturing technique, the obtained stator lamination stacking factor is relatively poor, namely 0.92. The stator diameter ratio was selected to be near the theoretical optimal value $\frac{1}{\sqrt{3}}$. In a proto-

type machine it is 0.6. However, this ratio was found to be slightly too small for the point of winding. It was rather time consuming to fit the end-winding in inner radius of machine to the available space. One of the machine stators is presented in Fig. 2 before and after winding.

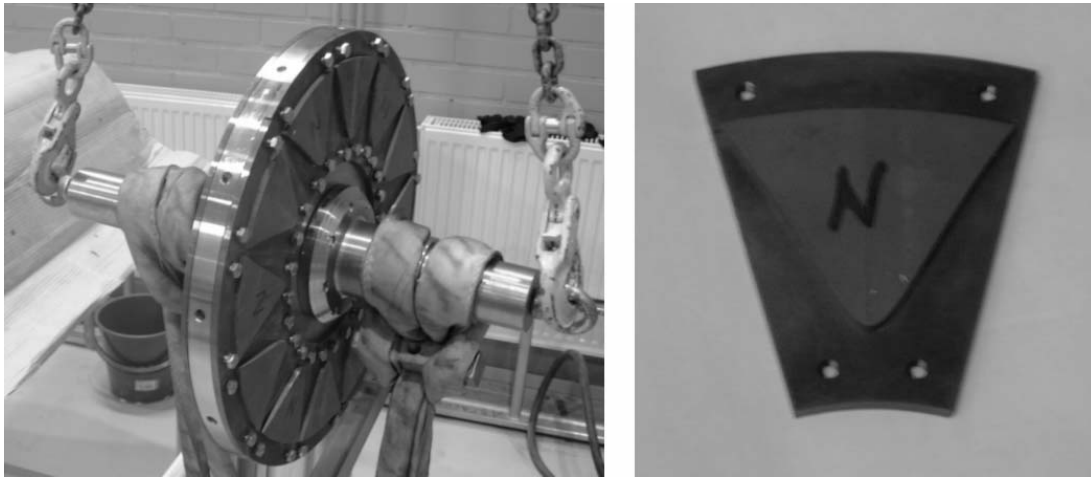


Fig. 1. Rotor during the magnet installation sequence and one of the used magnets glued to support plate.

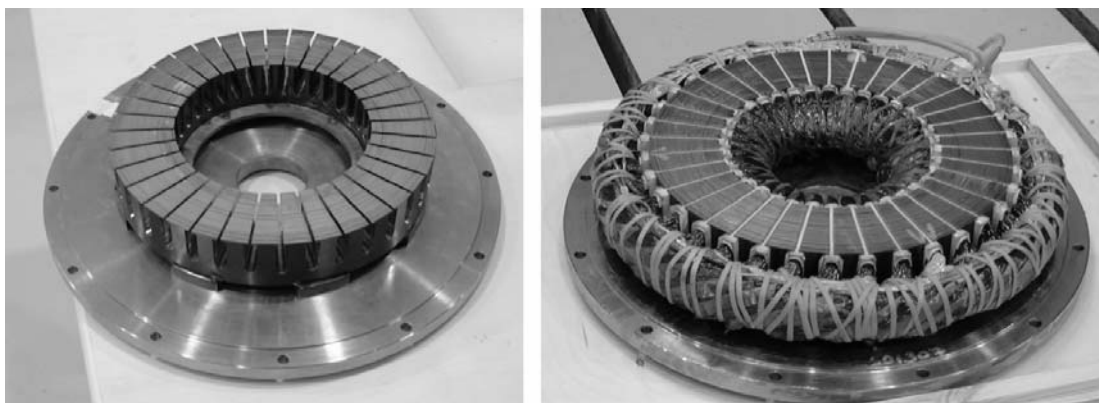


Fig. 2. One of the stators before and after winding.

Windings

In a stator winding the number of coils per pole and per phase is equal to one. Each phase coil includes 140 turns and the total number of phase turns is then 840. Both ends of the stators phase windings are available in a connection box. Thereby, it is possible to change the machine electrical connection from star connection to delta connection and to change the connection between the stators from parallel to series, or run the machine by using the one stator only. The machine is designed to operate in star connection while the stators are connected to parallel but it is possible to run the machine in different connections by modifying the machine operating point.

Temperature measurements

In order to develop an analytical lumped parameter thermal model for this machine, total 14 Pt100 thermo couples was installed to the machine frame and 6 thermo couples to the phase windings. Fig. 3 shows the machine in test bench and measured temperatures from D-side stator phase windings. Rotor

and magnet surface temperatures are measured via openings made to the frame by using infrared temperature measurement device. These openings may be closed via hatches in order to achieve a closed machine structure if needed. Internal airflow inside the machine is improved with fan arrangement. Removable fan plates are installed on the outer radii of the machine rotor forming centrifugal fan. It is shown in Fig. 3 that the improved internal airflow reduces phase winding temperature rise about 8 Celsius degrees compared to situation in which fan plates are missing.

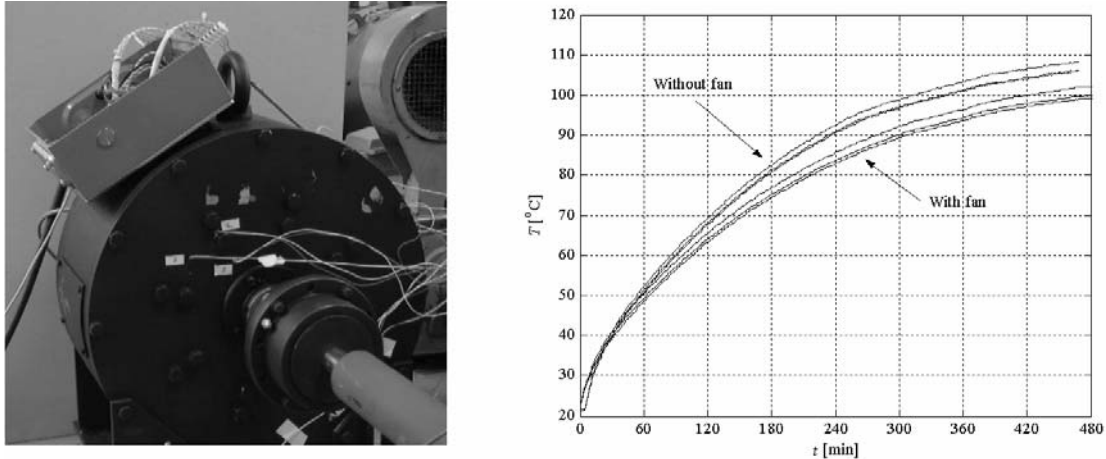


Fig. 3. Prototype machine in test bench and the measured phase winding temperatures at rated load with and without fan plates. Temperature curves are for D-side stator.

Conclusions

In a laboratory test use expensive modifications to present test machine or totally new prototypes are undesired if only small modifications are needed to introduce. In this paper a double-sided axial flux PM machine, designed to laboratory use, was described. This particular machine can be used in several studies by making modifications to machine modular construction or electrical connection with minimal work efforts.

Acknowledgements

This work was supported by ABB Oy, Finland.

References

- [1] A. Cavagnino, M. Lazzari, F. Profumo, A. Tenconi, Axial Flux Interior PM Synchronous Motor: Parameters Identification and Steady-State Performance Measurements, IEEE Transactions on Industry Applications, Vol. 36, pp. 1581-1588, 2000.
- [2] F. Caricchi, F.G. Capponi, F. Crescimbeni, L. Solero, Axial Flux Interior PM Synchronous Motor: Parameters Identification and Steady-State Performance Measurements, Conference Record of the 37th IAS Annual Meeting, Vol. 2, pp. 1295-1302, 2002.
- [3] J. Braid, A. van Zyl, C. Landy, Unbalanced Load Sharing in a Prototype Multistage Axial-Flux Permanent Magnet Synchronous Machine, Proceedings of IEMDC'03 conference, on CD: pp. 1935-1940, 2003
- [4] A. Parviainen, M. Niemelä, J. Pyrhönen, Modelling of Axial Flux PM Machines, Proceedings of IEMDC'03 conference, on CD: pp. 1955-1961, 2003

III-18. ELECTROMAGNETIC HYPERTHERMIA – FOUNDATIONS AND COMPUTER MODELLING

Jolanta Plewako, Andrzej Krawczyk, Barbara Grochowicz

Rzeszów University of Technology, Rzeszów, Poland, e-mail: jplewako@man.rzeszow.pl

Technical University of Częstochowa, Częstochowa, Poland, e-mail: krawczyk@iel.waw.pl

Technical University of Opole, Opole, Poland, e-mail: bgr@polo.po.opole.pl

Abstract – The usage of heating power as a healing system has been well-known for long time. A completely new motivation, however, came up when heat treating was recognized as a new and promising form of cancer therapy. It was found that cancer growth was stopped at temperature higher than about 42 C. It created new subject of research in the area of application of electromagnetic fields in medicine. In the paper the two main methods of heating have been described and two kinds of devices have been presented. Some advantages and drawbacks of the methods are discussed.

Introduction

Hyperthermia, a procedure in which body tissue is exposed to high temperatures (up to 42°C and above), is under investigation to assess its effectiveness in the treatment of cancer. Hyperthermia has by now become the chosen treatment for some important physiotherapeutic pathologies of the muscle-tendon apparatus, and plays a fundamental role integrating with other methodologies in the more general rehabilitating program.

Scientists believe that heat may help shrink tumors by damaging cells or depriving them of substances they need to live. They are studying *local*, *regional*, and *whole-body* hyperthermia, using external and internal heating devices. Hyperthermia is almost always used with other forms of therapy (radiation therapy, chemotherapy, and biological therapy) in attempt to increase their effectiveness.

Main problems

The wave propagates from the surface of the tissues towards the inside, and while it proceeds it is adsorbed, loosing electromagnetic energy that is transformed into heat. The mechanisms of heat deposition in tissues by electromagnetic fields is followed. When the tissue's electric dipoles (both permanent and induced) oscillate in response to the E -field of an applied wave, heat is generated by a process analogous to friction. Similarly, when free charges (electrons and ions) in the tissue are set in motion by the E -field, collisions with immobile atoms and molecules in the tissue generate heat. The propensity of the tissue to produce heat for a given sinusoidal E -field magnitude is determined by the values of the imaginary part of its relative permittivity ϵ'' and its conductivity σ . It is important that the internal E -field (i.e. the electric field inside the body) is responsible for the heat generation. In addition, the internal H -field is not directly responsible for heating because tissue has a permeability μ close to that of free space with no magnetic losses. But the time-varying H -field produces a resulting internal E -field (eddy currents) and in this way it causes heating of tissue.

The human body has an intricate structure (roughly stratified structure of the muscle-skeletal apparatus: skin, fat, muscle, bone), and that patients have a variety of physiological and psychological responses to hyperthermia treatment. The underlying principle is that a patient's responses must be monitored and considered in later designs, so as to reduce the patient's complaints and ultimately improve the efficiency by which the treatment is delivered.

From the very beginning of the application in question, there have been two essential problems to overcome:

- Generation of heat within the region of interest leaving all the vicinity of it unaffected.
- Monitoring and controlling the temperature, both in the region of interest and its vicinity.

The above problems are attempted to be solved by using different methods of heating, like capacitive, inductive, by microwave radiation, or by ultrasounds. It seems, however, that the therapy is still at the stage of medical research.

Hyperthermia in Cancer Treatment

Hyperthermia activates the immune system. In normal tissues, blood vessels open up, (dilate) when heat is applied, dissipating the heat and cooling down the cell environment. Unlike healthy cells, a tumor is a tightly packed group of cells, and circulation is restricted and sluggish. When heat is applied to the tumor, vital nutrients and oxygen are cut off from the tumor cells. Heat above 41°C also pushes cancer cells toward acidosis (decreased cellular pH) which decreases the cells' viability and transplantability. This results in a collapse of the tumor's vascular system and destruction of the cancer cells. Tumor masses tend to have hypoxic (oxygen deprived) cells within the inner part of the tumor. These cells are resistant to radiation, but they are very sensitive to heat. This is why, hyperthermia is an ideal companion to radiation: radiation kills the oxygenated outer cells, while hyperthermia acts on the inner low-oxygen cells, oxygenating them which makes them more susceptible to radiation damage. It is also thought that induced accumulation of proteins, induced by hyperthermia, inhibits the malignant cells from repairing the damage sustained.

Techniques in clinical hyperthermia can be classified into three categories:

- whole body,
- regional,
- local hyperthermia.

Whole-body heating is used to treat metastatic cancer¹ that has spread throughout the body. It can be accomplished using warm-water blankets, hot wax, inductive coils (like those in electric blankets), or thermal chambers (similar to large incubators). In *regional hyperthermia*, an organ or a limb is heated. Magnets and devices that produce high energy are placed over the region to be heated. In another approach, called perfusion², some of the patient's blood is removed, heated, and then pumped (perfused) into the region that is to be heated internally. *Local hyperthermia* refers to the heat that is applied to a very small area, such as a tumor. The area may be heated externally with high-frequency waves aimed at a tumor from a device outside the body. To achieve internal heating, one of several types of sterile probes may be used, including thin, heated wires or hollow tubes filled with warm water; implanted microwave antennae; and radio-frequency electrodes.

The two major categories of applicators are developed for electromagnetic hyperthermia:

- noninvasive applicators, which use devices external to the body to produce the internal *E*-field:
 - capacitive,
 - inductive,
 - radiative,
- invasive applicators, which penetrate the body either through the skin or in natural body orifices. The invasive applicators are listed in order of the types of external fields that are principally responsible for the internal *E*-field:
 - electrodes,
 - radiative antennas.

Capacitive Applicators

A capacitive applicator is composed of two conducting electrodes which are placed on or near the surface of the body (Fig. 1). The electrodes can have various shapes and sizes. A voltage source is connected across the electrodes, producing an *E*-field stretching throughout the volume between them. The *E*-field lines terminate on charges contained in the electrodes. Since these applicators are often intended to heat deeper tissues, the frequency of the voltage source is relatively low (in the high kHz to low MHz range).

The advantages of the capacitive-type applicator are based upon its simplicity. The placement and shape of the electrodes can be tailored to the location of the region that is to be heated. It is relatively easy to visualize the paths that the field lines take. Also, the electrodes can be curved to match the skin contour.

¹ Cancer that has spread from the place in which it started to other parts of the body

² Bathing an organ or tissue with a fluid. In regional perfusion, a specific area of the body (usually an arm or a leg) receives high doses of anticancer drugs through a blood vessel. Such a procedure is performed to treat cancer that has not spread

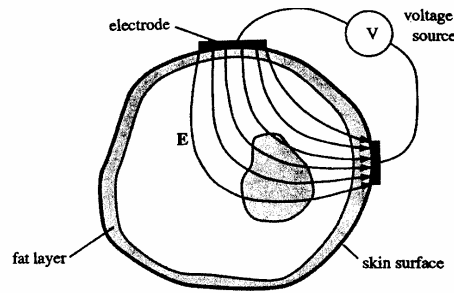


Fig. 1. Simple example of a capacitive applicator [1]

The drawbacks of this type of applicators are that the fields generated in the tissue are not optimum for preferentially heating deep tumors because the E -fields are mostly perpendicular to the body surface, where there are fat layers and if muscle or muscle-like, tissue is beneath the fat. The boundary conditions for normal E -field components combined with the lower permittivity of fat means that the E -field in the fat is much higher than in the muscle. Even though fat is less loss, the higher E -field results in higher energy deposition, often overheating the fat layer. A common tendency with capacitive applicators is to burn areas on the surface of the body when attempting to heat deeper tissue. The E -fields concentrates at the edges of metallic electrodes. Spots on the skin are vulnerable to burns near the corners of the applicator. To reduce this problem by spreading out the fields, water boluses (nonmetallic containers of water) are sometimes placed between the electrodes and the skin. The water in the bolus can even be chilled and recirculated to provide some conductive cooling of the skin.

Inductive Applicators

In this type of applicator, an external coil or some other means of generating high currents near the body is used to produce an H -field inside the body (Fig. 2). The magnetic field itself, according to the mechanism of heating described above, does not produce any heat, but if the H -field is time-varying it will induce an internal E -field for heating. These applicators are generally provided to deep heating, which suggests again lower frequency. However, since the generation of the *internal* E -field is proportional to the time rate of change of the H -field, the frequency should be high enough to produce a sufficient internal E -field. Operating frequencies are generally in the low MHz range.

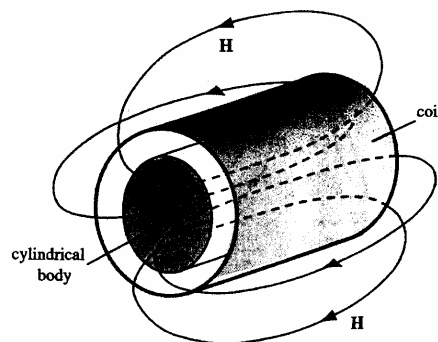


Fig. 2. Simple example of an inductive applicator for hyperthermia [1]

The H -field lines run longitudinally through the body, then encircle the coil outside the body because H -field lines must close upon themselves. Depending on the exact geometry of the coil windings and the size of the body, the density of the H -fields inside any cross section of the body can be fairly uniform. Other forms of coil applicators can also be used, such as pancake coils or saddle-shaped coils, or specially shaped conductors that bring currents to the surface of the body.

All inductive applicators share common advantages and disadvantages.

One advantage of this type of applicator is its relative insensitivity to the coupling conditions (since tissue is nonmagnetic, the exact position of the body with respect to the coil does not affect the H -field pattern). It is comfortable for patient because it allows him moving without any harm of treatment. In addition, the tuning of the coil in the resonant electrical circuit of the source is forgiving of exact body positioning.

One disadvantage is that centrally located tumors would not be heated effectively. Heating is greatest at the periphery, so surface heating is a major concern with inductive applicators, as it is with capacitive applicators. Because the E -field lines are produced by the time-varying H -field they encircle the H -field lines. There is a center of rotation for the E -field and here the field is zero. Also, eddy currents are zero in tissue. The field and current grow linearly toward the periphery of the cylinder. Because power deposition P is proportional to the square of the E -field, the heating pattern has a parabolic shape.

If the tissue properties are not uniform as in this simple example, eddy currents will not follow a radially linear profile and will be more irregular. This sometimes can be used to advantage. For example, a high-conductivity tumor surrounded by lower conductivity tissue will have a local eddy-current pattern flowing around the approximate center of the tumor. The local eddy-current patterns can lead to increased heating of a deep tumor, but the amount of improvement depends on the conductivities of the tissues involved, which may vary considerably from case to case.

Radiative Applicators

This class of applicators relies upon the coupling of E and H to carry electromagnetic energy into the tissue. They operate either at higher frequencies when localized surface heating is needed or at lower frequencies when deeper penetration is desired. The applicator and feed configurations are chosen to maximize the coupling of the launched wave into the tissues. One version of a radiative applicator is shown in Fig. 3. It basically consists of an open-ended waveguide that is coupled to the skin with a quarter-wavelength matching slab. The waveguide is loaded on both sides with dielectric strips. This produces a mode structure, thus giving a more uniform pattern in the transverse direction than an unloaded waveguide. The size of the waveguide dictates its relatively high operating frequency, namely 2450 MHz, so it is appropriate for heating superficial tumors.

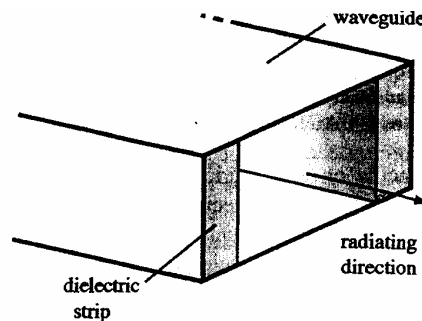


Fig. 3. A radiative hyperthermia applicator consisting of an open-ended waveguide[1]

To make the applicator size more compact, microstrip radiators have also been developed. These applicators are lightweight and can even be made flexible, so they are more convenient to use than the larger, heavier waveguides. They operate at higher frequencies (433 MHz to 2450 MHz), so they are meant for localized superficial heating. All electromagnetic radiative applicators face the same tradeoff between depth of penetration, applicator size, and localizing ability. Fig. 4 shows the penetration characteristics for planewaves of various frequencies into a dielectric halfspace whose properties are similar to those of muscle. The higher-frequency waves are clearly attenuated quickly by the tissue due to their high loss. Although the waves coming from practical applicators are not planewaves and the body certainly is not an infinite halfspace, this same general behavior is expected to apply to radiative applicators. Note from Fig. 4 that to penetrate to reasonable depths (say, beyond 7 or 8 cm), the frequency must be about 100 MHz or lower. The wavelength in muscle, therefore, is quite large—about 30 cm.

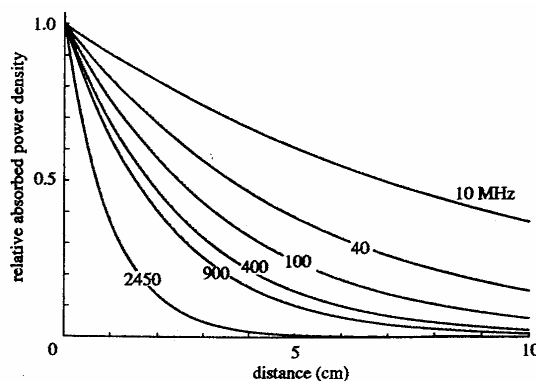


Fig. 4. The penetration of planewaves of various frequencies into a dielectric halfspace with the properties of muscle [1]

A radiator is not very effective unless at least one dimension of the radiating structure is one-half of a wavelength or larger. If the frequency is lower, the applicator will be even larger. This means it will be rather bulky and heavy, and more important, the energy coming from the applicator will spread out due to diffraction. Localized heating is difficult at the low frequencies that will penetrate deeply. They are drawbacks of this type of applicators.

Ultrasound waves obey these same laws but with different constants and with a much different outcome. Ultrasound's advantage of being able to penetrate deeply with small-wavelength beams is one reason ultrasound energy is being seriously considered for hyperthermia therapy. A disadvantage, however, is that ultrasound will not effectively penetrate bone or air, so treatment is limited to regions of the body where access is through soft tissue.

Invasive Applicators

To circumvent the difficulty of obtaining deep, localized heating patterns from external electromagnetic applicators, some investigators use invasive probes. These probes are placed in natural cavities of the body (if the tumor is nearby) or directly through the skin. The cavity applicators are often designed as thin radiating antennas. Higher frequencies are used to get good radiation efficiency from the small antennas, and penetration depth is not as critical as with external applicators. The probes that pierce the skin may also be small radiating antennas or may be an array of lower-frequency electrodes. In the latter case, conduction current in the tissues produces the heating.

The advantage of invasive probes is that the heat can be localized with more precision and in a smaller volume at depth than with external applicators. One disadvantage is much more uncomfortable for the patient. Also, even using multiple probes does not assure uniform heating; there still may be considerable non-uniformity to the power deposition pattern depending on the placement and individual patterns from the probes.

Hyperthermia Simulation and Treatment Planning

As part of a bigger research project (Sonderforschungsbereich "Hyperthermia: Scientific Methods and Clinical Applications") new algorithms for simulating and planning regional hyperthermia are developed at ZIB. These include methods for segmenting medical image data, generating tetrahedral patient models, solving Maxwell's equations and the problem of heat transport, as well as novel visualization methods. All these methods are integrated into a single, flexible, easy-to-use software system, called *HyperPlan*.

HyperPlan is able to simulate of the electric and thermal processes in the patient's body numerically. In order to perform a complete simulation some intermediate steps have to be executed. For every step a set of special-purpose modules is provided. All steps can be controlled by means of 3D visualization methods. In order to simulate the electric and thermal processes in the patient's body two different mathematical equations are solved in *HyperPlan*, Maxwell's equation in inhomogeneous media and the bio-heat transfer equation. This is achieved by means of modern adaptive multi-level finite-element methods. These methods require the user to create a tetrahedral model of the patient, describing the shape of the tumor and of other tissue compartments. Tools to carry out this task are integrated into *HyperPlan*. As a result, electromagnetic fields and power deposition in the patient's body are obtained. Using this information, a temperature distribution is calculated in a subsequent step. Finally, an optimized setting of applicator control parameters is computed.

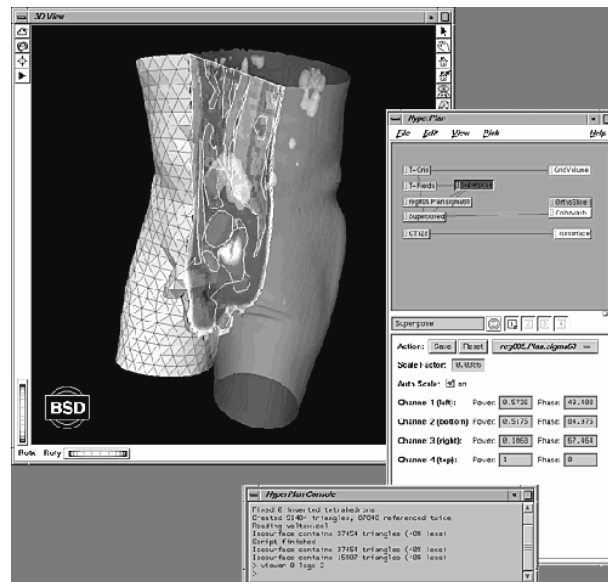


Fig. 5. System overview

Summary

It should be clear from the previous discussion that one area that remains problematic with electromagnetic hyperthermia is the ability to heat deeply in a well-controlled and localized manner. Too often there is surface overheating that accompanies deep heating, regardless of the type of applicator used. Based upon the concepts of electromagnetics, it seems unlikely that this problem will be easily solved. When localized superficial heating is desired, on the other hand, several of the approaches, in particular the small radiating applicators, are successful. Other engineering issues remain. These include the need for multiple-point temperature measurements for accurate and thorough monitoring. Treatment planning will require accurate characterization of the applicator deposition pattern and the tissue parameters, as well as a numerical technique to predict the resultant heating pattern. Tissue perfusion significantly modifies the temperature distribution for any given power deposition pattern, often in a time-variable and unpredictable way. Still, the promise of even a partially successful therapy for cancer spurs the continued study of hyperthermia.

References

- [1] C.H. Durney, D.A.Christensen, *The Basic Introduction to Bioelectromagnetics*, Boca Raton: CRC Press, 2000
- [2] W. Andra, H. Nowak, *Magnetism in Medicine*, Berlin:Wiley-VCH, 1999
- [3] M.W. Dewhirst, T.L. Phillips, T.V. Samulski., RTOG quality assurance guidelines for clinical trials using hyperthermia. *Int. J. Radiation Oncology Biol. Phys.*, 1990; 18:1249-1259.
- [4] M.J. Piket-May, A. Taflove, W.C. Lin, D.S. Katz, V. Sathiseelan, B.B. Mittal, Initial results for automated computational modeling of patient-specific electromagnetic hyperthermia, *IEEE Trans. Biomedical Engineering*, 1992; 39: 226-237
- [5] H.A.Vera, Q.J.E.Chong, S.L. Leija, M.Y.Hernández, Electromagnetic hyperthermia: an adjuvant treatment on cancerous cells, biological and physical principles, *Rev Mex Ing Biomed* 2001; 22 (2): 78-88
- [6] T. Sugahara, I.Yamamoto, V.Ostapenko, How to develop hyperthermia equipment for deep-seated tumors, <http://www.taishitsu.or.jp/hyperthermia/hp1-e.html>
- [7] <http://www.nebraskahealthsystem.com/cancer/cancer.cfm>
- [8] <http://www.esho.info/professionals/hyperthermia/>
- [9] <http://www.veramed.de/index2.html>
- [10] <http://www.hot-oncotherm.de/english/prof/index.htm>

III-19. 2D FEM ANALYSIS OF 3D MAGNETIC STRUCTURES BY USING TOPOLOGICAL TRANSFORMATIONS. APPLICATION TO THE DESIGN OF A MICRO-RELAY

J. Roger-Folch¹, E. Gómez², M. Riera¹, V. Lázaro¹

¹Dpto. de Ingeniería Eléctrica. ETSII. Universidad Politécnica de Valencia.
PO Box 22012, 46071 Valencia, Spain. E-mail: jroger@die.upv.es

²Dpto. de Ingeniería Eléctrica. Universidad Politécnica de Cartagena.
Campus Muralla del Mar, 30202 Cartagena (Murcia), Spain. E-mail: emilio.gomez@upct.es

Abstract— The main objective of this paper is to provide some specific ideas that are appropriate for the design of magnetic circuits, particularly a new industrial micro-relay prototype. The authors needed to obtain a micro-relay which had to comply with severe restrictions on volume, cost and technical –Ampere-turns, operational parameters–specifications. Given the lack of any symmetry in the relay, in the early analyses, a 3D Finite Element model was necessary to use. Due to the geometry of this device – particularly its airgap–, time consuming computations were required to obtain the torque with the required reduced margins for error. Therefore, this strategy was not considered suitable in the early steps, when a lot of parameters had to be set; consequently, to outline the preliminary design of the micro-relay, two different 2D Finite Element models were used. Particularly, approximate results using a single analysis were obtained with one of these methods, being verified with a computed –3D Finite Element Method. Subsequent 3D analyses were performed to calculate the effect on technical parameters –torque– of modifications in the preliminary design.

Introduction

The design of electrical devices using numerical techniques can be summarized as follows. Firstly, the design engineer, using relatively simple rules, obtains a design prototype. This prototype is analyzed using the Finite Element Method (FEM). In this way, performance is estimated before construction. If the computed performance meets the required specifications, the prototype is considered satisfactory; if not, adjustments are made and the new performance recomputed. Besides, these analysis strategies must be quick and accurate; speed is essential when several steady-state analyses for each design prototype are calculated, or several alternatives are taken into account. Accuracy is important to ensure that the performance is reliably predicted, so error is minimized and therefore the risk of manufacture modifications can be also reduced.

The design process mentioned above can be achieved with two ways. In the first method, the engineer evaluates each analysis modifying the model until reaching the initial specifications. In the second method, these modifications are achieved with automated mathematical methods. The design of electromagnetic devices using optimization techniques is a problem often complex, non-linear and multi-modal. Therefore, the optimization process is time-consuming if the finite element method is employed and so, many researchers are devoted to minimize this computational effort. Until recently, shape optimization of 2D electromagnetic devices by using sensitivity analysis has been widely used, [1][2][3][4]. However, the configuration of many of the electromagnetic devices has become increasingly complicated, and therefore in some cases 2D models can not be obtained, or at least a 2D model is not obvious and so, some authors are applying 3D models from the initial stages of the design process, [5]. Nevertheless, 2D simplified FE models have been obtained in certain problems, like induction machines with skewed slots, [6][7]. Here, the 2D simplified model is attacked from the point of view of the flux path in the magnetic structure.

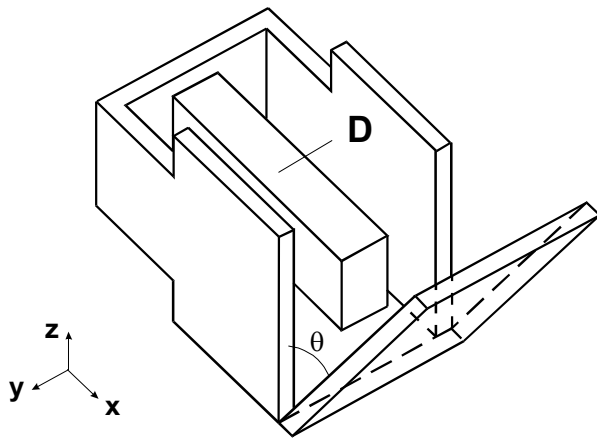


Figure 1. Magnetic structure (complete)

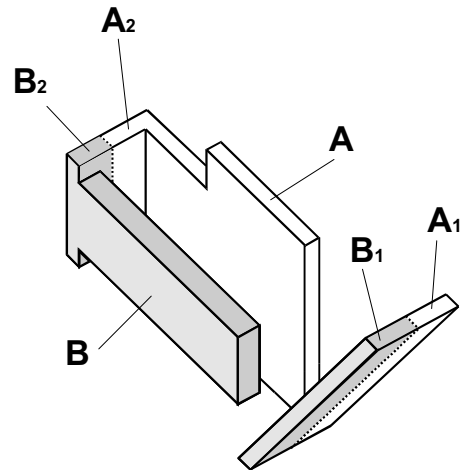


Figure 2. Magnetic structure (using symmetry)

Our research group, having experience in FEM, needed to develop a micro-relay in a short time. The aim of the work was to provide some prescribed performance (characteristic curve), taking into account behavior, geometry and cost, during the micro-relay design synthesis. The characteristic curve is the relationship between the torque (force) and the angle (air-gap distance) during the switching-on process. The group decided to search for a non-automated method for obtaining a prototype sufficiently optimized, even if it was not the mathematically optimal. This paper provides a brief summary of this study.

The initial design of the micro-relay (figure 1) was not symmetrical lengthways, being the coil wound on piece D. This characteristic made difficult that a simple 2D model was obtained, carrying out a time consuming 3D model, even when symmetry was taken into account (figure 2), as a first option. However, this strategy was not considered suitable for the early design stages where several alternatives had to be compared. To speed-up the calculations, several 2D models were developed. The reduction of CPU time of 2D models implied a reduction in accuracy as well. Therefore, a compromise solution was adopted, accomplishing a reasonable computing time in these steps of the design process, with limited margins for error in accuracy. Two 2D methods accomplished the above requirements. The first one is a 2D model obtained using several geometrical transformations. This 2D model is proposed as magnetically equivalent to the initial 3D model. In the other method, several parallel sections or slices are considered (2½D FEM). In the final steps of the design process, the margins for error in accuracy are reduced to minimize the post-manufacture modifications using complex and time consuming 3D models.

Proposed 2D FEM model

In the first model (proposed 2D FEM), a 2D analysis is applied using a modified 2D model. This 2D model is equivalent to the 3D model, from a magnetic point of view. It can be obtained by using several transformations. This transformation process can be described in three steps.

- 1) Figure 3 is obtained by cutting the 3D symmetrical model presented in figure 2, rotating AA_1A_2 and BB_1B_2 .
- 2) Figure 4 is obtained by rotating 90 degrees the pieces A1, B1 and A2, B2 and so, the magnetic flux path in 3D is “confined” in the same plane, where are placed all the components of the micro-relay.
- 3) Figure 2 and figure 4 will be magnetically equivalent when the path of the magnetic flux is the same. It can be achieved by adding two pieces of a material with ideal infinite permeability between A1 and B1 and A2 and B2, figure 5. In the same figure, some

observations can be taken into account: the coil is shown and termed C, and the pieces A1 and B1 are not fixed and their position depends on the angle θ , figure 1.

It can be observed that the reluctance of this modified magnetic circuit is the same as the real 3D circuit, with the exception of the value of the leakage flux.

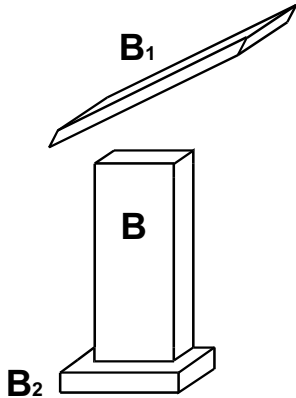


Figure 3 Proposed 2D FEM model. Step 1 of 3

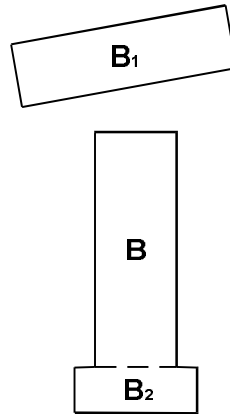
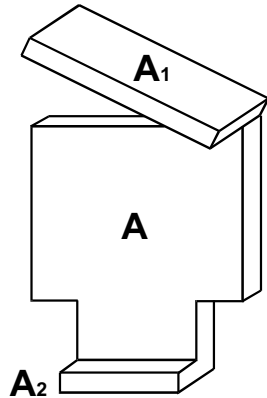


Figure 4. Proposed 2D FEM model. Step 2 of 3

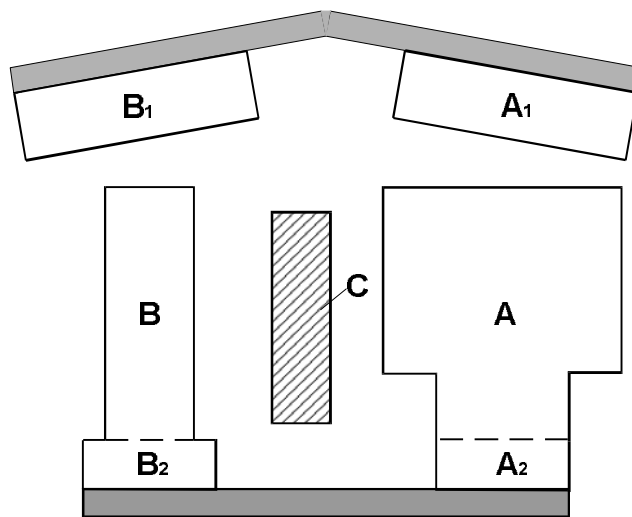
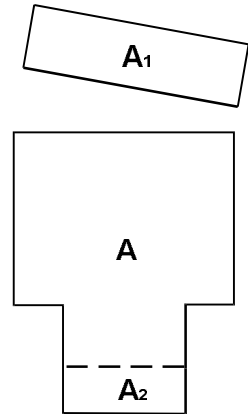


Figure 5. Proposed 2D FEM model. Step 3 of 3

2½D FEM

In the second model (2½D FEM or multi-slice) several sections parallel to the xy plane (figure 1) are considered. Each section is independently modeled with 2D FEM and the force on the mobile piece is computed as $f(x)$ in figure 6. The total torque on the mobile piece is calculated taking into account the contribution of the different sections. Using this method, the solution is accurate when the angle θ is null (all the sections are the same), and therefore the magnetic field is two dimensional. When the angle (θ) is not null, the density of the flux lines in the air gap is higher near the rotation axis, otherwise the density of the flux lines will be approximately constant in the core and therefore the magnetic flux density will be approximately constant as well. When the 2½D FE method is applied to a micro-relay with non-zero θ , the sections near the rotation axis will be much more saturated.

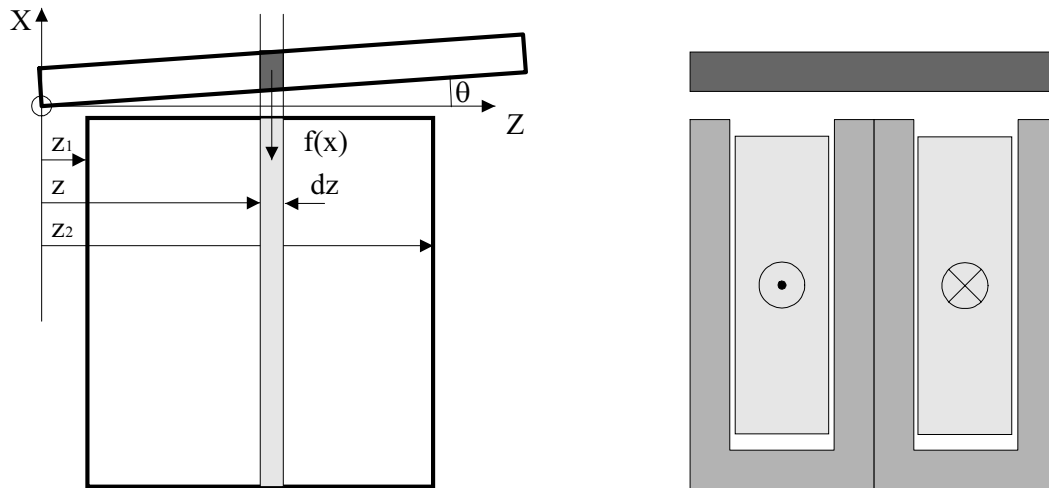


Figure 6. 2½D FE method

3D FEM

The validity of the previous 2D models was assessed by torque computations using this 3D model. Besides, this 3D model was used to obtain accurate torque calculations in the final stages of the design process where modifications in the micro-relay geometry could not be taken into account with the 2D FEM models.

To accomplish the above requirements, the 3D model of the micro-relay had to predict accurately the torque. So, to reduce the margins of error in the computation of torque in 3D FEM analysis, the density of elements and nodes must be adequate. The error in torque (force) computed using 2D/3D FEM depends on the quality of the mesh employed. Basically, all of the methods of force calculation compute small variations in the finite element solution. So, the flux density is obtained by calculating the curl of the magnetic vector potential, and therefore an error is introduced by these mathematical operations. Finally, the flux density computed in this way is squared and the error in the computed force is increased; therefore the density of the elements must be adequate in all the areas, especially in the airgap and its surroundings. Using a mesh with over 100.000 elements, several hours were necessary to solve the model, instead of several minutes in 2D computations, using the ANSYS© package on a Convex S-Class computer with 16 CPU's (PA-8000).

Results

The above models have reflected substantial differences in CPU resources, specifically between the proposed model with a single 2D analysis and the 3D FEM model. The use of this 2D model would speed up the preliminary design –by testing different modifications in the magnetic structure– if its results were accurate enough.

Several alternatives have been computed with the three methods. Figure 7 shows and the computed torque versus angle with the 3D FEM model ($T_{\text{FEM-3D}}$), the proposed method using 2D FEM ($T_{\text{FEM-Proposed-2D}}$) and the 2½D FE method using 2D FEM ($T_{\text{FEM-Multisection-2D}}$). The agreement between 3D FE model and 2D FE models is good, specifically in the proposed method. So, approximate results can be obtained solving one analysis with the proposed 2D FEM model instead of several analyses using the 2½D FEM. The differences are because of the leakage flux in 2D and 3D analyses are not the same.

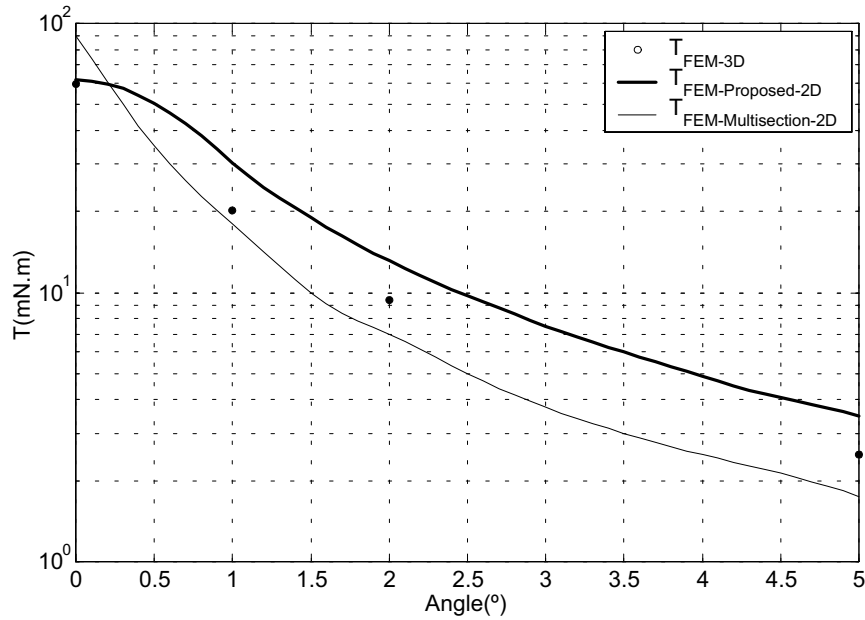


Figure 7. Computed torque versus angle (θ)

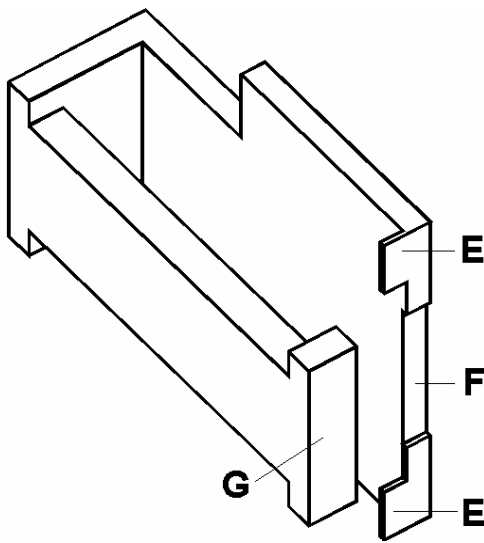


Figure 8. Magnetic structure with three new elements (E,F and G)

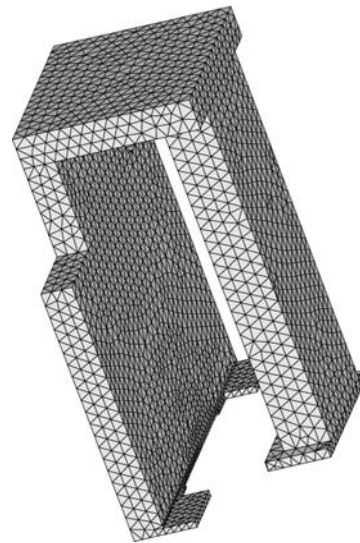


Figure 9. Mesh of the structure shown in figure 8

The 3D FEM has been employed to analyze the effect of the final modifications on the characteristic curve. The analyses showed that small changes in some parts of the magnetic circuit significantly modify the curves. Figure 8 shows the changes in the magnetic structure when three elements termed E, F and G were added to the initial 3D structure (figure 1), figure 9 shows its mesh. Table I shows the computed torque in the magnetic structures shown in figures 1 and 8 for four different values of θ (0, 1, 2 and 5 degrees). The torque calculated in the structure shown in figure 8 is seen to be significantly greater than the one obtained without these new added elements (figure 1) when θ is greater, even greater than the prescribed load torque. The performance of this new design met the required specifications (torque, volume and cost), considering this prototype satisfactory from these points of view.

Table I. Computed torque using 3D FEM

	Torque (mN.m)			
	0°	1°	2°	5°
Initial structure (figure 1)	59.66	20.22	9.39	2.49
Final structure (figure 8)	46.11	21.12	12.31	3.70

Conclusions

This paper has outlined three methods for analyzing a magnetic structure (micro-relay) using FEM. Two of the methods (2D FEM) gave a sufficiently accurate steady-state performance prediction in the early steps of the design process, using a modest amount of computer resource and therefore speeding up the results in these stages. This paper proposes a quick method to obtain approximate results using 2D instead of 3D models and solving the 2D FEM model obtained by geometrical transformations in just one step when the object is not symmetrical lengthways. This approach will be especially useful for the first steps of an industrial design process. The final steps are made with a 3D model. Besides, the 3D FEM model was employed to analyze the effect on the torque of small modifications, so that post-manufacture modifications could be minimized.

In conclusion: using the proposed method, we have obtained a prototype of a micro-relay which performs better than other relays – for the given operational parameters, meeting the initial geometrical restrictions, and exceeding the minimal prescribed characteristic curve.

References

- [1] P. Di Barba, A. Savini, Recent Advances of Automated Optimal Design in Low-Frequency Electromagnetics, COMPEL, Vol. 17 (1/2/3), pp 29-35, 1998
- [2] D. N. Dyck, D. A. Lowther, A Method of Computing the Sensitivity of Electromagnetic Quantities to Changes in Materials and Sources, IEEE Transactions on Magnetics, Vol. 30 (5), pp 3391-3394, 1994
- [3] P. Neittaanmäki, M. Rudnicki, A. Savini, Inverse Problems and Optimal Design in Electricity and Magnetism, Clarendon Press, 1996
- [4] K. Rashid, J.A. Ramírez, E.M. Freeman, M. Farina, J.K. Sykulski; A comparison of two generalized response surface methods for optimization in electromagnetics, COMPEL, Vol.20(3), pp.740-752 2001
- [5] S. Wang, J. Kang, Shape Optimization of BLDC Motor Using 3-D Finite Element Method, IEEE Transactions on Magnetics, Vol. 36 (4), pp 1119-1123, 2000
- [6] S. Williamson, T. J. Flack, A. F. Volschenk, Representation of Skew in Time-Stepped Two-Dimensional Finite Element Models of Electrical Machines, IEEE Transactions on Industry Applications, Vol. 31(5), pp 1009-1015, 1995
- [7] J. Roger-Folch, V. J. Lázaro, E. Gómez, Analysis of skewed slots in induction machines by using 2D finite element method, COMPEL, 17 N.1/2/3, pp 212-218, 1998

III-20. HEALTH EFFECTS OF BASE STATIONS

Ozge Sahin

Dokuz Eylul University, Department of Electrical and Electronics Eng.
35160 Buca, Izmir-TURKEY
ozge.sahin@eee.deu.edu.tr

Abstract - Mobile phones and their base stations transmit and receive signals using electromagnetic waves. In this study, effects of RF radiation from mobile phone base stations on human health have been examined extensively. Researches and international regulations in this matter are compared with the measured values in Turkey in order to make it clear if base stations are threatening our bodies, and so our lives. Then, a conclusion has been obtained related to the health effects of base stations.

Introduction

Radio frequencies constitute part of the overall electromagnetic spectrum. Cellular communications systems use frequencies in the 800-900MHz portion of the Radio Frequency (RF) spectrum, and transmitters in the Personal Communications Service (PCS) use frequencies in the range of 1850-1990MHz. Each base station is a low power radio station that serves users in a small geographic region called a cell. Cell phones operate by communicating with a nearby base station. The antenna of the base station is usually mounted on a tower, the roof of a building, or on another structure that provides the required height for proper coverage. Apart from concerns about aesthetic/visual impacts of antenna towers, many individuals have expressed concern about possible health risks of RF radiation from these installations, particularly for people residing close to the antennas.

Base Station Antennas

Cellular communication systems require the use of many base stations located throughout a service area. When a user places a call, his or her handset communicates with a nearby base station, which then relays the call to a central switching office and then to the conventional land line telephone network. As the user moves about, he or she is “handed off” to other base stations. As the system grows, base stations are installed closer together (to increase capacity) but operated at lower power levels (to prevent interference among base stations).

The RF patterns for different types of antennas are very different. For a low-gain antenna with a 1000W ERP (Effective Radiated Power) of the type formerly used by many cell phone base stations, the pattern can be shown in Fig.1, and for a high-gain (sector) antenna of the type used in many of the newer base stations, the pattern can be shown in Fig.2 [1].

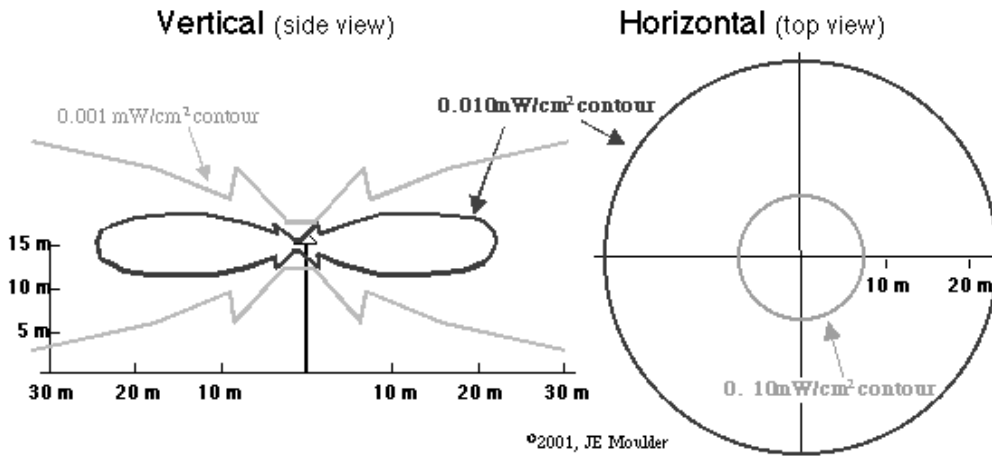


Fig. 1. Low gain antenna pattern

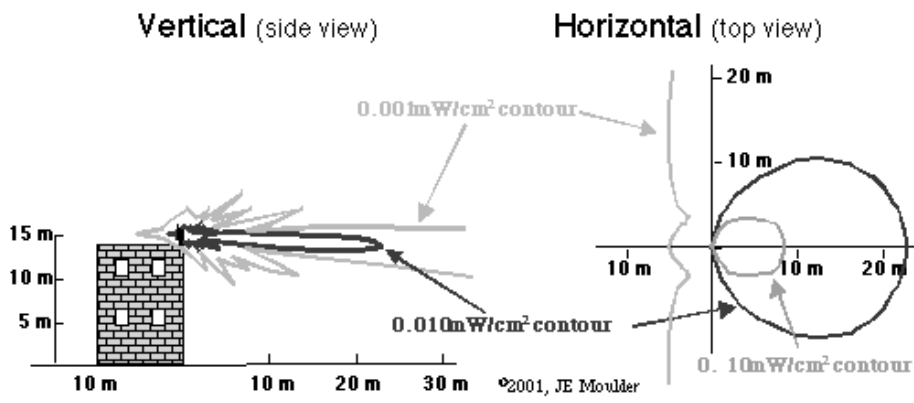


Fig. 2. High gain antenna pattern

Exposure Limits

There are various organizations in the world which produced guidelines for RF exposure limits [2]. Table 1-(a) and (b) summarizes FCC (U.S. Federal Communications Commission) major exposure guidelines at frequencies used by cellular and PCS communications systems for controlled and uncontrolled areas [3].

Table 1. FCC Limits for Maximum Permissible Exposure (MPE)

(a) Limits for Controlled* Exposure

Frequency Range (MHz)	Electric Field Strength (E) (V/m)	Magnetic Field Strength(H) (A/m)	Power Density (S) (mW/cm ²)	Avg. Time E ² , H ² or S (minutes)
0.3-3.0	614	1.63	(100)*	6
3.0-30	1842/f	4.89/f	(900/f ²)*	6
30-300	61.4	0.163	1.0	6
300-1500	--	--	f/300	6
1500-100,000	--	--	5	6

* Controlled environments are locations where there is exposure that may be incurred by persons who are aware of the potential for exposure.

(b) Limits for General Uncontrolled** Exposure

Frequency Range(MHz)	Electric Field Strength (E)(V/m)	Magnetic Field Strength (H)(A/m)	Power Density (S) (mW/cm ²)	Averaging Time E ² , H ² or S(minute)
0.3-1.34	614	1.63	(100)*	30
1.34-30	824/f	2.19/f	(180/f ²)*	30
30-300	27.5	0.073	0.2	30
300-1500	--	--	f/1500	30
1500-100,000	--	--	1.0	30

f = frequency in MHz

*Plane-wave equivalent power density

** Uncontrolled environments are locations where there is exposure of individuals who have no knowledge or control of their exposure.

The relevant interval for time-averaging for controlled exposures is six minutes. This means, for example, that during any given six-minute period a worker could be exposed to two times the applicable power density limit for three minutes as long as he or she were not exposed at all for the preceding or following three minutes.

Turkish Telecommunication Agency has also specified maximum permissible exposure limits [4]. Table 2 shows these limit values for a represents square- root of frequency, and f is the frequency in MHz.

Table 2. Limits specified by telecommunication agency in Turkey

frequency band MHz	Limits specified by telecommunication agency			
	E (V/m)		H A/m)	
	for one device	for all devices	for one device	for all devices
0.010-0.15	22	87	1,3	5
0.15-1	22	87	0.18/a	0.73/a
1.0-10.0	22/a	87/a	0.18/a	0.73/a
10-400	7	28	0.02	0.073
400-2000	0.341a	1.375a	0.0009a	0.0037a
2000-60000	15	61	0.04	0.16

Measurement Results in Turkey

In Turkey, there has been a great increase in the number of base stations in recent years. There are several GSM companies and each of them is trying to widen its own containment area. Many base stations are being set onto the roofs of buildings. That makes people anxious about the health effects of base stations. As a result, radiation measurements are being realized quite often.

Following pictures in Fig.3 are samples of radiation measurement of some base stations in Turkey [5]. When these results are compared, it can be seen that measured values are under limits specified by the Turkish Telecommunication Agency.



Fig.3. Maximum and minimum measured values for some base stations in Istanbul.

Effects of RF Radiation

A large body of data exists on the biological effects of exposure to RF EM fields. Much of this literature describes experimental investigations with laboratory animals, tissue preparations, or cells. There are also several epidemiologic studies. Consequences of exposure to RF EM energy that have been reported in the literature at various exposure levels can be classified as follows [6], [7]:

Thermal Effects

Thermal effects are those caused by the rise in temperature produced by the energy absorbed from oscillating electric fields. The force produced by an electric field on charged objects, such as the mobile ions present in the body, causes them to move, resulting in electric currents, and the electrical resistance of the material in which the currents are flowing results in heating. This heat input causes the temperature to rise and it continues to do so until the heat input is balanced by the rate at which it is removed, mostly by blood flowing to and from other parts of the body. It is estimated that it takes several minutes from the moment RF exposure occurs for the irradiated parts of the body to reach their final equilibrium temperatures. In view of this slow response, the equilibrium temperature arising from the pulsed fields of mobile telecommunications will essentially be determined by the *average* power absorbed. There will, however, be small oscillations about that temperature at the pulse frequency or frequencies.

The relationship between the SAR (Specific Absorption Rate: quantity used to measure how much RF energy is actually absorbed in a body) and the resulting temperature rise is complex, and significantly dependent on antenna configuration, location and frequency. The most problematic feature of a temperature calculation is modelling the effect of blood flow on heat transfer.

Non-thermal effects

The energy quanta of radiation at 0.9 and 1.8 GHz equal 4 and 7 μeV , respectively (1 μeV is a millionth of an eV). Both these values are extremely small compared with the energy of around 1 eV needed to break the weakest chemical bonds in genetic molecules (DNA). As already noted, it seems impossible. Therefore, that RF radiation could damage DNA directly, which might start cells on the path to cancer. In summarising the physical basis for non-thermal effects, it is convenient to consider separately the situations near to the antenna of a mobile phone and near to a base station.

Cellular Function

The cells of living organisms naturally maintain an electrical charge across their membranes that are essential for normal functioning of human tissues. This is extremely sensitive to very weak electromagnetic fields. Radiation of unnatural frequencies can rearrange and damage molecules and alter metabolism. A process of a chain-like reaction will firstly alter the organism's electrical stability and affect cell polarisation. The resulting disharmony may eventually lead to changes in hormonal activity, affect the synthesis of genetic material, interfere with the flow of substances in and out of cells, and change the behaviour of cancer cells.

Creating Free Radicals

The basic mechanism for damage involves *free radicals*. They damage proteins and cellular membranes, injure genes and DNA, reduce levels of antioxidant hormones, such as melatonin, affect enzymatic and biochemical processes essential to normal function, and disrupt patterns of electromagnetic energy in muscles.

Promoting Histamine Release

Mast cells (which secrete histamine and other substances) are destabilised by free radicals. When exposed to radiofrequency radiation, studies have shown a doubling of histamine release.

Upsetting Calcium Levels

Radio waves and their destructive agents, the free radicals, upset calcium levels in the body, especially in the central nervous system, the brain and the heart. It is thought that calcium (and possibly magnesium) levels diminish within the cells. This affects the growth, reproduction and division of cells and the communication.

Effects On Nerve System

There is a vast literature on the effects of RF fields on isolated nerve cells (neurons), on cultured nervous tissue, on living brain slices, on brain function in experimental animals, on the blood-brain barrier and on behavioural measures of brain function. The behaviour of animals, in particular, can be a very sensitive indicator of adverse health consequences. Early signs of potential result are often behavioural rather than anatomical.

Genetic Damage

There is a large body of evidence, from a variety of studies, indicating that neither isolated nor repeated exposure to radiofrequencies and microwave radiation acts as a tumour initiator. A few studies, however, suggested that radiofrequency fields might damage DNA. There have been other recent studies that did not find genotoxic effects from RF radiation. An Expert Panel of the Royal Society of Canada stated [8] "although some investigations have suggested that RF fields may damage DNA, most studies conducted to date in this area have been negative."

Effects on Cell Membranes

The lipid bilayer membrane that surrounds cells and the internal membranes within cells are vitally important for normal cellular function. It has been concluded from a review of the World Health Organization [7] that RF fields, continuous or pulsed, can affect membrane channels, mainly at fairly high intensities, but even at levels that do not cause significant heating. There have been reports of

decreased rates of channel formation, decreased frequency of channel openings, and increased rates of rapid, burst-like firing. However, there is no clear understanding of how low intensity RF fields have such effects.

Effects on Cancer

Some studies have also examined the possibility of a link between RF and microwave exposure and cancer. Results to date have been inconclusive. While some experimental data have suggested a possible link between exposure and tumor formation in animals exposed under certain specific conditions, the results have not been independently replicated. In fact, other studies have failed to find evidence for a causal link to cancer or any related condition. Further research is underway in several laboratories to help resolve this question.

Conclusion

In making decisions about the settling of base stations, planning authorities should have the power to ensure that the RF fields to which the public will be exposed will be kept to the lowest practical levels that will be commensurate with the telecommunications system operating effectively. It is recommended that particular attention should be paid initially to the auditing of base stations near to schools and other sensitive sites.

It should be noted that mobile phones threaten our health more than base stations because mobile phones are conventionally held close to the head. Recent reports in the media, for instance, have implied that the use of mobile phones can cause memory loss, changes in attention, and variation of blood pressure.

References

- [1] Federal Communications Commission Office of Engineering & Technology, "Questions and Answers about Biological Effects and Potential Hazards of Radiofrequency Electromagnetic Fields," OET BULLETIN 56, Fourth Edition, Washington, D.C., August 1999.
- [2] IEEE Standards Coordinating Committee, "ANSI/IEEE-C95.1: IEEE Standard for Safety Levels with Respect to Human Exposure to Radio Frequency Electromagnetic Fields, 3kHz to 300GHz", Piscataway, U.S.A., 1996.
- [3] Federal Communications Commission, <http://www.fcc.gov/oet/rfsafety> .
- [4] Turkish Telecommunication Agency, <http://www.tk.gov.tr> .
- [5] L. Sevgi, "Cep Telefonları ve Baz İstasyonları Tartışmaları Üzerine," İTÜ Fen Bilimleri Enstitüsü Savunma Araştırmaları, Istanbul, Turkey.
- [6] International Commission on Non-Ionizing Radiation Protection, ICNIRP (Europe), <http://www.icnirp.de> .
- [7] World Health Organization, "Electromagnetic Fields and Public Health Cautionary Policies," http://www.who.int/peh-emf/publications/facts_press/EMF-Precaution.htm .
- [8] An Expert Panel Report prepared at the request of the Royal Society of Canada for Health, "A Review of the Potential Health Risks of Radiofrequency Fields from Wireless Telecommunication Devices," March 1999.

III-21. TWO DIMENSIONAL FINITE-ELEMENT SIMULATION OF A HIGH TEMPERATURE SUPERCONDUCTING SYNCHRONOUS GENERATOR DURING THREE-PHASE SHORT-CIRCUIT FAULT CONDITION USING FULL TRANSIENT NON-LINEAR ROTATING MACHINE MODEL

K.S. Ship, K.F. Goddard, J.K. Sykulski

University of Southampton, Electronics and Computer Science Department
Highfield, Southampton, SO17 1BJ, United Kingdom
Email: kss00r@ecs.soton.ac.uk

Abstract - This paper describes fault analysis of a 100kVA high temperature superconducting synchronous generator (HTSSG) using two dimensional (2D) finite element modelling. The 100 kVA generator dimensions are based on the actual machine under construction in the Electrical Power Engineering Research Group at University of Southampton, United Kingdom. The non-linear transient modelling was simulated taking into account the relative movement between the stator and rotor. The high temperature superconducting field windings were analysed using external circuit equations as the equivalent supply voltage and resistance.

Introduction

It is important for electrical machine designer to understand the causes of instability in a machine especially due to sudden three-phase short-circuit condition. This will provide essential stability margins and hence suitable specification of control system and protective devices can be decided upon before the machine is built. In the past most designers relied on the use of complicated equivalent circuit machine models whose parameters are difficult to obtain with good accuracy during the design stage. The finite-element method provides better facilities to model complicated geometry of electrical machines, including saturation effects in iron, thus leading to better understanding of the short-circuit phenomenon. Many researchers, in particular Turner [1], has proved that numerical analysis using finite-element method gives answer consistent with test results for various machine designs.

The short-circuit analysis is of particular importance when considering devices operating in very low temperature environment. In this case the field winding of the HTSSG is made of silver clad $(\text{BiPb})_2\text{Sr}_2\text{Ca}_2\text{Cu}_3\text{O}_x$ or better known as BSCCO tapes which operate in a temperature range 73-77 K. During fault condition, large transport currents are expected to be induced in these windings; these cause large loss densities which may lead to thermal runaway and could damage the winding.

The design reported in this paper is based around an existing stator which has 48 slots and a balanced 2-pole 3-phase winding. The stator winding is short pitched (14/24) with two parallel circuits connected in each phase. The rotor of the generator (with hybrid salient pole design) is made of 9% Nickel steel plates of various sizes and shapes. The superconducting field winding consists of ten 40-turn identical flat coils placed in between 9% Nickel steel flux diverters. The flux diverters made of 9% nickel steel are placed between the coils to reduce the normal field in the coils by diverting flux around them. The required low temperatures are provided using a purpose built closed circuit liquid cryogen cooling system with pipe-network feeding liquid cryogen to the rotor body of the generator and to the copper radiation screen. Details of the design of the HTSSG may be found in [2].

2D Transient Rotating Machine Model

The generator is modelled by a transient 2D finite-element model which includes rigid body rotation of the rotor. External circuits are linked to the 2D model to simulate the connections between the coils. The resistance of the armature winding and the end winding leakage inductance are included in the definition of the external circuits. The value of the end winding leakage inductance was estimated using a formula based on Kilgore [3]; this gave a value of 0.125 mH. The rotor is set to rotate at a fixed speed of 3000 rpm and the time-step was chosen to hide the effects of tooth ripple, which in this case are believed not to be significant. Therefore, a fixed time step of 0.417 ms was used which is equivalent to a period for the rotor to pass one stator slot. Non-linear analysis was used throughout because the saturation of the rotor core was thought to be important. For simplicity, the coils are considered as being constructed from filamentary wires such that skin and proximity effects in the turns are ignored.

The symmetry of the machine is exploited to halve the area that needs to be modelled; regions are bounded by the rotor inter-polar axis and the back of the stator core: the later was taken as flux line with $A=0$ and the former had a periodicity boundary condition with A at $180^\circ = -A$ at 0° . The model was discretised into 24496 elements in order to obtain a solution with minimal error. The simulation of this time stepping rotating machine model was carried out using available finite-element OPERA software. Figure 1 shows the extent of the models used and the mesh near the coils.

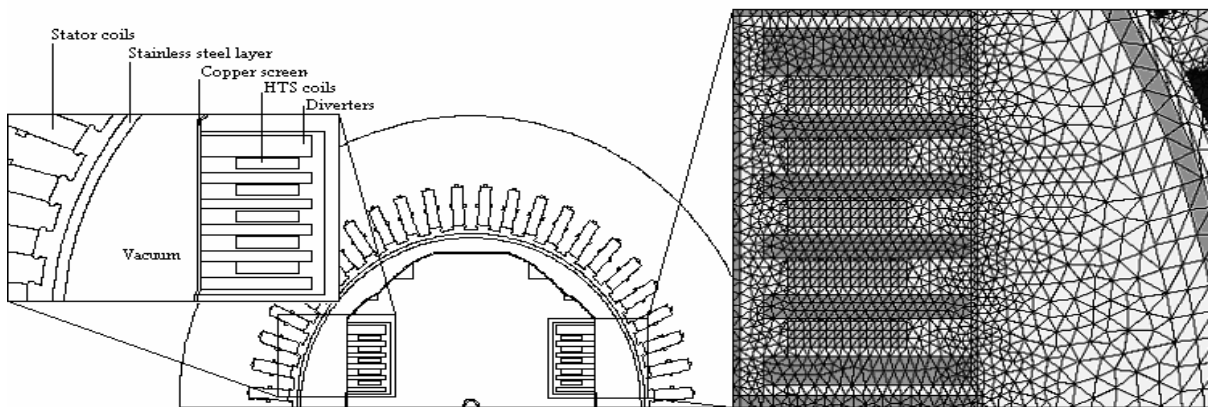


Fig. 1. 2D model of the high temperature superconducting synchronous generator.

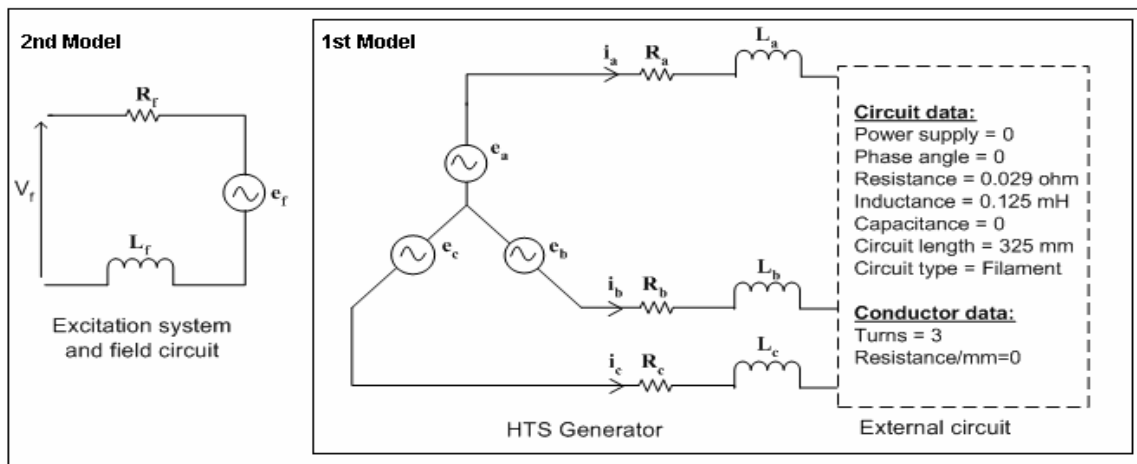


Fig. 2. The circuit arrangement for finite element modelling.

The generator was subjected to a three-phase balanced short-circuit at the terminals, starting from the no-load condition. Important parameters, such as direct axis reactances and time constants, were derived from the predicted waveforms. Finally, the use of a substantial negative field voltage to reduce the large fault currents in the field circuit was investigated.

Since it was unclear what value of resistance should be used for the field circuit, two models were produced. In the first approach, a constant value of field current was imposed by removing the field circuit from the model. In the second model, a low value of resistance (10 mΩ) was used to represent the resistance of the field circuit under normal operating conditions. Figure 2 shows the external circuit arrangement for the two models used for short-circuit analysis.

Results

The envelope of the AC component is high at the instant of short-circuit and decays ultimately to the sustained value I_S . If I_S is subtracted from the AC wave, the remainder is found to consist of two exponential components: transient component I' with long time constant, T_d' , and subtransient component I'' with short time constant, T_d'' . In addition to these AC currents, the waveforms of the stator currents each include a decaying DC component. The waveforms of the stator currents for the first and second model are shown in Figure 3 (a) and (b) respectively. In general, each short-circuit armature current waveform consists of a unidirectional or DC component and three AC components, and is given by an expression of the form

$$I_{SC} = I_{DC} e^{(-t/T_a)} + I_S \cos(\omega t + \phi_0) + I' e^{(-t/T_d')} \cos(\omega t + \phi_1) + I'' e^{(-t/T_d'')} \cos(\omega t + \phi_2) \quad (1)$$

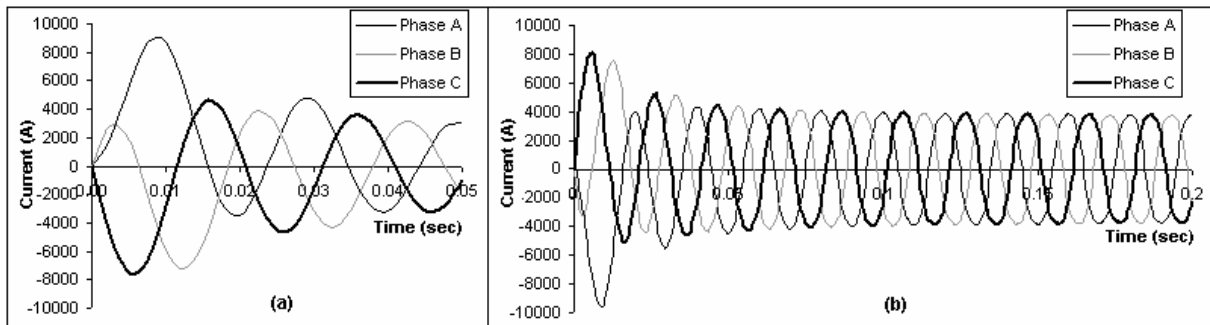


Fig. 3. Currents as a function of time for HTSSG short-circuited while running at no-load: (a) With constant value of field current and (b) With low resistance applied to the external field circuit.

The DC current components arise because, at the instant of short-circuit, the flux linking the stator windings differs from the value required to drive the sustained current. The DC components drive this additional flux, and are driven by the decay of the flux. The algebraic sum of the DC components is zero and they all decrease to zero exponentially with the same armature time constant, T_a . The transient and sub-transient currents arise from similar mechanism due to the flux trapped in the field winding and damper winding (radiation screen) respectively.

Due to the low resistance of the field circuit in the second model, the transient time constant is very long; the length of the simulation is therefore too short to give any estimate of the synchronous reactance or transient time constant. The synchronous reactance was therefore obtained by fitting the results from the first model into Equation 1 with the 3rd term removed. The difference between synchronous and transient reactances is due to eddy currents in the field circuit which are not allowed in the first model. This is due to the fact that the constant field current applied does not affect the transient term. Other parameters were obtained by curve fitting Equation 1 into the second model, and their values are shown in Table 1.

When a transient that is caused by a short-circuit, is induced into the field, a large positive fault current results. In order to investigate the voltage required to control this large current, a negative voltage was applied externally to the field winding 5 ms after fault initiation. It can be seen from Figure 4 that, with -175 V, the field fault current was successfully reduced.

Table 1. The direct reactances and time constants of the HTSSG

Reactances (p.u.)		Time Constants (sec)	
x_d	0.1191	T_d'	-
x_d'	0.0729	T_d''	0.0206
x_d''	0.0408	T_a	0.0120

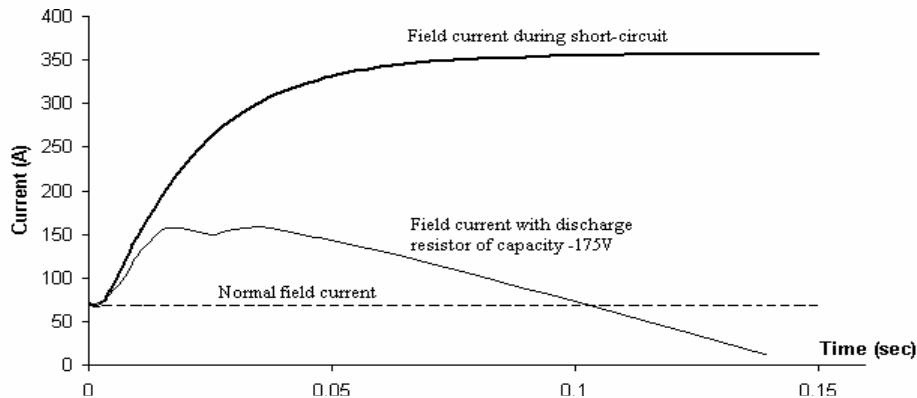


Fig. 4. The unidirectional component in the field current of the HTSSG

Conclusions

The simulation of the HTSSG during symmetrical three-phase short-circuit was successfully analysed using full transient rotating machine model. As expected the reactances were found to be of very low value compared to conventional generators. This is due to the large air gap needed to accommodate the thermal insulation. The field current during the fault condition was also analysed due to the anticipated large current that may cause damages to the superconducting field windings.

Acknowledgement

The development of the high-temperature superconducting rotor at the University of Southampton is sponsored by Engineering and Physical Science Research Council (United Kingdom) under research grant GR/N21253/01.

References

- [1] P. J. Turner, Finite-element simulation of turbine-generator terminal faults and application to machine parameter prediction, IEEE Transactions on Energy Conversion, vol. EC-2, no. 1, pp. 122-131, 1987
- [2] M. K. Al-Mosawi, C. Beduz, K. F. Goddard, J. K. Sykulski, Y. Yang, B. Xu, K. S. Ship, R. Stoll, and N. G. Stephen, 100kVA high temperature superconducting generator, Paper presented at Nineteenth International Cryogenic Engineering Conference, Genoble, France, July 2002.
- [3] L. A. Kilgore, Calculation of synchronous machine constants, AIEE Trans., vol. 50, pp. 1201-1214, 1932

III-22. COUPLED ELECTROMAGNETIC FIELDS AND TEMPERATURE FIELDS TO ANALYZE THE VOLTAGE FLUCTUATION OF A SYNCHRONOUS GENERATOR WITH THE CONSIDERATION OF INSULATION LAYERS

Li Weili*, Zhou Feng, Zhang Dong, Hou Yunpeng, Ding Shuye

College of Electrical and Electronic Engineering, P.O. Box 224, East Campus, Harbin University of Science and Technology, Harbin 150040, P.R China, Li.Weili@yeah.net.

Abstract – In this paper, electromagnetic fields and temperature fields of a synchronous generator with fractional stator slot are calculated. As a result, temperature distribution in this generator is obtained. When the terminal voltage fluctuate from +10% to -10%, the distribution of electromagnetic fields and temperature fields are analyzed. During the course of fields' calculation, the effect of strands insulation and turns insulation to the coupled fields is discussed. Longyang Gorge 320MW hydro generator is taken for example to test the accuracy of calculation.

Introduction

With the increasing of the single capability of synchronous generator, the problems of heat and ventilation are more and more cared by designers. Through Analyzing by coupled fields' method for synchronous generator, the more accurate distribution of temperature can be obtained. In 1999, the coupled field problems from the angles of weak-coupled problem and strong-coupled problem as well as common arithmetics for the two problems are expatiated by Kay Hameyer and other scholars [1]. In 2000, the maximum temperature point in the slot of an induction machine is calculated by coupling electromagnetic fields and temperature fields by Eric Chauveau and other scholars [2].

Because insulation layers in strands and turns are very thin, they are always be out of consideration when calculating electromagnetic field. However, the whole areas of stator strands insulation may exceed that of one piece of strand and it will have certain of effect on the calculation precision, it is the same for the turn's insulation. Therefore, calculation of the airgap magnetic field and rotor surface losses and comparison of the calculated result with and without the consideration of the stator strands insulation and rotor turns insulation will have reference significance for designing machine accurately [3]. In addition, the insulation layers are always ignored in the calculation and analyze of synchronous generator. However even a thin insulation layer may have a significant temperature drop and this will have a direct effect on the machine design. In 2001, small transition layers with a significant temperature drop were discussed and the mathematic model of thermal contact resistances and insulation layers were given by Johan Driesen and other scholars [4]. In 2002, electromagnetic fields and temperature fields of large salient synchronous generator are calculated with the consideration of turn's insulation layers from the angle of weak coupled problem [5].

The terminal voltage of generator should agree with that of electrify networks and an error from +10% to -10% is permitted. When the Voltage fluctuate from +10% to -10%, the distribution of electromagnetic fields and temperature fields are analyzed from the angle of weak-coupled problem. During the course of fields' calculation, the effect of strands insulation and turns insulation to the coupled fields is discussed. Longyang Gorge 320MW hydro generator (Fig. 1) is taken for example to test the accuracy of calculation.

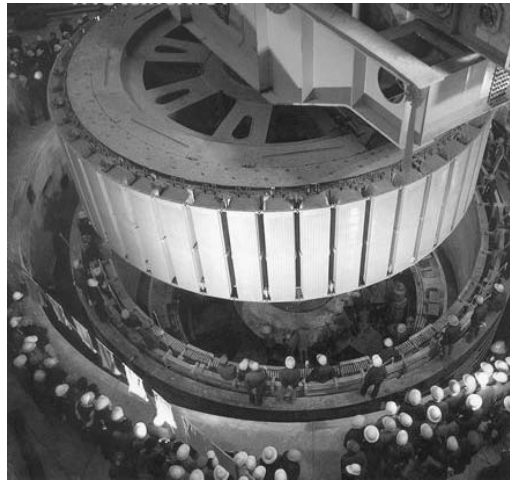


Fig.1. Longyang Gorge 320MW hydro generator

According to Maxwell's laws, magnetic vector potential is applied to solve the electromagnetic fields problem.

$$\nabla \times \mathbf{H} = \mathbf{J} \quad (1)$$

$$\nabla \times \mathbf{E} = -\frac{\partial \mathbf{B}}{\partial t} \quad (2)$$

$$\nabla \cdot \mathbf{B} = 0 \quad (3)$$

From (3), magnetic vector potential \mathbf{A} is

$$\mathbf{B} = \nabla \times \mathbf{A} \quad (4)$$

Form above equations, we can derive the equation as follows:

$$\nabla \times \nabla (\nabla \times \mathbf{A}) = \mathbf{J} \quad (5)$$

We can write the equation (5) as

$$\frac{\partial}{\partial x} \left(\nu \frac{\partial \mathbf{A}}{\partial x} \right) + \frac{\partial}{\partial y} \left(\nu \frac{\partial \mathbf{A}}{\partial y} \right) = -\mathbf{J} \quad (6)$$

Tab.1 Rated specifications of the machine

Characteristic	Value
Rated voltage	15750V
Rated current	13035A
Rated power	320000kW
Rated speed	125rpm
Rated power factor	0.9
Rated field winding current	1584.2A

Table 1 shows rated value of Longyang Gorge 320 MW hydro generator, which is the studied generator in this paper.

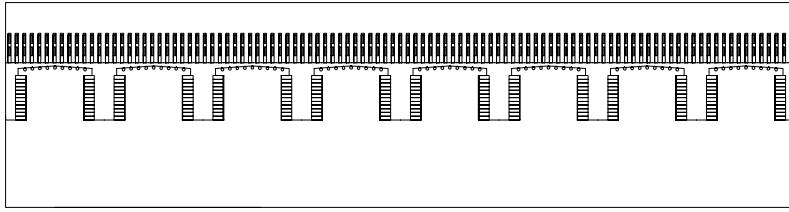


Fig.2. Solved region of 2D electromagnetic fields

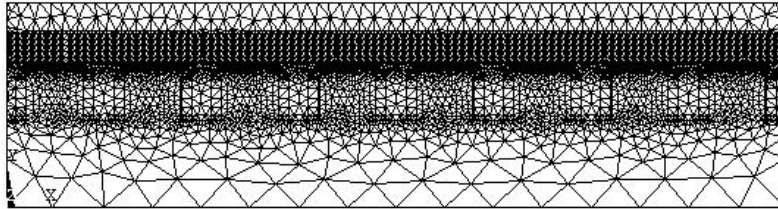


Fig.3. Mesh grid

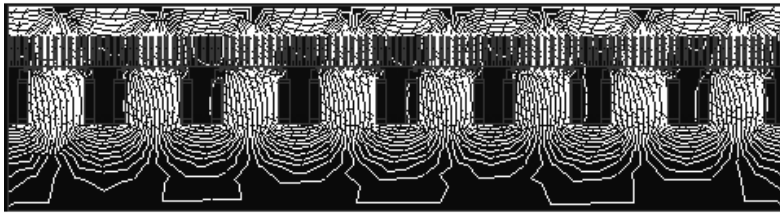


Fig.4. Isopotential line with the consideration of strands insulation and turns insulation when the terminal voltage don't fluctuate



Fig.5. Isopotential line with the consideration of strands insulation and turns insulation when the terminal voltage fluctuate +10%

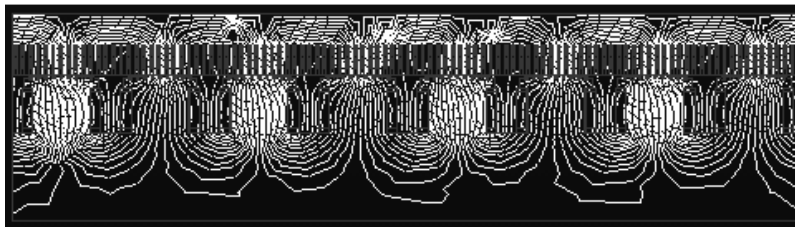


Fig.6. Isopotential line with the consideration of strands insulation and turns insulation when the terminal voltage fluctuate -10%

Fig. 2 and Fig. 3 are the solved region and mesh of Longyang Gorge 320 MW hydro generator respectively. Fig. 4, Fig. 5 and Fig. 6 are isopotential line under three conditions respectively.

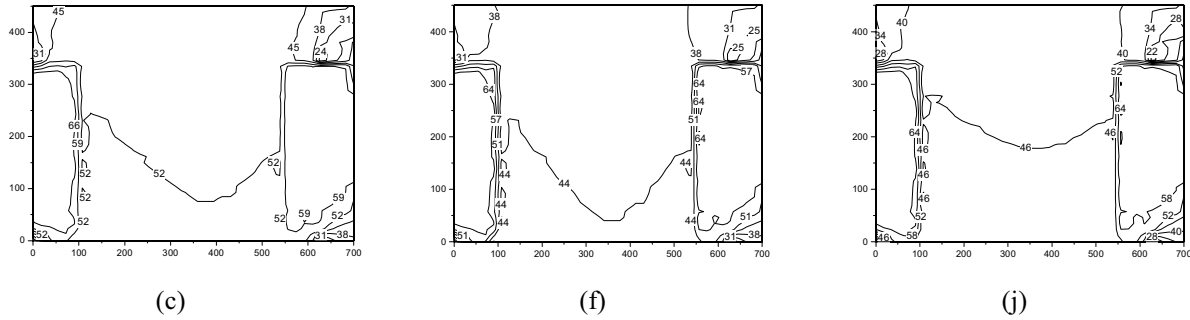


Fig.7. Comparison of temperature distribution along the axial direction of rotor with the consideration of strands insulation and turns insulation under three conditions (Figure (a) (b)(c) are temperature distribution along the axial direction of rotor under the condition of 1*; figure (d) (e)(f) are temperature distribution along the axial direction of rotor under the condition of 2*; figure (h)(i)(j) are temperature distribution along the axial direction of rotor under the condition of 3*)

Note: 1*: The terminal voltage do not fluctuate; 2*: The terminal voltage fluctuate +10%; 3*: The terminal voltage fluctuate -10%.

Fig. 6 is the solved region of 3D temperature fields and Fig. 7 is the comparison of temperature distribution along the axial direction of rotor under three conditions.

Results and Discussion

Tab.2. Comparison of temperature under three conditions

		Temperature when the terminal voltage doesn't fluctuate. (°C)	Temperature when the terminal voltage fluctuates +10%. (°C)	Temperature when the terminal voltage fluctuate -10%. (°C)
The field winding at the leeward side	The maximum temperature	70.00	67.60	68.45
	The minimum temperature	65.66	57.41	57.98
	The average temperature	68.67	66.30	67.16
The field winding at the windward side	The maximum temperature	62.72	60.61	61.36
	The minimum temperature	58.28	54.53	55.06
	The average temperature	61.29	59.24	59.98

Table 2 shows the comparison of temperature under three conditions. The measured results of the rotor winding of Longyang Gorge 320MW hydro generator is 56.6°C, which agree with the calculation results. Shown as the distribution of temperature under the three conditions, temperature when the terminal voltage do not fluctuate is higher than the other two conditions and the average temperature differences are 1.3~1.5 °C and 2.1~2.4 °C. The effect of voltage-fluctuate to the distribution of electromagnetic fields and temperature fields is little. Temperature of rotor from the end section to the middle section increase, which agree with the practical engineering condition. Therefore, the ventilation condition in the middle section should be improved to decrease the local temperature of rotor.

Conclusion

In this paper electromagnetic fields and temperature fields of a synchronous generator under three conditions from the angle of weak-coupled problem are calculated and the comparison the three conditions are listed and discussed. Longyang Gorge 320MW hydro generator is taken for example to test the accuracy of calculation.

References

- [1] Kay Hameyer, Johan Driesen, Herbert De Gersem, and Ronnie Belmans, The Classification of Coupled Field Problems, IEEE Transactions on Magnetics, Vol.35, pp 1618-1621, 1999
- [2] Eric Chauveau, El Hadi Zaïm, Didier Trichet, and Javad Fluladgar, A Statistical Approach of Temperature Calculation in Electrical Machines, IEEE Transactions on Magnetics, Vol.36, pp 1826-1829, 2000
- [3] Bai Yannian, Design and Calculation of Hydro Generator, Beijing: Mechanical Industry Press, 1982
- [4] Johan Driesen, Ronnie J.M.Belmans, Kay Hameyer, Finite-Element Modeling of Thermal Contact Resistances and Insulation Layers in Electrical Machines, IEEE Transactions on Industry Applications, Vol.37, pp 15-20, 2001
- [5] Zhang Dong, Li Weili, Zhou Feng, Hou Yunpeng, Numerical Calculation of Air Gap Magnetic Field of a Salient Synchronous Generator with the Consideration of the Effect of Turn Insulation, PowerCon 2002, pp 774-778, 2002
- [6] Kong Xiangqian, Applying of Finite Element Method in Heat Transfer, Beijing: Science Press, 1986

III-23. MAGNETIC DIAGNOSIS OF STRUCTURAL MATERIALS AND THESE MONTE-CARLO SIMULATIONS

K. Yamada, B. Liu, A. Shinagawa, Z. Honda, Y. Isobe¹, K. Yamaguchi² and A. Krawczyk³

Dept. of Functional Materials Sciences, Saitama University, 338-8570 Saitama, Japan,

yamasan@fms.saitama-u.ac.jp

¹Nuclear Fuel Ind., Kumatori-cho, Sen-nan-gun, 590-0481 Osaka, Japan, isobe@nfi.co.jp

²Dept. Education, Fukushima University, 960-1296 Fukushima, Japan, yama@educ.fukushima-u.ac.jp

³Electrotechnical Institute, Pożaryskiego 28, 04-703 Warszawa, Poland, krawczyk@iel.waw.pl

Abstract- Many magnetic techniques were developed for nondestructive evaluations for iron-based materials such as SUS304, A533B, S25C etc in a tensile stress range up to each fracture state. Magnetic tools are composed of a triple-fold coil for ac resistivity detections, a small Hall element for leakage flux observations after polarizations of the material and a pickup coil of magnetic Barkhausen noises combined with the excitation yoke. The degree of degradations was expressed by an average field for the discontinuous magnetization. Magnetic noises were simulated by Monte-Carlo method under the non-equilibrium condition with limited trials.

1. INTRODUCTION

Nowadays, nondestructive evaluations (NDE) of iron-based structural materials are of great importance for modern societies. However, NDE of the gigantic plants are not always performed by experienced specialists, and are mostly performed with high costs. We propose in this study the technologies with easy manipulations for inspectors by using electromagnetic tools. The presented approach consists of three different methods as follows. (1) Observation of ac resistivity by using a triple-fold coil [1,2]. The probe coil is integrated with an exciter coil and two equivalent receiver coils in a concentric configuration. This method exhibited the advantages of resistivity measurements without direct contacts to rusty samples and also the fixed configuration of the pick-up coils and the exciter coil. (2) Leakage flux measurements using a small size Hall element [3,4] after an adequate polarization for each material. The leakage flux distribution of the normal component to the surface reflects the inhomogeneous distribution of the material constants such as permeability or geometrical thickness. The local material degradations as a function of positions are well detected by the numerical derivations of the leakage flux distribution. (3) The observation of magnetic Barkhausen noises (MBN) with a pick-up coil [5,6] located in between exciting yokes. The MBN, in general, reflects the degree of the degradations via the lattice defects or via the pinning forces against the magnetic domain wall shifts. The signals of MBN are processed to derive an average field ($\langle H_D \rangle$) for the discontinuous magnetization to avoid the unstable amplitude measurements.

Our magnetic tools listed above are combined to judge the degradations as a function of positions. Especially the index ($\langle H_D \rangle$) was found an excellent parameter for exhibiting the degree of the local residual strains in addition to these anisotropic behaviors. Further, the theoretical simulations of 3-D moment arrays of 50x50x50 using Monte-Carlo method was performed for comparisons with the experimentally obtained MBN. We attained very close behaviors of our simulation as a function of applied magnetic fields at different temperatures. For the real evidences of degradations, we measured the residual strains by XRD using the relationship between the internal pressure in the material and the average inter-atomic distances. Therefore, the presented investigations are mainly based on the comparisons between complex phenomenological data and the residual stresses obtained by the thickness deformations or by the direct observations of XRD measurements. The overall judgments of degradations could be performed relatively by comparing the original calibrations of many parameters with those of fatigued samples and by the multilateral comparisons.

2 .EXPERIMENTALS

The samples of A533B, SUS304 and SUS316 were prepared in the typical shapes of 30x120x2^t mm or 60x165x5^t mm as shown in Fig.1. Static or repetitive tensile stresses were applied up to each fracture states along the sample elongating directions. The sample preparations before the stress applications are listed in the reference [6].

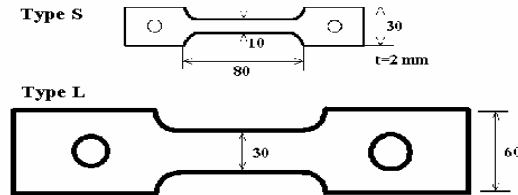


Fig.1. Sample shapes in this experiment

We performed ac resistivity measurements by using a triple-fold coil as shown in Fig. 2. Here the electromagnetic waves (EMW) were excited by the central coil (C_E) and received by the both side coils (C_1 and C_2) arranged in the symmetric positions. The output voltages of the two coils of C_1 and C_2 were connected in series and reversed to cancel the generated electromotive force (e.m.f.) each other when no sample is attached. In case of a sample is attached to one side, e.g. C_1 as in Fig. 2, output voltage ($V_0=V_{A_1-B_1}$) is generated.

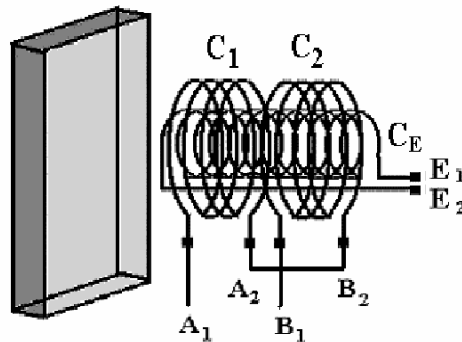


Fig.2. The experimental set-up of triple coil for ac resistivity measurement

For the more precise measurements, the signals deviated from a reference sample are obtainable to attach the reference sample to the side C_2 . The signals were sensitively obtained by using a Lock-in amplifier with the reference signal from the exciter. Fig. 3 shows some experimental results for the several materials of 1 mm thickness with an operating frequency at $f=10$ kHz and 100 kHz. The output voltages decreased with increasing resistivities of the materials. Here, it is worthwhile to note that the ferromagnetic materials like as Fe show anomalous responses deviated from those nonmagnetic materials. The physical mechanism will be discussed later. Fig 4 shows the results for a SUS304 samples with 1 mm and 25mm thickness, respectively with the residual strains of 0, 20 and 40 % given by static tensile stresses up to 740Mpa. In this experiment, a reference sample without strain was attached at C_2 side. As shown in this figure, V_0 increased with increasing frequencies up to 100kHz.

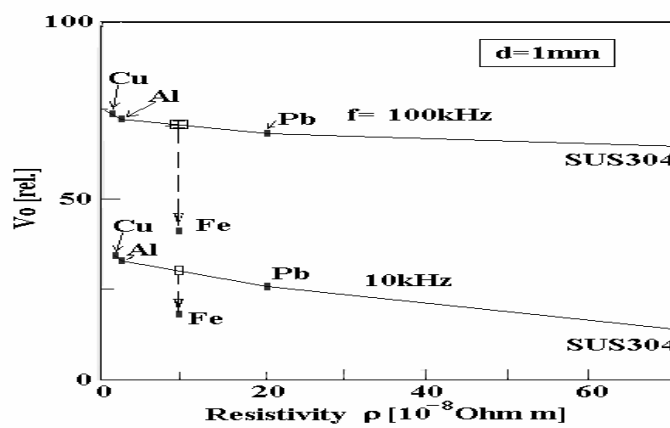


Fig.3. Pick-up voltages vs. resistivities observed for different materials

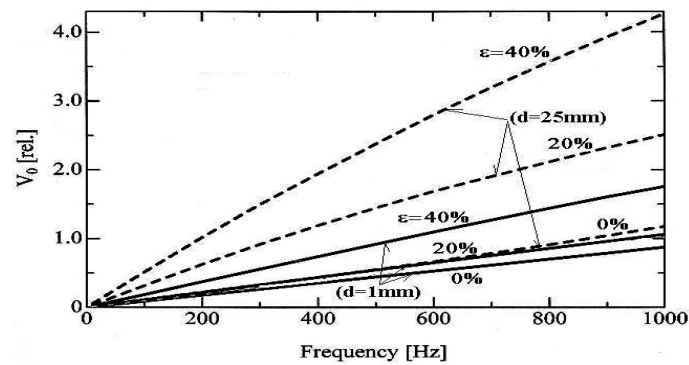


Fig.4. Pick-up coil vs. frequencies up to 1000Hz for differently strained SUS304 samples

However, the output voltages as a function of resistivities or strains for the samples with larger degradations are reversed against those in the characteristics as shown in Fig.3. In this case, the negative amplitudes increased with increasing resistivities of the samples in comparison with the reference sample, because the output voltages were obtained by subtracting those from the reference sample.

The experiment of the leakage flux observations was performed by using the experimental setup as shown in Fig.5. Here, we used a Hall sensor of $120 \times 120 \mu\text{m}^2$ with a lift-off distance of about $200 \mu\text{m}$ from the sample surface. The leakage fluxes were measured after an intentional polarization in $B=1\text{kOe}$ ($=0.1\text{T}$) to avoid any spurious polarizations by tools or electric machines. We observed densely over the sample surface by every 0.1mm of 500 points along the elongation direction ($=x$ direction) times 250 points in y direction. For high quality measurements available down to 1mOe ($=10^{-7}\text{T}$), the output voltages were amplified by a Lock-in amplifier operated at $f=20\text{kHz}$ as the optimum condition for the Hall element of GaAs. Fig.5 (a),(b) show the experimental results for an A533B sample with a tensile stress of 480MPa . Here, Fig.5(a) shows the leakage flux distribution $BZ(x,y)$ colored in black(-) and white (+), Fig.5(b), $\text{dBZ}(x,y)/\text{dx}$, respectively. The absolute values of the leakage flux intensities are large at the both ends (very black:S-pole, vice versa). It varies rapidly at the positions where the thickness deformations strongly occur. The location of Lüders band ("L") well coincided with the positions in white color of the distribution of $\text{dBZ}(x,y)/\text{dx}$.

We performed the experiments of MBN by using the device as shown in Fig.6, where the diameter of the pick-up coil is about 1mm . We applied magnetic fields up to 16kA/m (0.02T) in a constant increasing rate of 200kA/ms , at which field sweeping condition the maximum information of the magnetic domain wall shifts were obtained. This fact was examined by the 2-D fractal dimensions of the time dependent MBN signals [7]. The important notices for this device are that the pick-up coil must locate at an off-center position in between the magnetic

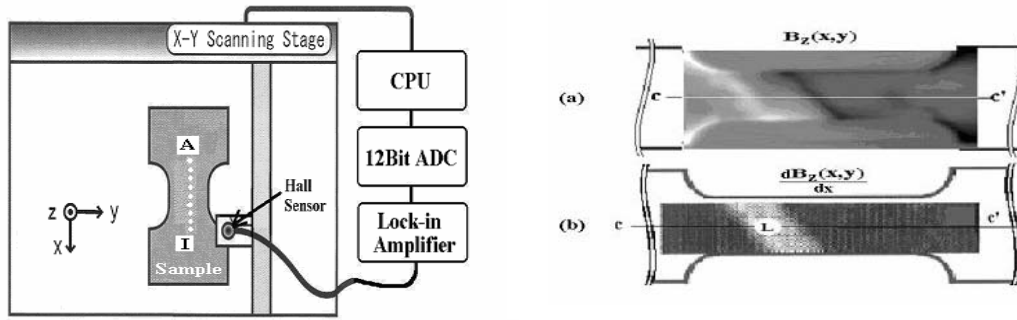


Fig. 5. The experimental setup for leakage flux observation and the examples of the observations (a) Leakage flux distribution $[B_z(x,y)]$, (b) the first derivative along positions $[dB_z(x,y)/dx]$.

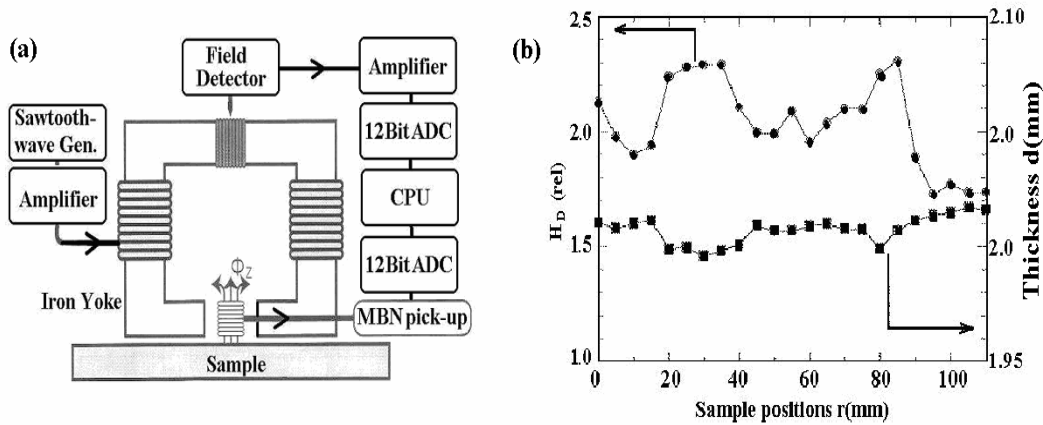


Fig. 6(a) Experimental setup for MBN measurement and (b) an example of the measurements for an A533B sample with a tensile stress of 540MPa

yokes and that the observations must be performed after several cycles of field sweeps by which the magnetic domain distribution are initialized to avoid the minor loop. For an example, Fig.6 (b) shows the processed index $\langle H_D \rangle$ of MBN as a function of positions defined [8] by

$$\langle H_D(\mathbf{R}, \theta) \rangle \equiv \frac{\int_0^{t_{\max}} H_{\text{int}}(t) V(x, y, h, \theta, t) dt}{\int_0^{t_{\max}} V(x, y, h, \theta, t) dt} \tag{1}$$

$$\cong \frac{\sum_{k=1}^N H_{\text{int } k} \cdot B_k}{\sum_{k=1}^N B_k} \tag{2}$$

Here, $V(x,y,\theta,h,t)$ denotes the pick-up voltage at a position $\mathbf{R}(x,y,h)$ with a lift-off distance h , with an observation angle of yoke tilted by θ against x -direction at time t . $H_{\text{int}}(t)$, an internal magnetic field at a time $t=t_k$ ($k=1,2,3, \dots, N$) in the pick-up coil, respectively. Here, $V(x,y,\theta,h,t)$ is a rapidly varying function of h and the time dependent part behaves like as the sequential delta-functions with different amplitudes [8]. Therefore, the k 'th signal of fields ($H_{\text{int } k}$) and the magnetic flux density (B_k) are countable to calculate the summation as in Eq.(2). As shown in Fig.6 (b), $\langle H_D \rangle$ behaves just reciprocally with thickness deformation change. It is also important to note that the pick-up voltages become larger when the pickup coil is closer to the surface. However, both the denominator and nominator in Eq.(1) increase simultaneously so that the derived index $\langle H_D \rangle$ was unchanged. Therefore, $\langle H_D \rangle$ is sensitive only to the distribution of MBN along with the applied field strength.

3. DISCUSSIONS

As we have shown in the former sections, the leakage flux distribution patterns reflects the inhomogeneous distributions of the material constants such as residual strains and/or lattice voids in addition to the apparent sample thickness change at each point. Here in discussions, we show briefly the physical mechanisms of the detected phenomena in each experiment. First of all, the output voltages in the triple-fold pick-up coils in Fig. 2 are generally explained by the time dependent flux changes (dB/dt), and the electromotive force (EMF) (V_H) in the coil C_1 and C_2 . When the sample is attached to C_1 , the effective EMF for the two coil become different due to the magnetic material is close to C_1 . Therefore the flux Φ inside of C_1 become modulated by the reflected fields from the material so that the unbalance EMF of $V_0=V_{C1}-V_{C2}$ occurs. As a magnetic circuit, the flux through the coil is given by the permeability $\mu(\ell)$ and the cross section $S(\ell)$ along the magnetic path ℓ in C_1 as expressed in Eq. (3). Here V_m is electro-magnetic force by the exciter coil. V_0 is given rise by the difference of $\mu(\ell)$ along of each coil. The voltage is, therefore, determined by the skin depth of the material as a function of permeability, thickness, resistivity and frequency.

$$\Phi_l = \frac{V_m}{\oint \frac{d\ell}{\mu(\ell)S(\ell)}} = \int_{C_1} \phi(x, y) \cdot dS$$

(3)

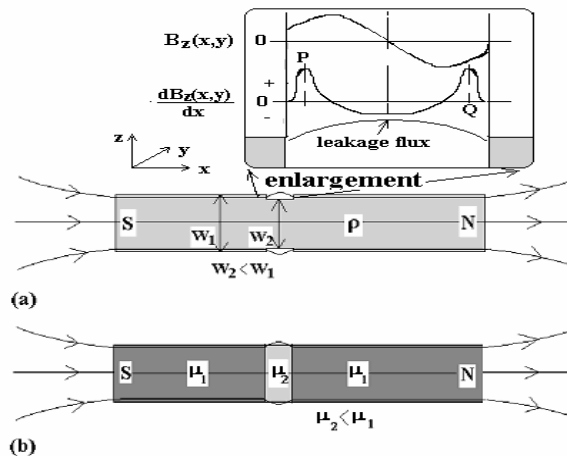


Fig. 7. The physical model of the leakage flux from sample surface

Secondly, we can show the physical origins of the leakage flux from the surface as shown in Fig. 7(a) and its enlargement. Namely, by the cross section decrease at a central position with a thickness $w_2 < w_1$, the leakage flux inevitably occurs and the $dB_z(x,y)/dx$ exhibit two peaks. In between the peaks, the degradations should be found due to the smaller value of μS in Eq.(3) and the situation is the same as that the permeability decrease as $\mu_1 > \mu_2$ at the center as shown in Fig.7(b). It is very plausible to consider the smaller permeability of the sample with increasing degradations. MBN are simulated by using Monte-Carlo simulations for 3-D spin arrays up to $50 \times 50 \times 50$ in the thermal equilibrium of a temperature T with various spin voids [9]. The Hamiltonian is simply composed of spin exchange interactions of $-J s_i \cdot s_j$ between the first nearest neighbor i th and j th spins, respectively with an exchange constant J . We consider the thermal equilibrium of spin system by comparing the lowest total energy, E of the system and the Boltzmann factor of $\exp(-E/k_B T)$. The non-equilibrium and ballistic behaviors of MBN were realized by stopping trials before the thermal equilibrium is obtained with the lowest energy. Fig.8(a) shows a result of the simulations for the spin array magnetizations for different array numbers vs. temperature. Fig. 8(b) shows MBN at the two temperatures of RT and 77K, respectively during a linearly increasing field sweep. These behaviors of MBN are quite similar with those obtained in our experiments.

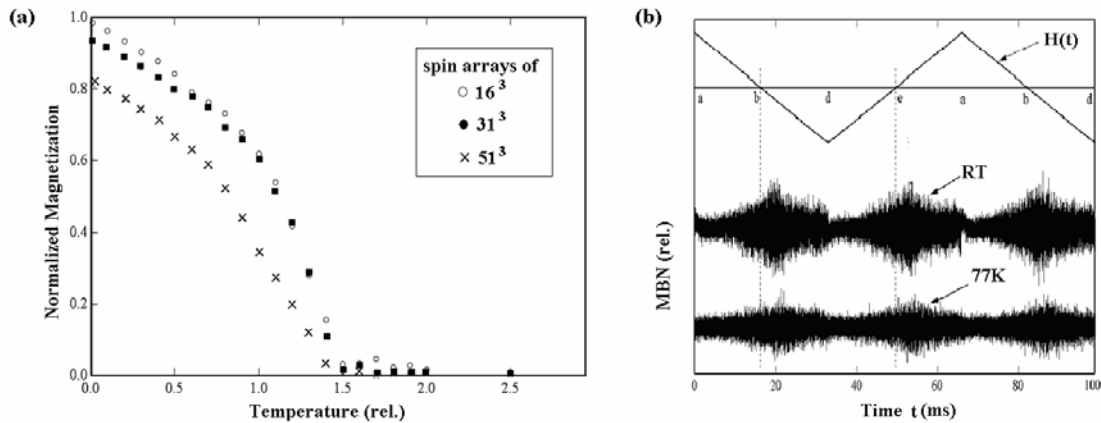


Fig. 8. Simulations of magnetizations as a function of temperature with different array numbers (a), and the MBN at $T=RT$, 77K as a function of time (b).

4. CONCLUSIONS

The experiments in this paper look successful for the aim of NDE. However, the phenomena are given rise by many parameter changes and also by the spatial inhomogeneities. Therefore, the calibrations of each material are indispensable before the real use in industries because each structural material was prepared characteristically for its own purpose and shows different behavior deviated from any standard properties.

References

- [1] M. Takanashi, Master Thesis of Grad. School of Saitama University, May 2001, in Japanese
- [2] M. Takanashi and K. Yamada, Proc. Int. Conf. Mechatronics and Information Techn. (ICMIT'01), Yamaguchi, Japan, Dec. 2001, pp292-297
- [3] K. Yamada, K. Yamaguchi, H. Takeda, S. Tonooka, T. Masuda and N. Hagiwara, "Nondestructive cross evaluations iron-based material by optical and magnetic diagnosis tools", Invited paper for 3rd Int. Workshop on Advanced Mechatronics (IWAM'99), Chunchon, Korea, Dec. (1999), pp1-6
- [4] K. Yamada, K. Yamaguchi et al., "Sensitive NDE of Stainless Steels by Magnetic Sensor", Trans. Mat. Res. Jpn., 25[2]481-486 (2001)
- [5] D.C. Jiles, Review of magnetic methods for NDE, NDT Int. 21,5(1988)pp311-319
- [6] K. Yamada, K. Yamaguchi et al. "Magnetic and Optical NDE for Iron-based Materials", Nondestructive Characterization of Material X, ed. By Green, pp333-340, Elsevier Publ.
- [7] K. Yamada and T. Saitoh, "Observation of Barkhausen effect in ferromagnetic amorphous ribbon by sensitive pulsed magnetometer", J. Mag. Magn. Mater. Vol. 104 (1991), p341-343
- [8] S. Shoji, Doctor Thesis (in Japanese), Saitama Univ., March (1999)
- [9] K. Yamaguchi, K. Yamada et al. Physica (to be published)